MASARYK UNIVERSITY

FACULTY OF SCIENCE

DEPARTMENT OF EXPERIMENTAL BIOLOGY

Novel molecular approaches to overcome therapy resistance in pediatric solid tumors

HABILITATION THESIS

Jan Škoda

MUNI
SCI

BRNO 2024

ACKNOWLEDGEMENTS

CONTENT

ABBREVIATIONS

ABC	ATP-binding cassette
ABCG2	ATP-binding cassette subfamily G member 2
ALK	Anaplastic lymphoma kinase
BAK	BCL-2 antagonist/killer
BAX	BCL-2-associated X protein
BCL-2	B-cell lymphoma 2
BimBH3	Death-activating BH3 domain peptide of BIM
CD	Cluster of differentiation
CHK1	Checkpoint kinase 1
CHK2	Checkpoint kinase 2
c-MYC	MYC proto-oncogene protein
COMBAT	Combined oral maintenance, biodifferentiating, antiangiogenic therapy
COX-2	Cyclooxygenase-2
CSC	Cancer stem cell
CXCR-4	C-X-C chemokine receptor type 4
DFO	Deferoxamine
Dp44mT	Di-2-pyridylketone-4,4-dimethyl-3-thiosemicarbazone
DpC	Di-2-pyridylketone-4-cyclohexyl-4-methyl-3-thiosemicarbazone
DRP1	Dynamin-related protein 1
DSB	Double strand break
E/M	Epithelial-mesenchymal
eIF2α	Eukaryotic translation initiation factor 2 alpha
EMT	Epithelial-mesenchymal transition
ER	Endoplasmic reticulum
ESC	Embryonic stem cell
GPX4	Glutathione peroxidase 4
IHC	Immunohistochemistry
INF2	Inverted formin 2
IP3R	Inositol 1,4,5-trisphosphate receptor
iPSCs	Induced pluripotent stem cells
ISR	Integrated stress response
MAM	Mitochondria-associated ER membrane
MCU	Mitochondrial calcium uniporter
MDM2	Mouse double minute 2 homolog
MDM4	Mouse double minute 4 homolog
MDR	Multidrug resistance
MGMT	O6-methylguanine DNA methyltransferase
MMR	Mismatch repair
MOMP	OMM permeabilization
mPTP	Mitochondrial permeability transition pore
MSC	Mesenchymal stem cell

MYC	Proteins c-MYC and N-MYC
MYC	MYC proto-oncogene
MYCN	MYCN proto-oncogene
NANOG	Nanog homeobox
NCC	Neural crest cell
NDRG1	N-MYC downstream regulated gene-1
N-MYC	MYCN proto-oncogene protein
NOD/SCID	Nonobese diabetic/severe combined immunodeficiency
NSG	NOD/SCID gamma
OCT4	Octamer-binding transcription factor 4
OMM	Outer mitochondrial membrane
PDX	Patient-derived xenograft
PHOX2B	Paired-like homeobox 2b
ROS	Reactive oxygen species
RTK	Receptor tyrosine kinase
SCP	Schwann cell precursor
scRNA-seq	Single-cell RNA sequencing
SERCA	Sarco/endoplasmic reticulum Ca2+-ATPase
SHH	Sonic Hedgehog
SIGLEC	Sialic acid-binding Ig-like lectin 10
SOX2	Sex-determining region y-box 2
tBid	Truncated BID
TFR1	Transferrin receptor-1
TKI	Tyrosine kinase inhibitor
TME	Tumor microenvironment
TOP2	Topoisomerase II
γ-H2AX	Phosphorylated histone H2AX

COMMENTARY

This habilitation thesis presents a compilation of selected scientific publications to which I contributed as a first, corresponding, or co-author. These works align with my long-term interest in pediatric cancer research with a major focus on the most aggressive solid tumors, including neuroblastoma and pediatric sarcomas.

Cancer remains the leading cause of death from disease in children. Although solid tumors represent only one-third of childhood malignancies, they account for about two-thirds of pediatric cancer deaths. This may be attributed to the limited insight into the complex nature and developmental origins of these relatively rare tumors, which hinders development of effective therapies. Therapy failure due to the multidrug resistant disease has generally been linked to the acquisition of a poorly differentiated, cancer stem cell (CSC) phenotype. This thesis summarizes the current understanding of CSC biology and the mechanisms driving therapy resistance in pediatric solid tumors, outlining recent advances in developing novel approaches for the treatment of aggressive tumors.

The first part of the thesis focuses on molecular determinants of CSCs and discusses their role in therapy resistance in pediatric solid tumors. Particular attention is given to pediatric sarcomas. Our studies on these tumor types have provided important insights into the molecular regulators of sarcoma stemness and identified previously unrecognized subcellular localizations of stemness-associated molecules, with important implications for cell physiology and/or potential clinical utility. Importantly, the key original findings (i) reveal that the transcription factor SOX2 is a crucial functionally relevant marker of CSCs across pediatric sarcomas and (ii) provide the first evidence that mesenchymal tumors may fine-tune their CSC traits by attaining a highly plastic, hybrid epithelial-mesenchymal phenotype, suggesting new targets for potential therapeutic interventions.

The second part of the thesis examines some of the current approaches for identifying novel strategies and therapeutic targets to overcome resistance in high-risk pediatric solid tumors. First, we showed in multiple pediatric tumor types that novel

iron-chelating agents exert context-dependent synergistic interactions with standard chemotherapy or molecularly targeted drugs, uncovering new mechanisms that provide an avenue for precision medicine-guided combination therapies. Second, we identified a novel mechanism of neuroblastoma multidrug resistance that is mediated by attenuated apoptotic signaling due to reduced connectivity between mitochondrial and endoplasmic reticulum membranes. Importantly, we demonstrated that this resistance is induced by both small molecule inhibitors and standard chemotherapy, but it is efficiently overcome by inhibiting mitochondrial translation with bacterial ribosome-targeting antibiotics. This study revealed mitochondrial ribosomes as a novel synthetic lethality target, potently downregulating MYC proteins and inducing cell death in MYC-driven neuroblastoma via mitochondrial stress-activated integrated stress response. Our findings pave the way for developing selective mitochondria-targeted therapies and highlight the potential of repurposing ribosomal antibiotics in the treatment of refractory *MYCN/MYC*-amplified neuroblastoma. Finally, we uncovered an antiproliferative role of serotonin signaling in aggressive neuroblastoma cells with stem-like traits, which aligned with its regulatory function in sympathoadrenal progenitors during adrenal gland development. By validating the biological relevance of a candidate protein inferred from developmental trajectories, this study serves as proof of concept for future single-cell transcriptomics-guided discovery of novel therapeutic targets in neuroblastoma.

Publications listed below represent selected peer-reviewed articles highlighting my contributions to the topic of this thesis. They comprise 15 original research articles and three reviews. I served as the first and/or corresponding author on ten of these papers, with the majority (eight) published in Q1 journals. My contribution to each work is detailed in the tables below. Respective manuscripts are attached as correspondingly numbered Appendixes and are highlighted in green in the main text for clarity.

[1] Pleskač P, Fargeas CA, Veselska R, Corbeil D, **Skoda J***. Emerging roles of prominin-1 (CD133) in the dynamics of plasma membrane architecture and cell signaling pathways in health and disease. *Cellular & Molecular Biology Letters*. 2024;29:41. (JCR 2023, IF = 9.2; Q1 - Cell Biology)

Experimental work (%)	Supervision (%)	Manuscript (%)	Research direction (%)
NA, review	80	30	75

[2] Borankova K, Krchniakova M, Leck LYW, Kubistova A, Neradil J, Jansson PJ, Hogarty MD, **Skoda J***. Mitoribosomal synthetic lethality overcomes multidrug resistance in MYC-driven neuroblastoma. *Cell Death & Disease*. 2023;14:747. (JCR 2023, IF = 8.1; Q1 - Cell Biology)

Experimental work (%)	Supervision (%)	Manuscript (%)	Research direction (%)
10	90	40	75

[3] Çoku J, Booth DM, **Skoda J**, Pedrotty MC, Vogel J, Liu K, Vu A, Carpenter EL, Ye JC, Chen MA, Dunbar P, Scadden E, Yun TD, Nakamaru-Ogiso E, Area-Gomez E, Li Y, Goldsmith KC, Reynolds CP, Hajnoczky G, Hogarty MD. Reduced ER-mitochondria connectivity promotes neuroblastoma multidrug resistance. *EMBO Journal*. 2022;41(8):e108272. doi: 10.15252/embj.2021108272. (JCR 2022, IF = 11.4; T10 - Biochemistry & Molecular Biology)

Experimental work (%)	Supervision (%)	Manuscript (%)	Research direction (%)
15	0	30	10

[4] Kameneva P, Melnikova VI, Kastriti ME, Kurtova A, Kryukov E, Murtazina A, Faure L, Poverennaya I, Artemov AV, Kalinina TS, Kudryashov NV, Bader M, **Skoda J**, Chlapek P, Curylova L, Sourada L, Neradil J, Tesarova M, Pasqualetti M, Gaspar P, Yakushov VD, Sheftel BI, Zikmund T, Kaiser J, Fried K, Alenina N, Voronezhskaya EE, Adameyko I. Serotonin limits generation of chromaffin cells during adrenal organ development. *Nature Communications*. 2022;13:2901. (JCR 2022, IF = 16.6; T10 - Multidisciplinary Sciences)

Experimental work (%)	Supervision (%)	Manuscript (%)	Research direction (%)
5	15	15	20

[5] Curylova L, Ramos H, Saraiva L, **Skoda J***. Noncanonical roles of p53 in cancer stemness and their implications in sarcomas. *Cancer Letters*. 2022;525:131-145. (JCR 2022, IF = 9.7; Q1 - Oncology)

Experimental work (%)	Supervision (%)	Manuscript (%)	Research direction (%)
NA, review	90	40	90

[6] Krchniakova M, Paukovcekova S, Chlapek P, Neradil J, **Skoda J***, Veselska R. Thiosemicarbazones and selected tyrosine kinase inhibitors synergize in pediatric solid tumors: NDRG1 upregulation and impaired prosurvival signaling in neuroblastoma cells. *Frontiers in Pharmacology*. 2022;13:976955. (JCR 2022, IF = 5.6; Q1 - Pharmacology & Pharmacy)

Experimental work (%)	Supervision (%)	Manuscript (%)	Research direction (%)
5	20	20	35

[7] Paukovcekova S, Krchniakova M, Chlapek P, Neradil J, **Skoda J***, Veselska R. Thiosemicarbazones Can Act Synergistically with Anthracyclines to Downregulate CHEK1 Expression and Induce DNA Damage in Cell Lines Derived from Pediatric Solid Tumors. *International Journal of Molecular Sciences*. 2022;23(15):8549. (JCR 2022; IF = 5.6, Q1 - Biochemistry & Molecular Biology)

Experimental work (%)	Supervision (%)	Manuscript (%)	Research direction (%)
5	20	20	35

[8] Macsek P, **Skoda J**, Krchniakova M, Neradil J, Veselska R. Iron-Chelation Treatment by Novel Thiosemicarbazone Targets Major Signaling Pathways in Neuroblastoma. *International Journal of Molecular Sciences*. 2022;23(1):376. (JCR 2022; IF = 5.6, Q1 - Biochemistry & Molecular Biology)

Experimental work (%)	Supervision (%)	Manuscript (%)	Research direction (%)
0	5	20	20

[9] Mikulenkova E, Neradil J, Vymazal O, **Skoda J***, Veselska R. NANOG/NANOGP8 Localizes at the Centrosome and is Spatiotemporally Associated with Centriole Maturation. *Cells*. 2020;9:692. (JCR 2020, IF = 6.600; Q2 – Cell Biology)

Experimental work (%)	Supervision (%)	Manuscript (%)	Research direction (%)
15	50	30	50

[10] <u>**Skoda J**</u>*, Neradil J, Staniczkova Zambo I, Nunukova A, Macsek P, Borankova K, Dobrotkova V, Nemec P, Sterba J, Veselska R. Serial Xenotransplantation in NSG Mice Promotes a Hybrid Epithelial/Mesenchymal Gene Expression Signature and Stemness in Rhabdomyosarcoma Cells. *Cancers*. 2020;12:196. (JCR 2020, IF = 6.639; Q1 – Oncology)

Experimental work (%)	Supervision (%)	Manuscript (%)	Research direction (%)
50	50	90	50

[11] Paukovcekova S, <u>**Skoda J**</u>, Neradil J, Mikulenkova E, Chlapek P, Sterba J, Richardson DR, Veselska R. Novel Thiosemicarbazones Sensitize Pediatric Solid Tumor Cell-Types to Conventional Chemotherapeutics through Multiple Molecular Mechanisms. *Cancers*. 2020;12:3781. (JCR 2020, IF = 6.639; Q1 – Oncology)

Experimental work (%)	Supervision (%)	Manuscript (%)	Research direction (%)
10	0	10	15

[12] <u>**Skoda J**</u>*, Borankova K, Jansson PJ, Huang ML, Veselska R, Richardson DR. Pharmacological targeting of mitochondria in cancer stem cells: An ancient organelle at the crossroad of novel anti-cancer therapies. *Pharmacological Research*. 2019;139:298-313. (JCR 2019, IF = 5.893; T10 - Pharmacology & Pharmacy)

Experimental work (%)	Supervision (%)	Manuscript (%)	Research direction (%)
NA, review	80	80	90

[13] Neradil J, Kyr M, Polaskova K, Kren L, Macigova P, <u>**Skoda J**</u>, Sterba J, Veselska R. Phospho-Protein Arrays as Effective Tools for Screening Possible Targets for Kinase Inhibitors and Their Use in Precision Pediatric Oncology. *Frontiers in Oncology*. 2019;9:930. (JCR 2019, IF = 4.848; Q2 – Oncology)

Experimental work (%)	Supervision (%)	Manuscript (%)	Research direction (%)
5	0	10	10

[14] <u>**Skoda J**</u>, Nunukova A, Loja T, Zambo I, Neradil J, Mudry P, Zitterbart K, Hermanova M, Hampl A, Sterba J, Veselska R. Cancer stem cell markers in pediatric sarcomas: Sox2 is associated with tumorigenicity in immunodeficient mice. *Tumor Biology*. 2016;37:9535-48. (JCR 2016, IF = 3.650; Q2 – Oncology)

Experimental work (%)	Supervision (%)	Manuscript (%)	Research direction (%)
40	0	60	50

[15] <u>Skoda J</u>, Hermanova M, Loja T, Nemec P, Neradil J, Karasek P, Veselska R. Co-Expression of Cancer Stem Cell Markers Corresponds to a Pro-Tumorigenic Expression Profile in Pancreatic Adenocarcinoma. *PLOS One.* 2016;11:e0159255. (JCR 2016, IF = 2.806; Q1 – Multidisciplinary Sciences)

Experimental work (%)	Supervision (%)	Manuscript (%)	Research direction (%)
75	50	80	50

[16] Zambo I, Hermanova M, Zapletalova D, **<u>Skoda J</u>**, Mudry P, Kyr M, Zitterbart K, Sterba J, Veselska R. Expression of nestin, CD133 and ABCG2 in relation to the clinical outcome in pediatric sarcomas. Cancer Biomarkers. 2016;17(1):107-16. (JCR 2016, IF = 2.274; Q3 – Oncology)

Experimental work (%)	Supervision (%)	Manuscript (%)	Research direction (%)
5	0	10	10

[17] Nunukova A, Neradil J, **<u>Skoda J</u>**, Jaros J, Hampl A, Sterba J, Veselska R. Atypical nuclear localization of CD133 plasma membrane glycoprotein in rhabdomyosarcoma cell lines. *International Journal of Molecular Medicine*. 2015;36:65-72. (JCR 2015, IF = 2.348; Q3 – Medicine, Research & Experimental)

Experimental work (%)	Supervision (%)	Manuscript (%)	Research direction (%)
20	0	10	10

[18] Sana J, Zambo I, **<u>Skoda J</u>**, Neradil J, Chlapek P, Hermanova M, Mudry P, Vasikova A, Zitterbart K, Hampl A, Sterba J, Veselska R. CD133 expression and identification of CD133/nestin positive cells in rhabdomyosarcomas and rhabdomyosarcoma cell lines. *Analytical Cellular Pathology*. 2011;34:303-18. (JCR 2011, IF = 0.917; Q4 – Oncology)

Experimental work (%)	Supervision (%)	Manuscript (%)	Research direction (%)
15	0	10	0

1 INTRODUCTION

More than 300,000 children and young people aged 0-19 are diagnosed with cancer each year worldwide [1]. Although pediatric cancers constitute just 1% of all cancer cases [2], they represent a serious health burden. In high-income countries and a growing body of middle-income countries, cancer is now the leading cause of death from disease in children [1]. These statistics are particularly alarming when considered in the light of the substantial progress made in the field of pediatric oncology, which has improved survival for patients with pediatric cancer from 60% to 85% over the past four decades, with survival rates of many hematologic malignancies now reaching over 95% (**Fig. 1A**) [3].

Despite advances in treatment, due to the complex etiology of pediatric cancers, their relative rarity, and their substantial biological differences from cancers that affect adults [4-6], pediatric cancer care has clearly lagged behind our capacity to manage infectious diseases in children [7]. This is reflected in the current prominence of cancer-related deaths in children and further highlights the need to focus our attention to better understand the etiology and biology of the most aggressive pediatric cancers.
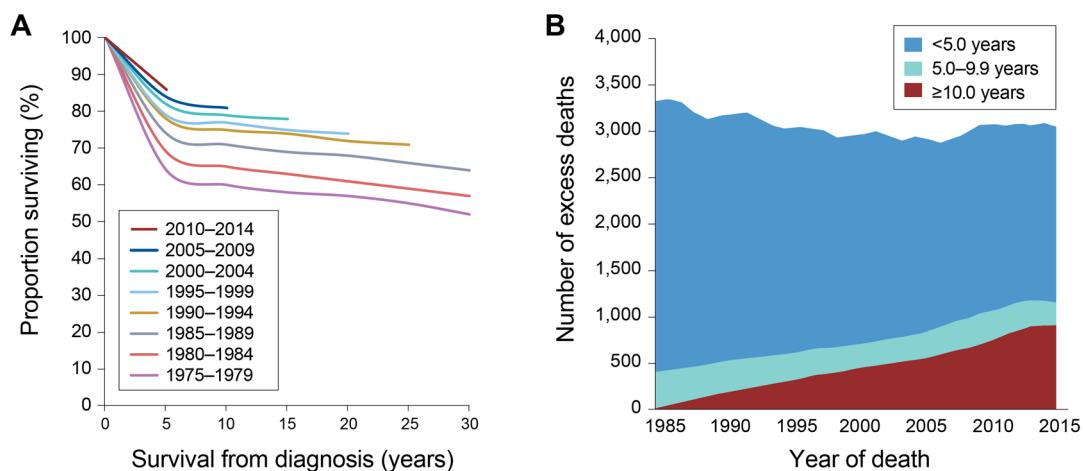
Figure 1. Trends in pediatric cancer mortality over time. A) 5-year overall survival for pediatric cancer patients (<20 years of age) in the USA. **B**) Number of annual excess deaths among pediatric cancer patients according to years after diagnosis. Note the steady increase in excess deaths in the group of long-term survivors, ≥10 years from diagnosis. Adapted from Ehrhardt et al. [8], reproduced with permission from Springer Nature.

Pediatric solid tumors are a heterogeneous group of nonhematologic cancers that arise from various tissues during embryonic or fetal life (congenital tumors are detected already during pregnancy or within three months after birth [9]) or later during childhood and adolescence. While these rare tumors represent 30% of all pediatric cancers, they are often highly aggressive and remain a significant cause of cancer-related mortality in children and young adults. Indeed, despite multimodal therapies, the survival rates of several pediatric solid tumor entities, such as high-risk neuroblastoma [10], certain brain tumors [3], pediatric osteosarcoma, rhabdomyosarcoma, and Ewing's sarcoma [3], have plateaued at only 60% to 70% over the last 20 years.

One of the reasons underlying this dismal prognosis is the development of multidrug resistance (MDR) phenotype, which is often observed in these aggressive tumors. MDR is a major cause of treatment failure and occurs when tumor cells become resistant to multiple structurally and functionally unrelated chemotherapeutic agents. However, from a broader perspective, MDR can be also perceived as resistance to anticancer therapy in general, because several MDR mechanisms have been shown to overlap with those that confer resistance to radiation therapy [11-14] or that drive metastasis via epithelial-mesenchymal transition (EMT) [15].

Along with the growing understanding of the tumor cell heterogeneity, cell hierarchies and cellular plasticity, the presence of cancer stem cells (CSCs) has been identified as a recuring aspect associated with the MDR tumors [16-18]. Unlike other tumor cells (often referred to as tumor bulk or transient-amplifying cells), CSCs possess long-term self-renewal and differentiation properties and are thought to be responsible for tumor initiation, maintenance, and resistance to therapy [17]. In line with the notion that undifferentiated cells, i.e., progenitor and stem cells, are preferentially primed for transformation and can often serve as the cell-of-origin for cancers [18], most, if not all, pediatric tumors are though to arise from aberrant maturation and dysregulated differentiation of these progenitors [19].

In contrast with cancers in adults, where exposure to environmental factors is a well-documented contributor to the accumulation of mutations during multistep tumorigenesis [20], the origins of pediatric tumors are closely intertwined with development [19]. Indeed, spatiotemporal distribution of pediatric tumors often coincide with waves of normal development and growth of the affected tissues. For example, the peak age-specific incidence of pediatric osteosarcoma overlaps with growth spurts in puberty [21], whereas the ongoing proliferation and migration of glial progenitors during the first years of life [22] likely underlies the development of pediatric brain tumors prevalent in younger children [23]. Similarly, about 20% of neuroblastoma cases are diagnosed congenitally, defining a group of perinatal neuroblastoma [24].

Thus, detailed understanding of developmental pathways and programs is pertinent for further progress in pediatric cancer research. Exploring these programs in the context of pediatric solid tumors might help us to identify therapeutic targets and approaches to either navigate the dysregulated tumor cells back toward differentiation or selectively eradicate them while sparing healthy progenitors. Such understanding, allowing us to clearly distinguish molecular actors and processes that differ between tumor cells and their normal tissue counterparts, is also vital for pinpointing selective vulnerabilities to overcome MDR. At the same time, decoding the cellular heterogeneity to establish molecular roadmaps of tumor cell fate regulators is key to identifying relevant markers that might be incorporated into better diagnostic and prognostic protocols. At this point, such resources are urgently needed to advance patient-tailored, precision medicine therapies [25,26], improve treatment outcomes, and reduce the late effects of cancer treatment and excess deaths among childhood cancer survivors (**Fig. 1B**).

The following chapters briefly overview some of the current approaches to identifying clinically relevant targets to maximize treatment outcomes and overcome MDR in pediatric solid tumors, while discussing the author's contributions to these efforts, particularly in pediatric sarcoma and neuroblastoma research.

2 CANCER STEM CELLS IN PEDIATRIC SOLID TUMORS

The idea that tumor development, metastasis and regrowth after therapy might be driven by a specific subset of self-renewing tumor cells, sitting at the apex of tumor cell hierarchy and exhibiting properties related to stem cells, is very old [27]. However, it was the seminal discoveries of Dick and colleagues studying hematological malignancies [28,29] that revived the CSC field. By introducing a gold-standard functional assay of the CSC phenotype, they demonstrated that only a small fraction of leukemia cells, isolated based on the expression of cluster of differentiation (CD) antigens, have the capacity to initiate tumors in immunocompromised mice [28]. Soon after, similar reports were made in breast [30] and brain cancer [31]. To isolate CSCs, the latter study used a newly discovered protein found to mark hematopoietic progenitors [31], prominin-1 (CD133) (reviewed in Appendix 1 [32]). Since then, CSCs have been described in a wide variety of cancers, including pediatric tumors [33-35]. Representing the pool of cells driving tumor progression and relapse, identification of CSCs via selective markers was considered an attractive approach towards development of CSC-targeted therapies. It is now well established that the CSC phenotypes are far more plastic and CSCs can arise by dedifferentiation and reprogramming of non-CSCs, e.g., in response to the tumor microenvironment (TME) [36] and therapy-induced stress [37-39]. However, the initial studies investigating various proteins in relation to their ability to discern CSCs in specific tumor types have provided important basis for our understanding of the molecular mechanisms that mediate CSC traits. Aside from pediatric brain tumors, including medulloblastomas and gliomas [31,40-42], and rather scarce reports in neuroblastoma (reviewed in Refs [43,44]), CSCs have been intensively studied in pediatric sarcomas [34].

Sarcomas are a highly heterogeneous group of bone and soft tissue tumors originating from primitive mesenchymal cells [34,45,46]. Although they are rare in adults, sarcomas account for ~15% of all pediatric malignancies, making them the third most common childhood tumor [34]. The most prevalent pediatric sarcomas include

rhabdomyosarcoma, osteosarcoma, and Ewing's sarcoma. These tumors are often highly aggressive, exhibiting enhanced therapy resistance and early metastasis. Despite intensive multimodal therapy, including surgery and systemic chemotherapy, about one-third of patients with localized disease eventually relapse. The prognosis of patients who present with advanced and metastatic tumors remains poor, with survival rates of only 20% [34,47]. As discussed in detail in the following chapter, several research groups, including our own, have demonstrated that these aggressive traits of pediatric sarcomas may be attributed to the presence of sarcoma CSCs.

Neuroblastoma is the most common and highly lethal extracranial pediatric solid tumor, accounting for ~15% of cancer deaths in children [48,49]. 90% of neuroblastoma arise in children younger than 10 years, with a median age of 18–24 months at diagnosis. Neuroblastoma is characterized by extensive intratumor and interpatient heterogeneity that dictates its clinical manifestation and complicates its management [48,50,51]. Indeed, spontaneous tumor regression without the need for treatment is often observed in infants with favorable biology. However, about half of the children with neuroblastoma present with more advanced disease and early metastasis associated with very poor prognosis, except for young children with stage 4S disease [48,49]. Amplification of *MYCN* (encoding N-MYC) and overexpression of *MYC* (encoding c-MYC) from the MYC family of transcription factors (collectively termed MYC proteins hereafter) are well-established drivers of high-risk neuroblastoma [51,52]. Several other aberrations, including 1p and 11q loss, 17q gain, activating mutations in *anaplastic lymphoma kinase* (*ALK*) or inactivating mutations in *paired-like homeobox 2b* (*PHOX2B)*, are associated with an inferior prognosis in neuroblastoma [51]. While the existence of neuroblastoma stem cells [48] remains elusive, neuroblastoma is closely linked to the dysregulation of developmental programs, with the most aggressive tumors exhibiting features of primitive multipotent sympathoadrenal progenitors [53-55].

2.1 Characterizing cancer stem cells in pediatric solid tumors

CD133 was the first protein reported to identify CSCs in pediatric sarcomas, i.e., osteosarcoma [56,57]. In line with results in established cell lines from Beat Schäfer's group [58], we were the first to demonstrate that CD133 is also expressed in rhabdomyosarcoma tumor tissues and patient-derived cell lines (Appendix 18 [59]). Rhabdomyosarcoma cells from a CD133-expressing cell line were found clonogenic *in vitro*, and initiated tumors in nonobese diabetic/severe combined immunodeficiency (NOD/SCID) mice, thus demonstrating CSC properties.

Interestingly, while CD133 is a pentaspan membrane glycoprotein found selectively associated with highly curved and prominent plasma membrane structures (reviewed in Appendix 1 [32]), immunohistochemistry (IHC) and immunofluorescence analyses revealed a significant pool of CD133 present in the cytoplasm of rhabdomyosarcoma cells (Appendix 18 [59]). Following this observation, we showed that intracellular localization of CD133 is a common feature found across a panel of cell lines derived from rhabdomyosarcoma (Appendix 17 [60]). Importantly, by utilizing confocal and transmission electron microscopy and subcellular fractionation, we demonstrated that CD133 is localized also within the nucleus of rhabdomyosarcoma cells [60], which opened new questions about alternative molecular roles of CD133 in different subcellular compartments (**Fig. 2**).

The nuclear localization of CD133 was confirmed by several independent reports, including studies in normal mouse incisor tooth epithelia [61] and various cancer types, i.e., melanoma [62], breast carcinoma [63], non-small cell lung carcinoma [64], and colorectal carcinoma [65]. However, the impact of nuclear CD133 on cancer progression appears to be context dependent and there are contradictory reports regarding its prognostic significance in different cancers. While high nuclear CD133 expression associates with poor outcomes in non-small cell lung carcinoma [64], it has been found to predict a favorable prognosis in colorectal adenocarcinoma [65].
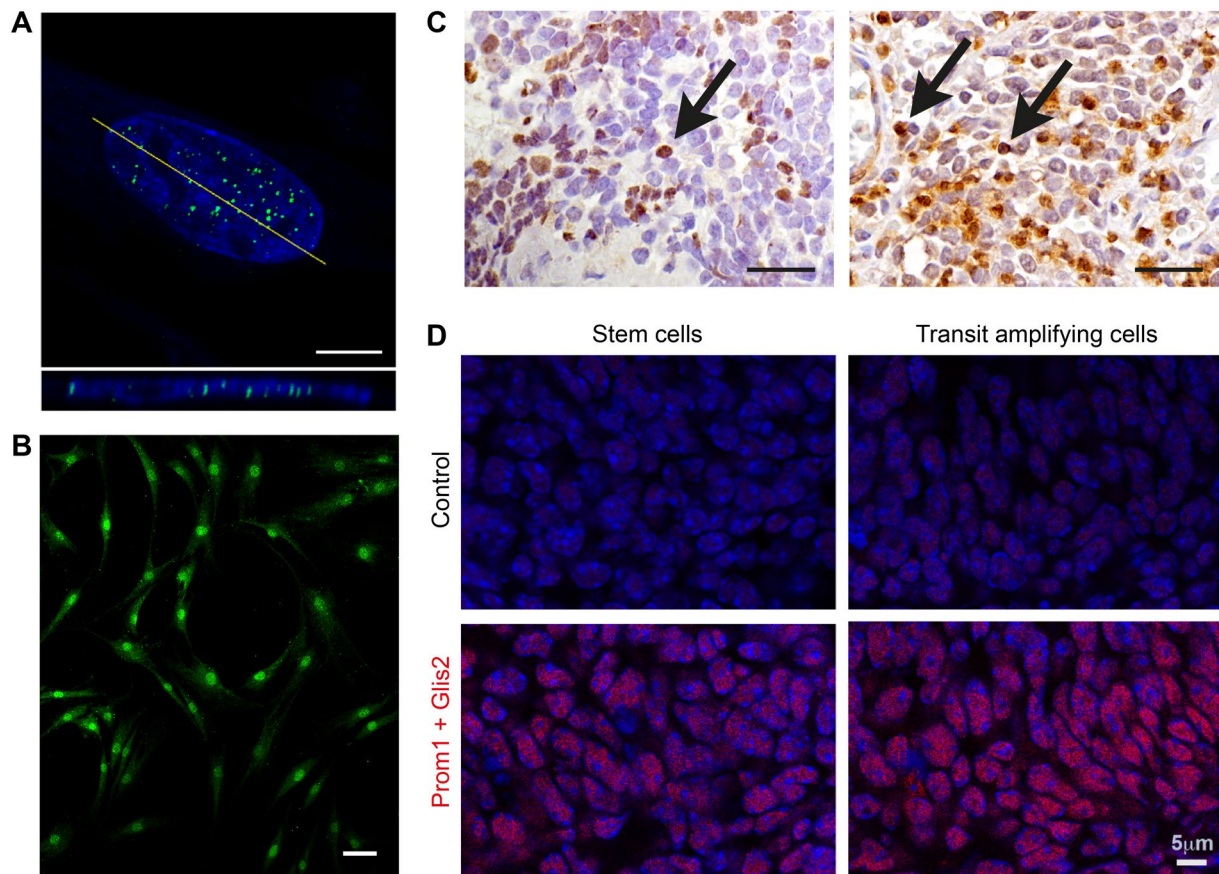
Figure 2. Nuclear localization of CD133 identified in pediatric sarcomas. A) A clear nuclear signal of CD133 (green) analyzed by confocal microscopy in rhabdomyosarcoma cells (top), with the software cross-section (bottom) indicated by a yellow line. Scale bar, 5 µm. Adopted from Nunukova et al. [60]. **B**) Subcellular distribution and marked nuclear localization of CD133 (green) in Ewing's sarcoma cells. Scale bar, 50 µm. Adapted from Skoda et al. [66], reproduced with permission from Springer Nature. **C**) IHC analysis of CD133 in rhabdomyosarcoma (left) and Ewing's sarcoma (right) tissues. Note the cells with pronounced nuclear CD133 expression (arrows). Scale bars, 100 5 µm. **D**) Proximity ligation assay confirms colocalization of Prom1 and Glis2 (red) in the nuclei of stem cells and transit amplifying cells in the mouse incisor cervical loop epithelium. Note the increased signal in transit amplifying cells. Control, detection with ommision of the anti-Glis2 antibody. Adapted from Singer et al. [61].

The molecular function of nuclear CD133 and its transport through the nuclear membrane are still poorly understood. However, a recent study by Singer at al. revealed that the translocation of CD133 into the nucleus might be involved in the regulation of stem cell maintenance and activation via Sonic Hedgehog (SHH) signaling [61]. CD133 was shown to form a complex with the transcription factor Glis2 at the primary cilium of mouse incisor epithelial stem cells. This led to the translocation of CD133-Glis2 into the

nucleus and the subsequent upregulation of Stat3, a direct transcriptional target of Glis2 [61]. Depletion of either CD133 or Glis2 inhibited Stat3 expression, highlighting the importance of CD133-Glis2 complex in Stat3 transcriptional regulation. Interestingly, the nuclear translocation of CD133-Glis2 was found to be associated with the transition of quiescent stem cells into proliferative transit amplifying cells (**Fig. 2D**) [61]. These findings suggest that differences in CD133 expression and subcellular distribution might reflect quiescent and active cycling states rather than cell stemness or differentiation status per se. Of note, CD133 protein has been detected in fully differentiated epithelial and non-epithelial cells (reviewed in Appendix 1 [32]).

These observations regarding the potential function of CD133 correspond with our findings in various tumor types. Along with the detected fluctuation of CD133 expression during cell culture [59], our results in rhabdomyosarcoma models suggested that CD133-positive (CD133+) and -negative (CD133-) phenotypes, routinely sorted at that time using immunodetection of CD133 at the cell surface, might not be as hardwired. We found that rhabdomyosarcoma cells have a substantial pool of intracellular CD133 that might allow a phenotype switch [59,60]. Such bidirectional conversion between CD133- and CD133+ tumor cell phenotypes during xenograft assays was reported in several studies [67-69], questioning CD133 as a selective CSC marker and indicating its function goes beyond stem cell activities (see Appendix 1 [32]). Indeed, we later showed that significant intracellular pools of CD133 can be detected in various pediatric sarcomas (Appendix 14 [66], Appendix 16 [70]) and other cancers (Appendix 15 [71]), pointing to the biological importance of intracellular CD133.

CD133 has been shown to be involved in various prosurvival and developmental signaling pathways, including PI3K/AKT, Src-FAK, WNT/β-catenin, TGF-β/SMAD, and MAPK/ERK pathways, and at least part of these roles are controlled by it subcellular distribution (Appendix 1 [32]). Consistently, the biological role of intracellular CD133 may be further substantiated by its clinical relevance identified in pediatric sarcomas. IHC analysis of pediatric sarcoma tissues revealed that high cytoplasmic CD133 expression is significantly associated with shorter survival in rhabdomyosarcoma patients (Appendix

16 [70]). This study also established that neuronal stem cell-associated protein nestin [72], another putative CSC marker that was found co-expressed with CD133 in our initial rhabdomyosarcoma study [59], indicates poor prognosis in Ewing's sarcoma patients [70]. Collectively, our findings show that intracellular CD133 has a prognostic power in pediatric sarcomas.

CSC phenotypes are routinely validated by functional assays which are designed to assess the various CSC traits [33]. Most importantly, these involve assays that test the capacity of long-term self-renewal, i.e., test the ability of individual cancer cells or their limiting numbers to re-initiate cancer growth [17,33]. Principally, *in vitro* CSC assays fit into two main categories: (i) colony formation assays (also termed clonogenic assays), testing the capacity of individual cells to produce colonies (defined by minimal cell numbers [73] or the area/diameter of the colony [74]) in adherent conditions, and (ii) sphere formation assays (also termed spheroid formation assays), which test the capacity of single cells to form a tumorsphere (a compact spheroid-like formation most often defined by the minimal diameter) [74-76].

With the development of advanced imaging and automated image analysis methods, overcoming the demand for laborious manual readout, the colony formation and sphere formation assays have been also successfully adopted for high-throughput analyses [77,78]. This makes them particularly useful for time- and cost-efficient large-scale screens for candidate CSC-targeting drugs, which cannot be paralleled by *in vivo* assays in animal models. Despite these advancements, the tumorigenicity assay in NOD/SCID gamma (NSG) mice remains the most comprehensive test and the 'gold standard' for identifying CSC phenotypes [79]. As multiple factors may affect xenografting efficiencies, including injection sites (ortothopic or heterotopic), tumor cell dissociation and sorting protocols, or the use of supporting matrices (e.g., Matrigel), it is important that studies carefully detail these parameters and that the CSC readouts of studies using different protocols are compared with caution [79]. Finally, although they provide important tools to study cancer stemness, current CSC assays may underestimate some CSC populations, as they test only for active (proliferative) CSC phenotypes, and thus

inherently overlook quiescent CSCs. However, it remains to be established whether the emerging biomarkers and tools for studying cell dormancy [80-83] can be adopted for the development of complex functional assays that will allow identification of both active and dormant CSC states.

Testing the *in vivo* tumorigenic capacity across a panel of nine patient-derive pediatric sarcoma cell lines, including osteosarcoma, rhabdomyosarcoma and Ewing's sarcoma models, we unequivocally demonstrated that CD133 is not sufficiently selective marker of pediatric sarcoma CSCs (Appendix 14 [66]). While the CD133 protein was highly expressed in all cell lines, with all of them showing at least 50% of CD133+ cells, only two of the cell lines were tumorigenic in NSG mice. These functional experiments provide valuable insights into the factors that determine stemness in pediatric sarcomas (Appendix 14 [66]). Previous studies in Ewing's sarcoma reported conflicting results, suggesting CD133+ sorted cells are either more tumorigenic [84] or less tumorigenic than unsorted (bulk) tumor cells [85]. Surprisingly, studies by other teams, reporting that CD133 identifies CSCs in osteosarcoma [56] and rhabdomyosarcoma [58], did not conduct functional assays to validate the CSC phenotype *in vivo*. Contrary to these initial reports, our results demonstrate that CD133 is a poor marker of CSCs in pediatric sarcomas (Appendix 14 [66]).

Although cell surface-expressed CD133 appeared as a tempting target for immunotherapies and drug delivery approaches, the current understanding implies that CD133-based anti-CSC strategies are likely to fail to induce durable tumor remission, as they may miss significant CSC populations [32,34,66]. Notably, several other cell surface antigens have been attributed to CSC phenotypes in aggressive pediatric tumors, e.g., ATP-binding cassette (ABC) subfamily G member 2 (ABCG2), CD117, and C-X-C chemokine receptor type 4 (CXCR-4) in pediatric sarcomas [34], or CD114, CD24, and LGR5 in neuroblastoma [44]. However, similar to CD133, expression of these molecules on tumor cells fluctuates in response to microenvironmental cues, including interactions with other cell types within the TME, raising doubts about their utility for CSC-targeted therapies [34]. For example, in Ewing's sarcoma cells, CXCR4 expression was found to be

highly plastic, being dynamically induced by stress caused by hypoxia or growth constraints, and reverting back to basal levels upon removal of these insults [86]. In addition, these putative CSC markers might have counterintuitive, context-dependent roles. For instance, while CD24 has been suggested to identify neuroblastoma cells with enhanced tumor-initiating properties, CD24-negative neuroblastoma cells also formed tumors in immunodeficient mice, albeit with greater latency [87]. A recent single-cell analysis of neuroblastoma tumors revealed that CD24 is exclusively expressed on tumor cells and it was proposed that this sialoglycoprotein might interact with sialic acid-binding Ig-like lectin 10 (SIGLEC10) on macrophages, preventing phagocytosis of neuroblastoma cells (**Fig. 3A**) [88]. Strikingly, high CD24 expression was found as a significant predictor of good prognosis in neuroblastoma patients [88], as also confirmed by our analysis in an independent dataset (**Fig. 3B**). While these results do not rule out the association of these cell surface molecules with more dedifferentiated, stem-like states, additional studies are needed to understand their biological roles in the context of the TME before they might be appropriately exploited to guide potential therapies.
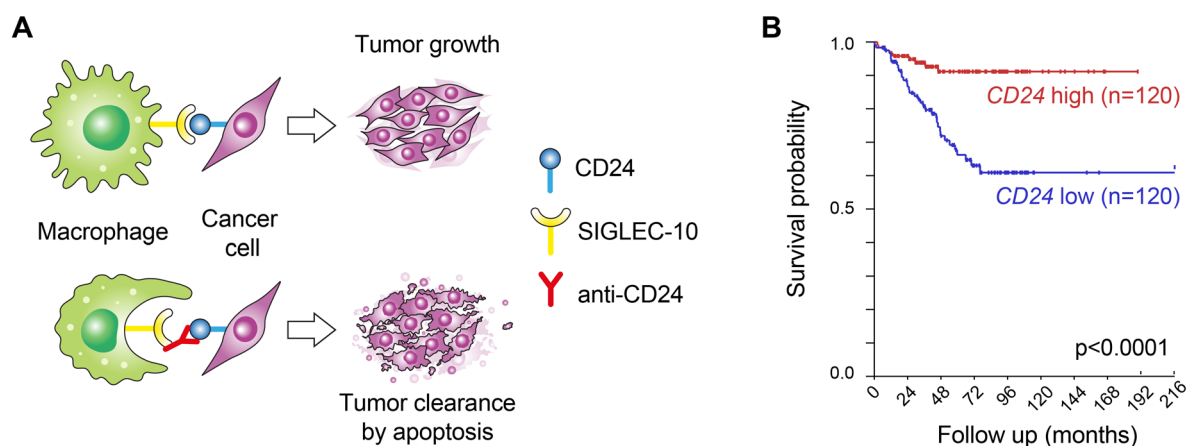
Figure 3. CD24-SIGLEC10 interactions in cancer and the prognosti power of *CD24* expression in neuroblastoma. A) A schematic of the CD24-SIGLEC10 interaction between cancer cells and macrophages. CD24 expressed on the cancer cell surface acts as a "don't eat me" signal, inhibiting phagocytic activity of tumor associated macrophages, which may be exploited for immunotherapy [89,90] **B**) Elevated expression of *CD24* mRNA associates with better survival in neuroblastoma patients. Analysis of the Kocak transcriptomics dataset [91] via the R2: Genomics Analysis and Visualization Platform.

There is a substantial body of evidence that master transcription factors associated with the self-renewal of embryonic stem cells (ESCs), i.e., sex-determining region y-box 2 (SOX2), octamer-binding transcription factor 4 (OCT4) and Nanog homeobox (NANOG), are also associated with cancer stemness [33,92]. These transcription factors are directly responsible for maintaining the expression profiles that preserve the stem cell phenotype and self-renewal capacity. Similarly to ESCs and induced pluripotent stem cells (iPSCs), these core stemness factors are found to be expressed in a wide range of tumors and are now generally accepted as essential for stemness [93-95]. Of these transcription factors, SOX2 appears to play a prominent role in the acquisition of stemness properties and plasticity in cancer [34,95-98].

Indeed, our work on pediatric sarcomas also demonstrates that SOX2, a canonical Yamanaka factor used for inducing the iPSC phenotype [99,100], is a crucial determinant of pediatric sarcoma stemness (Appendix 14 [66]). Among the examined marker proteins potentially associated with the CSCs phenotype (ABCG2, nestin, CD133, NANOG, OCT4, and SOX2), only the cell lines expressing SOX2 formed tumors in NSG mice. Our work in patient-derived cell lines confirmed previous observations in established osteosarcoma models [101] and was the first to show that SOX2 is a critical factor for the tumorigenic potential of other pediatric sarcoma subtypes, such as rhabdomyosarcoma and Ewing's sarcoma [66]. Several other studies have confirmed our findings and the significance of SOX2 expression as a specific marker of CSCs in pediatric sarcomas (reviewed in Ref [34]; see also Refs [102,103]).

Expression of SOX2 is positively regulated by several signaling pathways related to embryonic development, including SHH, Hippo, WNT/β-Catenin, and TGF-β/SMAD pathways, as well by the canonical prosurvival PI3K/AKT signaling pathway [97,98]. Interestingly, as discussed above, CD133 has been shown to be involved in the regulation of most of these pathways (Appendix 1 [32]), which may explain its function as a rather context-dependent contributor to the CSC phenotype. Overall, SOX2 stands out as the key marker of sarcoma CSCs (**Fig. 4**) and targeting SOX2 is being explored as an attractive therapeutic approach in aggressive cancers [104]. However, the undruggable nature of this

transcription factor has so far hindered progress in the development of direct SOX2 inhibitors [104].

Recently, we have proposed an alternative approach to target SOX2 and sarcoma CSCs via restoring the activity of the p53 pathway (Appendix 5 [46]). Deficiency of the wild-type p53 activity has been found crucial for the successful transformation of mesenchymal stem cells (MSCs) into various sarcomas. Conversely, aberrations in the p53 pathway due to *TP53* loss or mutation, as well as the amplification of mouse double minute homologs *MDM2* and *MDM4*, are common in sarcomas (reviewed in Appendix 5 [46]). Since p53 has been shown to directly and indirectly repress the expression of core stemness factors, including SOX2, therapeutic approaches that restore wild-type p53 activity could have potent anti-CSC effects and should be investigated in detail in future studies on pediatric sarcomas (Appendix 5 [46]).
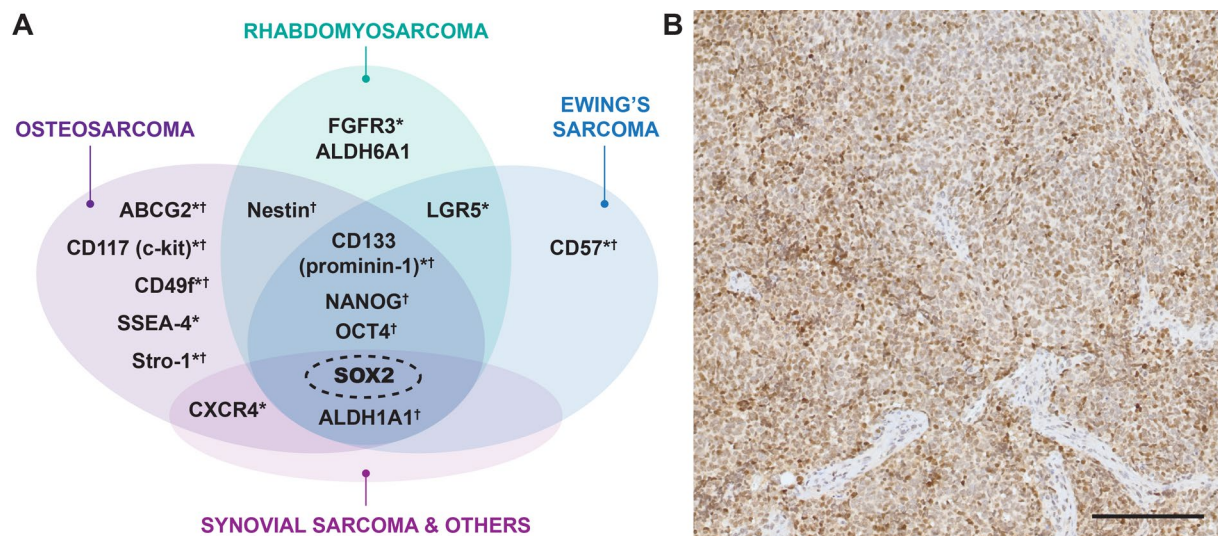
Figure 4. CSC markers in pediatric sarcomas. **A**) A Venn diagram showing the overlap of proteins reported to distinguish CSCs across sarcoma subtypes. Note the central position of the core ESC pluripotency factor, SOX2, which is shared among all major sarcoma subtypes. *Cell surface proteins; † Existing opposing evidence. Adapted from Skoda and Veselska [34] to incorporate data from Refs [74,105-107]. **B**) A representative IHC image of the Ewing's sarcoma xenograft tissue that displays high expression of SOX2 as the major determinant of sarcoma stemness. Scale bar, 200 μm.

The fundamental ability of CSCs is to initiate tumor growth, which is closely related to metastasis [33]. A prerequisite for metastasis formation is the ability of cells to enter the bloodstream and exit it again, thereby entering distant tissues and organs. In carcinomas, tumors of epithelial origin, the ability of cells to undergo EMT is crucial [33,108]. Transition towards a mesenchymal phenotype is essential for tumor cells to detach from the original microenvironment and to pass through the vascular endothelium into the bloodstream. Contrary to initial assumptions, it has been shown that CSCs do not exhibit a highly mesenchymal phenotype, but rather display characteristics corresponding to both epithelial and mesenchymal phenotypes [108,109]. This phenomenon is termed hybrid epithelial-mesenchymal (E/M) phenotype and it seems to provide CSCs with the highest plasticity, allowing them to adapt to various changes in the surrounding microenvironment and drive collective metastatic invasion [109-111].

However, sarcomas are tumors of mesenchymal origin, likely derived from MSCs and their progenitors (Appendix 5 [46]), which themselves exhibit a highly migratory phenotype. MSCs are known to exhibit a so-called homing capacity, where, in the case of injury, they migrate to the site of damaged tissue [112]. Repeated xenotransplantation is a method to unbiasedly select cells that exhibit a highly aggressive tumorigenic phenotype, representing the phenotype of active CSCs [33,113,114]. Using this approach to study rhabdomyosarcoma, we surprisingly demonstrated that the hybrid E/M phenotype also underlies the aggressiveness of sarcoma cells (Appendix 10 [74]). During repeated xenotransplantation, the rhabdomyosarcoma cells maintained their original phenotype in terms of SOX2 expression and other stemness-associated transcription factors; however, they gradually changed expression of many EMT-related genes. Interestingly, the distribution of differentially expressed mesenchymal and epithelial genes indicated a transition towards both epithelial and mesenchymal phenotypes. Notably, several epithelial genes, including *KRT5*, *LAMA3*, or *ANK3*, were significantly upregulated, while mesenchymal genes, such as *CDH2* (N-cadherin) or *SNAI1* (Snail), were downregulated after the third round of serial xenotransplantation. Consistent with findings in carcinomas, this is the first evidence that mesenchymal tumors, such as rhabdomyosarcoma, may fine-

tune their stem-like traits via progressive acquisition of the hybrid E/M expression signature (Appendix 10 [74]).

In case of rhabdomyosarcoma cells, this hybrid E/M signature was also linked with upregulation of transcription factors and markers that are associated with undifferentiated muscle precursors and proliferation of early muscle progenitors, such as *PAX3*, *HEYL*, *HEY2*, *PITX2*, *CDH15* (M-cadherin), and *MYOD1*. Along with the observed downregulation of MSC senescence-associated genes, these findings suggest a potential role of mesenchymal-to-epithelial transition (MET) in rhabdomyosarcoma, where cells acquire a highly aggressive phenotype by shifting their expression profiles towards a signature characteristic of primitive, undifferentiated cells resembling non-senescent myogenic precursors/mesenchymal stem cells (Appendix 10 [74]). This interpretation aligns with the notion that MET is one of the key cellular mechanisms in the process of reprogramming mesenchymal somatic cells, fibroblasts, towards pluripotency induced by transcription factors, including SOX2 [115,116]. Overall, emerging evidence suggest that hybrid E/M cells are more tumorigenic as compared to epithelial or mesenchymal ones, indicating that the hybrid E/M phenotype can endow tumor cells with a fitness advantage to drive metastatic dissemination [109,117]. However, whether this provides therapeutic opportunities to target cancer stemness by pharmacologically suppressing E/M cell states remains a pertinent question to be explored by future studies.

NANOG, a homeodomain transcription factor involved in ESC self-renewal and pluripotency, is often hijacked by aggressive cancers [118,119]. However, our studies provide strong evidence to reject NANOG as an important contributor to the CSC phenotype in pediatric sarcomas (Appendix 14 [66], Appendix 9 [120], Appendix 10 [74]). NANOGP8 is a functional paralog that differs from NANOG in only three amino acids and exhibits similar transcriptional activity [121]. Interestingly, contrary to their well-established role as regulators of gene expression in the cell nucleus, we found a substantial pool of NANOG/NANOGP8 in the cytoplasm, where they localize at the centrosome (Appendix 9 [120]). The centrosome, as the primary microtubule-organizing center plays a critical role in cell division, vesicle transport, cell signaling and modulating cell polarity

and morphology [122]. Centrosome duplication occurs once per cycle, preserving the temporal and structural differences between mother and daughter centrosomes. Notably, the centrosome age correlates with the cell fate during asymmetric stem cell division [123,124]. Strikingly, we discovered that centrosomal NANOG/NANOGP8 colocalize with the distal region of the mother centriole in various tumor and non-tumor cell types, indicating an association with centriole maturation (**Fig. 5**) (Appendix 9 [120]). These results provide the first evidence suggesting a centrosome-specific role of NANOG, raising important questions about whether and how centrosomal NANOG impacts cell division modes.
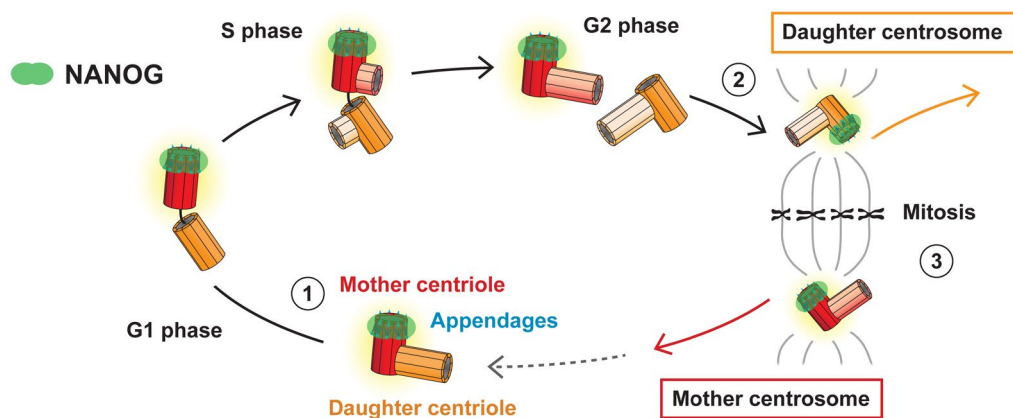

Figure 5. Spatiotemporal localization of NANOG/NANOGP8 at the centrosome during the cell cycle. NANOG colocalizes with mother centriole appendages (1) and its presence at the centrosome coincides with centriole maturation, leading to its appearance on the initially daughter centriole (orange) during the G2/mitosis transition. Centrosome duplication and cell division result in two daughter cells with centrosomes of different ages—mother and daughter centrosomes—both containing the older, mother centriole marked by NANOG protein (3). Adopted from Mikulenkova et al. (Appendix 9 [120]).

In summary, the studies discussed in this chapter have significantly advanced our understanding of the key molecular determinants of cancer stemness in pediatric solid tumors, particularly sarcomas. Current knowledge suggests that SOX2-related gene regulatory networks might provide more reliable risk stratification and prognostic tools, as exemplified by recent studies in Ewing's sarcoma [105] and other sarcomas [103].

Importantly, these networks may infer novel therapeutic targets to combat therapy resistance in aggressive tumors with stem-like traits.

2.2   The role of cancer stem cells in therapy resistance

A key characteristic of CSCs, and a major challenge in cancer treatment, is their intrinsic capacity to escape therapies. Numerous mechanisms have been shown to contribute to the MDR associated with the CSC phenotype. These mechanisms may be broadly divided into four categories: (i) enhanced expression and activity of detoxifying enzymes, drug efflux pumps and DNA repair mechanisms [125]; (ii) ability to switch into transiently dormant (quiescent) states that mediate resistance to standard chemotherapy targeting rapidly proliferating tumor cells [125,126]; (iii) cellular plasticity that unlocks tumor heterogeneity, allowing the selection of the fittest clones and enabling CSCs to evade immunosurveillance [35,127,128]; and (iv) reduced sensitivity to apoptotic signals [129] (see also Appendix 12 [130]). In fact, these mechanisms encompass all the different aspects of tumor cell resistance to therapy, underscoring the role of CSCs in tumor relapse and metastasis.

Conceptually, for a drug to be therapeutically effective, it must overcome all the abovementioned mechanisms of resistance. First, it must reach effective concentrations in the tumor cell (or within the tumor tissue for drugs targeting cell surface proteins). Second, it must efficiently bind to its cellular target(s), and this disturbance must be recognized by the cell to produce sufficient level of apoptotic stress signals. Third, the tumor cell must contain mitochondria responsive to these stress signals that principally converge on the mitochondria in the form proapoptotic B-cell lymphoma 2 (BCL-2) family proteins [131]. Only after overwhelming the capacity of antiapoptotic BCL-2 proteins, these drug-induced insults can efficiently trigger oligomerization of BCL-2-associated X protein (BAX) and BCL-2 antagonist/killer (BAK), forming pores in the mitochondrial outer membrane (OMM) and leading to OMM permeabilization (MOMP), cytochrome c release, and apoptosis [131]. Therefore, the inherently nonselective resistance arising from the

attenuated mitochondrial responses can protect tumor cells from a wide range of treatments, including anticancer drugs that are otherwise pharmacologically active and engage their targets, thereby rendering these treatments ineffective.

Although the ultimate decision for a cell to undergo apoptosis is a binary and switch-like process, its regulation by the BCL-2 family proteins is gradual and highly complex [131]. It has been demonstrated that the intrinsic potential of cells to undergo apoptosis (apoptotic threshold) upon chemotherapy treatment depends on their BCL-2 protein interactome, reflecting the ratio between proapoptotic and prosurvival proteins from the BCL-2 family [132,133]. Mitochondria that are "primed for apoptosis" readily respond to apoptotic signals, and trigger apoptosis through MOMP and cytochrome c release. Conversely, CSCs appear less sensitive to apoptotic stimuli and exhibit an increased apoptotic threshold due to an impairment in both intrinsic (mitochondrial) and extrinsic (death receptor) apoptotic pathways [129].

Interestingly, many primary therapy-naïve (pre-therapy) tumors, including neuroblastoma, are generally highly primed for apoptosis [132,134,135]. A decrease in mitochondrial priming in these tumors predicts a worse clinical response to conventional therapy. Although this has been commonly attributed to a shift in the balance favoring antiapoptotic BCL-2 proteins at the mitochondria [131,136], studies led by Michael Hogarty showed that expression of these proteins does not differ between pre-therapy and relapsed MDR (post-therapy) neuroblastoma cells [134,135]. Using paired patient-matched cell lines derived from tumors at diagnosis and at relapse after multimodal therapy, the authors demonstrated that the mechanism underlying the neuroblastoma MDR was not mediated by upregulation of BCL-2 homologues or loss of apoptotic priming, but by repressed BAK/BAX activation [135]. This has led to a recent discovery of a novel mechanism of mitochondria-mediated MDR in neuroblastoma (see Appendix 3 [14]), discussed in detail in Chapter 3.2.

Importantly, our work using the same patient-matched neuroblastoma models reveals that the MDR in post-therapy neuroblastoma cells associates with CSC traits

(Appendix 2 [137]). These cells showed markedly enhanced capacity to initiate tumors in NSG mice and to form neurospheres *in vitro*, while maintaining a similar growth rate compared with their pre-therapy counterparts. These results highlight the importance of cancer stemness and its relationship with therapy resistance in childhood tumors.

Unfortunately, it is well established that the failure of the first-line therapy to induce substantial and lasting tumor response selects for tumor cells with MDR and CSC traits, driving progressive, refractory disease [36-38,138]. In case of pediatric solid tumors, there are several studies replicating this phenomenon in neuroblastoma in the laboratory settings. For example, selection for cisplatin resistance induced cross-resistance to multiple chemotherapeutics and was associated with changes in the EMT expression signature [139], suggesting a fine-tuning of the CSC-associated hybrid E/M phenotype discussed above. Moreover, inducing resistance to molecularly targeted agents, such as BCL-2 and ALK inhibitors, has been also shown to lead to the neuroblastoma MDR (Appendix 3 [14]). Recently, a study investigating the effects of rapid COJEC induction therapy (combination of cisplatin, carboplatin, cyclophosphamide, etoposide, and vincristine) revealed that acquired resistance to COJEC is linked with the acquisition of immature mesenchymal-like phenotype, resembling that of multipotent progenitor cells in the adrenal medulla [53,54,140].

These findings highlight the need to improve current treatment regimens to account for the induction of a dedifferentiated CSC phenotype. For the reasons described above, single-agent therapies targeting fully prevalent stemness in heavily pretreated tumors have a very limited window for success. From the clinical perspective, combining novel anti-CSC approaches with the standard therapy appears as the most viable (and ethically sound) strategy to translate our findings from bench to bedside. Such strategies may involve enhancing the therapeutic index of standard chemotherapy with novel drugs, leveraging synthetic lethality arising from CSC maintenance, and preventing dedifferentiation by blocking pathways associated with CSC self-renewal.

3 DEFINING NOVEL MOLECULAR TARGETS AND THERAPEUTIC APPROACHES

3.1 Combination therapies and precision medicine approaches

Despite advances in available targeted therapies, conventional chemotherapeutics remain a standard component of the first-line therapy for high-risk pediatric tumors [141-143]. While intensified multiagent chemotherapy regimens initially improved survival for high-risk patients, they are associated with significant challenges.

First, in up to half of the high-risk patients, induction or neoadjuvant chemotherapy fails to elicit an adequate tumor response [141,144], leading to relapse and progression of resistant disease. In such case, the initial chemotherapy paradoxically selects for tumor cells with intrinsic or acquired resistance, an effect that can be modelled using patient-derived xenograft (PDX) models [140]. Such relapsed tumor cells are commonly cross-resistant to multiple classes of unrelated anticancer drugs as well as to radiation therapy, effectively limiting available options for successful treatment (Appendix 2 [137], Appendix 3 [14]).

Second, chemotherapy intensification is also associated with significant cytotoxicity and adverse late effects. Some of these chronic toxicities have been well recognized, including various cardiovascular conditions from anthracyclines, neurocognitive late effects caused by platinating agents and vinca alkaloids, gonadal dysfunction due to alkylating agent exposures, or secondary malignancies from topoisomerase inhibitors and alkylating agents (reviewed in Refs [8,145]). In fact, more than one-half of pediatric cancer survivors experience serious cancer therapy-related late effects [146,147]. Thus, there is an increasing need in pediatric oncology to focus not only on finding therapeutic strategies for those patients with high-risk refractory tumors but also on attempts to evaluate innovative personalized and combination strategies to reduce short- and long-term adverse effects and improve the quality of survivorship (**Fig. 1B**).

There is a strong biological rationale and empirical evidence suggesting that combining multiple drugs is likely to be more effective than monotherapy for most pediatric cancers, as combination therapy may help overcome resistance mechanisms through the synergistic interactions of the drugs [148]. Importantly, the synergistic effects of combination therapy can reduce the required dose of each drug, thereby minimizing associated toxicities [149-151]. Metronomic therapy, involving frequent low-dose administration of chemotherapeutic drugs (below maximum tolerated doses) without extended drug-free intervals, has proven promising by allowing the combination of drugs into low-toxicity regimens effective in heavily pretreated children with relapsed solid tumors [152-155].

The combined oral maintenance, biodifferentiating, antiangiogenic therapy (COMBAT) is a low-toxicity 4-drug treatment protocol designed for pediatric patients with relapsed or high-risk solid tumors [152,153]. This therapy combines low doses of an antiangiogenic drug (celecoxib) and cytotoxic agents (etoposide and temozolomide) with differentiation inducers (retinoids and calcitriol) [153]. Compared to maximum tolerated dose-based therapy, COMBAT significantly improved overall survival of pediatric patients with relapsed tumors [153]. The treatment is well tolerated with low acute toxicity, which makes it a viable option for maintenance and salvage therapy even in the modern era of emerging targeted therapies and immunotherapies [153,155]. However, the responses observed in patients treated with COMBAT were not durable, with the majority of patients (60-90%, depending on the diagnosis) eventually succumbing to the disease [153]. This is one of the examples illustrating the need to integrate novel therapeutics into the existing combined, metronomic chemotherapy framework to enhance its efficacy.

Thiosemicarbazones of the di-2-pyridylketone (DpT) class are iron chelators that have shown selective antitumor activity, overcoming chemoresistance *in vitro* an *in vivo* in various adult cancer types [156,157]. Besides chelation of iron and copper ions, which are crucial for tumor cell proliferation [158,159], the DpT thiosemicarbazones induce expression of the metastasis suppressor N-MYC downstream regulated gene-1 (NDRG1) [160] and have been shown to suppress major oncogenic signaling pathways [161-166].

Importantly, thiosemicarbazones have been also found to synergize with several standard chemotherapeutics [167], such as doxorubicin [168], gemcitabine or cisplatin [169], paclitaxel, 5-fluorouracil, methotrexate, and 4-hydroperoxycyclophosphamide [170].

Considering these activities, we investigated the potential of two lead DpT thiosemicarbazones, di-2-pyridylketone-4,4-dimethyl-3-thiosemicarbazone (Dp44mT) and its analog di-2-pyridylketone-4-cyclohexyl-4-methyl-3-thiosemicarbazone (DpC) (**Fig. 6A**), to potentiate the efficacy of the COMBAT protocol for therapy of pediatric solid tumors. In the COMBAT protocol, the cytotoxic agents are administered at different time periods, with etoposide followed by temozolomide, while the antiangiogenic agent, celecoxib, is given throughout the entire course of treatment [153]. Therefore, we focused on assessing the synergistic effects of DpT thiosemicarbazones with these drugs individually in three pediatric tumor cell-types, i.e., osteosarcoma, medulloblastoma, and neuroblastoma (Appendix 11 [171]). Combination index analysis revealed marked synergistic interactions of either DpC or Dp44mT with celecoxib across the examined pediatric tumor types. This synergism correlated with the upregulation of NDRG1, providing the first evidence that DpT thiosemicarbazones induce NDRG1 expression also in pediatric tumor cells (**Fig. 6B**).

Mechanistically, the synergistic effects of DpT thiosemicarbazones with celecoxib were independent of the expression of its target, cyclooxygenase-2 (COX-2), found upregulated in some cases upon thiosemicarbazone treatment (Appendix 11 [171]). Although the mechanism of synergy needs to be fully addressed in future studies, NDRG1 appears as the key candidate. In fact, several downstream molecular targets of celecoxib, including the PI3K/AKT pathway [172], overlap with those affected by the NDRG1-mediated activity of the DpT thiosemicarbazones [173] (Appendix 11 [171]).

In contrast, the interactions of either DpC or Dp44mT with cytotoxic agents, etoposide and temozolomide, showed more variable, likely context-dependent patterns among the pediatric tumor models (Appendix 11 [171]). This may be caused, at least in part, by the effects of the thiosemicarbazones on the molecular targets newly identified in
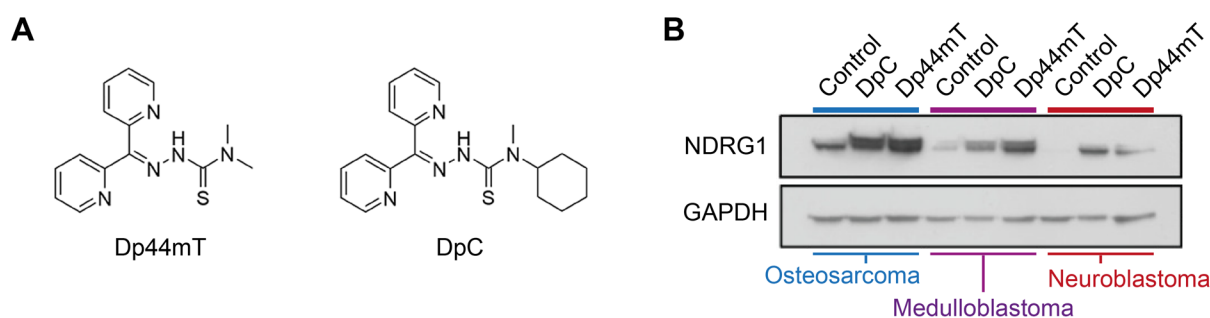
Figure 6. DpT thiosemicarbazones induce NDRG1 epression in various pediatric solid tumors. A) Chemical structures of Dp44mT and DpC chelators. **B**) Representative immonobloting analysis showing significant upregulation of NDRG1 upon treatment with 20µM DpC or Dp44mT in osteosarcoma (SAOS-2), medulloblastoma (Daoy), and neuroblastoma (SH-SY5Y) cells.

our study. We found that the two lead DpT thiosemicarbazone agents: (i) reduce levels of the DNA repair enzyme, O6-methylguanine DNA methyltransferase (MGMT), which is known to inhibit the anticancer activity of temozolomide [174], and (ii) downregulate mismatch repair (MMR) proteins, MSH2, MSH6 and MLH1, which have been also implicated in resistance to temozolomide [175-178]. Interestingly, thiosemicarbazones showed marked synergy in the cell line lacking MGMT protein expression, suggesting the thiosemicarbazones might provide synergistic effects in MGMT-deficient tumors by further promoting MMR machinery inhibition (Appendix 11 [171]). Indeed, inactivation of MMR genes has recently been shown to be associated with temozolomide-induced senescence [178] and increased sensitivity to immunotherapy [179-181], implicating that thiosemicarbazones may have potentially beneficial activity in this context.

In line with the MMR inactivation, by assessing the phosphorylated histone H2AX (γ-H2AX), we demonstrated that nanomolar concentrations of either DpC or Dp44mT induce double strand breaks (DSBs) in DNA across neuroblastoma, medulloblastoma, osteosarcoma, and rhabdomyosarcoma models (Appendix 7 [182]). While these aberrations are known to trigger mitotic catastrophe, leading to cell death or cell senescence [183], further research is needed to determine whether the effects of thiosemicarbazones are durable. Emerging evidence from neuroblastoma [184] and several adult cancers [185] suggest that therapy-induced senescence may, in fact, result in a senescent-like state, where tumor cells acquire a quiescent CSC phenotype, allowing

them to escape therapy and eventually re-enter the cell cycle leading to recurrence of the disease. Thus, senescence induction may act as a double-edge sword, highlighting the importance of further elucidating its complex roles in pediatric tumors. This understanding is key for identifying determinants and markers for tumors that may benefit from combination therapies with senolytics [186].

Etoposide, another cytotoxic agent in the COMBAT protocol, induces DNA DSBs by forming a complex with topoisomerase II (TOP2) and DNA, thereby inhibiting TOP2 and exerting its anticancer effects [187]. Our work in neuroblastoma, osteosarcoma and medulloblastoma models demonstrated that DpC and Dp44mT downregulate the *TOP2 alpha* (*TOP2α*) gene expression at both mRNA and protein levels in all three tumor types (Appendix 11 [171]). Importantly, in case of medulloblastoma cells expressing high levels of TOP2α, thiosemicarbazones showed synergism with etoposide treatment, which indicates that the converging activities of these pharmacologically different types of agents, inhibiting TOP2 by alternative mechanisms (i.e., expression and enzymatic activity), might be therapeutically effective in this setting.

Anthracyclines, another class of potent cytotoxic chemotherapeutic agents widely used in pediatric cancer treatment, are well known for their dose-dependent cardiotoxic side effects, which can lead to heart failure even decades after exposure [188]. In addition to the cardiotoxicity, limiting the maximum cumulative dose, emergence of chemoresistance is a major reason for the failure of anthracycline therapy [189]. One of the main mechanisms is associated with the acquisition of MDR due to the overexpression of drug efflux pumps of the ABC family, such as the *ABCB1* gene encoding P-glycoprotein (Pgp; a.k.a. multidrug resistance protein 1 (MDR1)) [189]. Besides active efflux of the drugs from tumor cells, ABC transporters also contribute to another mechanism underlying chemotherapy resistance, termed lysosomal sequestration. It is well known that hydrophobic weak-base drugs, such as anthracyclines, accumulate in the lysosomes, which impedes the sequestered drugs from acting against their intracellular targets [190,191]. One of the reasons why lysosomal sequestration is more pronounced in MDR cells may arise from the overexpression of the ABC transporters. It has been shown that

Pgp may become inverted during endocytosis, leading to the enhanced accumulation of Pgp substrates, like anthracyclines, within lysosomes, effectively trapping these drugs and preventing them from reaching their nuclear targets [192]. DpC and Dp44mT, also Pgp substrates, follow a similar trapping mechanism in the MDR cells. However, thiosemicarbazones can bind copper, leading to the generation of reactive oxygen species (ROS) that cause lysosomal membrane permeabilization [159]. This releases trapped anthracyclines and restores their cytotoxic effects [168]. It was suggested that combining anthracyclines with thiosemicarbazones could be particularly effective in MDR cells with high Pgp expression [168,193].

Exploring the potential of this strategy for overcoming MDR in pediatric tumors, we found that DpC and Dp44mT were synergistic with anthracyclines (doxorubicin, daunorubicin, and mitoxantrone) in osteosarcoma, neuroblastoma, and medulloblastoma models (Appendix 7 [182]). However, the mechanism of synergy was independent of Pgp expression. Fluorescence microscopy also did not reveal any significant accumulation of doxorubicin in the lysosomal compartment, as most of the doxorubicin autofluorescence signal localized in the cell nucleus. These findings rejected the inhibition of lysosomal sequestration as the mechanism of thiosemicarbazone-mediated synergistic effects in anthracycline-treated pediatric tumor cells. In contrast, we found that thiosemicarbazones downregulate expression of checkpoint kinase 1 and 2 (CHK1 and CHK2), revealing a previously unrecognized mode of synergistic interaction between anthracyclines and thiosemicarbazones (Appendix 7 [182]). DNA-damage induced cell death by mitotic catastrophe requires overriding the cell cycle checkpoints, which may be therapeutically exploited to sensitize tumor cells to DNA-targeted chemotherapeutics by pharmacological inhibition of the checkpoint regulators, including CHK1 and CHK2 [194-196]. We show that DpT thiosemicarbazones act as CHK1/CHK2 inhibitors, providing additional evidence for their newly recognized synergistic interaction with DNA-damaging agents by sensitizing tumor cells to mitotic catastrophe (Appendix 7 [182]).

As suggested by its name, NDRG1 is suppressed at the transcriptional level by transcription factor N-MYC, a major driver of high-risk neuroblastoma. N-MYC binds to

the *NDRG1* promoter in an MIZ-1-dependent manner and effectively downregulates NDRG1 expression [197,198]. Importantly, NDRG1 was found to be a positive prognostic factor in neuroblastoma, regardless of the *MYCN* amplification status [197]. In addition to its role as a marker of N-MYC dysregulation in neuroblastoma, this suggests a functional role of NDRG1 on its own [197].

Given the capacity of thiosemicarbazones to induce NDRG1 expression in pediatric tumor cells, including neuroblastoma cells [171], we decided to investigate the molecular effects of the leading, clinically trialed DpC as single agent in neuroblastoma cells. Marked NDRG1 upregulation upon DpC treatment was consistently detected in four neuroblastoma cell lines, and it was associated with a significantly decreased expression of N-MYC in *MYCN*-amplified and c-MYC in *MYCN*-nonamplified models (Appendix 8 [199]). These findings indicated that DpC-mediated inhibition of MYC proteins alleviates the suppression of NDRG1, further promoting NDRG1 upregulation and neuroblastoma cell death. This is in line with another study, showing that *MYCN*-amplified neuroblastoma cells rely on upregulated iron uptake and are highly sensitive to iron chelation by deferoxamine (DFO) [200]. N-MYC was found to bind to E-box sites in the promoter of *TRFC* gene, thus upregulating the encoded transferrin receptor-1 (TFR1) responsible for iron import [200,201]. Similar changes were observed following c-MYC overexpression, suggesting both MYC proteins generally promote iron accumulation by altering the expression of genes regulating iron uptake [200].

While iron is a well-known contributor to increased cancer proliferation and survival, it is also a major source of ROS production through the Fenton reaction [202,203]. Iron accumulation, therefore, imposes increased demands on ROS detoxification systems to sustain cell survival. Indeed, several studies have demonstrated that MYC-driven neuroblastomas overexpress cystine/glutamate-exchange transporter Xc−, which imports cystine as a precursor for glutathione synthesis, and they heavily depend on glutathione peroxidase 4 (GPX4), a powerful cellular ROS scavenger that utilizes glutathione to directly prevent lipid peroxidation [200,201,204]. Inhibition of cystine uptake and/or GPX4 in MYC-driven neuroblastoma cells results in ferroptosis [200,201,204], a new form of

regulated, iron-dependent cell death driven by lipid peroxidation and insufficient capacity to eliminate lipid peroxides [205]. Thus, the intricate link between the newly recognized addiction on iron and cysteine provides synthetic lethal targets in high-risk neuroblastoma overexpressing N-MYC or c-MYC proteins. Of note, our study showed that iron chelation by DpC leads to activation of oxidative stress response and accumulation of lipid droplets in neuroblastoma cells (Appendix 8 [199]). It is yet to be determined whether these effects are related to iron deficiency-induced mitochondrial stress [206], the ability of DpC to form copper complexes that potently generate ROS [168], or other unrecognized mechanism.

Besides downregulating MYC proteins, DpC was found to inhibit oncogenic EGFR signaling across multiple neuroblastoma cell lines (Appendix 8 [199]). Mechanistically, these effects were mediated in a NDRG1-dependent manner, pointing to the potential of thiosemicarbazones to enhance the efficacy of tyrosine kinase inhibitors (TKIs) in pediatric cancers. Indeed, receptor tyrosine kinases (RTKs) have been demonstrated as druggable targets in relapsed or refractory childhood solid tumors [207] (Appendix 13 [208]).

Recent studies evaluating precision-guided therapy in pediatric cancers most often rely on whole-genome and whole-transcriptome sequencing for target identification [25,26]. While mutant RTKs, serin/threonine kinases and other signaling molecules are among the most often identified druggable targets, the DNA/RNA-based approaches are agnostic to aberrations in cell signaling that are caused at the protein level, including protein translation, posttranslational modifications, and degradation. For that reason, we have established a phosphoproteomic-based approach. Using commercially available phosphoprotein arrays, this approach allows rapid analysis of phosphorylated RTKs and other signaling molecules in tumor tissues to identify potential therapeutic targets in individual patients (Appendix 13 [208]). This phosphoproteomic analysis has already proven to be informative for precision medicine by guiding treatment assignment in refractory pediatric tumors [207,209,210].

We have adopted the phosphoprotein arrays to assess the basal activity of prooncogenic RTKs in cell lines derived from various pediatric solid tumors, allowing us

to pinpoint major TKI targets (Appendix 6 [211]). To address the potential of combining thiosemicarbazones with TKIs, we further examined interactions of DpC and Dp44mT with sunitinib, gefitinib, and lapatinib. We found that the simultaneous treatment with thiosemicarbazones potentiates the anticancer activity of the selected TKIs across the examined tumor subtypes, comprising neuroblastoma, medulloblastoma, osteosarcoma, and rhabdomyosarcoma models. TKIs inhibited activation of their corresponding RTKs, while thiosemicarbazones further reduced the expression of several RTKs, including EGFR, PDGFRβ, and IGF-1R. This study also revealed upregulation of NDRG1 as a recuring response identified upon combined treatment (Appendix 6 [211]), suggesting NDRG1 as a candidate therapeutic target in pediatric solid tumors, although further investigation into its function is needed.

Overall, our results provide a strong rationale for combining iron-chelating agents with targeted small molecule inhibitors or standard chemotherapeutics for enhancing treatment of pediatric solid tumors. However, it remains unclear whether the DpT thiosemicarbazones have favorable profiles for translating these strategies into clinical practice or if alternative clinically trialed or FDA-approved iron chelators will be more suitable [212]. Although DpC entered a Phase I clinical trial (NCT02688101), there has been no progression to further phases since its completion in 2017.

3.2   Mitochondria-targeted therapeutic approaches

Over the last more than 10 years, mitochondria have been reinstated as attractive targets for cancer therapy, as their role in regulating traits of MDR- and CSC-like cells has become apparent (Appendix 12 [130]). Indeed, mitochondria are now recognized as organelles integrating many vital cellular processes, ranging from metabolism, immune regulation, cell signaling, and cell death to regulation of stem cell identity in development and cancer [130,213,214]. Conversely, many of these mitochondrial functions have been identified as promising targets for enhancing anticancer therapy and eliminating CSCs (**Fig. 7**).
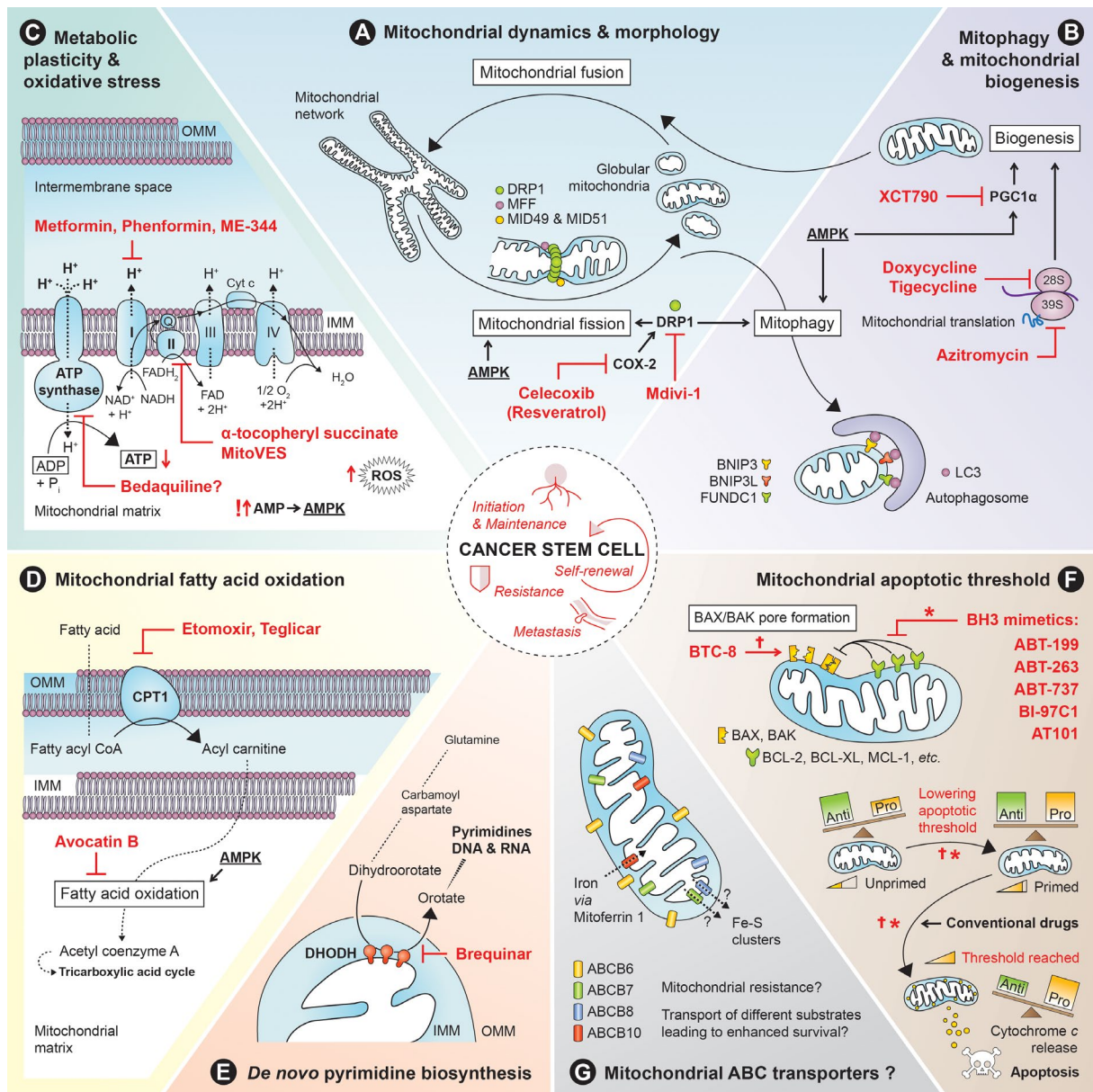
Figure 7. Illustration of therapeutic strategies targeting mitochondrial functions in CSCs. Potential therapeutic interventions (mitochondria-targeted drugs highlighted in bold red) against CSCs include: (**A**) modulating mitochondrial dynamics and morphology; (**B**) blocking mitochondrial autophagy (mitophagy) and biogenesis; (**C**) limiting metabolic plasticity and promoting oxidative stress (e.g., ROS generation); (**D**) inhibiting mitochondrial fatty acid oxidation; (**E**) suppressing *de novo* pyrimidine biosynthesis; (**F**) decreasing the mitochondrial apoptotic threshold to sensitize mitochondria to apoptosis; and (**G**) targeting mitochondrial ABC transporters and mitochondrial iron trafficking. For details, refer to Appendix 12 [130]. CPT1, carnitine palmitoyltransferase type 1; DHODH, dihydroorotate dehydrogenase; DRP1, dynamin-related protein 1; IMM, inner mitochondrial membrane; MFF, mitochondrial fission factor; MID49 and MID51, mitochondrial dynamics protein of 49- and 51-kDa; LC3, microtubule-associated protein 1 light chain 3; OMM, outer mitochondrial membrane. Adopted from Skoda et al. (Appendix 12 [130]).

Mitochondria are highly dynamic, continuously balancing between fragmented globular organelles and a fused tubular mitochondrial network. Mitochondrial dynamics, mitochondrial fission and fusion, is particularly critical for all mitochondrial functions and has been recently demonstrated as a major regulator of stem cell fate [213,215] (Appendix 12 [130]). The fused mitochondrial network usually shows a uniform, high mitochondrial membrane potential [216]. In contrast, mitochondrial fission produces more variation in the fragmented mitochondria, allowing the clearance of dysfunctional or damaged mitochondria via mitophagy, a selective form of autophagy, and maintaining the pool of healthy mitochondria for distribution into daughter cells [216].

Importantly, mitochondrial physiology is significantly affected by interactions of mitochondria with other organelles, namely with endoplasmic reticulum (ER). ER forms close physical contacts with mitochondria via mitochondria-associated ER membranes (MAMs; alternatively termed ER-mitochondria contacts, ERMCs) and plays a crucial role in mitochondrial fission, calcium (Ca^{2+}) transfer, and lipid biosynthesis and trafficking (**Fig. 8**) [217,218]. ER tubules associate with mitochondria and help define the sites of fission. Actin polymerization driven by ER-bound inverted formin 2 (INF2) generates force via myosin, leading to the initial constriction of mitochondria, which further promotes dynamin-related protein 1 (DRP1) oligomerization and DRP1-dependent constriction (**Fig. 8A**) [217].

Ca^{2+} is crucial for communication between ER and mitochondria, and its transfer to mitochondria promotes ATP production by favoring the enzymatic activity of key rate limiting dehydrogenases of the tricarboxylic acid cycle and the electron transport chain [218]. However, excessive mitochondrial transport may result in mitochondrial Ca^{2+} overload, leading to opening of the mitochondrial permeability transition pore (mPTP), rupture of the OMM and apoptosis initiated by cytochrome c release [219]. Thus, maintenance of Ca^{2+} homeostasis mediated by MAMs is essential for cell survival. Conversely, this mechanism may be prone to hijacking to sustain tumorigenesis, as the rewiring of Ca^{2+} signaling has been associated with various cancers, likely contributing to their chemoresistance [219].
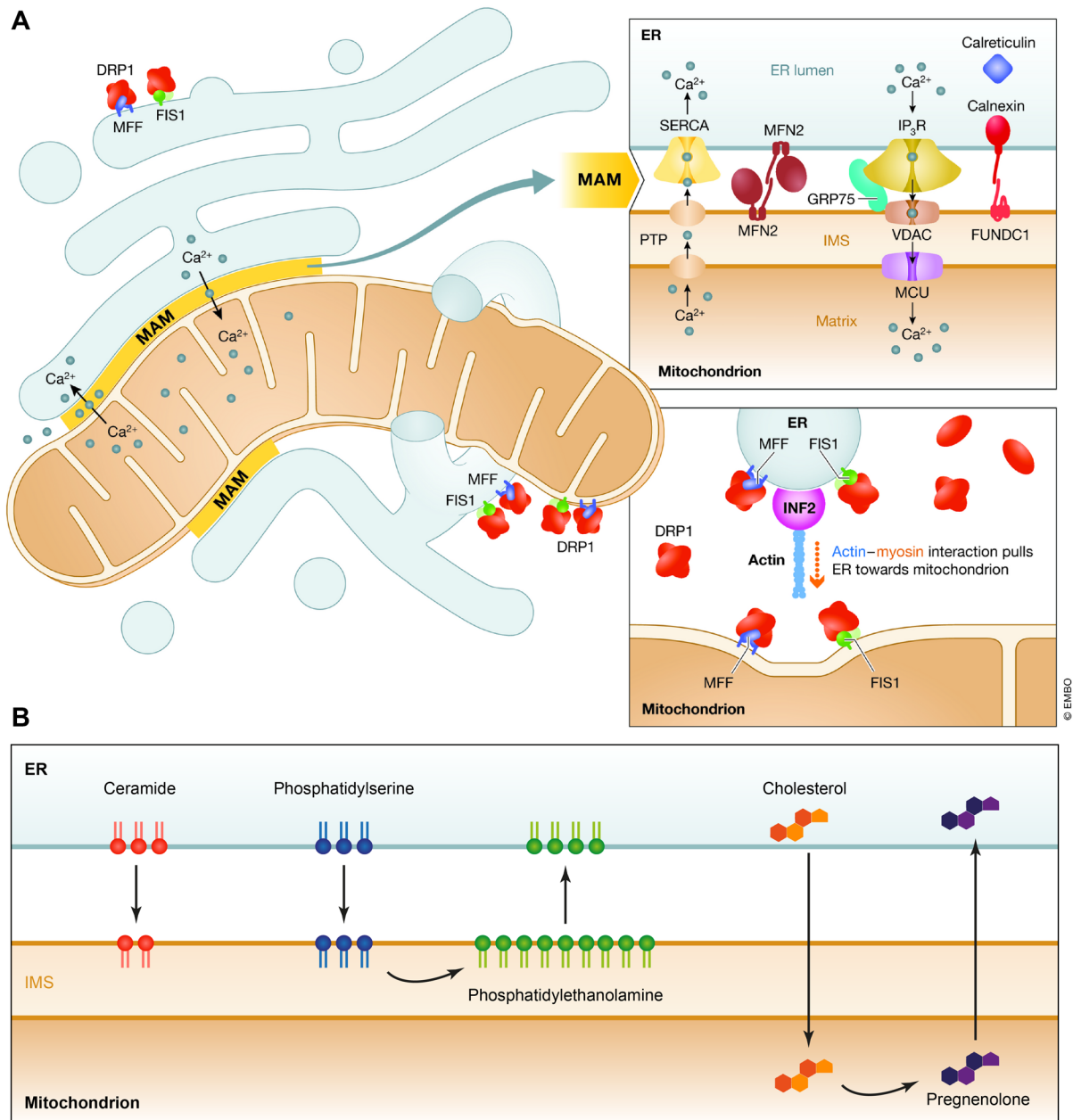
Figure 8. ER-mitochondria crosstalk. A) MAMs are enriched with mitochondria-specific proteins such as mitofusin (MFN) 1/2 and other tethering proteins, including glucose-regulated protein 75 (GRP75) and FUN14 domain-containing protein 1 (FUNDC1), which stabilize the MAM structure. Two crucial roles of MAMs are schematically illustrated: (i) facilitating efficient Ca^{2+} homeostasis between the ER and mitochondria and (ii) regulating mitochondrial dynamics. Refer to the main text and Ref [217] for further details. FIS1, mitochondrial fission 1 protein; MFF, mitochondrial fission factor. Adopted from Ref [217], reproduced with permission from Springer Nature. **B**) A schematic illustration of MAM-mediated lipid trafficking between ER and mitochondria. Major lipid species are depicted according to Ref [220]. Refer to the main text for further information.

Ca^{2+} is released from the ER through the inositol 1,4,5-trisphosphate receptor (IP3R), and subsequently taken up by mitochondria via the mitochondrial calcium uniporter (MCU). In the reverse process, Ca^{2+} is released from mitochondria through the mPTP, and is then reabsorbed by the ER through the sarco/endoplasmic reticulum Ca^{2+}-ATPase (SERCA) (**Fig. 8A**). Interestingly, impaired transfer of ER-derived Ca^{2+} to mitochondria and increased levels of cytosolic Ca^{2+} can influence dynamin activity, stimulate DRP1 translocation to mitochondria, and promote mitochondrial fission [217].

MAMs are also crucial sites of lipid transfer, maintaining the OMM lipid composition (**Fig. 8B**). The ER serves as the main organelle for bulk lipid synthesis and distribution. Mitochondria rely on lipid transfer from MAMs, including sphingolipids, which cooperate with proapoptotic proteins BAK and BAX to promote MOMP and cytochrome c release [221,222]. Ceramides appear to be the most important sphingolipid species involved in the regulation of apoptosis [222]. Ceramide in the OMM facilitates the oligomerization of BAK and/or BAX [223] and its production by sphingomyelinase targeted to mitochondria, but not to other organelles, leads to cell death [224]. In fact, ceramides have been linked with several forms of programmed cell death in cancer, including apoptosis, ferroptosis, autophagy-regulated cell death and necroptosis (see Ref. [225]). Sphingomyelin hydrolysis is a rapid pathway for ceramide production. Sphingomyelinases are found present in various compartments, including MAMs, and are often downregulated in cancer [225,226]. A recent lipidomics study found that early apoptosis is marked by increased sphingomyelinase activity in MAMs, leading to higher ceramide levels at mitochondria and reduced sphingomyelin in MAMs [222]. These data suggest that MAMs are crucial regulators of appropriate sphingolipid transfer necessary for the executive phase of apoptosis.

Following the finding that neuroblastoma MDR is mediated by repressed BAK/BAX activation unrelated to other significant changes in BCL-2 protein machinery [135], we focused on elucidating the underlying mechanism. To assay the apoptotic

sensitivity, we isolated heavy membrane fractions enriched with mitochondria and measured cytochrome c release upon incubation with BH3-only peptides that directly activate BAX and BAK, i.e., truncated BID (tBid) or the death-activating BH3 domain peptide of BIM (BimBH3) (Appendix 3 [14]). This assay efficiently bypasses the effects of drug transport, target engagement, metabolism and transcriptional response.

By applying this approach in seven patient-matched neuroblastoma cell line pairs, we demonstrated that majority of post-therapy tumors (6/7) show attenuated apoptotic signaling at mitochondrial level (Appendix 3 [14]). This renders neuroblastoma cells resistant to various unrelated classes of drugs, including BH3 mimetics, which displace proapoptotic BH3-only proteins from being sequestered by antiapoptotic BCL-2 proteins. Importantly, the same mitochondria-mediated MDR can be induced *in vitro* by selecting for resistance to targeted drugs, as demonstrated with the ALK inhibitor crizotinib. As a result, attenuated mitochondrial signaling that arises in response to therapy *in situ* may confer cross-resistance to chemotherapy, radiotherapy, and molecularly targeted drugs, even without prior selective pressure (Appendix 3 [14]).

Unexpectedly, by interrogating mitochondrial dynamics and physiology, our study revealed that attenuated apoptotic signaling correlates with decrease in the number of MAMs and their proximity to mitochondria, as detected by electron microscopy image analysis. Importantly, post-therapy neuroblastoma cells with depleted MAMs had significantly reduced ceramide levels. Depletion of mitofusin 2 (MFN2), a protein involved in the ER-mitochondria tethering, or inhibiting neutral sphingomyelinase in therapy-sensitive models phenocopied MDR observed in matched post-therapy counterparts. Reduced Ca^{2+} transfer was observed in some but not all resistant cells. However, inhibiting Ca^{2+} transfer did not attenuate apoptotic signaling, pointing to the key role of ceramide in MOMP and apoptosis induction. Together, we identified MAMs as physiologic regulators of apoptosis via ceramide transfer and uncovered a previously unrecognized mechanism for cancer MDR (Appendix 3 [14]). This work provides a novel framework for testing interventions to prevent emergent resistance or restore mitochondrial competence by modulating sphingolipid, namely ceramide, transfer in resistant tumors.

A pertinent aspect of the MYC-driven transcription is that it directly promotes mitochondrial biogenesis and function [227-229], highlighting mitochondria as potentially vulnerable therapeutic targets in high-risk neuroblastoma. To explore mitochondria-targeted approaches to overcome apoptotic insensitivity in MDR neuroblastoma, we used well-characterized matched (pre-therapy vs post-therapy) *MYC*-amplified cell line pair for screening drugs that inhibit various mitochondrial processes (**Fig. 9**) (Appendix 2 [137]). Despite their attenuated apoptotic signaling and the MDR phenotype, post-therapy neuroblastoma cells remained sensitive to mitochondria-targeted agents. Notably, one of the effective drugs was an FDA-aproved antibiotic, doxycycline, which is known to inhibit mitochondrial translation by binding to mitochondrial ribosomes (mitoribosomes) due to their structural similarity with bacterial ribsosomes [230]. At concentrations that show clinically safe profile even in young children [231,232], doxycycline elicited marked cytotoxic effects in neuroblastoma cells regardless of their MDR state (Appendix 2 [137]). This effect was further validated in a *MYCN*-amplified neuroblastoma pair, suggesting the mitoribosomal processivity as a shared vulnerability in high-risk neuroblastoma.
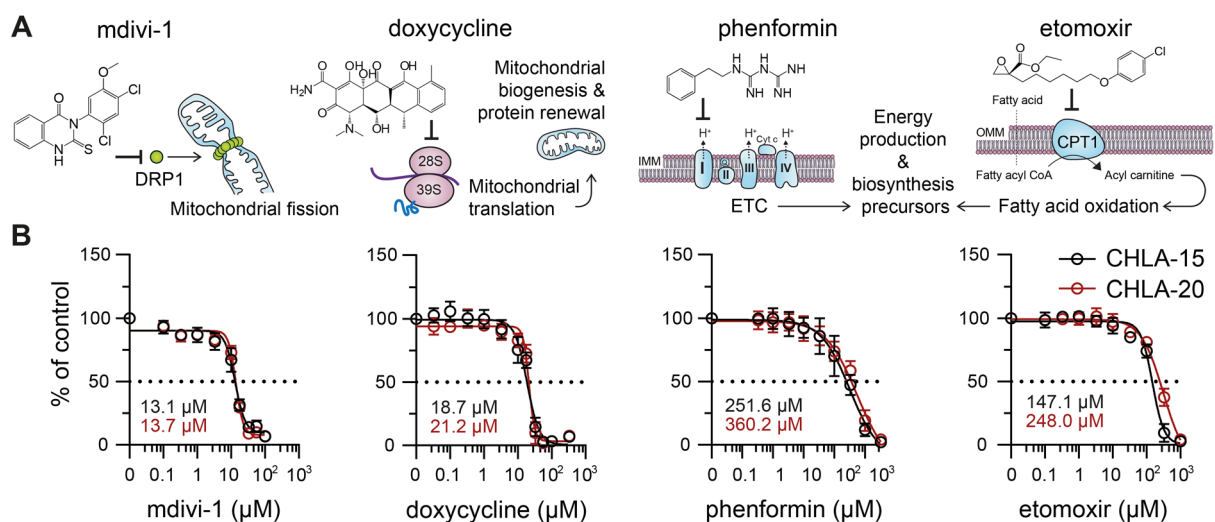

Figure 9. MDR neuroblastoma cells retain sensitivity to mitochondria-targeted drugs. A) A schematic illustrating the mechanisms of action of selected mitochondrial inhibitors. **B**) Therapy-naïve CHLA-15 (black) and MDR post-therapy CHLA-20 (red) neuroblastoma cells showed similar sensitivity to mitochondrial drugs (calculated IC_{50} values are indicated). MTT assay data are presented as mean ± SD, biological n ≥ 3, technical n = 3. Adopted from Borankova et al. [137]

Out of ~1,500 human mitochondrial proteins, only 13 proteins–all crucial components of the reparatory chain complexes–are encoded in the mitochondrial DNA (mtDNA) and synthesized at mitoribosomes in the mitochondrial matrix [233]. The rest, including mitochondrial ribosome proteins and translation factors, is transcribed from nuclear DNA and imported to mitochondria after synthesis at cytosolic ribosomes. Imbalance between mtDNA- and nuclear DNA-encoded mitochondrial proteins leads to mitochondrial dysfunction [234]. However, mitochondria do not encode stress-response genes and mitochondrial response to stress heavily relies on modulation of expression of nuclear-encoded mitochondrial and mitochondria-associated proteins [234]. Hence, stress signals from perturbed mitochondria must be efficiently relayed to cytosol and nucleus to orchestrate mitochondrial, and thus cellular homeostasis. In mammalian cells, mitochondrial stress principally converges on the integrated stress response (ISR) [235-238]. The ISR is an adaptive pathway mediated through the inhibiting phosphorylation of eukaryotic translation initiation factor 2 alpha (eIF2α). This attenuates global cap-dependent protein synthesis in favor of mRNAs with upstream open reading frames, such as the key ISR effectors, transcription factors ATF4 and CHOP [239]. ATF4 and CHOP then induce expression of cytoprotective genes to restore cellular homeostasis [239] and/or mitochondrial function [240,241]. However, when the ISR capacity is overwhelmed, the very same pathway leads to cell death [239].

Recently, the inner mitochondrial membrane (IMM) metalloprotease OMA1 has been identified as the major upstream regulator of retrograde signaling cascade that relays mitochondrial stress to the ISR [235,236]. Our mechanistic studies revealed that doxycycline-mediated inhibition of mitoribosomes dramatically reduced levels of mtDNA-encoded proteins, causing a mitochondrial protein imbalance and inducing mitochondrial stress, which was reflected in heavily fragmented/aberrant mitochondrial morphology and loss of mitochondrial membrane potential, priming mitochondria for apoptosis (Appendix 2 [137]). Importantly, this mitochondrial stress activated the ISR via OMA1-mediated pathway, leading to the phosphorylation of eIF2α, and synthesis of the ISR effectors ATF4 and CHOP. Interestingly, further analysis showed that these

mitochondrial ISR responses were consistent across neuroblastoma models, leading to downregulation of N-MYC/c-MYC proteins prior to neuroblastoma cell death.

Both N-MYC [242] and c-MYC [243] are known to have rapid turnover and are degraded through proteasome-dependent mechanisms with half-lives shorter than 1 hour. Our findings demonstrate that the activation of ISR upon mitochondrial stress favors rapid proteasomal degradation of MYC proteins, which is linked with neuroblastoma cell death. Restoring cap-dependent translation with the ISR inhibitor ISRIB rescued both the expression of MYC proteins and neuroblastoma cell viability. Using neuroblastoma models with tunable *MYCN* expression we demonstrated that overexpression of MYC proteins, found very common in high-risk tumors, is sensitizing neuroblastoma cells to cell death induced by mitoribosome inhibition. These results were also validated by a doxycycline-unrelated ribosome-targeting antibiotic, chloramphenicol.

To conclude, we identified mitoribosomes as a novel synthetic lethality target in MYC-driven neuroblastoma (**Fig. 10**). These findings open new avenues for targeting high-risk MDR tumors and warrant further investigation in preclinical *in vivo* studies. Our data from various tumor and non-tumor cell types provide evidence supporting a potentially promising therapeutic window for these mitoribosome-targeted approaches, as they confirm the high selectivity of rapid mitoribosomal inhibition-induced cell death, which was limited to neuroblastoma cells with supraphysiological levels of MYC proteins. A recent report suggested that MYC-driven tumors rely on enhanced ISR activity to prevent MYC-induced cell death [244]. However, the dual role of ISR and the identified regulatory networks imply that MYC-driven tumors might be primed to treatments that further promote the ISR, shifting its activity towards apoptosis. Indeed, the ISR overstimulation by ATF4 agonists [245] or proteasome inhibitors [246] has been shown synthetically lethal in MYC-driven neuroblastoma. Taken together, our work expands on these findings, indicating that mitoribosomal inhibition can be an approach to leverage ISR-related vulnerability while overcoming multidrug resistance (MDR) resulting from reduced sensitivity to apoptotic signaling at the mitochondria.
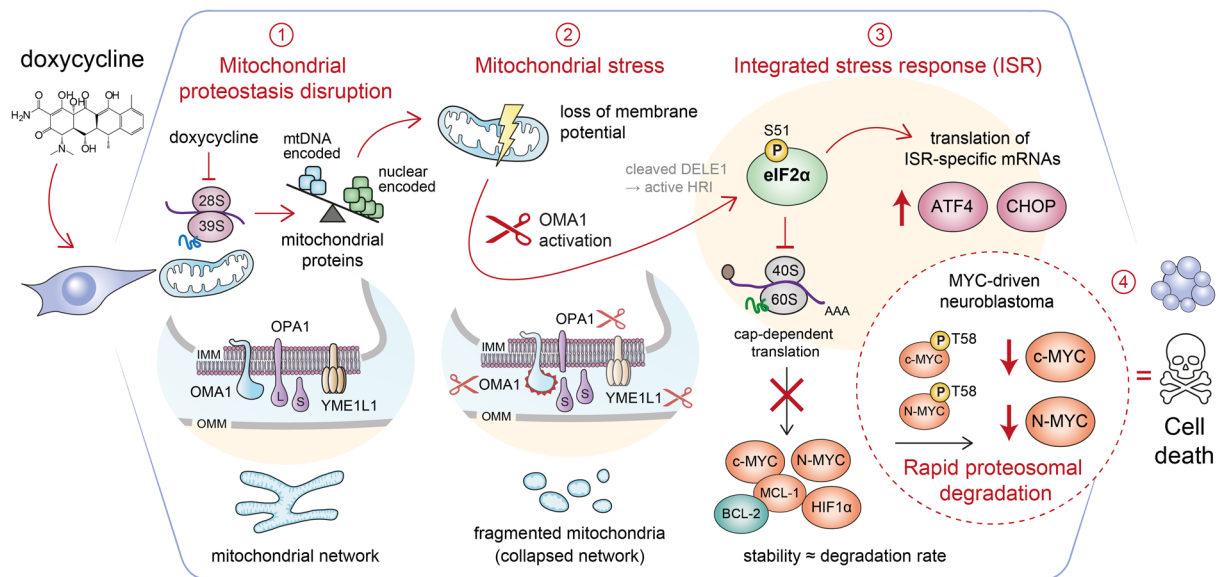
Figure 10. A schematic illustration of the synthetic lethal effects induced by mitoribosome inhibition in MYC-driven neuroblastoma. Blocking mitochondrial ribosomes with doxycycline disrupts mitochondrial proteostasis (1), leading to mitochondrial stress that activates OMA1 (2), which results in a collapse of the mitochondrial network and triggers the ISR (3), downregulating key short-lived proteins and sensitizing MYC-driven neuroblastoma to cell death (4) [137]. Adapted from Borankova et al. [137].

3.3 Target discovery guided by single-cell reconstruction of developmental trajectories

As described above, neuroblastoma is a pediatric malignancy characterized by an extremely heterogenous clinical manifestation. Accurate risk assessment is essential for selecting the optimal treatment strategy for each patient to maximize outcomes while minimizing toxicity and the long-term impact on quality of life [51]. While neuroblastoma risk classifiers have been evolving [10], biological understanding of some of the incorporated markers remains limited. For instance, exploring the impact of chromosome aberrations associated with poor neuroblastoma prognosis is an active area of research. Recently, gains of chromosomes 17q and 1q (found in up to 65% of neuroblastoma tumors [247]) have been shown to promote neuroblastoma initiation by potentiating immature neural crest progenitor phenotypes in a human neural crest model [248]. These early aneuploidization events likely lead to prolonged clonal evolution, underlying the development of highly aggressive neuroblastomas [247].

Neuroblastoma arises anywhere along the sympathetic nervous system, forming tumors localized in the adrenal medulla (≥ 50% of cases) and sympathetic ganglia [48,51]. Given the early onset of the disease, neuroblastoma initiation is thought to result from impaired/aberrant differentiation of neural crest cells (NCCs) and their derivatives that are produced during sympathoadrenal development [48,51,249]. Due to the limited understanding of the sympathoadrenal differentiation, the identification of neuroblastoma cell-of-origin has long remained largely elusive. Major discoveries from Igor Adameyko's group and recent single-cell RNA sequencing (scRNA-seq) studies shed new light on the NCC differentiation and provided state-of-the-art tools to study developmental processes at a single-cell level. In their seminal works [250-252], Adameyko and colleagues discovered that numerous neural crest-derived cell types, previously thought to originate directly from NCCs, are produced by NCC-derived multipotent progenitors, known as Schwann cell precursors (SCPs) (reviewed in Ref [253]).

During embryonic development, SCPs settle on developing nerves that guide them to different distant regions where they were found to give rise to various cell types and tissues, including chromaffin cells of adrenal medulla [254] or a portion of sympathetic nervous system [253,255]. The differentiation plasticity of SCPs is striking and seems to be dependent on local stimuli in a particular region, providing developing tissues and organs with necessary cell types [253,256]. Importantly, it has been shown that formation of adrenal medulla, the most common site of neuroblastoma, requires recruitment of SCPs that transiently proliferate and differentiate into chromaffin cells through a specific cell population, termed bridge cells [254]. Recently, two independent scRNA-seq studies revealed that SCPs give rise not only to chromaffin cells but also to sympathoblasts, making SCPs universal precursors of adrenal medulla formation (**Fig. 11**) [53,54].

By projecting individual cells of developing adrenal medulla according to their gene expression profiles, scRNA-seq data analysis allows reconstruction of differentiation trajectories that visualize distinct cell clusters, reflecting different cell types and potential transitions between them during adrenal gland development. These trajectories provide very useful resource to study neuroblastoma. As demonstrated by several recent studies,

expression profiles of neuroblastoma tumors relate to programs characteristic of various stages of normal sympathoadrenal development [53-55,257,258]. Interestingly, projecting high-risk/*MYCN*-amplified neuroblastoma tumors onto differentiation trajectories revealed their close similarity to the expression profiles of more primitive, undifferentiated progenitors – bridge/connecting progenitor cells [53] or multipotent SCPs [55]. While low-risk neuroblastomas comprise higher numbers of cells that transcriptionally match late neuroblasts, the proportion of undifferentiated tumor cells, resembling bridge cells, is elevated in high-risk tumors and advanced stage disease [53]. These findings demonstrate that developmental (cluster-specific) programs can infer neuroblastoma prognosis, suggesting their clinical importance and potential for unraveling neuroblastoma heterogeneity.
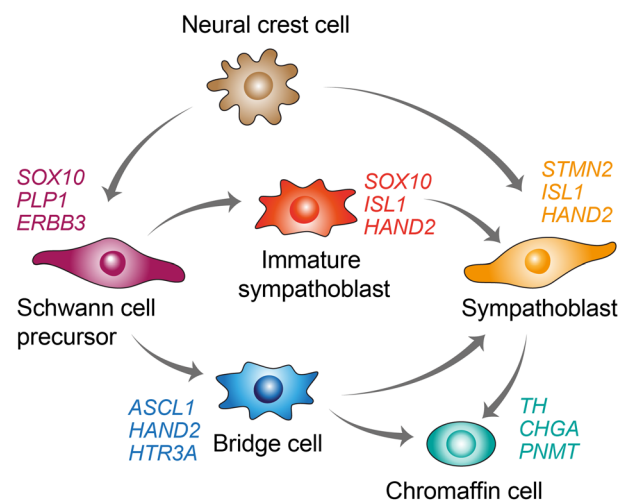

Figure 11. Normal sympathoadrenal lineage development in humans. A schematic summarizing current understanding of the differentiation trajectories during healthy adrenal gland development identified by scRNA-seq [53,54,75]. Note that SCPs can differentiate into both chromaffin cells and sympathobasts via transient cell states. Cluster-specific genes are indicated.

In the pioneering study, the serotonin receptor *Htr3a* was identified as a selective marker of bridge cells [254], indicating its important role in adrenal gland development. Indeed, Kameneva and colleagues recently demonstrated that serotonin signaling acts as a negative regulatory feedback loop controlling cell dynamics in the developing adrenal

medulla in mice (Appendix 4 [75]). Chromaffin cells, which arise directly from *Htr3a*-positive bridge cells, produce and secrete serotonin. It has been demonstrated that increased serotonin levels, in turn, activate *Htr3a* at bridge cells, leading to prolongation of the cell cycle and reduced proliferation. This implies that serotonin signaling functions as a feedback mechanism that prevents excessive proliferation of bridge cells, and thus chromaffin tissue overgrowth (Appendix 4 [75]).

Expanding on these findings, we interrogated the role of (human) HTR3A in neuroblastoma. Our results revealed that aggressive neuroblastoma cells overexpress HTR3A at both mRNA and protein levels. HTR3A^{high} neuroblastoma cell lines showed a significantly enhanced tumor-initiating capacity compared with their HTR3A^{low} counterparts, indicating that HTR3A expression is associated with stem cell-like traits resembling those of more undifferentiated progenitors. Consistent with the effects observed in normal bridge cells, we demonstrated that HTR3A^{high} neuroblastoma cells are highly responsive to HTR3A agonists, which effectively block their proliferation (Appendix 4 [75]), suggesting potential implications for novel combination therapies in neuroblastoma.

Collectively, recent scRNA-seq studies offer crucial insights into the functional parallels between adrenal gland development and neuroblastoma. Importantly, our study on HTR3A was the first to investigate candidate targets, inferred from scRNA-seq-based developmental trajectories, at the protein level to explore their biological relevance for neuroblastoma (Appendix 4 [75]). This work provides proof-of-concept evidence for utilizing recently generated scRNA-seq datasets for data-driven discovery of novel therapeutic targets. Finally, our recent results (unpublished) suggest that these may also be useful for identification of novel risk stratification markers that could be assessed by IHC and potentially integrated into improved protocols for neuroblastoma management.

4 FUTURE DIRECTIONS

Most cancer deaths are caused by progression of therapy-resistant disease. Although MDR may arise through various mechanisms, largely overlapping with mechanisms driving cancer stemness, our research has highlighted the role of mitochondria as key downstream regulators of the cell response to therapy.

Identification of the novel mitochondria-mediated mechanism of MDR raises important questions about the future directions of pediatric oncology research. A key consideration from these findings is that drugs developed to target molecules, structures, and pathways upstream of mitochondria may not always be effective, particularly in heavily pretreated tumors. Reduced sensitivity to apoptotic signals, regardless of the underlying mechanisms, may mask the pharmacological effects of newly developed drugs and compromise the results of Phase II/III clinical trials. From this perspective, combination therapies with standard treatment regimens present an ethically sound strategy of trialing novel molecularly targeted drugs in pediatric cancer patients. This is in line with the recently established international consensus [148]. Exploring agents that would block processes related to therapy-induced dedifferentiation could be particularly valuable in this setting for targeting emergent CSC phenotypes that drive tumor relapse.

Targeting mitochondria has emerged as a promising approach to overcoming therapy resistance in cancer, as exemplified by the identified mitoribosomal synthetic lethality in MDR neuroblastoma. Our results establish a foundation for testing novel selective anticancer drugs, as well as for the potential repurposing of many FDA-approved antibiotics and other drugs that perturb mitochondria. Additionally, attention should be directed towards better understanding of lipidomics in the context of MAMs and drug resistance. Investigating regulators of lipid trafficking, particularly ceramide transport, could reveal potential strategies to prevent MDR or resensitize refractory tumors.

Furthermore, expanding the understanding of developmental programs and regulatory networks is key for identifying effective targets for anti-CSC therapy. It is important to clearly distinguish functional regulators of stemness from mere bystanders, ensuring that anti-CSC strategies truly leverage vulnerabilities associated with molecular drivers of cancer stemness. An important challenge for future CSC research will be to incorporate *in vivo* models that more faithfully recapitulate immune interactome within the TME. Humanized NSG and other advanced humanized mouse models [259] are already available and may serve as effective tools for studying CSC-immune cell interactions and devising CSC-targeted immunotherapies.

Finally, employing rapidly evolving single-cell and spatial omics technologies to compare healthy development with neoplastic growth can open new avenues for targeting pediatric solid tumors. Currently, reducing the complexity of scRNA-seq data represents an exciting research opportunity for advancing clinical management of neuroblastoma. After all, while it is the big data that shapes our understanding of pediatric tumors, it is the key experimentally validated markers and targets that will guide the assignment of patient-tailored therapies.

5 REFERENCES

1. Bhakta N, Force LM, Allemani C, Atun R, Bray F, Coleman MP et al. (2019) Childhood cancer burden: a review of global estimates. *Lancet Oncol* 20 (1):e42-e53. https://doi.org/10.1016/s1470-2045(18)30761-7
2. Flores-Toro JA, Jagu S, Armstrong GT, Arons DF, Aune GJ, Chanock SJ et al. (2023) The Childhood Cancer Data Initiative: Using the Power of Data to Learn From and Improve Outcomes for Every Child and Young Adult With Pediatric Cancer. *J Clin Oncol* 41 (24):4045-4053. https://doi.org/10.1200/jco.22.02208
3. Siegel DA, Richardson LC, Henley SJ, Wilson RJ, Dowling NF, Weir HK et al. (2020) Pediatric cancer mortality and survival in the United States, 2001-2016. *Cancer* 126 (19):4379-4389. https://doi.org/10.1002/cncr.33080
4. Kattner P, Strobel H, Khoshnevis N, Grunert M, Bartholomae S, Pruss M et al. (2019) Compare and contrast: pediatric cancer versus adult malignancies. *Cancer Metastasis Rev* 38 (4):673-682. https://doi.org/10.1007/s10555-019-09836-y
5. Comitani F, Nash JO, Cohen-Gogo S, Chang AI, Wen TT, Maheshwari A et al. (2023) Diagnostic classification of childhood cancer using multiscale transcriptomics. *Nat Med* 29 (3):656-666. https://doi.org/10.1038/s41591-023-02221-x
6. Gröbner SN, Worst BC, Weischenfeldt J, Buchhalter I, Kleinheinz K, Rudneva VA et al. (2018) The landscape of genomic alterations across childhood cancers. *Nature* 555 (7696):321-327. https://doi.org/10.1038/nature25480
7. Cunningham RM, Walton MA, Carter PM (2018) The Major Causes of Death in Children and Adolescents in the United States. *N Engl J Med* 379 (25):2468-2475. https://doi.org/10.1056/NEJMsr1804754
8. Ehrhardt MJ, Krull KR, Bhakta N, Liu Q, Yasui Y, Robison LL, Hudson MM (2023) Improving quality and quantity of life for childhood cancer survivors globally in the twenty-first century. *Nat Rev Clin Oncol* 20 (10):678-696. https://doi.org/10.1038/s41571-023-00802-w
9. Alamo L, Beck-Popovic M, Gudinchet F, Meuli R (2011) Congenital tumors: imaging when life just begins. *Insights Imaging* 2 (3):297-308. https://doi.org/10.1007/s13244-011-0073-8
10. Irwin MS, Naranjo A, Zhang FF, Cohn SL, London WB, Gastier-Foster JM et al. (2021) Revised Neuroblastoma Risk Classification System: A Report From the Children's Oncology Group. *J Clin Oncol* 39 (29):3229-3241. https://doi.org/10.1200/jco.21.00278
11. Wu Y, Song Y, Wang R, Wang T (2023) Molecular mechanisms of tumor resistance to radiotherapy. *Mol Cancer* 22 (1):96. https://doi.org/10.1186/s12943-023-01801-2
12. Maier P, Fleckenstein K, Li L, Laufs S, Zeller WJ, Baum C et al. (2006) Overexpression of MDR1 using a retroviral vector differentially regulates genes involved in detoxification and apoptosis and confers radioprotection. *Radiat Res* 166 (3):463-473. https://doi.org/10.1667/rr0550.1
13. Ng IO, Lam KY, Ng M, Kwong DL, Sham JS (1998) Expression of P-glycoprotein, a multidrug-resistance gene product, is induced by radiotherapy in patients with oral squamous cell carcinoma. *Cancer* 83 (5):851-857. https://doi.org/10.1002/(sici)1097-0142(19980901)83:5<851::aid-cncr8>3.0.co;2-l
14. Çoku J, Booth DM, Skoda J, Pedrotty MC, Vogel J, Liu K et al. (2022) Reduced ER-mitochondria connectivity promotes neuroblastoma multidrug resistance. *EMBO J* 41 (8):e108272. https://doi.org/10.15252/embj.2021108272
15. Shibue T, Weinberg RA (2017) EMT, CSCs, and drug resistance: the mechanistic link and clinical implications. *Nat Rev Clin Oncol* 14 (10):611-629. https://doi.org/10.1038/nrclinonc.2017.44
16. Gupta PB, Chaffer CL, Weinberg RA (2009) Cancer stem cells: mirage or reality? *Nat Med* 15 (9):1010-1012. https://doi.org/10.1038/nm0909-1010
17. Batlle E, Clevers H (2017) Cancer stem cells revisited. *Nat Med* 23 (10):1124-1134. https://doi.org/10.1038/nm.4409
18. Lytle NK, Barber AG, Reya T (2018) Stem cell fate in cancer growth, progression and therapy resistance. *Nat Rev Cancer* 18 (11):669-680. https://doi.org/10.1038/s41568-018-0056-x
19. Puisieux A, Pommier RM, Morel AP, Lavial F (2018) Cellular Pliancy and the Multistep Process of Tumorigenesis. *Cancer Cell* 33 (2):164-172. https://doi.org/10.1016/j.ccell.2018.01.007

20. Zhang S, Xiao X, Yi Y, Wang X, Zhu L, Shen Y et al. (2024) Tumor initiation and early tumorigenesis: molecular mechanisms and interventional targets. *Signal Transduct Target Ther* 9 (1):149. https://doi.org/10.1038/s41392-024-01848-7

21. Gianferante DM, Mirabello L, Savage SA (2017) Germline and somatic genetics of osteosarcoma - connecting aetiology, biology and therapy. *Nat Rev Endocrinol* 13 (8):480-491. https://doi.org/10.1038/nrendo.2017.16

22. Zhou Y, Song H, Ming GL (2024) Genetics of human brain development. *Nat Rev Genet* 25 (1):26-45. https://doi.org/10.1038/s41576-023-00626-5

23. Baker SJ, Ellison DW, Gutmann DH (2016) Pediatric gliomas as neurodevelopmental disorders. *Glia* 64 (6):879-895. https://doi.org/10.1002/glia.22945

24. Nuchtern JG (2006) Perinatal neuroblastoma. *Semin Pediatr Surg* 15 (1):10-16. https://doi.org/10.1053/j.sempedsurg.2005.11.003

25. Acanda De La Rocha AM, Berlow NE, Fader M, Coats ER, Saghira C, Espinal PS et al. (2024) Feasibility of functional precision medicine for guiding treatment of relapsed or refractory pediatric cancers. *Nat Med* 30 (4):990-1000. https://doi.org/10.1038/s41591-024-02848-4

26. Lau LMS, Khuong-Quang DA, Mayoh C, Wong M, Barahona P, Ajuyah P et al. (2024) Precision-guided treatment in high-risk pediatric cancers. *Nat Med* 30 (7):1913-1922. https://doi.org/10.1038/s41591-024-03044-0

27. Wicha MS, Liu S, Dontu G (2006) Cancer stem cells: an old idea--a paradigm shift. *Cancer Res* 66 (4):1883-1890; discussion 1895-1886. https://doi.org/10.1158/0008-5472.Can-05-3153

28. Lapidot T, Sirard C, Vormoor J, Murdoch B, Hoang T, Caceres-Cortes J et al. (1994) A cell initiating human acute myeloid leukaemia after transplantation into SCID mice. *Nature* 367 (6464):645-648. https://doi.org/10.1038/367645a0

29. Bonnet D, Dick JE (1997) Human acute myeloid leukemia is organized as a hierarchy that originates from a primitive hematopoietic cell. *Nat Med* 3 (7):730-737. https://doi.org/10.1038/nm0797-730

30. Al-Hajj M, Wicha MS, Benito-Hernandez A, Morrison SJ, Clarke MF (2003) Prospective identification of tumorigenic breast cancer cells. *Proc Natl Acad Sci U S A* 100 (7):3983-3988. https://doi.org/10.1073/pnas.0530291100

31. Singh SK, Clarke ID, Terasaki M, Bonn VE, Hawkins C, Squire J, Dirks PB (2003) Identification of a cancer stem cell in human brain tumors. *Cancer Res* 63 (18):5821-5828

32. Pleskač P, Fargeas CA, Veselska R, Corbeil D, Skoda J (2024) Emerging roles of prominin-1 (CD133) in the dynamics of plasma membrane architecture and cell signaling pathways in health and disease. *Cell Mol Biol Lett* 29 (1):41. https://doi.org/10.1186/s11658-024-00554-0

33. Loh JJ, Ma S (2024) Hallmarks of cancer stemness. *Cell Stem Cell* 31 (5):617-639. https://doi.org/10.1016/j.stem.2024.04.004

34. Skoda J, Veselska R (2018) Cancer stem cells in sarcomas: Getting to the stemness core. *Biochim Biophys Acta Gen Subj* 1862 (10):2134-2139. https://doi.org/10.1016/j.bbagen.2018.07.006

35. Chu X, Tian W, Ning J, Xiao G, Zhou Y, Wang Z et al. (2024) Cancer stem cells: advances in knowledge and implications for cancer therapy. *Signal Transduct Target Ther* 9 (1):170. https://doi.org/10.1038/s41392-024-01851-y

36. Seebacher NA, Krchniakova M, Stacy AE, Skoda J, Jansson PJ (2021) Tumour Microenvironment Stress Promotes the Development of Drug Resistance. *Antioxidants (Basel)* 10 (11). https://doi.org/10.3390/antiox10111801

37. Pisco AO, Huang S (2015) Non-genetic cancer cell plasticity and therapy-induced stemness in tumour relapse: 'What does not kill me strengthens me'. *Br J Cancer* 112 (11):1725-1732. https://doi.org/10.1038/bjc.2015.146

38. Lambo S, Trinh DL, Ries RE, Jin D, Setiadi A, Ng M et al. (2023) A longitudinal single-cell atlas of treatment response in pediatric AML. *Cancer Cell* 41 (12):2117-2135.e2112. https://doi.org/10.1016/j.ccell.2023.10.008

39. Marine JC, Dawson SJ, Dawson MA (2020) Non-genetic mechanisms of therapeutic resistance in cancer. *Nat Rev Cancer* 20 (12):743-756. https://doi.org/10.1038/s41568-020-00302-4

40. Hemmati HD, Nakano I, Lazareff JA, Masterman-Smith M, Geschwind DH, Bronner-Fraser M, Kornblum HI (2003) Cancerous stem cells can arise from pediatric brain tumors. *Proc Natl Acad Sci U S A* 100 (25):15178-15183. https://doi.org/10.1073/pnas.2036535100

41. Čančer M, Hutter S, Holmberg KO, Rosén G, Sundström A, Tailor J et al. (2019) Humanized Stem Cell Models of Pediatric Medulloblastoma Reveal an Oct4/mTOR Axis that Promotes Malignancy. *Cell Stem Cell* 25 (6):855-870.e811. https://doi.org/10.1016/j.stem.2019.10.005

42. Da-Veiga MA, Rogister B, Lombard A, Neirinckx V, Piette C (2022) Glioma Stem Cells in Pediatric High-Grade Gliomas: From Current Knowledge to Future Perspectives. *Cancers (Basel)* 14 (9). https://doi.org/10.3390/cancers14092296

43. Garner EF, Beierle EA (2015) Cancer Stem Cells and Their Interaction with the Tumor Microenvironment in Neuroblastoma. *Cancers (Basel)* 8 (1). https://doi.org/10.3390/cancers8010005

44. Bahmad HF, Chamaa F, Assi S, Chalhoub RM, Abou-Antoun T, Abou-Kheir W (2019) Cancer Stem Cells in Neuroblastoma: Expanding the Therapeutic Frontier. *Front Mol Neurosci* 12:131. https://doi.org/10.3389/fnmol.2019.00131

45. WHO classification of tumours. (2020). Soft tissue and bone tumours., 5th edn. IARC Press, Lyon, France

46. Curylova L, Ramos H, Saraiva L, Skoda J (2022) Noncanonical roles of p53 in cancer stemness and their implications in sarcomas. *Cancer Lett* 525:131-145. https://doi.org/10.1016/j.canlet.2021.10.037

47. Perkins SM, Shinohara ET, DeWees T, Frangoul H (2014) Outcome for children with metastatic solid tumors over the last four decades. *PLoS One* 9 (7):e100396. https://doi.org/10.1371/journal.pone.0100396

48. Matthay KK, Maris JM, Schleiermacher G, Nakagawara A, Mackall CL, Diller L, Weiss WA (2016) Neuroblastoma. *Nat Rev Dis Primers* 2:16078. https://doi.org/10.1038/nrdp.2016.78

49. Newman EA, Nuchtern JG (2016) Recent biologic and genetic advances in neuroblastoma: Implications for diagnostic, risk stratification, and treatment strategies. *Semin Pediatr Surg* 25 (5):257-264. https://doi.org/10.1053/j.sempedsurg.2016.09.007

50. Boeva V, Louis-Brennetot C, Peltier A, Durand S, Pierre-Eugène C, Raynal V et al. (2017) Heterogeneity of neuroblastoma cell identity defined by transcriptional circuitries. *Nat Genet* 49 (9):1408-1413. https://doi.org/10.1038/ng.3921

51. Qiu B, Matthay KK (2022) Advancing therapy for neuroblastoma. *Nat Rev Clin Oncol* 19 (8):515-533. https://doi.org/10.1038/s41571-022-00643-z

52. Wang LL, Teshiba R, Ikegaki N, Tang XX, Naranjo A, London WB et al. (2015) Augmented expression of MYC and/or MYCN protein defines highly aggressive MYC-driven neuroblastoma: a Children's Oncology Group study. *Br J Cancer* 113 (1):57-63. https://doi.org/10.1038/bjc.2015.188

53. Jansky S, Sharma AK, Körber V, Quintero A, Toprak UH, Wecht EM et al. (2021) Single-cell transcriptomic analyses provide insights into the developmental origins of neuroblastoma. *Nat Genet* 53 (5):683-693. https://doi.org/10.1038/s41588-021-00806-1

54. Kameneva P, Artemov AV, Kastriti ME, Faure L, Olsen TK, Otte J et al. (2021) Single-cell transcriptomics of human embryos identifies multiple sympathoblast lineages with potential implications for neuroblastoma origin. *Nat Genet* 53 (5):694-706. https://doi.org/10.1038/s41588-021-00818-x

55. Gartlgruber M, Sharma AK, Quintero A, Dreidax D, Jansky S, Park YG et al. (2021) Super enhancers define regulatory subtypes and cell identity in neuroblastoma. *Nat Cancer* 2 (1):114-128. https://doi.org/10.1038/s43018-020-00145-w

56. Tirino V, Desiderio V, d'Aquino R, De Francesco F, Pirozzi G, Graziano A et al. (2008) Detection and characterization of CD133+ cancer stem cells in human solid tumours. *PLoS One* 3 (10):e3469. https://doi.org/10.1371/journal.pone.0003469

57. Veselska R, Hermanova M, Loja T, Chlapek P, Zambo I, Vesely K et al. (2008) Nestin expression in osteosarcomas and derivation of nestin/CD133 positive osteosarcoma cell lines. *BMC Cancer* 8:300. https://doi.org/10.1186/1471-2407-8-300

58. Walter D, Satheesha S, Albrecht P, Bornhauser BC, D'Alessandro V, Oesch SM et al. (2011) CD133 positive embryonal rhabdomyosarcoma stem-like cell population is enriched in rhabdospheres. *PLoS One* 6 (5):e19506. https://doi.org/10.1371/journal.pone.0019506

59. Sana J, Zambo I, Skoda J, Neradil J, Chlapek P, Hermanova M et al. (2011) CD133 expression and identification of CD133/nestin positive cells in rhabdomyosarcomas and rhabdomyosarcoma cell lines. *Anal Cell Pathol (Amst)* 34 (6):303-318. https://doi.org/10.3233/acp-2011-0018

60. Nunukova A, Neradil J, Skoda J, Jaros J, Hampl A, Sterba J, Veselska R (2015) Atypical nuclear localization of CD133 plasma membrane glycoprotein in rhabdomyosarcoma cell lines. *Int J Mol Med* 36 (1):65-72. https://doi.org/10.3892/ijmm.2015.2210

61. Singer D, Thamm K, Zhuang H, Karbanová J, Gao Y, Walker JV et al. (2019) Prominin-1 controls stem cell activation by orchestrating ciliary dynamics. *EMBO J* 38 (2). https://doi.org/10.15252/embj.201899845

62. Rappa G, Santos MF, Green TM, Karbanová J, Hassler J, Bai Y et al. (2017) Nuclear transport of cancer extracellular vesicle-derived biomaterials through nuclear envelope invagination-associated late endosomes. *Oncotarget* 8 (9):14443-14461. https://doi.org/10.18632/oncotarget.14804

63. Cantile M, Collina F, D'Aiuto M, Rinaldo M, Pirozzi G, Borsellino C et al. (2013) Nuclear localization of cancer stem cell marker CD133 in triple-negative breast cancer: a case report. *Tumori* 99 (5):e245-250. https://doi.org/10.1177/030089161309900523

64. Huang M, Zhu H, Feng J, Ni S, Huang J (2015) High CD133 expression in the nucleus and cytoplasm predicts poor prognosis in non-small cell lung cancer. *Dis Markers* 2015:986095. https://doi.org/10.1155/2015/986095

65. Lee YM, Yeo MK, Seong IO, Kim KH (2018) Nuclear Expression of CD133 Is Associated with Good Prognosis in Patients with Colorectal Adenocarcinoma. *Anticancer Res* 38 (8):4819-4826. https://doi.org/10.21873/anticanres.12792

66. Skoda J, Nunukova A, Loja T, Zambo I, Neradil J, Mudry P et al. (2016) Cancer stem cell markers in pediatric sarcomas: Sox2 is associated with tumorigenicity in immunodeficient mice. *Tumour Biol* 37 (7):9535-9548. https://doi.org/10.1007/s13277-016-4837-0

67. Wang J, Sakariassen P, Tsinkalovsky O, Immervoll H, Bøe SO, Svendsen A et al. (2008) CD133 negative glioma cells form tumors in nude rats and give rise to CD133 positive cells. *Int J Cancer* 122 (4):761-768. https://doi.org/10.1002/ijc.23130

68. Huang SD, Yuan Y, Tang H, Liu XH, Fu CG, Cheng HZ et al. (2013) Tumor cells positive and negative for the common cancer stem cell markers are capable of initiating tumor growth and generating both progenies. *PLoS One* 8 (1):e54579. https://doi.org/10.1371/journal.pone.0054579

69. Gaiser T, Camps J, Meinhardt S, Wangsa D, Nguyen QT, Varma S et al. (2011) Genome and transcriptome profiles of CD133-positive colorectal cancer cells. *Am J Pathol* 178 (4):1478-1488. https://doi.org/10.1016/j.ajpath.2010.12.036

70. Zambo I, Hermanova M, Zapletalova D, Skoda J, Mudry P, Kyr M et al. (2016) Expression of nestin, CD133 and ABCG2 in relation to the clinical outcome in pediatric sarcomas. *Cancer Biomark* 17 (1):107-116. https://doi.org/10.3233/cbm-160623

71. Skoda J, Hermanova M, Loja T, Nemec P, Neradil J, Karasek P, Veselska R (2016) Co-Expression of Cancer Stem Cell Markers Corresponds to a Pro-Tumorigenic Expression Profile in Pancreatic Adenocarcinoma. *PLoS One* 11 (7):e0159255. https://doi.org/10.1371/journal.pone.0159255

72. Neradil J, Veselska R (2015) Nestin as a marker of cancer stem cells. *Cancer Sci* 106 (7):803-811. https://doi.org/10.1111/cas.12691

73. Franken NA, Rodermond HM, Stap J, Haveman J, van Bree C (2006) Clonogenic assay of cells in vitro. *Nat Protoc* 1 (5):2315-2319. https://doi.org/10.1038/nprot.2006.339

74. Skoda J, Neradil J, Staniczkova Zambo I, Nunukova A, Macsek P, Borankova K et al. (2020) Serial Xenotransplantation in NSG Mice Promotes a Hybrid Epithelial/Mesenchymal Gene Expression Signature and Stemness in Rhabdomyosarcoma Cells. *Cancers (Basel)* 12 (1). https://doi.org/10.3390/cancers12010196

75. Kameneva P, Melnikova VI, Kastriti ME, Kurtova A, Kryukov E, Murtazina A et al. (2022) Serotonin limits generation of chromaffin cells during adrenal organ development. *Nat Commun* 13 (1):2901. https://doi.org/10.1038/s41467-022-30438-w

76. Weiswald LB, Bellet D, Dangles-Marie V (2015) Spherical cancer models in tumor biology. *Neoplasia* 17 (1):1-15. https://doi.org/10.1016/j.neo.2014.12.004

77. Chen YC, Ingram PN, Fouladdel S, McDermott SP, Azizi E, Wicha MS, Yoon E (2016) High-Throughput Single-Cell Derived Sphere Formation for Cancer Stem-Like Cell Identification and Analysis. *Sci Rep* 6:27301. https://doi.org/10.1038/srep27301

78. Esquer H, Zhou Q, Abraham AD, LaBarbera DV (2020) Advanced High-Content-Screening Applications of Clonogenicity in Cancer. *SLAS Discov* 25 (7):734-743. https://doi.org/10.1177/2472555220926921

79. Lan L, Behrens A (2023) Are There Specific Cancer Stem Cell Markers? *Cancer Res* 83 (2):170-172. https://doi.org/10.1158/0008-5472.Can-22-2053

80. Damen MPF, van Rheenen J, Scheele C (2021) Targeting dormant tumor cells to prevent cancer recurrence. *Febs j* 288 (21):6286-6303. https://doi.org/10.1111/febs.15626

81. Freter R, Falletta P, Omrani O, Rasa M, Herbert K, Annunziata F et al. (2021) Establishment of a fluorescent reporter of RNA-polymerase II activity to identify dormant cells. *Nat Commun* 12 (1):3318. https://doi.org/10.1038/s41467-021-23580-4

82.   Kim H, Wirasaputra A, Mohammadi F, Kundu AN, Esteves JAE, Heiser LM et al. (2023) Live Cell Lineage Tracing of Dormant Cancer Cells. *Adv Healthc Mater* 12 (14):e2202275. https://doi.org/10.1002/adhm.202202275

83.   Pérez-González A, Bévant K, Blanpain C (2023) Cancer cell plasticity during tumor progression, metastasis and response to therapy. *Nat Cancer* 4 (8):1063-1082. https://doi.org/10.1038/s43018-023-00595-y

84.   Suvà ML, Riggi N, Stehle JC, Baumer K, Tercier S, Joseph JM et al. (2009) Identification of cancer stem cells in Ewing's sarcoma. *Cancer Res* 69 (5):1776-1781. https://doi.org/10.1158/0008-5472.Can-08-2242

85.   Jiang X, Gwye Y, Russell D, Cao C, Douglas D, Hung L et al. (2010) CD133 expression in chemo-resistant Ewing sarcoma cells. *BMC Cancer* 10:116. https://doi.org/10.1186/1471-2407-10-116

86.   Krook MA, Nicholls LA, Scannell CA, Chugh R, Thomas DG, Lawlor ER (2014) Stress-induced CXCR4 promotes migration and invasion of ewing sarcoma. *Mol Cancer Res* 12 (6):953-964. https://doi.org/10.1158/1541-7786.Mcr-13-0668

87.   Hansford LM, McKee AE, Zhang L, George RE, Gerstle JT, Thorner PS et al. (2007) Neuroblastoma cells isolated from bone marrow metastases contain a naturally enriched tumor-initiating cell. *Cancer Res* 67 (23):11234-11243. https://doi.org/10.1158/0008-5472.Can-07-0718

88.   Verhoeven BM, Mei S, Olsen TK, Gustafsson K, Valind A, Lindström A et al. (2022) The immune cell atlas of human neuroblastoma. *Cell Rep Med* 3 (6):100657. https://doi.org/10.1016/j.xcrm.2022.100657

89.   Zhao K, Wu C, Li X, Niu M, Wu D, Cui X, Zhao H (2024) From mechanism to therapy: the journey of CD24 in cancer. *Front Immunol* 15:1401528. https://doi.org/10.3389/fimmu.2024.1401528

90.   Barkal AA, Brewer RE, Markovic M, Kowarsky M, Barkal SA, Zaro BW et al. (2019) CD24 signalling through macrophage Siglec-10 is a target for cancer immunotherapy. *Nature* 572 (7769):392-396. https://doi.org/10.1038/s41586-019-1456-0

91.   Kocak H, Ackermann S, Hero B, Kahlert Y, Oberthuer A, Juraeva D et al. (2013) Hox-C9 activates the intrinsic pathway of apoptosis and is associated with spontaneous regression in neuroblastoma. *Cell Death Dis* 4 (4):e586. https://doi.org/10.1038/cddis.2013.84

92.   Li M, Izpisua Belmonte JC (2018) Deconstructing the pluripotency gene regulatory network. *Nat Cell Biol* 20 (4):382-392. https://doi.org/10.1038/s41556-018-0067-6

93.   Ben-Porath I, Thomson MW, Carey VJ, Ge R, Bell GW, Regev A, Weinberg RA (2008) An embryonic stem cell-like gene expression signature in poorly differentiated aggressive human tumors. *Nat Genet* 40 (5):499-507. https://doi.org/10.1038/ng.127

94.   Hepburn AC, Steele RE, Veeratterapillay R, Wilson L, Kounatidou EE, Barnard A et al. (2019) The induction of core pluripotency master regulators in cancers defines poor clinical outcomes and treatment resistance. *Oncogene* 38 (22):4412-4424. https://doi.org/10.1038/s41388-019-0712-y

95.   Iglesias JM, Gumuzio J, Martin AG (2017) Linking Pluripotency Reprogramming and Cancer. *Stem Cells Transl Med* 6 (2):335-339. https://doi.org/10.5966/sctm.2015-0225

96.   Wuebben EL, Rizzino A (2017) The dark side of SOX2: cancer - a comprehensive overview. *Oncotarget* 8 (27):44917-44943. https://doi.org/10.18632/oncotarget.16570

97.   Schaefer T, Lengerke C (2020) SOX2 protein biochemistry in stemness, reprogramming, and cancer: the PI3K/AKT/SOX2 axis and beyond. *Oncogene* 39 (2):278-292. https://doi.org/10.1038/s41388-019-0997-x

98.   Niharika, Ureka L, Roy A, Patra SK (2024) Dissecting SOX2 expression and function reveals an association with multiple signaling pathways during embryonic development and in cancer progression. *Biochim Biophys Acta Rev Cancer* 1879 (5):189136. https://doi.org/10.1016/j.bbcan.2024.189136

99.   Takahashi K, Yamanaka S (2006) Induction of pluripotent stem cells from mouse embryonic and adult fibroblast cultures by defined factors. *Cell* 126 (4):663-676. https://doi.org/10.1016/j.cell.2006.07.024

100.   Takahashi K, Tanabe K, Ohnuki M, Narita M, Ichisaka T, Tomoda K, Yamanaka S (2007) Induction of pluripotent stem cells from adult human fibroblasts by defined factors. *Cell* 131 (5):861-872. https://doi.org/10.1016/j.cell.2007.11.019

101.   Basu-Roy U, Seo E, Ramanathapuram L, Rapp TB, Perry JA, Orkin SH et al. (2012) Sox2 maintains self renewal of tumor-initiating cells in osteosarcomas. *Oncogene* 31 (18):2270-2282. https://doi.org/10.1038/onc.2011.405

102. Maurizi G, Verma N, Gadi A, Mansukhani A, Basilico C (2018) Sox2 is required for tumor development and cancer cell proliferation in osteosarcoma. *Oncogene* 37 (33):4626-4632. https://doi.org/10.1038/s41388-018-0292-2

103. Menendez ST, Rey V, Martinez-Cruzado L, Gonzalez MV, Morales-Molina A, Santos L et al. (2020) SOX2 Expression and Transcriptional Activity Identifies a Subpopulation of Cancer Stem Cells in Sarcoma with Prognostic Implications. *Cancers (Basel)* 12 (4). https://doi.org/10.3390/cancers12040964

104. Zhang S, Xiong X, Sun Y (2020) Functional characterization of SOX2 as an anticancer target. *Signal Transduct Target Ther* 5 (1):135. https://doi.org/10.1038/s41392-020-00242-3

105. Sannino G, Marchetto A, Ranft A, Jabar S, Zacherl C, Alba-Rubio R et al. (2019) Gene expression and immunohistochemical analyses identify SOX2 as major risk factor for overall survival and relapse in Ewing sarcoma patients. *EBioMedicine* 47:156-162. https://doi.org/10.1016/j.ebiom.2019.08.002

106. Leung C, Murad KBA, Tan ALT, Yada S, Sagiraju S, Bode PK, Barker N (2020) Lgr5 Marks Adult Progenitor Cells Contributing to Skeletal Muscle Regeneration and Sarcoma Formation. *Cell Rep* 33 (12):108535. https://doi.org/10.1016/j.celrep.2020.108535

107. Haffner MR, Saiz AM, Jr., Darrow MA, Judge SJ, Laun T, Arora A et al. (2024) Effect of ALDH1A1 and CD44 on Survival and Disease Recurrence in Patients With Osteosarcoma. *Cureus* 16 (1):e52404. https://doi.org/10.7759/cureus.52404

108. Lambert AW, Weinberg RA (2021) Linking EMT programmes to normal and neoplastic epithelial stem cells. *Nat Rev Cancer* 21 (5):325-338. https://doi.org/10.1038/s41568-021-00332-6

109. Jolly MK, Somarelli JA, Sheth M, Biddle A, Tripathi SC, Armstrong AJ et al. (2019) Hybrid epithelial/mesenchymal phenotypes promote metastasis and therapy resistance across carcinomas. *Pharmacol Ther* 194:161-184. https://doi.org/10.1016/j.pharmthera.2018.09.007

110. Kröger C, Afeyan A, Mraz J, Eaton EN, Reinhardt F, Khodor YL et al. (2019) Acquisition of a hybrid E/M state is essential for tumorigenicity of basal breast cancer cells. *Proc Natl Acad Sci U S A* 116 (15):7353-7362. https://doi.org/10.1073/pnas.1812876116

111. Quan Q, Wang X, Lu C, Ma W, Wang Y, Xia G et al. (2020) Cancer stem-like cells with hybrid epithelial/mesenchymal phenotype leading the collective invasion. *Cancer Sci* 111 (2):467-476. https://doi.org/10.1111/cas.14285

112. Ullah M, Liu DD, Thakor AS (2019) Mesenchymal Stromal Cell Homing: Mechanisms and Strategies for Improvement. *iScience* 15:421-438. https://doi.org/10.1016/j.isci.2019.05.004

113. Ricci-Vitiani L, Lombardi DG, Pilozzi E, Biffoni M, Todaro M, Peschle C, De Maria R (2007) Identification and expansion of human colon-cancer-initiating cells. *Nature* 445 (7123):111-115. https://doi.org/10.1038/nature05384

114. Golan H, Shukrun R, Caspi R, Vax E, Pode-Shakked N, Goldberg S et al. (2018) In Vivo Expansion of Cancer Stemness Affords Novel Cancer Stem Cell Targets: Malignant Rhabdoid Tumor as an Example. *Stem Cell Reports* 11 (3):795-810. https://doi.org/10.1016/j.stemcr.2018.07.010

115. Li R, Liang J, Ni S, Zhou T, Qing X, Li H et al. (2010) A mesenchymal-to-epithelial transition initiates and is required for the nuclear reprogramming of mouse fibroblasts. *Cell Stem Cell* 7 (1):51-63. https://doi.org/10.1016/j.stem.2010.04.014

116. Høffding MK, Hyttel P (2015) Ultrastructural visualization of the Mesenchymal-to-Epithelial Transition during reprogramming of human fibroblasts to induced pluripotent stem cells. *Stem Cell Res* 14 (1):39-53. https://doi.org/10.1016/j.scr.2014.11.003

117. Sample RA, Nogueira MF, Mitra RD, Puram SV (2023) Epigenetic regulation of hybrid epithelial-mesenchymal cell states in cancer. *Oncogene* 42 (29):2237-2248. https://doi.org/10.1038/s41388-023-02749-9

118. Silva J, Nichols J, Theunissen TW, Guo G, van Oosten AL, Barrandon O et al. (2009) Nanog is the gateway to the pluripotent ground state. *Cell* 138 (4):722-737. https://doi.org/10.1016/j.cell.2009.07.039

119. Ervin EH, French R, Chang CH, Pauklin S (2022) Inside the stemness engine: Mechanistic links between deregulated transcription factors and stemness in cancer. *Semin Cancer Biol* 87:48-83. https://doi.org/10.1016/j.semcancer.2022.11.001

120. Mikulenkova E, Neradil J, Vymazal O, Skoda J, Veselska R (2020) NANOG/NANOGP8 Localizes at the Centrosome and is Spatiotemporally Associated with Centriole Maturation. *Cells* 9 (3). https://doi.org/10.3390/cells9030692

121. Palla AR, Piazzolla D, Abad M, Li H, Dominguez O, Schonthaler HB et al. (2014) Reprogramming activity of NANOGP8, a NANOG family member widely expressed in cancer. *Oncogene* 33 (19):2513-2519. https://doi.org/10.1038/onc.2013.196

122. Nigg EA, Holland AJ (2018) Once and only once: mechanisms of centriole duplication and their deregulation in disease. *Nat Rev Mol Cell Biol* 19 (5):297-312. https://doi.org/10.1038/nrm.2017.127

123. Yamashita YM, Mahowald AP, Perlin JR, Fuller MT (2007) Asymmetric inheritance of mother versus daughter centrosome in stem cell division. *Science* 315 (5811):518-521. https://doi.org/10.1126/science.1134910

124. Pelletier L, Yamashita YM (2012) Centrosome asymmetry and inheritance during animal development. *Curr Opin Cell Biol* 24 (4):541-546. https://doi.org/10.1016/j.ceb.2012.05.005

125. Steinbichler TB, Dudás J, Skvortsov S, Ganswindt U, Riechelmann H, Skvortsova, II (2018) Therapy resistance mediated by cancer stem cells. *Semin Cancer Biol* 53:156-167. https://doi.org/10.1016/j.semcancer.2018.11.006

126. Santos-de-Frutos K, Djouder N (2021) When dormancy fuels tumour relapse. *Commun Biol* 4 (1):747. https://doi.org/10.1038/s42003-021-02257-0

127. Lawson DA, Kessenbrock K, Davis RT, Pervolarakis N, Werb Z (2018) Tumour heterogeneity and metastasis at single-cell resolution. *Nat Cell Biol* 20 (12):1349-1360. https://doi.org/10.1038/s41556-018-0236-7

128. Bruschini S, Ciliberto G, Mancini R (2020) The emerging role of cancer cell plasticity and cell-cycle quiescence in immune escape. *Cell Death Dis* 11 (6):471. https://doi.org/10.1038/s41419-020-2669-8

129. Wang YH, Scadden DT (2015) Harnessing the apoptotic programs in cancer stem-like cells. *EMBO Rep* 16 (9):1084-1098. https://doi.org/10.15252/embr.201439675

130. Skoda J, Borankova K, Jansson PJ, Huang ML, Veselska R, Richardson DR (2019) Pharmacological targeting of mitochondria in cancer stem cells: An ancient organelle at the crossroad of novel anti-cancer therapies. *Pharmacol Res* 139:298-313. https://doi.org/10.1016/j.phrs.2018.11.020

131. Singh R, Letai A, Sarosiek K (2019) Regulation of apoptosis in health and disease: the balancing act of BCL-2 family proteins. *Nat Rev Mol Cell Biol* 20 (3):175-193. https://doi.org/10.1038/s41580-018-0089-8

132. Ni Chonghaile T, Sarosiek KA, Vo TT, Ryan JA, Tammareddi A, Moore Vdel G et al. (2011) Pretreatment mitochondrial priming correlates with clinical response to cytotoxic chemotherapy. *Science* 334 (6059):1129-1133. https://doi.org/10.1126/science.1206727

133. Sarosiek KA, Fraser C, Muthalagu N, Bhola PD, Chang W, McBrayer SK et al. (2017) Developmental Regulation of Mitochondrial Apoptosis by c-Myc Governs Age- and Tissue-Specific Sensitivity to Cancer Therapeutics. *Cancer Cell* 31 (1):142-156. https://doi.org/10.1016/j.ccell.2016.11.011

134. Goldsmith KC, Lestini BJ, Gross M, Ip L, Bhumbla A, Zhang X et al. (2010) BH3 response profiles from neuroblastoma mitochondria predict activity of small molecule Bcl-2 family antagonists. *Cell Death Differ* 17 (5):872-882. https://doi.org/10.1038/cdd.2009.171

135. Goldsmith KC, Gross M, Peirce S, Luyindula D, Liu X, Vu A et al. (2012) Mitochondrial Bcl-2 family dynamics define therapy response and resistance in neuroblastoma. *Cancer Res* 72 (10):2565-2577. https://doi.org/10.1158/0008-5472.Can-11-3603

136. Letai A (2015) Cell Death and Cancer Therapy: Don't Forget to Kill the Cancer Cell! *Clin Cancer Res* 21 (22):5015-5020. https://doi.org/10.1158/1078-0432.Ccr-15-1204

137. Borankova K, Krchniakova M, Leck LYW, Kubistova A, Neradil J, Jansson PJ et al. (2023) Mitoribosomal synthetic lethality overcomes multidrug resistance in MYC-driven neuroblastoma. *Cell Death Dis* 14 (11):747. https://doi.org/10.1038/s41419-023-06278-x

138. Elsayed AH, Cao X, Marrero RJ, Nguyen NHK, Wu H, Ni Y et al. (2024) Integrated drug resistance and leukemic stemness gene-expression scores predict outcomes in large cohort of over 3500 AML patients from 10 trials. *NPJ Precis Oncol* 8 (1):168. https://doi.org/10.1038/s41698-024-00643-5

139. Piskareva O, Harvey H, Nolan J, Conlon R, Alcock L, Buckley P et al. (2015) The development of cisplatin resistance in neuroblastoma is accompanied by epithelial to mesenchymal transition in vitro. *Cancer Lett* 364 (2):142-155. https://doi.org/10.1016/j.canlet.2015.05.004

140. Mañas A, Aaltonen K, Andersson N, Hansson K, Adamska A, Seger A et al. (2022) Clinically relevant treatment of PDX models reveals patterns of neuroblastoma chemoresistance. *Sci Adv* 8 (43):eabq4617. https://doi.org/10.1126/sciadv.abq4617

141. Garaventa A, Poetschger U, Valteau-Couanet D, Luksch R, Castel V, Elliott M et al. (2021) Randomized Trial of Two Induction Therapy Regimens for High-Risk Neuroblastoma: HR-NBL1.5 International Society of Pediatric Oncology European Neuroblastoma Group Study. *J Clin Oncol* 39 (23):2552-2563. https://doi.org/10.1200/jco.20.03144

142. Skapek SX, Ferrari A, Gupta AA, Lupo PJ, Butler E, Shipley J et al. (2019) Rhabdomyosarcoma. *Nat Rev Dis Primers* 5 (1):1. https://doi.org/10.1038/s41572-018-0051-2

143. Roelof, Nikolas H, Fredrik B, Daniel B, Kjetil B, Nathalie G et al. (2023) European standard clinical practice recommendations for children and adolescents with primary and recurrent osteosarcoma. *EJC Paediatric Oncology* 2:100029. https://doi.org/https://doi.org/10.1016/j.ejcped.2023.100029

144. Crist WM, Anderson JR, Meza JL, Fryer C, Raney RB, Ruymann FB et al. (2001) Intergroup rhabdomyosarcoma study-IV: results for patients with nonmetastatic disease. *J Clin Oncol* 19 (12):3091-3102. https://doi.org/10.1200/jco.2001.19.12.3091

145. Butler E, Ludwig K, Pacenta HL, Klesse LJ, Watt TC, Laetsch TW (2021) Recent progress in the treatment of cancer in children. *CA Cancer J Clin* 71 (4):315-332. https://doi.org/10.3322/caac.21665

146. Oeffinger KC, Mertens AC, Sklar CA, Kawashima T, Hudson MM, Meadows AT et al. (2006) Chronic health conditions in adult survivors of childhood cancer. *N Engl J Med* 355 (15):1572-1582. https://doi.org/10.1056/NEJMsa060185

147. Signorelli C, Wakefield CE, McLoone JK, Johnston KA, Mertens AC, Osborn M, Cohn RJ (2023) Childhood Cancer Survivors' Reported Late Effects, Motivations for Seeking Survivorship Care, and Patterns of Attendance. *Oncologist* 28 (5):e276-e286. https://doi.org/10.1093/oncolo/oyad004

148. Moreno L, DuBois SG, Glade Bender J, Mauguen A, Bird N, Buenger V et al. (2023) Combination Early-Phase Trials of Anticancer Agents in Children and Adolescents. *J Clin Oncol* 41 (18):3408-3422. https://doi.org/10.1200/jco.22.02430

149. Chou TC (2010) Drug combination studies and their synergy quantification using the Chou-Talalay method. *Cancer Res* 70 (2):440-446. https://doi.org/10.1158/0008-5472.Can-09-1947

150. Pomeroy AE, Schmidt EV, Sorger PK, Palmer AC (2022) Drug independence and the curability of cancer by combination chemotherapy. *Trends Cancer* 8 (11):915-929. https://doi.org/10.1016/j.trecan.2022.06.009

151. Jaaks P, Coker EA, Vis DJ, Edwards O, Carpenter EF, Leto SM et al. (2022) Effective drug combinations in breast, colon and pancreatic cancer cells. *Nature* 603 (7899):166-173. https://doi.org/10.1038/s41586-022-04437-2

152. Sterba J, Valik D, Mudry P, Kepak T, Pavelka Z, Bajciova V et al. (2006) Combined biodifferentiating and antiangiogenic oral metronomic therapy is feasible and effective in relapsed solid tumors in children: single-center pilot study. *Onkologie* 29 (7):308-313. https://doi.org/10.1159/000093474

153. Zapletalova D, André N, Deak L, Kyr M, Bajciova V, Mudry P et al. (2012) Metronomic chemotherapy with the COMBAT regimen in advanced pediatric malignances: a multicenter experience. *Oncology* 82 (5):249-260. https://doi.org/10.1159/000336483

154. Berthold F, Hömberg M, Proleskovskaya I, Mazanek P, Belogurova M, Ernst A, Sterba J (2017) Metronomic therapy has low toxicity and is as effective as current standard treatment for recurrent high-risk neuroblastoma. *Pediatr Hematol Oncol* 34 (5):308-319. https://doi.org/10.1080/08880018.2017.1373314

155. Chou SW, Chang HH (2024) Evolution and contemporary role of metronomic chemotherapy in the treatment of neuroblastoma. *Cancer Lett* 588:216617. https://doi.org/10.1016/j.canlet.2024.216617

156. Yuan J, Lovejoy DB, Richardson DR (2004) Novel di-2-pyridyl-derived iron chelators with marked and selective antitumor activity: in vitro and in vivo assessment. *Blood* 104 (5):1450-1458. https://doi.org/10.1182/blood-2004-03-0868

157. Whitnall M, Howard J, Ponka P, Richardson DR (2006) A class of iron chelators with a wide spectrum of potent antitumor activity that overcomes resistance to chemotherapeutics. *Proc Natl Acad Sci U S A* 103 (40):14901-14906. https://doi.org/10.1073/pnas.0604979103

158. Lane DJ, Merlot AM, Huang ML, Bae DH, Jansson PJ, Sahni S et al. (2015) Cellular iron uptake, trafficking and metabolism: Key molecules and mechanisms and their roles in disease. *Biochim Biophys Acta* 1853 (5):1130-1144. https://doi.org/10.1016/j.bbamcr.2015.01.021

159. Lovejoy DB, Jansson PJ, Brunk UT, Wong J, Ponka P, Richardson DR (2011) Antitumor activity of metal-chelating compound Dp44mT is mediated by formation of a redox-active copper complex that accumulates in lysosomes. *Cancer Res* 71 (17):5871-5880. https://doi.org/10.1158/0008-5472.Can-11-1218

160. Park KC, Menezes SV, Kalinowski DS, Sahni S, Jansson PJ, Kovacevic Z, Richardson DR (2018) Identification of differential phosphorylation and sub-cellular localization of the metastasis

suppressor, NDRG1. *Biochim Biophys Acta Mol Basis Dis* 1864 (8):2644-2663. https://doi.org/10.1016/j.bbadis.2018.04.011

161. Kovacevic Z, Menezes SV, Sahni S, Kalinowski DS, Bae DH, Lane DJ, Richardson DR (2016) The Metastasis Suppressor, N-MYC Downstream-regulated Gene-1 (NDRG1), Down-regulates the ErbB Family of Receptors to Inhibit Downstream Oncogenic Signaling Pathways. *J Biol Chem* 291 (3):1029-1052. https://doi.org/10.1074/jbc.M115.689653

162. Menezes SV, Kovacevic Z, Richardson DR (2019) The metastasis suppressor NDRG1 down-regulates the epidermal growth factor receptor via a lysosomal mechanism by up-regulating mitogen-inducible gene 6. *J Biol Chem* 294 (11):4045-4064. https://doi.org/10.1074/jbc.RA118.006279

163. Menezes SV, Fouani L, Huang MLH, Geleta B, Maleki S, Richardson A et al. (2019) The metastasis suppressor, NDRG1, attenuates oncogenic TGF-β and NF-κB signaling to enhance membrane E-cadherin expression in pancreatic cancer cells. *Carcinogenesis* 40 (6):805-818. https://doi.org/10.1093/carcin/bgy178

164. Geleta B, Park KC, Jansson PJ, Sahni S, Maleki S, Xu Z et al. (2021) Breaking the cycle: Targeting of NDRG1 to inhibit bi-directional oncogenic cross-talk between pancreatic cancer and stroma. *FASEB J* 35 (2):e21347. https://doi.org/10.1096/fj.202002279R

165. Geleta B, Tout FS, Lim SC, Sahni S, Jansson PJ, Apte MV et al. (2022) Targeting Wnt/tenascin C-mediated cross talk between pancreatic cancer cells and stellate cells via activation of the metastasis suppressor NDRG1. *J Biol Chem* 298 (3):101608. https://doi.org/10.1016/j.jbc.2022.101608

166. Shehadeh-Tout F, Milioli HH, Roslan S, Jansson PJ, Dharmasivam M, Graham D et al. (2023) Innovative thiosemicarbazones that induce multi-modal mechanisms to down-regulate estrogen-, progesterone-, androgen- and prolactin-receptors in breast cancer. *Pharmacol Res* 193:106806. https://doi.org/10.1016/j.phrs.2023.106806

167. Dharmasivam M, Azad MG, Afroz R, Richardson V, Jansson PJ, Richardson DR (2022) The thiosemicarbazone, DpC, broadly synergizes with multiple anti-cancer therapeutics and demonstrates temperature- and energy-dependent uptake by tumor cells. *Biochim Biophys Acta Gen Subj* 1866 (8):130152. https://doi.org/10.1016/j.bbagen.2022.130152

168. Seebacher NA, Richardson DR, Jansson PJ (2016) A mechanism for overcoming P-glycoprotein-mediated drug resistance: novel combination therapy that releases stored doxorubicin from lysosomes via lysosomal permeabilization using Dp44mT or DpC. *Cell Death Dis* 7 (12):e2510. https://doi.org/10.1038/cddis.2016.381

169. Lovejoy DB, Sharp DM, Seebacher N, Obeidy P, Prichard T, Stefani C et al. (2012) Novel second-generation di-2-pyridylketone thiosemicarbazones show synergism with standard chemotherapeutics and demonstrate potent activity against lung cancer xenografts after oral and intravenous administration in vivo. *J Med Chem* 55 (16):7230-7244. https://doi.org/10.1021/jm300768u

170. Potuckova E, Jansova H, Machacek M, Vavrova A, Haskova P, Tichotova L et al. (2014) Quantitative analysis of the anti-proliferative activity of combinations of selected iron-chelating agents and clinically used anti-neoplastic drugs. *PLoS One* 9 (2):e88754. https://doi.org/10.1371/journal.pone.0088754

171. Paukovcekova S, Skoda J, Neradil J, Mikulenkova E, Chlapek P, Sterba J et al. (2020) Novel Thiosemicarbazones Sensitize Pediatric Solid Tumor Cell-Types to Conventional Chemotherapeutics through Multiple Molecular Mechanisms. *Cancers (Basel)* 12 (12). https://doi.org/10.3390/cancers12123781

172. Arico S, Pattingre S, Bauvy C, Gane P, Barbat A, Codogno P, Ogier-Denis E (2002) Celecoxib induces apoptosis by inhibiting 3-phosphoinositide-dependent protein kinase-1 activity in the human colon cancer HT-29 cell line. *J Biol Chem* 277 (31):27613-27621. https://doi.org/10.1074/jbc.M201119200

173. Kovacevic Z, Chikhani S, Lui GY, Sivagurunathan S, Richardson DR (2013) The iron-regulated metastasis suppressor NDRG1 targets NEDD4L, PTEN, and SMAD4 and inhibits the PI3K and Ras signaling pathways. *Antioxid Redox Signal* 18 (8):874-887. https://doi.org/10.1089/ars.2011.4273

174. Hegi ME, Diserens AC, Gorlia T, Hamou MF, de Tribolet N, Weller M et al. (2005) MGMT gene silencing and benefit from temozolomide in glioblastoma. *N Engl J Med* 352 (10):997-1003. https://doi.org/10.1056/NEJMoa043331

175. Yip S, Miao J, Cahill DP, Iafrate AJ, Aldape K, Nutt CL, Louis DN (2009) MSH6 mutations arise in glioblastomas during temozolomide therapy and mediate temozolomide resistance. *Clin Cancer Res* 15 (14):4622-4629. https://doi.org/10.1158/1078-0432.Ccr-08-3012

176. Stark AM, Doukas A, Hugo HH, Mehdorn HM (2010) The expression of mismatch repair proteins MLH1, MSH2 and MSH6 correlates with the Ki67 proliferation index and survival in patients with recurrent glioblastoma. *Neurol Res* 32 (8):816-820. https://doi.org/10.1179/016164110x12645013515052

177. Sun Q, Pei C, Li Q, Dong T, Dong Y, Xing W et al. (2018) Up-regulation of MSH6 is associated with temozolomide resistance in human glioblastoma. *Biochem Biophys Res Commun* 496 (4):1040-1046. https://doi.org/10.1016/j.bbrc.2018.01.093

178. Aasland D, Götzinger L, Hauck L, Berte N, Meyer J, Effenberger M et al. (2019) Temozolomide Induces Senescence and Repression of DNA Repair Pathways in Glioblastoma Cells via Activation of ATR-CHK1, p21, and NF-κB. *Cancer Res* 79 (1):99-113. https://doi.org/10.1158/0008-5472.Can-18-1733

179. Crisafulli G, Sartore-Bianchi A, Lazzari L, Pietrantonio F, Amatu A, Macagno M et al. (2022) Temozolomide Treatment Alters Mismatch Repair and Boosts Mutational Burden in Tumor and Blood of Colorectal Cancer Patients. *Cancer Discov* 12 (7):1656-1675. https://doi.org/10.1158/2159-8290.Cd-21-1434

180. Indraccolo S, Lombardi G, Fassan M, Pasqualini L, Giunco S, Marcato R et al. (2019) Genetic, Epigenetic, and Immunologic Profiling of MMR-Deficient Relapsed Glioblastoma. *Clin Cancer Res* 25 (6):1828-1837. https://doi.org/10.1158/1078-0432.Ccr-18-1892

181. Guan J, Li GM (2023) DNA mismatch repair in cancer immunotherapy. *NAR Cancer* 5 (3):zcad031. https://doi.org/10.1093/narcan/zcad031

182. Paukovcekova S, Krchniakova M, Chlapek P, Neradil J, Skoda J, Veselska R (2022) Thiosemicarbazones Can Act Synergistically with Anthracyclines to Downregulate CHEK1 Expression and Induce DNA Damage in Cell Lines Derived from Pediatric Solid Tumors. *Int J Mol Sci* 23 (15). https://doi.org/10.3390/ijms23158549

183. Sazonova EV, Petrichuk SV, Kopeina GS, Zhivotovsky B (2021) A link between mitotic defects and mitotic catastrophe: detection and cell fate. *Biol Direct* 16 (1):25. https://doi.org/10.1186/s13062-021-00313-7

184. Zanotti S, Decaesteker B, Vanhauwaert S, De Wilde B, De Vos WH, Speleman F (2022) Cellular senescence in neuroblastoma. *Br J Cancer* 126 (11):1529-1538. https://doi.org/10.1038/s41416-022-01755-0

185. Riviere-Cazaux C, Carlstrom LP, Neth BJ, Olson IE, Rajani K, Rahman M et al. (2023) An untapped window of opportunity for glioma: targeting therapy-induced senescence prior to recurrence. *NPJ Precis Oncol* 7 (1):126. https://doi.org/10.1038/s41698-023-00476-8

186. Schmitt CA, Wang B, Demaria M (2022) Senescence and cancer - role and therapeutic opportunities. *Nat Rev Clin Oncol* 19 (10):619-636. https://doi.org/10.1038/s41571-022-00668-4

187. Burden DA, Kingma PS, Froelich-Ammon SJ, Bjornsti MA, Patchan MW, Thompson RB, Osheroff N (1996) Topoisomerase II.etoposide interactions direct the formation of drug-induced enzyme-DNA cleavage complexes. *J Biol Chem* 271 (46):29238-29244. https://doi.org/10.1074/jbc.271.46.29238

188. Armenian S, Bhatia S (2018) Predicting and Preventing Anthracycline-Related Cardiotoxicity. *Am Soc Clin Oncol Educ Book* 38:3-12. https://doi.org/10.1200/edbk_100015

189. Capelôa T, Benyahia Z, Zampieri LX, Blackman M, Sonveaux P (2020) Metabolic and non-metabolic pathways that control cancer resistance to anthracyclines. *Semin Cell Dev Biol* 98:181-191. https://doi.org/10.1016/j.semcdb.2019.05.006

190. Mlejnek P, Havlasek J, Pastvova N, Dolezel P, Dostalova K (2022) Lysosomal sequestration of weak base drugs, lysosomal biogenesis, and cell cycle alteration. *Biomed Pharmacother* 153:113328. https://doi.org/10.1016/j.biopha.2022.113328

191. Dey D, Marciano S, Poryvai A, Groborz O, Wohlrábová L, Slanina T, Schreiber G (2024) Reversing protonation of weakly basic drugs greatly enhances intracellular diffusion and decreases lysosomal sequestration. eLife Sciences Publications, Ltd. doi:10.7554/elife.97255.1

192. Yamagishi T, Sahni S, Sharp DM, Arvind A, Jansson PJ, Richardson DR (2013) P-glycoprotein mediates drug resistance via a novel mechanism involving lysosomal sequestration. *J Biol Chem* 288 (44):31761-31771. https://doi.org/10.1074/jbc.M113.514091

193. Jansson PJ, Yamagishi T, Arvind A, Seebacher N, Gutierrez E, Stacy A et al. (2015) Di-2-pyridylketone 4,4-dimethyl-3-thiosemicarbazone (Dp44mT) overcomes multidrug resistance by a novel mechanism involving the hijacking of lysosomal P-glycoprotein (Pgp). *J Biol Chem* 290 (15):9588-9603. https://doi.org/10.1074/jbc.M114.631283

194. Castedo M, Perfettini JL, Roumier T, Andreau K, Medema R, Kroemer G (2004) Cell death by mitotic catastrophe: a molecular definition. *Oncogene* 23 (16):2825-2837. https://doi.org/10.1038/sj.onc.1207528

195. Castedo M, Perfettini JL, Roumier T, Yakushijin K, Horne D, Medema R, Kroemer G (2004) The cell cycle checkpoint kinase Chk2 is a negative regulator of mitotic catastrophe. *Oncogene* 23 (25):4353-4361. https://doi.org/10.1038/sj.onc.1207573

196. Drápela S, Khirsariya P, van Weerden WM, Fedr R, Suchánková T, Búzová D et al. (2020) The CHK1 inhibitor MU380 significantly increases the sensitivity of human docetaxel-resistant prostate cancer cells to gemcitabine through the induction of mitotic catastrophe. *Mol Oncol* 14 (10):2487-2503. https://doi.org/10.1002/1878-0261.12756

197. Li J, Kretzner L (2003) The growth-inhibitory Ndrg1 gene is a Myc negative target in human neuroblastomas and other cell types with overexpressed N- or c-myc. *Mol Cell Biochem* 250 (1-2):91-105. https://doi.org/10.1023/a:1024918328162

198. Zhang J, Chen S, Zhang W, Zhang J, Liu X, Shi H et al. (2008) Human differentiation-related gene NDRG1 is a Myc downstream-regulated gene that is repressed by Myc on the core promoter region. *Gene* 417 (1-2):5-12. https://doi.org/10.1016/j.gene.2008.03.002

199. Macsek P, Skoda J, Krchniakova M, Neradil J, Veselska R (2021) Iron-Chelation Treatment by Novel Thiosemicarbazone Targets Major Signaling Pathways in Neuroblastoma. *Int J Mol Sci* 23 (1). https://doi.org/10.3390/ijms23010376

200. Floros KV, Cai J, Jacob S, Kurupi R, Fairchild CK, Shende M et al. (2021) MYCN-Amplified Neuroblastoma Is Addicted to Iron and Vulnerable to Inhibition of the System Xc-/Glutathione Axis. *Cancer Res* 81 (7):1896-1908. https://doi.org/10.1158/0008-5472.Can-20-1641

201. Lu Y, Yang Q, Su Y, Ji Y, Li G, Yang X et al. (2021) MYCN mediates TFRC-dependent ferroptosis and reveals vulnerabilities in neuroblastoma. *Cell Death Dis* 12 (6):511. https://doi.org/10.1038/s41419-021-03790-w

202. Bystrom LM, Guzman ML, Rivella S (2014) Iron and reactive oxygen species: friends or foes of cancer cells? *Antioxid Redox Signal* 20 (12):1917-1924. https://doi.org/10.1089/ars.2012.5014

203. Salnikow K (2021) Role of iron in cancer. *Semin Cancer Biol* 76:189-194. https://doi.org/10.1016/j.semcancer.2021.04.001

204. Alborzinia H, Flórez AF, Kreth S, Brückner LM, Yildiz U, Gartlgruber M et al. (2022) MYCN mediates cysteine addiction and sensitizes neuroblastoma to ferroptosis. *Nat Cancer* 3 (4):471-485. https://doi.org/10.1038/s43018-022-00355-4

205. Stockwell BR (2022) Ferroptosis turns 10: Emerging mechanisms, physiological functions, and therapeutic applications. *Cell* 185 (14):2401-2421. https://doi.org/10.1016/j.cell.2022.06.003

206. Danielli M, Perne L, Jarc Jovičić E, Petan T (2023) Lipid droplets and polyunsaturated fatty acid trafficking: Balancing life and death. *Front Cell Dev Biol* 11:1104725. https://doi.org/10.3389/fcell.2023.1104725

207. Mudry P, Slaby O, Neradil J, Soukalova J, Melicharkova K, Rohleder O et al. (2017) Case report: rapid and durable response to PDGFR targeted therapy in a child with refractory multiple infantile myofibromatosis and a heterozygous germline mutation of the PDGFRB gene. *BMC Cancer* 17 (1):119. https://doi.org/10.1186/s12885-017-3115-x

208. Neradil J, Kyr M, Polaskova K, Kren L, Macigova P, Skoda J et al. (2019) Phospho-Protein Arrays as Effective Tools for Screening Possible Targets for Kinase Inhibitors and Their Use in Precision Pediatric Oncology. *Front Oncol* 9:930. https://doi.org/10.3389/fonc.2019.00930

209. Polaskova K, Merta T, Martincekova A, Zapletalova D, Kyr M, Mazanek P et al. (2019) Comprehensive Molecular Profiling for Relapsed/Refractory Pediatric Burkitt Lymphomas-Retrospective Analysis of Three Real-Life Clinical Cases-Addressing Issues on Randomization and Customization at the Bedside. *Front Oncol* 9:1531. https://doi.org/10.3389/fonc.2019.01531

210. Mahdal M, Neradil J, Mudry P, Paukovcekova S, Staniczkova Zambo I, Urban J et al. (2021) New Target for Precision Medicine Treatment of Giant-Cell Tumor of Bone: Sunitinib Is Effective in the Treatment of Neoplastic Stromal Cells with Activated PDGFRβ Signaling. *Cancers (Basel)* 13 (14). https://doi.org/10.3390/cancers13143543

211. Krchniakova M, Paukovcekova S, Chlapek P, Neradil J, Skoda J, Veselska R (2022) Thiosemicarbazones and selected tyrosine kinase inhibitors synergize in pediatric solid tumors: NDRG1 upregulation and impaired prosurvival signaling in neuroblastoma cells. *Front Pharmacol* 13:976955. https://doi.org/10.3389/fphar.2022.976955

212. Ibrahim O, O'Sullivan J (2020) Iron chelators in cancer therapy. *Biometals* 33 (4-5):201-215. https://doi.org/10.1007/s10534-020-00243-3

213. Lisowski P, Kannan P, Mlody B, Prigione A (2018) Mitochondria and the dynamic control of stem cell homeostasis. *EMBO Rep* 19 (5). https://doi.org/10.15252/embr.201745432

214. Wang Y, Barthez M, Chen D (2024) Mitochondrial regulation in stem cells. *Trends Cell Biol* 34 (8):685-694. https://doi.org/10.1016/j.tcb.2023.10.003

215. Giacomello M, Pyakurel A, Glytsou C, Scorrano L (2020) The cell biology of mitochondrial membrane dynamics. *Nat Rev Mol Cell Biol* 21 (4):204-224. https://doi.org/10.1038/s41580-020-0210-7

216. Sebastián D, Palacín M, Zorzano A (2017) Mitochondrial Dynamics: Coupling Mitochondrial Fitness with Healthy Aging. *Trends Mol Med* 23 (3):201-215. https://doi.org/10.1016/j.molmed.2017.01.003

217. Sharma A, Smith HJ, Yao P, Mair WB (2019) Causal roles of mitochondrial dynamics in longevity and healthy aging. *EMBO Rep* 20 (12):e48395. https://doi.org/10.15252/embr.201948395

218. Li YE, Sowers JR, Hetz C, Ren J (2022) Cell death regulation by MAMs: from molecular mechanisms to therapeutic implications in cardiovascular diseases. *Cell Death Dis* 13 (5):504. https://doi.org/10.1038/s41419-022-04942-2

219. Kerkhofs M, Bittremieux M, Morciano G, Giorgi C, Pinton P, Parys JB, Bultynck G (2018) Emerging molecular mechanisms in chemotherapy: Ca(2+) signaling at the mitochondria-associated endoplasmic reticulum membranes. *Cell Death Dis* 9 (3):334. https://doi.org/10.1038/s41419-017-0179-0

220. Rieusset J (2011) Mitochondria and endoplasmic reticulum: mitochondria-endoplasmic reticulum interplay in type 2 diabetes pathophysiology. *Int J Biochem Cell Biol* 43 (9):1257-1262. https://doi.org/10.1016/j.biocel.2011.05.006

221. Chipuk JE, McStay GP, Bharti A, Kuwana T, Clarke CJ, Siskind LJ et al. (2012) Sphingolipid metabolism cooperates with BAK and BAX to promote the mitochondrial pathway of apoptosis. *Cell* 148 (5):988-1000. https://doi.org/10.1016/j.cell.2012.01.038

222. Mignard V, Dubois N, Lanoé D, Joalland MP, Oliver L, Pecqueur C et al. (2020) Sphingolipid distribution at mitochondria-associated membranes (MAMs) upon induction of apoptosis. *J Lipid Res* 61 (7):1025-1037. https://doi.org/10.1194/jlr.RA120000628

223. Ganesan V, Perera MN, Colombini D, Datskovskiy D, Chadha K, Colombini M (2010) Ceramide and activated Bax act synergistically to permeabilize the mitochondrial outer membrane. *Apoptosis* 15 (5):553-562. https://doi.org/10.1007/s10495-009-0449-0

224. Birbes H, El Bawab S, Hannun YA, Obeid LM (2001) Selective hydrolysis of a mitochondrial pool of sphingomyelin induces apoptosis. *FASEB J* 15 (14):2669-2679. https://doi.org/10.1096/fj.01-0539com

225. Taniguchi M, Okazaki T (2021) Role of ceramide/sphingomyelin (SM) balance regulated through "SM cycle" in cancer. *Cell Signal* 87:110119. https://doi.org/10.1016/j.cellsig.2021.110119

226. Morad SA, Cabot MC (2013) Ceramide-orchestrated signalling in cancer cells. *Nat Rev Cancer* 13 (1):51-65. https://doi.org/10.1038/nrc3398

227. Morrish F, Hockenbery D (2014) MYC and mitochondrial biogenesis. *Cold Spring Harb Perspect Med* 4 (5). https://doi.org/10.1101/cshperspect.a014225

228. Casinelli G, LaRosa J, Sharma M, Cherok E, Banerjee S, Branca M et al. (2016) N-Myc overexpression increases cisplatin resistance in neuroblastoma via deregulation of mitochondrial dynamics. *Cell Death Discov* 2:16082. https://doi.org/10.1038/cddiscovery.2016.82

229. Li F, Wang Y, Zeller KI, Potter JJ, Wonsey DR, O'Donnell KA et al. (2005) Myc stimulates nuclearly encoded mitochondrial genes and mitochondrial biogenesis. *Mol Cell Biol* 25 (14):6225-6234. https://doi.org/10.1128/mcb.25.14.6225-6234.2005

230. Moullan N, Mouchiroud L, Wang X, Ryu D, Williams EG, Mottis A et al. (2015) Tetracyclines Disturb Mitochondrial Function across Eukaryotic Models: A Call for Caution in Biomedical Research. *Cell Rep* 10 (10):1681-1691. https://doi.org/10.1016/j.celrep.2015.02.034

231. Todd SR, Dahlgren FS, Traeger MS, Beltrán-Aguilar ED, Marianos DW, Hamilton C et al. (2015) No visible dental staining in children treated with doxycycline for suspected Rocky Mountain Spotted Fever. *J Pediatr* 166 (5):1246-1251. https://doi.org/10.1016/j.jpeds.2015.02.015

232. Pöyhönen H, Nurmi M, Peltola V, Alaluusua S, Ruuskanen O, Lähdesmäki T (2017) Dental staining after doxycycline use in children. *J Antimicrob Chemother* 72 (10):2887-2890. https://doi.org/10.1093/jac/dkx245

233. Pfanner N, Warscheid B, Wiedemann N (2019) Mitochondrial proteins: from biogenesis to functional networks. *Nat Rev Mol Cell Biol* 20 (5):267-284. https://doi.org/10.1038/s41580-018-0092-0

234. Shpilka T, Haynes CM (2018) The mitochondrial UPR: mechanisms, physiological functions and implications in ageing. *Nat Rev Mol Cell Biol* 19 (2):109-120. https://doi.org/10.1038/nrm.2017.110

235. Fessler E, Eckl EM, Schmitt S, Mancilla IA, Meyer-Bender MF, Hanf M et al. (2020) A pathway coordinated by DELE1 relays mitochondrial stress to the cytosol. *Nature* 579 (7799):433-437. https://doi.org/10.1038/s41586-020-2076-4

236. Guo X, Aviles G, Liu Y, Tian R, Unger BA, Lin YT et al. (2020) Mitochondrial stress is relayed to the cytosol by an OMA1-DELE1-HRI pathway. *Nature* 579 (7799):427-432. https://doi.org/10.1038/s41586-020-2078-2

237. Mick E, Titov DV, Skinner OS, Sharma R, Jourdain AA, Mootha VK (2020) Distinct mitochondrial defects trigger the integrated stress response depending on the metabolic state of the cell. *Elife* 9. https://doi.org/10.7554/eLife.49178

238. Kim Y, Park J, Kim S, Kim M, Kang MG, Kwak C et al. (2018) PKR Senses Nuclear and Mitochondrial Signals by Interacting with Endogenous Double-Stranded RNAs. *Mol Cell* 71 (6):1051-1063.e1056. https://doi.org/10.1016/j.molcel.2018.07.029

239. Pakos-Zebrucka K, Koryga I, Mnich K, Ljujic M, Samali A, Gorman AM (2016) The integrated stress response. *EMBO Rep* 17 (10):1374-1395. https://doi.org/10.15252/embr.201642195

240. Quirós PM, Prado MA, Zamboni N, D'Amico D, Williams RW, Finley D et al. (2017) Multi-omics analysis identifies ATF4 as a key regulator of the mitochondrial stress response in mammals. *J Cell Biol* 216 (7):2027-2045. https://doi.org/10.1083/jcb.201702058

241. Kaspar S, Oertlin C, Szczepanowska K, Kukat A, Senft K, Lucas C et al. (2021) Adaptation to mitochondrial stress requires CHOP-directed tuning of ISR. *Sci Adv* 7 (22). https://doi.org/10.1126/sciadv.abf0971

242. Bonvini P, Nguyen P, Trepel J, Neckers LM (1998) In vivo degradation of N-myc in neuroblastoma cells is mediated by the 26S proteasome. *Oncogene* 16 (9):1131-1139. https://doi.org/10.1038/sj.onc.1201625

243. Paul I, Ahmed SF, Bhowmik A, Deb S, Ghosh MK (2013) The ubiquitin ligase CHIP regulates c-Myc stability and transcriptional activity. *Oncogene* 32 (10):1284-1295. https://doi.org/10.1038/onc.2012.144

244. Tameire F, Verginadis, II, Leli NM, Polte C, Conn CS, Ojha R et al. (2019) ATF4 couples MYC-dependent translational activity to bioenergetic demands during tumour progression. *Nat Cell Biol* 21 (7):889-899. https://doi.org/10.1038/s41556-019-0347-9

245. Qing G, Li B, Vu A, Skuli N, Walton ZE, Liu X et al. (2012) ATF4 regulates MYC-mediated neuroblastoma cell death upon glutamine deprivation. *Cancer Cell* 22 (5):631-644. https://doi.org/10.1016/j.ccr.2012.09.021

246. Wang J, Jiang J, Chen H, Wang L, Guo H, Yang L et al. (2019) FDA-approved drug screen identifies proteasome as a synthetic lethal target in MYC-driven neuroblastoma. *Oncogene* 38 (41):6737-6751. https://doi.org/10.1038/s41388-019-0912-5

247. Körber V, Stainczyk SA, Kurilov R, Henrich KO, Hero B, Brors B et al. (2023) Neuroblastoma arises in early fetal development and its evolutionary duration predicts outcome. *Nat Genet* 55 (4):619-630. https://doi.org/10.1038/s41588-023-01332-y

248. Saldana-Guerrero IM, Montano-Gutierrez LF, Boswell K, Hafemeister C, Poon E, Shaw LE et al. (2024) A human neural crest model reveals the developmental impact of neuroblastoma-associated chromosomal aberrations. *Nat Commun* 15 (1):3745. https://doi.org/10.1038/s41467-024-47945-7

249. Erickson AG, Kameneva P, Adameyko I (2023) The transcriptional portraits of the neural crest at the individual cell level. *Semin Cell Dev Biol* 138:68-80. https://doi.org/10.1016/j.semcdb.2022.02.017

250. Adameyko I, Lallemend F, Aquino JB, Pereira JA, Topilko P, Müller T et al. (2009) Schwann cell precursors from nerve innervation are a cellular origin of melanocytes in skin. *Cell* 139 (2):366-379. https://doi.org/10.1016/j.cell.2009.07.049

251. Dyachuk V, Furlan A, Shahidi MK, Giovenco M, Kaukua N, Konstantinidou C et al. (2014) Neurodevelopment. Parasympathetic neurons originate from nerve-associated peripheral glial progenitors. *Science* 345 (6192):82-87. https://doi.org/10.1126/science.1253281

252. Kaukua N, Shahidi MK, Konstantinidou C, Dyachuk V, Kaucka M, Furlan A et al. (2014) Glial origin of mesenchymal stem cells in a tooth model system. *Nature* 513 (7519):551-554. https://doi.org/10.1038/nature13536

253. Kameneva P, Kastriti ME, Adameyko I (2021) Neuronal lineages derived from the nerve-associated Schwann cell precursors. *Cell Mol Life Sci* 78 (2):513-529. https://doi.org/10.1007/s00018-020-03609-5

254. Furlan A, Dyachuk V, Kastriti ME, Calvo-Enrique L, Abdo H, Hadjab S et al. (2017) Multipotent peripheral glial cells generate neuroendocrine cells of the adrenal medulla. *Science* 357 (6346). https://doi.org/10.1126/science.aal3753

255. Kamenev D, Sunadome K, Shirokov M, Chagin AS, Singh A, Irion U et al. (2021) Schwann cell precursors generate sympathoadrenal system during zebrafish development. *J Neurosci Res* 99 (10):2540-2557. https://doi.org/10.1002/jnr.24909

256. Kastriti ME, Faure L, Von Ahsen D, Bouderlique TG, Boström J, Solovieva T et al. (2022) Schwann cell precursors represent a neural crest-like state with biased multipotency. *EMBO J* 41 (17):e108780. https://doi.org/10.15252/embj.2021108780

257. Fredlund E, Andersson S, Hilgert E, Monferrer E, Álvarez-Hernán G, Karakaya S et al. (2024) MOXD1 is a lineage-specific gene and a tumor suppressor in neuroblastoma. *Sci Adv* 10 (25):eado1583. https://doi.org/10.1126/sciadv.ado1583

258. Kildisiute G, Kholosy WM, Young MD, Roberts K, Elmentaite R, van Hooff SR et al. (2021) Tumor to normal single-cell mRNA comparisons reveal a pan-neuroblastoma cancer cell. *Sci Adv* 7 (6). https://doi.org/10.1126/sciadv.abd3311

259. Chuprin J, Buettner H, Seedhom MO, Greiner DL, Keck JG, Ishikawa F et al. (2023) Humanized mouse models for immuno-oncology research. *Nat Rev Clin Oncol* 20 (3):192-206. https://doi.org/10.1038/s41571-022-00721-2

6 APPENDICES

Selected publications related to the thesis.

APPENDIX 1

Pleskač P, Fargeas CA, Veselska R, Corbeil D, **Skoda J***. Emerging roles of prominin-1 (CD133) in the dynamics of plasma membrane architecture and cell signaling pathways in health and disease. *Cellular & Molecular Biology Letters*. 2024;29:41. (JCR 2023, IF = 9.2; Q1 - Cell Biology)

REVIEW

Emerging roles of prominin-1 (CD133) in the dynamics of plasma membrane architecture and cell signaling pathways in health and disease

Petr Pleskač[1,2], Christine A. Fargeas[3,4], Renata Veselska[1,2], Denis Corbeil[3,4]* and Jan Skoda[1,2]*

*Correspondence:
denis.corbeil@tu-dresden.de; jan.
skoda@sci.muni.cz

[1] Laboratory of Tumor Biology, Department of Experimental Biology, Faculty of Science, Masaryk University, Kamenice 5, 625 00 Brno, Czech Republic
[2] International Clinical Research Center, St. Anne's University Hospital, Brno, Czech Republic
[3] Biotechnology Center (BIOTEC) and Center for Molecular and Cellular Bioengineering (CMCB), Technische Universität Dresden, Tatzberg 47/49, 01307 Dresden, Germany
[4] Tissue Engineering Laboratories, Medizinische Fakultät der Technischen Universität Dresden, Dresden, Germany

Abstract

Prominin-1 (CD133) is a cholesterol-binding membrane glycoprotein selectively associated with highly curved and prominent membrane structures. It is widely recognized as an antigenic marker of stem cells and cancer stem cells and is frequently used to isolate them from biological and clinical samples. Recent progress in understanding various aspects of CD133 biology in different cell types has revealed the involvement of CD133 in the architecture and dynamics of plasma membrane protrusions, such as microvilli and cilia, including the release of extracellular vesicles, as well as in various signaling pathways, which may be regulated in part by posttranslational modifications of CD133 and its interactions with a variety of proteins and lipids. Hence, CD133 appears to be a master regulator of cell signaling as its engagement in PI3K/Akt, Src-FAK, Wnt/β-catenin, TGF-β/Smad and MAPK/ERK pathways may explain its broad action in many cellular processes, including cell proliferation, differentiation, and migration or intercellular communication. Here, we summarize early studies on CD133, as they are essential to grasp its novel features, and describe recent evidence demonstrating that this unique molecule is involved in membrane dynamics and molecular signaling that affects various facets of tissue homeostasis and cancer development. We hope this review will provide an informative resource for future efforts to elucidate the details of CD133's molecular function in health and disease.

Keywords: Cancer, Cancer stem cell, Cell signaling, CD133, Cilium, Exosome, Lipid raft, Microvillus, Prominin-1, Stem cell

Introduction

Prominin-1 (Prom1, a.k.a. cluster of differentiation (CD)133; hereafter, CD133 refers to the mammalian molecule) has attracted global interest in the fields of regenerative medicine and oncology, as its expression on the cell surface allows the identification and isolation of stem cells and cancer stem cells (CSCs). In 1997, the discovery of CD133 was reported by two independent research teams studying the cell biology of murine neuroepithelial progenitor cells [1] and the surface markers of human hematopoietic

stem and progenitor cells (HSPCs) [2, 3]. Soon after, CD133 protein was detected in fully differentiated cells and cancer cells in both rodents and humans, demonstrating that its expression is not restricted to stem and progenitor cell populations [1, 4–10].

Murine CD133 was originally cloned using a cDNA library prepared from adult kidney [1], while the human ortholog was obtained from retinoblastoma cell lines [3]. Indeed, CD133 is highly expressed in the proximal tubules of the kidney and other epithelial cells in embryonic and adult tissues, where it is expressed solely on the apical domain of polarized cells [1, 7, 11, 12]. CD133 expression has also been identified in the epithelial cells of the epididymal tract, where sperm maturation occurs [10, 13, 14], and in various glands [15–17], such as mammary glands [11, 17, 18], liver [17, 19, 20], pancreas [17, 21] and salivary glands [22–24]. Of note, differentiated nonepithelial cells, particularly photoreceptor cells [8, 23, 25] and glial cells [26], also express CD133, indicating that CD133 plays a general role that is not necessarily linked to a particular condition (e.g., cell stemness or differentiation status) or specific cellular type (epithelial versus nonepithelial) [27].

General interest in CD133 grew exponentially after 2003 when Dirks and colleagues, and others, reported its expression in tumor brain tissues and its use as a marker to isolate human CSCs [28–30]. These reports aroused enormous enthusiasm not only in the field of oncology, where the CD133 expression has been correlated with cancer progression, metastasis, recurrence and poor survival [31, 32] (reviewed in Ref. [33]), but also in that of stem cells. Since then, CD133 has been regularly used as a molecular marker/target to isolate cells with stem cell properties in a wide range of human and murine tissues and tumors (reviewed in Refs [27, 34]). In addition to their detection in neural and hematopoietic systems [1, 35–37], CD133$^+$ cells with stem cell properties have been found in healthy and cancerous prostate [38–42], kidney [43–46], liver [47–49], pancreas [50, 51], intestine, colon [52–55], lung [56], and other organ tissues [57, 58]. CD133 was also associated with leukemic cells [3, 5, 59–62]. Importantly, in the context of cancer and regenerative medicine, CD133 is a marker of endothelial progenitor cells that could contribute to tumor vasculature in cancer and tissue regeneration upon injury [63–69]. It cannot be excluded that CD133 plays a role in facultative stem cells, i.e., fully differentiated cells that exhibit stem and progenitor activities through their ability to re-enter the cell cycle in particular tissues and/or under specific conditions [70–72]. In fact, certain differentiated CD133$^+$ cells (e.g., in kidney and liver) may have such ability upon injury or in disease states [70] (reviewed in Ref. [73]). Regardless of the mechanism of regeneration, CD133 can mark cells with stem cell properties and thus has clinical value.

The utility of CD133 as an organ-specific stem cell marker in humans and its importance for determining cancer prognosis and progression have been nonetheless called into question [74]. This controversy stemmed in part from the apparent contradiction between the limited expression of CD133 protein in human adult tissues, based on immunodetection using an antibody named AC133 directed against a specific epitope of CD133 (CD133/1) [3], and the wide expression of its transcript as detected via Northern blot and polymerase chain reaction analyses [2, 3, 7, 11, 17, 21, 75]. However, the murine CD133 (both protein and transcript) has been known to be widely expressed well beyond stem cells [1], particularly in epithelial cells (see above) and photoreceptors [8]. The mapping of CD133 to differentiated epithelial cells using LacZ reporter-based

Pleskač *et al. Cellular & Molecular Biology Letters*   (2024) 29:41

Page 3 of 47

mice further contributed to the debate [76]. The use of alternative antibodies against human CD133 has confirmed its wide protein expression [11, 17, 21, 24], similar to that of its ortholog in rodents [9, 10, 22]. Therefore, it is important to note that the AC133 immunoreactivity is not necessarily equivalent to the human CD133 protein, and a link between CD133/1 detection and cellular status (i.e., stem cell versus differentiation) has been proposed [11, 77]. The use of the AC133 antibody and the accessibility of the CD133/1 epitope have been extensively discussed in the literature, and we invite readers to consult the relevant publications [11, 15–17, 78–83].

It should be noted that stem cells are functional without CD133, as illustrated by the various *Prominin-1* (*Prom1*)-knockdown mouse models (reviewed in Ref. [84]) in which no major defects are detected, except for retinal degeneration [23]; this retinal phenotype is consistent with the expression of CD133 in photoreceptor cells [8] (see below). Likewise, no major phenotype, other than blindness, has been detected in patients carrying dominant or recessive mutations in the *PROM1* gene [85], suggesting that CD133 is dispensable for general stem cell properties under physiological conditions [8, 86–88]. For example, total loss of CD133 did not affect the regenerative capacity of mammary epithelium in *Prom-1*$^{-/-}$ mice, although it did impact ductal branching and increased the ratio of luminal to basal cells [18]. This study is in agreement with the earlier report that transplantation of CD133-enriched murine cells from the mammary luminal cell population demonstrated a low regenerative capacity compared with CD133-negative fraction or basal cells, suggesting that in normal mammary tissue, CD133 is not a stem cell marker and that its function goes beyond stem cell activity [89]. Similar conclusions were drawn for mouse oviduct epithelial progenitors [90]. Finally, CD133 is not essential for normal hematopoiesis, as observed in *Prom-1*$^{-/-}$ mice, but nonetheless it modifies the frequencies of growth-factor responsive hematopoietic progenitor cells during steady state and under myelotoxic stress conditions in vivo [91]. These findings suggest that CD133 plays a redundant role in the differentiation of the mature myeloid cell population during hematopoiesis, yet CD133 is important for the recovery of red blood cells after hematopoietic stress [91]. It cannot be ruled out that, in these models, a compensatory mechanism involving the CD133 paralog prominin-2 occurs in CD133-depleted cells in tissues that typically express both proteins [92], which is not the case of retina [93].

Clearly, it is time to re-examine the function of CD133, including its role in cancers, and translate this knowledge into new and biologically relevant CD133-based approaches for tissue engineering, regenerative medicine and cancer therapy. Here, we summarize the current knowledge of the molecular and cellular biology of CD133, including its preferential association with highly curved membrane protrusions such as microvilli and cilia as well as tunneling nanotubes (TNTs) that mediate exchange of CD133 between interconnected stem or cancer cells. We will also discuss the role of CD133$^+$ extracellular membrane vesicles (EVs), which have received considerable attention in recent years, and the lessons learned from studies using CD133-deficient animals and CD133-silenced human CD34$^+$ HSPCs as well as studies focused on cancers in which CD133 is upregulated. Particular attention will be given to the impact of CD133 on various cell signaling pathways and its potential involvement in cell proliferation, differentiation, autophagy and migration. We hope that this review will promote the

development of future functional studies on CD133 as a molecule essential for multiple cellular processes.

Molecular biology of CD133

Structure and splice variants

CD133 is a membrane glycoprotein with an apparent molecular mass of ≈ 120 kDa, of which N-glycans represent ≈ 20 kDa, consistent with its predicted molecular weight of 97,202 Da (referring here to the human splice variant s2, see below) [1, 3, 11]. It contains five transmembrane segments; delimiting an extracellular N-terminal domain (referred to as EC1), two large extracellular loops (EC2 and EC3) alternating with two small intracellular loops (IC1 and IC2) and an intracytoplasmic C-terminal domain (IC3). The approximate size of each structural domain is indicated (Fig. 1a, see the corresponding legend for more details) [22]. Eight asparagine residues in consensus N-glycosylation sites (Asn-X-Ser/Thr-X sequons, where X is any amino acid except proline) are found in human and murine CD133 and distributed between EC2 and EC3 [1, 3]. An additional site, Asn_{206}-Glu-Thr-Pro, was shown to be glycosylated in human CD133 [94].

CD133 belongs to the prominin family of pentaspan membrane proteins [93]. Two distinct mammalian *Prominin* genes have been described [93, 95], while three prominin molecules have been identified in nonmammalian species [25, 96, 97]. Two *Prominin*-related genes, prominin and prominin-like, were identified in *Drosophila melanogaster* [93, 98–100] and other holometabolous insects [101]. However, in contrast to prominin-like, fly prominin has a predicted sixth transmembrane domain [101, 102]. Interestingly, the *Prom1* gene is duplicated in zebrafish, and the two gene products are referred to as *prominin-1a* and *-1b* [25, 103]. Structurally related prominin-like proteins have been identified in an amoeba, i.e., *Naegleria gruberi* (GenBank accession numbers JN679227.1 and JN679228.1), suggesting the expression of prominin in unicellular organisms. Interestingly, amino acid sequences are poorly conserved between paralogs as well as within one orthologous group, notably CD133/prominin-1. For example, only 60% identity has been observed between primates and rodents, while their sequence identities with other species (fish, amphibians, birds) are below 50%; and less than 25% with invertebrates (flies, worms) [25, 93, 96]. Yet, the analysis of the primary sequence of all prominin molecules, regardless of the species, revealed no potential enzymatic/catalytic motif or domain that could explain their molecular function [95].

PROM1/Prom1 genes are located on chromosome 4 and 5 in humans and mice, respectively (see also Online Mendelian Inheritance in Man (OMIM) entry number 604365). The organization of these genes and of the *PROM2* genes (OMIN 617150) is highly conserved in terms of exon–intron boundaries, across most of species (Fig. 1b) [25, 93, 104, 105]. At least six alternative promoters (named P1-P6; discussed in detail below) have been identified in the human *PROM1* gene. The primary transcripts may undergo extensive alternative splicing [8, 10, 106]. Considering mammalian and nonmammalian vertebrates, more than 20 splice variants from at least 28 exons affecting the open reading frame (ORF) have been described [10, 25, 105]. In rodents and primates, the resulting proteins would be from 804 to 865 amino acids in length [95]. A nomenclature of CD133 splice variants proposing to add a suffix "s" and number the variants according to the chronology of publication regardless of species was presented [10, 25,
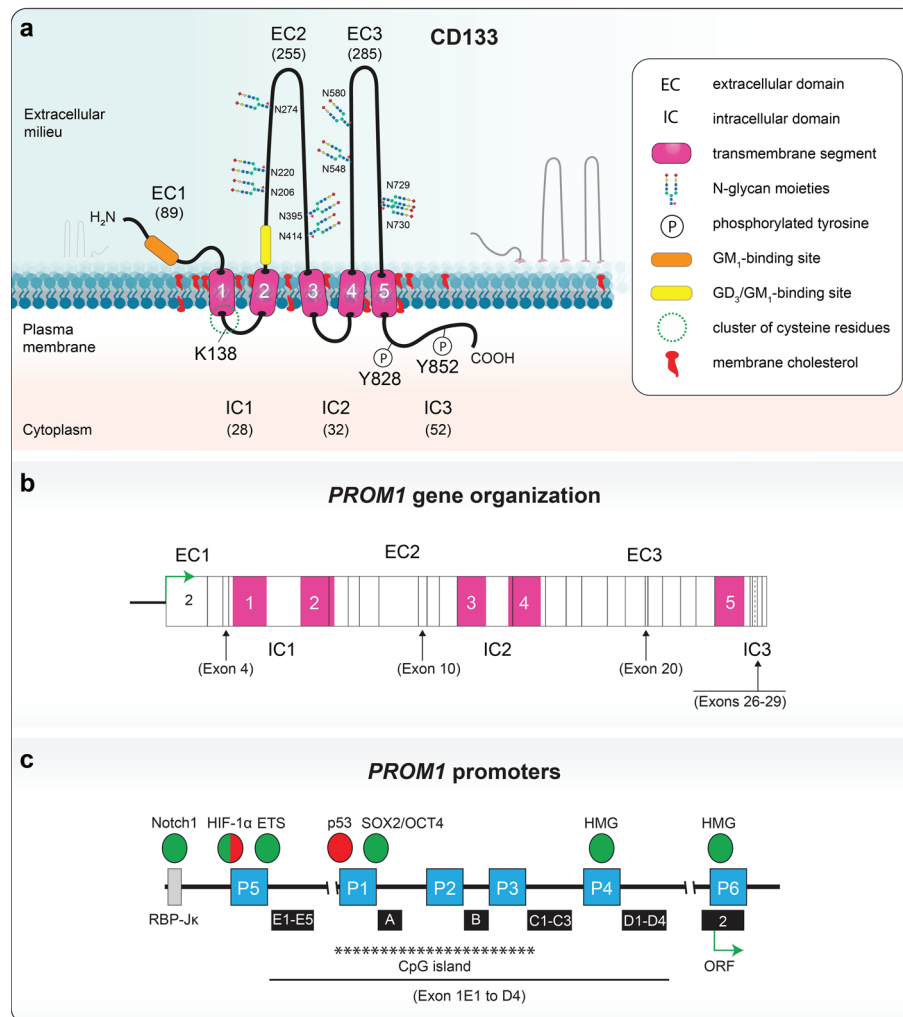
Fig. 1 Structural features of CD133. **a** Membrane topology. The human CD133 protein comprises three extracellular domains (EC1–3), an N-terminal domain (EC1) and two larger loops (EC2 and EC3) bearing nine glycosylation sites. N-glycan structures vary with the subcellular localization of CD133 and the state of cell differentiation, which may influence its interaction with protein partners. The intracellular domains (IC1–3) consist of two small cytoplasmic loops (IC1–2) and the C-terminal domain (IC3). ECs and ICs are separated by five transmembrane domains (1–5, pink cylinders). CD133 carries a cluster of cysteine residues located at the boundary of the first transmembrane segment and the IC1 domain (dotted green line). These residues may be subject to palmitoylation. Two potential ganglioside-binding sites are located in the EC1 and EC2 domains (orange and yellow cylinders). Two major tyrosine (Y) residues, 828 and 852, in IC3 can be phosphorylated and regulate the activity of several signaling pathways. Lysine (K) 138 interacts with HDAC6 and Arl13b. The outer and inner leaflets of the plasma membrane are shown with membrane cholesterol (red), highlighting the association of CD133 with cholesterol-dependent membrane microdomains. Amino acid numbering is based on the human splice variant CD133.s2; the approximate number of amino acid residues in a given domain, which may vary from one splice variant to another, is indicated in parentheses. **b** Genomic organization of mammalian CD133. Vertical lines indicate exon boundaries, the dashed line the presence of an alternative splice acceptor site, while transmembrane domains are highlighted in pink. Major facultative exons within ORF are indicated in brackets. The exons are numbered as the initial start codon is located in exon 2. **c** *PROM1* promoters. Six distinct promoters were identified (blue boxes) in human *PROM1* gene with various facultative exons (A-E5, black boxes) that are part of exon 1. The P1-P3 promoters show high proportion of CpG islands. The major transcription factors impacting positively or negatively on *PROM1* gene expression are indicated in green and red, respectively. Figures are not to scale. Illustration in **a** is adapted from Ref [3] and incorporates data from Refs [94, 161, 209, 219], while those in panels b and c are adapted from Refs [95] and [111], respectively

Pleskač *et al. Cellular & Molecular Biology Letters*   (2024) 29:41

Page 6 of 47

77, 104]. The majority of these splice variants differ in the N- and C-terminal domain sequences. Splice variants s1 and s2 differ from each other by the inclusion or exclusion of a small exon [numbered 4 as we refer to exon 2 as carrying the initial codon] in EC1, respectively, while IC3 shows a greater propensity for alternative splicing of small exons (exons 26–29), suggesting interactions with distinct extracellular and cytoplasmic partners (Fig. 1b, see legend for more details) [10, 104]. At least 10 distinct cytoplasmic C-termini were described [25] (reviewed in Ref. [95]). The final four C-terminal amino acid residues in some variants exhibit the characteristics of PSD-95/Dig-1/ZO-1 (PDZ)-binding domains (classes I-III), which is consistent with the ability of the CD133 variants to bind various proteins [104].

The expression of CD133 splice variants is often cell- and tissue-type dependent and may reflect its particular role in the given organ [10, 26, 34, 107]. For example, CD133.s1 is predominantly expressed in the brain tissue of mouse embryos, and its expression decreases during brain development to barely detectable levels in the brains of adult mice [26]. An opposite trend was observed for CD133.s3 expression in the early postnatal period, which correlated with the onset of neuronal myelination. This splice variant is a component of the myelin sheath [22, 26], and hypomyelination has been observed in *Prom1*-null mice [108]. Exons splicing in the EC2 appears to impact cell surface expression and overall folding of the protein, as evidenced by the absence of the 25 residues encoded by murine exon 10 leading to the CD133 degradation in the endoplasmic reticulum (ER) (Fig. 1b) [10]. A 16-kDa truncated variant of the CD133 protein has also been reported in glioblastoma cell lines [109]. Yet, the precise nature of this potential short form would require further investigation. Importantly, the coexpression of distinct CD133 splice variants has been reported [10], confirming the need to include systematic analyses of CD133 variants in future studies to unravel their potentially complex involvement in various cellular processes.

Regulation of PROM1 gene expression

In relation to its multiple roles and differential expression in normal tissues, stem cells and cancer cells, the transcriptional regulation of CD133 expression is complex with human *PROM1* gene being driven by six promoters [106, 110–112]. Consequently, at least 14 distinct transcripts are generated depending on the tissue with different or optional exons 1 (namely 1A-E) constituting the 5' untranslated region (UTR) (Fig. 1c) [106, 111, 113]. The P1, P2 and P3 promoters of *PROM1* gene show high proportion of CpG islands and are differentially methylated in normal and cancer tissues such as glioma or colon cancer [110, 114–117]. These promoters may also be polycomb-repressed in acute leukemia [118] and divers cell lines [111]. The proximal P6 promoter identified in melanoma cells was found to be enriched in binding sites for high mobility group (HMG) proteins—nonhistone chromatin-associated proteins that are aberrantly expressed in a variety of cancers (Fig. 1c) [111].

PROM1 gene expression may also be regulated through histone modification, which may depend on DNA hypermethylation [114, 117]. Histone H3 lysine-79 (H3K79) methylation was first identified to be a regulator of *PROM1* gene expression in an investigation aimed at identifying targets of mixed lineage leukemia (MLL) fusion proteins responsible for aberrant gene expression in patients with leukemia [119]. *PROM1* gene

was found to be a target of the MLL fusion-associated gene AF4 (MLL-AF4) in human colon cancer Caco-2 cells [120] and in some MLL cells [118], where its transcription is upregulated through H3K79 methylation and the presence of an intragenic H3K79me2/3 enhancer element. Notably, polycomb-repression inactivates such enhancer. Transforming growth factor (TGF)-β1 has been shown to induce the demethylation of *PROM1* promoter P1 by inhibiting the expression of DNA methyltransferase-1 and 3β (DNMT1 and DNMT3ß) in hepatoma cells, leading to a significant upregulation of CD133 [121]. Collectively, TGF-β signaling in different solid malignancies leads to the induction of stem-like characteristics [122], the epithelial-mesenchymal transition (EMT), or increased tumorigenicity [123] and initiates the expression of CD133. The mechanisms that regulate the interplay between TGF-β1 and CD133, thereby contributing to the stem cell phenotype among various normal and cancer cell types, remains to be explored in greater detail.

Interestingly, a thorough analysis of the relationship between promoter hypomethylation and increased CD133 expression in glioma revealed novel transcriptional coregulators of CD133 expression, specificity protein 1 and c-MYC, which can bind only to a hypomethylated *PROM1* promoter [110]. However, although such epigenetic regulation has been shown to exist in prostate cell lines, this is not the case in primary prostate epithelial cultures, suggesting evidence for dysregulated CD133 expression during long-term culture in vitro [124]. In basal-like breast carcinoma cells with p53 deficiency, which leads to an autocrine interleukin (IL)-6 loop driving cell reprogramming, IL-6 was found to regulate *PROM1* expression by inducing *PROM1* P1 promoter demethylation that resulted in enhanced transcription and, in parallel, an increased methylation of the *PROM1* P2 promoter that carries putative repressor sites [125].

Cells exposed to stresses, such as DNA damage, hypoxia, oncogene activation, or ribosomal stress, react by stabilizing p53, which in turn orchestrates the transcription of genes involved in major stress response processes, i.e., cell cycle arrest, DNA repair, and cell death [126]. The expression pattern of CD133 was reported to be inversely related to the expression of p53 in different cancer cell lines and tumor tissue samples [127]. Noncanonical p53 binding sites were identified in the P1 promoter enabling p53 interaction (Fig. 1c), which led to the recruitment of histone deacetylase (HDAC) 1 and thus inhibition of CD133 expression due to reduced histone H3 acetylation. Interestingly, the downregulation of CD133 was also accompanied by suppression of stemness-associated transcription factors, such as NANOG, octamer-binding transcription factor 4 (OCT4, also called POU5F1), sex-determining region Y-box 2 (SOX2), and c-MYC, and reduced cell growth and tumor formation capacity [127].

Hypoxia is a key factor in the tumor microenvironment and was shown to increase the CD133$^+$ population in medulloblastoma and glioma cells [128, 129]. Prolonged hypoxia exposure (i.e., 1% O_2 for a period of 72 h) stimulated glioblastoma cells to express CD133 and the stemness markers Kruppel-like factor 4 (KLF4) and SOX2 via a hypoxia inducible factor (HIF)-1α-dependent mechanism (Fig. 2a) [130]. Interestingly, these stemness traits as well as the significantly higher clonogenicity and capacity to form spheres during serial passaging were maintained after normoxic conditions were restored [130]. A similar hypoxia-induced coexpression of CD133 and HIF-1α in glioma cells has been reported by other groups [131, 132], and it was shown to be associated with enhanced
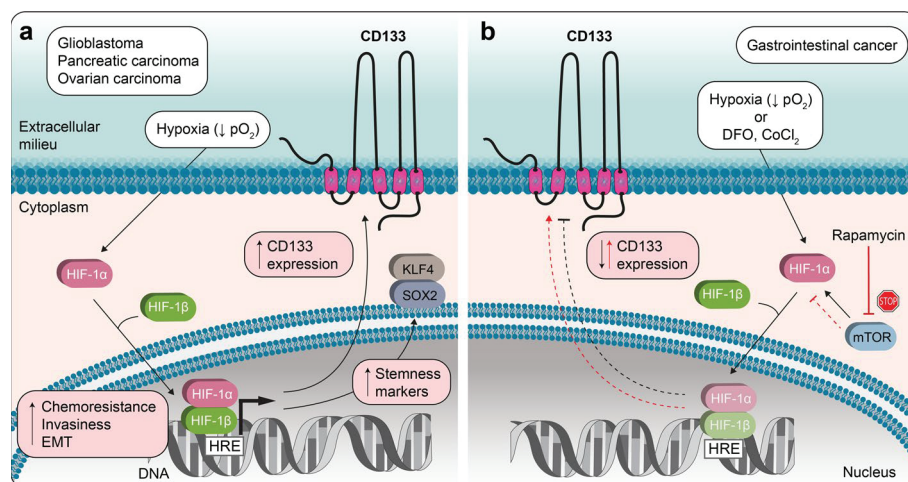
Fig. 2 Cell type-dependent impact of hypoxic conditions on CD133 expression. **a** Under hypoxic conditions and in certain types of cancer as indicated, HIF-1α and HIF-1β are translocated into the nucleus, where they form a heterodimeric transcription factor that binds to hypoxia-responsive elements (HRE), resulting in increased expression of CD133 and other stemness markers (e.g., KLF4 and SOX2). Thus, hypoxia can promote chemoresistance, invasiveness and EMT. **b** In gastrointestinal carcinoma cells, the induction of hypoxia either by lowering the partial pressure of oxygen or by applying hypoxia-mimicking agents such as DFO and CoCl$_2$ downregulates CD133 expression (black dashed arrow). Reciprocally, rapamycin-mediated inhibition of mammalian TOR (red dashed arrow), an upstream regulator of HIF-1α signaling, results in the downregulation of HIF-1α and elevated levels of CD133 (red arrow). Illustrations in panels a and b are based on data presented in Refs [130] and [139], respectively, among others

chemoresistance, invasiveness, and EMT, which is in line with results obtained with cell lines derived from pancreatic [133] and ovarian cancer samples [134]. HIF-1 is a heterodimeric protein that regulates tissue responses to changes in the oxygen level [135]. It is composed of two subunits, α and β. Although HIF-1β subunit expression is constitutive, HIF-1α subunit expression is regulated by the partial pressure of oxygen level. Under normoxic conditions, the levels of HIF-1α are reduced because of proteasomal degradation. Hypoxia induces the dimerization of HIF-1α and HIF-1β, which form a transcription complex that recognizes E-box-like hypoxia response elements and initiates the transcription of genes involved not only in cellular oxygen homeostasis but also in pathways that coordinate cell proliferation, metabolism reprogramming, apoptosis, or resistance to tumor therapy [135].

Elevated levels of HIF-1α and HIF-2α were shown to simulated the transcription of the *PROM1* gene at the P5 promoter in colon cancer cells; specifically, it was initiated by the binding of the HIF-1-Elk1 complex to the E-twenty-six (ETS)-binding motif present in P5 [113, 136]. In contrast, in lung cancer cell lines, hypoxia-induced CD133 transcription was mainly initiated via HIF inducible-OCT4 and SOX2 binding at the P1 promoter that is devoid of HIF-binding site [137]. Interestingly, in hepatocellular carcinoma, a functional cooperation between IL-6/signal transducer and activator of transcription 3 (STAT3) signaling and nuclear factor kappa-light-chain-enhancer of activated B cells and HIF-1α was reported to upregulate CD133 expression that was associated with poor prognosis [138].

However, in addition to the positive regulation of CD133 under hypoxic conditions, contradictory results have also been reported for different tumor types. Induction of

hypoxia, either by lowering the partial pressure of oxygen or by applying hypoxia-mimicking agents [e.g., desferrioxamine (DFO) and cobalt chloride (CoCl$_2$)] in three gastrointestinal carcinoma cell lines, suppressed the expression of CD133 (Fig. 2b) [139]. In line with these findings, rapamycin-mediated inhibition of mammalian target of rapamycin (TOR), an upstream positive regulator of HIF-1α signaling, resulted in downregulation of HIF-1α and upregulation of CD133 transcription [139]. This negative correlation between CD133 and HIF-1α expression may be tissue specific. A focus on potential interaction partners of the HIF transcription complex in future studies may help to decipher the mechanisms responsible for the different impacts of hypoxia on CD133 expression.

Notch1 has also been shown to control the proportion of CD133$^+$ cells in lung adenocarcinoma [140] and to regulate CD133 expression in glioblastoma [141]. Konishi and colleagues reported that in diffuse gastric cancer, CD133 expression was induced by Notch1 through the binding of the activated Notch1 intracellular domain to a recombination signal binding protein for immunoglobulin kappa J region (RBP-Jκ)-binding motif identified in the *PROM1* gene promoter (Fig. 1c) [142]. In melanoma cell lines from both mice and humans, Notch1 also induced CD133 expression by the binding of activated Notch1 to the *Prom1/PROM1* promoter [143].

The *PROM1* gene promoter sequence carries a putative tandem β-catenin-T-cell factor (TCF)/lymphoid enhancer factor (LEF) complex binding sites within intron 2 that are conserved among mammalian *PROM1* genes [144]. Moreover, specific inhibition of CREB-binding protein (CBP), a coactivator of β-catenin/TCF-mediated transcription [145], also suppressed CD133 expression at both the mRNA and protein levels in hepatocellular carcinoma cells, reducing the anchorage-independent growth and colony formation capacity of these cells [146]. These observations suggest that *PROM1* is a Wnt target gene, which may allow a feedback loop between CD133 and β-catenin-Wnt signaling, as is discussed below.

Posttranscriptional regulation of CD133 expression by microRNAs (miRNAs) has also been documented, and these findings are in line with CD133 expression in CSCs, as these short noncoding RNAs play important roles in cancer initiation and progression and in the control of signaling pathways activity [147, 148]. For instance, miR-29b downregulated *CD133* mRNA by targeting its 3'-UTR in transfected human hepatocellular carcinoma cells [149]. Similar observations were made in esophageal cancer cells, where miR-377 expression was inversely correlated with CD133 expression [150]. High levels of miR-181a inhibited CD133 in glioblastoma cells; however, whether the miRNA acted directly or indirectly remains to be determined [151].

Interestingly, the 3'-UTR of human *CD133* transcripts bears a noncanonical iron-responsive element that may mediate their stabilization after the binding of cytosolic iron-regulatory protein 1, a key controller of iron metabolism that posttranscriptionally regulates the expression of iron metabolism genes. This possibility is in line with the reduced CD133 protein levels observed in Caco-2 cells after treatment with iron chelators or iron supplementation [152]. This regulatory mechanism appears to be related to the cholesterol-dependent negative impact of CD133 on transferrin uptake through endocytosis observed in undifferentiated Caco-2 cells. As transferrin plays the major role in the delivery of iron to cells via endocytosis, it may interfere with hypoxia-induced

Pleskač *et al. Cellular & Molecular Biology Letters*   (2024) 29:41

Page 10 of 47

regulation of CD133 expression. These data justify interest in further studying the CD133/transferrin-iron network and its potential role in endocytosis [152].

Overall, it appears that, in relation with the implication of CD133 in different biological and pathological processes, such as cancer and degenerative diseases, numerous gene expression regulatory mechanisms confer the diverse expression patterns of CD133.

Posttranslational modifications of CD133

In addition to alternative splicing, CD133 undergoes various posttranslational modifications that regulate its intracellular trafficking, stability and interactions with cytoplasmic enzymes and/or other classes of proteins. One of these CD133 modifications is N-glycosylation, in which differential processing of the glycan moiety can lead to distinct glycosylation profiles between tissues and organs [10]. Different glycoforms may coexist in a given tissue, but little is known about these complex structures. The terminal N-glycans of human CD133 contain sialyl residues, which seem to regulate CD133 stability in neural stem cells and glioma-initiating cells [153]. In the mouse embryonic brain, N-glycans of CD133 bind to *Phaseolus vulgaris* erythroagglutinating lectin, which allows cells with stem cell properties to be isolated [154]. Notably, the CD133 glycosylation is altered during early pregnancy in uterine epithelial cells under the influence of maternal ovarian hormones [155].

Similarly, hypoxic conditions can influence the glycosylation status of CD133, as demonstrated with pediatric glioblastoma cell lines [156]. Interestingly, the glycosyltransferase 8 domain containing 1 (GLT8D1) was recently shown to contribute to the stabilization of CD133 by interacting with it and influencing its glycosylation in glioma cells [157]. Similarly, the interaction of the high-mannose N-glycan form of CD133 with cytoplasmic DNA methyltransferase 1 (DNMT1) maintains the slow-cycling state of glioma stem cells, and favors chemotherapy resistance and tumorigenesis [158]. These observations are in line with the differential glycosylation status of CD133 in relation to cell differentiation [7, 11]. Although DNMT1 interaction is mediated by CD133 cytoplasmic C-terminal domain, the mechanism underlying the contribution of high-mannose N-glycans of CD133 remains unclear. The mutation of individual N-linked glycosylation sites in CD133 had no effect on its stability [159], although the loss of N-linked glycosylation at Ans548 decreased the ability of CD133 to associate with β-catenin and activate the β-catenin signaling pathway, and thus reduced CD133-driven cell proliferation [94].

Similar to differential splicing, alternative glycosylation patterns should be considered when selecting specific antibodies against CD133, especially those used for its immunodetection in a tissue of interest. For example, N-glycosylation of human CD133 seems to contribute to the recognition of the CD133/1 epitope on the cell surface by the AC133 antibody [159] (see above). Therefore, the use of two distinct antibodies to analyze CD133 expression in a given tissue and/or under specific physiological and pathological conditions is recommended [11, 17, 21–24, 83, 160].

Importantly, CD133 is also subject to other posttranslational modifications, such as phosphorylation, ubiquitination, and acetylation [24, 161, 162]. Phosphorylation, as one of the reversible posttranslational modifications, is essential for the regulation of protein functions in cell signaling. Human CD133 can be phosphorylated at two distinct tyrosine

residues (namely, Y828 and Y852 in the human CD133.s2 sequence) in its cytoplasmic C-terminus (Fig. 1a) [161]. The phosphorylation of these residues is mediated by the Src and Fyn tyrosine kinases, members of the Src nonreceptor tyrosine kinase family [161]. The amino acid sequence flanking Y828 is highly conserved in vertebrates and conforms to the tyrosine kinase phosphorylation motif [R/K]xxx[D/E]xxY. Y828 is found in the YDDV Src SH2-binding motif, and its phosphorylation may regulate the CD133 interaction with SH2 domain-containing proteins involved in intracellular signaling events [161]. A highly significant activity mediated by Y828 phosphorylation of CD133 is its interaction with the p85 regulatory subunit of phosphoinositide 3-kinase (PI3K), which thereby regulates PI3K activity at plasma membrane [163]. After overexpression, both Src and Fyn enzymes induced tyrosine phosphorylation of the complex N-glycosylated form of CD133 associated with the plasma membrane, but only Src modified the high-mannose N-glycan form associated with the ER [161]. The significance of this selectivity as well as whether Src-dependent phosphorylation of the high-mannose form of CD133 contributes to its interaction with DNMT1 (see above) remains to be determined.

Y852 is encoded by a facultative exon, the sequence of which is relatively less conserved and does not conform to the phosphorylation motif or the SH2-binding domain. It is present in some mammals, including rats, mice, chimpanzees, and humans [9, 104], but not in others, such as dogs [105]. Nevertheless, the phosphorylation of Y852 has been shown to play a critical role in the activation of Src-focal adhesion kinase (FAK) signaling [164].

Ubiquitination is another posttranslational modification of CD133 [24] that might regulate its internalization from the cell surface and sorting into small intralumenal vesicles within late endosome/multivesicular bodies (LE/MVB) *en route* to exosomes [165]. Lysine 848 (K848) is one of the sites of CD133 ubiquitination. Ubiquitinated CD133 interacts with the tumor susceptibility gene 101 (TSG101) protein [165], a component of the endosomal sorting complex required for transport (ESCRT) machinery involved in LE/MVB formation [166], and possibly with syntenin-1 [24], a PDZ domain-containing scaffold protein that regulates the biogenesis of exosomes in conjunction with ALIX and syndecan (see below) [167]. Together, these findings suggest a role for ubiquitination in the intracellular trafficking of CD133 and its release in association with exosomes into physiological bodily fluids (see below). CD133 is also subjected to acetylation by acetyltransferase 1 and 2, two acetyl-CoA:lysine acetyltransferases associated with the ER/ER–Golgi intermediate compartment. Three lysine residues (K216, K248 and K255) in the EC2 are acetylated during the anterograde transport of CD133 to the plasma membrane, and perturbation of this posttranslational modification affects the stability of CD133 and impedes its appearance at the cell membrane [162, 168].

Cellular biology of CD133

CD133: an organizer of plasma membrane protrusions

Prominin-1 owes its name to its specific subcellular distribution on prominent cellular protrusions [1]. It localizes to highly curved membrane subdomains, such as microvilli, cilia, filopodia, and other membrane structures that protrude from flat regions of the plasma membrane regardless of cell type, i.e., stem cells versus differentiated cells, or epithelial versus nonepithelial cells, as described in a review article published two

decades ago [22]. Its expression in the flagellum of immature spermatozoa present in murine testis and in the myelin sheath produced by oligodendrocytes and Schwann cells is consistent with its specific localization to membrane protrusions [10, 26].

The importance of this subcellular localization was initially demonstrated in photoreceptor cells in which CD133 is enriched at the base of the outer segment of rod cells [8]; more specifically, in precursor membranes of photoreceptor disks emerging from the connecting cilium (reviewed in Refs [169, 170]). The outer segment is a specialized ciliary organelle that allows sensory neurons to detect light and convert it into cellular signals relayed to downstream neurons [171]. The interaction of CD133 with the membrane protein protocadherin 21 regulates the proper biogenesis and maintenance of these large nascent membrane evaginations [87]. CD133 knockdown in murine models impaired these processes, leading to the disorganization of the photoreceptor outer segment and progressive degeneration of the photoreceptor [23]. Variations in the genetic background could influence the progression of photoreceptor cell degeneration [172]. Han and colleagues demonstrated that frog prominin-1 localized to highly curved open rims of outer segment lamellae in the rod and cone cells of *Xenopus laevis* retinas [173]. Retinal phenotypes were observed in frogs and zebrafish when prominin-1 or prominin-1b paralog was silenced, respectively [174, 175]. Although zebrafish prominin-1a is also highly expressed in photoreceptors, its role has not been established [25, 175, 176]. As observed in frog eyes, CD133 was expressed throughout all the disk membranes of human cone cells [170], and clinically, all patients with recessive or dominant *PROM1* mutations show cone–rod dystrophy. Interestingly, although the recessive diseases were associated with early-onset severe panretinal degeneration with early central loss of vision, the dominant diseases were linked with late-onset dystrophy predominantly involving the macula [85].

The structural impact of CD133 expression on membrane protrusions concerns more than disk morphogenesis in photoreceptor cells, as recently demonstrated in one of our laboratories. For example, overexpression of human CD133 in polarized Madin-Darby canine kidney (MDCK) cells resulted in an increase in the number of microvilli, branched microvilli and microvilli clusters within the apical surface (Fig. 3a), whereas its silencing in human CD34^{+} HSPCs abolished uropod-associated microvilli-like structures at the rear pole [177]. Similarly, CD133 overexpression impacted the structure of filopodia in fibroblasts or other membrane extensions in retinal pigmented epithelium cells [177, 178] (see below). The interaction of CD133 with the actin-related protein 2/3 (Arp2/3) complex, which mediates the branching of actin networks, may favor such microvilli-related and filopodial alterations in epithelial and nonepithelial cells, respectively (Fig. 3a, see below) [177]. The latter case might explain, at least partially, the involvement of CD133 in cancer metastasis, as both CD133 and actin filament branching are found at the leading edge of motile cell lamellipodia, which are the driving force of cell migration [1, 179]. The interaction between CD133 and the Arp2/3 complex is mediated by the phosphorylation of CD133 Y828, and the mutation of this tyrosine (Tyr $\rightarrow$ Phe, Y828F) resulted in short microvilli (Fig. 3a) [177]. The CD133-Arp2/3 complex interaction is also of interest in the context of photoreceptor biogenesis since it could stimulate the growth of membrane evaginations from the connecting cilium at the base of the outer segment to generate a new photoreceptor disk [180].
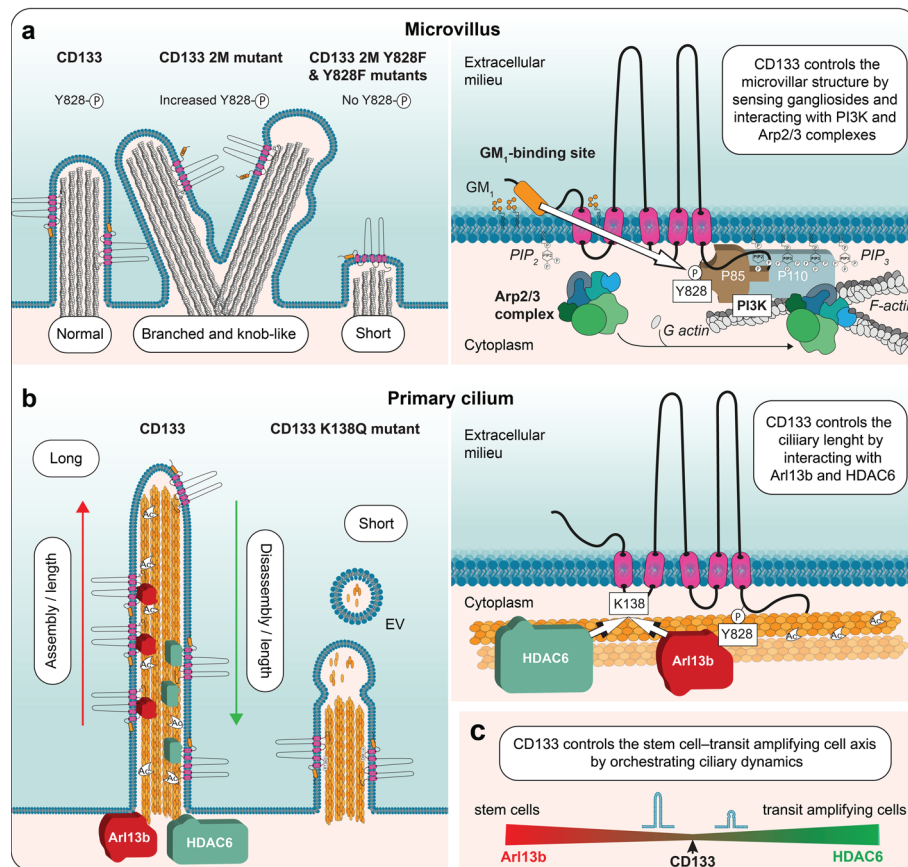
Fig. 3 CD133 impacts the architecture of actin-based microvilli and microtubule-based primary cilia. **a, b** CD133 is involved in the architecture of microvilli (**a**) and primary cilia (**b**), two distinct types of membrane protrusions based on actin filaments and microtubules, respectively. In microvilli, mutation (2 M) in the GM$_1$-binding domain of CD133 creates branched microvilli and/or microvilli with a knob-like structure, while the mutation of tyrosine 828 by phenylalanine (2 M Y828F or Y828F mutants; numbered according to CD133. s2) abolishes these phenotypes and creates short microvilli (**a**, left panel). Branching of the microvilli results from the interaction of phosphorylated CD133 with the Arp2/3 complex, whereas the interaction with PI3K, which stimulates the conversion of PIP$_2$ to PIP$_3$ in the inner leaflet of the plasma membrane, uncouples the plasma membrane and the underlying cytoskeleton, resulting in irregularly shaped microvilli (**a**, right panel). Both subunits (p85 and p110) of PI3K and all seven subunits of the Arp2/3 complex are represented. In primary cilium, overexpression of CD133 increased cilium length, while K138Q mutation led to the formation of short cilia and the appearance of EVs derived therefrom (**b**, left panel). The dual interaction of CD133, mediated by K138, with Arl13b and HDAC6 regulate the assembly and disassembly, respectively, of the ciliary structure. Arl13b binding to CD133 also depends on tyrosine 828 phosphorylation (**b**, right panel). Ac, acetylated tubulin. **c** CD133 plays an essential role in the recruitment of molecular regulators (Arl13b and HDAC6) controlling the dynamics of the ciliary compartment during the activation of quiescent stem cells into transit amplifying cells, as demonstrated in incisor tooth epithelial cells—a process impaired in CD133-null mice. Illustrations in **a**–**c** are based on data presented in Refs [177, 182, 183]

The implication of CD133 in ciliary structures has been reported in different cell types. The spatiotemporal activation of stem cells is based on coordinated cell signaling. The primary cilium, acting as a sensory organelle, participates in the transmission of extracellular signals into a cell, triggering downstream cascades responsible for the cell renewal and differentiation [181]. The proper function of the primary cilium depends on the balanced assembly and disassembly of the microtubular apparatus through the cell cycle. Accumulating evidence shows that CD133 plays a critical role in controlling

the length of the primary cilium in both mammalian and nonmammalian vertebrates [182, 183], via either its interaction with regulators of ciliary morphology or CD133$^+$ EV budding from the ciliary membrane (Fig. 3b). The distribution of CD133 within the ciliary compartment is complex and often asymmetrical along the axoneme [182, 184, 185]. CD133 is found either at the base or the tip of a cilium or within the ciliary shaft [182, 183]. A good example of the physiological involvement of CD133 in ciliogenesis was demonstrated by Singer and colleagues using dental epithelium stem cells as a model, showing that CD133 controls the stem cell–transit amplifying cell axis by orchestrating ciliary dynamics, which was disrupted in *Prom-1$^{-/-}$* mice (Fig. 3c) [182]. The mechanism by which CD133 regulates primary cilium length has been further dissected using kidney MDCK cells [182, 183]. Two regulators of ciliary morphology have been shown to interact with CD133 [182]: ADP-ribosylation factor-like GTPase 13B (Arl13b) and HDAC6. Both of these CD133-interacting proteins compete for cytoplasmic K138 (numbered as in splice variant s2) in the CD133 IC1 [182]. Arl13b is a member of the Ras superfamily of small GTPases that regulates ciliary length [186, 187], while HDAC6 catalyzes the deacetylation of alpha-tubulin and is involved in the disassembly of the primary cilium, a process required for cell cycle progression (Fig. 3b) [188, 189]. The dual interaction of CD133 with Arl13b and HDAC6 may orchestrate cilium functionality and ciliary length dynamics in a positive and negative manner, respectively, and consequently regulate the activation of dental stem cells (Fig. 3c). Of note, the phosphorylation of Y828 has also been implicated in the CD133-Arl13b interaction, and its mutation resulted in a reduction in ciliary length and the number of cells with a primary cilium [183]. In such context, it remains to be determined whether CD133 phosphorylation impacts its interaction with HDCA6, as suggested in the process of autophagy [190] (see below), or whether other posttranslational modifications that would promote or hinder CD133-Arl13b/HDAC6 interactions control the ciliary architecture, and functionally influence cellular proliferation versus differentiation.

Beyond dental stem cells, ciliary CD133 may have an impact on the activity of other cells with stem cell properties, including those associated with the nervous system [191–196] (reviewed in Ref [197]). In addition to primary cilia, CD133 affects motile cilia, such as those found in ependymal cells or multiciliated cells of the airway epithelium, as the absence of CD133 impaired ciliary beating [198, 199]. CD133 is also associated with multiciliated cells found in oviduct epithelium [90]. In zebrafish, *prominin-3* silencing alters the number and length of monocilia in Kupffer's vesicles, resulting in molecular and anatomical defects in left–right asymmetry [183]. Thus, the involvement of CD133 (or its paralogs) in ciliogenesis and/or ciliary functions may have consequences in many ciliopathies [200].

The association of CD133 with cellular protrusions and its involvement in their proper organization is not unique to vertebrate cells, as *Drosophila melanogaster* Prominin has been found in the microvilli-based rhabdomere of the photoceptor cells. Therein, Prominin concentrated at the apical tips of microvilli, and by interacting with the secreted protein Eyes Shut/Spacemaker, it prevented unwarranted contacts between adjacent membrane protrusions and conferred structural integrity onto rhabdomeres [98]. The knockdown of fly Prominin led to the altered arrangement of the photoreceptor compartment. Yet, this phenotype was rescued by the expression of mammalian CD133,

Pleskač *et al. Cellular & Molecular Biology Letters*   (2024) 29:41

Page 15 of 47

indicating the cross-species conservation of CD133 activity in invertebrate and vertebrate photoreceptor cells [100]. Similarly, *Drosophila melanogaster* Prominin-like showed a preferential affinity for apical protrusions of wing imaginal disc cells [99].

Altogether, CD133 shows a profound preference for plasma membrane protrusions, the morphology and organization of which are regulated through multiple interactions of CD133 with various protein and lipid interactors (see below) and/or its posttranslational modification. Of note, almost all CD133-knockout mouse models described so far are viable and fertile [23, 54, 84, 90, 91, 177, 201–204] even though CD133 is normally expressed in the male reproductive tract and spermatozoa and may play a role in sperm maturation [10, 13, 202, 205–207]. This indicates potential functional redundancy of CD133 in specific tissues [84, 92], despite a recent study reporting male infertility after deletion of the *Prom1* gene in a particular mouse background [208]. Compromised spermatogenesis has also been reported for some individuals of *Prom-1*-deficient males showing no interference with development or fertility in general [203]. It remains to be determined whether the genetic background and/or other factors, e.g., expression levels of CD133 interactors, can influence the impact of CD133 on the biogenesis and/or maintenance of functional membrane protrusions.

Thus, advancing our basic knowledge of CD133 may help in understanding not only its impact on protruding membrane structures, but also its involvement in various cell signaling pathways and processes, including proliferation/differentiation, autophagy and cell migration.

CD133 and lipid rafts

The subcellular localization of CD133 in plasma membrane protrusions (e.g., microvilli) relies, at least in part, on its association with a specific membrane microdomain [209, 210]. These submembrane domains, called "lipid rafts", are rich in specific membrane lipids such as cholesterol and sphingolipids [211]. The integrity of these lipid rafts particularly depends on membrane cholesterol. Lipid rafts play an essential role in cellular processes, including membrane trafficking, epithelial polarity, membrane budding and fission, and signal transduction [212–214]. The implication of lipid rafts in CSC self-renewal, quiescence and EMT, which are mediated by various signaling pathways, has made them putative targets for cancer eradication (reviewed in Ref [215]).

The classical biochemical method used to determine the association of a given protein with lipid rafts is based on protein resistance to extraction with certain nonionic detergents under cold conditions; Triton X-100 is the most commonly used detergent for these assays [216, 217]. Although CD133 was completely soluble after incubation with Triton X-100, cholesterol-dependent detergent resistance of CD133 was observed with other detergents, such as Lubrol WX, Triton X-102, or Brij 58, making these CD133-containing lipid rafts different from others [209, 210]. These biochemical observations were corroborated by morphological data where the specific retention of CD133 in microvillar structures was disrupted after the depletion of membrane cholesterol [209] (reviewed in Ref [218]). A relationship between CD133 and lipid rafts is supported by its direct interaction with membrane cholesterol, as demonstrated using a photoactivatable cholesterol analog [209].

Other lipid species may also interact with CD133, including gangliosides such monosialoganglioside 1 (GM_1) and disialoganglioside 3 (GD_3). Taïeb and colleagues have proposed two ganglioside-binding motifs in the EC1 and EC2 of CD133 [219], corroborating the colocalization of CD133 with GM_1 at the membrane protrusions of epithelial and nonepithelial cells [185, 220, 221]. The importance of the GM_1-binding motif in CD133 was further dissected by creating point mutations, as one CD133 mutant (named 2 M) produced microvilli or filopodia with altered morphology in MDCK cells and fibroblasts, respectively [177]. Notably, branched microvilli and/or with a "pearling" state were observed (Fig. 3a, see legend). These effects were related to an increased phospho-Y828-dependent interaction of CD133 with either Arp2/3 complex (see above) or PI3K leading to their activation [177]. How does the extracellular domain of CD133 influence the activity of cytosolic proteins, and subsequently the organization of membrane protrusions? The interaction of CD133 with gangliosides in the plasma membrane outer leaflet may determine the phospholipid composition of the inner leaflet (e.g., the phosphatidylinositol 4,5-bisphosphate (PIP_2)/phosphatidylinositol (3,4,5)-trisphosphate (PIP_3) ratio), by regulating CD133-driven PI3K activation, which may be responsible for the uncoupling of the microvillar membrane from the underlying cytoskeleton, resulting in irregularly shaped microvilli [177]. Linker proteins that interact with actin filaments, such as myosin and ezrin, are involved in the membrane binding which is regulated by clusters of PIP_2 [222, 223]. An increase in the PIP_3 level might also induce the activation of the Arp2/3 complex [224, 225]. By promoting membrane lipid clustering, CD133 may thus mediate direct crosstalk between lipid bilayer leaflets (Fig. 3a). Together with its lipid interactors, CD133 might control the shape and organization of highly curved membranes, such as those found in microvilli, cilia, filopodia and TNTs (see below) [213, 226–228] (reviewed in Ref [218]).

Importantly, cholesterol and gangliosides are not merely structural components of the membrane microdomains affecting membrane structure but, either alone or as a part of lipid rafts, can also modulate signal transduction [214, 229, 230]. Thus, in addition to acting as structural units involved in the architecture of membrane protrusions, CD133 and associated lipid rafts can constitute membrane signaling platforms. The involvement of CD133 as a signaling transduction component in different aspects of cell physiology and tissue regeneration is discussed in subsequent sections.

CD133: intra- and extra-cellular trafficking

As an organizer of the plasma membrane, especially protrusions, CD133 may be involved in membrane turnover and/or recycling [177]. The proper composition of biological membranes is essential for their physical properties and functionality, as in the case of the plasma membrane, which mediates the activation of signaling pathways [231]. The dynamic movement of CD133 from the plasma membrane to intracellular compartments via endocytosis and/or its release into the extracellular medium in association with membrane particles (see next section) may affect the homeostasis of fully differentiated cells and perhaps the proliferation of cells with stem cell properties. The expression of a ganglioside-binding mutant of CD133, stimulating its ubiquitination and interaction with syntenin-1, coincided with an increase in intracellular multivesicular structures, which highlights the importance of proper interaction between CD133 and

certain plasma membrane lipids [177]. CD133 internalization may also indirectly impact various signaling pathways associated with the cell surface, such as those linked to ciliary structures and/or those in other subcellular compartments.

The presence of CD133 in the cytoplasmic compartment, probably in association with the endosomal system, was found to be a high-risk factor for cancer patients survival [232–235]. In blood-derived stem and progenitor cells [81], the intracellular pool of CD133 may contribute to the vasculogenic potential of the cell [68]. The underlying mechanism remains to be established, but the interaction of CD133 with vascular endothelial growth factor, which potentiates its action on angiogenesis, could be part of the answer [236].

Several reports have suggested a positive role for cytoplasmic CD133 in autophagy, which regulates the survival of cancer cells and normal retinal epithelial cells under stress signals, such as those from a nutrient-deprived environment [237–239]. Autophagy is a conserved multistep intracellular process involving autophagosome initiation, elongation and maturation and subsequent fusion with a lysosome, which acts as an indispensable mechanism for removing damaged, denatured, or senescent aggregated proteins and/or organelles. CD133 might participate in autophagosome maturation through its interaction with the autophagy receptor p62/sequestosome 1 (SQSTM1) and HDAC6 [239]. p62/SQSTM1 acts as an adapter molecule that links autophagic cargoes to autophagosomes [240]. These observations may show clinical promise, as targeting CD133-related signaling and autophagy may enhance cancer therapy. Recently, Izumi and colleagues reported an intriguing mechanism affecting the subcellular localization of CD133 and regulating autophagy in colorectal carcinoma and neuroblastoma cell lines [190]. The authors proposed that after endocytosis under severe growth conditions, recycling endosome-associated CD133 is redistributed towards the pericentrosomal region via its interaction with HDAC6 and dynein motor-dependent trafficking along microtubules. Therein, binding of CD133 to the γ-aminobutyric type A receptor-associated protein (GABARAP) prevented autophagy by impeding the interaction of GABARAP with Unc-51-like autophagy activating kinase 1 (ULK1), which contributes to the initiation of the autophagy process (Fig. 4a) [241, 242]. Of note, a microtubule-associated protein 1 light chain 3 (LC3)-interacting region (LIR) [243] spanning positions 828–831 in CD133 might mediate the interaction of CD133 with GABARAP [190]. However, this interaction remains to be formally demonstrated. Importantly, the aforementioned process specifically involved unphosphorylated CD133, as the phosphorylated form did not interact with HDAC6 and remained at the plasma membrane [190]. By inhibiting autophagy, pericentrosomal CD133 suppresses cell differentiation and primary cilium formation and allows maintenance of the undifferentiated state [190]. How phosphorylation impedes HDAC6 binding still needs to be elucidated.

The internalization of CD133 and its transport to intralumenal vesicles (precursors of exosomes) found in the MVBs of CD34^{+} HSPCs might determine the fate of these cells, as the partial or complete loss of CD133, either by degradation in the lysosomal system and/or discharge in association with exosomes, is somehow linked to cell differentiation [81] (see below). Remarkably, in the endosomal compartment of CD34^{+} HSPCs, CD133 has been shown to be distributed symmetrically or asymmetrically during cytokinesis, which may support proliferation or differentiation, respectively [27, 244].
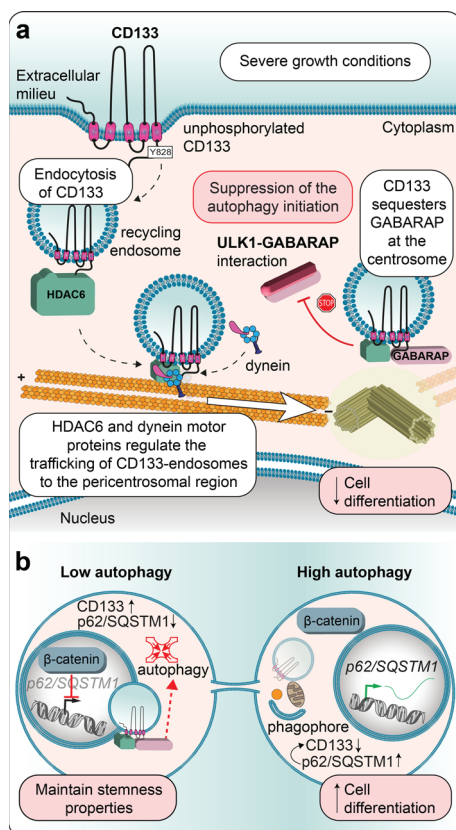
Fig. 4 The impact of CD133 on autophagy relies on its phosphorylation status. **a** Under severe growth conditions, the absence of Src-dependent phosphorylation of CD133 Y828 favors its internalization into recycling endosomes. Through its interaction with HDAC6, CD133 is redistributed via motor protein dynein and microtubules to the pericentrosomal region, where its binding to GABARAP prevents autophagy by hindering the GABARAP interaction with ULK1. Suppression of perinuclear CD133-mediated autophagy in cells with stem cell properties favors the maintenance of an undifferentiated state. **b** The asymmetric distribution of CD133 in dividing neuroblastoma cells impacts autophagic activity in nascent cells. During cytokinesis, the presence of CD133 together with GABARAP and HDAC6 in recycling endosomes located asymmetrically in the pericentrosomal region and the nuclear translocation of β-catenin cooperatively suppress the autophagic activity in a nascent daughter cell by inhibiting GABARAP-mediated initiation of autophagy and repressing the expression of SQSTM1, which may also protect CD133 from degradation. Such interplay may promote the maintenance of stem characteristics via a reduction in autophagy, while the absence of CD133 and increased autophagy may favor cell differentiation. Illustrations in panels a and b are adapted from Refs [190] and [247], respectively

Similar features have been observed in cancer cells [245, 246]. As demonstrated in neuroblastoma cells, the asymmetric distribution of pericentrosomal CD133 and nuclear β-catenin cooperatively suppressed autophagic activity in a nascent daughter cell during cytokinesis by inhibiting *p62/SQSTM1* expression (Fig. 4b) [247]. Further investigation is needed to decipher the positive or negative implication of CD133 in the autophagy processes, which might depend on the basal autophagic activity of the cell of interest and/or external cues [247].

In glioblastoma stem cells, the asymmetric redistribution of the CD133 pool and perhaps of the associated lipid rafts during cell division could produce a progeny with coenriched growth factor receptors, which may contribute to the generation of a more drug-resistant CSC population [248]. In neuroepithelial progenitor cells, the asymmetric

inheritance of CD133 that occurs during neurogenic cell division relies on the apical localization of CD133 [249]. Together with other constituents in the apical domain, including those associated with membrane protrusions such as microvilli and the primary cilium, CD133 may contribute to the cell fate determination [249]. The spatiotemporal relationship between CD133 and the autophagy machinery in neural progenitors remains to be further studied. Nevertheless, as autophagy has been implicated in differentiation and primary ciliogenesis [250–254], it is tempting to speculate that CD133 mediates the crosstalk between these processes in a phosphorylation-dependent manner. These cellular processes could be involved in fate decision that upon dysregulation could lead to cancer [247].

Surprisingly, CD133 has also been reported to localize to the nucleus of tumor cells derived from rhabdomyosarcoma [255] and other childhood sarcoma subtypes, such as osteosarcoma and Ewing's sarcoma [256]. Several independent studies confirmed that CD133 may localize to the nucleus of various normal and cancer cell types, including mouse incisor tooth epithelia [182], breast carcinoma [257], non-small cell lung carcinoma [258], melanoma [259] and colorectal carcinoma [260]. Contradictory results have been reported regarding its prognostic significance when it is located in the nuclear compartment of different cancers. Although high nuclear CD133 expression has been correlated with poor outcome in non-small cell lung carcinoma [258], it has been associated with a favorable prognosis in patients with colorectal adenocarcinoma [260]. The role of nuclear CD133 and its transport through the nuclear membrane are still poorly understood, but the aforementioned study by Singer and colleagues provided the first insights into potential mechanisms. In mouse incisor epithelial stem cells, CD133 was found to orchestrate the transition of stem cells towards more differentiated cells via a primary cilia-dependent process in which it associates with Glis2 [182], a transcription factor involved in Sonic Hedgehog signaling, one of the major regulators of stem cell differentiation [261]. The CD133-Glis2 complex is translocated from the primary cilium to the nucleus via an importin β1-mediated cytoplasmic-nuclear transport to induce the expression of Glis2 downstream targets, such as STAT3, a transcription factor implicated in stem cell maintenance and activation [262]. Knockdown of CD133 in mice lowered the expression of Glis2 and vice versa, implying their functional relationship, and moreover, knockdown of either gene resulted in the suppression of STAT3 expression [182]. Of note, molecular crosstalk between CD133 and STAT3 signaling reportedly controlled autophagy [263], further linking ciliogenesis and autophagy, which in turn may regulate stem cell proliferation and differentiation.

Here again, the various subcellular localization and the intracellular transport dynamics of CD133 are not unique to mammals, as they have been observed in fruit flies [102, 264, 265]. For instance, in addition to membrane protrusions, Prominin-like has been shown to be located in mitochondria, where it directly interacts with ND20, a complex I subunit in the respiratory chain [102]. The inhibition of Prominin-like expression increased the levels of reactive oxygen species, reduced cytoplasmic and mitochondrial ATP, and led to total mitochondrial dysfunction. Similarly, Prominin-like has been proposed to be involved in the control of body size in adult flies, as a mutant lacking this protein was larger with excess weight accompanied by higher fat deposits [264]. The accumulation of lipid droplets in fat body cells and decreased mitochondrial β-oxidation

rates in whole flies were observed. The impact of CD133 on energy-consuming metabolic processes has been linked to the *Drosophila* homolog of the TOR and insulin-like peptide 6 signaling pathways. A link between CD133 and mTOR signaling has also been reported in mammals, where cytoplasm-located CD133 influenced autophagosome maturation and trafficking (see above) [239]. Another loss-of-function study demonstrated that a Prominin-like mutant exhibited an extended life span and metabolic defects such as an increase in circulating carbohydrate levels, lipid storage, and starvation resistance [265]. These phenotypes were related to glucose metabolism by the control of insulin signaling. In agreement with this physiological impact, Prominin-like expression has been mapped in the adult brain to the pars intercerebralis region containing insulin-producing cells [265]. Prominin-like protein was found to affect the morphological features of primary neural cells [266]. The observations regarding *Drosophila* Prominin-like protein are in agreement with earlier studies proposing a link between CD133 and glucose metabolism in myotubes, as elevated glucose levels increased CD133 expression, while CD133 overexpression promoted glucose uptake [267]. Similarly, CD133 has been shown to be involved in hepatoma cell survival through its regulation of autophagy and glucose uptake [237]. A relationship between CD133 expression and bioenergetic stress affecting mitochondrial functions has also been proposed in the context of glioma [268] (reviewed in Ref [269]).

Altogether, the dynamics of the subcellular localization of CD133 and its relatives, which influence various cellular processes and metabolism, must be considered when studying its function under particular conditions. From a technical point of view, the presence of intracellular (cytoplasmic and/or nuclear) pools of CD133 must be taken into account when analyzing its expression by immunocytochemistry and flow cytometry, particularly in the absence of cell permeabilization, or when CD133 is chosen as a prognostic biomarker or as the cell surface target of a therapeutic strategy [68, 81].

CD133 and extracellular vesicles

Besides its association with various types of plasma membrane protrusions or specific organelles, CD133 is released into the extracellular milieu, including various bodily fluids, in association with EVs [81, 191]. Although the initially proposed function of EVs was to remove "cell dust" from cells and thus maintain their homeostasis, EVs are now recognized as mediators of intercellular communication in a variety of biological processes, including embryogenesis and immune responses, as well as in cancer progression and metastasis [270–272]. EVs carry specific sets of biological materials (e.g., proteins, lipids and nucleic acids) that often reflect the physiological state of the cells from which they originate [273]. Once released, EVs interact with and/or are potentially internalized by recipient cells, whose characteristics may thus be altered. The release of specific cellular components through EVs may also alter the fate of donor cells.

These nanosized particles are classified into two main categories based on their biogenesis: exosomes (typically approximately 40–100 nm in diameter) and ectosomes/microvesicles (hereafter MVs; 50–1000 nm in diameter) [271]. Exosomes are of endosomal origin, as they are formed by the inward budding of endosome-limiting membranes, leading to the formation of MVBs that subsequently fuse with the plasma membrane and discharge their small intralumenal vesicles into the extracellular medium [271, 274].

In contrast, MVs are derived directly from the plasma membrane as they often bud or shed from protruding membranes (reviewed in Refs [275–277]). Depending on the cell type, CD133 has been associated with exosomes or MVs [81, 191]. However, CD133 may be associated with both entities in a given biological fluid, reflecting the different cellular sources in contact with these fluids and/or the release by both mechanisms from a particular cell under specific conditions or in diseases such as cancer.

In 2005, Marzesco and colleagues were the first to report the release of CD133 into the external environment; they described its release both in physiological fluids, notably cerebrospinal fluid and urine, and in conditioned medium of a cancer cell line in culture [191]. They showed that CD133$^+$ MVs were released from neuroepithelial progenitor cells and that their appearance in the extracellular milieu coincided with a reduction in CD133$^+$ microvilli, which were most likely the origins of the MVs (Fig. 5a). Consistent with this hypothesis, the CD133$^+$ MVs did not contain the bona fide exosome marker CD63 [191]. The budding of CD133$^+$ MVs from microvillar structures depends on specific cholesterol-rich lipid rafts, suggesting that the interaction of CD133 with membrane cholesterol is the main driver of MV release [278, 279]. Indeed, a reduction in membrane cholesterol increases the release of CD133$^+$ MVs from microvilli [278], while mutations in the GM$_1$-binding domain of CD133 reduce their release [177]. The GM$_1$-binding-dependent interaction of CD133 with the Arp2/3 complex may
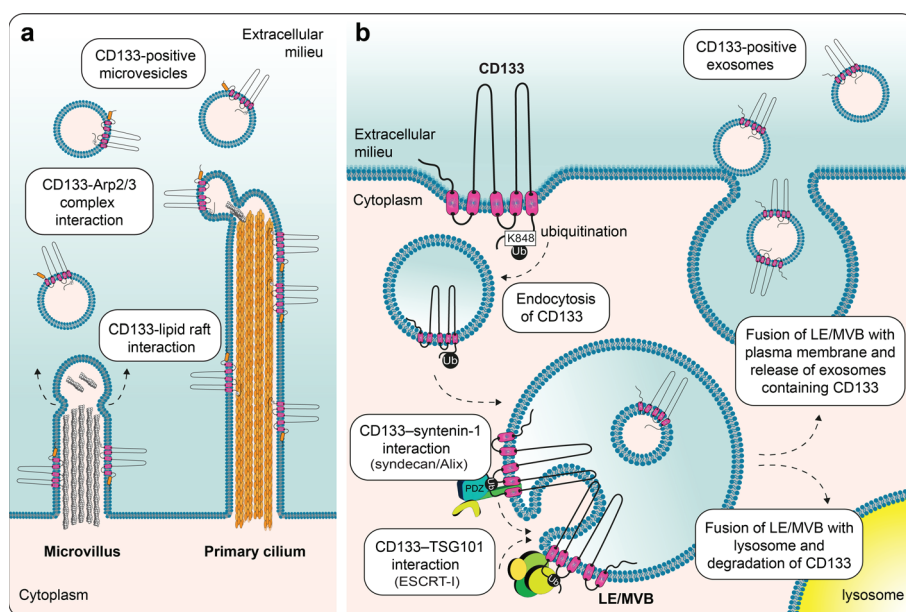
Fig. 5 Release of CD133 into the extracellular environment in association with microvesicles and/or exosomes. **a** CD133 is extracellularly released in association with MVs after budding from microvilli or the primary cilium. The association of CD133 with cholesterol-rich lipid rafts and/or its interaction with Arp2/3 complexes, among other interactors, might favor the formation and budding of MVs. **b** CD133 is released in association with exosomes after the fusion of the late endosome/multivesicular body (LE/MVB) with the plasma membrane. Alternatively, LE/MVB can fuse with lysosomes, resulting in the CD133 degradation. CD133 endocytosis and sorting into intralumenal vesicles within the LE/MVB may be promoted via its ubiquitination at lysine (K) 848 and its interactions with TSG101 and/or syntenin-1 that are involved with Alix, syndecan, and the ESCRT machinery in the exosome biogenesis. Illustrations in panels a and b are based on data presented in Refs [177, 182, 278] and [24, 81, 165], respectively

also be relevant, as the Arp2/3 complex has recently been shown to be involved in MV release [280, 281]. The primary cilium and midbody, i.e., a transient structure that connects two nascent daughter cells at the end of cytokinesis, are other sources of CD133^{+} MVs (Fig. 5a) [192]. The midbody itself can be released and thus constitutes a large and particular CD133^{+} EV [191, 192, 282]. Overall, the interest in CD133 as a microvillar lipid-binding membrane protein, in parallel with research on cytoskeletal regulators [283, 284], has led to more studies into MV shedding from plasma membrane protrusions [276]. For example, it has recently been shown that the fruit fly Prominin-like is important for both the integrity of microvilli and the release of MVs, contributing to the proper morphogenesis of wing imaginal discs through long-distance signaling of the Hedgehog morphogen [285].

In addition to MVs, as mentioned above, CD133 is associated with exosomes, as demonstrated in primary human CD34^{+} HSPCs (Fig. 5b) [81]. CD133 sorting into exosomes may be related to its ubiquitination and interactions with TSG101 and/or syntenin-1 (see above). Whether lipid rafts and/or certain gangliosides are involved in these processes remains to be determined. It is noteworthy that in addition to GM_1, CD133 bears a potential GD_3-binding site in the EC2 domain near its second transmembrane domain [219], possibly contributing to its incorporation into intralumenal vesicles of MVBs, as the GD_3 ganglioside has been reported in exosomes [286].

Although the function(s) of CD133^{+} EVs is poorly documented, a correlation between their release, irrespective of the mechanism, and the onset of the cell differentiation have been reported in three distinct cellular systems: murine neural progenitors, human Caco-2 cells and primary human CD34^{+} HSPCs [81, 191]. For example, the release of CD133^{+} MVs from neuroepithelial progenitors occurs at the very beginning and early phase of neurogenesis, resulting in apical membrane remodeling with loss of microvilli, promoting cell differentiation [191] (reviewed in Refs [218, 287]). In epithelial Caco-2 cells, which in confluent culture show spontaneous differentiation leading to mature colonic epithelial cells, the release of CD133^{+} MVs coincides perfectly with the differentiation process [191]. Similarly, the differentiation of CD34^{+} HSPCs in culture has also been associated with the release of CD133^{+}CD34^{−} exosomes, a phenomenon that can be stimulated by phorbol esters such as phorbol 12-myristate 13-acetate, further linking HSPC differentiation and CD133 release [81].

Interestingly, CD133^{+} EVs contain all the characteristics of lipid rafts (reviewed in Ref. [279]), including the binding of CD133 to membrane cholesterol [81, 278, 288, 289]. As initially proposed by Marzesco and colleagues, these nano(micro)membrane entities may contain the determinants and/or some components of certain signaling pathways necessary for the maintenance of stem (cancer stem) cell properties [191]. The loss of lipid rafts via the release of CD133^{+} EVs may promote cell differentiation. This concept of "*stem cell-specific lipid rafts*" is attractive in the context of stem cell-based tissue regeneration and CSCs. Interfering with CD133^{+} EV release that promotes differentiation may thus favor cell proliferation [191] (reviewed in Ref [27]). In support of this hypothesis, blocking MVB maturation with ammonium chloride impeded both sodium butyrate-induced differentiation and CD133 depletion in two colon cancer cell lines, suggesting that the release of CD133^{+} EVs is essential for cell differentiation [290]. With the asymmetric distribution of CD133 during cell division (see above), the release

of CD133+ EVs may act as a complementary process for the expulsion of CD133-related signaling components and/or its associated lipid rafts [191].

The release of CD133+ EVs may not only constitute a clearance process that leads to cell differentiation but may also produce the vehicles necessary for intercellular communication, delivering information and signaling factors to surrounding tissues (reviewed in Ref [275]). The uptake of CD133+ EVs by stem cells or cancer cells has been demonstrated in several studies [81, 288, 290]. For instance, metastatic melanoma FEMX-I cells released CD133+ EVs carrying proteins and microRNAs, which promoted tumorigenic/prometastatic activity in recipient cells. Thus, the transfer of CD133+ EVs to bone marrow-derived mesenchymal stem cells significantly increased their invasive capacity in vitro [288, 289]. Similarly, CD133+ EVs released by HT29 colon cancer cells increased the proliferation and motility of both colorectal cancer cells and normal fibroblasts [290]. These effects were coupled with an increase in phosphorylation of Src proteins and extracellular signal-regulated kinases as well as in the expression of genes associated with EMT. CD133+ EVs, such as those released from Kirsten rat sarcoma virus oncogene homolog (*KRAS*) mutant colon cancer cells, can also be involved in oncoprotein trafficking [291]. The small GTPase KRAS is a well-characterized oncoprotein that increases the malignancy and metastatic potential of cancer cells by acting as an epidermal growth factor receptor (EGFR) signaling transducer [292, 293]. Specifically, Kang and colleagues reported that the transfer of KRAS mutants via CD133+ EVs (in this case, MVs) to surrounding nontumorigenic cells activated downstream KRAS signaling, leading to an increased cell motility, proliferation and resistance to anti-EGFR drugs [291]. Interestingly, the amount and sizes of budding MVs depended on the level of CD133 expression, which stimulated and inhibited the activities of the small GTPases RhoA and Rac1, respectively [291].

CD133+ EVs in various bodily fluids, notably cerebrospinal fluid, urine and seminal fluid, may have, in addition to their biological and physiological impact, clinical value as noninvasive biological tools to monitor disease progression or tissue regeneration after organ transplantation [191]. For example, Huttner and colleagues demonstrated in a series of publications that CD133+ EVs associated with cerebrospinal fluid can be used as a biomarker to monitor neural diseases such as cancer or brain injury [294–297]. The expression of CD133 in various renal cell types (e.g., cells in proximal tubules and parietal layer of Bowman's capsule of juxtamedullary nephrons) [1, 11, 12, 43, 45] and derived urinary EVs that mirror in some way the tissue expression profile may also be useful for monitoring kidney disease and tissue recovery after kidney transplantation [298–300] (reviewed in Ref [301]). In all cases, the potential use of CD133+ EVs as bodily fluid-associated biomarkers requires further assessment, particularly with a large cohort of patients.

CD133 and tunneling nanotubes

In the context of intercellular communication and signaling, the exchange of CD133 between cells can be mediated via TNTs, which connect adjacent cells over a short or long distance. Discovered by Gerdes and colleagues, TNTs are thin, straight and long protruding membrane structures that are not in direct contact with the extracellular matrix, in contrast to other protruding structures such as filopodia [302]. Most TNTs

are composed of microfilaments (F-actin), although tubulin has been detected in some TNTs [302–304]. They are categorized based on the junctional connections between cells as closed-ended or open-ended, with the latter type of TNTs leading to cytoplasmic continuity between interconnected cells [305]. Open-ended TNTs have been implicated in the transport of diverse cellular components, including cytoplasmic molecules and organelles (e.g., mitochondria), whereas closed-ended TNTs have been reported to mediate the transport of electrical impulses between cells [303, 306, 307].

One of our laboratories reported that closed-ended TNTs were involved in the selective intercellular transport of certain membrane proteins, such as CD133, between primary human CD34$^+$ HSPCs and KG1a hematopoietic leukemia cells [308]. The association of CD133 with lipid rafts may explain its selective and directional transport along the surface of TNTs in small clusters, similar to cytoplasmic phospho-myosin light chain 2, suggesting that this actin motor protein might be implicated in CD133 transport along TNTs (Fig. 6, see the corresponding legend for the potential mechanism of CD133 transfer) [308]. Accumulation of CD133 occurs at the junctional complex before its transfer
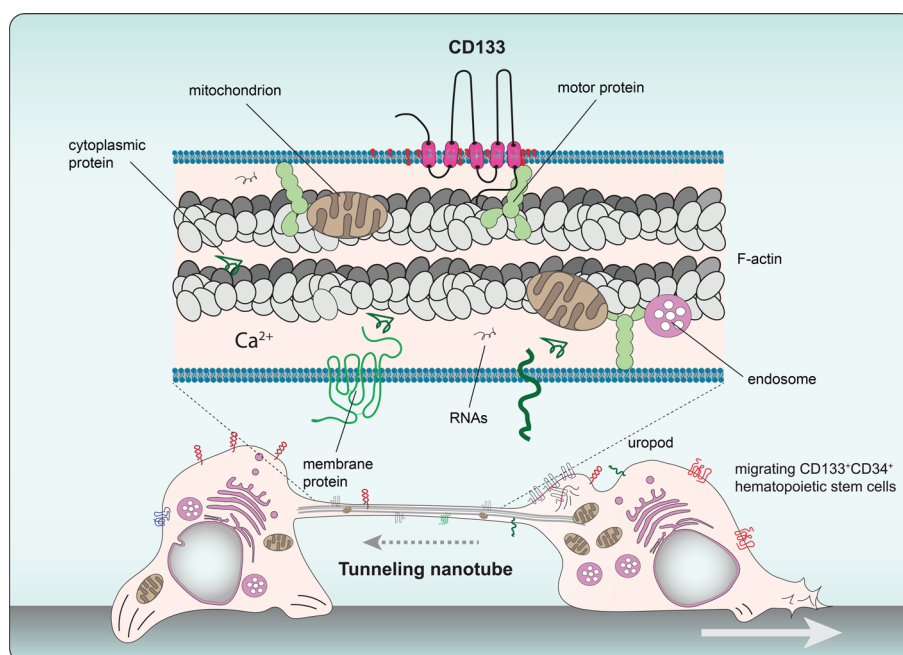
Fig. 6 Tunneling nanotubes mediate the transfer of CD133 between hematopoietic stem and progenitor cells. CD133 is exchanged between CD133$^+$CD34$^+$HSPCs (or KG1a hematopoietic leukemic cells) via TNTs. In various cellular systems, these transient narrow actin-based tubular connections have been reported to mediate the transfer of organelles, soluble and membrane proteins and nucleic acids or to contribute to calcium signaling, thereby promoting intercellular communication between adjacent or distant cells. In cells of hematopoietic origin, TNT biogenesis depends on cell polarization and occurs during cell migration (solid arrow) with one of two cells in direct contact forming membrane extensions from the uropod membrane at its rear pole, where CD133 is concentrated. Mechanistically, the biological properties of CD133, including its direct interaction with membrane cholesterol (red lipid) and its incorporation into cholesterol-rich membrane microdomains, may modulate the lipid composition and the local organization of the plasma membrane in TNTs. The CD133 interaction with PI3K may lead to the conversion of the docking PIP$_2$ into PIP$_3$ at the inner leaflet of CD133-containing membrane microdomains, thereby regulating their interaction with the underlying actin cytoskeleton. The binding of the actin motor protein myosin to PIP$_3$ clusters may promote the selective movement of such CD133-containing membrane microdomains along the actin filament and mediate their transfer between TNT-connected cells (dashed arrow). Illustration is adapted from Ref [308]

from donor to acceptor cells, but the mechanism underlying this transfer of membrane remains to be determined [308]. Interestingly, CD34$^+$CD133$^+$ HSPCs were more likely to generate TNTs than their CD34$^+$CD133$^-$ counterparts, suggesting that more primitive stem cells deploy this means of communication to exchange or share materials among themselves [308]. Differentiation may be triggered in donor HSPCs by the reduction in CD133 level and/or that of its associated lipid rafts, while their increase in recipient cells may promote proliferation, thus contributing to the replenishment of the bone marrow stem cell niche and the formation of new mature blood cells [308]. Nonetheless, the impact of CD133 transfer on recipient cells, the composition of the associated lipid rafts that may harbor specific components of signaling pathways and whether CD133 directly contributes to TNT formation still need to be answered by further studies.

Collectively, these molecular and cell biological findings underscore the importance for future studies of examining the subcellular localization of CD133 (or its orthologs across species) and the posttranslational modifications that may influence it. Elucidation of the regulatory factors may be essential to determine the function and/or involvement of CD133 in membrane organization and dynamics, which, in addition to its structural and physical properties, may impact various signaling networks.

CD133 and signaling pathways

In recent years, the involvement of CD133 in various signaling pathways has been postulated. As no study has reported any soluble ligand that could demonstrates a functional role for CD133 as a membrane receptor, it is important to determine its interactors, especially those directly involved in signaling pathways [33, 309, 310]. In this section, we highlight the pathways in which CD133 has been shown to play a role or exert an influence, particularly in cancer cells.

CD133 and RhoA/ROCK signaling influence cell morphology

Rho GTPases orchestrate various biological processes including cell cycle progression, vesicular transport pathways, cell migration and cytoskeleton dynamics [311]. Among them, RhoA and its main downstream effectors, Rho-associated coiled-coil-containing protein kinase (ROCK) 1 and 2, are key players in the regulation of cytoskeletal remodeling and cell polarity, acting on actin, intermediate filaments and microtubules [312–314].

In addition to the link between RhoA and CD133 in the formation of MVs mentioned above, it has been reported that overexpression of CD133 in retinal pigmented epithelium cells or mouse embryonic fibroblasts leads to the formation of multiple RhoA-dependent long membrane extensions (named fibres by the authors) oriented in an opposite direction to that of cell movement [178]. These fibres, although somewhat similar to the retraction fibers left behind by migrating cells, were surprisingly formed independently of F-actin or α-tubulin polymerization and, consistent with the lipid-binding properties of CD133, were highly enriched in membrane cholesterol. Interestingly, five critical residues (KLAKY818) mapped to the end of the last transmembrane domain (TM5) of CD133 were found to be essential for the formation of these fibres [178]. In contrast, the phosphorylation of the tyrosine at site 818 (or 828 in the case of CD133.s2) was not required [178], suggesting that these membrane structures are

generated independently of the PI3K activity, making them different from the other protruding structures involving PI3K and the Arp2/3 complex, described in the previous section [177]. Of note, KLAKY818 residues in CD133 are in a motif similar to the linear Cholesterol Recognition/interaction Amino acid Consensus sequence (CRAC) domain (L/V-X_{1-5}-Y-X_{1-5}-K/R) [315, 316]. However, whether they act as cholesterol-binding sites on the cytoplasmic leaflet of the plasma membrane is unknown, and further analysis is required. Interestingly, CD133 appeared to colocalize with active RhoA at sites of fibre formation initialization, and silencing of ROCK1/2 disrupted CD133-induced fibre formation, suggesting that the RhoA/ROCK pathway mediated the biogenesis of these cellular extensions [178]. It remains to be determined how CD133 and Rho activation act synergistically, what the target of ROCK1/2 is in the biogenesis of these CD133-dependent membrane extensions and whether these fibres contain other types of cytoskeletal elements, such as intermediate filaments [178]. Despite the questions, these observations are consistent with the impact of CD133 on the architecture of membrane protrusions and cell migration and are in line with the previous findings that in migrating CD34$^+$ HSPCs, CD133 was selectively concentrated in the uropod at the posterior pole, the latter structure being regulated by the RhoA/ROCK1 signaling pathway [317, 318].

The same study by Hori and colleagues demonstrated that fibre formation is induced by the overexpression of Tweety homolog (TTYH) 1/2 proteins, similar to CD133, suggesting that both types of molecules may show functional similarity [178]. TTYH1/2 were reported to act as anion channels that were activated either by calcium ions or cell swelling [319]. Recent structural studies on TTYH based on cryo-electron microscopy combined with functional data refuted their potential functions as the pore-forming subunits of ion channels, although they may act as accessory molecules to these channels [320, 321]. Instead, the hypothesis that these proteins might play a role in the dynamics of membrane lipids was proposed [320]. More interestingly, TTYH1/2 proteins are structurally similar to CD133, including their membrane topology and dimer/tetramer formation [210, 322], suggesting that they may all regulate membrane organization leading to fibre formation. Whether this process is directly related to the chloride efflux activity mediated by TTYH1/2 (or CD133) or to their interaction with other molecules remains to be demonstrated [178].

Signaling via phosphorylated CD133

The regulation of protein phosphorylation involves specific protein tyrosine phosphatases. Two studies indicated that protein tyrosine phosphatase κ (PTPRκ) was involved in the dephosphorylation of CD133 IC3 [323, 324]. PTPRκ is a member of the group of transmembrane receptors in the classical tyrosine phosphatases family [325]. Its two catalytic intracellular domains dephosphorylate target proteins, and thus regulate intercellular adhesion and cell proliferation [325, 326]. Both catalytic domains of PTPRκ interact with the CD133 C-terminal domain, independently of the phosphorylation status, resulting in the dephosphorylation of residues Y828 and Y852, thereby inhibiting the ability of CD133 to activate two major signaling pathways, namely, the PI3K-Rac-alpha serine/threonine-protein kinase (Akt) and Src-FAK pathways [323, 324]. The importance of the phosphorylation of CD133 in the regulation of cell signaling was strengthened by the discovery of a novel small compound (LDN193189, a derivative of Dorsomorphin)

that binds to the IC3 and prevents its phosphorylation [327]. As a result, the interaction of CD133 with PI3K was effectively abolished, leading to the inhibition of Akt signaling and decreased self-renewal and tumorigenicity in liver tumor-initiating cells [327].

Tyrosine 828 phosphorylation of CD133 regulates PI3K-Akt signaling

Increasing evidence suggests a role for CD133 as an upstream activator of the PI3K/Akt pathway [163, 328]. PI3K, a heterodimeric protein composed of a catalytic (p110) and a regulatory (p85) subunit (reviewed in Ref [329]), affects several cellular processes, including cell proliferation, apoptosis, and growth and cytoskeleton remodeling [330, 331]. The main downstream molecule of the PI3K pathway is the serine/threonine kinase Akt (also known as protein kinase B), which stimulates the proliferation and survival of stem cells and CSCs [332, 333]. Indeed, upregulated PI3K-Akt signaling is common in a wide spectrum of tumors [334–339], and it is indispensable for the increased self-renewal and tumorigenicity of CD133$^+$ cancer cells [163].

Mechanistically, as demonstrated in glioma cells, Src-dependent phosphorylation of CD133 at cytoplasmic residue Y828 promotes its interaction with the PI3K p85 subunit, leading to the translocation of PI3K to the plasma membrane and the initiation of Akt signaling (Fig. 7a), which may promote self-renewal, cell survival and tumorigenicity [163]. Manoranjan and colleagues reported an association between overexpressed
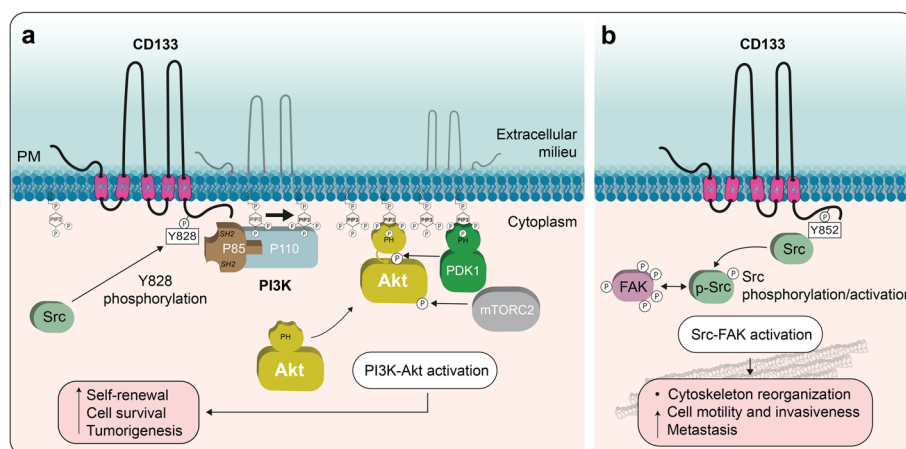
Fig. 7 Phosphorylated CD133 regulates the PI3K-Akt and Src-FAK signaling pathways. **a** The Src-dependent phosphorylated tyrosine 828 in the CD133 IC3 binds to the PI3K regulatory subunit p85 via the SH2 domain in the latter, resulting in the translocation of the kinase to the plasma membrane and the phosphorylation of PIP$_2$ to yield PIP$_3$. Accumulation of the PIP$_3$ enables Akt to interact via its pleckstrin homology (PH) domain with the plasma membrane (PM), resulting in a conformational change in the Akt kinase domain, which allows the phosphorylation of a critical residue required for Akt kinase activity by the 3-phosphoinositide-dependent protein kinase 1 (PDK1). The mammalian TOR complex 2 (mTORC2) also phosphorylates Akt, promoting its kinase activity. It should be noted that PDK1 binding to PIP$_3$ is not essential for its activity, in contrast to the dependence of Akt on PIP$_3$. Then, the resulting activation of the PI3K/Akt pathway promotes self-renewal, cell survival and tumor formation. **b** The phosphorylated tyrosine 852 residue of CD133 directly interacts with Src and mediates its activation. The phosphorylated (p)-Src protein phosphorylates, and then forms a complex with, the FAK protein, triggering EMT-related events and cytoskeletal reorganization. This leads to increased cell motility and invasiveness, among other processes. Inhibition of Src activity by PP2, a known Src activity inhibitor, blocks the activation of FAK phosphorylation and cell migration induced by CD133 (not shown). Illustration in panel a is adapted from Ref [163], while in panel b is based on data from Ref [352]

Pleskač *et al. Cellular & Molecular Biology Letters* (2024) 29:41

Page 28 of 47

CD133 and elevated levels of phosphorylated Akt and Wnt in glioblastoma cell lines [340]. Phosphorylated Akt, which inhibits glycogen synthase kinase-3 activity through its phosphorylation at serine 9 [341], may lead to stabilization of β-catenin and thus mediate CD133-Akt-Wnt signaling axis activity, resulting in increased proliferation and self-renewal potential of CD133$^+$ cells [340]. Thus, as a putative cell surface receptor, CD133 may mediate Akt-dependent activation of Wnt signaling, which may drive glioblastoma tumor-initiating cells in the brain [340]. The CD133-dependent interplay between pathways might explain the correlation of CD133 with progression and recurrence of brain cancer and poor survival for patients [31, 309, 342].

In thyroid cancer, the activation of Src kinase is facilitated by the close proximity of CD133$^+$ cancer cells to acetylcholine-secreting neurons [343]. The released acetylcholine binds to the M3R acetylcholine receptor of thyroid cancer cells, which induces the activation of Src through the phosphorylation at Y416. The latter promotes Y828 phosphorylation of CD133 and activation of the PI3K/Akt pathway, leading to increased resistance of thyroid cancer cells to cytotoxic CD8$^+$ T cells [343]. In melanoma, the same phosphorylation of CD133 conferred chemoresistance to an alkylating agent, namely, fotemustine, via the activation of both the PI3K/Akt/mitogen-activated protein kinase-1 and PI3K/mouse double minute 2 pathways [344].

Tyrosine 852 phosphorylation of CD133 activates Src-FAK signaling

EMT is a reversible shift in the epithelial phenotype of a cell toward the mesenchymal phenotype, allowing migration of originally adherent cells [345]. Phosphorylated Src kinase (p-Src) controls the onset of EMT in many tumors [346, 347]. Active Src signaling leads to the disintegration of cell–cell adhesion; promotes cell invasiveness, motility, and proliferation; induces the reorganization of the cytoskeleton; and affects the tumor microenvironment [348].

A link between Src signaling and CD133 has been suggested in the head and neck squamous cell carcinoma (HNSCC). CD133$^+$ HNSCC cells exhibited higher levels of p-Src and concurrently displayed properties of mesenchymal cells, such as lower expression of E-cadherin and higher expression of vimentin, fibronectin, and transcription factors OCT4 and NANOG [164]. Moreover, the suppression of *PROM1* transcription downregulated p-Src and favored the acquisition the epithelial phenotype associated with E-cadherin re-expression and OCT4 and NANOG depletion in HNSCC cells [164]. Yet, this phenotype switching did not seem to involve the Src SH2-binding motif, as the expression of the CD133 Y828F mutant did not impair Src activation. The authors therefore proposed that other tyrosine residues in CD133, including Y852, may be the main sites of regulation of Src activity.

One of the p-Src downstream molecules is FAK, a cytoplasmic tyrosine kinase involved in integrin signaling [349, 350]. Once activated, FAK and Src form a Src-FAK complex, which facilitates actin remodeling and cell motility and hence promotes the invasiveness of cancer cells [346, 348, 351]. In this context, CD133$^+$ cells of the SW620 colorectal carcinoma cell line exhibited high levels of phosphorylated FAK and Src that were decreased after the knockdown of CD133 expression [352]. This relationship was further supported by the demonstration that CD133 phosphorylated on tyrosine Y852 interacted with Src, leading to Src activation and subsequent formation of a Src-FAK

complex which stimulates the invasive behavior of these cancer cells (Fig. 7b) [352]. Altogether, the presence of several tyrosine residues in the IC3 of CD133, with two of them being encoded by a facultative exon, suggest that signaling cascades could be differentially mediated depending on the cellular context.

CD133, HDAC6, and Wnt/β-catenin signaling

Wnt proteins (the name of which was derived from Drosophila Wingless and mouse Int proteins [353]) are signaling molecules that orchestrate tissue development [354, 355] by regulating the expression of target genes as well as by modifying the cytoskeleton or the mitotic spindle [356, 357]. Activation of the Wnt pathway stabilizes β-catenin, a canonical Wnt downstream molecule, which is then translocated from the cytoplasm to the nucleus, where it forms a complex with members of the TCF family of transcription factors and initiates the transcription of β-catenin-TCF-dependent genes [355].

Wnt signaling has been implicated in the early phase of human hair follicle morphogenesis [358]. During this phase, CD133 expression in a subset of invaginating placode cells was associated with Wnt activation [359]. In early placodes, CD133 was detected in adherens junctions rich in E-cadherin and β-catenin, while in later phases, its expression was spatially and mechanistically correlated with a reduction in membrane β-catenin and E-cadherin levels, a crucial process for proper adherens junction disassembly, suggesting a functional role for CD133 in placode remodeling [359]. The link between CD133 and E-cadherin was supported by Brossa and colleagues, who provided evidence showing that CD133 directly bound E-cadherin and β-catenin to form a complex restraining the β-catenin degradation [360]. Stabilized β-catenin in turn activated a regeneration program by initiating the transcription of Wnt pathway-responsive genes in cisplatin-damaged kidney tubular cells [360]. In the same line, a Glis3/CD133/Wnt signaling axis implicated in the maintenance of the self-renewing capacity of these cells, was uncovered in mouse pancreatic colony-forming units [361]. In general, CD133 seems to be an important upstream regulator of the Wnt signaling pathway in various normal tissues, which in turn may promote CD133 expression via β-catenin-TCF/LEF complex-binding sites present in the *PROM1* gene.

Indeed, the activity of the Wnt pathway is most likely also modulated by CD133 in tumor cells [33, 309, 310]. While the silencing of CD133 expression leads to a suppression of the Wnt pathway, inhibition of Wnt signaling results in the downregulation of CD133 expression [289, 362]. In a metastatic melanoma cell line, the downregulation of CD133 expression mediated by short hairpin RNA was associated with an upregulation of Wnt pathway inhibitors (e.g., Dickkopf-related protein 1 and Dishevelled binding antagonist of β-catenin 1) [363]. Similarly, CD133-depleted metastatic melanoma and ovarian carcinoma cell lines displayed low basal Wnt signaling and a very limited nuclear localization of β-catenin, which was restored after supplementation with the exogenous ligand Wnt3a [289, 362].

As mentioned above, CD133 interacts with another modulator of Wnt signaling, HDAC6 [190, 359, 362], a cytoplasmic histone deacetylase involved in the regulation of β-catenin stability and microtubular remodeling [364, 365]. Besides its interactions with acetylated microtubules, polyubiquitinated misfolded proteins and dynein motors [364, 366, 367], HDAC6 binds via its second catalytic domain to the CD133 IC1, and
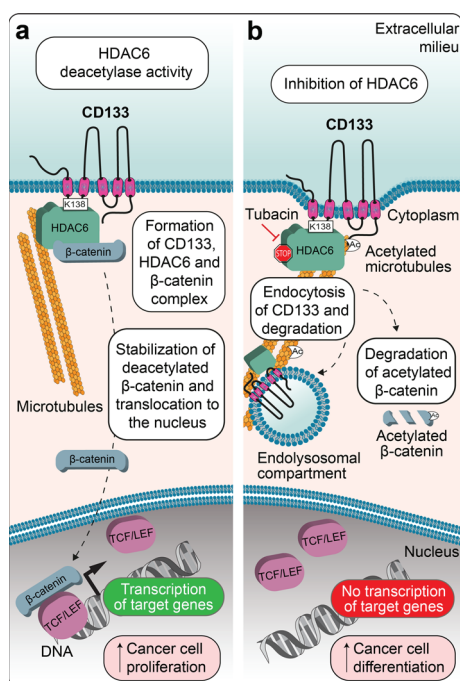
Fig. 8 CD133 regulates β-catenin signaling via its interaction with HDAC6. **a** CD133 regulates the formation of a tripartite complex involving HDAC6 and β-catenin, leading to the stabilization of the latter, which may then translocate to the nuclear compartment, where it activates the expression of genes, notably those associated with the Wnt/β-catenin pathway via its interaction with the TCF/LEF transcription factor. The interaction between CD133 and HDAC6 is mediated by IC1 and potentially lysine (K) 138 (numbered according to the splice variant s2). **b** Treatment of cells with tubacin, a specific inhibitor of HDAC6 deacetylase activity, leads to the degradation of acetylated β-catenin (Ac) and thus the impairment of transcriptional activity, while CD133 is endocytosed and degraded upon its transport to the endolysosomal compartment. Therefore, CD133/HDAC6/β-catenin interactions will have an impact on cancer cell proliferation and differentiation. Illustrations in panels a and b are adapted from Ref [362]

thus stabilizes CD133 and prevents its degradation in the endosomal-lysosomal pathway [190, 362]. Indeed, CD133 creates a ternary complex with HDAC6 and β-catenin at the plasma membrane that protects the HDAC6 activity, thereby reducing β-catenin acetylation and degradation [362]. This action favors the translocation of β-catenin to the nuclear compartment, and subsequently influence the gene regulation (Fig. 8a) [362]. This process depends on HDAC6 deacetylase activity, as treatment with tubacin, a specific inhibitor of HDAC6 deacetylase activity [368], led to the degradation of acetylated β-catenin (Fig. 8b). Mechanistically, given that the phosphorylation of HDAC6 has been associated with a decrease of its deacetylase activity [369] and that phospho-mimicking mutants of HDAC6 failed to interact with CD133, it has been suggested that the interaction of HDAC6 with CD133 prevents the loss of HDAC6 activity by impeding HDAC6 phosphorylation, thereby increasing its β-catenin-stabilizing and nuclear transfer effects, essential steps to induce the expression of Wnt/β-catenin target genes [362].

CD133 and TGF-β/Smad2 signaling

The TGF-β family of cytokines comprises more than thirty secreted proteins that are highly conserved among a broad group of organisms [370]. By binding to specific receptors

on the cell membrane, TGF-β cytokines regulate diverse cellular processes from proliferation, adhesion, differentiation, and metabolism to cell death. TGF-β receptors act as heterodimeric serine/threonine protein kinases, which phosphorylate the C-terminal domain of Smad proteins. Once phosphorylated, Smad proteins form a heterocomplex that is translocated to the nucleus and activates the transcription of target genes [370]. Aside from the implication of TGF-β in the regulation of CD133 expression in cancer (see above), an intriguing relationship between CD133 and TGF-β/Smad signaling has been observed in a study focused on peripheral axon regeneration after crush injury [371]. CD133 is expressed on dorsal root ganglia neurons and is developmentally downregulated. After injury, neuronal intrinsic signals trigger a regenerative program for axonal regrowth and CD133 was found to regulate this regenerative potential. Indeed, CD133 interacted with activin-like kinase (ALK) 4, a type I TGF-β receptor, to synergistically induce phosphorylation of Smad2, which regulates the expression of genes involved in lipid metabolic pathways. Notably, among a set of differentially expressed genes in response to neuronal injury, the downregulation of those associated with cholesterol biosynthesis was specifically observed after CD133 overexpression (Fig. 9) [371]. Thus, this CD133-dependent regulation of cholesterol metabolism associated with TGF-β/Smad signaling may explain the involvement of CD133 as a neuronal intrinsic factor responsible for the regulation of axonal regenerative potential. This exciting example of CD133-related regenerative processes highlights the fact that this lipid raft-associated protein not only directly organizes membrane topology by interacting with membrane cholesterol and gangliosides, but also regulates, in association with certain signaling pathways, sterol and lipid metabolisms.
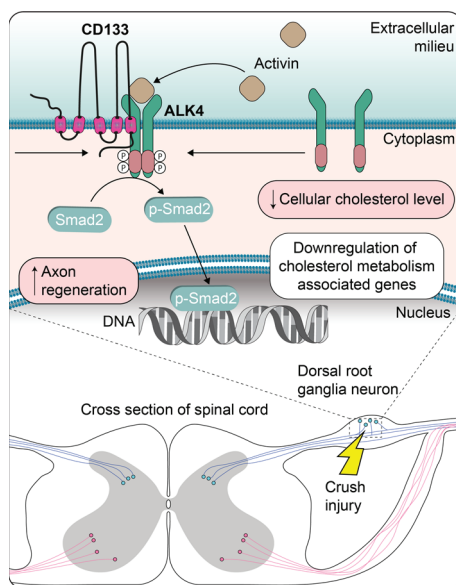
Fig. 9 CD133 regulates cholesterol metabolism and peripheral axon regeneration through TGF-β/Smad2 signaling. Mouse dorsal root ganglion crush injury induces the formation of functional ALK4, a TGF-β type I receptor that binds to its ligand activin, a TGF-β superfamily member and a determinant of axon regenerative capacity. At the plasma membrane, the interaction of ALK4 with CD133 stimulates the phosphorylation of Smad2, which inhibits, after translocation into the nuclear compartment, the expression of genes involved in cholesterol metabolism, thereby promoting a positive effect on axon regeneration. Illustration is based on data presented in Ref [371]

In a murine model of liver fibrosis, Lee and colleagues reported that CD133 was upregulated in the plasma membrane of fibrotic liver hepatocytes and could interact via its IC1 domain with the N-terminal domain of Smad7 [372], a feedback inhibitor of TGF-β signaling that prevents the TGF-β-induced phosphorylation of Smad2/3 [373, 374]. This CD133–Smad7 interaction inhibited the SMURF2-induced ubiquitination of Smad7 and increased its half-life, resulting in a reduction in the TGF-β-induced liver fibrosis and apoptosis rates of hepatocytes [372]. It is of note that an opposite role for CD133 in fibrogenesis has been proposed on the basis of another murine model of liver injury, where the profibrogenic activity of TGF-β depended on the presence of CD133 [375]. Differences in the identification of CD133-expressing cells, i.e., whether CD133 expression was restricted to progenitor cells or extended to hepatocytes, may account for this discrepancy [372, 375].

During liver regeneration after injury, cytokine IL-6 secreted upon inflammation activation binds to the IL-6 receptor complexed with the signal transducer glycoprotein 130 (gp130) on hepatocytes and triggers various downstream signaling pathways [376]. Recent evidence suggests that CD133 in hepatocytes positively regulates IL-6 signaling by interacting via its EC1 with gp130. This interaction recruits gp130 to lipid rafts, consequently promoting IL-6-induced STAT3 phosphorylation, and thus cell proliferation and liver regeneration [377].

CD133–radixin signaling regulates cAMP-mediated PKA activation

Spatiotemporal organization of signaling pathway components is a complex process involving intermolecular interactions. Scaffolding proteins play indispensable roles in maintaining the organization of all molecular components. Radixin, a member of the A kinase-anchored protein family, is a scaffolding protein that binds to cyclic adenosine monophosphate (cAMP)-dependent protein kinase A (PKA) to enable phosphorylation of downstream targets [378]. In the mouse liver, radixin mediated the interaction between PKA and proteins involved in glucagon-initiated gluconeogenesis [20, 379]. Interestingly, mouse CD133 directly interacted with radixin through its C-terminal domain and recruited the radixin-PKA complex to the proximity of the glucagon G protein-coupled receptor and adenylyl cyclase at the plasma membrane [20]. This resulted in the activation of adenylyl cyclase and production of cAMP that promoted the separation of the PKA regulatory subunit from the catalytic subunit, which in turn phosphorylated key initiators of gluconeogenesis [20].

CD133–MAPK/ERK signaling

The crucial role of mitogen-activated protein kinase/extracellular signal-regulated kinase (MAPK/ERK) signaling in cell proliferation, growth, and differentiation is well documented [380]. In a pancreatic carcinoma cell line, CD133 interacts with the ERK1/2/Src complex to enable signal transduction mediated through endothelial growth factor-stimulated ERK1/2 to downstream mediators, including slug (also known as snail family transcriptional repressor 2) [381]. Activation of Slug leads to subsequent N-cadherin expression, which is accompanied by the acquisition of an invasive and pro-metastatic phenotype. Moreover, both ERK1/2 and Src are able to positively regulate the expression of CD133 and thus further promote the CD133-dependent activation of EMT

[381, 382]. A similar feedback loop between the MAPK pathway and CD133 expression, which directly affects self-renewal and tumorigenesis, has been described in hepatocellular carcinoma cell lines treated with C-X-C motif chemokine ligand (CXCL)3 [383]. CXCL3 promoted ERK1/2 phosphorylation and the subsequent phosphorylation of the transcription factor ETS proto-oncogene 1, leading to CD133 upregulation. Upregulated CD133 then acted as an upstream activator of CXCL3 and stimulated the growth of hepatocellular carcinoma cells [383].

The importance of CD133-MAPK/ERK signaling in EMT has also been confirmed in vivo. When compared with CD133$^-$ counterparts, mouse CD133$^+$ melanoma cells were observed to preferentially interact with tumor endothelial cells and establish metastatic foci [143]. The positive regulation of CD133 expression by Notch1 was shown to lead, via CD133-dependent MAPK activation, to the upregulation of activator protein 1 transcription factor, which in turn initiated the expression of matrix metalloproteinases 2 and 9 as well as vascular endothelial growth factor, promoting metastatic potential and tumorigenesis in mouse models [143].

Conclusion and perspectives

Since its discovery in 1997, the study of CD133 has been an active field covering a wide range of biological topics. In particular, this molecule has been studied in relation to stem cells and CSCs, as well as photoreceptors biogenesis. CD133 has rapidly garnered considerable interest as a prognostic marker and potential target in cancer therapy despite little information about its molecular function in physiological and pathological conditions. Naturally, some conflicting data have been reported as a matter of course. Although there is still no agreement regarding the function of this cholesterol-binding membrane protein, CD133 appears to be involved in a wide array of cellular processes that may be hijacked by cancer cells. These diverse areas nonetheless converge to suggest a fundamental role for CD133 in the dynamics of the cell membrane, including the activity of membrane protrusions, notably the primary cilium, and the release of EVs.

Emerging findings related to various subcellular locations of CD133 (i.e., in membrane protrusions, including microvilli, primary cilium and midbody, or in pericentrosomal and perinuclear regions as well as its inclusion in the nucleus) call for further study of its role(s) in these diverse compartments, and of the mechanisms regulating its intracellular trafficking. As the activation of molecular pathways orchestrating cancer cell self-renewal and metastasis, such as the PI3K-Akt and Src-FAK pathways, depends on the tyrosine phosphorylation status of CD133, particular attention to this specific posttranslational modification may be worthwhile. Although the kinases and tyrosine phosphatases involved have been characterized, the conditions under which these processes are triggered are not fully understood. To fill this gap, we face the challenge of studying the spatiotemporal characteristics of CD133 phosphorylation and associated signal transduction, which may provide important insights into the role of CD133 in different cellular compartments.

CD133$^+$ EVs, derived from both normal and cancer cells, have garnered considerable attention in recent years, with ongoing research into the clinical potential of these particles for the diagnosis and monitoring of pathological conditions such as neurodegeneration and other neurological disorders. As reviewed herein, by the means of CD133$^+$

EVs delivering various pro-tumorigenic cargoes, cancer cells may communicate to the healthy cells in their vicinity, or at distant sites, the instruction for malignant transformation. From a therapeutic perspective, selective targeting of CD133 with inhibitory anti-CD133 antibodies or small-molecule drugs may, not only eliminate cancer cells [384], but also prevent the release, spreading or uptake of CD133$^+$ EVs and thus disrupt tumor tissue growth, and possibly the process of metastasis [272]. A better understanding of the contribution of CD133 to the biogenesis of CD133$^+$ EVs is crucial for developing these therapeutic approaches.

As we learned in the past two decades, the mechanisms by which CD133 affects various signaling pathways and cellular processes are diverse and largely relate to the inherent involvement of CD133 at cell membranes as well as to its posttranslational modifications. Therefore, it is important that in future, researchers pay close attention to the subcellular localization of CD133 and its phosphorylation status when reporting correlational or even mechanistic findings describing the role of CD133. Only this detailed information may prevent the misuse of CD133 as a universal marker of cells with stem cell properties, as currently seen in many cancer and stem cell studies. Finally, this knowledge should accelerate ongoing efforts to exploit CD133 in cancer treatment and regenerative medicine.

Abbreviations

Akt	Rac-alpha serine/threonine-protein kinase
ALK	Activin-like kinase
Arl13b	ADP-ribosylation factor-like GTPase 13B
Arp2/3	Actin-related protein 2/3
cAMP	Cyclic adenosine monophosphate
CD	Cluster of differentiation
CXCL	C-X-C motif chemokine ligand
CSC	Cancer stem cell
DFO	Desferrioxamine
DNMT	DNA methyltransferase
ECX	Extracellular domain X (where is 1 to 3)
EGFR	Epidermal growth factor receptor
EMT	Epithelial-mesenchymal transition
ER	Endoplasmic reticulum
ERK	Extracellular signal-regulated kinase
ESCRT	Endosomal sorting complex required for transport
ETS	E-twenty-six or erythroblast transformation specific
EV	Extracellular vesicle
FAK	Focal adhesion kinase
GABARAP	γ-aminobutyric type A receptor-associated protein
GLT8D1	Glycosyltransferase 8 domain containing 1
GM$_1$	Monosialoganglioside 1
GD$_3$	Disialoganglioside 3
HDAC	Histone deacetylase
HIF	Hypoxia inducible factor
HMG	High-mobility group of nuclear proteins
HNSCC	Head and neck squamous cell carcinoma
HSPC	Hematopoietic stem and progenitor cell
ICX	Intracellular domain X (where is 1 to 3)
IL	Interleukin
KRAS	Kirsten rat sarcoma virus oncogene homolog
KLF4	Kruppel-like factor 4
LE/MVB	Late endosome/multivesicular body
LEF	Lymphoid enhancer factor
MAPK	Mitogen-activated protein kinase
MDCK	Madin-Darby canine kidney
MLL	Mixed lineage leukemia
MV	Microvesicle
OCT4	Octamer-binding transcription factor 4

Pleskač *et al. Cellular & Molecular Biology Letters*   (2024) 29:41

Page 35 of 47

OMIM	Online Mendelian inheritance in man
ORF	Open reading frame
PDK1	3-Phosphoinositide-dependent protein kinase 1
PDZ	PSD-95/Dig-1/ZO-1
PI3K	Phosphoinositide 3-kinase
PIP_2	Phosphatidylinositol 4,5-bisphosphate
PIP_3	Phosphatidylinositol (3,4,5)-trisphosphate
PKA	Protein kinase A
PTPRκ	Protein tyrosine phosphatase κ
RBP-Jκ	Recombination signal binding protein for immunoglobulin kappa J region
ROCK	Rho-associated coiled-coil-containing protein kinase
SOX2	Sex-determining region Y-box 2
SQSTM1	Sequestosome 1
STAT3	Signal transducer and activator of transcription 3
TCF	T-cell factor
TGF	Transforming growth factor
TOR	Target of rapamycin
TNT	Tunneling nanotube
TSG101	Tumor susceptibility gene 101
TTYH	Tweety homolog
ULK1	Unc-51-like autophagy activating kinase 1
UTR	Untranslated region

Declarations

Ethics approval and consent to participate
Not applicable.

Consent for publication
Not applicable.

Competing interests
The authors declare no conflicts of interest.

References

1. Weigmann A, Corbeil D, Hellwig A, Huttner WB. Prominin, a novel microvilli-specific polytopic membrane protein of the apical surface of epithelial cells, is targeted to plasmalemmal protrusions of non-epithelial cells. Proc Natl Acad Sci U S A. 1997;94:12425–30.
2. Yin AH, Miraglia S, Zanjani ED, Almeida-Porada G, Ogawa M, Leary AG, et al. AC133, a novel marker for human hematopoietic stem and progenitor cells. Blood. 1997;90:5002–12.
3. Miraglia S, Godfrey W, Yin AH, Atkins K, Warnke R, Holden JT, et al. A novel five-transmembrane hematopoietic stem cell antigen: isolation, characterization, and molecular cloning. Blood. 1997;90:5013–21.
4. Horn PA, Tesch H, Staib P, Schoch C, Kube D, Diehl V, et al. Significance of AC133 and CD34 expression on acute myeloid leukemia cells. In: Büchner T, Hiddemann W, Wörmann B, Schellong G, Ritter J, Creutzig U, editors., Acute Leukemias VIII: Prognostic Factors and Treatment Strategies. Berlin Heidelberg: Springer; 2001. p. 160–5.
5. Bühring HJ, Seiffert M, Marxer A, Weiss B, Faul C, Kanz L, Brugger W. AC133 antigen expression is not restricted to acute myeloid leukemia blasts but is also found on acute lymphoid leukemia blasts and on a subset of CD34+ B-cell precursors. Blood. 1999;94:832–3.
6. Bühring HJ, Seiffert M, Bock TA, Scheding S, Thiel A, Scheffold A, et al. Expression of novel surface antigens on early hematopoietic cells. Ann N Y Acad Sci. 1999;872:25–39.

7. Corbeil D, Röper K, Hellwig A, Tavian M, Miraglia S, Watt SM, et al. The human AC133 hematopoietic stem cell antigen is also expressed in epithelial cells and targeted to plasma membrane protrusions. J Biol Chem. 2000;275:5512–20.

8. Maw MA, Corbeil D, Koch J, Hellwig A, Wilson-Wheeler JC, Bridges RJ, et al. A frameshift mutation in prominin (mouse)-like 1 causes human retinal degeneration. Hum Mol Genet. 2000;9:27–34.

9. Corbeil D, Fargeas CA, Huttner WB. Rat prominin, like its mouse and human orthologues, is a pentaspan membrane glycoprotein. Biochem Biophys Res Commun. 2001;285:939–44.

10. Fargeas CA, Joester A, Missol-Kolka E, Hellwig A, Huttner WB, Corbeil D. Identification of novel Prominin-1/CD133 splice variants with alternative C-termini and their expression in epididymis and testis. J Cell Sci. 2004;117:4301–11.

11. Florek M, Haase M, Marzesco AM, Freund D, Ehninger G, Huttner WB, et al. Prominin-1/CD133, a neural and hematopoietic stem cell marker, is expressed in adult human differentiated cells and certain types of kidney cancer. Cell Tissue Res. 2005;319:15–26.

12. Jászai J, Farkas LM, Fargeas CA, Janich P, Haase M, Huttner WB, et al. Prominin-2 is a novel marker of distal tubules and collecting ducts of the human and murine kidney. Histochem Cell Biol. 2010;133:527–39.

13. Gashaw I, Dushaj O, Behr R, Biermann K, Brehm R, Rubben H, et al. Novel germ cell markers characterize testicular seminoma and fetal testis. Mol Hum Reprod. 2007;13:721–7.

14. Pereira MF, Fernandes SA, Nascimento AR, Siu ER, Hess RA, Oliveira CA, et al. Effects of the oestrogen receptor antagonist Fulvestrant on expression of genes that affect organization of the epididymal epithelium. Andrology. 2014;2:559–71.

15. Jászai J, Janich P, Farkas LM, Fargeas CA, Huttner WB, Corbeil D. Differential expression of Prominin-1 (CD133) and Prominin-2 in major cephalic exocrine glands of adult mice. Histochem Cell Biol. 2007;128:409–19.

16. Immervoll H, Hoem D, Sakariassen PØ, Steffensen OJ, Molven A. Expression of the "stem cell marker" CD133 in pancreas and pancreatic ductal adenocarcinomas. BMC Cancer. 2008;8:48.

17. Karbanová J, Missol-Kolka E, Fonseca A-V, Lorra C, Janich P, Hollerová H, et al. The stem cell marker CD133 (Prominin-1) is expressed in various human glandular epithelia. J Histochem Cytochem. 2008;56:977–93.

18. Anderson LH, Boulanger CA, Smith GH, Carmeliet P, Watson CJ. Stem cell marker prominin-1 regulates branching morphogenesis, but not regenerative capacity, in the mammary gland. Dev Dyn. 2011;240:674–81.

19. Suzuki A, Sekiya S, Onishi M, Oshima N, Kiyonari H, Nakauchi H, et al. Flow cytometric isolation and clonal identification of self-renewing bipotent hepatic progenitor cells in adult mouse liver. Hepatology. 2008;48:1964–78.

20. Lee H, Yu DM, Park JS, Lee H, Kim JS, Kim HL, et al. Prominin-1-Radixin axis controls hepatic gluconeogenesis by regulating PKA activity. EMBO Rep. 2020;21: e49416.

21. Lardon J, Corbeil D, Huttner WB, Ling Z, Bouwens L. Stem cell marker prominin-1/AC133 is expressed in duct cells of the adult human pancreas. Pancreas. 2008;36:e1-6.

22. Corbeil D, Röper K, Fargeas CA, Joester A, Huttner WB. Prominin: a story of cholesterol, plasma membrane protrusions and human pathology. Traffic. 2001;2:82–91.

23. Zacchigna S, Oh H, Wilsch-Bräuninger M, Missol-Kolka E, Jászai J, Jansen S, et al. Loss of the cholesterol-binding protein prominin-1/CD133 causes disk dysmorphogenesis and photoreceptor degeneration. J Neurosci. 2009;29:2297–308.

24. Karbanová J, Laco J, Marzesco A-M, Janich P, Voborníková M, Mokrý J, et al. Human prominin-1 (CD133) is detected in both neoplastic and non-neoplastic salivary gland diseases and released into saliva in a ubiquitinated form. PLoS ONE. 2014;9: e98927.

25. Jászai J, Fargeas CA, Graupner S, Tanaka EM, Brand M, Huttner WB, et al. Distinct and conserved prominin-1/CD133–positive retinal cell populations identified across species. PLoS ONE. 2011;6: e17590.

26. Corbeil D, Joester A, Fargeas CA, Jászai J, Garwood J, Hellwig A, et al. Expression of distinct splice variants of the stem cell marker prominin-1 (CD133) in glial cells. Glia. 2009;57:860–74.

27. Fargeas CA, Fonseca A-V, Huttner WB, Corbeil D. Prominin-1 (CD133): from progenitor cells to human diseases. Future Lipidol. 2006;1:213–25.

28. Singh SK, Clarke ID, Terasaki M, Bonn VE, Hawkins C, Squire J, et al. Identification of a cancer stem cell in human brain tumors. Cancer Res. 2003;63:5821–8.

29. Singh SK, Hawkins C, Clarke ID, Squire JA, Bayani J, Hide T, et al. Identification of human brain tumour initiating cells. Nature. 2004;432:396–401.

30. Hemmati HD, Nakano I, Lazareff JA, Masterman-Smith M, Geschwind DH, Bronner-Fraser M, et al. Cancerous stem cells can arise from pediatric brain tumors. Proc Natl Acad Sci U S A. 2003;100:15178–83.

31. Zeppernick F, Ahmadi R, Campos B, Dictus C, Helmke BM, Becker N, et al. Stem cell marker CD133 affects clinical outcome in glioma patients. Clin Cancer Res. 2008;14:123–9.

32. Zhang M, Song T, Yang L, Chen R, Wu L, Yang Z, et al. Nestin and CD133: valuable stem cell-specific markers for determining clinical outcome of glioma patients. J Exp Clin Cancer Res. 2008;27:85.

33. Liou GY. CD133 as a regulator of cancer metastasis through the cancer stem cells. Int J Biochem Cell Biol. 2019;106:1–7.

34. Grosse-Gehling P, Fargeas CA, Dittfeld C, Garbe Y, Alison MR, Corbeil D, et al. CD133 as a biomarker for putative cancer stem cells in solid tumours: limitations, problems and challenges. J Pathol. 2013;229:355–78.

35. Uchida N, Buck DW, He D, Reitsma MJ, Masek M, Phan TV, et al. Direct isolation of human central nervous system stem cells. Proc Natl Acad Sci U S A. 2000;97:14720–5.

36. Lee A, Kessler JD, Read TA, Kaiser C, Corbeil D, Huttner WB, et al. Isolation of neural stem cells from the postnatal cerebellum. Nat Neurosci. 2005;8:723–9.

37. Beier D, Hau P, Proescholdt M, Lohmeier A, Wischhusen J, Oefner PJ, et al. CD133(+) and CD133(-) glioblastoma-derived cancer stem cells show differential growth characteristics and molecular profiles. Cancer Res. 2007;67:4010–5.

38. Richardson GD, Robson CN, Lang SH, Neal DE, Maitland NJ, Collins AT. CD133, a novel marker for human prostatic epithelial stem cells. J Cell Sci. 2004;117:3539–45.

39. Miki J, Furusato B, Li H, Gu Y, Takahashi H, Egawa S, et al. Identification of putative stem cell markers, CD133 and CXCR4, in hTERT–immortalized primary nonmalignant and malignant tumor-derived human prostate epithelial cell lines and in prostate cancer specimens. Cancer Res. 2007;67:3153–61.

40. Vander Griend DJ, Karthaus WL, Dalrymple S, Meeker A, Demarzo AM, Isaacs JT. The role of CD133 in normal human prostate stem cells and malignant cancer-initiating cells. Cancer Res. 2008;68:9703–11.

41. Missol-Kolka E, Karbanová J, Janich P, Haase M, Fargeas CA, Huttner WB, et al. Prominin-1 (CD133) is not restricted to stem cells located in the basal compartment of murine and human prostate. Prostate. 2011;71:254–67.

42. Collins AT, Berry PA, Hyde C, Stower MJ, Maitland NJ. Prospective identification of tumorigenic prostate cancer stem cells. Cancer Res. 2005;65:10946–51.

43. Bussolati B, Bruno S, Grange C, Buttiglieri S, Deregibus MC, Cantino D, et al. Isolation of renal progenitor cells from adult human kidney. Am J Pathol. 2005;166:545–55.

44. Angelotti ML, Ronconi E, Ballerini L, Peired A, Mazzinghi B, Sagrinati C, et al. Characterization of renal progenitors committed toward tubular lineage and their regenerative potential in renal tubular injury. Stem Cells. 2012;30:1714–25.

45. Sagrinati C, Netti GS, Mazzinghi B, Lazzeri E, Liotta F, Frosali F, et al. Isolation and characterization of multipotent progenitor cells from the Bowman's capsule of adult human kidneys. J Am Soc Nephrol. 2006;17:2443–56.

46. Lindgren D, Boström AK, Nilsson K, Hansson J, Sjölund J, Möller C, et al. Isolation and characterization of progenitor-like cells from human renal proximal tubules. Am J Pathol. 2011;178:828–37.

47. Suetsugu A, Nagaki M, Aoki H, Motohashi T, Kunisada T, Moriwaki H. Characterization of CD133+ hepatocellular carcinoma cells as cancer stem/progenitor cells. Biochem Biophys Res Commun. 2006;351:820–4.

48. Kordes C, Sawitza I, Müller-Marbach A, Ale-Agha N, Keitel V, Klonowski-Stumpe H, et al. CD133+ hepatic stellate cells are progenitor cells. Biochem Biophys Res Commun. 2007;352:410–7.

49. Dorrell C, Erker L, Schug J, Kopp JL, Canaday PS, Fox AJ, et al. Prospective isolation of a bipotential clonogenic liver progenitor cell in adult mice. Genes Dev. 2011;25:1193–203.

50. Oshima Y, Suzuki A, Kawashimo K, Ishikawa M, Ohkohchi N, Taniguchi H. Isolation of mouse pancreatic ductal progenitor cells expressing CD133 and c-Met by flow cytometric cell sorting. Gastroenterology. 2007;132:720–32.

51. Hermann PC, Huber SL, Herrler T, Aicher A, Ellwart JW, Guba M, et al. Distinct populations of cancer stem cells determine tumor growth and metastatic activity in human pancreatic cancer. Cell Stem Cell. 2007;1:313–23.

52. O'Brien CA, Pollett A, Gallinger S, Dick JE. A human colon cancer cell capable of initiating tumour growth in immunodeficient mice. Nature. 2007;445:106–10.

53. Ricci-Vitiani L, Lombardi DG, Pilozzi E, Biffoni M, Todaro M, Peschle C, et al. Identification and expansion of human colon-cancer-initiating cells. Nature. 2007;445:111–5.

54. Zhu L, Gibson P, Currle DS, Tong Y, Richardson RJ, Bayazitov IT, et al. Prominin 1 marks intestinal stem cells that are susceptible to neoplastic transformation. Nature. 2009;457:603–7.

55. Snippert HJ, van Es JH, van den Born M, Begthel H, Stange DE, Barker N, et al. Prominin-1/CD133 marks stem cells and early progenitors in mouse small intestine. Gastroenterology. 2009;136:2187-2194.e2181.

56. Eramo A, Lotti F, Sette G, Pilozzi E, Biffoni M, Di Virgilio A, et al. Identification and expansion of the tumorigenic lung cancer stem cell population. Cell Death Differ. 2008;15:504–14.

57. Monzani E, Facchetti F, Galmozzi E, Corsini E, Benetti A, Cavazzin C, et al. Melanoma contains CD133 and ABCG2 positive cells with enhanced tumourigenic potential. Eur J Cancer. 2007;43:935–46.

58. Ito Y, Hamazaki TS, Ohnuma K, Tamaki K, Asashima M, Okochi H. Isolation of murine hair-inducing cells using the cell surface marker prominin-1/CD133. J Invest Dermatol. 2007;127:1052–60.

59. Kratz-Albers K, Zühlsdorp M, Leo R, Berdel WL, Büchner T, Serve H. Expression of a AC133, a novel stem cell marker, on human leukemic blasts lacking CD34-antigen and on a human CD34+ leukemic line:MUTZ-2. Blood. 1998;92:4485–7.

60. Horn PA, Tesch H, Staib P, Kube D, Diehl V, Voliotis D. Expression of AC133, a novel hematopoietic precursor antigen, on acute myeloid leukemia cells. Blood. 1999;93:1435–7.

61. Wuchter C, Ratei R, Spahn G, Schoch, C, Harbott J, Schnittger, S et al. Impact of CD133 (AC133) and CD90 expression analysis for acute leukemia immunophenotyping. Haematologica. 2001;86:154-61.

62. Cox CV, Diamanti P, Evely RS, Kearns PR, Blair A. Expression of CD133 on leukemia-initiating cells in childhood ALL. Blood. 2009;113:3287–96.

63. Peichev M, Naiyer AJ, Pereira D, Zhu Z, Lane WJ, Williams M, et al. Expression of VEGFR-2 and AC133 by circulating human CD34(+) cells identifies a population of functional endothelial precursors. Blood. 2000;95:952–8.

64. Gehling UM, Ergün S, Schumacher U, Wagener C, Pantel K, Otte M, et al. In vitro differentiation of endothelial cells from AC133-positive progenitor cells. Blood. 2000;95:3106–12.

65. Hilbe W, Dirnhofer S, Oberwasserlechner F, Schmid T, Gunsilius E, Hilbe G, et al. CD133 positive endothelial progenitor cells contribute to the tumour vasculature in non-small cell lung cancer. J Clin Pathol. 2004;57:965–9.

66. Quirici N, Soligo D, Caneva L, Servida F, Bossolasco P, Deliliers GL. Differentiation and expansion of endothelial cells from human bone marrow CD133(+) cells. Br J Haematol. 2001;115:186–94.

67. Sekine A, Nishiwaki T, Nishimura R, Kawasaki T, Urushibara T, Suda R, et al. Prominin-1/CD133 expression as potential tissue-resident vascular endothelial progenitor cells in the pulmonary circulation. Am J Physiol Lung Cell Mol Physiol. 2016;310:L1130-1142.

68. Rossi E, Poirault-Chassac S, Bieche I, Chocron R, Schnitzler A, Lokajczyk A, et al. Human endothelial colony forming cells express intracellular CD133 that modulates their vasculogenic properties. Stem Cell Rev Rep. 2019;15:590–600.

69. Sun S, Meng Y, Li M, Tang X, Hu W, Wu W, et al. CD133(+) endothelial-like stem cells restore neovascularization and promote longevity in progeroid and naturally aged mice. Nat Aging. 2023;3:1401–14.

70. Corbeil D, Fargeas CA, Jászai J. CD133 might be a pan marker of epithelial cells with dedifferentiation capacity. Proc Natl Acad Sci U S A. 2014;111:E1451–2.

71. Jászai J, Graupner S, Tanaka EM, Funk RHW, Huttner WB, Brand M, et al. Spatial distribution of prominin-1 (CD133)—positive cells within germinative zones of the vertebrate brain. PLoS ONE. 2013;8: e63457.

72. Kusaba T, Lalli M, Kramann R, Kobayashi A, Humphreys BD. Differentiated kidney epithelial cells repair injured proximal tubule. Proc Natl Acad Sci U S A. 2014;111:1527–32.

73. Kramann R, Kusaba T, Humphreys BD. Who regenerates the kidney tubule? Nephrol Dial Transplant. 2015;30:903–10.

74. Cheng JX, Liu BL, Zhang X. How powerful is CD133 as a cancer stem cell marker in brain tumors? Cancer Treat Rev. 2009;35:403–8.

75. Miraglia S, Godfrey W, Buck D. A response to AC133 hematopoietic stem cell antigen: human homologue of mouse kidney prominin or distinct member of a novel protein family? Blood. 1998;91:4390–1.

76. Shmelkov SV, Butler JM, Hooper AT, Hormigo A, Kushner J, Milde T, et al. CD133 expression is not restricted to stem cells, and both CD133(+) and CD133(-) metastatic colon cancer cells initiate tumors. J Clin Invest. 2008;118:2111–20.

77. Fargeas CA, Corbeil D, Huttner WB. AC133 antigen, CD133, prominin-1, prominin-2, etc.: prominin family gene products in need of a rational nomenclature. Stem Cells. 2003;21:506–8.

78. Bidlingmaier S, Zhu X, Liu B. The utility and limitations of glycosylated human CD133 epitopes in defining cancer stem cells. J Mol Med. 2008;86:1025–32.

79. Jaksch M, Múnera J, Bajpai R, Terskikh A, Oshima RG. Cell cycle-dependent variation of a CD133 epitope in human embryonic stem cell, colon cancer, and melanoma cell lines. Cancer Res. 2008;68:7882–6.

80. Kemper K, Sprick MR, de Bree M, Scopelliti A, Vermeulen L, Hoek M, et al. The AC133 epitope, but not the CD133 protein, is lost upon cancer stem cell differentiation. Cancer Res. 2010;70:719–29.

81. Bauer N, Wilsch-Bräuninger M, Karbanová J, Fonseca AV, Strauss D, Freund D, et al. Haematopoietic stem cell differentiation promotes the release of prominin-1/CD133-containing membrane vesicles—a role of the endocytic–exocytic pathway. EMBO Mol Med. 2011;3:398–409.

82. Fargeas CA, Karbanová J, Jászai J, Corbeil D. CD133 and membrane microdomains: old facets for future hypotheses. World J Gastroenterol. 2011;17:4149.

83. Barrantes-Freer A, Renovanz M, Eich M, Braukmann A, Sprang B, Spirin P, et al. CD133 expression is not synonymous to immunoreactivity for AC133 and fluctuates throughout the cell cycle in glioma stem-like cells. PLoS ONE. 2015;10: e0130519.

84. Fargeas CA, Büttner E, Corbeil D. Commentary: "Prom1 function in development, intestinal inflammation, and intestinal tumorigenesis." Front Oncol. 2015;5:91.

85. Cehajic-Kapetanovic J, Birtel J, McClements ME, Shanks ME, Clouston P, Downes SM, et al. Clinical and molecular characterization of PROM1-related retinal degeneration. JAMA Netw Open. 2019;2: e195752.

86. Zhang Q, Zulfiqar F, Xiao X, Riazuddin S, Ahmad Z, Caruso R, et al. Severe retinitis pigmentosa mapped to 4p15 and associated with a novel mutation in the PROM1 gene. Hum Genet. 2007;122:293–9.

87. Yang Z, Chen Y, Lillo C, Chien J, Yu Z, Michaelides M, et al. Mutant prominin 1 found in patients with macular degeneration disrupts photoreceptor disk morphogenesis in mice. J Clin Invest. 2008;118:2908–16.

88. Pras E, Abu A, Rotenstreich Y, Avni I, Reish O, Morad Y, et al. Cone-rod dystrophy and a frameshift mutation in the PROM1 gene. Mol Vis. 2009;15:1709–16.

89. Sleeman KE, Kendrick H, Robertson D, Isacke CM, Ashworth A, Smalley MJ. Dissociation of estrogen receptor expression and in vivo stem cell activity in the mammary gland. J Cell Biol. 2007;176:19–26.

90. Ford MJ, Harwalkar K, Kazemdarvish H, Yamanaka N, Yamanaka Y. CD133/Prom1 marks proximal mouse oviduct epithelial progenitors and adult epithelial cells with a low generative capacity. Biol Open. 2023;12:bio059963.

91. Arndt K, Grinenko T, Mende N, Reichert D, Portz M, Ripich T, et al. CD133 is a modifier of hematopoietic progenitor frequencies but is dispensable for the maintenance of mouse hematopoietic stem cells. Proc Natl Acad Sci U S A. 2013;110:5582–7.

92. Walker TL, Wierick A, Sykes AM, Waldau B, Corbeil D, Carmeliet P, et al. Prominin-1 allows prospective isolation of neural stem cells from the adult murine hippocampus. J Neurosci. 2013;33:3010–24.

93. Fargeas CA, Florek M, Huttner WB, Corbeil D. Characterization of Prominin-2, a new member of the prominin family of pentaspan membrane glycoproteins. J Biol Chem. 2003;278:8586–96.

94. Liu Y, Ren S, Xie L, Cui C, Xing Y, Liu C, et al. Mutation of N-linked glycosylation at Asn548 in CD133 decreases its ability to promote hepatoma cell growth. Oncotarget. 2015;6:20650–60.

95. Corbeil D, Karbanová J, Fargeas CA, Jászai J. Prominin-1 (CD133): molecular and cellular features across species. Adv Exp Med Biol. 2013;777:3–24.

96. Han Z, Papermaster DS. Identification of three prominin homologs and characterization of their messenger RNA expression in Xenopus laevis tissues. Mol Vis. 2011;17:1381–96.

97. Fargeas CA. Prominin-2 and other relatives of CD133. Adv Exp Med Biol. 2013;777:25–40.

98. Zelhof AC, Hardy RW, Becker A, Zuker CS. Transforming the architecture of compound eyes. Nature. 2006;443:696–9.

99. Demontis F, Dahmann C. Apical and lateral cell protrusions interconnect epithelial cells in live Drosophila wing imaginal discs. Dev Dyn. 2007;236:3408–18.

100. Nie J, Mahato S, Mustill W, Tipping C, Bhattacharya SS, Zelhof AC. Cross species analysis of Prominin reveals a conserved cellular role in invertebrate and vertebrate photoreceptor cells. Dev Biol. 2012;371:312–20.

101. Mahato S, Nie J, Plachetzki DC, Zelhof AC. A mosaic of independent innovations involving eyes shut are critical for the evolutionary transition from fused to open rhabdoms. Dev Biol. 2018;443:188–202.

102. Wang X, Zheng H, Jia Z, Lei Z, Li M, Zhuang Q, et al. Drosophila Prominin-like, a homolog of CD133, interacts with ND20 to maintain mitochondrial function. Cell Biosci. 2019;9:101.

103. McGrail M, Batz L, Noack K, Pandey S, Huang Y, Gu X, et al. Expression of the zebrafish CD133/prominin1 genes in cellular proliferation zones in the embryonic central nervous system and sensory organs. Dev Dyn. 2010;239:1849–57.

104. Fargeas CA, Huttner WB, Corbeil D. Nomenclature of prominin-1 (CD133) splice variants—an update. Tissue Antigens. 2007;69:602–6.

105. Thamm K, Graupner S, Werner C, Huttner WB, Corbeil D. Monoclonal antibodies 13A4 and AC133 do not recognize the canine ortholog of mouse and human stem cell antigen prominin-1 (CD133). PLoS ONE. 2016;11: e0164079.

106. Shmelkov SV, Jun L, St Clair R, McGarrigle D, Derderian CA, Usenko JK, et al. Alternative promoters regulate transcription of the gene that encodes stem cell surface protein AC133. Blood. 2004;103:2055–61.

107. Kemper K, Tol MJPM, Medema JP. Mouse tissues express multiple splice variants of prominin-1. PLoS ONE. 2010;5: e12325.

108. Choi M-H, Na JE, Yoon YR, Rhyu IJ, Ko Y-G, Baik J-H. Hypomyelination and cognitive impairment in mice lacking CD133 (Prominin-1). Biochem Biophys Res Commun. 2018;502:291–8.

109. Osmond TL, Broadley KWR, McConnell MJ. Glioblastoma cells negative for the anti-CD133 antibody AC133 express a truncated variant of the CD133 protein. Int J Mol Med. 2010;25:883–8.

110. Gopisetty G, Xu J, Sampath D, Colman H, Puduvalli VK. Epigenetic regulation of CD133/PROM1 expression in glioma stem cells by Sp1/myc and promoter methylation. Oncogene. 2013;32:3119–29.

111. Sompallae R, Hofmann O, Maher C, Gedye C, Behren A, Vitezic M, et al. A comprehensive promoter landscape identifies a novel promoter for CD133 in restricted tissues, cancers, and stem cells. Front Genet. 2013;4:209.

112. Tabu K, Bizen N, Taga T, Tanaka S. Gene regulation of prominin-1 (CD133) in normal and cancerous tissues. Adv Exp Med Biol. 2013;777:73–85.

113. Tabu K, Kimura T, Sasai K, Wang L, Bizen N, Nishihara H, et al. Analysis of an alternative human CD133 promoter reveals the implication of Ras/ERK pathway in tumor stem-like hallmarks. Mol Cancer. 2010;9:39.

114. Tabu K, Sasai K, Kimura T, Wang L, Aoyanagi E, Kohsaka S, et al. Promoter hypomethylation regulates CD133 expression in human gliomas. Cell Res. 2008;18:1037–46.

115. Pleshkan VV, Vinogradova TV, Sverdlov ED. Methylation of the prominin 1 TATA-less main promoters and tissue specificity of their transcript content. Biochim Biophys Acta. 2008;1779:599–605.

116. Yi JM, Tsai HC, Glöckner SC, Lin S, Ohm JE, Easwaran H, et al. Abnormal DNA methylation of CD133 in colorectal and glioblastoma tumors. Cancer Res. 2008;68:8094–103.

117. Baba T, Convery PA, Matsumura N, Whitaker RS, Kondoh E, Perry T, et al. Epigenetic regulation of CD133 and tumorigenicity of CD133+ ovarian cancer cells. Oncogene. 2009;28:209–18.

118. Godfrey L, Crump NT, O'Byrne S, Lau IJ, Rice S, Harman JR, et al. H3K79me2/3 controls enhancer-promoter interactions and activation of the pan-cancer stem cell marker PROM1/CD133 in MLL-AF4 leukemia cells. Leukemia. 2021;35:90–106.

119. Guenther MG, Lawton LN, Rozovskaia T, Frampton GM, Levine SS, Volkert TL, et al. Aberrant chromatin at genes encoding stem cell regulators in human mixed-lineage leukemia. Genes Dev. 2008;22:3403–8.

120. Mak AB, Nixon AML, Moffat J. The mixed lineage leukemia (MLL) fusion-associated gene AF4 promotes CD133 transcription. Cancer Res. 2012;72:1929–34.

121. You H, Ding W, Rountree CB. Epigenetic regulation of cancer stem cell marker CD133 by transforming growth factor-β. Hepatology. 2010;51:1635–44.

122. Chen Z, Chen Y, Li Y, Lian W, Zheng K, Zhang Y, et al. Prrx1 promotes stemness and angiogenesis via activating TGF-β/smad pathway and upregulating proangiogenic factors in glioma. Cell Death Dis. 2021;12:615.

123. Cave DD, Di Guida M, Costa V, Sevillano M, Ferrante L, Heeschen C, et al. TGF-β1 secreted by pancreatic stellate cells promotes stemness and tumourigenicity in pancreatic cancer cells through L1CAM downregulation. Oncogene. 2020;39:4271–85.

124. Pellacani D, Packer RJ, Frame FM, Oldridge EE, Berry PA, Labarthe M-C, et al. Regulation of the stem cell marker CD133 is independent of promoter hypermethylation in human epithelial differentiation and cancer. Mol Cancer. 2011;10:94.

125. D'Anello L, Sansone P, Storci G, Mitrugno V, D'Uva G, Chieco P, et al. Epigenetic control of the basal-like gene expression profile via Interleukin-6 in breast cancer cells. Mol Cancer. 2010;9:300.

126. Hafner A, Bulyk ML, Jambhekar A, Lahav G. The multiple mechanisms that regulate p53 activity and cell fate. Nat Rev Mol Cell Biol. 2019;20:199–210.

127. Park EK, Lee JC, Park JW, Bang SY, Yi SA, Kim BK, et al. Transcriptional repression of cancer stem cell marker CD133 by tumor suppressor p53. Cell Death Dis. 2015;6:e1964–e1964.

128. Blazek ER, Foutch JL, Maki G. Daoy medulloblastoma cells that express CD133 are radioresistant relative to CD133– cells, and the CD133+ sector is enlarged by hypoxia. Int J Radiat Oncol Biol Phys. 2007;67:1–5.

129. Platet N, Liu SY, Atifi ME, Oliver L, Vallette FM, Berger F, et al. Influence of oxygen tension on CD133 phenotype in human glioma cell cultures. Cancer Lett. 2007;258:286–90.

130. Bar EE, Lin A, Mahairaki V, Matsui W, Eberhart CG. Hypoxia increases the expression of stem-cell markers and promotes clonogenicity in glioblastoma neurospheres. Am J Pathol. 2010;177:1491–502.

131. Filatova A, Seidel S, Böğürcü N, Gräf S, Garvalov BK, Acker T. Acidosis acts through HSP90 in a PHD/VHL-independent manner to promote HIF function and stem cell maintenance in glioma. Cancer Res. 2016;76:5845–56.

132. Soeda A, Park M, Lee D, Mintz A, Androutsellis-Theotokis A, McKay RD, et al. Hypoxia promotes expansion of the CD133-positive glioma stem cells through activation of HIF-1alpha. Oncogene. 2009;28:3949–59.

133. Maeda K, Ding Q, Yoshimitsu M, Kuwahata T, Miyazaki Y, Tsukasa K, et al. CD133 modulate HIF-1α expression under hypoxia in EMT phenotype pancreatic cancer stem-like cells. Int J Mol Sci. 2016;17:1025.

134. Qin J, Liu Y, Lu Y, Liu M, Li M, Li J, et al. Hypoxia-inducible factor 1 alpha promotes cancer stem cells-like properties in human ovarian cancer cells by upregulating SIRT1 expression. Sci Rep. 2017;7:10592.

135. Choudhry H, Harris AL. Advances in hypoxia-inducible factor biology. Cell Metab. 2018;27:281–98.

136. Ohnishi S, Maehara O, Nakagawa K, Kameya A, Otaki K, Fujita H, et al. Hypoxia-inducible factors activate CD133 promoter through ETS family transcription factors. PLoS ONE. 2013;8: e66255.

137. Iida H, Suzuki M, Goitsuka R, Ueno H. Hypoxia induces CD133 expression in human lung cancer cells by up-regulation of OCT3/4 and SOX2. Int J Oncol. 2012;40:71–9.

138. Won C, Kim BH, Yi EH, Choi KJ, Kim EK, Jeong JM, et al. Signal transducer and activator of transcription 3-mediated CD133 up-regulation contributes to promotion of hepatocellular carcinoma. Hepatology. 2015;62:1160–73.

139. Matsumoto K, Arao T, Tanaka K, Kaneda H, Kudo K, Fujita Y, et al. mTOR signal and hypoxia-inducible factor-1 regulate CD133 expression in cancer cells. Cancer Res. 2009;69:7160–4.
140. Liu YP, Yang CJ, Huang MS, Yeh CT, Wu AT, Lee YC, et al. Cisplatin selects for multidrug-resistant CD133+ cells in lung adenocarcinoma by activating Notch signaling. Cancer Res. 2013;73:406–16.
141. Fan X, Khaki L, Zhu TS, Soules ME, Talsma CE, Gul N, et al. NOTCH pathway blockade depletes CD133-positive glioblastoma cells and inhibits growth of tumor neurospheres and xenografts. Stem Cells. 2010;28:5–16.
142. Konishi H, Asano N, Imatani A, Kimura O, Kondo Y, Jin X, et al. Notch1 directly induced CD133 expression in human diffuse type gastric cancers. Oncotarget. 2016;7:56598–607.
143. Kumar D, Kumar S, Gorain M, Tomar D, Patil HS, Radharani NNV, et al. Notch1-MAPK signaling axis regulates CD133+ cancer stem cell-mediated melanoma growth and angiogenesis. J Invest Dermatol. 2016;136:2462–74.
144. Katoh Y, Katoh M. Comparative genomics on PROM1 gene encoding stem cell marker CD133. Int J Mol Med. 2007;19:967–70.
145. Emami KH, Nguyen C, Ma H, Kim DH, Jeong KW, Eguchi M, et al. A small molecule inhibitor of beta-catenin/CREB-binding protein transcription. Proc Natl Acad Sci U S A. 2004;101:12682–7.
146. Tang Y, Berlind J, Mavila N. Inhibition of CREB binding protein-beta-catenin signaling down regulates CD133 expression and activates PP2A-PTEN signaling in tumor initiating liver cancer cells. Cell Commun Signal. 2018;16:9.
147. Inui M, Martello G, Piccolo S. MicroRNA control of signal transduction. Nat Rev Mol Cell Biol. 2010;11:252–63.
148. Yoshida K, Yamamoto Y, Ochiya T. miRNA signaling networks in cancer stem cells. Regen Ther. 2021;17:1–7.
149. Bai H-Y, Liao Y-J, Cai M-Y, Ma N-F, Zhang Q, Chen J-W, et al. Eukaryotic initiation factor 5A2 contributes to the maintenance of CD133(+) hepatocellular carcinoma cells via the c-Myc/microRNA-29b Axis. Stem Cells. 2018;36:180–91.
150. Li B, Xu WW, Han L, Chan KT, Tsao SW, Lee NPY, et al. MicroRNA-377 suppresses initiation and progression of esophageal cancer by inhibiting CD133 and VEGF. Oncogene. 2017;36:3986–4000.
151. Huang S-X, Zhao Z-Y, Weng G-H, He X-Y, Wu C-J, Fu C-Y, et al. Upregulation of miR-181a suppresses the formation of glioblastoma stem cells by targeting the Notch2 oncogene and correlates with good prognosis in patients with glioblastoma multiforme. Biochem Biophys Res Commun. 2017;486:1129–36.
152. Bourseau-Guilmain E, Griveau A, Benoit J-P, Garcion E. The importance of the stem cell marker prominin-1/CD133 in the uptake of transferrin and in iron metabolism in human colon cancer Caco-2 cells. PLoS ONE. 2011;6: e25515.
153. Zhou F, Cui C, Ge Y, Chen H, Li Q, Yang Z, et al. α2,3-Sialylation regulates the stability of stem cell marker CD133. J Biochem. 2010;148:273–80.
154. Hamanoue M, Matsuzaki Y, Sato K-I, Okano HJ, Shibata S, Sato I, et al. Cell surface N-glycans mediated isolation of mouse neural stem cells. J Neurochem. 2009;110:1575–84.
155. Dowland SN, Madawala RJ, Poon CE, Lindsay LA, Murphy CR. Prominin-1 glycosylation changes throughout early pregnancy in uterine epithelial cells under the influence of maternal ovarian hormones. Reprod Fertil Dev. 2017;29:1194–208.
156. Lehnus KS, Donovan LK, Huang X, Zhao N, Warr TJ, Pilkington GJ, et al. CD133 glycosylation is enhanced by hypoxia in cultured glioma stem cells. Int J Oncol. 2013;42:1011–7.
157. Liu K, Jiang L, Shi Y, Liu B, He Y, Shen Q, et al. Hypoxia-induced GLT8D1 promotes glioma stem cell maintenance by inhibiting CD133 degradation through N-linked glycosylation. Cell Death Differ. 2022;29:1834–49.
158. Wei Y, Chen Q, Huang S, Liu Y, Li Y, Xing Y, et al. The interaction between DNMT1 and high-mannose CD133 maintains the slow-cycling state and tumorigenic potential of glioma stem cell. Adv Sci. 2022;9:2202216.
159. Mak AB, Blakely KM, Williams RA, Penttilä P-A, Shukalyuk AI, Osman KT, et al. CD133 protein N-glycosylation processing contributes to cell surface recognition of the primitive cell marker AC133 epitope. J Biol Chem. 2011;286:41046–56.
160. Joo KM, Kim SY, Jin X, Song SY, Kong DS, Lee JI, et al. Clinical and biological implications of CD133-positive and CD133-negative cells in glioblastomas. Lab Invest. 2008;88:808–15.
161. Boivin D, Labbé D, Fontaine N, Lamy S, Beaulieu ED, Gingras D, et al. The stem cell marker CD133 (Prominin-1) is phosphorylated on cytoplasmic tyrosine-828 and tyrosine-852 by Src and Fyn tyrosine kinases. Biochemistry. 2009;48:3998–4007.
162. Mak AB, Pehar M, Nixon AML, Williams RA, Uetrecht AC, Puglielli L, et al. Post-translational regulation of CD133 by ATase1/ATase2-mediated lysine acetylation. J Mol Biol. 2014;426:2175–82.
163. Wei Y, Jiang Y, Zou F, Liu Y, Wang S, Xu N, et al. Activation of PI3K/Akt pathway by CD133-p85 interaction promotes tumorigenic capacity of glioma stem cells. Proc Natl Acad Sci U S A. 2013;110:6829–34.
164. Chen Y-S, Wu M-J, Huang C-Y, Lin S-C, Chuang T-H, Yu C-C, et al. CD133/Src axis mediates tumor initiating property and epithelial-mesenchymal transition of head and neck cancer. PLoS ONE. 2011;6: e28053.
165. Yang F, Xing Y, Li Y, Chen X, Jiang J, Ai Z, et al. Monoubiquitination of cancer stem cell marker CD133 at lysine 848 regulates its secretion and promotes cell migration. Mol Cell Biol. 2018;38:e00024-e118.
166. Babst M, Odorizzi G, Estepa EJ, Emr SD. Mammalian tumor susceptibility gene 101 (TSG101) and the yeast homologue, Vps23p, both function in late endosomal trafficking. Traffic. 2000;1:248–58.
167. Baietti MF, Zhang Z, Mortier E, Melchior A, Degeest G, Geeraerts A, et al. Syndecan-syntenin-ALIX regulates the biogenesis of exosomes. Nat Cell Biol. 2012;14:677–85.
168. Ding Y, Dellisanti CD, Ko MH, Czajkowski C, Puglielli L. The endoplasmic reticulum-based acetyltransferases, ATase1 and ATase2, associate with the oligosaccharyltransferase to acetylate correctly folded polypeptides. J Biol Chem. 2014;289:32044–55.
169. Jászai J, Fargeas CA, Florek M, Huttner WB, Corbeil D. Focus on molecules: prominin-1 (CD133). Exp Eye Res. 2007;85:585–6.
170. Gurudev N, Florek M, Corbeil D, Knust E. Prominent role of prominin in the retina. Adv Exp Med Biol. 2013;777:55–71.
171. Goldberg AFX, Moritz OL, Williams DS. Molecular basis for photoreceptor outer segment architecture. Prog Retin Eye Res. 2016;55:52–81.

172. Dellett M, Sasai N, Nishide K, Becker S, Papadaki V, Limb GA, et al. Genetic background and light-dependent progression of photoreceptor cell degeneration in prominin-1 knockout Mice. Invest Ophthalmol Vis Sci. 2015;56:164–76.

173. Han Z, Anderson DW, Papermaster DS. Prominin-1 localizes to the open rims of outer segment lamellae in xenopus laevis rod and cone photoreceptors. Invest Ophthalmol Vis Sci. 2012;53:361–73.

174. Carr BJ, Stanar P, Moritz OL. Distinct roles for prominin-1 and photoreceptor cadherin in outer segment disc morphogenesis in CRISPR-altered *X. laevis*. J Cell Sci. 2021;134:jcs253906.

175. Lu Z, Hu X, Reilly J, Jia D, Liu F, Yu S, et al. Deletion of the transmembrane protein Prom1b in zebrafish disrupts outer-segment morphogenesis and causes photoreceptor degeneration. J Biol Chem. 2019;294:13953–63.

176. Corbeil D, Fargeas CA, Jászai J. Deciphering the roles of prominins in the visual system. J Biol Chem. 2019;294:17166.

177. Thamm K, Šimaitė D, Karbanová J, Bermúdez V, Reichert D, Morgenstern A, et al. Prominin-1 (CD133) modulates the architecture and dynamics of microvilli. Traffic. 2019;20:39–60.

178. Hori A, Nishide K, Yasukuni Y, Haga K, Kakuta W, Ishikawa Y, et al. Prominin-1 modulates Rho/ROCK-mediated membrane morphology and calcium-dependent intracellular chloride flux. Sci Rep. 2019;9:15911.

179. Freund D, Bauer N, Boxberger S, Feldmann S, Streller U, Ehninger G, et al. Polarization of human hematopoietic progenitors during contact with multipotent mesenchymal stromal cells: effects on proliferation and clonogenicity. Stem Cells Dev. 2006;15:815–29.

180. Spencer WJ, Schneider NF, Lewis TR, Castillo CM, Skiba NP, Arshavsky VY. The WAVE complex drives the morphogenesis of the photoreceptor outer segment cilium. Proc Natl Acad Sci U S A. 2023;120: e2215011120.

181. Goetz SC, Anderson KV. The primary cilium: a signalling centre during vertebrate development. Nat Rev Genet. 2010;11:331–44.

182. Singer D, Thamm K, Zhuang H, Karbanová J, Gao Y, Walker JV, et al. Prominin-1 controls stem cell activation by orchestrating ciliary dynamics. EMBO J. 2019;38: e99845.

183. Jászai J, Thamm K, Karbanová J, Janich P, Fargeas CA, Huttner WB, et al. Prominins control ciliary length throughout the animal kingdom: new lessons from human prominin-1 and zebrafish prominin-3. J Biol Chem. 2020;295:6007–22.

184. Florek M, Bauer N, Janich P, Wilsch-Braeuninger M, Fargeas CA, Marzesco AM, et al. Prominin-2 is a cholesterol-binding protein associated with apical and basolateral plasmalemmal protrusions in polarized epithelial cells and released into urine. Cell Tissue Res. 2007;328:31–47.

185. Janich P, Corbeil D. GM1 and GM3 gangliosides highlight distinct lipid microdomains within the apical domain of epithelial cells. FEBS Lett. 2007;581:1783–7.

186. Larkins CE, Aviles GDG, East MP, Kahn RA, Caspary T. Arl13b regulates ciliogenesis and the dynamic localization of Shh signaling proteins. Mol Biol Cell. 2011;22:4694–703.

187. Lu H, Toh MT, Narasimhan V, Thamilselvam SK, Choksi SP, Roy S. A function for the Joubert syndrome protein Arl13b in ciliary membrane extension and ciliary length regulation. Dev Biol. 2015;397:225–36.

188. Pugacheva EN, Jablonski SA, Hartman TR, Henske EP, Golemis EA. HEF1-dependent Aurora A activation induces disassembly of the primary cilium. Cell. 2007;129:1351–63.

189. Ran J, Yang Y, Li D, Liu M, Zhou J. Deacetylation of α-tubulin and cortactin is required for HDAC6 to trigger ciliary disassembly. Sci Rep. 2015;5:12917.

190. Izumi H, Li Y, Shibaki M, Mori D, Yasunami M, Sato S, et al. Recycling endosomal CD133 functions as an inhibitor of autophagy at the pericentrosomal region. Sci Rep. 2019;9:2236.

191. Marzesco AM, Janich P, Wilsch-Bräuninger M, Dubreuil V, Langenfeld K, Corbeil D et al. Release of extracellular membrane particles carrying the stem cell marker prominin-1 (CD133) from neural progenitors and other epithelial cells. J Cell Sci. 2005;118:2849–58.

192. Dubreuil V, Marzesco AM, Corbeil D, Huttner WB, Wilsch-Bräuninger M. Midbody and primary cilium of neural progenitors release extracellular membrane particles enriched in the stem cell marker prominin-1. J Cell Biol. 2007;176:483–95.

193. Mirzadeh Z, Merkle FT, Soriano-Navarro M, Garcia-Verdugo JM, Alvarez-Buylla A. Neural stem cells confer unique pinwheel architecture to the ventricular surface in neurogenic regions of the adult brain. Cell Stem Cell. 2008;3:265–78.

194. Codega P, Silva-Vargas V, Paul A, Maldonado-Soto AR, Deleo AM, Pastrana E, et al. Prospective identification and purification of quiescent adult neural stem cells from their in vivo niche. Neuron. 2014;82:545–59.

195. Coskun V, Wu H, Blanchi B, Tsao S, Kim K, Zhao J, et al. CD133+ neural stem cells in the ependyma of mammalian postnatal forebrain. Proc Natl Acad Sci U S A. 2008;105:1026–31.

196. Zhong A, Short C, Xu J, Fernandez GE, Malkoff N, Noriega N, et al. Prominin-1 promotes restitution of the murine extrahepatic biliary luminal epithelium following cholestatic liver injury. Hepatol Commun. 2023;7: e0018.

197. Jászai J, Corbeil D, Fargeas CA. Comprehensive overview of CD133 biology in neural tissues across species. In: Pruszak J, editor. Neural surface antigens–from basic biology towards biomedical applications. Academic Press; 2015. p. 113–129.

198. Bachor TP, Karbanová J, Büttner E, Bermúdez V, Marquioni-Ramella M, Carmeliet P, et al. Early ciliary and prominin-1 dysfunctions precede neurogenesis impairment in a mouse model of type 2 diabetes. Neurobiol Dis. 2017;108:13–28.

199. Serra CFH, Liu H, Qian J, Mori M, Lu J, Cardoso WV. Prominin 1 and Notch regulate ciliary length and dynamics in multiciliated cells of the airway epithelium. iScience. 2022;25:104751.

200. Badano JL, Mitsuma N, Beales PL, Katsanis N. The ciliopathies: an emerging class of human genetic disorders. Annu Rev Genomics Hum Genet. 2006;7:125–48.

201. Xiao YS, Liang J, Gao M, Sun JR, Liu Y, Chen JQ, et al. Deletion of prominin-1 in mice results in disrupted photoreceptor outer segment protein homeostasis. Int J Ophthalmol. 2021;14:1334–44.

202. Fargeas CA, Jászai J, Corbeil D. Prominin-1 expression in the testis/epididymis and fertility. Reprod Med Biol. 2023;22: e12544.

203. Karim BO, Rhee KJ, Liu G, Yun K, Brant SR. Prom1 function in development, intestinal inflammation, and intestinal tumorigenesis. Front Oncol. 2014;4:323.

204. Nishide K, Nakatani Y, Kiyonari H, Kondo T. Glioblastoma formation from cell population depleted of Prominin1-expressing cells. PLoS ONE. 2009;4: e6869.

205. Jászai J, Fargeas CA, Haase M, Farkas LM, Huttner WB, Corbeil D. Robust expression of Prominin-2 all along the adult male reproductive system and urinary bladder. Histochem Cell Biol. 2008;130:749–59.

206. Asano A, Nelson JL, Zhang S, Travis AJ. Characterization of the proteomes associating with three distinct membrane raft sub-types in murine sperm. Proteomics. 2010;10:3494–505.

207. Yukselten Y, Aydos OSE, Sunguroglu A, Aydos K. Investigation of CD133 and CD24 as candidate azoospermia markers and their relationship with spermatogenesis defects. Gene. 2019;706:211–21.

208. Matsukuma H, Kobayashi Y, Oka S, Higashijima F, Kimura K, Yoshihara E, et al. Prominin-1 deletion results in spermatogenic impairment, sperm morphological defects, and infertility in mice. Reprod Med Biol. 2023;22: e12514.

209. Röper K, Corbeil D, Huttner WB. Retention of prominin in microvilli reveals distinct cholesterol-based lipid microdomains in the apical plasma membrane. Nat Cell Biol. 2000;2:582–92.

210. Karbanová J, Lorico A, Bornhäuser M, Corbeil D, Fargeas CA. Prominin-1/CD133: lipid raft association, detergent resistance, and immunodetection. Stem Cells Transl Med. 2018;7:155–60.

211. Sezgin E, Levental I, Mayor S, Eggeling C. The mystery of membrane organization: composition, regulation and roles of lipid rafts. Nat Rev Mol Cell Biol. 2017;18:361–74.

212. Ikonen E, Simons K. Protein and lipid sorting from the trans-Golgi network to the plasma membrane in polarized cells. Semin Cell Dev Biol. 1998;9:503–9.

213. Huttner WB, Zimmerberg J. Implications of lipid microdomains for membrane curvature, budding and fission. Curr Opin Cell Biol. 2001;13:478–84.

214. Simons K, Toomre D. Lipid rafts and signal transduction. Nat Rev Mol Cell Biol. 2000;1:31–9.

215. Zhang S, Zhu N, Li HF, Gu J, Zhang CJ, Liao DF, et al. The lipid rafts in cancer stem cell: a target to eradicate cancer. Stem Cell Res Ther. 2022;13:432.

216. Brown DA, Rose JK. Sorting of GPI-anchored proteins to glycolipid-enriched membrane subdomains during transport to the apical cell surface. Cell. 1992;68:533–44.

217. Lingwood D, Simons K. Detergent resistance as a tool in membrane research. Nat Protoc. 2007;2:2159–65.

218. Corbeil D, Marzesco AM, Wilsch-Bräuninger M, Huttner WB. The intriguing links between prominin-1 (CD133), cholesterol-based membrane microdomains, remodeling of apical plasma membrane protrusions, extracellular membrane particles, and (neuro)epithelial cell differentiation. FEBS Lett. 2010;584:1659–64.

219. Taïeb N, Maresca M, Guo X-J, Garmy N, Fantini J, Yahi N. The first extracellular domain of the tumour stem cell marker CD133 contains an antigenic ganglioside-binding motif. Cancer Lett. 2009;278:164–73.

220. Gillette JM, Larochelle A, Dunbar CE, Lippincott-Schwartz J. Intercellular transfer to signalling endosomes regulates an ex vivo bone marrow niche. Nat Cell Biol. 2009;11:303–11.

221. Freund D, Fonseca A-V, Janich P, Bornhäuser M, Corbeil D. Differential expression of biofunctional GM1 and GM3 gangliosides within the plastic-adherent multipotent mesenchymal stromal cell population. Cytotherapy. 2010;12:131–42.

222. Mazerik JN, Tyska MJ. Myosin-1A targets to microvilli using multiple membrane binding motifs in the tail homology 1 (TH1) domain. J Biol Chem. 2012;287:13104–15.

223. Hokanson DE, Ostap EM. Myo1c binds tightly and specifically to phosphatidylinositol 4,5-bisphosphate and inositol 1,4,5-trisphosphate. Proc Natl Acad Sci U S A. 2006;103:3118–23.

224. Insall RH, Weiner OD. PIP3, PIP2, and cell movement—similar messages, different meanings? Dev Cell. 2001;1:743–7.

225. Spillane M, Ketschek A, Jones SL, Korobova F, Marsick B, Lanier L, et al. The actin nucleating Arp2/3 complex contributes to the formation of axonal filopodia and branches through the regulation of actin patch precursors to filopodia. Dev Neurobiol. 2011;71:747–58.

226. Iglič A, Hägerstrand H, Veranič P, Plemenitaš A, Kralj-Iglič V. Curvature-induced accumulation of anisotropic membrane components and raft formation in cylindrical membrane protrusions. J Theor Biol. 2006;240:368–73.

227. Schara K, Jansa V, Sustar V, Dolinar D, Pavlic JI, Lokar M, et al. Mechanisms for the formation of membranous nanostructures in cell-to-cell communication. Cell Mol Biol Lett. 2009;14:636–56.

228. Kabaso D, Bobrovska N, Góźdź W, Gov N, Kralj-Iglič V, Veranič P, et al. On the role of membrane anisotropy and BAR proteins in the stability of tubular membrane structures. J Biomech. 2012;45:231–8.

229. Kinnebrew M, Iverson EJ, Patel BB, Pusapati GV, Kong JH, Johnson KA, et al. Cholesterol accessibility at the ciliary membrane controls hedgehog signaling. Elife. 2019;8:e50051.

230. Radhakrishnan A, Rohatgi R, Siebold C. Cholesterol access in cellular membranes controls Hedgehog signaling. Nat Chem Biol. 2020;16:1303–13.

231. Adhyapak P, Kapoor S. Membrane dynamics in health and disease: impact on cellular signalling. J Membr Biol. 2019;252:213–26.

232. Sasaki A, Kamiyama T, Yokoo H, Nakanishi K, Kubota K, Haga H, et al. Cytoplasmic expression of CD133 is an important risk factor for overall survival in hepatocellular carcinoma. Oncol Rep. 2010;24:537–46.

233. Zhang J, Guo X, Chang DY, Rosen DG, Mercado-Uribe I, Liu J. CD133 expression associated with poor prognosis in ovarian cancer. Mod Pathol. 2012;25:456–64.

234. Brescia P, Ortensi B, Fornasari L, Levi D, Broggi G, Pelicci G. CD133 is essential for glioblastoma stem cell maintenance. Stem Cells. 2013;31:857–69.

235. Chen Y-L, Lin P-Y, Ming Y-Z, Huang W-C, Chen R-F, Chen P-M, et al. The effects of the location of cancer stem cell marker CD133 on the prognosis of hepatocellular carcinoma patients. BMC Cancer. 2017;17:474.

236. Adini A, Adini I, Ghosh K, Benny O, Pravda E, Hu R, et al. The stem cell marker prominin-1/CD133 interacts with vascular endothelial growth factor and potentiates its action. Angiogenesis. 2013;16:405–16.

237. Chen H, Luo Z, Dong L, Tan Y, Yang J, Feng G, et al. CD133/Prominin-1-mediated autophagy and glucose uptake beneficial for hepatoma cell survival. PLoS ONE. 2013;8: e56878.

238. Sun H, Zhang M, Cheng K, Li P, Han S, Li R, et al. Resistance of glioma cells to nutrient-deprived microenvironment can be enhanced by CD133-mediated autophagy. Oncotarget. 2016;7:76238–49.

239. Bhattacharya S, Yin J, Winborn CS, Zhang Q, Yue J, Chaum E. Prominin-1 is a novel regulator of autophagy in the human retinal pigment epithelium. Invest Ophthalmol Vis Sci. 2017;58:2366.

240. Cha-Molstad H, Yu JE, Feng Z, Lee SH, Kim JG, Yang P, et al. p62/SQSTM1/Sequestosome-1 is an N-recognin of the N-end rule pathway which modulates autophagosome biogenesis. Nat Commun. 2017;8:102.

241. Weidberg H, Shvets E, Shpilka T, Shimron F, Shinder V, Elazar Z. LC3 and GATE-16/GABARAP subfamilies are both essential yet act differently in autophagosome biogenesis. EMBO J. 2010;29:1792–802.

242. Joachim J, Jefferies HB, Razi M, Frith D, Snijders AP, Chakravarty P, et al. Activation of ULK kinase and autophagy by GABARAP trafficking from the centrosome is regulated by WAC and GM130. Mol Cell. 2015;60:899–913.

243. Rogov V, Dötsch V, Johansen T, Kirkin V. Interactions between autophagy receptors and ubiquitin-like proteins form the molecular basis for selective autophagy. Mol Cell. 2014;53:167–78.

244. Fonseca AV, Bauer N, Corbeil D. The stem cell marker CD133 meets the endosomal compartment–new insights into the cell division of hematopoietic stem cells. Blood Cells Mol Dis. 2008;41:194–5.

245. Pine SR, Ryan BM, Varticovski L, Robles AI, Harris CC. Microenvironmental modulation of asymmetric cell division in human lung cancer cells. Proc Natl Acad Sci U S A. 2010;107:2195–200.

246. Lathia JD, Hitomi M, Gallagher J, Gadani SP, Adkins J, Vasanji A, et al. Distribution of CD133 reveals glioma stem cells self-renew through symmetric and asymmetric cell divisions. Cell Death Dis. 2011;2: e200.

247. Izumi H, Li Y, Yasunami M, Sato S, Mae T, Kaneko Y, et al. Asymmetric pericentrosomal CD133 endosomes induce the unequal autophagic activity during cytokinesis in CD133-positive human neuroblastoma cells. Stem Cells. 2022;40:371–84.

248. Hitomi M, Chumakova AP, Silver DJ, Knudsen AM, Pontius WD, Murphy S, et al. Asymmetric cell division promotes therapeutic resistance in glioblastoma stem cells. JCI Insight. 2021;6: e130510.

249. Kosodo Y, Röper K, Haubensak W, Marzesco AM, Corbeil D, Huttner WB. Asymmetric distribution of the apical plasma membrane during neurogenic divisions of mammalian neuroepithelial cells. EMBO J. 2004;23:2314–24.

250. Mizushima N, Levine B. Autophagy in mammalian development and differentiation. Nat Cell Biol. 2010;12:823–30.

251. Pampliega O, Orhon I, Patel B, Sridhar S, Díaz-Carretero A, Beau I, et al. Functional interaction between autophagy and ciliogenesis. Nature. 2013;502:194–200.

252. Orhon I, Dupont N, Pampliega O, Cuervo AM, Codogno P. Autophagy and regulation of cilia function and assembly. Cell Death Differ. 2015;22:389–97.

253. Cao M, Zhong Q. Cilia in autophagy and cancer. Cilia. 2015;5:4.

254. Morleo F. The autophagy-cilia axis: an intricate relationship. Cells. 2019;8:905.

255. Nunukova A, Neradil J, Skoda J, Jaros J, Hampl A, Sterba J, et al. Atypical nuclear localization of CD133 plasma membrane glycoprotein in rhabdomyosarcoma cell lines. Int J Mol Med. 2015;36:65–72.

256. Skoda J, Nunukova A, Loja T, Zambo I, Neradil J, Mudry P, et al. Cancer stem cell markers in pediatric sarcomas: Sox2 is associated with tumorigenicity in immunodeficient mice. Tumor Biol. 2016;37:9535–48.

257. Cantile M, Collina F, D'Aiuto M, Rinaldo M, Pirozzi G, Borsellino C, et al. Nuclear localization of cancer stem cell marker CD133 in triple-negative breast cancer: a case report. Tumori. 2013;99:e245-250.

258. Huang MJ, Zhu HJ, Feng J, Ni SS, Huang JF. High CD133 expression in the nucleus and cytoplasm predicts poor prognosis in non-small cell lung cancer. Dis Markers. 2015;2015: 986095.

259. Rappa G, Santos MF, Green TM, Karbanová J, Hassler J, Bai Y, et al. Nuclear transport of cancer extracellular vesicle-derived biomaterials through nuclear envelope invagination-associated late endosomes. Oncotarget. 2017;8:14443–61.

260. Lee YM, Yeo MK, Seong IO, Kim KH. Nuclear expression of CD133 is associated with good prognosis in patients with colorectal adenocarcinoma. Anticancer Res. 2018;38:4819–26.

261. Briscoe J, Thérond PP. The mechanisms of Hedgehog signalling and its roles in development and disease. Nat Rev Mol Cell Biol. 2013;14:416–29.

262. Tierney MT, Aydogdu T, Sala D, Malecova B, Gatto S, Puri PL, et al. STAT3 signaling controls satellite cell expansion and skeletal muscle repair. Nat Med. 2014;20:1182–6.

263. Bhattacharya S, Yin J, Yang C, Wang Y, Sims M, Pfeffer LM, et al. STAT3 suppresses the AMPKα/ULK1-dependent induction of autophagy in glioblastoma cells. J Cell Mol Med. 2022;26:3873–90.

264. Zheng H, Zhang Y, Chen Y, Guo P, Wang X, Yuan X, et al. Prominin-like, a homolog of mammalian CD133, suppresses di lp6 and TOR signaling to maintain body size and weight in Drosophila. FASEB J. 2019;33:2646–58.

265. Ryu TH, Yeom E, Subramanian M, Lee K-S, Yu K. Prominin-like regulates longevity and glucose metabolism via insulin signaling in drosophila. J Gerontol A Biol Sci Med Sci. 2018;74:1557–63.

266. Sepp KJ, Hong P, Lizarraga SB, Liu JS, Mejia LA, Walsh CA, et al. Identification of neural outgrowth genes using genome-wide RNAi. PLoS Genet. 2008;4: e1000111.

267. Yang C, Yang Y, Gupta N, Liu X, He A, Liu L, et al. Pentaspan membrane glycoprotein, prominin-1, is involved in glucose metabolism and cytoskeleton alteration. Biochemistry (Mosc). 2007;72:854–62.

268. Griguer CE, Oliva CR, Gobin E, Marcorelles P, Benos DJ, Lancaster JR, et al. CD133 is a marker of bioenergetic stress in human glioma. PLoS ONE. 2008;3: e3655.

269. Zobalova R, Prokopova K, Stantic M, Stapelberg M, Dong LF, Ralph SJ, et al. The potential role of CD133 in immune surveillance and apoptosis: a mitochondrial connection? Antioxid Redox Signal. 2011;15:2989–3002.

270. Raposo G, Nijman HW, Stoorvogel W, Liejendekker R, Harding CV, Melief CJ, et al. B lymphocytes secrete antigen-presenting vesicles. J Exp Med. 1996;183:1161–72.

271. van Niel G, D'Angelo G, Raposo G. Shedding light on the cell biology of extracellular vesicles. Nat Rev Mol Cell Biol. 2018;19:213–28.

272. Arena GO, Forte S, Abdouh M, Vanier C, Corbeil D, Lorico A. Horizontal transfer of malignant traits and the involvement of extracellular vesicles in metastasis. Cells. 2023;12:1566.

273. Yáñez-Mó M, Siljander PR, Andreu Z, Zavec AB, Borràs FE, Buzas EI, et al. Biological properties of extracellular vesicles and their physiological functions. J Extracell Vesicles. 2015;4:27066.

274. Raposo G, Stoorvogel W. Extracellular vesicles: exosomes, microvesicles, and friends. J Cell Biol. 2013;200:373–83.
275. Corbeil D, Santos MF, Karbanová J, Kurth T, Rappa G, Lorico A. Uptake and fate of extracellular membrane vesicles: nucleoplasmic reticulum-associated late endosomes as a new gate to intercellular communication. Cells. 2020;9:1931.
276. Rilla K. Diverse plasma membrane protrusions act as platforms for extracellular vesicle shedding. J Extracell Vesicles. 2021;10: e12148.
277. Gustafson CM, Gammill LS. Extracellular vesicles and membrane protrusions in developmental signaling. J Dev Biol. 2022;10:39.
278. Marzesco AM, Wilsch-Bräuninger M, Dubreuil V, Janich P, Langenfeld K, Thiele C, et al. Release of extracellular membrane vesicles from microvilli of epithelial cells is enhanced by depleting membrane cholesterol. FEBS Lett. 2009;583:897–902.
279. Corbeil D, Marzesco AM, Fargeas CA, Huttner WB. Prominin-1: a distinct cholesterol-binding membrane protein and the organisation of the apical plasma membrane of epithelial cells. Subcell Biochem. 2010;51:399–423.
280. de Poret A, Dibsy R, Merida P, Trausch A, Inamdar K, Muriaux D. Extracellular vesicles containing the I-BAR protein IRSp53 are released from the cell plasma membrane in an Arp2/3 dependent manner. Biol Cell. 2022;114:259–75.
281. Nager AR, Goldstein JS, Herranz-Pérez V, Portran D, Ye F, Garcia-Verdugo JM, et al. An actin network dispatches ciliary GPCRs into extracellular vesicles to modulate signaling. Cell. 2017;168:252-263.e214.
282. Ettinger AW, Wilsch-Bräuninger M, Marzesco A-M, Bickle M, Lohmann A, Maliga Z, et al. Proliferating versus differentiating stem and cancer cells exhibit distinct midbody-release behaviour. Nat Commun. 2011;2:503.
283. McConnell RE, Higginbotham JN, Shifrin DA Jr, Tabb DL, Coffey RJ, Tyska MJ. The enterocyte microvillus is a vesicle-generating organelle. J Cell Biol. 2009;185:1285–98.
284. Muralidharan-Chari V, Clancy J, Plou C, Romao M, Chavrier P, Raposo G, et al. ARF6-regulated shedding of tumor cell-derived plasma membrane microvesicles. Curr Biol. 2009;19:1875–85.
285. Hurbain I, Macé A-S, Romao M, Prince E, Sengmanivong L, Ruel L, et al. Microvilli-derived extracellular vesicles carry Hedgehog morphogenic signals for Drosophila wing imaginal disc development. Curr Biol. 2022;32:361-373.e366.
286. Shenoy GN, Loyall J, Berenson CS, Kelleher RJ, Iyer V, Balu-Iyer SV, et al. Sialic acid-dependent inhibition of T cells by exosomal ganglioside GD3 in ovarian tumor microenvironments. J Immunol. 2018;201:3750–8.
287. Marzesco AM. Prominin-1-containing membrane vesicles: origins, formation, and utility. Adv Exp Med Biol. 2013;777:41–54.
288. Rappa G, Mercapide J, Anzanello F, Pope RM, Lorico A. Biochemical and biological characterization of exosomes containing prominin-1/CD133. Mol Cancer. 2013;12:62.
289. Rappa G, Mercapide J, Anzanello F, Le TT, Johlfs MG, Fiscus RR, et al. Wnt interaction and extracellular release of prominin-1/CD133 in human malignant melanoma cells. Exp Cell Res. 2013;319:810–9.
290. Lucchetti D, Calapa F, Palmieri V, Fanali C, Carbone F, Papa A, et al. Differentiation affects the release of exosomes from colon cancer cells and their ability to modulate the behavior of recipient cells. Am J Pathol. 2017;187:1633–47.
291. Kang M, Kim S, Ko J. Roles of CD133 in microvesicle formation and oncoprotein trafficking in colon cancer. FASEB J. 2019;33:4248–60.
292. Moon B-S, Jeong W-J, Park J, Kim TI, Min DS, Choi K-Y. Role of oncogenic K-Ras in cancer stem cell activation by aberrant Wnt/β-catenin signaling. J Natl Cancer Inst. 2014;106:djt373.
293. Deng Y, Wang L, Tan S, Kim GP, Dou R, Chen D, et al. KRAS as a predictor of poor prognosis and benefit from post-operative FOLFOX chemotherapy in patients with stage II and III colorectal cancer. Mol Oncol. 2015;9:1341–7.
294. Huttner HB, Janich P, Kohrmann M, Jászai J, Siebzehnrubl F, Blumcke I, et al. The stem cell marker prominin-1/CD133 on membrane particles in human cerebrospinal fluid offers novel approaches for studying central nervous system disease. Stem Cells. 2008;26:698–705.
295. Huttner HB, Corbeil D, Thirmeyer C, Coras R, Köhrmann M, Mauer C, et al. Increased membrane shedding—indicated by an elevation of CD133-enriched membrane particles—into the CSF in partial epilepsy. Epilepsy Res. 2012;99:101–6.
296. Bobinger T, May L, Lücking H, Kloska SP, Burkardt P, Spitzer P, et al. CD133-positive membrane particles in cerebrospinal fluid of patients with inflammatory and degenerative neurological diseases. Front Cell Neurosci. 2017;11:77.
297. Bobinger T, Roeder SS, Spruegel MI, Froehlich K, Beuscher VD, Hoelter P, et al. Variation of membrane particle–bound CD133 in cerebrospinal fluid of patients with subarachnoid and intracerebral hemorrhage. J Neurosurg. 2020;134:1–8.
298. Dimuccio V, Ranghino A, Praticò Barbato L, Fop F, Biancone L, Camussi G, et al. Urinary CD133+ extracellular vesicles are decreased in kidney transplanted patients with slow graft function and vascular damage. PLoS ONE. 2014;9: e104490.
299. Dimuccio V, Peruzzi L, Brizzi MF, Cocchi E, Fop F, Boido A, et al. Acute and chronic glomerular damage is associated with reduced CD133 expression in urinary extracellular vesicles. Am J Physiol Renal Physiol. 2020;318:F486–95.
300. Burrello J, Monticone S, Burrello A, Bolis S, Cristalli CP, Comai G, et al. Identification of a serum and urine extracellular vesicle signature predicting renal outcome after kidney transplant. Nephrol Dial Transplant. 2023;38:764–77.
301. Ranghino A, Dimuccio V, Papadimitriou E, Bussolati B. Extracellular vesicles in the urine: markers and mediators of tissue damage and regeneration. Clin Kidney J. 2015;8:23–30.
302. Rustom A, Saffrich R, Markovic I, Walther P, Gerdes HH. Nanotubular highways for intercellular organelle transport. Science. 2004;303:1007–10.
303. Cordero Cervantes D, Zurzolo C. Peering into tunneling nanotubes-The path forward. EMBO J. 2021;40: e105789.
304. Kolba MD, Dudka W, Zaręba-Kozioł M, Kominek A, Ronchi P, Turos L, et al. Tunneling nanotube-mediated intercellular vesicle and protein transfer in the stroma-provided imatinib resistance in chronic myeloid leukemia cells. Cell Death Dis. 2019;10:817.
305. Wang X, Gerdes HH. Transfer of mitochondria via tunneling nanotubes rescues apoptotic PC12 cells. Cell Death Differ. 2015;22:1181–91.

306. Wang X, Veruki ML, Bukoreshtliev NV, Hartveit E, Gerdes HH. Animal cells connected by nanotubes can be electrically coupled through interposed gap-junction channels. Proc Natl Acad Sci U S A. 2010;107:17194–9.

307. Wang X, Bukoreshtliev NV, Gerdes HH. Developing neurons form transient nanotubes facilitating electrical coupling and calcium signaling with distant astrocytes. PLoS ONE. 2012;7: e47429.

308. Reichert D, Scheinpflug J, Karbanová J, Freund D, Bornhäuser M, Corbeil D. Tunneling nanotubes mediate the transfer of stem cell marker CD133 between hematopoietic progenitor cells. Exp Hematol. 2016;44:1092-1112. e1092.

309. Rappa G, Fargeas CA, Le TT, Corbeil D, Lorico A. Letter to the editor: an intriguing relationship between lipid droplets, cholesterol-binding protein CD133 and Wnt/β-catenin signaling pathway in carcinogenesis. Stem Cells. 2015;33:1366–70.

310. Jang JW, Song Y, Kim SH, Kim J, Seo HR. Potential mechanisms of CD133 in cancer stem cells. Life Sci. 2017;184:25–9.

311. Etienne-Manneville S, Hall A. Rho GTPases in cell biology. Nature. 2002;420:629–35.

312. Riento K, Ridley AJ. Rocks: multifunctional kinases in cell behaviour. Nat Rev Mol Cell Biol. 2003;4:446–56.

313. Amano M, Nakayama M, Kaibuchi K. Rho-kinase/ROCK: a key regulator of the cytoskeleton and cell polarity. Cytoskeleton (Hoboken). 2010;67:545–54.

314. Guan G, Cannon RD, Coates DE, Mei L. Effect of the Rho-kinase/ROCK signaling pathway on cytoskeleton components. Genes (Basel). 2023;14:272.

315. Li H, Papadopoulos V. Peripheral-type benzodiazepine receptor function in cholesterol transport. Identification of a putative cholesterol recognition/interaction amino acid sequence and consensus pattern. Endocrinology. 1998;139:4991–7.

316. Fantini J, Barrantes FJ. How cholesterol interacts with membrane proteins: an exploration of cholesterol-binding sites including CRAC, CARC, and tilted domains. Front Physiol. 2013;4:31.

317. Fonseca A-V, Freund D, Bornhäuser M, Corbeil D. Polarization and migration of hematopoietic stem and progenitor cells rely on the RhoA/ROCK I pathway and an active reorganization of the microtubule network. J Biol Chem. 2010;285:31661–71.

318. Fonseca A-V, Corbeil D. The hematopoietic stem cell polarization and migration. Commun Integr Biol. 2011;4:201–4.

319. Suzuki M. The Drosophila tweety family: molecular candidates for large-conductance Ca2+ activated Cl- channels. Exp Physiol. 2006;91:141–7.

320. Sukalskaia A, Straub MS, Deneka D, Sawicka M, Dutzler R. Cryo-EM structures of the TTYH family reveal a novel architecture for lipid interactions. Nat Commun. 2021;12:4893.

321. Li B, Hoel CM, Brohawn SG. Structures of tweety homolog proteins TTYH2 and TTYH3 reveal a Ca2+-dependent switch from intra- to intermembrane dimerization. Nat Commun. 2021;12:6913.

322. Melvin E, Kalaninová Z, Shlush E, Man P, Giladi M, Haitin Y. TTYH family members form tetrameric complexes at the cell membrane. Commun Biol. 2022;5:886.

323. Shimozato O, Waraya M, Nakashima K, Souda H, Takiguchi N, Yamamoto H, et al. Receptor-type protein tyrosine phosphatase κ directly dephosphorylates CD133 and regulates downstream AKT activation. Oncogene. 2015;34:1949–60.

324. Matsushita M, Mori Y, Uchiumi K, Ogata T, Nakamura M, Yoda H, et al. PTPRK suppresses progression and chemoresistance of colon cancer cells via direct inhibition of pro-oncogenic CD133. FEBS Open Bio. 2019;9:935–46.

325. Tonks NK. Protein tyrosine phosphatases: from genes, to function, to disease. Nat Rev Mol Cell Biol. 2006;7:833–46.

326. Xu Y, Tan L-J, Grachtchouk V, Voorhees JJ, Fisher GJ. Receptor-type protein-tyrosine phosphatase-κ regulates epidermal growth factor receptor function. J Biol Chem. 2005;280:42694–700.

327. Liang Z, Wu B, Ji Z, Liu W, Shi D, Chen X, et al. The binding of LDN193189 to CD133 C-terminus suppresses the tumorigenesis and immune escape of liver tumor-initiating cells. Cancer Lett. 2021;513:90–100.

328. Takenobu H, Shimozato O, Nakamura T, Ochiai H, Yamaguchi Y, Ohira M, et al. CD133 suppresses neuroblastoma cell differentiation via signal pathway modification. Oncogene. 2011;30:97–105.

329. Fruman DA, Chiu H, Hopkins BD, Bagrodia S, Cantley LC, Abraham RT. The PI3K pathway in human disease. Cell. 2017;170:605–35.

330. Engelman JA, Luo J, Cantley LC. The evolution of phosphatidylinositol 3-kinases as regulators of growth and metabolism. Nat Rev Genet. 2006;7:606–19.

331. Vanhaesebroeck B, Guillermet-Guibert J, Graupera M, Bilanges B. The emerging mechanisms of isoform-specific PI3K signalling. Nat Rev Mol Cell Biol. 2010;11:329–41.

332. Hambardzumyan D, Squatrito M, Carbajal E, Holland EC. Glioma formation, cancer stem cells, and akt signaling. Stem Cell Rev. 2008;4:203–10.

333. Manning BD, Toker A. AKT/PKB signaling: navigating the network. Cell. 2017;169:381–405.

334. Vivanco I, Sawyers CL. The phosphatidylinositol 3-Kinase–AKT pathway in human cancer. Nat Rev Cancer. 2002;2:489–501.

335. Getz G, Gabriel SB, Cibulskis K, Lander E, Sivachenko A, Sougnez C, et al. Integrated genomic characterization of endometrial carcinoma. Nature. 2013;497:67–73.

336. Bass AJ, Thorsson V, Shmulevich I, Reynolds SM, Miller M, Bernard B, et al. Comprehensive molecular characterization of gastric adenocarcinoma. Nature. 2014;513:202–9.

337. Gao D, Vela I, Sboner A, Iaquinta PJ, Karthaus WR, Gopalan A, et al. Organoid cultures derived from patients with advanced prostate cancer. Cell. 2014;159:176–87.

338. Lawrence MS, Sougnez C, Lichtenstein L, Cibulskisl K, Lander E, Gabriel SB, et al. Comprehensive genomic characterization of head and neck squamous cell carcinomas. Nature. 2015;517:576–82.

339. Liu Y, Easton J, Shao Y, Maciaszek J, Wang ZM, Wilkinson MR, et al. The genomic landscape of pediatric and young adult T-lineage acute lymphoblastic leukemia. Nat Genet. 2017;49:1211–8.

340. Manoranjan B, Chokshi C, Venugopal C, Subapanditha M, Savage N, Tatari N, et al. A CD133-AKT-Wnt signaling axis drives glioblastoma brain tumor-initiating cells. Oncogene. 2020;39:1590–9.

341. Cross DA, Alessi DR, Cohen P, Andjelkovich M, Hemmings BA. Inhibition of glycogen synthase kinase-3 by insulin mediated by protein kinase B. Nature. 1995;378:785–9.

342. Shibahara I, Sonoda Y, Saito R, Kanamori M, Yamashita Y, Kumabe T, et al. The expression status of CD133 is associated with the pattern and timing of primary glioblastoma recurrence. Neuro Oncol. 2013;15:1151–9.

343. Wang Z, Liu W, Wang C, Li Y, Ai Z. Acetylcholine promotes the self-renewal and immune escape of CD133+ thyroid cancer cells through activation of CD133-Akt pathway. Cancer Lett. 2020;471:116–24.

344. Jamal SME, Alamodi A, Wahl RU, Grada Z, Shareef MA, Hassan S-Y, et al. Melanoma stem cell maintenance and chemo-resistance are mediated by CD133 signal to PI3K-dependent pathways. Oncogene. 2020;39:5468–78.

345. Brabletz T, Kalluri R, Nieto MA, Weinberg RA. EMT in cancer. Nat Rev Cancer. 2018;18:128–34.

346. Olea-Flores M, Zuñiga-Eulogio M, Tacuba-Saavedra A, Bueno-Salgado M, Sánchez-Carvajal A, Vargas-Santiago Y, et al. Leptin promotes expression of EMT-related transcription factors and invasion in a Src and FAK-dependent pathway in MCF10A mammary epithelial cells. Cells. 2019;8:1133.

347. Tian Q, Yuan P, Quan C, Li M, Xiao J, Zhang L, et al. Phosphorylation of BCKDK of BCAA catabolism at Y246 by Src promotes metastasis of colorectal cancer. Oncogene. 2020;39:3980–96.

348. Patel A, Sabbineni H, Clarke A, Somanath PR. Novel roles of Src in cancer cell epithelial-to-mesenchymal transition, vascular permeability, microinvasion and metastasis. Life Sci. 2016;157:52–61.

349. Tai Y-L, Chen L-C, Shen T-L. Emerging roles of focal adhesion kinase in cancer. Biomed Res Int. 2015;2015: 690690.

350. Lee BY, Timpson P, Horvath LG, Daly RJ. FAK signaling in human cancer as a target for therapeutics. Pharmacol Ther. 2015;146:132–49.

351. Tai Y-L, Chu P-Y, Lai IR, Wang M-Y, Tseng H-Y, Guan J-L, et al. An EGFR/Src-dependent β4 integrin/FAK complex contributes to malignancy of breast cancer. Sci Rep. 2015;5:16408.

352. Liu C, Li Y, Xing Y, Cao B, Yang F, Yang T, et al. The interaction between cancer stem cell marker CD133 and Src protein promotes focal adhesion kinase (FAK) phosphorylation and cell migration. J Biol Chem. 2016;291:15540–50.

353. Nusse R, Brown A, Papkoff J, Scambler P, Shackleford G, McMahon A, et al. A new nomenclature for int-1 and related genes: the Wnt gene family. Cell. 1991;64:231.

354. Logan CY, Nusse R. The Wnt signaling pathway in development and disease. Annu Rev Cell Dev Biol. 2004;20:781–810.

355. Nusse R, Clevers H. Wnt/β-catenin signaling, disease, and emerging therapeutic modalities. Cell. 2017;169:985–99.

356. Klaus A, Birchmeier W. Wnt signalling and its impact on development and cancer. Nat Rev Cancer. 2008;8:387–98.

357. Sawa H. Control of cell polarity and asymmetric division in *C. elegans*. Curr Top Dev Biol. 2012;101:55–76.

358. Huelsken J, Vogel R, Erdmann B, Cotsarelis G, Birchmeier W. beta-Catenin controls hair follicle morphogenesis and stem cell differentiation in the skin. Cell. 2001;105:533–45.

359. Gay DL, Yang CC, Plikus MV, Ito M, Rivera C, Treffeisen E, et al. CD133 expression correlates with membrane beta-catenin and E-cadherin loss from human hair follicle placodes during morphogenesis. J Invest Dermatol. 2015;135:45–55.

360. Brossa A, Papadimitriou E, Collino F, Incarnato D, Oliviero S, Camussi G, et al. Role of CD133 molecule in Wnt response and renal repair. Stem Cells Transl Med. 2018;7:283–94.

361. Tremblay JR, Lopez K, Ku HT. A GLIS3–CD133–WNT-signaling axis regulates the self-renewal of adult murine pancreatic progenitor-like cells in colonies and organoids. J Biol Chem. 2019;294:16634–49.

362. Mak AB, Nixon AML, Kittanakom S, Stewart JM, Chen GI, Curak J, et al. Regulation of CD133 by HDAC6 promotes β-catenin signaling to suppress cancer cell differentiation. Cell Rep. 2012;2:951–63.

363. Rappa G, Fodstad O, Lorico A. The stem cell-associated antigen CD133 (Prominin-1) is a molecular therapeutic target for metastatic melanoma. Stem Cells. 2008;26:3008–17.

364. Hubbert C, Guardiola A, Shao R, Kawaguchi Y, Ito A, Nixon A, et al. HDAC6 is a microtubule-associated deacetylase. Nature. 2002;417:455–8.

365. Li Y, Zhang X, Polakiewicz RD, Yao TP, Comb MJ. HDAC6 is required for epidermal growth factor-induced beta-catenin nuclear localization. J Biol Chem. 2008;283:12686–90.

366. Miyake Y, Keusch JJ, Wang LL, Saito M, Hess D, Wang XN, et al. Structural insights into HDAC6 tubulin deacetylation and its selective inhibition. Nat Chem Biol. 2016;12:748–54.

367. Kawaguchi Y, Kovacs JJ, McLaurin A, Vance JM, Ito A, Yao TP. The deacetylase HDAC6 regulates aggresome formation and cell viability in response to misfolded protein stress. Cell. 2003;115:727–38.

368. Haggarty SJ, Koeller KM, Wong JC, Grozinger CM, Schreiber SL. Domain-selective small-molecule inhibitor of histone deacetylase 6 (HDAC6)-mediated tubulin deacetylation. Proc Natl Acad Sci U S A. 2003;100:4389–94.

369. Deribe YL, Wild P, Chandrashaker A, Curak J, Schmidt MHH, Kalaidzidis Y, et al. Regulation of epidermal growth factor receptor trafficking by lysine deacetylase HDAC6. Sci Signal. 2009;2:ra84.

370. David CJ, Massagué J. Contextual determinants of TGFβ action in development, immunity and cancer. Nat Rev Mol Cell Biol. 2018;19:419–35.

371. Lee J, Shin JE, Lee B, Kim H, Jeon Y, Ahn SH, et al. The stem cell marker Prom1 promotes axon regeneration by down-regulating cholesterol synthesis via Smad signaling. Proc Natl Acad Sci U S A. 2020;117:15955–66.

372. Lee H, Yu D-M, Bahn M-S, Kwon Y-J, Um MJ, Yoon SY, et al. Hepatocyte-specific Prominin-1 protects against liver injury-induced fibrosis by stabilizing SMAD7. Exp Mol Med. 2022;54:1277–89.

373. Nakao A, Afrakhte M, Morén A, Nakayama T, Christian JL, Heuchel R, et al. Identification of Smad7, a TGFbeta-inducible antagonist of TGF-beta signalling. Nature. 1997;389:631–5.

374. Hayashi H, Abdollah S, Qiu Y, Cai J, Xu YY, Grinnell BW, et al. The MAD-related protein Smad7 associates with the TGFbeta receptor and functions as an antagonist of TGFbeta signaling. Cell. 1997;89:1165–73.

375. Fenlon M, Short C, Xu J, Malkoff N, Mahdi E, Hough M, et al. Prominin-1-expressing hepatic progenitor cells induce fibrogenesis in murine cholestatic liver injury. Physiol Rep. 2020;8: e14508.

376. Schmidt-Arras D, Rose-John S. IL-6 pathway in the liver: from physiopathology to therapy. J Hepatol. 2016;64:1403–15.

377. Bahn M-S, Yu D-M, Lee M, Jo S-J, Lee J-W, Kim H-C, et al. Central role of Prominin-1 in lipid rafts during liver regeneration. Nat Commun. 2022;13:6219.

378. Deming PB, Campbell SL, Stone JB, Rivard RL, Mercier AL, Howe AK. Anchoring of protein kinase A by ERM (Ezrin-Radixin-Moesin) proteins is required for proper netrin signaling through DCC (deleted in colorectal cancer). J Biol Chem. 2015;290:5783–96.
379. Dema A, Perets E, Schulz MS, Deák VA, Klussmann E. Pharmacological targeting of AKAP-directed compartmentalized cAMP signalling. Cell Signal. 2015;27:2474–87.
380. Lavoie H, Gagnon J, Therrien M. ERK signalling: a master regulator of cell behaviour, life and fate. Nat Rev Mol Cell Biol. 2020;21:607–32.
381. Ding Q, Miyazaki Y, Tsukasa K, Matsubara S, Yoshimitsu M, Takao S. CD133 facilitates epithelial-mesenchymal transition through interaction with the ERK pathway in pancreatic cancer metastasis. Mol Cancer. 2014;13:15.
382. Xin B, He X, Wang J, Cai J, Wei W, Zhang T, et al. Nerve growth factor regulates CD133 function to promote tumor cell migration and invasion via activating ERK1/2 signaling in pancreatic cancer. Pancreatology. 2016;16:1005–14.
383. Zhang L, Zhang L, Li H, Ge C, Zhao F, Tian H, et al. CXCL3 contributes to CD133+ CSCs maintenance and forms a positive feedback regulation loop with CD133 in HCC via Erk1/2 phosphorylation. Sci Rep. 2016;6:27426.
384. Vora P, Venugopal C, Salim SK, Tatari N, Bakhshinyan D, Singh M, et al. The rational development of CD133-targeting immunotherapies for glioblastoma. Cell Stem Cell. 2020;26:832-844.e836.

Publisher's Note

APPENDIX 2

Borankova K, Krchniakova M, Leck LYW, Kubistova A, Neradil J, Jansson PJ, Hogarty MD, **Skoda J***. Mitoribosomal synthetic lethality overcomes multidrug resistance in MYC-driven neuroblastoma. *Cell Death & Disease*. 2023;14:747. (JCR 2023, IF = 8.1; Q1 - Cell Biology)

ARTICLE   OPEN

Check for updates

Mitoribosomal synthetic lethality overcomes multidrug resistance in MYC-driven neuroblastoma

Karolina Borankova [1,2], Maria Krchniakova[1,2], Lionel Y. W. Leck[3,4], Adela Kubistova[1], Jakub Neradil [1,2], Patric J. Jansson [3,4], Michael D. Hogarty[5,6] and Jan Skoda [1,2 ✉]

Mitochondria are central for cancer responses to therapy-induced stress signals. Refractory tumors often show attenuated sensitivity to apoptotic signaling, yet clinically relevant molecular actors to target mitochondria-mediated resistance remain elusive. Here, we show that MYC-driven neuroblastoma cells rely on intact mitochondrial ribosome (mitoribosome) processivity and undergo cell death following pharmacological inhibition of mitochondrial translation, regardless of their multidrug/mitochondrial resistance and stem-like phenotypes. Mechanistically, inhibiting mitoribosomes induced the mitochondrial stress-activated integrated stress response (ISR), leading to downregulation of c-MYC/N-MYC proteins prior to neuroblastoma cell death, which could be both rescued by the ISR inhibitor ISRIB. The ISR blocks global protein synthesis and shifted the c-MYC/N-MYC turnover toward proteasomal degradation. Comparing models of various neuroectodermal tumors and normal fibroblasts revealed overexpression of MYC proteins phosphorylated at the degradation-promoting site T58 as a factor that predetermines vulnerability of MYC-driven neuroblastoma to mitoribosome inhibition. Reducing N-MYC levels in a neuroblastoma model with tunable *MYCN* expression mitigated cell death induction upon inhibition of mitochondrial translation and functionally validated the propensity of neuroblastoma cells for MYC-dependent cell death in response to the mitochondrial ISR. Notably, neuroblastoma cells failed to develop significant resistance to the mitoribosomal inhibitor doxycycline over a long-term repeated (pulsed) selection. Collectively, we identify mitochondrial translation machinery as a novel synthetic lethality target for multidrug-resistant MYC-driven tumors.

INTRODUCTION

Acquisition of aggressive dedifferentiated phenotype and therapy-induced multidrug resistance is the major cause of cancer therapy failure. Despite efforts, therapies that would overcome resistance mechanisms to kill all cancer cells including tumor-repopulating cancer stem-like cells remain elusive. Mitochondria have recently emerged as therapeutic targets in refractory cancers [1]. Besides serving as metabolic hubs, mitochondria integrate crucial roles in stemness maintenance [1], drug resistance [2], and cell death regulation [3]. Inhibiting mitochondrial processes has shown promising results in the most common tumor types, sensitizing resistant cancer cells to conventional chemotherapeutics [1]. However, our understanding of mitochondrial vulnerabilities in pediatric malignancies is limited.

Neuroblastoma is the most common extracranial childhood tumor. High-risk neuroblastomas are frequently driven by either N-MYC or c-MYC upregulation and have an extremely poor prognosis with 5-year overall survival of ~50% [4, 5]. Among other functions, MYC oncogenic transcription factors induce expression

of genes involved in mitochondrial biogenesis [6–9] and mitochondria-dependent metabolism [10–12]. Importantly, we have recently demonstrated that mitochondria from therapy-resistant tumor cells often show attenuated apoptotic signaling, which largely contributes to neuroblastoma multidrug resistance [13]. Here, we therefore investigated potential mitochondrial dependencies, testing mitochondria as direct targets to overcome multidrug resistance in neuroblastoma. For this purpose, we took advantage of diverse mitochondrial inhibitors repurposed to target drug-resistant and/or stem-like cells in other cancers [14–18].

While mitochondria carry their own genome (mtDNA) and distinct transcription and translation machinery, their function heavily relies on nuclear-encoded mitochondrial proteins. Hence, mitochondrial perturbations must be efficiently relayed to cytosol and nucleus to orchestrate mitochondrial homeostasis, including proper stoichiometry of mitochondrial proteins [19]. Mitochondrial components of this retrograde signaling were only recently discovered, with inner mitochondrial membrane metalloprotease OMA1 identified as the major upstream regulator [20, 21]. We

[1]Department of Experimental Biology, Faculty of Science, Masaryk University, 62500 Brno, Czech Republic. [2]International Clinical Research Center, St. Anne's University Hospital, 65691 Brno, Czech Republic. [3]Cancer Drug Resistance & Stem Cell Program, School of Medical Science, Faculty of Medicine and Health, The University of Sydney, Camperdown, NSW 2006, Australia. [4]Bill Walsh Translational Cancer Research Laboratory, Kolling Institute, Faculty of Medicine and Health, The University of Sydney, St. Leonards, NSW 2065, Australia. [5]Division of Oncology and Center for Childhood Cancer Research, The Children's Hospital of Philadelphia, Philadelphia, PA, USA. [6]Department of Pediatrics, Perelman School of Medicine, University of Pennsylvania, Philadelphia, PA, USA. ✉email: jan.skoda@sci.muni.cz
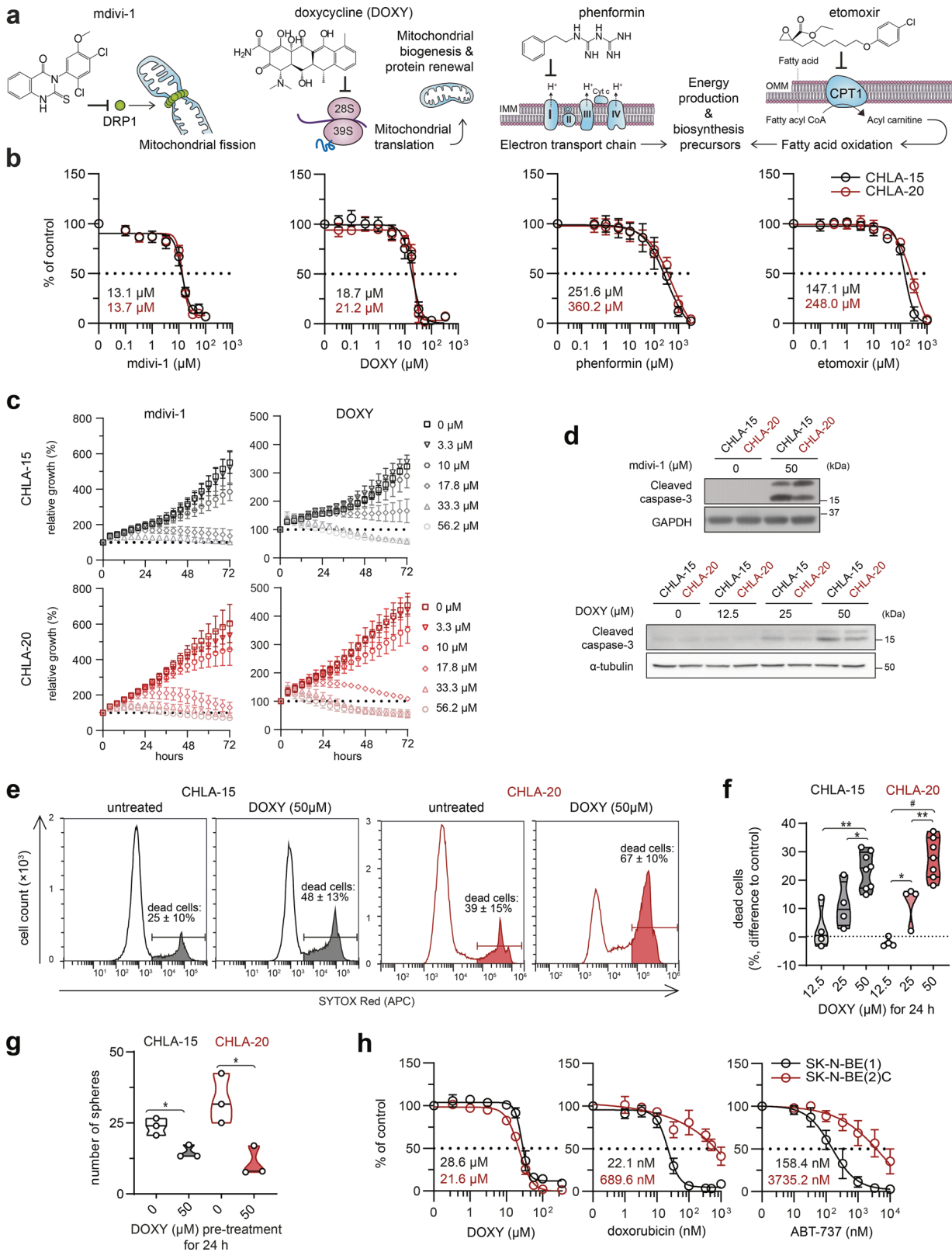Edited by Professor Stephen Tait
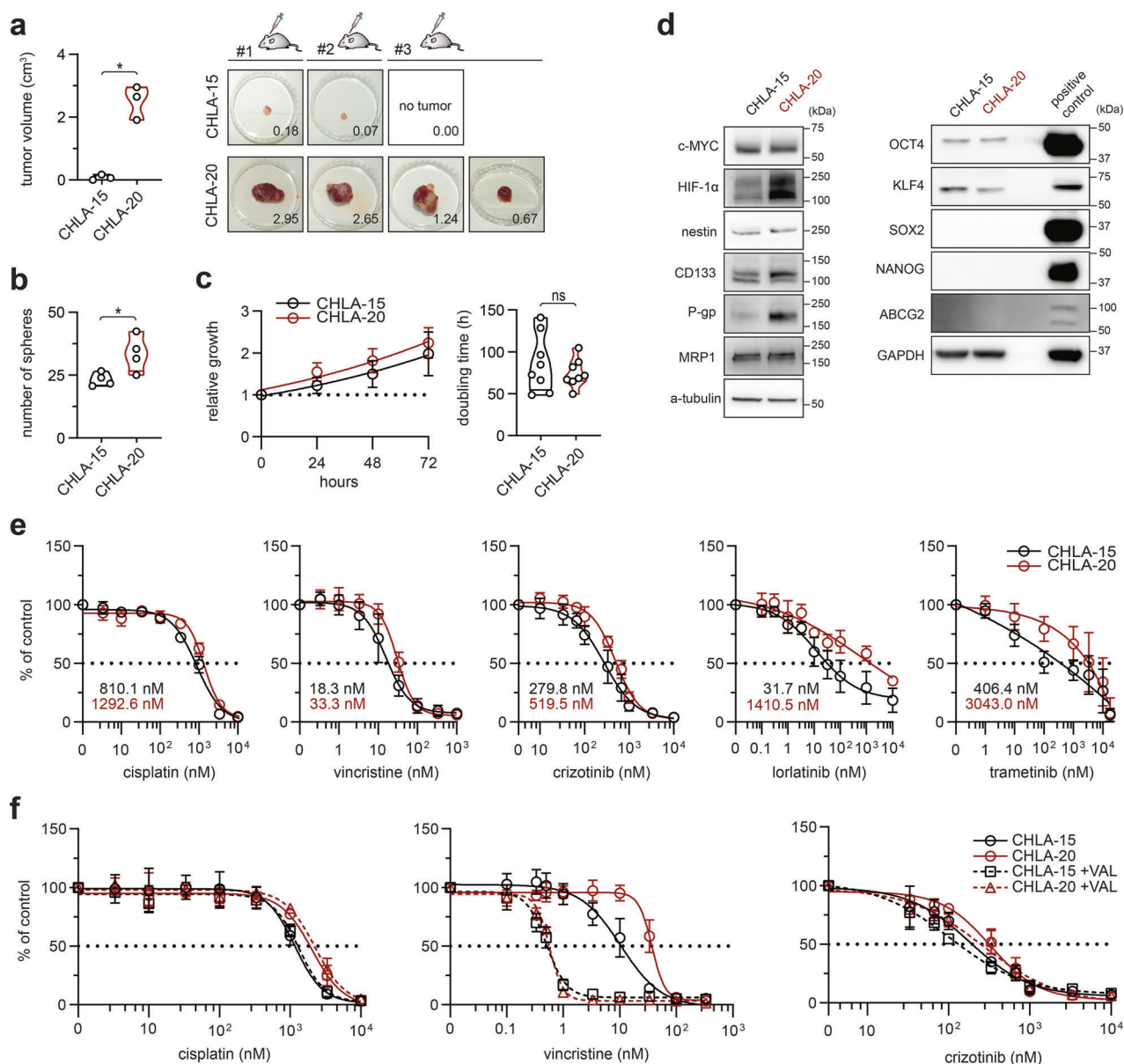
Fig. 1 Therapy-naive CHLA-15 and post-therapy CHLA-20 near-isogenic cell lines provide a useful model of therapy-induced drug resistance and cancer stemness in neuroblastoma. a Mean volume of tumors per mice (left panel) and individual xenograft tumors (right panel) formed by CHLA-15 and CHLA-20 cells respectively after 29 days of injection in NSG mice. Right panel, numbers indicate the volume (cm³) of individual tumors. Also note the difference in the absolute tumor-forming efficiency (CHLA-15, 2/3 mice vs. CHLA-20, 3/3 mice). Left panel, data are presented as mean ± SD, biological $n = 3$ mice per group. **b** CHLA-20 are endowed with increased neurosphere formation capacity compared with CHLA-15, biological $n = 4$, technical $n = 3$. **c** MTT cell viability assay analysis showed no significant difference in growth rate (left panel; data are mean ± SD) or calculated doubling times (right panel) of the cell line pair, biological $n = 8$, technical $n \geq 4$. **d** Western blot analysis of stemness transcription factors and CSC-related markers. Blots are representative of at least three experiments. Densitometric analysis is provided in Fig. S1. **e** Sensitivity to diverse chemotherapeutics tested by MTT assay after 72 h of treatment (calculated IC$_{50}$ values are indicated). Data are presented as mean ± SD, biological $n = 4$, technical $n = 3$. **f** In vitro viability curves after 72 h exposure to drugs alone or with 0.5 μM of P-gp inhibitor valspodar (VAL). MTT data presented as mean ± SD, biological $n = 3$, technical $n = 3$. Statistical significance was determined by unpaired two-tailed Student's t-test (**a–c**), *$p < 0.05$, ns not significant.

now provide insights into how this conserved mitochondrial stress-induced signaling might be exploited in neuroblastoma treatment. We demonstrate that disruption of mitochondrial proteostasis by mitoribosome inhibitors activates integrated stress response (ISR), in part via OMA1, which leads to c-MYC/N-MYC downregulation and cell death preferentially in neuroblastoma cells that rely on elevated MYC proteins. Our results reveal a novel mechanism of synthetic lethality that offers a promising therapeutic strategy to treat otherwise refractory MYC-driven tumors.

RESULTS

Mitochondria-targeting inhibitors overcome emergent multidrug resistance in post-therapy neuroblastoma cells

To establish a suitable model for our study, we first characterized a pair of *MYC*-amplified therapy-naive CHLA-15 and drug-resistant CHLA-20 neuroblastoma cell lines derived from tumors of the same patient at diagnosis and at relapse after multimodal therapy, respectively [22]. Functionally, these cell lines differed in their stem cell-like characteristics, with CHLA-20 cells showing a markedly enhanced capacity to initiate tumors in NSG mice (Fig. 1a) and form

a mdivi-1 · doxycycline (DOXY) · phenformin · etomoxir

b Dose-response curves: mdivi-1 (13.1 µM / 13.7 µM), DOXY (18.7 µM / 21.2 µM), phenformin (251.6 µM / 360.2 µM), etomoxir (147.1 µM / 248.0 µM); CHLA-15, CHLA-20

c Relative growth curves for mdivi-1 and DOXY in CHLA-15 and CHLA-20

d Western blots: Cleaved caspase-3, GAPDH, α-tubulin

e Flow cytometry SYTOX Red (APC): CHLA-15 untreated (dead cells: 25 ± 10%), DOXY (50µM) (48 ± 13%); CHLA-20 untreated (39 ± 15%), DOXY (50µM) (67 ± 10%)

f dead cells (%, difference to control) vs DOXY (µM) for 24 h

g number of spheres vs DOXY (µM) pre-treatment for 24 h

h Dose-response: DOXY (28.6 µM / 21.6 µM), doxorubicin (22.1 nM / 689.6 nM), ABT-737 (158.4 nM / 3735.2 nM); SK-N-BE(1), SK-N-BE(2)C

neurospheres in vitro (Fig. 1b) while maintaining a similar growth rate (Fig. 1c). Pointing to a complex fine-tuning of stem-like traits [23, 24], both cell lines expressed similar levels of the c-MYC oncoprotein and other common stemness-associated markers, except for the upregulation of HIF-1α and OCT4 in CHLA-20 (Figs. 1d, S1a).

Previously, CHLA-20 cells were reported more resistant to diverse chemotherapeutics than CHLA-15 [13, 22]. Validating this phenotype in our experimental settings, CHLA-20 cells exhibited broad resistance (1.6-fold to 44.5-fold difference vs. CHLA-15) to both DNA and non-DNA targeting drugs. The latter even included modern targeted

Fig. 2 Therapy-naive and drug-resistant neuroblastoma cells retain sensitivity to inhibitors of mitochondrial quality control. a An overview of utilized mitochondrial inhibitors with indicated mechanism of action. **b** MTT cell viability assay analysis after 72-h treatment showed no significant difference in sensitivity to mitochondrial inhibitors between therapy-naive CHLA-15 and post-therapy CHLA-20 cell lines (calculated IC_{50} values are indicated). Data are presented as mean ± SD, biological $n \geq 3$, technical $n = 3$. **c** Live-cell imaging growth rate analysis of CHLA-15 and CHLA-20 treated with indicated concentrations of mdivi-1 and DOXY. Data are presented as mean ± SD, biological $n \geq 3$, technical $n = 3$. Supporting Supplementary Videos 1, 2 are provided. **d** Western blotting of the cleaved caspase-3 showed that DOXY and mdivi-1 treatment for 24 h induced apoptosis in both CHLA-15 and CHLA-20. Blots are representative of three experiments. **e, f** Flow cytometry analysis of cell viability after DOXY treatment for 24 h. Representative histograms including percentages of SYTOX Red-positive dead cells as mean ± SD, biological $n \geq 7$ (**e**) and the difference in percentages of SYTOX Red-positive dead cells after indicated treatment vs. untreated controls (**f**). **g** Pretreating neuroblastoma cells with 50 µM DOXY for 24 h reduced their neurosphere formation capacity. Notably, the inhibition of sphere-formation capacity was more pronounced in CHLA-20 cells which exhibit enhanced stem-like traits (3-fold reduction relative to untreated control) compared with CHLA-15 (1.6-fold reduction); biological $n = 3$, technical $n = 3$. **h** CellTiter-Glo cell viability assay analysis of therapy-naive SK-N-BE(1) and post-therapy SK-N-BE(2)C after 72-h treatment (calculated IC_{50} are indicated) showed their similar sensitivity to DOXY whereas post-therapy SK-N-BE(2)C were found resistant to conventional chemotherapy drugs (see also Fig. S2) or a BH3 mimetic, ABT-737, inhibiting multiple anti-apoptotic BCL-2 proteins. Data are presented as mean ± SD, biological $n = 3$, technical $n = 3$. Statistical significance was determined by one-way ANOVA followed by Tukey's multiple comparisons test (**f**) and by unpaired two-tailed Student's t-test (**g**), *$p < 0.05$, **$p < 0.01$, #$p < 0.0001$.

agents never used to treat the donor patient's tumor, i.e., crizotinib and lorlatinib, inhibiting ALK kinase (both CHLA-15 and CHLA-20 harbor the same *ALK*R1275Q activating mutation), or the MEK inhibitor trametinib (Fig. 1e). Of the common multidrug efflux pumps examined, only P-glycoprotein (P-gp) was upregulated in CHLA-20 compared with the therapy-naive CHLA-15 (Figs. 1d, S1b). However, P-gp upregulation was unlikely the mechanism underlying the broad resistance of CHLA-20 cells. First, it cannot explain resistance to cisplatin that is not a P-gp substrate. Second, when we inhibited P-gp by valspodar, CHLA-20 still retained enhanced resistance to drugs that are known P-gp substrates, such as crizotinib [25] (Fig. 1f). This is in line with our previous findings demonstrating that CHLA-20 has diminished sensitivity to apoptosis induction directly at the level of isolated mitochondria [13]. Together, the CHLA-15/CHLA-20 pair represents a useful model of emergent therapy resistance and cancer stemness in neuroblastoma.

To investigate potential mitochondrial vulnerabilities in this model, we treated both cell lines with several mitochondria-targeting drugs (Fig. 2a, b). Mitochondrial ATP production inhibitors, phenformin (inhibits complex I in the electron transport chain [1, 15]) and etomoxir (inhibits carnitine-palmitoyl transferase-1 [1, 14]), showed inefficient and reduced cell viability only at concentrations multiple times exceeding their selective or clinically tolerable profiles [26–29], with CHLA-20 still retaining a slightly increased resistance to these drugs (1.4-fold to 1.7-fold vs. CHLA-15; Fig. 2b). In contrast, inhibition of dynamin-related protein 1 (DRP1) by mdivi-1 and blocking mitochondrial protein synthesis by doxycycline (DOXY) substantially suppressed cell growth and induced apoptosis with a similar efficiency in both cell lines (Fig. 2b–d, Supplementary Videos 1, 2). Importantly, the effective DOXY concentrations (IC_{50} ~20 µM for 72 h) were within the range that shows a great clinical safety profile even during prolonged treatment [30, 31] and in young children [32, 33].

Both mitochondrial translation and DRP1-mediated mitochondrial fission are crucial for mitochondrial renewal [34], suggesting that survival of neuroblastoma cells was dependent on efficient mitochondrial quality control irrespective of their drug-resistant state. We decided to explore this dependency by focusing on mitochondrial translation inhibition, using DOXY as one of the FDA-approved ribosome-targeting antibiotics that might be readily repurposed for potential anticancer therapies. Flow cytometric analysis confirmed the dose-dependent effects of DOXY leading to the induction of cell death in the CHLA-15/CHLA-20 pair (Fig. 2e, f). Viable DOXY-pretreated cells also formed significantly fewer spheres (Fig. 2g) which is a proxy for the capacity of DOXY to eliminate stem-like tumor-initiating neuroblastoma cells. We next validated the therapeutic potential of mitochondrial translation inhibition in another model pair of *MYCN*-amplified therapy-naive SK-N-BE(1) and drug-resistant SK-N-BE(2)C neuroblastoma cells,

the latter being even more sensitive to DOXY (Figs. 2h, S2). Collectively, these results revealed that targeting mitochondrial translation is efficient against bulk as well as drug-resistant/stem-like neuroblastoma cells.

Inhibiting mitochondrial translation downregulates major oncoproteins and reveals a vulnerability shared across multiple neuroblastoma cell lines

Given the significant anticancer effects of DOXY, we further examined mechanisms underlying its activity. In line with previous studies [35–37], DOXY treatment induced an imbalance of mtDNA-encoded and nuclear-encoded mitochondrial proteins. While mtDNA-encoded cytochrome c oxidase I (MT-CO1) was down-regulated in DOXY-treated cells, the levels of nuclear-encoded ATP synthase alpha-subunit 1 (ATP5A1) or mitochondrial import receptor subunit TOM20 homolog (TOMM20) were unaffected (Fig. 3a, b). Validating the general significance of our observations, we also detected similar growth inhibitory effects using other antibiotics that target bacterial, and thus mitochondrial ribosomes. Both tigecycline, a DOXY-related tetracycline derivate, and DOXY-unrelated antibiotics, linezolid and chloramphenicol, reduced cell viability in a dose-dependent manner (Fig. 3c). In contrast, ampicillin, a bacterial cell wall synthesis inhibitor not interfering with ribosome activity, did not affect the neuroblastoma cell growth (Fig. 3d). These results confirmed that the anti-neuroblastoma effects of DOXY were mediated by its specific binding to mitoribosomes leading to suppression of mitochondrial protein synthesis.

We next utilized a panel of twelve neuroblastoma cell lines, including MYC- or MYCN-amplified and non-amplified clones, to test whether mitochondrial translation might be a common vulnerability in high-risk neuroblastoma. Using two different viability assays, we found all examined cell lines highly sensitive to DOXY (Fig. 3e, f). On the contrary, when tested in nonmalignant neonatal dermal fibroblasts NDF-2 and NDF-3, DOXY limited proliferation only at much higher concentrations and did not deteriorate cell viability (Figs. 3g, S3, Supplementary Video 2), which suggests a potentially favorable therapeutic window of mitochondrial translation-targeted therapies in neuroblastoma.

Independent of genomic amplification, overexpression of N-MYC or c-MYC associates with the worst outcomes in neuroblastoma [38]. Yet, strategies targeting the MYC proteins for neuroblastoma treatment remain limited to preclinical studies [39]. Together with HIF-1α, another transcription factor associated with poor neuroblastoma prognosis, MYC proteins are known to affect mitochondrial biogenesis and metabolism [6–12]. Strikingly, DOXY-mediated inhibition of mitochondrial translation led to a dose-dependent downregulation of these transcription factors (Figs. 3h, i, S4), pointing to a novel therapeutically promising approach for inhibiting MYC proteins in multidrug-resistant high-risk neuroblastoma.
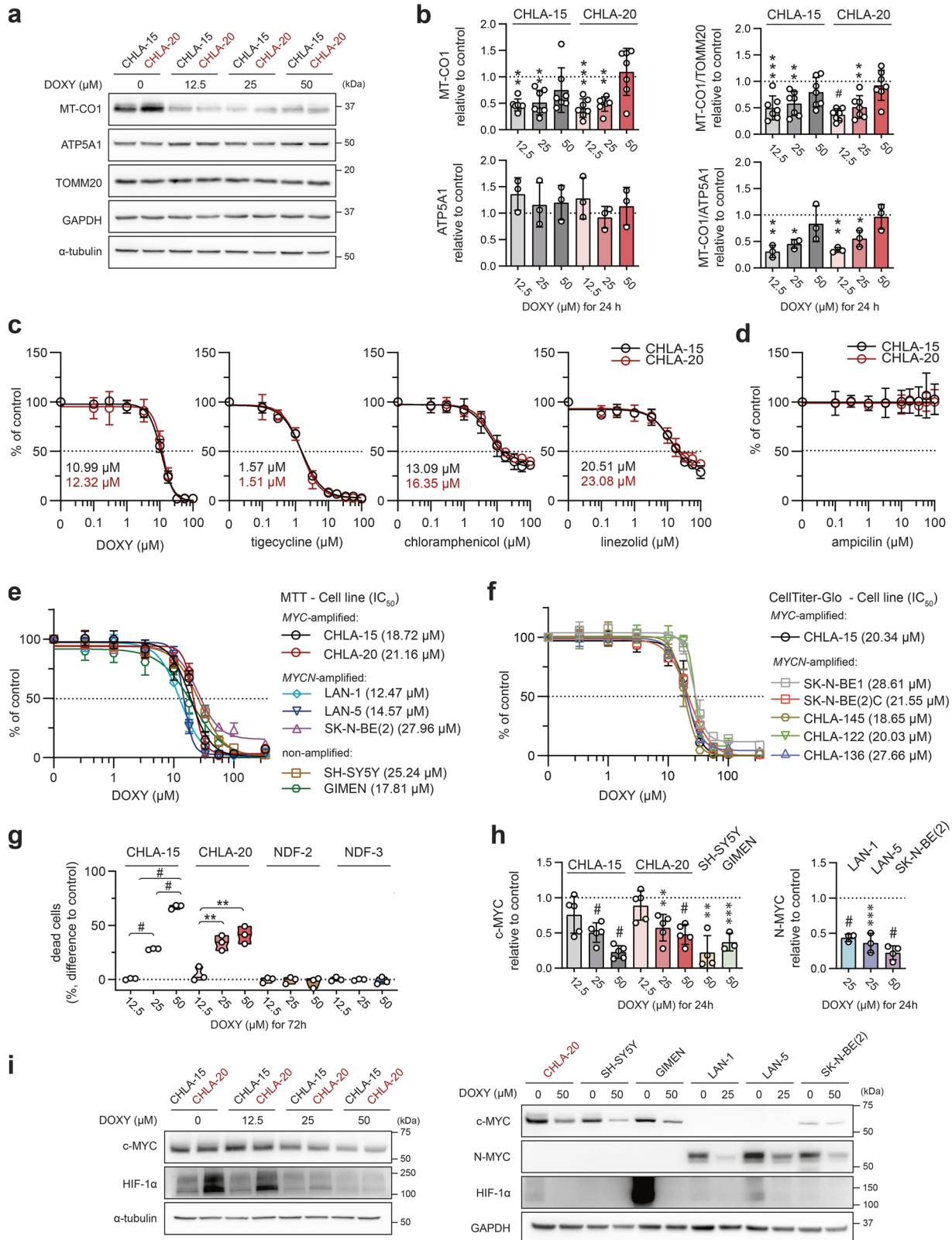
DOXY disrupts mitochondrial morphology, suppresses mitochondrial fission machinery and primes mitochondria for apoptosis

Microscopically, most DOXY-treated neuroblastoma cells showed substantially impaired mitochondrial morphology and disrupted mitochondrial network (Fig. 4a, b). However, cleaved caspase-3 was detected only in a fraction of these cells, which suggests that the collapse of mitochondrial network was an early event after DOXY-induced inhibition of mitochondrial translation, priming mitochondria to apoptosis (Fig. 4a). As demonstrated by JC-1

Fig. 3 DOXY-mediated inhibition of mitochondrial protein synthesis impairs cell viability and reduces oncogenic transcription factors across a panel of neuroblastoma cells. a, b Expression of mitochondrial proteins, mitochondrial-encoded MT-CO1 and nuclear-encoded proteins ATP5A1 and TOMM20, after 24-h DOXY treatment analyzed by western blotting (**a**) and subsequent densitometry (**b**). Normalized protein levels are plotted relative to untreated controls, mean ± SD. **c, d** MTT cell viability assay analysis of 6-day treatment with DOXY and other FDA-approved antibiotics targeting procaryotic ribosomes, tigecycline, chloramphenicol, and linezolid (**c**), and targeting bacterial cell wall synthesis, ampicillin (**d**). Calculated IC$_{50}$ are indicated. Data presented as mean ± SD, biological $n = 4$, technical $n = 3$. **e** MTT and **f** CellTiter-Glo cell viability assay analysis after 72-h treatment revealed all neuroblastoma cell lines to be highly sensitive to DOXY. Respective IC$_{50}$ values are indicated in brackets. Data points are mean ± SD, biological $n \geq 3$, technical $n = 3$. **g** Cell death rate of neuroblastoma cells (CHLA-15 and CHLA-20) and neonatal dermal fibroblasts (NDF-2 and NDF-3) was analyzed after 72 h of DOXY treatment by flow cytometry using SYTOX Red staining. Data are presented as the difference in percentages of SYTOX Red-positive dead cells after indicated treatment vs. respective untreated controls, biological $n = 3$. **h, i** Densitometric analysis (**h**) of western blotting detection (**i**) revealed downregulation of c-MYC, N-MYC, and HIF-1α across a panel of neuroblastoma cell lines treated with indicated concentrations of DOXY for 24 h. Normalized protein levels are plotted relative to untreated controls, mean ± SD. Densitometric analysis of HIF-1α is provided in Fig. S4. Statistical significance was determined by one-way ANOVA followed by Tukey's multiple comparisons test (**b, g, h**), *$p < 0.05$, **$p < 0.01$, ***$p < 0.001$, #$p < 0.0001$.

probe, DOXY treatment disrupted mitochondrial membrane potential in a dose-dependent manner (Fig. 4c), which corresponded with the cleaved caspase-3 levels detected in cells treated with increasing concentrations of DOXY (Fig. 2d).

The inhibition of mitochondrial translation did not affect the master regulator of mitochondrial biogenesis PGC1α (Fig. 4d, e). However, mitochondrial fission machinery, essential for the maintenance of mitochondrial health [40] and adjustment of mitochondrial functions [41], was suppressed after DOXY treatment. We found significant downregulation of fission-active DRP1 phosphorylated at Ser616, p-DRP1(S616), whereas its inactive form phosphorylated at Ser637, p-DRP1(S637), remained unaffected. Mitochondrial fission factor (MFF), a DRP1 adaptor protein, was also decreased upon DOXY treatment (Fig. 4d, e). At the level of anti-apoptotic BCL-2 family proteins, we identified a marked ~4-fold decrease of MCL-1 together with a ~2-fold BCL-2 upregulation (Fig. 4d, e). As CHLA-15 and CHLA-20 are both BCL-2-dependent [42, 43], these changes unlikely contributed to the DOXY-induced apoptosis.

Mitochondrial stress-activated ISR is an early event during DOXY-mediated inhibition of mitochondrial translation
The identified mitochondrial protein imbalance, disrupted morphology and dynamics, and the loss of membrane potential collectively underpin a severe mitochondrial stress induced in DOXY-treated neuroblastoma cells. Recent studies showed that mitochondrial stress activates the OMA1-DELE1-HRI cascade, inducing the ISR by phosphorylation of its core mediator eIF2α [20, 21]. Due to the lack of reliable DELE1- or activated HRI kinase-specific antibodies, we assessed the activity of the key upstream and downstream regulators of this pathway. This analysis revealed consistent effects across a panel of neuroblastoma cells. DOXY-mediated inhibition of mitochondrial translation activated mitochondrial stress sensor OMA1, marked by its autocatalytic depletion and cleavage of its substrate optic atrophy-1 (OPA1) [44], and led to the induction of ISR, marked by upregulation of phosphorylated eIF2α, p-eIF2α(S51), and the key ISR effector, CHOP [45] (Figs. 5a, b, S5).

Long, intact L-OPA1 isoforms are crucial for the inner mitochondrial membrane fusion and their specific cleavage into short, fusion-inactive S-OPA1 forms by OMA1 induces the collapse of the mitochondrial network and promotes apoptosis [46, 47]. Consistently, the apparent degradation of L-OPA1 (Fig. 5a–d) likely explains the mitochondrial fragmentation observed in DOXY-treated cells, which counterintuitively showed impaired mitochondrial fission machinery (Fig. 4). Importantly, OMA1 activation (assessed by L-OPA1 processing) and increased levels of p-eIF2α(S51) and ATF4, a transcription factor promoting CHOP expression, were detected already after 2-h DOXY treatment (Fig. 5c, d), indicating the importance of mitochondrial ISR during the initial phase of mitochondrial translation inhibition by DOXY.

PERK is a canonical kinase that phosphorylates eIF2α in response to endoplasmic reticulum (ER) stress from unfolded proteins. To evaluate whether ER stress was involved in the DOXY-induced ISR, we treated cells with ER stressor thapsigargin. However, PERK activation was detected only in thapsigargin-treated cells and, conversely, reciprocal degradation of mitochondrial stress-activated proteases OMA1 and YME1L1 and cleavage of L-OPA1 [44, 48] was found only in DOXY-treated samples (Figs. 5c, d, S5, S6a, b). These results demonstrate that DOXY-mediated inhibition of mitochondrial translation leads to mitochondrial stress that directly activates ISR independently of PERK and ER stress signaling.

Prolonged mitochondrial dysfunction is associated with ATP depletion, known to induce AMPK activity [49], and with overproduction of reactive oxygen species (ROS), activating redox-sensitive signaling cascades including p38 MAPK [50]. Indeed, we detected activation of these pathways, marked by increased levels of p-AMPKα(T172/T173) and p-p38 MAPK(T180/Y182), at later time points and DOXY concentrations that resulted in almost fully processed OPA1 and markedly degraded OMA1 (Figs. 5a–d, S5, S6c). Thus, the induction of AMPK and p38 MAPK signaling is a subsequent event following the mitochondrial stress-activated ISR in an OMA1-dependent fashion. However, we demonstrated that these late effects of DOXY-mediated inhibition of mitochondrial translation further contribute to neuroblastoma apoptosis, as inhibiting p38 MAPK by its specific inhibitor SB203580 partially prevented DOXY-induced activation of caspase-3 (Fig. S6d).

Mitochondrial ISR links inhibited mitochondrial translation with degradation of short-lived oncoproteins and induction of cell death
Phosphorylation of eIF2α attenuates cap-dependent translation in favor of ISR-specific mRNAs, allowing for efficient degradation of accumulated proteins and restoration of proteostasis [51]. We hypothesized that the ISR-mediated blockage of global protein synthesis might concurrently downregulate proteins with rapid turnover, as these are more readily targeted for degradation. Notably, c-MYC [52], N-MYC [53], HIF-1α [54], and MCL-1 [55], all significantly downregulated by DOXY treatment (Fig. 3h, i), are known to undergo rapid proteasome-dependent degradation with half-lives of <1 h. Indeed, the early mitochondrial stress-activated ISR was accompanied by the c-MYC, HIF-1α, and MCL-1 downregulation that was detectable already upon 2-h treatment and progressed with time (Figs. 6a, b, S6c). In contrast, levels of BCL-2 that has a substantially longer half-life of ~20 h [56] were not significantly affected even after 16 h of DOXY treatment. Preferential downregulation of short-lived proteins upon the DOXY-induced ISR was further substantiated by the constant levels of the protein loading control GAPDH, which is a substrate for proteasome-independent chaperone-mediated autophagy
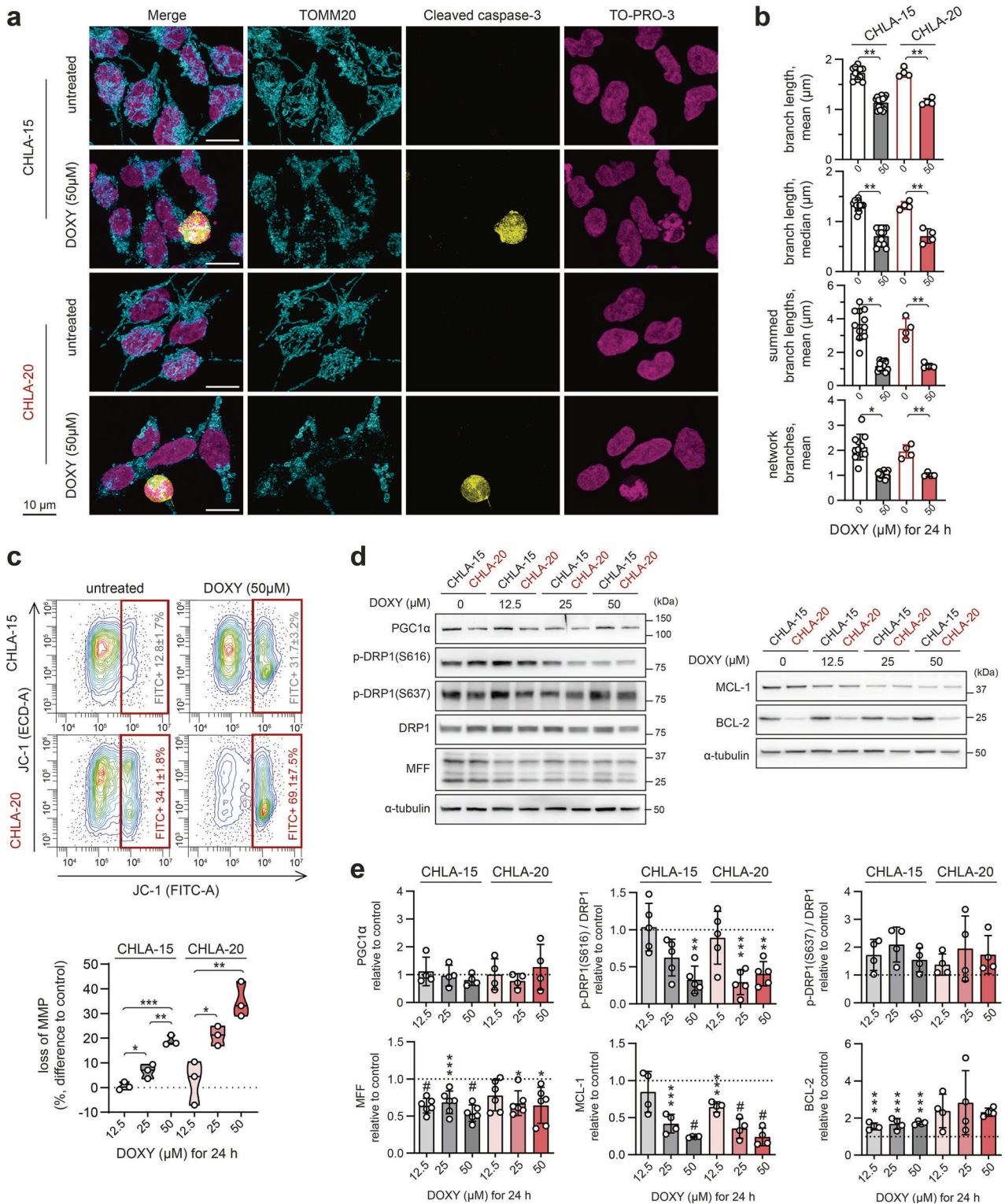
with a half-life of ~40 h [57] (Fig. 6a, b). In line with this reasoning, activation of the ISR by thapsigargin was also sufficient to downregulate c-MYC, HIF-1α, and MCL-1 in neuroblastoma cells already within 1 h of treatment, whereas BCL-2 levels remained unchanged (Fig. S6a).

We next confirmed that DOXY treatment did not affect expression of c-MYC, HIF-1α, and MCL-1 at transcriptional levels (Fig. 6c). In contrast, proteasome inhibition by MG-132 almost

completely reverted the DOXY-induced downregulation of c-MYC (Fig. 6d, e), including its phosphorylated form p-c-MYC(T58) (Fig. S7) prone to proteasomal degradation [58], and significantly rescued expression of HIF-1α and MCL-1 (Fig. 6d, e). Importantly, pretreating cells with the ISR inhibitor ISRIB, which reverses the effects of phosphorylated eIF2α and restores cap-dependent translation [59] (Fig. 6f), partially rescued the N-MYC down-regulation in DOXY-treated cells (Fig. 6g). Thus, the attenuated

Fig. 4 DOXY-mediated inhibition of mitochondrial translation disrupts mitochondrial morphology and fission machinery and primes mitochondria for apoptosis. a Mitochondrial morphology–visualized by immunofluorescence staining of TOMM20 (cyan)–revealed signs of fragmentation and swelling in most cells after 24-h treatment with 50 μM DOXY. At this timepoint, apoptosis marked by cleaved caspase-3 (yellow) and fragmented nuclei (TO-PRO-3; magenta) was detected only in a subset of cells. Maximum intensity projections of confocal microscopy Z-stacks are shown. **b** Image analysis by ImageJ plug-in tool MiNA - Mitochondrial Network Analysis confirmed disrupted mitochondrial morphology in cells treated with 50 μM DOXY for 24 h. Data are presented as parameters determined for individual field of vision images, mean ± SD. **c** Flow cytometry using JC-1 probe after 24-h DOXY treatment revealed dose-dependent loss of mitochondrial potential. Upper panel, representative contour plots; percentages of cells with depolarized mitochondria are presented as mean ± SD, biological $n = 3$. Bottom panel, the differences in percentages of cells with depolarized mitochondria after indicated treatment vs. untreated cells. **d**, **e** Western blotting detection (**d**) and densitometric analysis (**e**) of proteins related to mitochondrial dynamics and BCL-2 anti-apoptotic proteins after 24-h DOXY treatment in indicated concentrations. Normalized protein levels are plotted relative to untreated controls, mean ± SD. Statistical significance was determined by unpaired two-tailed Student's t-test (**b**) and by one-way ANOVA followed by Tukey's multiple comparisons test (**e**), *$p < 0.05$, **$p < 0.01$, ***$p < 0.001$, #$p < 0.0001$.

cap-dependent protein synthesis and enhanced proteasomal degradation upon mitochondrial stress-activated ISR are the major mechanisms causing the downregulation of short-lived oncoproteins, including MYC proteins in neuroblastoma cells.

Following this finding, we asked whether inhibiting the DOXY-induced mitochondrial ISR also rescues the viability of neuroblastoma cells. Indeed, combining DOXY treatment with ISRIB suppressed expression of the ISR effectors ATF4 and CHOP (Fig. 6h), and reduced the cell death induction (Fig. 6i) and cell growth inhibition (Fig. 6j) when compared with cells treated with DOXY alone. Together, these results demonstrate mitochondrial ISR as the key pathway responsible for both downregulation of MYC proteins and induction of neuroblastoma cell death upon the mitoribosome inhibition.

Rapid turnover of MYC proteins associates with sensitivity of MYC-driven neuroblastoma to DOXY-induced cell death

To explore if the effects of DOXY-mediated mitochondrial translation inhibition are neuroblastoma specific, we introduced seven cell lines derived from different nervous system tumors. Consistent with our results in neuroblastoma, inhibiting mitochondrial translation by DOXY limited cell proliferation across the tested cell lines, except for NSTS-5 schwannoma cells (Fig. 7a). Similarly, induction of mitochondrial stress, activation of ISR and decrease of HIF-1α were detected in DOXY-responsive glioblastoma, astrocytoma, and medulloblastoma cells (Figs. 7b–d, S8). Intriguingly, markers of mitochondrial stress and ISR activation were also found in neonatal dermal fibroblasts (Fig. S9) that partially reduced proliferation but retained their viability in response to DOXY treatment (Figs. 3g, S3). This may suggest that the ISR is a conserved retrograde pathway that relays DOXY-induced imbalance in mitochondrial proteins but leads to cell type-dependent outcomes.

In contrast to neuroblastoma, we did not observe consistent downregulation of c-MYC in cell lines derived from other nervous system tumors (Figs. 7b–d, S8) or neonatal dermal fibroblasts (Fig. S9). Compared with other tumor types, *MYC*-amplified CHLA-20 neuroblastoma cells express markedly higher levels of c-MYC together with its phosphorylated forms, p-c-MYC(T58) and p-c-MYC(S62) (Fig. 7e). Phosphorylation at threonine 58 (T58), subsequent to serine 62 (S62) phosphorylation, is known to promote proteasomal degradation and rapid turnover of both c-MYC [58] and N-MYC [60].

Strikingly, we found cell types with relatively low levels of c-MYC and its phosphorylated forms to be substantially resistant to DOXY-induced cell death, as demonstrated in Daoy (Fig. S10), NSTS-5 (Fig. 7a) and NDF-3 cells (Figs. 3g, S3). Immunoblots using the antibody recognizing both p-c-MYC(T58) and p-N-MYC(T58) showed that these phosphorylated forms are markedly upregulated in MYC-driven neuroblastoma and their levels correlated with sensitivity to DOXY-induced cell death in a panel of neuroblastoma and medulloblastoma models (Figs. 7f, g, S11a, c, d). To functionally validate this MYC-dependent sensitivity, we

utilized Tet21N neuroblastoma cells [61] with tunable N-MYC expression (for details refer to Methods section). Tet21N cells that expressed high levels of N-MYC and its T58-phosphorylated form (Tet21N *MYCN*-on) were significantly more sensitive to DOXY-induced cell death compared to their counterparts (Tet21N *MYCN*-off) where N-MYC expression was switched off (Figs. 7h, S12a). Of note, both *MYCN*-on and *MYCN*-off untreated cells showed very similar growth rates (Fig. S12b), which supports the conclusion that the outcomes of mitoribosome inhibition are MYC-dependent. Our data indicate that the high c-MYC/N-MYC levels and extensive T58 phosphorylation, priming MYC proteins for rapid degradation upon the mitochondrial ISR (Fig. S7), determine the propensity of MYC-driven neuroblastoma cells to cell death in response to inhibition of mitochondrial translation. Conversely, cell types lacking aberrantly upregulated expression and phosphorylation of MYC proteins, such as normal fibroblasts (Figs. 3g, 7e), did not undergo cell death after mitochondrial ISR activation, which suggests a promising opportunity for developing mitoribosome targeting therapies that would be efficient against MYC-driven neuroblastomas while sparing healthy tissues.

Long-term repeated inhibition of mitochondrial translation does not induce highly resistant neuroblastoma phenotype

Target-specific resistance often develops between chemotherapy cycles. We therefore repeatedly exposed CHLA-15/CHLA-20 cells to DOXY to mimic multiple rounds of therapy and gradually select for the DOXY-resistant phenotype (DOXY-sel; Fig. 8a). However, even after 11 months and 30 cycles of selection, the cells remained highly sensitive to 2-fold of the initial IC$_{50}$ of DOXY and the finally established DOXY-sel cell lines showed only ~1.5-fold resistance compared with parental cells (Fig. 8b). Both DOXY-sel cell lines exhibited downregulation of several proteins associated with poor neuroblastoma prognosis, including HIF-1α [62], P-gp, or MCL-1 (Fig. S13a, b). Given the marked P-gp downregulation in DOXY-sel cells, we next asked whether P-gp modulates sensitivity to DOXY. However, pharmacological inhibition of P-gp did not change the viability of parental cells treated with DOXY (Fig. S13c). Additional cell line-specific changes involved proteins targeted by DOXY treatment, including MT-CO1, eIF2α, or OMA1 (Fig. S13a, b). How these potentially compensatory events affect mitochondrial functions and the overall phenotype of DOXY-sel neuroblastoma cells will require further investigation.

Collectively, our data establish that perturbing mitochondrial function by DOXY-mediated targeting of mitochondrial protein synthesis triggers the mitochondrial ISR which in the context of MYC-driven neuroblastoma efficiently overcomes existing multi-drug resistance mechanisms and eradicates aggressive tumor cells without inducing clinically relevant resistance (Fig. 8c). To confirm this concept of mitoribosomal synthetic lethality, we also replicated the key experiments with a tetracycline-unrelated mitoribosome inhibitor, chloramphenicol. This antibiotic was selected as it is known to bind to the large ribosomal subunit (DOXY binds to the small subunit of the mitoribosome), and as it
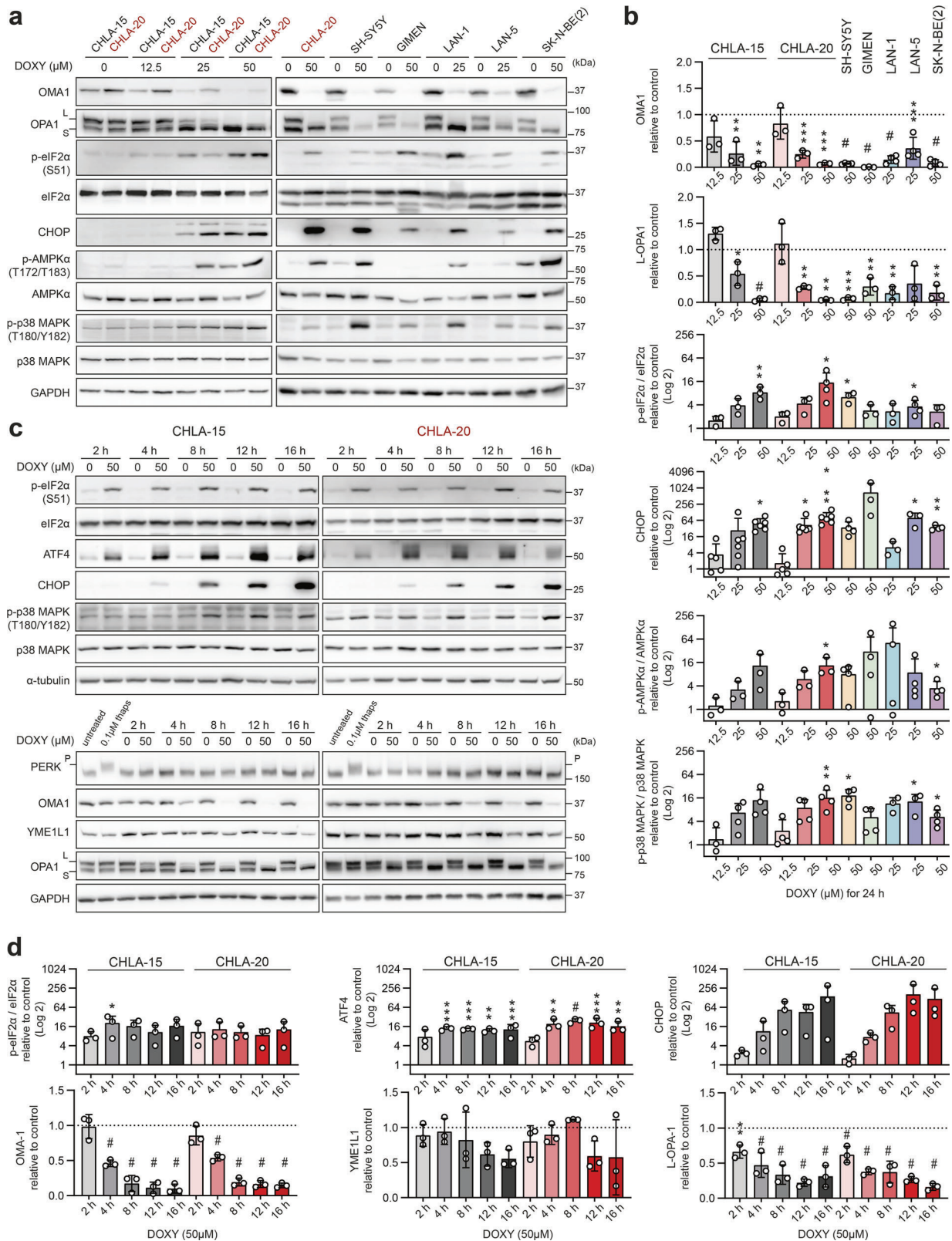
Fig. 5 Inhibition of mitochondrial protein synthesis leads to early activation of OMA1-mediated ISR. a–d Western blotting detection and densitometric analysis of markers of mitochondrial stress, ISR and stress signaling kinases in a panel of neuroblastoma cells after DOXY treatment for 24 h (**a**, **b**) and over a 16-h time course (**c**, **d**). Normalized protein levels are plotted relative to untreated controls, mean ± SD. Treatment with 0.1 μM thapsigargin for 1 h served as a positive control of PERK phosphorylation, assessed by a reduced electrophoretic mobility in 6% polyacrylamide gel. Western blotting and densitometric analysis of YME1L1 after 24-h DOXY treatment and densitometric analysis of p-p38 MAPK (T180/Y182)/p38 MAPK during 16-h DOXY treatment are provided in Fig. S6b, c, respectively. Statistical significance was determined by one-way ANOVA followed by Tukey's multiple comparisons test (**b**, **d**), *$p < 0.05$, **$p < 0.01$, ***$p < 0.001$, #$p < 0.0001$.
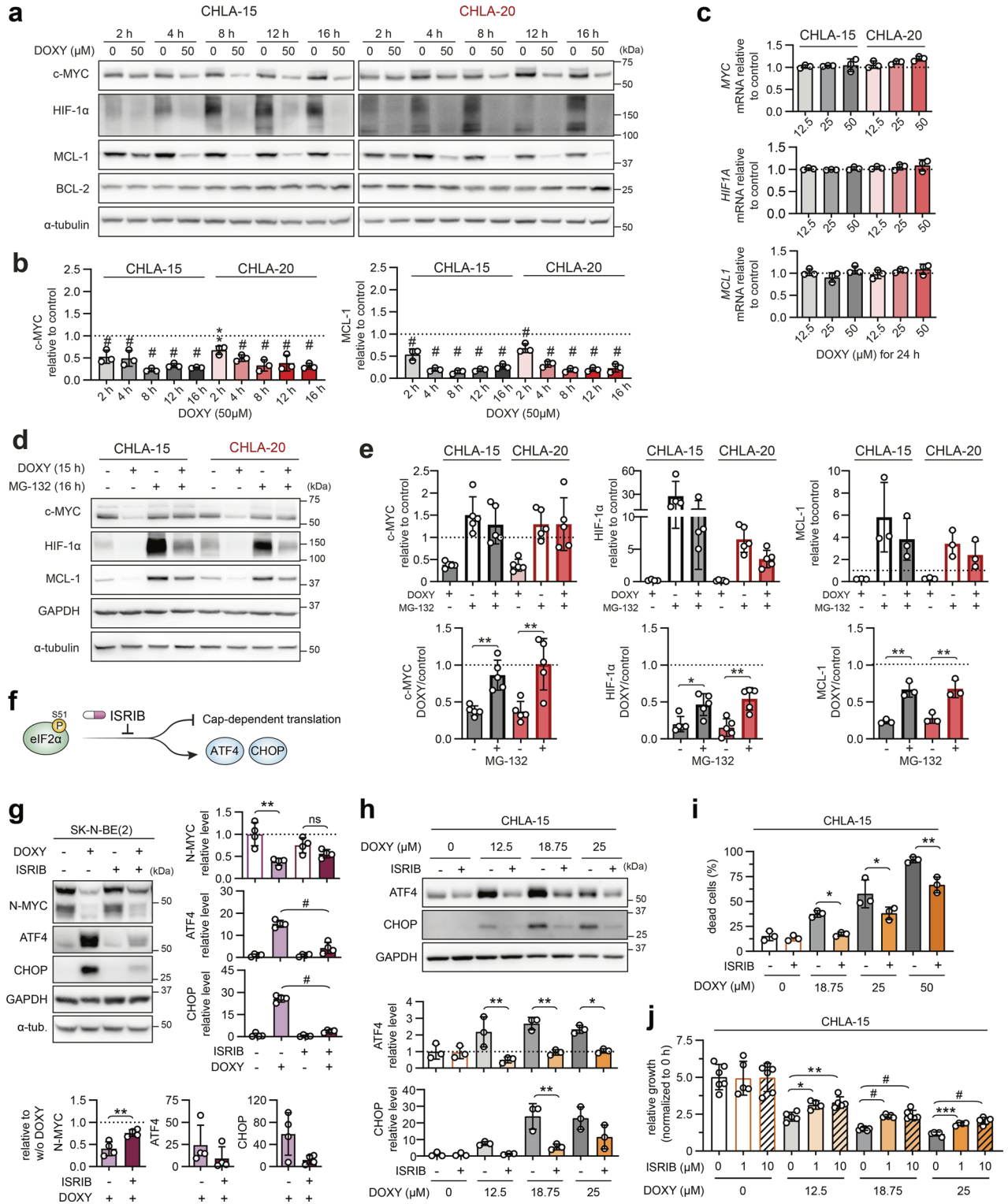
was already found efficient against therapy-naive and drug-resistant neuroblastoma cells in this study (Fig. 3c). In line with the effects observed after DOXY treatment, chloramphenicol selectively inhibited mitochondrial translation (Fig. S14a) and induced mitochondrial ISR leading to the downregulation of c-MYC in neuroblastoma cells (Fig. S14b, c). Consistently, sensitivity of Tet21N cells to chloramphenicol-mediated inhibition of proliferation was also diminished by N-MYC downregulation (Fig. S14d). In

contrast to DOXY, chloramphenicol did not induce OMA1 activity but degradation of other mitochondrial stress-activated protease YME1L1 was detected (Fig. S14b, c). This suggests that an alternative pathway distinct from the OMA1-DELE1-HRI cascade might relay the mitochondrial stress signals to eIF2α upon blocking the large mitoribosomal subunit. Nevertheless, the key effects observed after chloramphenicol treatment, i.e., the mitochondrial ISR activation leading to impaired neuroblastoma

Fig. 6 DOXY-induced ISR activation corresponds with early downregulation of short-lived oncoproteins and contributes to neuroblastoma growth inhibition and cell death. a, b Western blotting detection (**a**) of c-MYC, HIF-1α, and anti-apoptotic BCL-2 family proteins in CHLA-15 and CHLA-20 treated with 50 µM DOXY for 2–16 h followed by densitometric analysis (**b**) of c-MYC and MCL-1. Normalized protein levels are plotted relative to untreated controls, mean ± SD. Densitometric analysis of HIF-1α and BCL-2 is provided in Fig. S6c. **c** No change in the transcription of *MYC*, *HIF1A*, and *MCL1* was detected by RT-qPCR upon 24-h DOXY treatment. Normalized mRNA levels plotted relative to untreated controls, mean ± SD. **d, e** Western blotting detection (**d**) and densitometric analysis (**e**) of c-MYC, HIF-1α, and MCL-1 after DOXY treatment of neuroblastoma cells with inhibited proteasome. To block proteasome activity, CHLA-15 and CHLA-20 were pretreated with MG-132 (1 µM for MCL-1 analysis, 5 µM for c-MYC and HIF-1α) and after 1 h, 50 µM DOXY was added for additional 15 h. Upper panel, normalized protein levels are plotted relative to fully untreated controls (dashed line). Lower panel, ratios of normalized protein levels in DOXY-treated cells (w/o or with MG-132) and respective controls (w/o or with MG-132), mean ± SD. **f** ISRIB reverts p-eIF2α(S51)-mediated attenuation of cap-dependent translation [59], thus restores global protein synthesis while suppressing translation of mRNAs encoding ISR effectors such as ATF4 and CHOP. **g** Western blotting detection and densitometric analysis of N-MYC, ATF4, and CHOP in *MYCN*-amplified SK-N-BE(2) treated for 24 h with 50 µM DOXY in the presence or absence of 1 µM ISRIB. To efficiently block the induction of ISR, cells were pretreated with ISRIB for 4 h prior to addition of DOXY. Right panel, normalized protein levels plotted relative to the average of all samples, mean ± SD. Lower panel, ratios of normalized protein levels in DOXY-treated cells and their respective controls (w/o or with ISRIB), mean ± SD. **h** Western blotting detection and densitometric analysis of ATF4 and CHOP in CHLA-15 treated for 72 h with different concentrations of DOXY w/o or with 1 µM ISRIB. Normalized protein levels are plotted relative to the average of all samples, mean ± SD. **i** Cell death rate of CHLA-15 analyzed by flow cytometry using SYTOX Red staining after 72-h treatment with 18.75–50 µM DOXY in the presence or absence of 1µM ISRIB. Data shown as percentages of SYTOX Red-positive dead cells after the indicated treatments, biological $n = 3$. **j** Live-cell imaging growth rate analysis of CHLA-15 concomitantly treated with DOXY and ISRIB in indicated concentrations for 72 h. Data are normalized to 0 h and presented as mean ± SD, biological $n \geq 4$, technical $n = 3$. Statistical significance was determined by one-way ANOVA followed by Tukey's multiple comparisons test (**b**, **c**, **g**–**j**) and unpaired two-tailed Student's t-test (**e**, **g**), $*p < 0.05$, $**p < 0.01$, $***p < 0.001$, $\#p < 0.0001$.

cell viability in a MYC-dependent manner, provide further evidence for the newly identified mitoribosomal synthetic lethality, highlighting the potential of repurposing ribosome-targeting antibiotics in neuroblastoma therapy.

DISCUSSION

Targeting mitochondria is an emerging strategy to overcome cancer drug resistance. Yet, molecular determinants that would guide efficient mitochondrial therapies are poorly understood, particularly in pediatric tumors. Here, we identified mitochondrial translation as a promising MYC-dependent target in multidrug-resistant neuroblastoma. Our results also implicate that mitochondrial quality control mechanisms, including mitochondrial dynamics and translation control, are essential for neuroblastoma cell survival irrespective of the drug resistance status, as demonstrated by inhibition of mitochondrial fission by mdivi-1 and disruption of mitoribosome processivity by DOXY (Fig. 2c–h, Supplementary Videos 1, 2).

Mechanistically, time course experiments showed that inhibition of mitoribosomes by DOXY induces the activity of mitochondrial metalloprotease OMA1 and initiates mitochondrial retrograde signaling via the central ISR mediator eIF2α. Short-running ISR normally orchestrates gene expression and protein translation to restore cellular homeostasis and maintain cell survival, in line with its reported pro-tumorigenic effects [63]. However, excessive or prolonged ISR is known to induce cell death in various cell types [51]. Interestingly, the ISR effector ATF4 was already shown to mediate cell death upon glutamine deprivation in *MYCN*-amplified neuroblastoma [64]. Consistently, we provide evidence that MYC-driven neuroblastoma cells are particularly vulnerable to the ISR-mediated cell death, while p38 MAPK appears to further favor apoptosis induced by the mitochondrial ISR. p38 MAPK is known to promote apoptosis [65–67] and likely synergizes with the ISR by directly phosphorylating CHOP [68], enhancing its pro-apoptotic activity [69].

Previously, DOXY-mediated inhibition of mitochondrial translation was shown to enhance ER-mitochondria connectivity [70] and was suggested to activate ISR via inducing ER stress in carcinomas [70, 71] and melanoma [18, 72]. On the contrary, we demonstrate that ER stress is not involved in DOXY-induced ISR in neuroblastoma, as eIF2α phosphorylation was not mediated by its upstream ER stress-activated kinase PERK. Our data are consistent with recent studies demonstrating mitochondrial stress sensor OMA1 as the major inducer of ISR via the OMA1-DELE1-HRI

pathway [20, 21]. Similarly, we demonstrate that DOXY-induced mitochondrial protein imbalance disrupts mitochondrial morphology and membrane potential, inducing the ISR along the OMA1 activity detected already in early phases of the treatment. These results indicate that targeting the small mitoribosomal subunit by DOXY induces ISR via OMA1 signaling.

However, our data also revealed a potentially alternative, OMA1-independent mechanism of mitochondrial ISR upon blocking mitoribosomes, as targeting the large mitoribosomal subunit by chloramphenicol induced ISR without apparent OMA1 activation (Fig. S14). Of note, additional cell context-dependent signaling pathways cannot be excluded. Previously, knocking down components of the OMA1-DELE1-HRI pathway showed insufficient to completely block the DOXY-mediated ISR in embryonal kidney HEK293T cells [20]. However, in contrast to our models (Figs. 5, 7d, S5a, b), DOXY-treated HEK293T cells did not show any signs of L-OPA1 cleavage [20], suggesting cell type-dependent activation of OMA1 in response to the DOXY-mediated inhibition of mitochondrial translation. Similarly, DOXY structural analog tigecycline was recently shown to induce ISR via GCN2 signaling in colorectal adenocarcinoma and chronic myelogenous leukemia cells [73]. Together, these findings suggest that mitoribosomal inhibitors induce ISR via multiple signaling pathways and further investigation is needed to explore the context dependency.

A chronic ISR has been recently suggested to predict the sensitivity of melanoma cells to tigecycline-mediated inhibition of mitoribosomes [18]. In contrast, we did not observe any association between DOXY-induced cell death and the extent of ISR activation prior or after treatment. In fact, we found p-eIF2α(S51) and one of the major ISR effectors, CHOP, to be consistently upregulated by DOXY in nearly all tested cell lines (neuroblastoma: 11/11; other nerve tissue tumors: 6/7; normal fibroblasts: 1/1) regardless their vulnerability to DOXY-induced cell death. High c-MYC levels have been associated with the susceptibility of hematological malignancies to inhibition of mitochondrial protein synthesis [37, 74]. In this study, we found that the mitoribosome inhibition-induced ISR leads to degradation of short-lived MYC proteins and that the upregulation of their T58-phosphorylated forms, tagging MYC proteins for rapid proteasome degradation [58, 60, 75, 76], sensitizes MYC-driven neuroblastoma to inhibition of mitoribosomes.

Based on these findings, we propose mitochondrial translation as a novel synthetic lethal target that might be exploited to overcome multidrug resistance in MYC-driven neuroblastoma

K. Borankova et al.
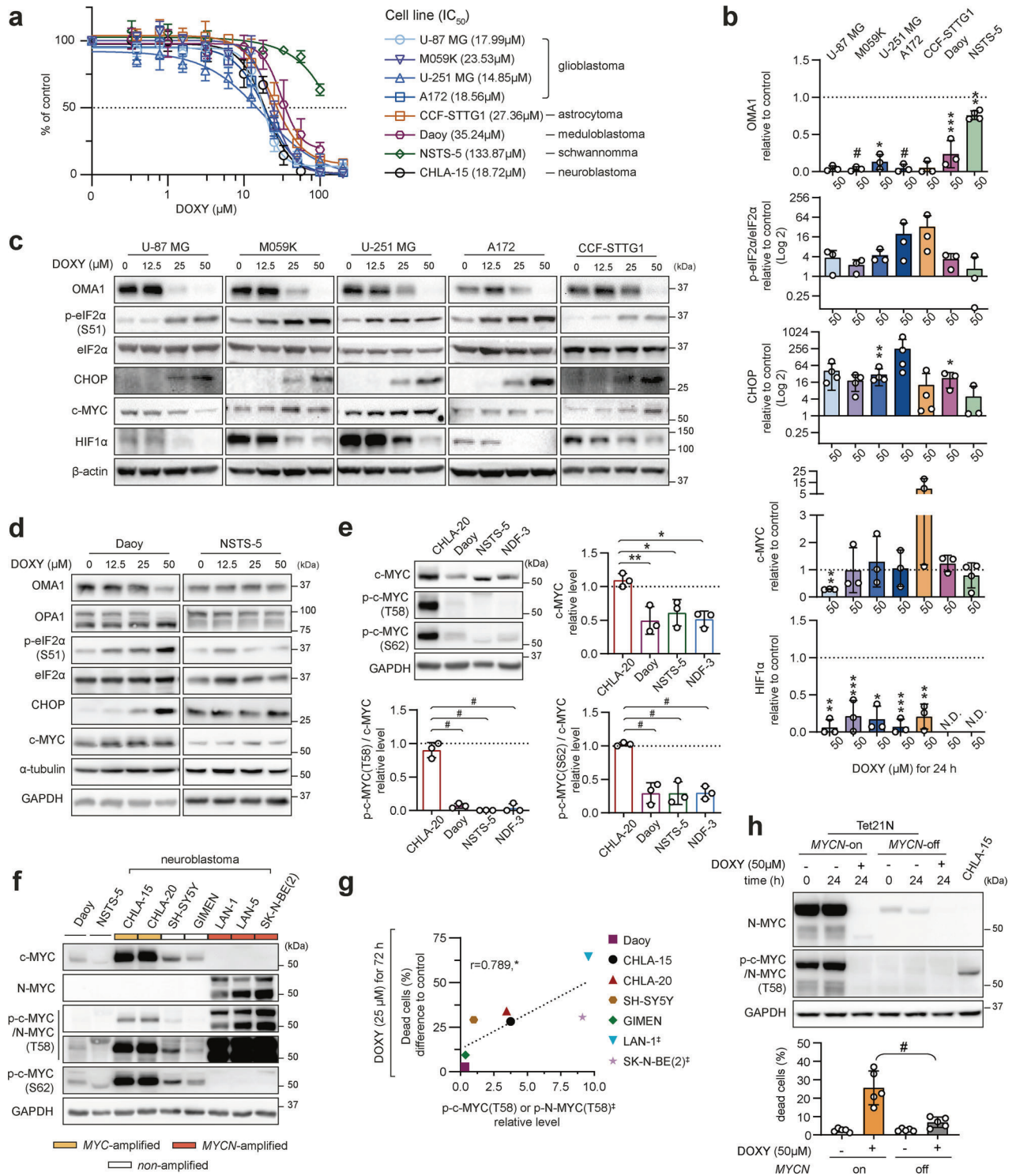
(Fig. 8c). We anticipate that further dissection of mitochondrial stress signaling pathways might enable identification of additional clinically relevant targets for the treatment of MYC-addicted tumors.

METHODS
Cell culture and treatment
The following cell lines were used in the study: (i) neuroblastoma cell lines CHLA-15, CHLA-20, CHLA-122, CHLA-136, CHLA-145, SK-N-BE(1), SK-N-BE(2)

C (obtained from the COG/ALSF Childhood Cancer Repository; www.cccells.org), GIMEN, LAN-1, LAN-5 (a kind gift of Prof. Lumír Krejčí), SH-SY5Y, SK-N-BE(2) (purchased from ECACC), and Tet21N (kindly provided by Dr. Frank Westermann); (ii) glioblastoma cell lines U-87 MG, M059K, U-251 MG, A-172 and astrocytoma cell line CCF-STTG1 (all purchased from ATCC); (iii) medulloblastoma cell line Daoy (purchased from ECACC); (iv) schwannoma cell line NSTS-5 (in-house derived from tumor tissue with written informed consent under IGA MZCR NR/9125-4 project approved by the Research Ethics Committee of the School of Medicine, Masaryk University, Brno, Czech Republic – approval no. 23/2005); (v) human neonatal dermal fibroblast cell lines NDF-2 and NDF-3 (#CC-2509; Lonza

Fig. 7 Overexpression and phosphorylation of MYC proteins correlate with sensitivity to cell death via mitochondrial ISR, conserved across various models of nervous system tumors. a MTT cell viability assay analysis was used to determine sensitivity of cell lines derived from various nervous system tumors to DOXY. Respective IC_{50} values for 72-h treatment are indicated in brackets. Data presented as mean ± SD, biological $n \geq 3$, technical $n = 3$. **b–d** Densitometric analysis (**b**) of immunoblots (**c, d**) from lysates after 24-h DOXY treatment showed dose-dependent induction of mitochondrial stress and ISR in a panel of cell lines derived from different nervous system tumors. Contrary to neuroblastoma, this did not lead to consistent downregulation of c-MYC, although HIF-1α was significantly downregulated in nervous system tumors. Normalized protein levels are plotted relative to untreated controls, mean ± SD; N.D. – not detectable. Complete densitometric analysis is provided in Fig. S8. **e** Western blotting detection and densitometric analysis of c-MYC, p-c-MYC(T58), and p-c-MYC(S62) revealed that CHLA-20 neuroblastoma cells have significantly higher c-MYC level and extensively enhanced phosphorylation of c-MYC compared with Daoy, NSTS-5 and NDF-3 cells that were less sensitive to DOXY. Normalized protein levels are plotted relative to untreated control, mean ± SD. **f** Western blotting detection of c-MYC, p-CMYC/N-MYC(T58) and p-c-MYC(S62) in a panel of nervous system tumors. **g** A significant positive correlation between the percentage of dead cells after 72-h treatment with 25 μM DOXY and the basal levels of p-CMYC/N-MYC(T58) in untreated neuroblastoma models and Daoy medulloblastoma cells, r = Pearson correlation coefficient; ‡, *MYCN*-amplified. Related flow cytometry and protein densitometry data are provided in Fig. S10. **h** Western blotting detection of N-MYC and p-c-MYC/N-MYC(T58) (upper panel; densitometric analysis is provided in Fig. S12a) and cell death rate flow cytometric analysis (lower panel) revealed that Tet21N *MYCN*-off cells with extensively downregulated N-MYC and p-c-MYC/N-MYC(T58) levels are significantly less sensitive to DOXY-induced cell death compared with N-MYC overexpressing Tet21N *MYCN*-on cells. Cell death rate was analyzed using SYTOX Red staining after 24-h treatment with 50 μM DOXY. Data are presented as percentages of SYTOX Red-positive dead cells after indicated treatment, biological $n = 5$. Statistical significance was determined by one-way ANOVA followed by Tukey's multiple comparisons test (**b, e, h**) and by Pearson correlation (**g**), *$p < 0.05$, **$p < 0.01$, ***$p < 0.001$, #$p < 0.0001$.

Bioscience, Durham, NC, USA; a kind gift of Dr. Tomáš Bárta). In addition, human pluripotent embryonal carcinoma cell line NTERA-2 (clone D1) purchased from ECACC (#01071221) served as a positive control shown in Fig. 1d. All cell lines were authenticated by STR profiling (Generi Biotech, Hradec Králové, Czech Republic; Westmead Institute of Medical Research, Westmead, NSW, Australia; Promega Geneprint 10, Madison, Wisconsin, USA) and routinely tested for mycoplasma by PCR [77].

Cell lines were cultured in a humidified atmosphere of 5% CO_2 at 37 °C in media with supplements as detailed in Supplementary Tables 1, 2. Drug treatments were always performed the day after cell seeding. A detailed overview of the drugs used is provided in Supplementary Table 3. Tet21N cells express N-MYC from a *MYCN* Tet-off construct [61]. To induce *MYCN*-off state, Tet21N cells (*MYCN*-on) were pretreated with a non-cytotoxic and non-cytostatic dose of DOXY (2.25 μM) for 72 h, blocking *MYCN* expression under the control of Tet-off promoter. If not treated with 50 μM of DOXY, Tet21N *MYCN*-off cells were always maintained in media supplemented with 2.25 μM DOXY during subsequent experiments.

Cell viability assays
For 24–72-h and 6-day experiments, cells were seeded into 96-well plates in a density of 5000 and 2500 cells/well, respectively, except for neonatal dermal fibroblast NDF-2 and NDF-3 (2000 cells/well for 72-h experiments) and Tet21N cells (700 cells/well for 6-day experiments). After the incubation time, cell viability was measured. Performing MTT assay, thiazolyl blue tetrazolium bromide (#M2128, Sigma-Aldrich, St. Louis, MO, USA) was added to each well to reach the final concentration of 0.455 mg/ml. After 3-h incubation under standard conditions, the medium was replaced with 200 μL of DMSO to solubilize the formazan crystals. The absorbance of each well was determined by Sunrise Absorbance Reader (Tecan, Männedorf, Switzerland). For CellTiter-Glo® assay (#G7571, Promega, Madison, WI, USA), cells were seeded in Corning® 96-well Flat Clear Bottom White Polystyrene TC-treated luminescent microplates (#3610, Corning, Corning, NY, USA) and manufacturer instructions were followed. Luminescence was measured by Synergy™ 2 microplate reader (BioTek Instruments, Winooski, VT, USA).

Absolute half maximal inhibitory concentration (IC_{50}) of drugs and inhibitors was determined from non-linear regression of datasets of MTT assay and CellTiter-Glo® assay with individual tested concentrations normalized to untreated control cells. Non-linear regression with variable slope was calculated using GraphPad Prism 8.0.2. software (GraphPad Software, San Diego, CA, US). Determined parameters were then used to calculate absolute IC_{50} values according to the following formula: relative $IC_{50}*(((50\text{-top})/(\text{bottom-}50))^{\wedge}(-1/\text{hill slope}))$.

Growth analysis
Cells were seeded into 96-well plates (CHLA-15, CHLA-20: 5000 cells/well; NDF-3: 2000 cells/well) and treated the day after seeding with respective drugs. To validate that 2.25 μM DOXY shows no cytotoxic and cytostatic activity in Tet21N cells during the 6-day treatment, Tet21N cells were seeded at low density in 6-well plates and replenished with fresh media w/o DOXY (*MYCN*-on) or with 2.25 μM DOXY (*MYCN*-off) the day after seeding.

Subsequently, cell confluency was determined every 4 h using live cell imaging system Incucyte® SX1 (Sartorius, Göttingen, Germany) and plotted relative to initial values. Cell line doubling times were calculated by GraphPad Prism 8.0.2. software using non-linear regression – exponential (Malthusian) growth model.

Sphere formation assay
Cells were harvested and dissociated into single-cell suspension using Accutase (#LM-T1735, Biosera) and seeded into ultra-low attachment 6-well plates (#CLS3471-24EA, Corning) at a density of 1000 cells/well in a defined serum-free medium: DMEM/F12 based (as detailed in Supplementary Table 1) w/o fetal bovine serum, supplemented with 1× B27 w/o vitamin A (#12587, Gibco), 10 ng/ml EGF (#E9644, Sigma-Aldrich), and 20 ng/ml FGF2 (#SRP4037, Sigma-Aldrich). Cells were replenished with 200 μl of the freshly prepared medium three times a week. The number of spheres (diameter ≥ 50 μm) was manually counted after 21 days of incubation using PROView software analysis of images taken under IM-3 light microscope equipped with C-B5 digital camera (all Optika, Ponteranica, Italy).

Tumorigenicity assay in vivo
Cells were harvested, enzymatically dissociated and a single cell suspension of 1×10^6 cells in 100 μl of pure DMEM/F/12 medium (#LM-D-1224, Biosera) was injected subcutaneously into the right flank of 9-week-old female NSG (NOD/ShiLtSz-*scid/Il2ry*null) mice. All animal experiments were conducted in accordance with a study (MSMT-4408/2016-6) approved by the Institutional Animal Care and Use Committee of Masaryk University and registered by the Ministry of Education, Youth and Sports of the Czech Republic as required by national legislation. After 29 days, the mice were sacrificed and surgically examined. The xenograft tumors were excised and photographed, and the final tumor volume was determined using the following formula: tumor volume (mm³) = length (mm) × width (mm) × width (mm) × 1/2. The adequate sample size ($n = 3$ animals/ experimental arm) was chosen based on our previous studies [24, 78] in accordance with the reduction principle. Animal exclusion criteria, randomization, and blinding were not applied in this study.

Western blotting
Whole-cell extracts were collected using RIPA lysis buffer (2 mM EDTA, 1% IGEPAL® CA-630, 0.1% SDS, 8.7 mg/ml sodium chloride, 5 mg/ml sodium deoxycholate, 50 mM Tris-HCl) supplemented with cOmplete™ Mini Protease Inhibitor Cocktail (#11836170001, Roche, Basel, Switzerland) and PhosSTOP (#4906837001, Roche). 20 μg of total proteins were resolved on 10% polyacrylamide gels (except for 6% gels used for PERK detection) and blotted onto PVDF membranes (#1620177, Bio-Rad Laboratories, Hercules, CA, USA). The membranes were blocked with 5% not-fat dry milk or bovine serum albumin (#A7906, Sigma-Aldrich) in Tris-buffered saline with 0.05% Tween-20 (#93773, Sigma-Aldrich) for at least 1 h and incubated with primary antibodies overnight on rocking platform at 4 °C. The incubation with secondary HRP-linked antibody was conducted at RT for at least 1 h.
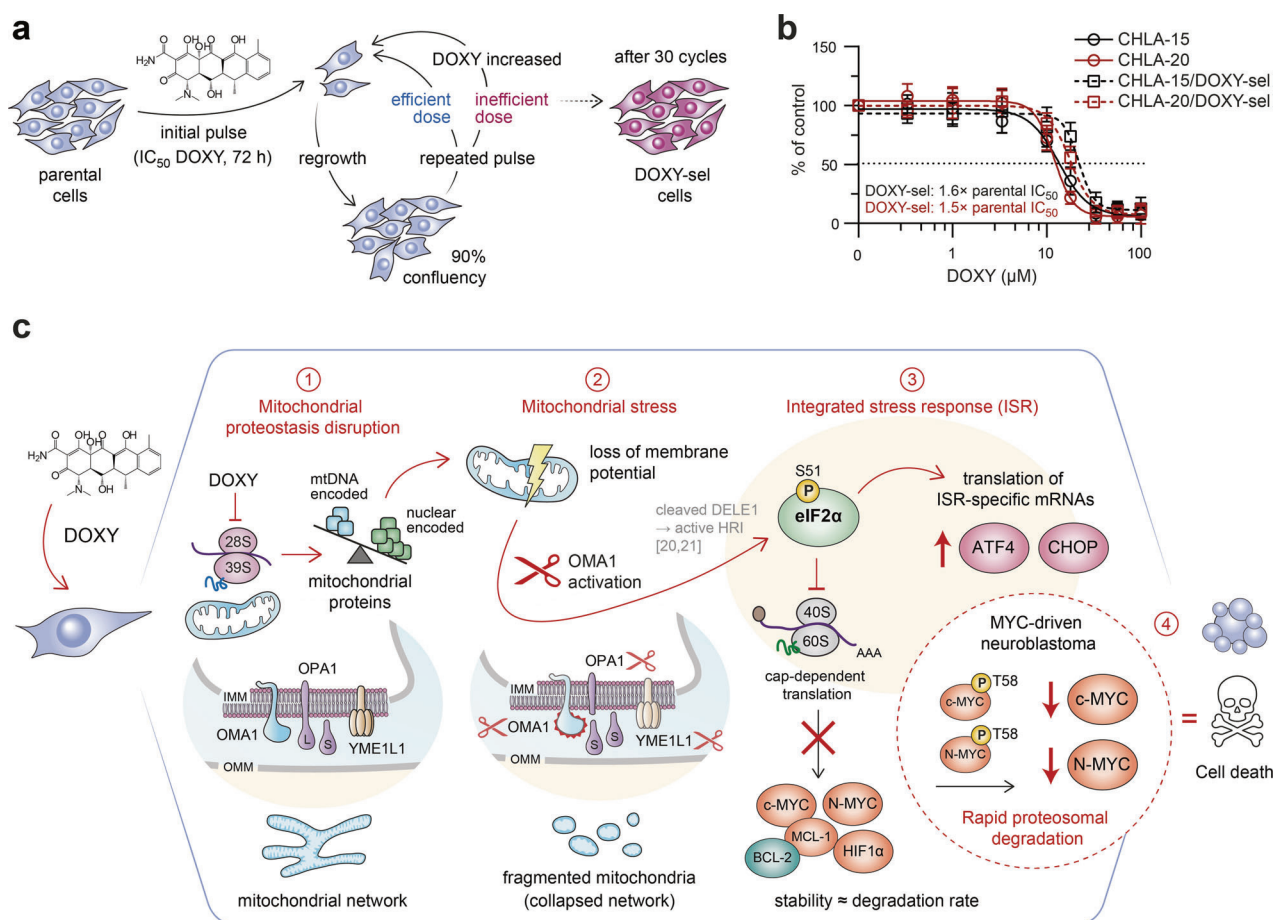
Fig. 8 Inhibiting mitochondrial translation does not induce clinically relevant resistance and offers a promising therapeutic strategy for MYC-driven neuroblastoma. a A schematic overview of the pulsed-selection strategy mimicking the chemotherapy cycles in the clinic. Parental cells CHLA-15 and CHLA-20 were repeatedly exposed to gradually increasing concentrations of DOXY, starting from IC_{50} (determined for each cell line by MTT assay upon 72-h treatment) as follows: 3 cycles of IC_{50}, followed by 3 cycles of 1.5-fold IC_{50} and finally 2-fold IC_{50} that remained highly efficient for additional 24 cycles. In each cycle, cells were treated for 72 h and let to regrow to approx. 90% confluency in fresh drug-free culture media before another round of DOXY treatment. **b** The sensitivity of parental cells and established DOXY-selected cells (CHLA-15/DOXY-sel and CHLA-20/DOXY-sel) to DOXY was compared by MTT cell viability assay after 72 h of treatment. Data are presented as mean ± SD, biological $n = 3$, technical $n = 3$. **c** A model summarizing synthetic lethal effects induced by inhibition of mitochondrial translation in MYC-driven neuroblastoma. Blocking mitochondrial ribosomes by DOXY disrupts mitochondrial proteostasis (1) which impairs mitochondrial function and leads to the mitochondrial stress-induced activation of OMA1 (2). Activated OMA1 mediates OPA1 cleavage, eventually resulting in collapsed mitochondrial network, and relays mitochondrial stress directly via the mitochondrial ISR without involving ER stress signaling (3). Besides preferential translation of ISR-specific mRNAs, attenuated cap-dependent translation leads to downregulation of short-lived proteins primed for rapid degradation, including p-c-MYC(T58) and p-N-MYC(T58), which sensitizes MYC-driven neuroblastoma to cell death induced by the inhibition of mitochondrial translation (4).

The list of antibodies used, including dilutions and respective blocking agents, is provided in Supplementary Table 4. Chemiluminescent detection was performed following a 5-min incubation with ECL™ Prime Western Blotting Detection Reagent (#RPN2236, Cytiva, Marlborough, MA, USA) using either Azure C600 imaging system (Azure Biosystems, Dublin, CA, USA) or light sensitive films (#CP-BU NEW 100 NIF, Agfa, Mortsel, Belgium).

Densitometric analysis of western blotting images was done using gel analysis tool in ImageJ (Fiji) software (NIH, Bethesda, MD, USA), version 2.1.0/1.53c. The signal of a protein of interest was normalized to that of a loading control, α-tubulin, β-actin, or GAPDH, detected on the same gel. For all relevant figures, original uncropped blots including all replicates are provided as supplementary Original Data file.

Immunostaining
Cells were seeded on coverslips coated with Matrigel (#734-1440, Corning). After the incubation period, the coverslips were rinsed by PBS and cells were fixed by 3% paraformaldehyde (#158127, Sigma-Aldrich). The cells were then permeabilized using 0.2% Triton X-100 (#04807423, MP Biomedicals, Irvine, CA, USA) for 1 min and blocking was performed by 3% bovine serum albumin (#A7906, Sigma-Aldrich) for 10 min at RT. The

primary and secondary antibodies (Supplementary Table 4) were diluted in blocking solution. The incubation with antibodies lasted for at least 60 min. Nuclei were stained by TO-PRO3 (#T3605, Invitrogen, Carlsbad, CA, USA). The cells were mounted by ProLong™ Diamond Antifade (#P36961, Invitrogen) and imaged using Leica SP8 confocal microscope (Leica, Wetzlar, Germany). Z-stacked images were captured and processed as maximum intensity projections using software LAS X (Leica, 3.4.218368).

Mitochondrial morphology analysis
Mitochondrial morphology was determined from maximum intensity projection of z-stack confocal images of TOMM20 fluorescence channel using ImageJ (Fiji) plug-in tool MiNA (Mitochondrial Network Analysis) [79]. The pre-processing parameters were applied as follows: 3rd-order median filter with radius 1; 1st-order unsharp mask with radius 2 and mask weight 0.9; contrast enhancement using 2nd-order CLAHE with block size 127 pixels, histogram bins 256 and maximum slope 3.

Flow cytometry
For all experiments, cells were harvested using Accutase (#LM-T1735, Biosera) and diluted in PBS with 3% fetal bovine serum (#FB-1101, Biosera)

and 2 mM EDTA (#ED2SS, Sigma-Aldrich) and immediately processed for measurements using CytoFLEX S flow cytometer (Beckman Coulter, Brea, CA, USA). Cell viability was measured following 15-min incubation with 5 nM SYTOX™ Red Dead Cell Stain (#S34859, Invitrogen) on ice as per manufacturer's instructions.

Mitochondrial membrane potential was assessed by 10 μg/ml JC-1 Probe (#65-0851-38, Invitrogen) after 10-min incubation at 37 °C. Fluorescence of JC-1 monomers and aggregates was excited by 488 nm laser and detected using FITC (525/40) and ECD (610/20) channels, respectively. To eliminate the spillover signal of JC-1 monomers marking depolarized mitochondria into ECD channel, fluorescence compensation was performed as previously described [80].

To analyze DOXY absorption by neonatal dermal fibroblasts, NDF-3 cells were treated with different concentrations of DOXY for 72 h. DOXY fluorescence was excited by 405 nm laser and detected using the KO525 (550/40) channel [81].

RT-qPCR
RNA isolation, reverse transcription, and qPCR were performed as previously described [78]. The list of primer sequences used is provided in Supplementary Table 5. The qPCR reactions were performed in technical triplicates.

Statistical analysis
All experiments were replicated at least three times, as detailed in the figure legends. For violin plots and bar graphs, individual data points show independent biological replicates. For all violin plots, median and quartiles are shown. Bar graphs and line graphs are presented as mean ± standard deviation (SD). Statistical analysis was performed using GraphPad Prism 8.0.2. software. Unpaired two-tailed Student's t-test was applied when comparing 2 groups, otherwise one-way ANOVA followed by Tukey's multiple comparison test was used, assuming normal data distribution and similar variance between the compared groups. Linear correlation between 2 datasets was tested by Pearson correlation coefficient (r). p values < 0.05 were considered statistically significant; $*p < 0.05$, $**p < 0.01$, $***p < 0.001$, $\#p < 0.0001$.

DATA AVAILABILITY
The data analyzed during this study are included in this published article and the supplemental data files. Additional supporting data are available from the corresponding author upon reasonable request.

REFERENCES
1. Skoda J, Borankova K, Jansson PJ, Huang MLH, Veselska R, Richardson DR. Pharmacological targeting of mitochondria in cancer stem cells: an ancient organelle at the crossroad of novel anti-cancer therapies. Pharm Res. 2019;139:298–313.
2. Guerra F, Arbini AA, Moro L. Mitochondria and cancer chemoresistance. Biochim Biophys Acta Bioenerg. 2017;1858:686–99.
3. Bock FJ, Tait SWG. Mitochondria as multifaceted regulators of cell death. Nat Rev Mol Cell Biol. 2020;21:85–100.
4. Wang LL, Teshiba R, Ikegaki N, Tang XX, Naranjo A, London WB, et al. Augmented expression of MYC and/or MYCN protein defines highly aggressive MYC-driven neuroblastoma: a Children's Oncology Group study. Br J Cancer. 2015;113:57–63.
5. Irwin MS, Naranjo A, Zhang FF, Cohn SL, London WB, Gastier-Foster JM, et al. Revised neuroblastoma risk classification system: a report from the Children's Oncology Group. J Clin Oncol. 2021;39:3229–41.
6. Graves JA, Wang YD, Sims-Lucas S, Cherok E, Rothermund K, Branca MF, et al. Mitochondrial structure, function and dynamics are temporally controlled by c-Myc. PLoS ONE. 2012;7:13.
7. Oran AR, Adams CM, Zhang XY, Gennaro VJ, Pfeiffer HK, Mellert HS, et al. Multi-focal control of mitochondrial gene expression by oncogenic MYC provides potential therapeutic targets in cancer. Oncotarget. 2016;7:72395–414.
8. Zeineldin M, Federico S, Chen X, Fan YP, Xu BS, Stewart E, et al. MYCN amplification and ATRX mutations are incompatible in neuroblastoma. Nat Commun. 2020;11:20.
9. Popay TM, Wang J, Adams CM, Howard GC, Codreanu SG, Sherrod SD, et al. MYC regulates ribosome biogenesis and mitochondrial gene expression programs through its interaction with host cell factor-1. eLife. 2021;10:39.
10. Oliynyk G, Ruiz-Perez MV, Sainero-Alcolado L, Dzieran J, Zirath H, Gallart-Ayala H, et al. MYCN-enhanced oxidative and glycolytic metabolism reveals vulnerabilities for targeting neuroblastoma. iScience. 2019;21:188–204.
11. Camarda R, Zhou AY, Kohnz RA, Balakrishnan S, Mahieu C, Anderton B, et al. Inhibition of fatty acid oxidation as a therapy for MYC-overexpressing triple-negative breast cancer. Nat Med. 2016;22:427–32.
12. Gao P, Tchernyshyov I, Chang TC, Lee YS, Kita K, Ochi T, et al. c-Myc suppression of miR-23a/b enhances mitochondrial glutaminase expression and glutamine metabolism. Nature. 2009;458:762–U100.
13. Coku J, Booth DM, Skoda J, Pedrotty MC, Vogel J, Liu KN, et al. Reduced ER-mitochondria connectivity promotes neuroblastoma multidrug resistance. EMBO J. 2022;41:20.
14. Viale A, Pettazzoni P, Lyssiotis CA, Ying HQ, Sanchez N, Marchesini M, et al. Oncogene ablation-resistant pancreatic cancer cells depend on mitochondrial function. Nature. 2014;514:628–32.
15. Veiga SR, Ge XM, Mercer CA, Hernandez-Alvarez MI, Thomas HE, Hernandez-Losa J, et al. Phenformin-induced mitochondrial dysfunction sensitizes hepatocellular carcinoma for dual inhibition of mTOR. Clin Cancer Res. 2018;24:3767–80.
16. Jiang W, Finniss S, Cazacu S, Xiang C, Brodie Z, Mikkelsen T, et al. Repurposing phenformin for the targeting of glioma stem cells and the treatment of glioblastoma. Oncotarget. 2016;7:56456–70.
17. Xie Q, Wu Q, Horbinski CM, Flavahan WA, Yang K, Zhou W, et al. Mitochondrial control by DRP1 in brain tumor initiating cells. Nat Neurosci. 2015;18:501–10.
18. Vendramin R, Katopodi V, Cinque S, Konnova A, Knezevic Z, Adnane S, et al. Activation of the integrated stress response confers vulnerability to mitoribosome-targeting antibiotics in melanoma. J Exp Med. 2021;218:e20210571.
19. Quirós PM, Mottis A, Auwerx J. Mitonuclear communication in homeostasis and stress. Nat Rev Mol Cell Biol. 2016;17:213–26.
20. Guo XY, Aviles G, Liu Y, Tian RL, Unger BA, Lin YHT, et al. Mitochondrial stress is relayed to the cytosol by an OMA1-DELE1-HRI pathway. Nature. 2020;579:427–32.
21. Fessler E, Eckl EM, Schmitt S, Mancilla IA, Meyer-Bender MF, Hanf M, et al. A pathway coordinated by DELE1 relays mitochondrial stress to the cytosol. Nature. 2020;579:433–7.
22. Keshelava N, Seeger RC, Reynolds CP. Drug resistance in human neuroblastoma cell lines correlates with clinical therapy. Eur J Cancer. 1997;33:2002–6.
23. Shibue T, Weinberg RA. EMT, CSCs, and drug resistance: the mechanistic link and clinical implications. Nat Rev Clin Oncol. 2017;14:611–29.
24. Skoda J, Neradil J, Zambo IS, Nunukova A, Macsek P, Borankova K, et al. Serial Xenotransplantation in NSG Mice Promotes a Hybrid Epithelial/Mesenchymal Gene Expression Signature and Stemness in Rhabdomyosarcoma Cells. Cancers. 2020;12:24.
25. Tang SC, Nguyen LN, Sparidans RW, Wagenaar E, Beijnen JH, Schinkel AH. Increased oral availability and brain accumulation of the ALK inhibitor crizotinib by coadministration of the P-glycoprotein (ABCB1) and breast cancer resistance protein (ABCG2) inhibitor elacridar. Int J Cancer. 2014;134:1484–94.
26. Yao CH, Liu GY, Wang R, Moon SH, Gross RW, Patti GJ. Identifying off-target effects of etomoxir reveals that carnitine palmitoyltransferase I is essential for cancer cell proliferation independent of β-oxidation. PLoS Biol. 2018;16:e2003782.
27. Raud B, Roy DG, Divakaruni AS, Tarasenko TN, Franke R, Ma EH, et al. Etomoxir actions on regulatory and memory T cells are independent of Cpt1a-mediated fatty acid oxidation. Cell Metab. 2018;28:504–515.e507.
28. Di Magno L, Manni S, Di Pastena F, Coni S, Macone A, Cairoli S, et al. Phenformin inhibits hedgehog-dependent tumor growth through a complex I-independent redox/corepressor module. Cell Rep. 2020;30:1735–1752.e1737.
29. García Rubiño ME, Carrillo E, Ruiz Alcalá G, Domínguez-Martín A, Marchal JA, Boulaiz H. Phenformin as an anticancer agent: challenges and prospects. Int J Mol Sci. 2019;20:3316.
30. Baxter BT, Pearce WH, Waltke EA, Littooy FN, Hallett JW, Kent KC, et al. Prolonged administration of doxycycline in patients with small asymptomatic abdominal aortic aneurysms: Report of a prospective (Phase II) multicenter study. J Vasc Surg. 2002;36:1–12.
31. Prall AK, Longo GM, Mayhan WG, Waltke EA, Fleckten B, Thompson RW, et al. Doxycycline in patients with abdominal aortic aneurysms and in mice: comparison of serum levels and effect on aneurysm growth in mice. J Vasc Surg. 2002;35:923–8.
32. Todd SR, Dahlgren FS, Traeger MS, Beltrán-Aguilar ED, Marianos DW, Hamilton C, et al. No visible dental staining in children treated with doxycycline for suspected Rocky Mountain Spotted Fever. J Pediatr. 2015;166:1246–51.
33. Pöyhönen H, Nurmi M, Peltola V, Alaluusua S, Ruuskanen O, Lähdesmäki T. Dental staining after doxycycline use in children. J Antimicrob Chemother. 2017;72:2887–90.
34. Lima T, Li TY, Mottis A, Auwerx J. Pleiotropic effects of mitochondria in aging. Nat Aging. 2022;2:199–213.

35. Moullan N, Mouchiroud L, Wang X, Ryu D, Williams EG, Mottis A, et al. Tetracyclines disturb mitochondrial function across eukaryotic models: a call for caution in biomedical research. Cell Rep. 2015;10:1681–91.

36. Houtkooper RH, Mouchiroud L, Ryu D, Moullan N, Katsyuba E, Knott G, et al. Mitonuclear protein imbalance as a conserved longevity mechanism. Nature. 2013;497:451–7.

37. Skrtic M, Sriskanthadevan S, Jhas B, Gebbia M, Wang X, Wang Z, et al. Inhibition of mitochondrial translation as a therapeutic strategy for human acute myeloid leukemia. Cancer Cell. 2011;20:674–88.

38. Wei SJ, Nguyen TH, Yang IH, Mook DG, Makena MR, Verlekar D, et al. MYC transcription activation mediated by OCT4 as a mechanism of resistance to 13-cisRA-mediated differentiation in neuroblastoma. Cell Death Dis. 2020;11:20.

39. Llombart V, Mansour MR. Therapeutic targeting of "undruggable" MYC. EBioMedicine. 2022;75:103756.

40. Ni HM, Williams JA, Ding WX. Mitochondrial dynamics and mitochondrial quality control. Redox Biol. 2015;4:6–13.

41. Sprenger HG, Langer T. The good and the bad of mitochondrial breakups. Trends Cell Biol. 2019;29:888–900.

42. Goldsmith KC, Gross M, Peirce S, Luyindula D, Liu X, Vu A, et al. Mitochondrial Bcl-2 family dynamics define therapy response and resistance in neuroblastoma. Cancer Res. 2012;72:2565–77.

43. Bierbrauer A, Jacob M, Vogler M, Fulda S. A direct comparison of selective BH3-mimetics reveals BCL-X(L), BCL-2 and MCL-1 as promising therapeutic targets in neuroblastoma. Br J Cancer. 2020;122:1544–51.

44. Rainbolt TK, Lebeau J, Puchades C, Wiseman RL. Reciprocal degradation of YME1L and OMA1 adapts mitochondrial proteolytic activity during stress. Cell Rep. 2016;14:2041–9.

45. Anderson NS, Haynes CM. Folding the mitochondrial UPR into the integrated stress response. Trends Cell Biol. 2020;30:428–39.

46. Baker MJ, Lampe PA, Stojanovski D, Korwitz A, Anand R, Tatsuta T, et al. Stress-induced OMA1 activation and autocatalytic turnover regulate OPA1-dependent mitochondrial dynamics. EMBO J. 2014;33:578–93.

47. Gilkerson R, De La Torre P, St Vallier S. Mitochondrial OMA1 and OPA1 as gatekeepers of organellar structure/function and cellular stress response. Front Cell Dev Biol. 2021;9:626117.

48. Rainbolt TK, Saunders JM, Wiseman RL. YME1L degradation reduces mitochondrial proteolytic capacity during oxidative stress. EMBO Rep. 2015;16:97–106.

49. Herzig S, Shaw RJ. AMPK: guardian of metabolism and mitochondrial homeostasis. Nat Rev Mol Cell Biol. 2018;19:121–35.

50. Ito K, Hirao A, Arai F, Takubo K, Matsuoka S, Miyamoto K, et al. Reactive oxygen species act through p38 MAPK to limit the lifespan of hematopoietic stem cells. Nat Med. 2006;12:446–51.

51. Pakos-Zebrucka K, Koryga I, Mnich K, Ljujic M, Samali A, Gorman AM. The integrated stress response. EMBO Rep. 2016;17:1374–95.

52. Paul I, Ahmed SF, Bhowmik A, Deb S, Ghosh MK. The ubiquitin ligase CHIP regulates c-Myc stability and transcriptional activity. Oncogene. 2013;32:1284–95.

53. Bonvini P, Nguyen P, Trepel J, Neckers LM. In vivo degradation of N-myc in neuroblastoma cells is mediated by the 26S proteasome. Oncogene. 1998;16:1131–9.

54. Berra E, Roux D, Richard DE, Pouysségur J. Hypoxia-inducible factor-1 alpha (HIF-1 alpha) escapes O(2)-driven proteasomal degradation irrespective of its subcellular localization: nucleus or cytoplasm. EMBO Rep. 2001;2:615–20.

55. Slomp A, Moesbergen LM, Eldering E, Kersten MJ, Minnema MC, Peperzak V. Phosphatase PP2A enhances MCL-1 protein half-life in multiple myeloma cells. Cell Death Dis. 2021;12:229.

56. Rooswinkel RW, van de Kooij B, de Vries E, Paauwe M, Braster R, Verheij M, et al. Antiapoptotic potency of Bcl-2 proteins primarily relies on their stability, not binding selectivity. Blood. 2014;123:2806–15.

57. Franch HA, Sooparb S, Du J, Brown NS. A mechanism regulating proteolysis of specific proteins during renal tubular cell growth. J Biol Chem. 2001;276:19126–31.

58. Sears R, Nuckolls F, Haura E, Taya Y, Tamai K, Nevins JR. Multiple Ras-dependent phosphorylation pathways regulate Myc protein stability. Genes Dev. 2000;14:2501–14.

59. Zyryanova AF, Kashiwagi K, Rato C, Harding HP, Crespillo-Casado A, Perera LA, et al. ISRIB blunts the integrated stress response by allosterically antagonising the inhibitory effect of phosphorylated eIF2 on eIF2B. Mol Cell. 2021;81:88–103.e106.

60. Otto T, Horn S, Brockmann M, Eilers U, Schüttrumpf L, Popov N, et al. Stabilization of N-Myc is a critical function of Aurora A in human neuroblastoma. Cancer Cell. 2009;15:67–78.

61. Lutz W, Stöhr M, Schürmann J, Wenzel A, Löhr A, Schwab M. Conditional expression of N-myc in human neuroblastoma cells increases expression of alpha-prothymosin and ornithine decarboxylase and accelerates progression into S-phase early after mitogenic stimulation of quiescent cells. Oncogene 1996;13:803–12.

62. Cimmino F, Pezone L, Avitabile M, Acierno G, Andolfo I, Capasso M, et al. Inhibition of hypoxia inducible factors combined with all-trans retinoic acid treatment enhances glial transdifferentiation of neuroblastoma cells. Sci Rep. 2015;5:15.

63. Costa-Mattioli M, Walter P. The integrated stress response: from mechanism to disease. Science. 2020;368:eaat5314.

64. Qing GL, Li B, Vu A, Skuli N, Walton ZE, Liu XY, et al. ATF4 regulates MYC-mediated neuroblastoma cell death upon glutamine deprivation. Cancer Cell. 2012;22:631–44.

65. Bragado P, Armesilla A, Silva A, Porras A. Apoptosis by cisplatin requires p53 mediated p38 alpha MAPK activation through ROS generation. Apoptosis. 2007;12:1733–42.

66. Chen J, Chen JQ, Cheng YH, Fu YF, Zhao HZ, Tang MY, et al. Mesenchymal stem cell-derived exosomes protect beta cells against hypoxia-induced apoptosis via miR-21 by alleviating ER stress and inhibiting p38 MAPK phosphorylation. Stem Cell Res Ther. 2020;11:12.

67. Ibraheem K, Yhmed AMA, Qayyum T, Bryan NP, Georgopoulos NT. CD40 induces renal cell carcinoma-specific differential regulation of TRAF proteins, ASK1 activation and JNK/p38-mediated, ROS-dependent mitochondrial apoptosis. Cell Death Discov. 2019;5:14.

68. Wang XZ, Ron D. Stress-induced phosphorylation and activation of the transcription factor CHOP (GADD153) by p38 MAP kinase. Science. 1996;272:1347–9.

69. Sari FR, Widyantoro B, Thandavarayan RA, Harima M, Lakshmanan AP, Zhang SS, et al. Attenuation of CHOP-mediated myocardial apoptosis in pressure-overloaded dominant negative p38 alpha mitogen-activated protein kinase mice. Cell Physiol Biochem. 2011;27:487–96.

70. Lopez-Crisosto C, Diaz-Vegas A, Castro PF, Rothermel BA, Bravo-Sagua R, Lavandero S. Endoplasmic reticulum-mitochondria coupling increases during doxycycline-induced mitochondrial stress in HeLa cells. Cell Death Dis. 2021;12:12.

71. Matsumoto T, Uchiumi T, Monji K, Yagi M, Setoyama D, Amamoto R, et al. Doxycycline induces apoptosis via ER stress selectively to cells with a cancer stem cell-like properties: importance of stem cell plasticity. Oncogenesis. 2017;6:397.

72. Mortison JD, Schenone M, Myers JA, Zhang ZY, Chen LF, Ciarlo C, et al. Tetracyclines modify translation by targeting key human rRNA substructures. Cell Chem Biol. 2018;25:1506–1518.e13.

73. Sanchez-Burgos I, Navarro-Gonzalez B, Garcia-Martin S, Sirozh O, Mota-Pino J, Fueyo-Marcos E, et al. Activation of the integrated stress response is a vulnerability for multidrug-resistant FBXW7-deficient cells. EMBO Mol Med. 2022;14:18.

74. D'Andrea A, Gritti I, Nicoli P, Giorgio M, Doni M, Conti A, et al. The mitochondrial translation machinery as a therapeutic target in Myc-driven lymphomas. Oncotarget. 2016;7:72415–30.

75. Lutterbach B, Hann SR. Hierarchical phosphorylation at N-terminal transformation-sensitive sites in c-Myc protein is regulated by mitogens and in mitosis. Mol Cell Biol. 1994;14:5510–22.

76. Sjostrom SK, Finn G, Hahn WC, Rowitch DH, Kenney AM. The Cdk1 complex plays a prime role in regulating N-myc phosphorylation and turnover in neural precursors. Dev Cell. 2005;9:327–38.

77. Young L, Sung J, Stacey G, Masters JR. Detection of Mycoplasma in cell cultures. Nat Protoc. 2010;5:929–34.

78. Kameneva P, Melnikova VI, Kastriti ME, Kurtova A, Kryukov E, Murtazina A, et al. Serotonin limits generation of chromaffin cells during adrenal organ development. Nat Commun. 2022;13:21.

79. Valente AJ, Maddalena LA, Robb EL, Moradi F, Stuart JA. A simple ImageJ macro tool for analyzing mitochondrial network morphology in mammalian cell culture. Acta Histochem. 2017;119:315–26.

80. Perelman A, Wachtel C, Cohen M, Haupt S, Shapiro H, Tzur A. JC-1: alternative excitation wavelengths facilitate mitochondrial membrane potential cytometry. Cell Death Dis. 2012;3:7.

81. Khader H, Solodushko V, Al-Mehdi AB, Audia J, Fouty B. Overlap of doxycycline fluorescence with that of the redox-sensitive intracellular reporter roGFP. J Fluoresc. 2014;24:305–11.

AUTHOR CONTRIBUTIONS

FUNDING

COMPETING INTERESTS

The authors declare no competing interests.

ETHICS APPROVAL

The study was conducted according to the guidelines of the Declaration of Helsinki, and approved by the Research Ethics Committee of the Masaryk University (approval no. EKV-2019-025). All noncommercial cell lines were derived from tumor tissues with written informed consent obtained from patients or their legal guardians. The animal experiments were approved by the Institutional Animal Care and Use Committee of the Masaryk University and registered by the Ministry of Education, Youth and Sports of the Czech Republic (ref. no. MSMT-4408/2016-6) as required by national legislation.

ADDITIONAL INFORMATION

Supplementary information The online version contains supplementary material available at https://doi.org/10.1038/s41419-023-06278-x.

Correspondence and requests for materials should be addressed to Jan Skoda.

Reprints and permission information is available at http://www.nature.com/reprints

Publisher's note Springer Nature remains neutral with regard to jurisdictional claims in published maps and institutional affiliations.

APPENDIX 3

Çoku J, Booth DM, **Skoda J**, Pedrotty MC, Vogel J, Liu K, Vu A, Carpenter EL, Ye JC, Chen MA, Dunbar P, Scadden E, Yun TD, Nakamaru-Ogiso E, Area-Gomez E, Li Y, Goldsmith KC, Reynolds CP, Hajnoczky G, Hogarty MD. Reduced ER-mitochondria connectivity promotes neuroblastoma multidrug resistance. *EMBO Journal*. 2022;41(8):e108272. (JCR 2022, IF = 11.4; T10 - Biochemistry & Molecular Biology)

Article

Reduced ER–mitochondria connectivity promotes neuroblastoma multidrug resistance

Jorida Çoku[1], David M Booth[2], Jan Skoda[3,4] (iD), Madison C Pedrotty[5,†], Jennifer Vogel[6,‡], Kangning Liu[5], Annette Vu[5], Erica L Carpenter[7], Jamie C Ye[5], Michelle A Chen[5,§], Peter Dunbar[5,¶], Elizabeth Scadden[5,#] (iD), Taekyung D Yun[8], Eiko Nakamaru-Ogiso[9,10], Estela Area-Gomez[8] (iD), Yimei Li[11], Kelly C Goldsmith[12], C Patrick Reynolds[13], Gyorgy Hajnoczky[2] (iD) & Michael D Hogarty[5,10,*] (iD)

Abstract

Most cancer deaths result from progression of therapy resistant disease, yet our understanding of this phenotype is limited. Cancer therapies generate stress signals that act upon mitochondria to initiate apoptosis. Mitochondria isolated from neuroblastoma cells were exposed to tBid or Bim, death effectors activated by therapeutic stress. Multidrug-resistant tumor cells obtained from children at relapse had markedly attenuated Bak and Bax oligomerization and cytochrome c release (surrogates for apoptotic commitment) in comparison with patient-matched tumor cells obtained at diagnosis. Electron microscopy identified reduced ER–mitochondria-associated membranes (MAMs; ER–mitochondria contacts, ERMCs) in therapy-resistant cells, and genetically or biochemically reducing MAMs in therapy-sensitive tumors phenocopied resistance. MAMs serve as platforms to transfer Ca^{2+} and bioactive lipids to mitochondria. Reduced Ca^{2+} transfer was found in some but not all resistant cells, and inhibiting transfer did not attenuate apoptotic signaling. In contrast, reduced ceramide synthesis and transfer was common to resistant cells and its inhibition induced stress resistance. We identify ER–mitochondria-associated membranes as physiologic regulators of apoptosis via ceramide transfer and uncover a previously unrecognized mechanism for cancer multidrug resistance.

Introduction

Over 600,000 people die of cancer each year in the USA, most with progression of disease that is resistant to available treatments. Our understanding of the mechanisms underlying broad resistance to diverse drug classes and therapeutic modalities includes altered drug transport into or out of the cancer cell, such as from increased activity of ATP-binding cassette transporters (Holohan *et al*, 2013), and mutations in genotoxic response genes like *TP53* (Olivier *et al*, 2010). The former have not been shown to contribute to resistance *in vivo* (Cripe *et al*, 2010) and does not explain resistance to drugs that are not substrates for such transporters, and the latter does not explain therapy resistance in tumors with retained p53 activity. More recently, the focus has shifted to studying resistance to inhibitors of oncogenic kinases, with secondary mutations in the drug target, activation of bypass signals, and cellular plasticity identified as causal, yet even here a large proportion of acquired resistance remains

1 Cancer Biology Program, Perelman School of Medicine, University of Pennsylvania, Philadelphia, PA, USA
2 MitoCare Center, Department of Pathology, Anatomy & Cell Biology, Thomas Jefferson University, Philadelphia, PA, USA
3 Department of Experimental Biology, Faculty of Science, Masaryk University, Brno, Czech Republic
4 International Clinical Research Center, St. Anne's University Hospital, Brno, Czech Republic
5 Division of Oncology and Center for Childhood Cancer Research, The Children's Hospital of Philadelphia, Philadelphia, PA, USA
6 Department of Radiation Oncology, Perelman School of Medicine, University of Pennsylvania, Philadelphia, PA, USA
7 Department of Medicine, Perelman School of Medicine, University of Pennsylvania, Philadelphia, PA, USA
8 Department of Neurology, Columbia University Irving Medical Center, New York, NY, USA
9 Mitochondrial Medicine Frontier Program, Division of Human Genetics, The Children's Hospital of Philadelphia, Philadelphia, PA, USA
10 Department of Pediatrics, Perelman School of Medicine, University of Pennsylvania, Philadelphia, PA, USA
11 Department of Biostatistics, Perelman School of Medicine, University of Pennsylvania, Philadelphia, PA, USA
12 Department of Pediatrics, Emory University School of Medicine, Atlanta, GA, USA
13 TTUHSC Cancer Center, Texas Tech University Health Sciences Center, Lubbock, TX, USA
 *Corresponding author. Tel: +1 215 590 3931; Fax: +1 215 590 3770; E-mail: hogartym@chop.edu
 †M.C. Pedrotty is deceased (see acknowledgements)
 ‡Present address: St. Francis Cancer Center, Bon Secours, Greenville, SC, USA
 §Present address: Howard University College of Medicine, Washington, DC, USA
 ¶Present address: Departments of Pediatrics and Medicine, Brigham and Women's Hospital, Boston, MA, USA
 #Present address: Center for Regenerative Medicine, Massachusetts General Hospital, Boston, MA, USA

unexplained (Katayama *et al*, 2012; Chong & Janne, 2013; Lito *et al*, 2013; Lord & Ashworth, 2013; Hugo *et al*, 2015; Wilson *et al*, 2015). Our incomplete understanding of the contributors to therapy resistance remains a principal barrier to improving cancer outcomes.

We used the highly lethal childhood tumor, neuroblastoma, as a model system to investigate therapy resistance. Children with high-risk neuroblastoma are treated with intensive chemoradiotherapy, stem cell rescue, surgery, and immunotherapy (Pinto *et al*, 2015). Many patients have metastatic disease at diagnosis, yet the tumors are chemosensitive and respond to treatment, including complete responses. Still, half of all patients subsequently relapse with lethal therapy-resistant disease (Keshelava *et al*, 1997, 1998; Matthay *et al*, 2009). To study emergent therapy resistance, we established tumor cell lines from the same patients at diagnosis prior to treatment, and again at the time of relapse during or after treatment, providing near-isogenic tumor models in which post-relapse tumors demonstrate therapy resistance acquired *in situ* in response to multimodal therapy (Keshelava *et al*, 1998). Since mitochondria serve as platforms for integrating cellular stress and survival signals in real time, largely governed by Bcl2 family interactions, we hypothesized they harbor information related to therapeutic stress sensitivity. We used an unbiased assay in which cancer mitochondria are exposed to tBid protein or BimBH3 peptides, death effectors activated downstream of most therapeutic stress (Tan *et al*, 2005; Kim *et al*, 2006; Ren *et al*, 2010; Sarosiek *et al*, 2013a), to define their sensitivity for activating mitochondrial outer membrane permeabilization (MOMP) as a surrogate for apoptotic commitment. We discovered that mitochondria from therapy-resistant tumors have markedly attenuated MOMP responses in comparison with patient-matched therapy-sensitive tumors, demonstrating that mitochondrial apoptotic signaling dysfunction arises during the course of clinical therapy and contributes to emergent multidrug resistance.

Many mitochondrial functions, including sensitivity to apoptosis, are regulated by signals derived from endoplasmic reticulum (ER) at contact sites with mitochondria [reviewed in (Rowland & Voeltz, 2012; Csordas *et al*, 2018)]. ER–mitochondria contact sites (ERMCs) consist of a multitude of ER–mitochondria protein bridges that tether the organelles and facilitate inter-organelle communication. Cell fractionation can isolate these specialized ER domains as mitochondria-associated ER membranes (MAMs). For simplicity, we use MAM to refer to both ERMCs and MAMs herein. How cells regulate these contacts is incompletely understood, however, the importance of MAMs in tuning the cross-talk between these dynamic organelle networks is proposed to contribute to many pathophysiologic states, such as diabetes, neurodegeneration, and cancer (Area-Gomez *et al*, 2012; Cali *et al*, 2013; Hedskog *et al*, 2013; Arruda *et al*, 2014). Here, we show that post-relapse tumor cell mitochondria have reduced MAMs (altered numbers, lengths, and gap distances) that directly contribute to their stress resistance, and lead to the multidrug resistance phenotype seen clinically. Depleted MAMs contribute to resistance to chemotherapy, radiotherapy, and molecularly targeted drugs. It acts at a terminal signaling node to imbue cancer cells with resistance to diverse therapy-induced stressors yet is not exclusive to other resistance mechanisms operative upstream. Ca^{2+} transfer that occurs at MAMs is reduced in a subset of multidrug-resistant neuroblastomas but not all, and genetically or biochemically inhibiting this does not attenuate apoptotic signaling. However, synthesis and transfer of the bioactive sphingolipid,

ceramide that is enriched at MAMs, is reduced in all multidrug-resistant neuroblastomas studied and chemical inhibition of this transfer leads to attenuated MOMP. This new framework for understanding therapy resistance may provide opportunities to enhance cancer care, including the measurement of relative resistance by characterizing MAM abundance and proximity, and enabling interventions to restore ER–mitochondrial communication or sphingolipid homeostasis in resistant cancers.

Results

Mitochondria from drug-resistant tumor cells have attenuated apoptotic signal transduction

Optimizing approaches developed by Letai (Deng *et al*, 2007), we isolated mitochondria from paired neuroblastoma cell lines derived from the same patients at diagnosis (DX) before therapy, and at relapse (REL) during or after completion of therapy (Fig 1A). Mitochondria-enriched heavy-membrane fractions from tumor cells were incubated with recombinant truncated Bid or the death-activating BH3 domain peptide of Bim (tBid and BimBH3, respectively) across a range of concentrations. Bid and Bim proteins are direct activators of intrinsic apoptosis liberated by diverse cell stressors to either engage Bak or Bax to induce MOMP and cell death, or be sequestered and neutralized by pro-survival Bcl2 family proteins (Gavathiotis *et al*, 2008; Sarosiek *et al*, 2013a). The sensitivity for release of cytochrome c in response to tBid or BimBH3 reflects a cell's proximity to its apoptotic threshold (Tan *et al*, 2005; Goldsmith *et al*, 2012). By delivering terminal death effectors directly to mitochondria, the assay bypasses the contributions of drug transport, metabolism, target engagement, and transcriptional response. Instead, mitochondrial responses reflect the state of the Bcl2 family and related apoptosis-regulating processes present in the tumor cell at the time of testing [reviewed in (Sarosiek *et al*, 2013b)]. A Bid BH3 domain with substitution of two highly conserved residues served as a negative control and induced release of < 10% of available cytochrome c in all experiments.

Seven DX/REL matched cell line pairs were studied, each pair tested concurrently under identical culture conditions. Six of seven pairs showed attenuated cytochrome c release from tumor cells derived at relapse (Figs 1B and C, and EV1A). For five of the seven pairs, REL mitochondria had reduced cytochrome c release in response to both tBid and BimBH3 in every biological replicate, with both reduced sensitivity for release and reduced maximal release. One pair demonstrated reduced cytochrome c release in response to BimBH3 peptide but not tBid; and one pair showed similar release (CHLA122/CHLA136; maximal release differed < 10% in all but one replicate). Overall, in 41 of 44 (93%) assays with tBid or BimBH3, the mitochondria from post-relapse tumor cells released less cytochrome c than their patient-matched counterparts from the time of diagnosis. Recombinant tBid was more potent at inducing cytochrome c release than BimBH3 peptide (all experiments), and maximal tBid-induced release exceeded that of BimBH3 in 39 of 42 (93%) experiments, despite BimBH3 peptide being used to > 1 log higher concentrations.

Relative cytochrome c release from tumor cell mitochondria was reproducible (Figs 1C and EV1). Mitochondria from CHLA15 (DX)
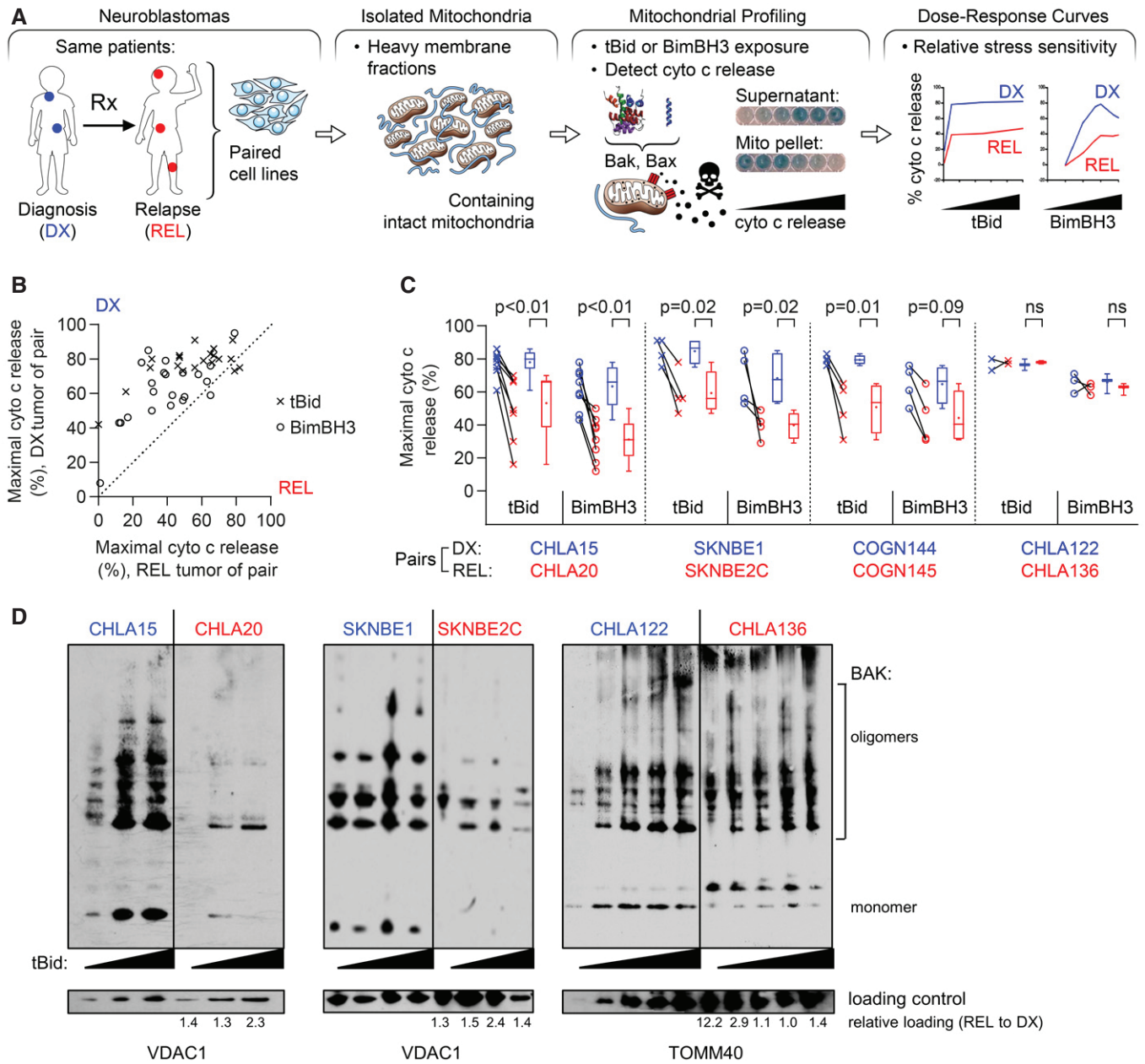
Figure 1. Mitochondria from REL neuroblastomas have attenuated apoptotic responses.

A   Tumor models were derived at DX and REL following treatment. Mitochondria-rich fractions were exposed to tBid or BimBH3 peptide and cytochrome c release measured as a surrogate for apoptotic commitment.

B   Maximal cytochrome c release in response to tBid or BimBH3 peptide for each replicate of a DX/REL tumor pair (1–9 biological replicates per DX/REL pair; $n = 44$ total).

C   Maximal cytochrome c release for all DX/REL pairs with ≥ 3 biological replicates; box-whisker plots summarize data (box 25–75%; belt = median; dot = mean; and whiskers = minimum and maximum values).

D   Bak oligomerization in response to escalating tBid concentration for DX/REL pairs. Relative mitochondrial protein loading per lane is assessed by densitometry, showing ration of loading control in REL lane with patient-matched DX lane at same tBid exposure (no REL lane is underloaded compared to DX lane).

Data information: Statistical analyses in C were performed using an unpaired two-sided Student's *t*-test, with significance $P < 0.05$ (trend $P < 0.10$). Cyto c, cytochrome c; mito, mitochondria.

and CHLA20 (REL) were profiled in 9 biological replicates with both tBid and BimBH3, and maximal cytochrome c release for CHLA15 was greater than CHLA20 in all 18 experiments. The SKNBE1 (DX)/

SKNBE2 (REL) and COGN144 (DX)/COGN145 (REL) pairs were profiled in 4 biological replicates each, and DX tumor mitochondria released more cytochrome c to both tBid and BimBH3 in all 16

experiments. In contrast, CHLA122 (DX) and CHLA136 (REL) showed nearly equivalent cytochrome c release in four of five experiments (in one, DX cells released > 10% more cytochrome c than REL cells in response to BimBH3). In all, maximal cytochrome c release in response to tBid or BimBH3 peptide was significantly higher for DX tumor cells compared with patient-matched REL tumor cells for the CHLA15/CHLA20, SKNBE1/SKNBE2C, and COGN144/COGN145 pairs, consistent with apoptosis resistance at relapse (Table 1). Overall, DX neuroblastomas released > 50% of available cytochrome c in 38 of 43 of experiments (88%) using either tBid or BimBH3 as a stimulus, whereas REL neuroblastomas released > 50% in just 19 of 44 of experiments (43%), further reflecting their attenuated response to stress ($P < 0.01$). Only the CHLA122/CHLA136 pair demonstrated no difference in cytochrome c release in response to tBid or BimBH3.

To confirm that MOMP was being induced by Bak and/or Bax oligomerization in our cytochrome c release assays, we compared their sensitivity to form homo-oligomers in response to increasing concentrations of tBid. Bak sensitivity to tBid, its preferential target (Sarosiek *et al*, 2013a), was reduced in CHLA20 and BE2C mitochondria compared with matched DX cells. Bax oligomerization was also reduced in CHLA20, while CHLA136 did not have differential oligomerization of Bak or Bax in response to tBid (Figs 1D and EV2A).

Cytochrome c release from isolated mitochondria correlates with tumor cell sensitivity to diverse therapeutic stressors

Attenuated mitochondrial responses to tBid and Bim, the stress sentinels activated by chemotherapy (Tan *et al*, 2005; Kim *et al*, 2006; Ren *et al*, 2010; Sarosiek *et al*, 2013a), predicts for reduced cytotoxicity in response to such drugs. We compared sensitivity to chemotherapeutics of different drug classes used to treat neuroblastoma, including cisplatin, mafosfamide, etoposide, and doxorubicin. Etoposide and doxorubicin are substrates for the multidrug resistance protein, P-glycoprotein-1, whereas cisplatin and mafosfamide are not. Both the CHLA15/CHLA20 and SKNBE1/SKNBE2C pairs that had attenuated release of cytochrome c from REL mitochondria, showed relative chemoresistance in REL tumor cells to both P-glycoprotein-1 substrates and non-substrates (Fig 2A; Appendix Fig S1A; Table 1). In contrast, the CHLA122/CHLA136 pair without attenuated mitochondrial release of cytochrome c did not show differential chemosensitivity. Comparing IC_{50} values for DX/REL pairs showed 1.6-fold to 33-fold resistance for CHLA15/CHLA20 (three of four drugs with > 3-fold difference); 4.2-fold to 122-fold for SKNBE1/SKNBE2C (all four drugs with > 3-fold difference); and 1.2-fold to 2.6-fold for CHLA122/CHLA136 (no drugs with > 3-fold difference). We next assessed sensitivity to ionizing radiation as a treatment modality to which there is less cross-resistance than chemotherapy. Radiation bypasses drug transport and metabolism contributions to deliver genotoxic stress that can be quantified as γ-H2AX foci. SKNBE2C (REL) cells had a larger induction of γ-H2AX foci post-radiation (~10-fold compared with ~5-fold for SKNBE1; $P = 0.04$), yet they were 2-fold more radiation resistant (Fig EV3). However, SKNBE2C cells harbor an acquired *TP53* mutation (C135F) contributing to their resistance, and fail to induce p53, p21, or noxa. CHLA20 (REL) cells, however, are *TP53* wild type and were also > 2-fold radiation resistant in comparison with CHLA15 (DX)

cells despite both inducing p53 response genes and deriving equivalent DNA damage, confirming attenuated apoptotic signaling downstream of radiation-induced genotoxic damage (Fig 2B and C).

To determine whether attenuated mitochondrial responses also contribute to resistance to molecularly targeted drugs, we tested Bcl2 inhibitors since their mechanism of activity is localized at mitochondria. We previously showed that CHLA15 (DX) cells are sensitive to Bcl2 inhibitors as they use Bcl2 to sequester Bim and prevent its activation of Bak or Bax (Goldsmith *et al*, 2012). Both CHLA15 (DX) and CHLA20 (REL) cells have Bim sequestered by Bcl2 and the Bcl2/Bclx inhibitor ABT-737 displaces Bim with equal potency, yet CHLA20 cells are > 40-fold more resistant despite the patient the cell line derived from never having been treated with a Bcl2 inhibitor (IC_{50}: CHLA15 = 260 nM, CHLA20 = 11.4 μM; Fig 2 D). In contrast, the CHLA122/CHLA136 pair also have Bim sequestered by Bcl2, but these cells have similar cytochrome c release and Bcl2 inhibitor responses (~1.8-fold IC_{50} difference). We did not test SKNBE1/SKNBE2C cells with ABT-737 as they use Mcl1, rather than Bcl2, to neutralize Bim (Goldsmith *et al*, 2012). We next studied anaplastic lymphoma kinase (Alk) inhibitors since mutations in the *ALK* gene are found in 10–14% of neuroblastomas, and Alk inhibition has anti-tumor activity (Bresler *et al*, 2014). Both CHLA15 (DX) and CHLA20 (REL) cells harbor an *ALK* R1275Q mutation (variant allele frequency of 0.46 and 0.49, respectively). The patient this tumor pair was obtained from had not been treated with an Alk inhibitor, yet REL cells were > 3-fold more resistant to the Alk inhibitors crizotinib, ceritinib, and lorlatinib, without having a secondary resistance-encoding *ALK* mutation (e.g., crizotinib IC_{50}: CHLA15 = 96 nM and CHLA20 = 349 nM; Fig 2E). SKNBE1/SKNBE2C and CHLA122/CHLA136 have wild-type *ALK* and are resistant to Alk inhibitors (Appendix Fig S1B). Therefore, attenuated mitochondrial signaling that arises in response to multimodal therapy *in situ* confers resistance to chemotherapy, radiotherapy, and molecularly targeted drugs (the latter in the absence of prior selective pressure). We next assessed the reverse: whether selection for resistance to a molecularly targeted agent can induce this mitochondrial phenotype. We exposed SH-SY5Y (*ALK* F1174L) and NB1643 (*ALK* R1275Q) cells to escalating concentrations of crizotinib to generate crizotinib-resistant clones, and both demonstrated attenuated MOMP responses to tBid and BimBH3 in the absence of secondary *ALK* mutations, phenocopying REL cells (Fig 2F). In addition, such Alk inhibitor-resistant cells were more resistant to chemotherapy drugs such as etoposide (> 20-fold) and molecularly targeted drugs like Bcl2 inhibitors (> 40-fold; Fig 2G).

Attenuated mitochondrial apoptotic responses are accompanied by reductions in MAMs

We confirmed that loss of Bak or Bax, or upregulation of pro-survival Bcl2-family proteins, were not drivers of attenuated MOMP [Fig EV2B and C and (Goldsmith *et al*, 2012)]. We next compared mitochondrial mass, size, shape, and mitochondrial DNA (mtDNA) from DX and REL pairs, as these have been correlated with apoptotic signaling in other systems. Mitochondrial mass assessed by citrate synthase activity was unchanged in CHLA15 and CHLA20, and reduced in SKNBE2C (relative to SKNBE1) and CHLA136 (relative to CHLA122; Fig EV4A). Mitochondrial DNA content was measured

Table 1. Summary of paired diagnostic (DX) and relapse (REL) neuroblastoma models.

	CHLA15	CHLA20		SKNBE1	SKNBE2C		CHLA122	CHLA136	
Mitochondrial response									
Max % cyto c release, tBid (mean ± SD)	78 ± 8	53 ± 19	$P < 0.01$	85 ± 7	59 ± 11	$P < 0.02$	77 ± 5	78 ± 1	P = ns
Max % cyto c release, BimBH3 (mean ± SD)	63 ± 13	31 ± 12	$P < 0.01$	68 ± 14	40 ± 7	$P < 0.02$	66 ± 6	62 ± 4	P = ns
Tumor cell response (fold-resistance, IC_{50})									
Mafosfamide		3.9			12.9			1.2	
Doxorubicin		33.0			28.6			1.7	
Cisplatin		1.6			4.2			2.6	
Etoposide		3.5			122.0			2.1	
Ionizing Radiation		2.1			2.0			n.d.	
Crizotinib		5.0			n.d.			n.d.	
ABT737		44.0			n.d.			1.8	
Mitochondria									
Number analyzed	196	241		137	160		206	143	
Perimeter, mean (nm)	2,207	1,725	$P < 0.01$	1,653	1,810	$P = 0.06$	1,626	1,454	P = ns
Perimeter, median (nm)	2,055	1,675		1,503	1,725		1,404	1,330	
Circularity, median	0.902	0.920	$P < 0.01$	0.910	0.898	P = ns	0.913	0.905	P = ns
Roundness, median	0.996	0.745	P = ns	0.714	0.692	P = ns	0.676	0.655	P = ns
% with 0 MAMs	18%	32%	$P < 0.01$	18%	40%	$P < 0.01$	17%	8%	$P < 0.01$ (REL fewer)
% with 1 MAMs	39%	39%		37%	35%		33%	34%	
% with 2–3 MAMs	41%	25%	$P < 0.01$	38%	22%	$P < 0.01$	42%	43%	P = ns
% with ≥ 4 MAMs	3%	3%		6%	4%		7%	15%	
%OMM with MAM gap width ≤ 10 nm	0.7%	0.4%	(↓43%)	2.3%	1.1%	(↓52%)	2.1%	2.7%	(↑29%)
%OMM with MAM gap width ≤ 25 nm	2.5%	2.1%	(↓16%)	6.0%	3.5%	(↓42%)	6.1%	6.8%	(↑11%)
%OMM with MAM gap width ≤ 50 nm	6.8%	6.3%	(↓7%)	12.4%	7.6%	(↓39%)	12.8%	14.2%	(↑13%)
%OMM with MAM gap width ≤ 100 nm	16.9%	15.5%	(↓8%)	24.4%	15.2%	(↓38%)	24.0%	25.5%	(↑6%)
MAM									
Number analyzed	267	266		203	154		334	386	
MAMs per mitochondria	1.36	1.10	$P < 0.01$	1.48	0.96	$P < 0.01$	1.62	2.00	$P = 0.01$ (REL more)
MAM frequency (per nm perimeter)	1,651	1,556		1,116	1,880		710	1,134	
%MAM with gap width ≤ 10 nm	18%	12%	$P = 0.05$	30%	21%	$P < 0.01$	36%	39%	P = ns
%MAM with gap width ≤ 25 nm	40%	36%	P = ns	57%	46%	$P < 0.01$	65%	69%	P = ns
%MAM with gap width ≤ 50 nm	70%	63%		80%	73%		86%	93%	
%MAM with gap width ≤ 100 nm	100%	100%		100%	100%		100%	100%	
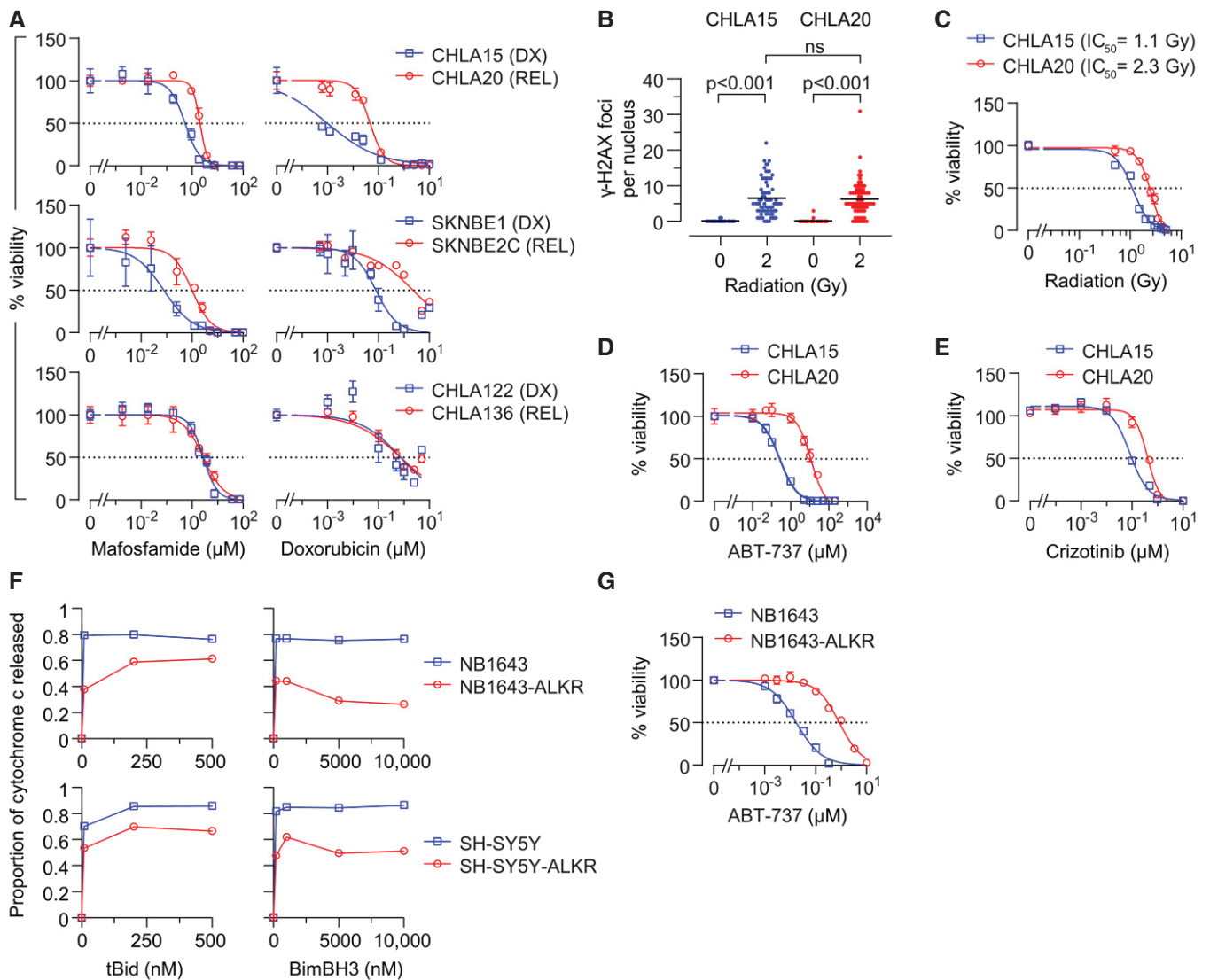
Figure 2. REL neuroblastomas are resistant to multimodal cancer therapeutics.

A   *In vitro* viability curves after 72 h exposure to mafosfamide or doxorubicin. Results are shown for three DX/REL neuroblastoma cell line pairs, two with attenuated cytochrome c release (CHLA15/CHLA20 and SKNBE1/SKNBE2C), and one without (CHLA122/CHLA136).

B   DNA damage induced by 2 Gy ionizing radiation as measured by γ-H2AX foci at 1 h ($n = 53$–77 cell nuclei/condition scored; mean shown); statistical analyses performed using two-tailed Mann–Whitney U test.

C–E   *In vitro* viability for CHLA15 (DX) and CHLA20 (REL) following ionizing radiation at 7 days, 48 h exposure to the Bcl2/Bclx inhibitor, ABT-737, or 120 h exposure to the Alk inhibitor, crizotinib.

F   Cytochrome c release from mitochondria after exposure to tBid or BimBH3 peptide for parental NB1643 and SY5Y cells, in comparison to cells cultured in escalating concentrations of crizotinib until resistant (NB1643-ALKR and SY5Y-ALKR).

G   *In vitro* viability of NB1643 and NB1643-ALKR cells following 72 h exposure to ABT-737.

Data information: For A, C–E, and G, data points are mean and SD from triplicate wells, experiments are representative of at least three biological replicates, dotted line represents 50% viability. For F, data points are mean of duplicate wells (SD < 0.05 at all points) in a representative experiment from at least two biological replicates.

using quantitative PCR for two mitochondrial genes (*MT-CO1* and *MT-ATP6*), each normalized to two nuclear genes (*CFAP410* and *MTTP*) that are disomic in > 85% of neuroblastomas. *TP53* mutant SKNBE2C cells had markedly reduced mtDNA content compared with *TP53* wild-type SKNBE1 cells, consistent with p53 mutation effects on mtDNA content (Park *et al*, 2016). CHLA15/CHLA20 and CHLA122/CHLA136 had less divergent mtDNA quantity with

modest reductions in REL cells at a subset of loci (Fig EV4B). We next used transmission electron micrographs of each cell line to assess mitochondrial size (circumference) and shape (roundness and circularity; Fig 3A–C). These did not differ for the SKNBE1/SKNBE2C and CHLA122/CHLA136 pairs, although there was a trend toward larger mitochondria in SKNBE2C ($P = 0.06$). The CHLA15 (DX) and CHLA20 (REL) pair did differ, with REL cells having
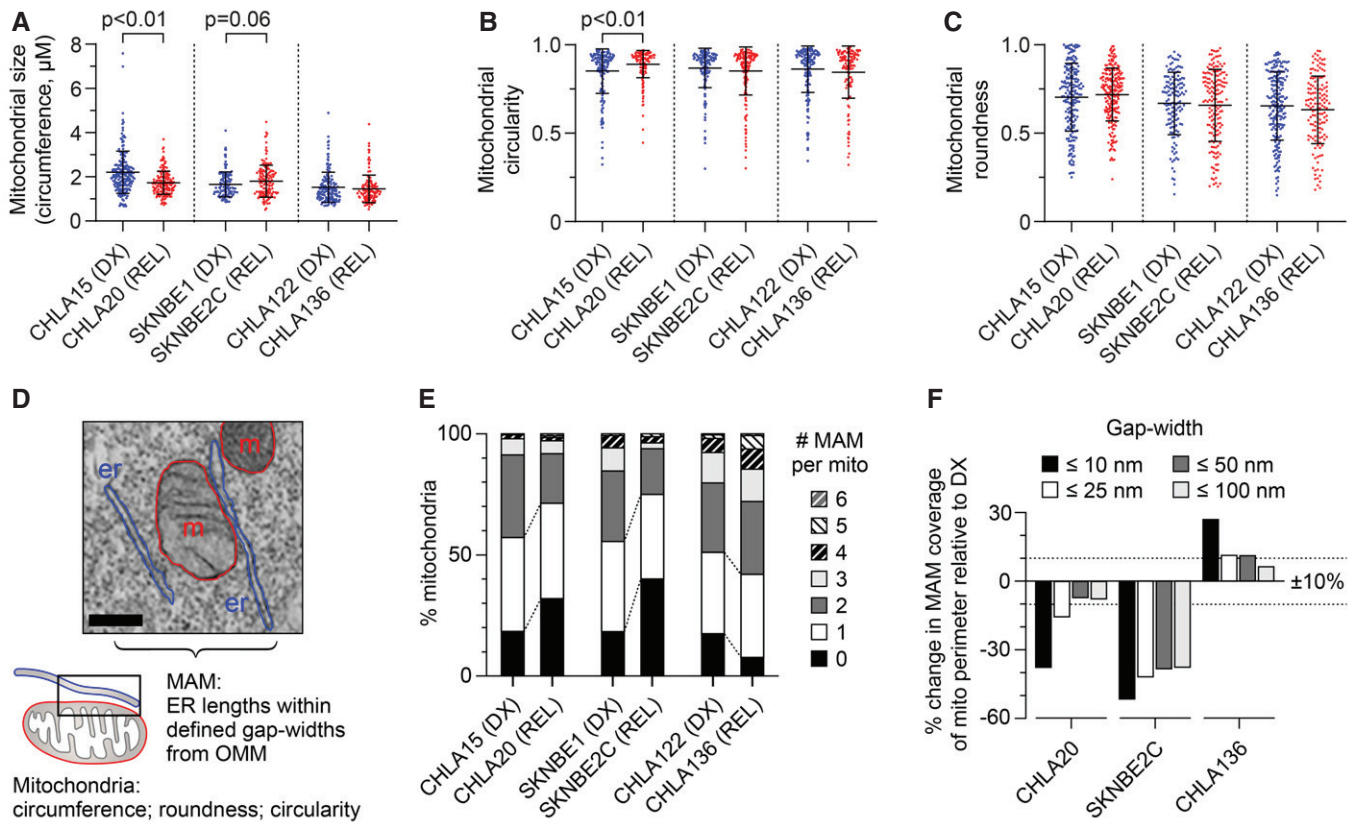
Figure 3. REL neuroblastomas have reduced mitochondria-associated membranes compared with patient-matched tumors from DX.

A–C   Transmission electron microscopy image analysis was used to quantify mitochondrial size, circularity, and roundness in DX/REL neuroblastoma pairs (mean ± SD shown).

D   Electron micrograph illustrating organelle masking of MAM interfaces; scale bar = 500 nm.

E   Proportion of mitochondria with 0–6 or more MAMs are shown for each cell line, as DX/REL pairs.

F   Percentage of mitochondria perimeter with an apposed ER within defined gap widths for DX/REL neuroblastoma cell line pairs; dotted lines denote +10% and −10% change.

Data information: For A–C and E, F, $n = 137$–241 mitochondria per cell line; er, endoplasmic reticulum; m, mitochondria. For A-C, statistical analyses were performed using a two-tailed Mann–Whitney U test, with significance $P < 0.05$ (trend $P < 0.10$).

smaller more circular mitochondria ($P < 0.01$). No feature correlated with mitochondrial cytochrome c release sensitivity across all pairs.

We applied electron microscopy to visualize the mitochondria-enriched heavy-membrane fractions tested in our mitochondrial profiling assays. Non-mitochondria organellar membranes were abundant yet there was an increase in the proportion of mitochondria in fractions from REL cells, despite their reduced cytochrome c release when stimulated (Fig EV4C and D). ER, including MAM, is a major contributor to heavy-membrane fractions. We postulated that fewer ER–mitochondria contacts cause reduced MAM content to be pulled down in heavy-membrane fractions. We further fractionated these to resolve purified mitochondria from MAMs (Annunziata *et al*, 2013). With equal cellular input, more MAMs were present from DX cells than REL cells for the CHLA15/CHLA20 and SKNBE1/SKNBE2C pairs, while the CHLA122/CHLA136 pair that lacks attenuated mitochondrial signaling had slightly more MAM from REL cells (Fig EV4E). We also assessed ER-specific proteins in heavy-

membrane fractions from DX and REL cells but were unable to detect differential expression (Fig EV4F).

We directly visualized MAM interfaces using transmission electron micrographs of DX and REL tumor cells (all MAM interface data can be found in Dataset EV1). We defined MAMs as regions of ER within 100 nm of the outer mitochondrial membrane (OMM), and characterized their number, length, and gap width from the OMM, binned as ≤10 nm, >10–25 nm, >25–50 nm, and >50–100 nm (Fig 3D). CHLA20 (REL) cells had reduced MAM content compared with CHLA15 (DX) cells (Table 1). The number of MAMs per mitochondria was reduced ($P < 0.01$), the frequency of mitochondria with ≥ 2 MAMs was reduced while those with absent MAMs were increased (both $P < 0.01$). Because CHLA20 mitochondrial had a mean circumference 22% smaller ($P < 0.01$), MAMs occurred at equal frequency in DX/REL cells: every 1,651 nm in CHLA15 and every 1,556 nm in CHLA20. However, there was a marked reduction in closely apposed MAMs and MAM lengths in REL cells. The proportion of MAM that came within 10 nm of the OMM was reduced

($P = 0.05$), as was the proportion of the OMM perimeter in contact with a MAM at < 10 nm. In contrast, the proportion approximated by a MAM at larger gap distances was less reduced (Fig 3E and F). Similarly, SKNBE2C (REL) cells were reduced in the number of MAMs per mitochondria compared to SKNBE1 (DX) cells ($P < 0.01$), and the frequency of mitochondria with ≥ 2 MAMs was reduced, while those absent MAMs were increased > 2-fold (both $P < 0.01$). MAMs occurred on average every 1,116 nm along the OMM of SKNBE1 but only every 1,880 nm in SKNBE2C. In addition to reduced frequency, the total length and proximity of MAMs were reduced in SKNBE2C cells, adjacent to 24% of the mitochondrial perimeter in SKNBE1 but only 15% in SKNBE2C cells, and MAMs were markedly reduced across all gap widths (Fig 3E and F).

In contrast, CHLA136 (REL) cells do not have attenuated mitochondrial responses, multidrug resistance, reduced MAM content by fractionation, nor reduced MAM interfaces in comparison with CHLA122 (DX) cells. In fact, CHLA136 (REL) cells had a trend toward more mitochondria with ≥ 2 MAMs ($P = 0.10$) and fewer orphan mitochondria ($P < 0.01$), more MAMs per mitochondria overall ($P = 0.01$), and a slightly higher proportion of MAMs along the OMM across all gap widths. The characteristics of individual MAMs by their length and relative proximity to the mitochondrial outer membrane were otherwise similar (Fig 3E and F; Table 1). In all, reduced ER–mitochondria connectivity (in particular, a reduction in the proportion of MAMs in close proximity to the OMM) was recurrently present in tumor cells with multidrug resistance and attenuated mitochondrial responses to death stimuli, nominating this feature as a contributor to therapy resistance.

The role of MAMs in mitochondrial apoptotic signaling can be functionally demonstrated

Murine liver and HeLa cell mitochondria separated from MAMs using limiting proteolysis have reduced cytochrome c release in response to Bid and BimBH3 domains (Chipuk *et al*, 2012). We tested limited proteolysis and immunomagnetic bead separation to mechanically isolate mitochondria from ER in DX neuroblastoma cells. Both induced non-specific cytochrome c release, dampening the dynamic range of the assay. Neither process reduced the integrity or abundance of Bak (the preferential target of tBid), although the latter led to reduced MAM markers such as Facl4 protein (Fig EV2D and E). Immunomagnetic bead separation induced less membrane disruption, and MOMP sensitivity in response to BimBH3 was greater for CHLA15 heavy-membrane fractions (intact MAMs) compared with purified mitochondria (reduced MAMs; Fig 4A; SKNBE1 could not be reliably assessed due to high non-specific release with both methods).

We next knocked-down expression of phosphofurin acid cluster sorting protein-2 (*PACS2*) and mitofusin-2 (*MFN2*) as these have been shown to reduce MAMs (Simmen *et al*, 2005; de Brito & Scorrano, 2008; Moulis *et al*, 2019). Mitochondria in CHLA15-shPACS2 cells with Pacs2 expression reduced > 50% were larger than CHLA15-shCtrl cells but similar in roundness and circularity (Fig 4B–E). There was a trend toward reduced MAM per mitochondria, although the distribution of MAMs to mitochondria was preserved (Fig 4F; Table 2). MAM length and proximity were reduced, with Pacs2 knockdown cells having a reduced MAM per mitochondrial perimeter across all gap widths (Fig 4F and G; Table 2). The

proportion of MAM that came within 10 or 25 nm of the OMM was reduced ($P = 0.02$ and $P < 0.05$, respectively), as was the proportion of the OMM perimeter in contact with a MAM at all gap widths (Fig 4G). By comparison, mitochondria in CHLA15-shMFN2 cells with Mfn2 reduced ~60% had reduced circularity and roundness ($P = 0.03$ and $P < 0.01$, respectively) but size was maintained (Fig 4B–E). There were fewer MAMs per mitochondria ($P < 0.01$), and the frequency of mitochondria with ≥ 2 MAMs was reduced while those absent MAMs were increased (both $P < 0.01$; Fig 4F). Moreover, MAM lengths were reduced across all gap widths (Fig 4G). We tested the sensitivity of these cells to the Bcl2/Bclx-inhibitor, ABT-737, a pharmacological enhancer of MOMP in CHLA15 cells, and knockdown of Mfn2 or Pacs2 phenocopied the ABT-737 resistance seen in CHLA20 cells, shifting the $IC_{50} > 18$-fold and 8-fold, respectively (Fig 4H). In addition, CHLA15-shMFN2 cells, which had more substantial MAM alterations than did CHLA15-shPACS2 cells, showed a resistance to tBid and BimBH3 in mitochondrial profiles that phenocopied multidrug-resistant neuroblastomas (Fig 4I).

Reduced transfer of Ca^{2+} from MAMs to mitochondria is not required for attenuated apoptotic signaling

Mitochondria-associated ER membranes support mitochondria as platforms to integrate stress signals. ER provides the major intracellular reservoir for Ca^{2+}, and MAMs are enriched with Ca^{2+} release constituents to create localized microdomains that enable calcium transfer into mitochondria through the low-affinity mitochondrial calcium uniporter [mtCU; (Rizzuto & Pozzan, 2006)], which has been linked to Bcl2 family function and apoptotic sensitivity (Hajnoczky *et al*, 2000; Rizzuto & Pozzan, 2006). Indeed, synthetically decreasing ER–mitochondria tethering in rat liver cells and basophils reduces Ca^{2+} transfer and apoptotic sensitivity, while augmenting tethering increases both (Csordas *et al*, 2006).

We posited that the reduction in MAMs in REL tumors reduces ER-to-mitochondria Ca^{2+} transfer to attenuate apoptotic signaling. We measured Ca^{2+} transfer in two DX/REL pairs with differential MAM content. Mitochondrial calcium concentration ($[Ca^{2+}]_m$) was detected with a fluorescent protein-based Ca^{2+} sensor targeted to the mitochondrial matrix, GCamp6f. Cytoplasmic calcium concentration ($[Ca^{2+}]_c$) was monitored with fura2 loaded to the cells as fura2AM. Calcium responses evoked by the IP_3R-linked stimulus, carbachol, were recorded and the time courses for the corresponding fluorescence signals calculated. CHLA20 (REL) cells have attenuated MOMP responses, multidrug-resistant phenotype, and reduced MAM content in comparison with CHLA15 cells (DX), yet both have similar $[Ca^{2+}]_c$ and $[Ca^{2+}]_m$ signals and coupling time (< 2 s), the time difference between $[Ca^{2+}]_c$ and $[Ca^{2+}]_m$ achieving 50% of maximum (Fig 5A; Appendix Fig S2E). Like CHLA20, SKNBE2C (REL) cells also have attenuated MOMP responses, multidrug-resistant phenotype, and reduced MAM content in comparison with SNKBE1 (DX) cells. However, unlike CHLA20, SKNBE2C cells have markedly reduced Ca^{2+} transfer compared with SKNBE1 (DX) cells, with a > 3-fold increase in coupling time ($P < 0.01$; Fig 5B). We genetically augmented MAMs in SKNBE2C cells using a monomeric linker composed of a fluorescent protein extended with ER and OMM membrane anchor domains (Csordas *et al*, 2006). Linker-induced augmentation of MAMs normalized the Ca^{2+} transfer coupling time to ~1.5 s, compared with a control
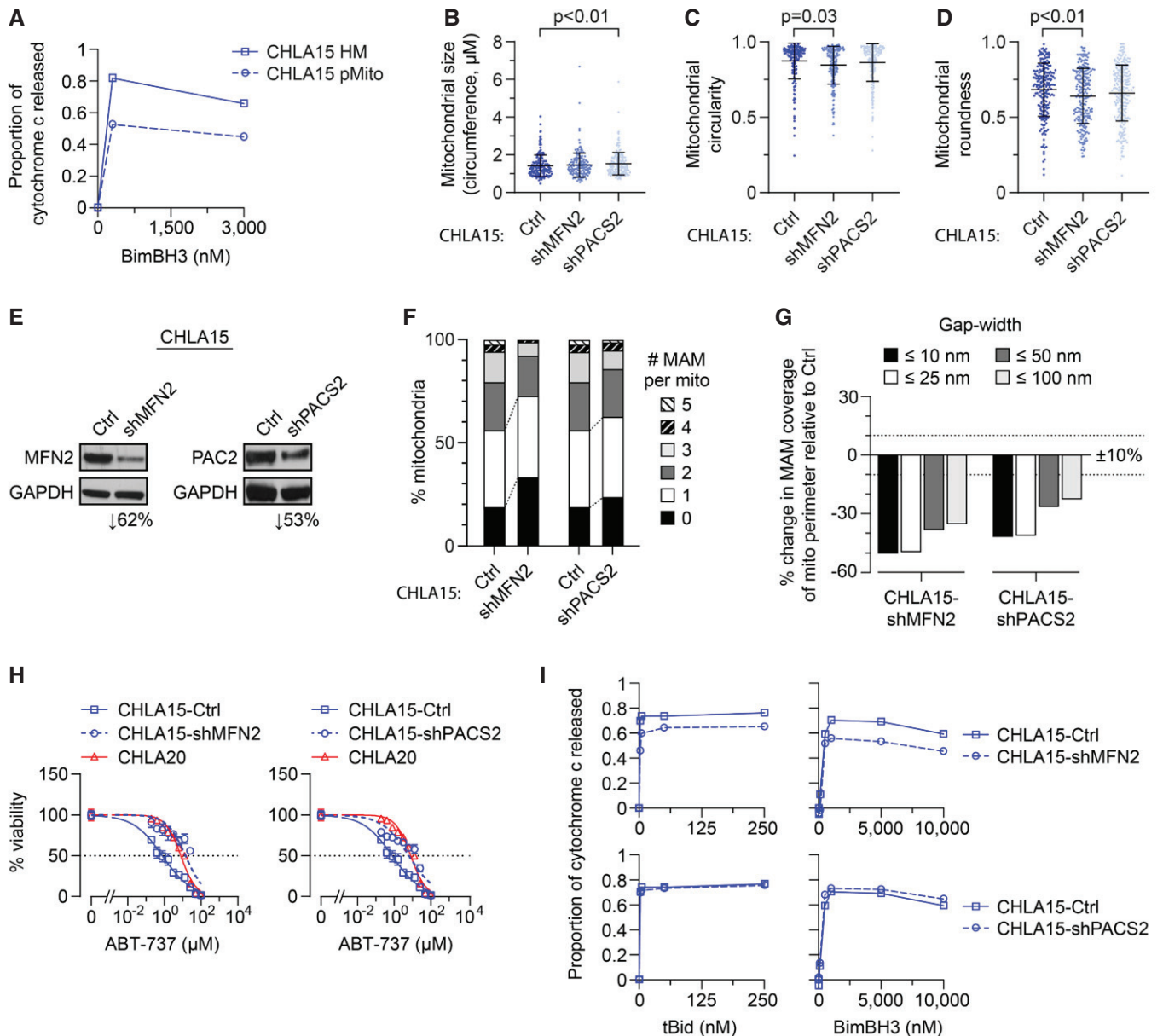
Figure 4. Chemically or genetically reducing MAMs leads to MOMP resistance.

A   Heavy-membrane (HM) fractions of CHLA15 were rendered MAM depleted by immunomagnetic separation to derive purified mitochondria (pMito), and cytochrome c release measured in response to BimBH3 peptide.

B–D   TEM analyses were used to quantify mitochondrial size, circularity, and roundness in CHLA15 cells transfected with a sh-control (Ctrl), shMFN2 or shPACS2 constructs (mean ± SD shown).

E   Immunoblot assessment of Mfn2 and Pacs2 protein knockdown.

F   Proportion of mitochondria with 0–5 MAMs are shown for each.

G   Percentage of mitochondria perimeter with an apposed ER within defined gap widths; dotted lines denote +10% and −10% change.

H   *In vitro* viability of CHLA15-ctrl, CHLA15-shMFN2, CHLA15-shPACS2, and CHLA20 cells following 72 h exposure to ABT-737; dotted line represents 50% viability.

I   Mitochondrial cytochrome c release in response to tBid and BimBH3 peptide in CHLA15-Ctrl, CHLA15-shMFN2, and CHLA15-shPACS2 cells.

Data information: For B–D and F, G, n = 214–246 mitochondria per cell line. For A and I, data points are mean of duplicate wells (SD < 0.05 at all points) in a representative experiment from at least two biological replicates; for H, data points are mean and SD from triplicate wells, experiments, are representative of at least two biological replicates. For B–D, statistical analyses were performed using a two-tailed Mann–Whitney *U* test, with significance *P* < 0.05.

OMM-only linker, confirming the reduction was a consequence of reduced MAMs (Fig 5C). In both the CHLA15/CHLA20 and SKNBE1/SKNBE2C pairs, the REL cells showed similar

proportional reductions in MAM coverage at ≤10 nm ER–mitochondrial gap width (Table 1). However, CHLA20 cells had preserved MAM coverage at larger gap widths capable of

Table 2. Summary of CHLA15-Ctrl (DX) and CHLA15-shMFN2 and -shPACS2 models.

	CHLA15-ctrl	CHLA15-shMFN2		CHLA15-shPACS2	
Mitochondria					
Number analyzed	214	234		246	
Perimeter, mean (nm)	1,416	1,468	P = ns	1,530	P < 0.01
Perimeter, median (nm)	1,319	1,381		1,453	
Circularity, median	0.918	0.892	P = 0.03	0.914	P = ns
Roundness, median	0.715	0.655	P < 0.01	0.686	P = ns
% with 0 MAMs	19%	33%	P < 0.01	24%	P = ns
% with 1 MAMs	37%	39%		39%	
% with 2–3 MAMs	37%	26%	P < 0.01	22%	P = ns
% with ≥ 4 MAMs	6%	1%		5%	
%OMM with MAM gap width ≤ 10 nm	1.7%	0.9%	(↓47%)	1.0%	(↓41%)
%OMM with MAM gap width ≤ 25 nm	5.9%	3.0%	(↓49%)	3.5%	(↓41%)
%OMM with MAM gap width ≤ 50 nm	12.6%	7.8%	(↓38%)	9.3%	(↓26%)
%OMM with MAM gap width ≤ 10 nm	27.4%	17.8%	(↓35%)	21.2%	(↓23%)
MAM					
Number analyzed	330	241		331	
MAMs per mitochondria	1.54	1.03	P < 0.01	1.35	P = 0.07
MAM frequency (per nm perimeter)	918	1,425		1,137	
%MAM with gap width ≤ 10 nm	22%	17%	P = 0.09	15%	P = 0.02
%MAM with gap width ≤ 25 nm	47%	43%	P = ns	40%	P < 0.05
%MAM with gap width ≤ 50 nm	68%	73%	P = ns	71%	P = ns
%MAM with gap width ≤ 100 nm	100%	100%		100%	

accommodating the Ca^{2+} transfer machinery, while SKNBE2C cells were reduced at all gap widths, limiting Ca^{2+} transfer.

We used biochemical and genetic approaches to further evaluate Ca^{2+} transfer and stress sensitivity. We treated CHLA15 heavy-membrane fractions with Ru360 that inhibits the mtCU, before measuring cytochrome c release in response to tBid or BimBH3. No reduction in release was seen (Fig 5D). Similarly, CHLA20 (REL) cells did not have further attenuated cytochrome c release following exposure to Ru360. We next used siRNA to reduce expression of MCU, the pore-forming component of the mtCU (Baughman *et al*, 2011; De Stefani *et al*, 2011). MCU was not differentially expressed in DX/REL pairs (Appendix Fig S2A). MCU knockdown of ~45% and 60% was achieved in two CHLA15 subclones and MOMP sensitivity was only modestly reduced (Fig 5E and F). We also tested MCU knockdown and Ru360 exposure in SKNBE1 cells and obtained similar results (Appendix Fig S2B–D). Collectively, these data support that reduced Ca^{2+} transfer from ER to mitochondria is not required for the attenuated MOMP phenotype.

MAM-reduced tumor cells have diminished ceramide pools, and repressing ceramide generation at MAMs induces relative MOMP resistance

Mitochondria are dependent on the transfer of lipids from MAMs to maintain their OMM composition, including sphingolipids that are implicated in regulating Bak and Bax sensitivity to stress signals

(Chipuk *et al*, 2012). ER is the primary organelle for bulk lipid synthesis and distribution, and regulatory enzymes are highly compartmentalized within ER subdomains, including MAMs. Neutral sphingomyelinases are enriched at MAMs where they hydrolyze sphingomyelin to ceramide and facilitate its transfer to the OMM through incompletely understood mechanisms (Morad & Cabot, 2013). Ceramide in the OMM facilitates the oligomerization of Bak and/or Bax (Ganesan *et al*, 2010).

We quantified bioactive sphingolipids in DX and REL cell pairs with altered MAM content, focusing on ceramide (Cer) and sphingo-myelin (SM) species. SKNBE2C cells demonstrated the most altered sphingolipid profile in comparison with matched DX SKNBE1 cells, consistent with their markedly disrupted MAM content. This included reductions in multiple bioactive Cer species (chain length C32-C36) and total Cers, elevation in SMs, and an elevated SM:Cer ratio. CHLA20 cells also had reductions in bioactive Cers, although no alterations in SMs or SM:Cer ratio. Finally, CHLA136 cells did not have alterations in Cers, SMs, or their ratio, consistent with their intact MAM content at DX and REL (Fig 6A–F and Fig EV5). To determine whether reduced MAM-synthesized ceramides specifically were relevant in regulating MOMP in our models, we inhibited neutral sphingomyelinase in isolated mitochondria by pre-incubating them with the inhibitor, GW4869. Prolonged incubation of isolated mitochondria with GW4869 led to mitochondrial dysfunction and failure to elicit specific cytochrome c release, but drug incubation for 30 min was tolerated, albeit with a reduced dynamic
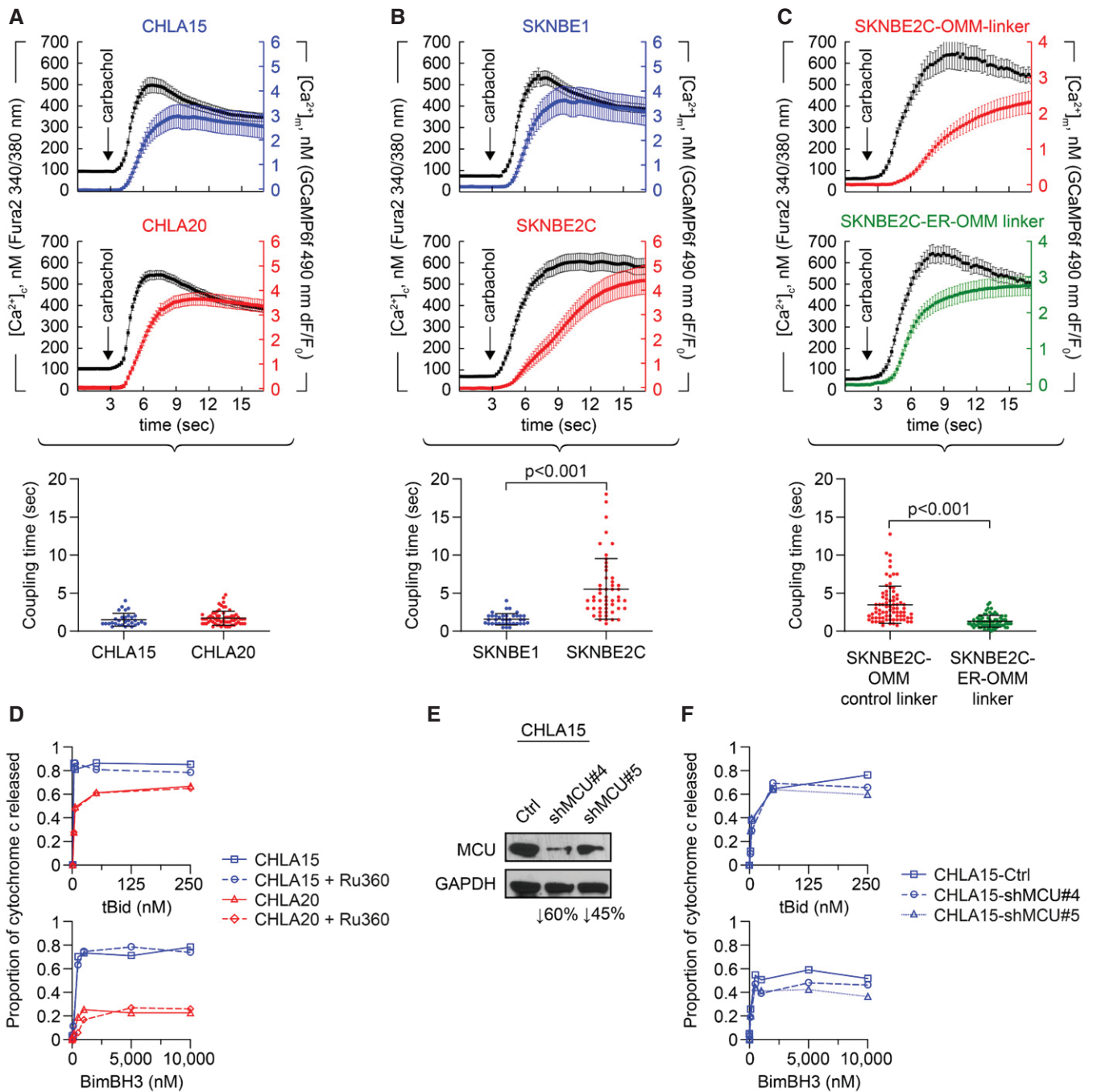
Figure 5. Reduced Ca²⁺ transfer at MAMs is not required for attenuated mitochondrial responses to stress.

A, B Cytosolic (black tracing) and mitochondrial (colored tracing) Ca²⁺ concentration measured using fluorescent reporters in the CHLA15 ($n = 29$ cells)/CHLA20 ($n = 65$ cells) and SKNBE1 ($n = 37$ cells)/SKNBE2C ($n = 52$ cells) pairs. ER Ca²⁺ release was induced by 100 μM carbachol, an IP3R-agonist; time added indicated by arrow; tracings are mean ± SD error bars. Coupling time (time between achieving 50% of maximal cytosolic and mitochondrial concentrations) is an index of ER–mitochondrial proximity and transfer efficiency; plotted below.

C MAM proximity was enforced in SKNBE2C cells using an ER-OMM linker construct, with Ca²⁺ transfer coupling time ($n = 57$ cells) compared with cells expressing an OMM-only control linker ($n = 70$ cells); tracings are mean ± SEM error bars.

D Mitochondrial cytochrome c release for CHLA15 and CHLA20 cells following exposure to tBid or BimBH3 peptide, with or without Ru360 treatment.

E Silencing of the mitochondrial calcium uniporter (MCU) was achieved in two CHLA15-shMCU clones.

F Cytochrome c release in response to tBid and BimBH3 assessed.

Data information: For A–C, data are derived from at least three separate cell transfections (biological replicates). For D and F, data points are mean of duplicate wells (SD < 0.05 at all points) in a representative experiment from at least two biological replicates. For A–C, statistical analyses were performed using an unpaired two-sided Student's *t*-test, with significance *P* < 0.05.

range. Thirty minutes of sphingomyelinase inhibition reduced tBid-induced cytochrome c release in DX therapy-sensitive CHLA15 (median 35% inhibition; $P = 0.09$) and SKNBE1 (median 34%; $P < 0.01$; Fig 6G and H). CHLA15 cells were most inhibited at lower tBid concentrations and Bax oligomerization was also inhibited at these concentrations (Fig EV2F). To exclude direct effects of GW4869 on cytochrome c release, as opposed to lipid-mediated mechanisms, we pre-incubated mitochondria without the inhibitor, and added it at the time of tBid, and no inhibition of cytochrome c release was observed (Fig 6G).

Discussion

Most cancer deaths result from progression of disease that is resistant to available therapies, yet its principal contributors remain incompletely understood. The diversity of targets and stress signals engaged by cancer treatments, and the myriad adaptations cancer cells use to subvert them, pose fundamental challenges. Cancer therapies activate stress signals that converge on mitochondria (Danial & Korsmeyer, 2004; Deng et al, 2007; Ni Chonghaile et al, 2011; Vo et al, 2012; Sarosiek et al, 2013b; Montero et al, 2015), whose ability to undergo MOMP is regulated by MAMs, essential contacts for the transfer of metabolites. Here, we identify reduced MAMs as a novel convergence-based mechanism of resistance arising from attenuation of stress-induced MOMP. Since mitochondria act at a terminal node integrating stress signals, this attenuated responsiveness contributes to multidrug resistance. Importantly, this mechanism is not exclusive to other mechanisms of resistance operative upstream of mitochondria.

We identified the MOMP-attenuated phenotype measuring mitochondrial responses to the Bak and Bax activators, tBid and Bim. Mitochondrial profiling was developed by Letai (Deng et al, 2007) and used to define Bcl2 family dependencies and predict responses to chemotherapy (Ni Chonghaile et al, 2011; Vo et al, 2012; Montero et al, 2015) and molecularly targeted drugs (Hata et al, 2015; Montero et al, 2015). We studied neuroblastoma, a tumor that often responds to chemoradiotherapy with tumor regression (Uccini et al, 2006) followed by lethal relapse (Matthay et al, 2009). Limited clinical samples had constrained such investigations, so we derived patient-matched tumor models at diagnosis and relapse, the latter frequently manifesting multidrug resistance (Keshelava et al, 1998). We show that in six of seven pairs, mitochondria from relapsed neuroblastomas have reduced MOMP responses to tBid and Bim compared with their at-diagnosis counterparts, providing evidence that attenuated mitochondrial signaling arises during multimodal therapy. Attenuated MOMP was identified in response to either death activator, although tBid was more potent. Indeed, BimBH3 is an intrinsically unstructured peptide (Hinds et al, 2007) that engages Bak or Bax at micromolar exposures, while recombinant tBid binds lipid membranes to activate Bak or Bax at nanomolar exposures, highlighting the importance of lipid membranes in facilitating MOMP (Walensky et al, 2006; Sarosiek et al, 2013a). Quantitative variability among biological replicates reflects myriad events impinging on Bak/Bax-mediated pore formation, including temperature, pH, detergents, and metabolites (Kale et al, 2018), but working with patient-matched pairs in parallel enabled reproducible qualitative differences to be identified. A mitochondrial basis has been proposed for the selective killing of tumor cells by chemotherapy (Vo et al, 2012; Sarosiek et al, 2013b), and here we expand this notion to demonstrate a mitochondrial basis for multidrug resistance in response to therapeutic pressure during multimodal therapy.

Neuroblastoma cell lines represent oligoclonal outgrowths from tumors. If MOMP sensitivity were highly heterogeneous within a tumor, we predict some diagnosis–relapse pairs to have attenuated mitochondrial responses present at diagnosis from chance alone. Instead, our data support that contributions from intra-tumoral heterogeneity are minor compared with the effect of therapeutic selective pressure. We confirmed that attenuated mitochondrial responses correlated with resistance to chemotherapy and ionizing radiation. For the latter, differential cell death follows equivalent genotoxic stress, emphasizing this as a post-target resistance mechanism. Resistance is also conferred to molecularly targeted drugs such as Bcl2 and Alk inhibitors in the absence of prior exposure, since these operate upstream of mitochondria. More surprising is evidence that selecting for resistance to targeted agents in vitro can induce the attenuated MOMP phenotype and multidrug resistance. This provides a potential mechanism for the significant proportion of patients with emergent resistance to therapeutic kinase inhibitors that have no on-pathway mechanism identified (Katayama et al, 2012; Chong & Janne, 2013; Lito et al, 2013; Hugo et al, 2015; Wilson et al, 2015).

We identified reductions in MAM content from tumors with attenuated MOMP when visualized by fractionation or quantified by EM morphometry. ER–mitochondria contacts at MAMs regulate fission/fusion dynamics to optimize mitochondrial shape (Hoppins & Nunnari, 2012), which impacts Bax-induced MOMP in murine hepatocytes and embryonic fibroblasts (MEFs) by altering cooperation among Bcl2 family members. Smaller mitochondria with increased membrane curvature are more resistant to stress-induced MOMP, possibly contributing to chemoresistance (Renault et al, 2015). Consistent with this, the CHLA15/CHLA20 pair had smaller more circular mitochondria in the post-relapse MOMP-resistant tumor cells, however, the reverse was true for the SKNBE1/SKNBE2C pair. While mitochondrial size, shape, mass, and mtDNA content differed, only the reduction in MAMs was present across all models with attenuated MOMP, while absent in the single pair without this feature.

Our image analyses were done in 2D, so to ensure representative findings we analyzed > 2,400 MAMs from > 1,700 mitochondria across nine tumor models. In both the CHLA15/CHLA20 and SKNBE1/SKNBE2C pairs, MAMs were markedly reduced in the therapy-resistant post-relapse model, as was the proportion of mitochondrial surface with an apposed MAM. In contrast, the only tumor pair without attenuated MOMP responses or chemoresistance, CHLA122/CHLA136, did not have such alterations. That MAMs are reduced in cancer cells was originally posited by Howatson and Ham from EM studies of mouse liver tumors (Howatson & Ham, 1955). A role in mediating apoptotic sensitivity was demonstrated using MEF heavy-membrane fractions, as MOMP sensitivity to Bid was reduced when mitochondria were purified away from their associated MAMs (Chipuk et al, 2012). Similarly, we could phenocopy attenuated MOMP responses in DX tumors by reducing MAMs from mitochondria with chemical proteolysis or genetic perturbation. In the latter, we used EM morphometry to confirm the MAM-reduced phenotype.
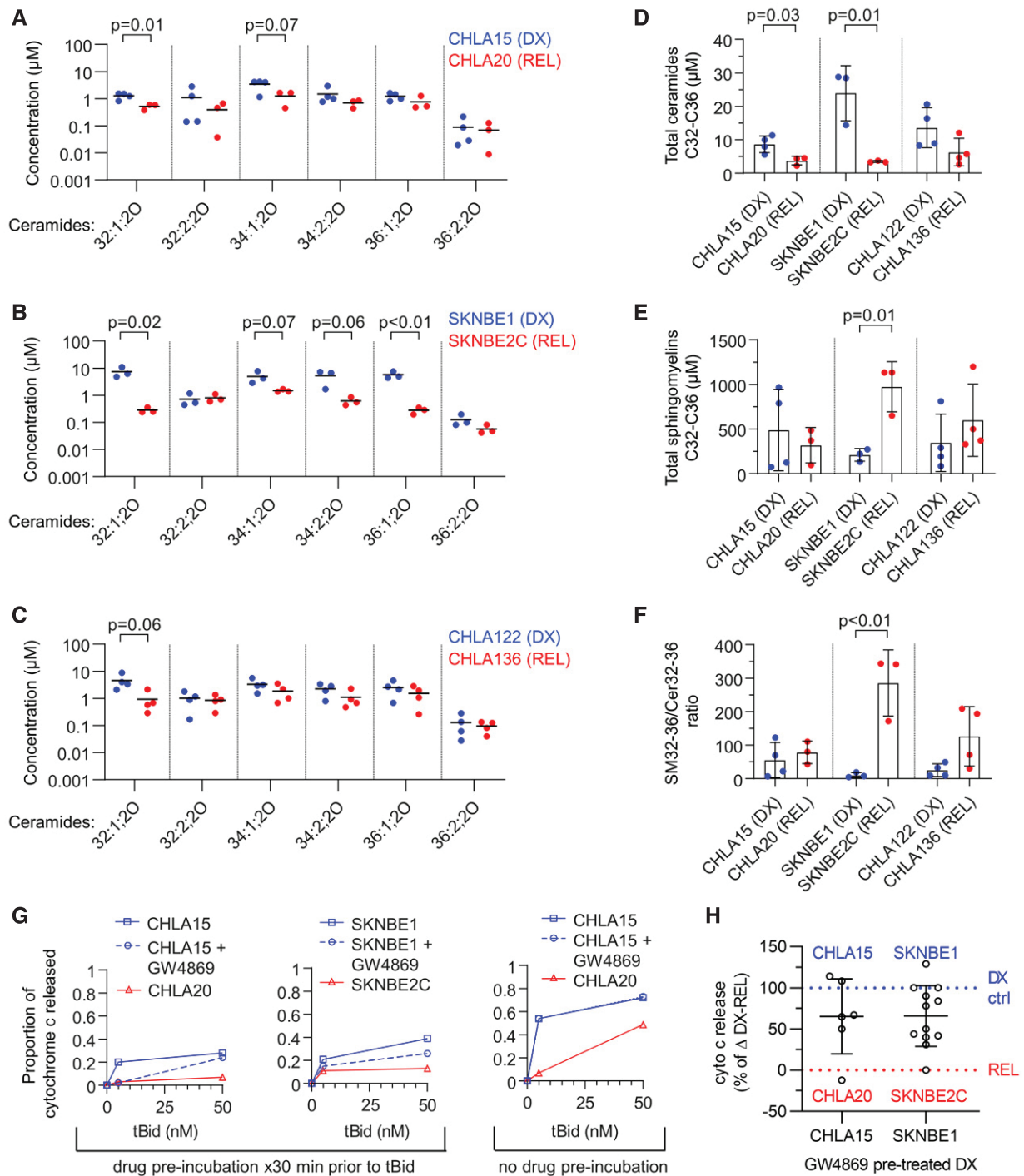
Figure 6. Reduced ceramides are present in REL cells with depleted MAMs.

A–C Concentration of ceramide species as measured by LC/MS from DX and REL pair whole-cell pellets.

D, E Cumulative ceramides and sphingomyelins (of C32–C36 chain length) for DX/REL pairs.

F Ratio of total C32-C36 sphingomyelins:ceramides for DX/REL pairs.

G Cytochrome c release for CHLA15 and SKNBE1 mitochondria following exposure to tBid, pre-incubated for 30 min with or without GW4869, and CHLA20 and SKNBE2C pre-incubated without GW4869 (left panel); same experiment but with GW4869 added with tBid, after the 30 min pre-incubation (right panel).

H Summary data for CHLA15/CHLA20 and SKNBE1/SKNBE2C showing relative cytochrome c release when pre-incubated with GW4869 to inhibit ceramide generation, compared with untreated cells.

Data information: A–F show mean of three to four biological replicates plotted; three technical replicates each; D–F error bars are ± SD. For G, data points are mean of duplicate wells (SD < 0.05 at all points) in a representative experiment from at least two biological replicates. All data points from two (CHLA15) or three (SKNBE1) biological replicates are depicted in H. Statistical analyses were performed using an unpaired two-sided Student's *t*-test, with significance *P* < 0.05 (trend, *P* < 0.10).
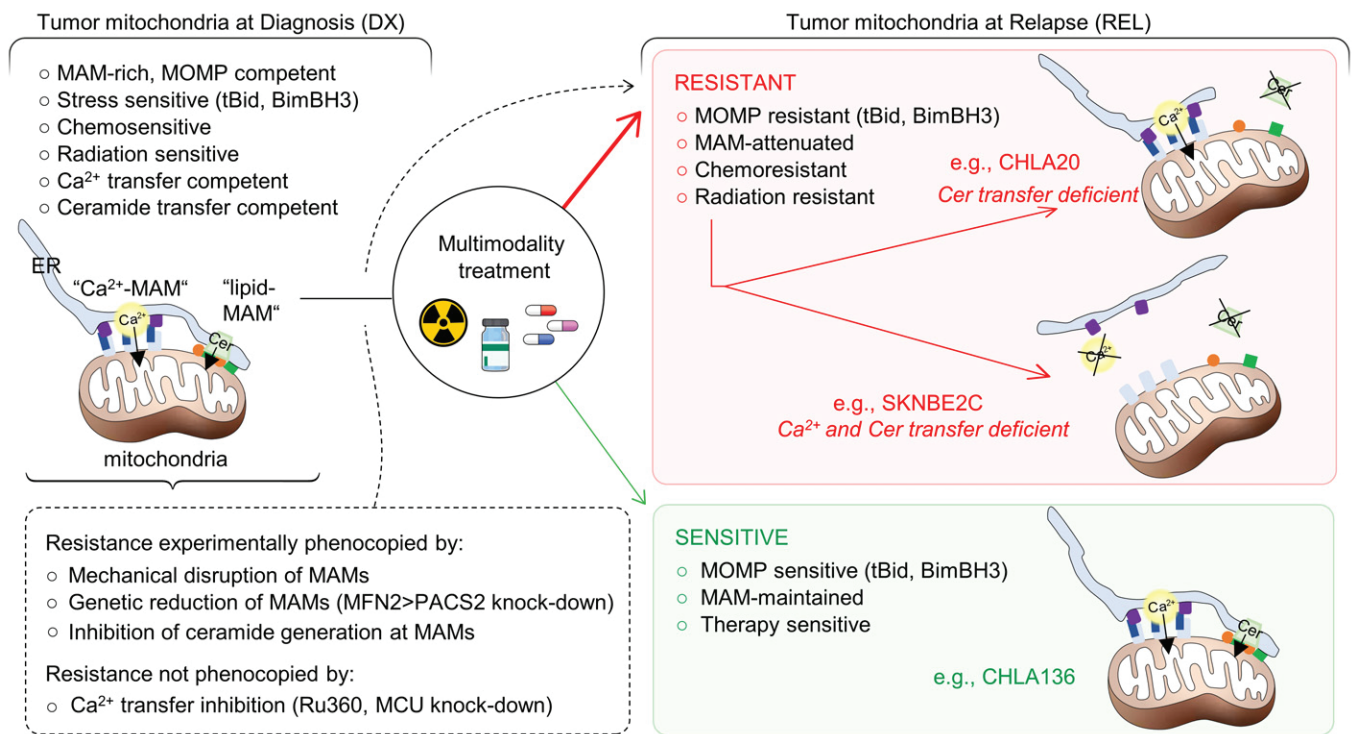
Figure 7. MAM-mediated mitochondrial resistance model.

DX neuroblastoma cells have MAM-replete mitochondria that are MOMP competent and sensitive to therapeutic stress. REL tumor cells have reduced MAMs (by number and/or proximity) and are relatively multidrug resistant due to attenuated MOMP (red box). Rare tumors at relapse retain MOMP competence and relative therapy sensitivity (green box). Ca^{2+} transfer may be reduced but is not essential for the multidrug-resistant phenotype. Reduced transfer of sphingolipids such as ceramides (Cer) at MAMs is common in REL cells and contributes to attenuated MOMP via altered Bak/Bax oligomerization in response to stress.

These data support that an essential factor for mitochondrial sensitization to MOMP is provided by MAMs. Korsmeyer's group showed that many intrinsic cell death signals require both functional Bak or Bax and ER-released Ca^{2+} (Scorrano *et al*, 2003), and deficiencies in MAM-derived Ca^{2+} transfer can confer apoptosis resistance in mesothelioma cells (Patergnani *et al*, 2015). We found a > 3-fold increase in Ca^{2+} transfer coupling time (reflecting reduced transfer) in therapy-resistant SKNBE2C cells compared with DX cells, which was normalized using a linker that tightens MAM contacts. However, we found no change in coupling time for the CHLA15/CHLA20 pair. CHLA20 have reduced MAMs with tight gap widths with relative preservation at larger gap widths that enable Ca^{2+} transfer (Csordas *et al*, 2006, 2010). While altered Ca^{2+} transfer may contribute to MOMP regulation, it is not indispensable for therapy resistance in neuroblastoma and disrupted Ca^{2+} transfer did not phenocopy MOMP attenuation. It is postulated that Ca^{2+} transfer at MAMs regulates the mitochondrial permeability transition pore and sphingolipid transfer regulates MOMP (Lemasters *et al*, 2009; Bauer & Murphy, 2020).

Narrow gap width MAMs are unable to accommodate the Ca^{2+} transfer machinery but are critical for lipid transport, and tight contacts (< 10 nm) have been referred to as lipid-ERMCs or lipid-MAMs (Schauder *et al*, 2014; Martino Adami *et al*, 2019). We show that resistant neuroblastoma cells have reduced ceramide levels reflecting reduced MAM activities and inhibiting the hydrolysis of sphingomyelin that occurs at MAMs for only 30 min partially phenocopies the attenuated MOMP phenotype. Ceramides are synthesized by neutral sphingomyelinases enriched at MAMs, and transferred to the OMM where they synergize with Bak and Bax to induce pore formation (Ganesan *et al*, 2010). Multiple ceramide regulators (including sphingomyelinase) were identified as determinants of multidrug resistance in an siRNA screen across diverse carcinoma cell lines. That work was agnostic to consideration of MAM content yet knockdown of six of six ceramide-metabolizing enzymes led to drug sensitivity changes (increased or decreased) predicted by a ceramide–OMM–MOMP model (Swanton *et al*, 2007). Chipuk and Green demonstrated that the reduced MOMP sensitivity of mitochondria purified away from MAMs results from loss of neutral sphingomyelinase activity. Sensitivity was restored by the addition of microsomes containing MAM domains, active sphingomyelinase and sphingomyelin, or ceramide and/or ceramide-derived lipids (Chipuk *et al*, 2012). Walensky's group identified a covalent lipid-binding site on Bax regulating its oligomerization potential (Cohen *et al*, 2020), and crystal structures have revealed Bak sites preferentially bound by lipids and necessary to support its oligomerization (Cowan *et al*, 2020). Targeting neutral sphingomyelinases to various organelles demonstrated that ceramide's effect on apoptosis induction requires its presence at mitochondria (Birbes *et al*, 2001) where it creates ceramide-rich macrodomains that enhance Bak or Bax oligomerization (Lee *et al*,

2011). Finally, mistargeting of the ceramide transporter, CERT, to mitochondria enhances Bax-dependent MOMP and this requires its ceramide transfer domain (Jain *et al*, 2017). Here, we propose that MAMs serve this "targeting" role to facilitate ceramide transfer to the OMM, and this is frequently disrupted in REL tumor cells.

Since MAMs serve as physiological regulators of apoptosis by maintaining an OMM lipid milieu that supports Bak and/or Bax oligomerization (Renault & Chipuk, 2014), MAM reductions may comprise an adaptive response providing a novel multidrug resistance mechanism (Fig 7). Additional work defining the lipid requirements downstream of ceramide that support MOMP, and how they are disrupted in cancer, is warranted. Alterations in MAMs have increasingly been linked to diverse pathological states, including cardiomyocyte recovery after reperfusion injury (Paillard *et al*, 2013), neurodegeneration (Zampese *et al*, 2011; Area-Gomez *et al*, 2012; Cali *et al*, 2013; Hedskog *et al*, 2013; Ottolini *et al*, 2013), obesity-related diabetes (Rieusset, 2011; Arruda *et al*, 2014), and systemic lipid homeostasis (Anastasia *et al*, 2021). Importantly, our attenuated MOMP model proposes that multidrug resistance does not reflect an absence of death signals but their insufficiency to trigger MOMP. Investigational cancer drugs are often tested in patients with multidrug resistance. For drugs that do not induce a tumor response, we cannot differentiate those that engaged their target to liberate death-activating signals that remain subthreshold for MOMP versus those that did not. This may lead to drugs that might have clinical efficacy in other settings being abandoned. Finally, recognition of this phenotype can facilitate the development of tools to measure ER–mitochondria interactions for clinical use in predicting therapy resistance and provide a novel framework for testing interventions to prevent emergent resistance or restore mitochondrial competence to resistant cancers.

Materials and Methods

Cell lines

Cell lines were obtained from the COG/ALSF Childhood Cancer Repository (www.CCcells.org) and grown in IMDM Media 12440 (Life Technologies, Gaithersburg, MD) supplemented with 10% fetal bovine serum, 2 mM L-glutamine, 1% ITS, 100 U/ml of penicillin, and 100 µg/ml gentamycin. Those obtained at diagnosis (DX) were kept physically separate from those at relapse (REL) to avoid cross-contamination. All were subjected to STR identity and pathogen testing every 4–6 months. Culture conditions were 37°C in a humidified atmosphere of 5% CO_2. Cell lines were interrogated for cancer gene mutations using the FoundationOne CDx assay (Foundation Medicine) to confirm *TP53*, *ALK,* and additional cancer gene mutation status, including variant allele frequencies.

Isolation of heavy-membrane, purified mitochondria, and MAM fractions

Heavy-membrane fractions were obtained by rupturing cells in isolation buffer A (250 mM Sucrose, 20 mM HEPES, 1 mM DTT, 10 mM KCl, 1 mM EDTA, 1 mM EGTA, and 1.5 mM $MgCl_2$) with protease inhibitor cocktail by 20 strokes in a 2-ml glass Dounce homogenizer, followed by removal of debris and nuclei by

centrifugation at 800 *g* for 10 min and then 1,050 *g* for 10 min at 4°C. Mitochondria-enriched fractions were collected by centrifuging the supernatant of the second spin at 12,000 *g* for 10 min at 4°C. To visualize MAM content, heavy-membrane fractions were resuspended in 2 ml Isolation Medium (250 mM Mannitol, 5 mM HEPES pH 7.4, 0.5 mM EGTA, and 0.1% BSA) with freshly added protease inhibitors and slowly layered onto 8 ml of 30% Percoll gradient prepared with Gradient Buffer (225 mM Mannitol, 25 mM HEPES pH 7.5, 1 mM EGTA, and 0.1% BSA) in an Ultra-Clear Beckman Centrifuge Tube, and spun at 95,000 *g* for 60 min to resolve MAM from more pure mitochondria, as described (Annunziata *et al*, 2013).

To prepare purified mitochondria, we used Magnetic Activated Cell Sorting (MACS) according to the MidiMACS™ Starting Kit (LS) protocol (130-042-301, Mitenyi Biotec, Germany). Cells were collected in cold PBS and resuspended in cold Buffer A with protease inhibitor at 10 million cells/ml. After 20–25 strokes of homogenization using a 7 ml Dounce homogenizer, 1 ml of cell lysate was mixed with 9 ml of ice-cold 1× Separation Buffer (130-091-221, Mitenyi Biotec) and incubated with 50 µl anti-TOM22 microbeads at 4°C on a shaker for 1 h. The mixture was passed stepwise through an LS column (130-042-401, Mitenyi Biotec), pre-rinsed with 3 ml of 1× Separation Buffer, and installed in the magnetic field of the MidiMACS Separator (130-042-302, Mitenyi Biotec). After washing three times with 3 ml of 1× Separation Buffer, the column was removed and magnetically labeled mitochondria were flushed into a collection tube using 1.5 ml of 1× Separation Buffer. Purified mitochondria were used immediately for analysis or centrifuged at 13,000 *g* for 2 min at 4°C and stored in 100 µl storage buffer on ice.

Mitochondrial profiling

Heavy-membrane or purified mitochondria fractions were resuspended in buffer C [10 mM Tris-MOPS (pH 7.4), 1 mM KH_2PO_4, 10 mcM Tris-EGTA, 5 mM glutamate, 2 mM malate, and 125 mM KCl]. Mitochondria (50 µl of 1 µg/µl protein) were treated with caspase-8-cleaved tBid from 5 to 500 nM (882-B8-050, R&D Systems, Minneapolis, MN), Bim-BH3 from 10 to 10,000 nM (Ac-DMRPEIWIAQELRRIGDEFNAYYARR-amide; New England Peptide, Gardner, MA), or 300 µM BidAltBH3 (Ac-EDIIRNIARHAA QVGASMDR-amide; New England Peptide, Inc.). Reactions were incubated at 37°C for 30 mins and spun at 12,000 *g* for 10 min at 4°C: 10 µl of the supernatant (SN) and the 10 µl pellet (mitochondria; MITO) fractions were resuspended in 50 µl of 0.1% Triton X in PBS in duplicate in Quantikine, Human Cyto C Immunoassay 96-well plates followed by ELISA detection (R&D Systems, Minneapolis, MN). The fractional release of mitochondrial cytochrome c was calculated for each condition as [mean intensity$_{SN}$/(mean intensity$_{MITO}$ + mean intensity$_{SN}$)]. We report percent cytochrome c release normalized to the non-specific release induced by DMSO as [(fractional release$_{RX}$ - fractional release$_{DMSO}$)/(1-fractional release$_{DMSO}$)]*100. To test GW4869 (D1692, Sigma Aldrich), the drug (0–250 nM) was pre-incubated with mitochondria for 30 min at 30°C prior to tBid (pre-incubation), or added with tBid after 30 min pre-incubation (control). Experiments with < 30% cytochrome c release to DMSO and BidAltBH3 peptide were analyzed.

Bak and Bax oligomerization

Mitochondria (1 µg/µl) suspended in buffer A/C were treated with tBid (0–250 nM) or DMSO for 30 min at 37°C followed by a 30 min incubation with 0.9 mM of 1,6-bismaleimidohexane (Pierce, #22330) at RT to crosslink oligomers, and centrifuged at 12,000 g (4°C) to pellet mitochondria. Supernatant was removed and the pellet dissolved in NuPage loading buffer (Invitrogen) and immunoblotted for Bak and Bax.

Cytotoxicity

Cells were seeded into Corning® 96-well Flat Clear Bottom White Polystyrene TC-treated luminescent microplates (3610, Corning, Corning, NY) in triplicate at a density of 10,000 cells/well and allowed a 24-h recovery period, then treated with 100 µl of control Gibco™ IMDM full culture media (12440-053, Gibco by Life Technologies, Carlsbad, CA). ABT-737 was tested from 1 nM to 200 µM, added to IMDM culture media for 48 h. Chemotherapy exposure was 72 h, concentrations tested were as follows: etoposide (341205-25MG, EMD Millipore, Billerica, MA) 10 nM to 10 µM, cisplatin (63323-103-51, Fresenius Kabi, Lake Zurich, IL) 0.5 nM to 75 µM, carboplatin (216100-25MG, EMD Millipore) 6 nM to 10 µM, doxorubicin (5927S, Cell Signaling Technology, Danvers, MA) 0.5 nM to 10 µM, and mafosfamide (M110300 Toronto Research Chemicals, Inc., Toronto, Canada) 2 nM to 75 µM. ALK inhibitors [crizotinib (C-7900, LC Laboratories, Woburn, MA), ceritinib (C-2086, LC Laboratories), and lorlatinib (5640, Tocris Bioscience, Minneapolis, MN)] were tested from 0.01 nM to 10 µM and assessed after 5 days. Cells were irradiated on a Cs-137 Gammacell 40 irradiator S/N 186 (Nordion Ltd, Kanata, Ontario, Canada) at a dose rate of 1.3 cGy/s from 0.5 to 5 Gy and assessed after 7 days. Viability was assessed using CellTiter-Glo® Assay according to the manufacturer's instructions (Promega, Madison, WI; #G7571). A Synergy™ 2 microplate reader with Gen5™ software (BioTek Instruments, Winooski, VT) was used to measure luminescence. For each plate, mean relative luminescence was calculated from at least three technical replicates, normalized to control samples. Non-linear regression algorithms in Prism software (GraphPad8) were used to calculate IC_{50} values.

Real-time qPCR detection of mtDNA

mtDNA content was quantified by qPCR to define the mtDNA/nucDNA ratio using each of the two mitochondrial genome (MT-C01 and MT-ATPase6) and two nuclear genome (CFAP410 and MTTP) genes. Assays were run in triplicate using Taqman Gene Expression Mastermix (4369016, Applied Biosystems) and the following primer/probes from Invitrogen: MT-CO1 (Hs02596864_g1), MT-ATPase6 (Hs02596862_g1), CFAP410 (Hs00223770_cn), and MTTP (HS0405900_cn). mtDNA/nucDNA ratio was determined as the mean and SD of all biological replicates.

Citrate synthase measurements

Mitochondrial mass was assessed by measuring citrate synthase activity from 4 million whole cells normalized to protein input (U/mg) in triplicate from three biological replicates using the Citrate Synthase Assay kit (CS0720, Sigma-Aldrich, St, Louis, MO).

Electron microscopy

Intact cells for 2D electron microscopic morphometry were fixed with 2% glutaraldehyde with 1% tannic acid in 0.1 M sodium cacodylate buffer, pH 7.4, overnight at 4°C. After buffer washes, the samples were post-fixed in 2.0% osmium tetroxide with 1.5% K_3Fe $(CN)_6$ for 1 h at room temperature, and rinsed in ddH_2O prior to *en bloc* staining with 2% uranyl acetate. After dehydration through a graded ethanol series, the tissue was infiltrated and embedded in EMbed-812 (Electron Microscopy Sciences, Fort Washington, PA). Thin 70 nm sections were stained with uranyl acetate and SATO lead and examined with a JEOL 1010 electron microscope (JEOL, Peabody, MA) at 70 kV fitted with a Hamamatsu digital camera and AMT Advantage NanoSprint500 software. MAM and mitochondria characteristics were obtained from TEM images at 50,000× magnification analyzed blinded in Image J after hand masking the mitochondria perimeter and ER interface. Analysis of the ER–mitochondria interfaces were extracted with a custom macro (Bartok *et al*, 2019) available at: http://sites.imagej.net/MitoCare/ that quantifies ER interface metrics binned within a 10, 25, 50, or 100 nm gap distance from the mitochondria (Csordas *et al*, 2006).

Calcium transfer

Mitochondria-targeted calcium reporter 4mtGCamp6f was electroporated into cells with Amaxa Nucleofactor (Lonza, Basel, Switzerland). Cells recovered in full IMDM media for 24 h and were plated on poly-D lysine covered slides, washed three times with Ca^{2+}-free HBSS medium (Life Technologies Inc., Grand Island, NY), and loaded with 1 µM Fura 2-AM (Life Technologies Inc., Eugene, OR) cytoplasmic calcium indicator in the presence of 0.03% Pluronic F127 and 100 µM sulfinpyrazone at 35°C for 30 min. Fura-2AM-loaded cells were washed with Ca^{2+}-free HBSS medium and mounted into microscope loading chambers on a thermostat-controlled (37°C) stage of Olympus IX70 inverted microscope with LambdaDG4 wavelength-switch xenon light source (Sutter, Novato, CA) optimized by custom Spectralyzer software. Fura2 fluorescence was recorded with 340/11 nm and 380/11 nm excitation while 485/15 nm excitation was used for the mitochondrial matrix-targeted GCaMP6f using dual-band dichroic and emission filters (Chroma, customized set 59022). Images were collected on a high quantum efficiency cooled CCD camera every 0.25 s. $[Ca^{2+}]_c$ measurements with fura2 were calibrated *in vitro* by adding 1 mM $CaCl_2$, followed by 10 mM EGTA/Tris, pH 8.5. Basal fluorescent levels were measured for 120 s, after which calcium release was evoked by addition of 100 µM carbachol. To determine $[Ca^{2+}]$, the following formula was used:

$$[Ca^{2+}] = K_d \times (S_{f2}/S_{b2}) \times (R - R_{min})/(R_{max} - R),$$

where K_d is the Ca^{2+} dissociation constant (0.224 µM), R is the ratio of the fluorescence intensities at 340/380 nm excitation, R_{min} and R_{max} are the fluorescence ratios in Ca^{2+}-free and Ca^{2+}-saturated conditions, respectively, and S_{f2}/S_{b2} is the ratio of fluorescence intensities measured at 380 nm excitation in Ca^{2+}-free (f)/Ca^{2+}-saturated (Ca^{2+} bound, b) conditions (Csordas & Hajnoczky, 2001). $[Ca^{2+}]$ is measured over regions of interest (cells) and cells with cytosolic distributed GCaMP6f were excluded from analyses.

To determine coupling time, the delay between ½ max $[Ca^{2+}]_c$ and ½ max $[Ca^{2+}]_m$ was calculated for each cell.

Lipidomics

Modified Bligh and Dyer lipid extraction was used. Cell pellets were added to 900 μl ice-chilled chloroform/methanol (1:2; v/v) and vortexed 15 s, then incubated in 4°C on a mixer (300 rpm) for 1 h. After agitation, 300 μl of ice-chilled chloroform and 250 μl of ice-chilled MQ water were added sequentially, followed by vortex for 15 s and centrifugation at 9,000 rpm for 2 min to separate the phase. Bottom organic phases were collected, and the aqueous phases were re-extracted with 500 μl of chilled chloroform. Collected organic phases were dried in a vacuum concentrator and stored lyophilized at −80°C. Samples were solubilized in 100 μl chloroform/methanol (1:1; v/v) and analyzed using a Waters Acquity UPLC I class coupled with a Waters Synapt G2-Si (Waters Corp, Milford, MA). Lipids were separated in reverse phase using an Acquity UPLC HSS T3 1.8 μm column with the following conditions: mobile phase A (water:acetonitrile, 40:60, with 10 μM ammonium acetate and 0.1% acetic acid), B (water:acetonitrile:isopropanol:acetic acid, 5:10:85:0.1, with 10 μM ammonium acetate and 0.1% acetic acid); flow rate of 300 μl/min; injection volume of 5 μl; column temperature at 55°C; 20% B for 1.5 min; linear change to 100% B over next 16.5min; and maintained at 100% B for 3 min. Then, the gradient was reverted back to initial state 20% B for 1 min then held for next 1 min at 20% B. QC samples were injected prior to, and after every 5 samples, to monitor the stability of the instrument. Samples were run under untargeted positive and negative electrospray ionization (ESI) modes in a data-independent manner (MSE mode). The following ESI conditions were used: for positive, capillary at 2 kV, sampling cone at 35 V, source temperature at 100°C, desolvation gas at 500 l/h, and nebulizer at 6.5 bar; and for negative, capillary at 2.2 kV, sampling cone at 40 V, source temperature at 80°C, desolvation gas at 500 l/h, and nebulizer at 6.5 bar. For lock mass correction, leucine enkephain was used at 1 ng/ml in acetonitrile/water (1:1, v/v) with 0.1% formic acid and at a flow rate of 10 μl/min. The low collision energy was set to 4 eV and high collision energy was set between 25 and 40 eV for both positive and negative modes. Raw data were converted into ABF format using Reifycs Analysis Base File Converter, then used in MS-Dial (ver. 4.60) for peak picking and retention time alignment using default settings. Lipid species were manually verified and named using Lipid Maps abbreviations. The intensities were normalized with total ionic current. These species were exported into R (ver. 4.0.3) to calculate the concentration using the known concentration of spiked internal standards.

Plasmids, retroviral constructs, and reagents

A synthetic mitochondria–ER linker was used to recouple ER and mitochondria, as described (Csordas et al, 2006). Lentiviral shRNAs to MFN2 (RHS5086-EG9927-GIPZ MFN2), PACS2 (RHS5086-EG23241-GIPZ PACS2) and GIPZ non-silencing lentiviral shRNA control were purchased from GE Health Dharmacon, Inc., Lafayette, CO. 4mtGCamp6f was provided by Dr. Diego De Stefani. Primary antibodies were as follows: Bak (3814, Cell Signaling Technologies, Danvers, MA), Bax (2774, Cell Signaling), Bap31 (ab109304, Abcam Inc., Cambridge, MA), β-tubulin (T8328, Sigma-Aldrich, St. Louis,

MO), calnexin (C7617, Sigma-Aldrich), FACL4 (22401-1-AP, Proteintech, Rosemond, IL), Gapdh (2118, Cell Signaling), γ-H2AX (NB100-384, Novus, Littleton, CO), Mfn2 (ab56889, Abcam Inc.), Mcu (HPA016480, Sigma-Aldrich), noxa (OP180, Calbiochem/EMD Chemicals, San Diego, CA), PACS2 (ab129402, Abcam Inc.), p53 (sc-126, Santa Cruz Biotechnology, Dallas, TX), p21 (sc-6246, Santa Cruz Biotechnology), Tmx1 (256-270, SAB1105403, Sigma-Aldrich), Tomm40 (18409-1-AP, Proteintech), and Vdac1 (D73D12, Cell Signaling). To quantify protein abundance, densitometry was performed using Image J. The intensity of each band was normalized to its respective loading control for comparison.

DNA damage detection

A total of 10,000 cells were plated onto poly-L lysine-coated microscope slides, allowed to adhere 24 h, and irradiated at 2 Gy for 1 h on a Cs-137 Gammacell 40 irradiator S/N 186 (Nordion Ltd, Kanata, Ontario, Canada) at a dose rate of 1.3 cGy/s. Cells were washed once with warm PBS and fixed with pre-warmed paraformaldehyde for 10 min, permeabilized with 2% Triton-PBS for 5 min at 4°C, washed twice with PBS-5% triton, and blocked for 10 min in Duolink blocking solution. Cells were then incubated for 1 h at 37°C with γ-H2AX primary antibody (NB100-384, Novus Biologicals, Centennial, CO) at 1:1,000 dilution, washed twice with PBS-T, and incubated at 37°C with AlexaFluor goat anti-rabbit 488 (ab150077; Abcam Inc., Cambridge, MA) at 1:500 dilution for 45 min. After washing four times with PBS-T, they were stained with VectaShield DAPI staining, covered with a microscope coverslip, and analyzed using a Leica DMR fluorescent microscope at 40× magnification, and the number of γ-H2AX foci/cell quantified.

Statistical analyses

Statistical comparisons for mitochondrial size, roundness, circularity, MAM content per mitochondria, and γ-H2AX foci were performed with the Mann–Whitney U test, two tailed; comparisons for cytochrome c release, Ca^{2+} transfer coupling time, lipid content, mtDNA content, and mass were performed with the Student's t-test, independent values, two tailed; and comparisons for the proportion of mitochondria with diverse tether numbers were performed using the Chi-Square test. For all, significance was defined as $P < 0.05$, trend $P < 0.10$, and non-significant as $P \geq 0.10$.

Data availability

This study includes lipidomics data that are available for public access at the NIH Common Fund's National Metabolomics Data Repository (NMDR) website, the Metabolomics Workbench (https://www.metabolomicsworkbench.org), where it has been assigned Study ID ST002054 (Sur et al, 2016).

Expanded View for this article is available online.

Author contributions

Jorida Çoku: Conceptualization; Data curation; Formal analysis; Validation; Investigation; Visualization; Methodology; Writing—original draft; Project administration; Writing—review and editing. **David M Booth:** Software; Validation; Investigation; Visualization; Methodology; Writing—review and editing. **Jan Skoda:** Formal analysis; Validation; Investigation; Visualization; Writing—review and editing. **Madison C Pedrotty:** Data curation; Formal analysis; Investigation. **Jennifer Vogel:** Data curation; Formal analysis; Investigation; Methodology; Writing—review and editing. **Kangning Liu:** Conceptualization; Data curation; Formal analysis; Supervision; Validation; Investigation; Methodology; Writing—review and editing. **Annette Vu:** Data curation; Formal analysis; Investigation; Methodology; Writing—review and editing. **Erica L Carpenter:** Data curation; Formal analysis; Investigation; Visualization; Methodology; Writing—review and editing. **Jamie C Ye:** Data curation; Formal analysis; Investigation; Methodology. **Michelle A Chen:** Data curation; Formal analysis; Investigation; Methodology. **Peter Dunbar:** Data curation; Formal analysis; Validation; Investigation; Visualization; Methodology. **Elizabeth Scadden:** Data curation; Formal analysis; Investigation; Methodology; Writing—review and editing. **Taekyung D Yun:** Validation; Investigation; Visualization; Methodology; Writing—review and editing. **Eiko Nakamaru-Ogiso:** Data curation; Formal analysis; Supervision; Validation; Investigation; Visualization; Methodology; Writing—review and editing. **Estela Area-Gomez:** Conceptualization; Funding acquisition; Investigation; Methodology; Project administration; Writing—review and editing. **Yimei Li:** Data curation; Software; Formal analysis; Validation; Writing—review and editing. **Kelly C Goldsmith:** Data curation; Formal analysis; Funding acquisition; Validation; Investigation; Visualization; Methodology; Writing—review and editing. **C Patrick Reynolds:** Conceptualization; Data curation; Formal analysis; Supervision; Funding acquisition; Investigation; Visualization; Methodology; Writing—original draft; Project administration; Writing—review and editing. **Gyorgy Hajnoczky:** Conceptualization; Data curation; Funding acquisition; Validation; Investigation; Visualization; Methodology; Project administration; Writing—review and editing. **Michael D Hogarty:** Conceptualization; Data curation; Formal analysis; Supervision; Funding acquisition; Investigation; Visualization; Methodology; Writing—original draft; Project administration; Writing—review and editing.

In addition to the CRediT author contributions listed above, the contributions in detail are:

JC, DMB, JV, CPR, JS, GH, EA-G, and MDH designed the experiments; CPR provided tumor models and model validation; JC, DMB, KCG, MCP, JV, KL, JCY, MAC, ES, PD, EN-O, ELC, JS, and AV conducted the experiments and acquired data related to ER–mitochondria connectivity, signaling, and stress response; JC, DMB, and GH conducted the experiments and acquired data related to calcium transfer; TDY and EA-G conducted lipidomic experiments; YL performed statistical analyses; JC, DMB, MCP, JV, KL, JCY, ELC, ES, AV, CPR, JS, GH, TDY, EA-G, and MDH analyzed the data; and JC, JS, DMB, CPR, KCG, GH, EA-G, and MDH wrote and edited the manuscript.

Disclosure and competing interests statement

The authors declare that they have no conflict of interest.

References

Anastasia I, Ilacqua N, Raimondi A, Lemieux P, Ghandehari-Alavijeh R, Faure G, Mekhedov SL, Williams KJ, Caicci F, Valle G *et al* (2021) Mitochondria-rough-ER contacts in the liver regulate systemic lipid homeostasis. *Cell Rep* 34: 108873

Annunziata I, Patterson A, d'Azzo A (2013) Mitochondria-associated ER membranes (MAMs) and glycosphingolipid enriched microdomains (GEMs): isolation from mouse brain. *J uis Exp* 73: e50215

Area-Gomez E, del Carmen Lara Castillo M, Tambini MD, Guardia-Laguarta C, de Groof AJC, Madra M, Ikenouchi J, Umeda M, Bird TD, Sturley SL *et al* (2012) Upregulated function of mitochondria-associated ER membranes in Alzheimer disease. *EMBO J* 31: 4106–4123

Arruda AP, Pers BM, Parlakgul G, Guney E, Inouye K, Hotamisligil GS (2014) Chronic enrichment of hepatic endoplasmic reticulum-mitochondria contact leads to mitochondrial dysfunction in obesity. *Nat Med* 20: 1427–1435

Bartok A, Weaver D, Golenár T, Nichtova Z, Katona M, Bánsághi S, Alzayady KJ, Thomas VK, Ando H, Mikoshiba K *et al* (2019) IP3 receptor isoforms differently regulate ER-mitochondrial contacts and local calcium transfer. *Nat Commun* 10: 3726

Bauer TM, Murphy E (2020) Role of mitochondrial calcium and the permeability transition pore in regulating cell death. *Circ Res* 126: 280–293

Baughman JM, Perocchi F, Girgis HS, Plovanich M, Belcher-Timme CA, Sancak Y, Bao XR, Strittmatter L, Goldberger O, Bogorad RL *et al* (2011) Integrative genomics identifies MCU as an essential component of the mitochondrial calcium uniporter. *Nature* 476: 341–345

Birbes H, El Bawab S, Hannun YA, Obeid LM (2001) Selective hydrolysis of a mitochondrial pool of sphingomyelin induces apoptosis. *FASEB J* 15: 2669–2679

Bresler S, Weiser D, Huwe P, Park J, Krytska K, Ryles H, Laudenslager M, Rappaport E, Wood A, McGrady P *et al* (2014) ALK mutations confer differential oncogenic activation and sensitivity to ALK inhibition therapy in neuroblastoma. *Cancer Cell* 26: 682–694

de Brito OM, Scorrano L (2008) Mitofusin 2 tethers endoplasmic reticulum to mitochondria. *Nature* 456: 605–610

Cali T, Ottolini D, Brini M (2013) Calcium and endoplasmic reticulum-mitochondria tethering in neurodegeneration. *DNA Cell Biol* 32: 140–146

Chipuk JE, McStay GP, Bharti A, Kuwana T, Clarke CJ, Siskind LJ, Obeid LM, Green DR (2012) Sphingolipid metabolism cooperates with BAK and BAX to promote the mitochondrial pathway of apoptosis. *Cell* 148: 988–1000

Chong CR, Janne PA (2013) The quest to overcome resistance to EGFR-targeted therapies in cancer. *Nat Med* 19: 1389–1400

Chonghaile TN, Sarosiek KA, Vo T-T, Ryan JA, Tammareddi A, Moore VDG, Deng J, Anderson KC, Richardson P, Tai Y-T *et al* (2011) Pretreatment mitochondrial priming correlates with clinical response to cytotoxic chemotherapy. *Science* 334: 1129–1133

Cohen DT, Wales TE, McHenry MW, Engen JR, Walensky LD (2020) Site-dependent cysteine lipidation potentiates the activation of proapoptotic BAX. *Cell Rep* 30: 3229–3239

Cowan AD, Smith NA, Sandow JJ, Kapp EA, Rustam YH, Murphy JM, Brouwer JM, Bernardini JP, Roy MJ, Wardak AZ *et al* (2020) BAK core dimers bind lipids and can be bridged by them. *Nat Struct Mol Biol* 27: 1024–1031

Cripe LD, Uno H, Paietta EM, Litzow MR, Ketterling RP, Bennett JM, Rowe JM, Lazarus HM, Luger S, Tallman MS (2010) Zosuquidar, a novel modulator

of P-glycoprotein, does not improve the outcome of older patients with newly diagnosed acute myeloid leukemia: a randomized, placebo-controlled trial of the Eastern Cooperative Oncology Group 3999. *Blood* 116: 4077–4085

Csordas G, Hajnoczky G (2001) Sorting of calcium signals at the junctions of endoplasmic reticulum and mitochondria. *Cell Calcium* 29: 249–262

Csordas G, Renken C, Varnai P, Walter L, Weaver D, Buttle KF, Balla T, Mannella CA, Hajnoczky G (2006) Structural and functional features and significance of the physical linkage between ER and mitochondria. *J Cell Biol* 174: 915–921

Csordas G, Varnai P, Golenar T, Roy S, Purkins G, Schneider TG, Balla T, Hajnoczky G (2010) Imaging interorganelle contacts and local calcium dynamics at the ER-mitochondrial interface. *Mol Cell* 39: 121–132

Csordas G, Weaver D, Hajnoczky G (2018) Endoplasmic reticulum-mitochondrial contactology: structure and signaling functions. *Trends Cell Biol* 28: 523–540

Danial NN, Korsmeyer SJ (2004) Cell death: critical control points. *Cell* 116: 205–219

De Stefani D, Raffaello A, Teardo E, Szabo I, Rizzuto R (2011) A forty-kilodalton protein of the inner membrane is the mitochondrial calcium uniporter. *Nature* 476: 336–340

Deng J, Carlson N, Takeyama K, Dal Cin P, Shipp M, Letai A (2007) BH3 profiling identifies three distinct classes of apoptotic blocks to predict response to ABT-737 and conventional chemotherapeutic agents. *Cancer Cell* 12: 171–185

Ganesan V, Perera MN, Colombini D, Datskovskiy D, Chadha K, Colombini M (2010) Ceramide and activated Bax act synergistically to permeabilize the mitochondrial outer membrane. *Apoptosis* 15: 553–562

Gavathiotis E, Suzuki M, Davis ML, Pitter K, Bird GH, Katz SG, Tu H-C, Kim H, Cheng E-Y, Tjandra N *et al* (2008) BAX activation is initiated at a novel interaction site. *Nature* 455: 1076–1081

Goldsmith KC, Gross M, Peirce S, Luyindula D, Liu X, Vu A, Sliozberg M, Guo R, Zhao H, Reynolds CP *et al* (2012) Mitochondrial Bcl-2 family dynamics define therapy response and resistance in neuroblastoma. *Cancer Res* 72: 2565–2577

Hajnoczky G, Csordas G, Madesh M, Pacher P (2000) Control of apoptosis by IP(3) and ryanodine receptor driven calcium signals. *Cell Calcium* 28: 349–363

Hata AN, Engelman JA, Faber AC (2015) The BCL2 family: key mediators of the apoptotic response to targeted anticancer therapeutics. *Cancer Discov* 5: 475–487

Hedskog L, Pinho CM, Filadi R, Ronnback A, Hertwig L, Wiehager B, Larssen P, Gellhaar S, Sandebring A, Westerlund M *et al* (2013) Modulation of the endoplasmic reticulum-mitochondria interface in Alzheimer's disease and related models. *Proc Natl Acad Sci USA* 110: 7916–7921

Hinds MG, Smits C, Fredericks-Short R, Risk JM, Bailey M, Huang DC, Day CL (2007) Bim, Bad and Bmf: intrinsically unstructured BH3-only proteins that undergo a localized conformational change upon binding to prosurvival Bcl-2 targets. *Cell Death Differ* 14: 128–136

Holohan C, Van Schaeybroeck S, Longley DB, Johnston PG (2013) Cancer drug resistance: an evolving paradigm. *Nat Rev Cancer* 13: 714–726

Hoppins S, Nunnari J (2012) Cell Biology. Mitochondrial dynamics and apoptosis–the ER connection. *Science* 337: 1052–1054

Howatson AF, Ham AW (1955) Electron microscope study of sections of two rat liver tumors. *Cancer Res* 15: 62–69

Hugo W, Shi H, Sun LU, Piva M, Song C, Kong X, Moriceau G, Hong A, Dahlman K, Johnson D *et al* (2015) Non-genomic and immune evolution of melanoma acquiring MAPKi resistance. *Cell* 162: 1271–1285

Jain A, Beutel O, Ebell K, Korneev S, Holthuis JC (2017) Diverting CERT-mediated ceramide transport to mitochondria triggers Bax-dependent apoptosis. *J Cell Sci* 130: 360–371

Kale J, Osterlund EJ, Andrews DW (2018) BCL-2 family proteins: changing partners in the dance towards death. *Cell Death Differ* 25: 65–80

Katayama R, Shaw AT, Khan TM, Mino-Kenudson M, Solomon BJ, Halmos B, Jessop NA, Wain JC, Yeo AT, Benes C *et al* (2012) Mechanisms of acquired crizotinib resistance in ALK-rearranged lung Cancers. *Sci Transl Med* 4: 120ra117

Keshelava N, Seeger RC, Reynolds CP (1997) Drug resistance in human neuroblastoma cell lines correlates with clinical therapy. *Eur J Cancer* 33: 2002–2006

Keshelava N, Seeger RC, Groshen S, Reynolds CP (1998) Drug resistance patterns of human neuroblastoma cell lines derived from patients at different phases of therapy. *Cancer Res* 58: 5396–5405

Kim H, Rafiuddin-Shah M, Tu HC, Jeffers JR, Zambetti GP, Hsieh JJ, Cheng EH (2006) Hierarchical regulation of mitochondrion-dependent apoptosis by BCL-2 subfamilies. *Nat Cell Biol* 8: 1348–1358

Lee H, Rotolo JA, Mesicek J, Penate-Medina T, Rimner A, Liao W-C, Yin X, Ragupathi G, Ehleiter D, Gulbins E *et al* (2011) Mitochondrial ceramide-rich macrodomains functionalize Bax upon irradiation. *PLoS One* 6: e19783

Lemasters JJ, Theruvath TP, Zhong Z, Nieminen AL (2009) Mitochondrial calcium and the permeability transition in cell death. *Biochim Biophys Acta* 1787: 1395–1401

Lito P, Rosen N, Solit DB (2013) Tumor adaptation and resistance to RAF inhibitors. *Nat Med* 19: 1401–1409

Lord CJ, Ashworth A (2013) Mechanisms of resistance to therapies targeting BRCA-mutant cancers. *Nat Med* 19: 1381–1388

Martino Adami PV, Nichtova Z, Weaver DB, Bartok A, Wisniewski T, Jones DR, Do Carmo S, Castano EM, Cuello AC, Hajnoczky G *et al* (2019) Perturbed mitochondria-ER contacts in live neurons that model the amyloid pathology of Alzheimer's disease. *J Cell Sci* 132: jcs229906

Matthay KK, Reynolds CP, Seeger RC, Shimada H, Adkins ES, Haas-Kogan D, Gerbing RB, London WB, Villablanca JG (2009) Long-term results for children with high-risk neuroblastoma treated on a randomized trial of myeloablative therapy followed by 13-cis-retinoic acid: a children's oncology group study. *J Clin Oncol* 27: 1007–1013

Montero J, Sarosiek K, DeAngelo J, Maertens O, Ryan J, Ercan D, Piao H, Horowitz N, Berkowitz R, Matulonis U *et al* (2015) Drug-induced death signaling strategy rapidly predicts cancer response to chemotherapy. *Cell* 160: 977–989

Morad SA, Cabot MC (2013) Ceramide-orchestrated signalling in cancer cells. *Nat Rev Cancer* 13: 51–65

Moulis M, Grousset E, Faccini J, Richetin K, Thomas G, Vindis C (2019) The multifunctional sorting protein PACS-2 controls mitophagosome formation in human vascular smooth muscle cells through mitochondria-ER contact sites. *Cells* 8: 638

Olivier M, Hollstein M, Hainaut P (2010) TP53 mutations in human cancers: origins, consequences, and clinical use. *Cold Spring Harb Perspect Biol* 2: a001008

Ottolini D, Cali T, Negro A, Brini M (2013) The Parkinson disease-related protein DJ-1 counteracts mitochondrial impairment induced by the tumour suppressor protein p53 by enhancing endoplasmic reticulum-mitochondria tethering. *Hum Mol Genet* 22: 2152–2168

Paillard M, Tubbs E, Thiebaut P-A, Gomez L, Fauconnier J, Crola Da Silva C, Teixeira G, Mewton N, Belaidi E, Durand A *et al* (2013) Depressing mitochondria-reticulum interactions protects cardiomyocytes from lethal hypoxia-reoxygenation injury. *Circulation* 128: 1555–1565

Park JH, Zhuang J, Li J, Hwang PM (2016) p53 as guardian of the mitochondrial genome. *FEBS Lett* 590: 924–934

Patergnani S, Giorgi C, Maniero S, Missiroli S, Maniscalco P, Bononi I, Martini F, Cavallesco G, Tognon M, Pinton P (2015) The endoplasmic reticulum mitochondrial calcium cross talk is downregulated in malignant pleural mesothelioma cells and plays a critical role in apoptosis inhibition. *Oncotarget* 6: 23427–23444

Pinto NR, Applebaum MA, Volchenboum SL, Matthay KK, London WB, Ambros PF, Nakagawara A, Berthold F, Schleiermacher G, Park JR *et al* (2015) Advances in risk classification and treatment strategies for neuroblastoma. *J Clin Oncol* 33: 3008–3017

Ren D, Tu HC, Kim H, Wang GX, Bean GR, Takeuchi O, Jeffers JR, Zambetti GP, Hsieh JJ, Cheng EH (2010) BID, BIM, and PUMA are essential for activation of the BAX- and BAK-dependent cell death program. *Science* 330: 1390–1393

Renault TT, Chipuk JE (2014) Death upon a kiss: mitochondrial outer membrane composition and organelle communication govern sensitivity to BAK/BAX-dependent apoptosis. *Chem Biol* 21: 114–123

Renault T, Floros K, Elkholi R, Corrigan K-A, Kushnareva Y, Wieder S, Lindtner C, Serasinghe M, Asciolla J, Buettner C *et al* (2015) Mitochondrial shape governs BAX-induced membrane permeabilization and apoptosis. *Mol Cell* 57: 69–82

Rieusset J (2011) Mitochondria and endoplasmic reticulum: mitochondria-endoplasmic reticulum interplay in type 2 diabetes pathophysiology. *Int J Biochem Cell Biol* 43: 1257–1262

Rizzuto R, Pozzan T (2006) Microdomains of intracellular Ca^{2+}: molecular determinants and functional consequences. *Physiol Rev* 86: 369–408

Rowland AA, Voeltz GK (2012) Endoplasmic reticulum-mitochondria contacts: function of the junction. *Nat Rev Mol Cell Biol* 13: 607–625

Sarosiek KA, Chi X, Bachman JA, Sims JJ, Montero J, Patel L, Flanagan A, Andrews DW, Sorger P, Letai A (2013a) BID preferentially activates BAK while BIM preferentially activates BAX, affecting chemotherapy response. *Mol Cell* 51: 751–765

Sarosiek KA, Ni Chonghaile T, Letai A (2013b) Mitochondria: gatekeepers of response to chemotherapy. *Trends Cell Biol* 23: 612–619

Schauder CM, Wu X, Saheki Y, Narayanaswamy P, Torta F, Wenk MR, De Camilli P, Reinisch KM (2014) Structure of a lipid-bound extended synaptotagmin indicates a role in lipid transfer. *Nature* 510: 552–555

Scorrano L, Oakes SA, Opferman JT, Cheng EH, Sorcinelli MD, Pozzan T, Korsmeyer SJ (2003) BAX and BAK regulation of endoplasmic reticulum Ca^{2+}: a control point for apoptosis. *Science* 300: 135–139

Simmen T, Aslan JE, Blagoveshchenskaya AD, Thomas L, Wan L, Xiang Y, Feliciangeli SF, Hung CH, Crump CM, Thomas G (2005) PACS-2 controls endoplasmic reticulum-mitochondria communication and Bid-mediated apoptosis. *EMBO J* 24: 717–729

Sur M, Fahy E, Cotter D, Azam K, Vadivelu I, Burant C, Edison A, Fiehn O, Higashi R, Sreekumaran Nair K *et al* (2016) Metabolomics workbench: an international repository for metabolomics data and metadata, metabolite standards, protocols, tutorials and training, and analysis tools. *Nuc Acids Res* 44: D463–D470

Swanton C, Marani M, Pardo O, Warne PH, Kelly G, Sahai E, Elustondo F, Chang J, Temple J, Ahmed AA *et al* (2007) Regulators of mitotic arrest and ceramide metabolism are determinants of sensitivity to paclitaxel and other chemotherapeutic drugs. *Cancer Cell* 11: 498–512

Tan TT, Degenhardt K, Nelson DA, Beaudoin B, Nieves-Neira W, Bouillet P, Villunger A, Adams JM, White E (2005) Key roles of BIM-driven apoptosis in epithelial tumors and rational chemotherapy. *Cancer Cell* 7: 227–238

Uccini S, Colarossi C, Scarpino S, Boldrini R, Natali PG, Nicotra MR, Perla FM, Mannarino O, Altavista P, Boglino C *et al* (2006) Morphological and molecular assessment of apoptotic mechanisms in peripheral neuroblastic tumours. *Br J Cancer* 95: 49–55

Vo TT, Ryan J, Carrasco R, Neuberg D, Rossi DJ, Stone RM, Deangelo DJ, Frattini MG, Letai A (2012) Relative mitochondrial priming of myeloblasts and normal HSCs determines chemotherapeutic success in AML. *Cell* 151: 344–355

Walensky LD, Pitter K, Morash J, Oh KJ, Barbuto S, Fisher J, Smith E, Verdine GL, Korsmeyer SJ (2006) A stapled BID BH3 helix directly binds and activates BAX. *Mol Cell* 24: 199–210

Wilson F, Johannessen C, Piccioni F, Tamayo P, Kim J, Van Allen E, Corsello S, Capelletti M, Calles A, Butaney M *et al* (2015) A functional landscape of resistance to ALK inhibition in lung cancer. *Cancer Cell* 27: 397–408

Zampese E, Fasolato C, Kipanyula MJ, Bortolozzi M, Pozzan T, Pizzo P (2011) Presenilin 2 modulates endoplasmic reticulum (ER)-mitochondria interactions and Ca^{2+} cross-talk. *Proc Natl Acad Sci USA* 108: 2777–2782

Kameneva P, Melnikova VI, Kastriti ME, Kurtova A, Kryukov E, Murtazina A, Faure L, Poverennaya I, Artemov AV, Kalinina TS, Kudryashov NV, Bader M, **Skoda J**, Chlapek P, Curylova L, Sourada L, Neradil J, Tesarova M, Pasqualetti M, Gaspar P, Yakushov VD, Sheftel BI, Zikmund T, Kaiser J, Fried K, Alenina N, Voronezhskaya EE, Adameyko I. Serotonin limits generation of chromaffin cells during adrenal organ development. *Nature Communications*. 2022;13:2901. (JCR 2022, IF = 16.6; T10 - Multidisciplinary Sciences)

ARTICLE

Check for updates

Serotonin limits generation of chromaffin cells during adrenal organ development

Polina Kameneva[1,2,19], Victoria I. Melnikova [3,19], Maria Eleni Kastriti [1,2], Anastasia Kurtova [3], Emil Kryukov [1,2], Aliia Murtazina[2], Louis Faure [1], Irina Poverennaya[1], Artem V. Artemov[1,4], Tatiana S. Kalinina[5], Nikita V. Kudryashov [5,6], Michael Bader[7,8,9,10], Jan Skoda [11,12], Petr Chlapek[11,12], Lucie Curylova [11,12], Lukas Sourada [11,12], Jakub Neradil [11,12], Marketa Tesarova [13], Massimo Pasqualetti [14,15], Patricia Gaspar [16], Vasily D. Yakushov[17], Boris I. Sheftel[17], Tomas Zikmund [13], Jozef Kaiser [13], Kaj Fried[18], Natalia Alenina[7,8], Elena E. Voronezhskaya[3✉] & Igor Adameyko [1,2✉]

Adrenal glands are the major organs releasing catecholamines and regulating our stress response. The mechanisms balancing generation of adrenergic chromaffin cells and protecting against neuroblastoma tumors are still enigmatic. Here we revealed that serotonin (5HT) controls the numbers of chromaffin cells by acting upon their immediate progenitor "bridge" cells via 5-hydroxytryptamine receptor 3A (HTR3A), and the aggressive HTR3A^{high} human neuroblastoma cell lines reduce proliferation in response to HTR3A-specific agonists. In embryos (in vivo), the physiological increase of 5HT caused a prolongation of the cell cycle in "bridge" progenitors leading to a smaller chromaffin population and changing the balance of hormones and behavioral patterns in adulthood. These behavioral effects and smaller adrenals were mirrored in the progeny of pregnant female mice subjected to experimental stress, suggesting a maternal-fetal link that controls developmental adaptations. Finally, these results corresponded to a size-distribution of adrenals found in wild rodents with different coping strategies.

[1] Department of Neuroimmunology, Center for Brain Research, Medical University Vienna, Vienna, Austria. [2] Department of Physiology and Pharmacology, Karolinska Institute, Stockholm, Sweden. [3] Koltsov Institute of Developmental Biology, Russian Academy of Sciences, Moscow, Russia. [4] National Medical Research Center for Endocrinology, Moscow, Russia. [5] Federal state budgetary institution "Research Zakusov Institute of Pharmacology" (FSBI "Zakusov Institute of Pharmacology"), Russian Academy of Sciences, Moscow, Russia. [6] Sechenov First Moscow State Medical University (Sechenov University), Moscow, Russia. [7] Max-Delbrück Center for Molecular Medicine (MDC), 13125 Berlin-Buch, Germany. [8] German Center for Cardiovascular Research (DZHK), Partner Site Berlin, Germany. [9] Charité-Universitätsmedizin Berlin, 10117 Berlin, Germany. [10] Institute for Biology, University of Lübeck, 23562 Lübeck, Germany. [11] Department of Experimental Biology, Faculty of Science, Masaryk University, Brno, Czech Republic. [12] International Clinical Research Center, St. Anne's University Hospital, Brno, Czech Republic. [13] Central European Institute of Technology, Brno University of Technology, Brno, Czech Republic. [14] Unit of Cell and Developmental Biology, Department of Biology, University of Pisa, Pisa, Italy. [15] Center for Neuroscience and Cognitive Systems @UniTn, Istituto Italiano di Tecnologia, Rovereto, Italy. [16] INSERM, Paris Brain Institute, Paris, France. [17] Severtsov Institute of Ecology and Evolution, Russian Academy of Sciences, Moscow, Russia. [18] Department of Neuroscience, Karolinska Institute, Stockholm, Sweden. [19]These authors contributed equally: Polina Kameneva, Victoria I. Melnikova. ✉email: elena.voronezhskaya@idbras.ru; igor.adameyko@ki.se

A drenal glands are key hormonal regulators in our body, as they control major physiological processes of our daily life, and homeostasis cannot be maintained without their normal function. The structure of adrenal glands includes the cortical matter, consisting of cells that produce steroid hormones, and the centrally positioned medulla (adrenal medulla—AM), which orchestrates the response of our body to stress by releasing catecholamines (adrenaline and noradrenaline). Quite remarkably, there is another similar catecholamine-producing organ transiently present in our body, namely the Organ of Zuckerkandl (ZO)[1]. The ZO eventually disappears during the first years of human life. Chromaffin cells represent the major catecholamine-producing cell type in the AM and in ZO (together called chromaffin organs).

Despite the importance for our physiology, the key details of adrenal gland development remain unclear. These details are important not only for the adrenal gland engineering attempts or for understanding associated congenital abnormalities, but also for coping with tumors arising from sympathoadrenal lineage, namely neuroblastoma, pheochromocytoma, and paraganglioma. According to a recent paradigm, tumor cells exploit and re-play developmental programs to elicit intra-tumoral plasticity and resist treatment[2]. In addition, the good knowledge of developmental steps and molecular profiles assists better classification of tumors and helps to pinpoint the tumor-initiating cell types using transcriptional similarity of malignant cells to particular developmental cell states[3–5].

In line with this reasoning, recent studies showed that the initial stages of chromaffin cell development depend on the recruitment of local nerve-associated Schwann cell precursors (SCPs), which turn into a short-living transient population of "bridge" cells that rapidly transitions towards mature chromaffin cells in mouse and human embryos[6–9]. This finding complicated the old picture of adrenal development (where migratory neural crest cells immediately generate chromaffin tissues), and raised a series of questions regarding the control of the number of chromaffin progenitors operating during the differentiation steps. These "bridge" cells are characterized by the expression of *Htr3a*[6,8]—a gene encoding for a subunit of HTR3 receptor to serotonin (5-hydroxytryptamine, 5HT). Based on that, 5HT was recently hinted to be a part of the mechanism related to the development of adrenal medulla[6].

More generally, 5HT is crucial for the embryonic development[10] and for postnatal growth in the animal kingdom[11–13], including the formation of the nervous system[14–16]. Moreover, 5HT is one of the main players shaping mood, fight-or-flight stress response, and aggressive behavior in mammals[17]. One of the key connection between embryonic development, chromaffin organs and 5HT comes from studies of animal domestication. Domesticated animals have higher levels of 5HT and less catecholamine-triggered aggressive behaviors[18]. Genetic differences between wild and tame animals of the same species include genes encoding for the enzymes of 5HT synthesis and degradation[19]. Moreover, the adrenal glands of domesticated animals are smaller than their wild relatives[20,21]. Therefore, behavioral differences can be attributed to variations in 5HT and catecholamine systems and to the size of the respective endocrine organs, particularly the adrenal glands, which are shaped during embryonic development.

In this study, by analysing cellular composition and cell dynamics in the developing adrenal medulla and ZO, we show a 5HT-mediated regulatory negative feedback loop between chromaffin cells and their immediate precursor "bridge" cells. In line with this, we demonstrate that neuroblastoma cell lines with high expression of HTR3A are more tumorigenic and respond to HTR3A agonists with reduced proliferation rate. Finally, we

discover that high levels of mother-derived 5HT affect the development of embryonic adrenal medulla in a systemic way, being possibly involved in transmission of environmental signals and stress-related states from pregnant mother to her progeny. Indeed, we find that maternal mild stress induces smaller adrenal medullae in the progeny of stressed animals. Furthermore, the wild rodent population demonstrate a natural distribution of adrenal medulla sizes correlated with their preferred individual lifestyles. Taken together, these results support a major ecological and evolutionary role of the mechanisms controlling the development of adrenal glands and, in particular, chromaffin cells via a 5HT pathway.

Results

5HT-secreting and 5HT-sensitive cells in chromaffin organs. To address the role of 5HT signaling in adrenal gland development, we re-analyzed the expression of related enzymes and receptors using previously published single-cell transcriptomics dataset of chromaffin and sympathetic development at E12.5 and E13.5 stages[6] (Supplementary Fig. 1). As shown earlier by Furlan et al., chromaffin cells originate from SCPs and the differentiation progresses through the transitory "bridge" population. Thus "bridge" cells are immediate progenitors of chromaffin cells (Supplementary Fig. 1a). According to our analysis at E12.5, *Htr3a/3b* (encoding 5HT-receptor 3A/3B) are strongly expressed in the population of "bridge" cells and are only sporadically expressed in cells from other clusters. At E13.5, *Htr3a/3b* specifically marks the "bridge" cell population and also appears to be present in a minor portion of sympathoblasts (Supplementary Fig. 1b). To check if *HTR3A* is expressed in human adrenal medulla during development, we isolated adrenal glands at weeks 5-to-7 and subjected them to single-cell transcriptomics analysis with Chromium 10X approach. The results showed the sparse expression of *HTR3A* in "bridge" cells and rather consistent expression in sympathoblasts (Supplementary Fig. 2a, b). Although we detected only 6 *HTR3A*+ cells in a "bridge" population, the statistical test supports the significance of this find (Supplementary Fig. 2c). At the same time, this suggests low expression level of *HTR3A*, which we experimentally validated with RNAscope in situ hybridisation on slices of week 6 and week 8 human adrenal tissue (Supplementary Fig. 2d). Indeed, if the expression of *HTR3A* is truly present, it is weak and at the border of detection, which leaves the question about the role of *HTR3A* in human "bridge" cells open. Consistently, the data from other groups show almost absent expression of *HTR3A* from SCPs and "bridge" cells in developing human adrenal medulla despite its clear presence in sympathoblasts[22]. Again, a question of whether *HTR3A* is sufficiently present in "bridge" cells of human adrenal glands requires further investigation with more sensitive methods.

5HT, the ligand activating the ion channel receptor formed by HTR3A/3B proteins, can be supplied through the embryonic bloodstream, although it might be also produced locally by other cells of the developing adrenal medulla (AM). Thus, we explored different cell types in AM for the presence of enzymatic cascades necessary to produce local 5HT. It turned out that nearly all cells in AM express *Ddc* gene encoding the enzyme responsible for decarboxylating 5HTP (5-hydroxytryptophan) into 5HT, and *Maoa* gene encoding the enzyme responsible for monoamine degradation. At the same time, the synthesis of 5HT from tryptophan does not take place in AM cells, as most cells do not express the *Tph1* and *Tph2* genes at E12.5 and E13.5 (Supplementary Fig. 1c). Thus, the majority of immature and mature chromaffin cells, and a subset of SCPs and "bridge" cells are capable of producing 5HT from the chemical precursor

5HTP, but not from tryptophan. In addition to this, at E12.5, chromaffin cells are positive for *Slc29a4*, which encodes Plasma Membrane Monoamine Transporter (PMAT)—a non-selective transporter responsible for pumping 5HT inside the cells (Supplementary Fig. 1d). Therefore, embryonic chromaffin cells are capable of taking 5HT from the bloodstream, especially given that the adrenal glands are heavily vascularized. Moreover, chromaffin cells and sympathoblasts express *Slc18a1* and *Slc18a2*, which encode for VMAT1 and VMAT2, non-selective vesicular monoamine transporters responsible for the storage of monoamines in intracellular secretory vesicles. Therefore, chromaffin cells possess the necessary molecular machinery to uptake, synthesize, and secrete 5HT, and they originate from the 5HT-sensitive HTR3A^{+} "bridge" cells.

To characterize the local cell type composition and to assess the physical contacts between different cell types in AM and ZO, we took advantage of a standard combination of immunohistochemical markers (SOX10 for SCPs, tyrosine hydroxylase (TH) for chromaffin cells, and 5HT) together with genetically modified *Htr3a*[EGFP] mice in order to visualize "bridge" cells and their newly-differentiated progeny[23]. Because EGFP can be retained in cells up to 48 h after the cease of active expression[24], we additionally visualized "bridge" cells by *Htr3a* mRNA in situ hybridization, which revealed a proportion of *Htr3a*[EGFP+] cells actively expressing *Htr3a* mRNA in developing AM at the time of the observations (Supplementary Fig. 3a). This result shows that *Htr3a*[EGFP+] cells negative for *Htr3a* mRNA (post-bridge cells) rapidly differentiate into TH^{+} chromaffin cells. No chromaffin cells were found positive for *Htr3a* mRNA (Supplementary Fig. 3b). Therefore, the *Htr3a*[EGFP] mouse strain can be used to trace the transition from the intermediate "bridge" cell population to the chromaffin cells by assessing the proportions of TH[−]/*Htr3a*[EGFP+] "bridge" cells, TH[+]/*Htr3a*[EGFP+] early chromaffin cells and TH[+]/*Htr3a*[EGFP−] mature chromaffin cells.

AM and ZO are dynamically developing organs, and, therefore, the proportion of cells building AM and ZO changes between E12.5 and E14.5 towards more mature cell types (Fig. 1). Indeed, TH[−]/*Htr3a*[EGFP+] "bridge" cells compose most of the AM and ZO at E12.5 (Fig. 1a–d, Supplementary Fig. 4a–d), and they rapidly differentiate into TH[+]/*Htr3a*[EGFP+] early chromaffin cells and TH[+]/*Htr3a*[EGFP−] mature chromaffin cells, composing most of the AM and ZO at E13.5 and E14.5 (Fig. 1f–o, Supplementary Fig. 4f–o). We validated the active transition from SCPs to "bridge" cells by visualizing the presence of SOX10^{+}/*Htr3a*[EGFP+] cells at E12.5 and E13.5 (Fig. 1b, g insets, Supplementary Fig. 4), as well as by assessing *Htr3a* mRNA expression at E13.5 (Supplementary Fig. 3a).

Next, our analysis revealed that already at E12.5, nearly 32% of early and mature chromaffin cells are 5HT[+] in the AM (Fig. 1e). Soon after, around 58% and 77.8% of chromaffin cells became 5HT[+] in the AM at E13.5 and E14.5 correspondingly (Fig. 1f–o). At the same time, SCPs did not show 5HT immunoreactivity (Supplementary Fig. 5a), and only 1.7–5.1% of all *Htr3a*[EGFP] cells were *Htr3a*[EGFP+]/TH[−]/5HT[+] (5HT-positive "bridge" cells) at E12.5–E14.5 (Fig. 1e, j, o). In ZO the proportion of 5HT^{+} cells among TH[+] and *Htr3a*[EGFP+] cells followed a similar pattern (Supplementary Fig. 4). Therefore, chromaffin cells contribute most of the local 5HT to the surrounding and neighboring cell types in the adrenal gland. In line with these observations, at E12.5–E13.5, *Htr3a*[EGFP+]/TH[−] "bridge" cells (sensitive to 5HT) are intermingled with chromaffin cells in the primordium of AM and ZO (Fig. 1a, e, Supplementary Fig. 4a–h), and are susceptible to 5HT generated by neighboring chromaffin cells. Based on this, we propose a mechanism of a paracrine control, where chromaffin cells release 5HT acting on neighboring "bridge" cells, with some contribution of the autocrine regulation, where

few 5HT[+] "bridge" cells act on themselves and other HTR3A^{+} "bridge" cells in their vicinity. As the SCPs and few chromaffin cells express other receptors to 5HT, additional modes of local autocrine and paracrine control might be also present (Fig. 1p).

When the differentiation of chromaffin cells slows down around E14.5 (E13.5 in ZO)[6,8], the proportion of SOX10^{+}/ *Htr3a*[EGFP+] cells decreases gradually (from 6.3% at E13.5 to 4.7% at E14.5), as the SOX10^{+} SCPs engage into the "bridge" fate at a decreasing rate (Fig. 1k–o, Supplementary Fig. 4f–o). Consistently, after E14.5, the majority of SOX10^{+} cells of AM and ZO are supporting glial cells and immature Schwann cells, as reported in the literature[25].

Thus, the observed transitions between SCPs, "bridge" and chromaffin cells suggest that the key 5HT-mediated regulatory phase occurs predominantly in a limited time window during chromaffin organ development (E11.5–E14.5). This is substantiated by the fact that *Htr3a*[EGFP+]/TH[+]/5HT[+] early chromaffin cells (reflecting the transition from *Htr3a*[EGFP+] cells to chromaffin cells) are observed already at E12.5 within the AM (Fig. 1a, f insets), whereas at E14.5 the proportion of these cells drops two-fold in comparison with E13.5 (Fig. 1j, o). Moreover, at E14.5, a subset of TH^{+} chromaffin cells in AM undergoes further functional specialization as shown by the onset of expression of *Pnmt* gene encoding phenylethanolamine N-methyltransferase (PNMT) (Supplementary Fig. 5b), the enzyme responsible for converting noradrenaline to adrenaline. Even though the contribution of SCPs to "bridge" cells and their differentiation towards early chromaffin cells peaks at E13.5 and is reduced significantly after E15.5 in AM, in E14.5 ZO 90% of cells are represented by newly-generated *Htr3a*[EGFP+]/TH[+]/5HT[+] early chromaffin cells (Supplementary Fig. 4o). Importantly, during this time window and up to postnatal day 14 (P14) (the latest stage we checked), chromaffin cells in AM and ZO maintain 5HT-immunoreactivity (Supplementary Fig. 5c). Thus, chromaffin cells in mice are capable of releasing both 5HT and catecholamines during embryonic development and later during postnatal life[26–30] being involved into a system of cell number control, which we specify below.

High 5HT causes developmental reduction of chromaffin organs. To reveal the effects of 5HT on the developing AM, we performed a gain-of-function experiment by administering its biochemical precursor, 5HTP, to pregnant rats (Fig. 2a). The administration of 5HTP enables to increase the physiological concentrations of 5HT in embryos without disruption of pregnancy caused by direct 5HT administration[31]. Moreover, 5HTP is converted to 5HT by the placenta[14]. As expected, administration of 5HTP to pregnant females led to a significant increase of 5HT concentration in the placenta and trunks of E14.5 embryos (Fig. 2b), and enhanced the release of 5HT by the fetal adrenal glands (Fig. 2c), as measured by HPLC-ED. Thus, the administration of 5HTP to pregnant rodent females causes a stable and physiological increase of 5HT concentration in embryos, as previously shown for other tissues including the uterus[32,33].

Pregnant Wistar rats received 5HTP during E11.5–E15.5 stages, and the adrenal glands of E15.5 embryos were investigated in 3D by micro computerized tomography (microCT) (Fig. 2d). We observed a 37.2% reduction of the mean volume of adrenal glands in embryos upon 5HTP treatment (Fig. 2e, f). Immunohistochemical analysis of adrenal glands of littermates revealed a significant reduction of the AM, whereas the area of the adrenal cortex was similar in control and experimental offspring (Fig. 2g). The volume of kidneys in treated embryos did not change, confirming the lack of general developmental delay.
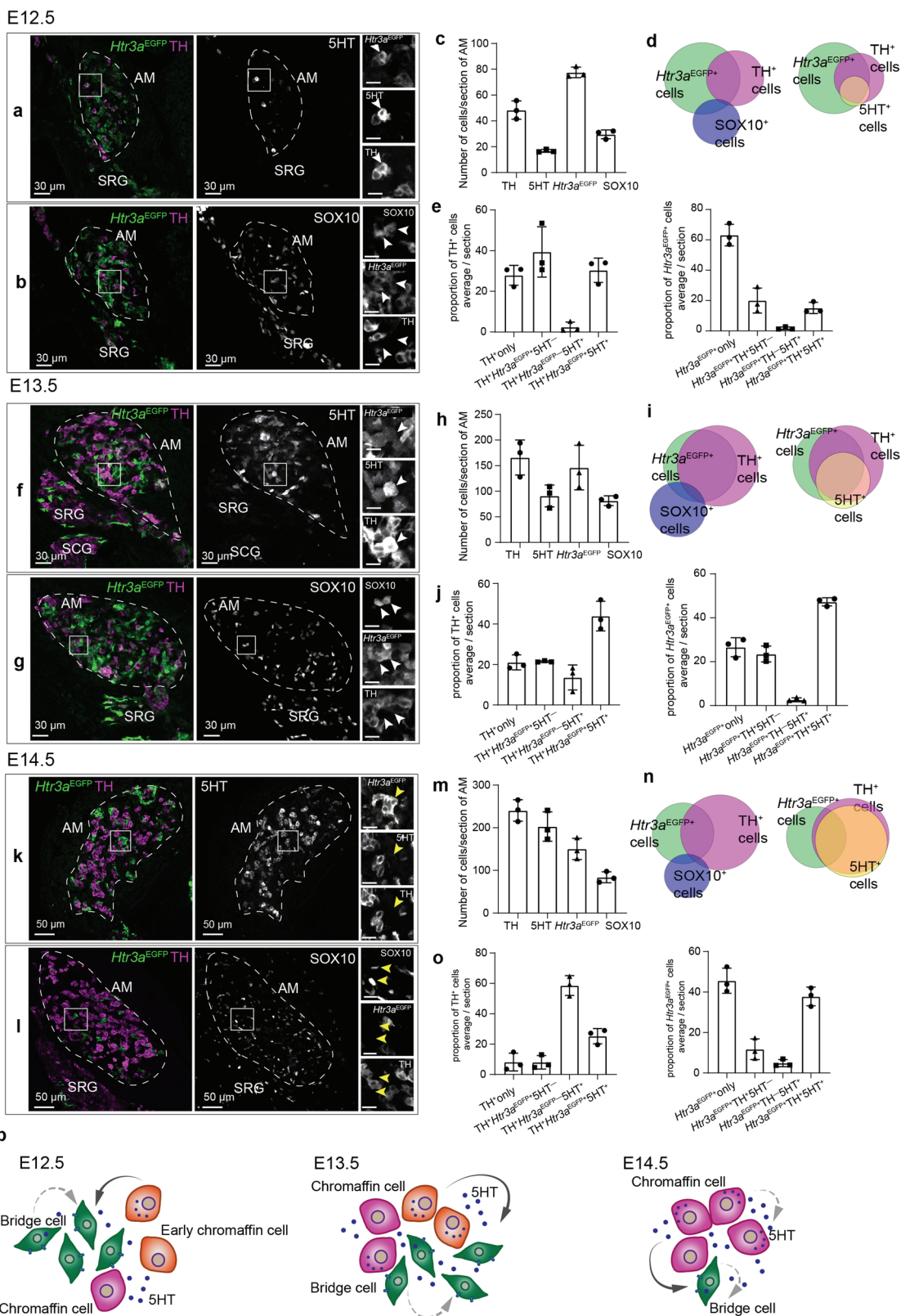
To make sure that the effect of 5HT on the AM size is consistent in a different rodent model, we analyzed the adrenal glands of mice and obtained consistent results (Fig. 2h). 5HTP treatment of pregnant rats and mice during the active differentiation of "bridge" cells into chromaffin cells resulted in a long-lasting reduction of AM size in embryonic and postnatal life in both species. Administration of 5HTP outside this critical time window led to a less pronounced effect (Fig. 2h). Thus, we were able to influence the size of the adrenal glands in rodent offspring through the elevation of 5HT levels in pregnant animals during a limited developmental time window corresponding to the peak of chromaffin cell generation.

To pinpoint the specific medullary population affected by the increased levels of 5HT in developing AM and ZO, we repeated

Fig. 1 5HT-sensitive "bridge" cells and 5HT-producing chromaffin cells are present together in developing adrenal glands. a, **b** Transversal section of adrenal gland of $Htr3a^{EGFP+/-}$ embryos immunostained for TH (marker chromaffin cells and sympathoblasts), EGFP (indicating expression of $Htr3a$), and 5HT (5-hydroxytryptamine, serotonin) (**a**), and for SOX10 (marker of SCPs) (**b**) at E12.5. White arrows point at TH$^+$/$Htr3a^{EGFP+}$/5HT$^+$ (**a**) and SOX10$^+$/$Htr3a^{EGFP+}$/TH$^-$ (**b**) cells, indicating formation of "bridge" cells and their differentiation into 5HT$^+$ early chromaffin cells. **c** Cell numbers at E12.5. **d** Venn diagrams of $Htr3a^{EGFP+}$, TH$^+$, SOX10$^+$ (left), and 5HT$^+$ (right) cells at E12.5. **e** Proportions of TH$^+$ cells also positive for $Htr3a^{EGFP}$ and 5HT (left), and proportions of $Htr3a^{EGFP+}$ cells with TH and 5HT signal (right). **f**, **g** Immunohistochemistry on the transversal section of adrenal glands of $Htr3a^{EGFP+/-}$ embryos stained for TH, EGFP, 5HT (**f**) and for SOX10 (**g**) at E13.5. White arrows point at TH$^+$/$Htr3a^{EGFP+}$/5HT$^+$ cells in (**f**) and SOX10$^+$/$Htr3a^{EGFP+}$/TH$^-$ cells in (**g**) at E13.5. **h** Cell numbers at E13.5. **i** Venn diagrams of $Htr3a^{EGFP+}$, TH$^+$, SOX10$^+$ (left), and 5HT$^+$ (right) cells at E13.5. **j** Proportions of TH$^+$ cells positive for $Htr3a^{EGFP}$, 5HT (left) and proportions of $Htr3a^{EGFP+}$ cells positive for TH, 5HT (right). **k**, **l** Transversal sections of adrenal glands from $Htr3a^{EGFP+/-}$ embryos stained for TH, EGFP, and 5HT in (**k**), and for SOX10 in (**l**) at E14.5. Yellow arrows point at TH$^-$/$Htr3a^{EGFP+}$/5HT$^-$ cells (**k**) and SOX10$^+$/$Htr3a^{EGFP-}$/TH$^-$ cells (**l**) indicating the end of "bridge" differentiation, SOX10$^+$ represent supporting glial cells. **m** Cell numbers at E14.5. **n** Venn diagrams of $Htr3a^{EGFP+}$, TH$^+$, SOX10$^+$ (left), and 5HT$^+$ cells (right) at E14.5. **o** Proportions of TH$^+$ cells positive for $Htr3a^{EGFP}$, 5HT (left), and proportions of $Htr3a^{EGFP+}$ cells positive for TH and 5HT (rigth). **p** Schematic representation of the proposed paracrine/autocrine regulation: chromaffin cells release 5HT activating HTR3A receptors on the surface of "bridge" cells (solid lines). Note that few "bridge" cells produce 5HT and can stimulate "bridge" population in an autocrine mode as well as some chromaffin cells can sense 5HT with other 5HT receptors (dashed lines). Scale bars for the insets are 10 µm. Quantification is presented as mean ± SD, biological $n = 3$. Adrenal medulla (AM) is outlined by the dashed line in all sections. SRG: suprarenal ganglion, SCG: sympathetic chain ganglion.

the 5HTP treatment in the transgenic $Htr3a^{EGFP}$ mice. In order to target the same consistent stages across species, 5HTP was administered to pregnant mice at E11.5–E12.5, corresponding to E13.0–E15.0 in rats[34] (Fig. 3a). As a result, at E13.5, the numbers of early chromaffin cells (TH$^+$/$Htr3a^{EGFP+}$) and mature chromaffin cells (TH$^+$/$Htr3a^{EGFP-}$) were reduced by 39.1% and 38.8%, respectively (difference between mean values of control and 5HTP groups), in AM of the embryos from the treated mice (Fig. 3c). We did not detect a significant change in "bridge" cells number at E13.5. In the ZO, the number of "bridge" cells ($Htr3a^{EGFP+}$/TH$^-$) was twice higher, and the number of mature chromaffin cells (TH$^+$/$Htr3a^{EGFP-}$) was reduced (Fig. 3c). Schwann cell precursors (SOX10$^+$) cell numbers were unaffected in both chromaffin organs (Fig. 3c).

To control for the systemic effect, we checked the cells in the sympathetic chain ganglia (SCG), which are directly derived from the migratory neural crest cells and do not transition through a "bridge" stage[6,35]. Thus, SCG served as an internal control for the changes in size of chromaffin organs. 5HTP administration did not influence the size or cellular composition of SCG (Supplementary Fig. 6). Therefore, the reduction of chromaffin organs is specific and occurs at the expense of chromaffin cells.

To confirm that the observed phenotype emerged due to the activation of HTR3A, we used SR57227 hydrochloride, a potent and selective HTR3A agonist. Administration of SR57227 to pregnant mice at E11.5 and E12.5 caused a 30.6% reduction (difference between mean values of DMSO control and SR57227 groups) of early and mature TH$^+$ chromaffin cells in AM at E13.5 (Fig. 3d). This is similar to the effect caused by 5HTP administration to pregnant mice during the same developmental time. To rescue the phenotype caused by the elevated 5HT level, we co-administered granisetron, a HTR3A antagonist, in combination with 5HTP. In this condition, the number of TH$^+$ cells in AM turned out to be similar (Fig. 3d), whereas the administration of 5HTP alone caused a 34.5% reduction (difference between mean values of DMSO control and 5HTP groups) of the chromaffin cells in AM. The SCG (representing a control tissue with different genesis) showed the same numbers of TH$^+$ sympathoblasts in all groups (Fig. 3d). Therefore, the HTR3A activation mediated 5HT-dependent signaling in the development of the chromaffin cell lineage and caused the decrease of chromaffin cells in AM and ZO upon 5HTP treatment.

To further investigate the reasons for the observed reduction in chromaffin cell numbers, we checked the dynamics of cell cycle in various populations of cells in the chromaffin lineage. For this purpose, we administered consecutively 5-ethynyl-2′-deoxyuridine (EdU) and 5-chloro-2′-deoxyuridine (CldU) thymidine

analogues at E12.5 with 4-h intervals to $Htr3a^{EGFP}$ mice treated with 5HTP (Fig. 4a). At the time of CldU injection, EdU is not available for cells due to its rapid pharmacokinetics[36]. This approach allowed calculating the proliferation rate as well as the proportion of EdU$^+$CldU$^-$, EdU$^-$CldU$^+$, and EdU$^+$CldU$^+$ cells.

Despite the overall numbers of proliferating (incorporating one or both thymidine analogues) cells among SCPs, "bridge" cells, early chromaffin cells or mature chromaffin cells did not show a significant change in comparison with control (Fig. 4b), the length of a cell cycle in "bridge" cells appeared significantly increased in the 5HTP-treated group (Fig. 4c, d, Supplementary Fig. 7a). Delayed cell cycle progression resulted in the reduced number of "bridge" cells observed at this stage, soon after the injection (Fig. 4b). Such reduction of "bridge" cells was not observed at E13.5, due to a fast turnover of "bridge" cells and subsequent recruitment of new "bridge" cells from SCPs. Moreover, 5HTP and 5HT are rapidly depleted after the injection-dependent concentration peak due to pharmacokinetics. At the same time, the dynamics of cell cycle progression in SCPs and early chromaffin cells in AM did not change in control vs treatment group (Fig. 4c). The majority of mature chromaffin cells were negative for EdU or CldU, as they temporarily exit cell cycle in agreement with previous studies[37]. Due to fast differentiation of chromaffin cells from progenitors in 14 h[7], reduction of the progenitor pool has a major effect of chromaffin cell population. A majority of chromaffin cells do not proliferate at E12.5–E13.5 and are unable to compensate for the loss.

Contrary to the AM, in the E12.5 ZO, we observed a lower proportion and reduced absolute numbers of SOX10$^+$ SCPs incorporating EdU only in the 5HTP-treated group (Supplementary Fig. 7), which suggests another mechanism of cell number control or delayed dynamics of 5HT's effects in the ZO.

As we did not observe cleaved caspase-3 immunopositive (CASP3$^+$) cells in any cell population in the AM and ZO (excluding exceptionally rare cases), the reduction of chromaffin cells in 5HTP-treated group cannot be mediated via increased apoptosis (Fig. 4e). Thus, the increase of 5HT causes a prolongation of the cell cycle of "bridge" progenitors leading to a decrease in their number, which results in a reduction of derived chromaffin cells (Fig. 4f).

Next, to dissect the potential changes of gene expression upon 5HTP administration, we performed single-cell RNA sequencing of the AM and ZO at E13.5 from 5HTP-treated and untreated embryos (Fig. 5a). We sequenced 1528 cells (both conditions combined) using Smart-seq2 technology, which allows an extraordinary deep sequencing of individual cells (7000/8000
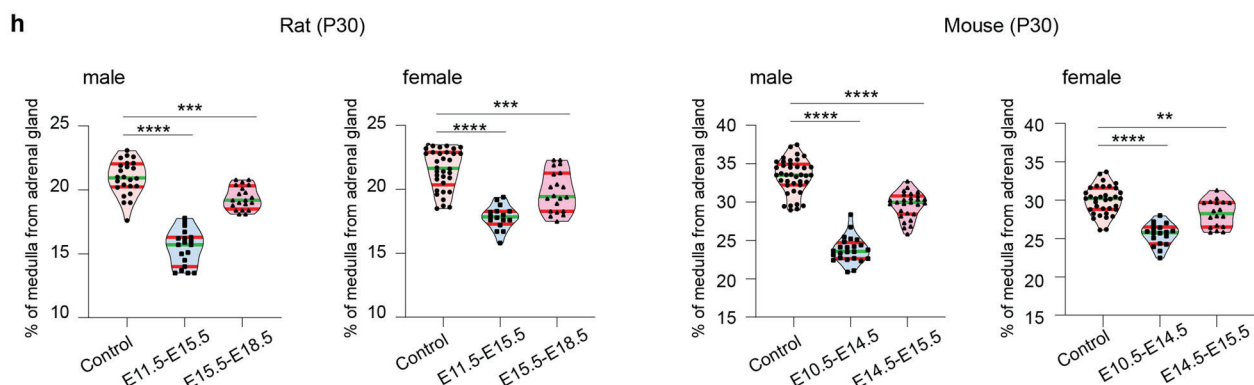
Serotonin is increased in adrenal glands after 5HTP treatment
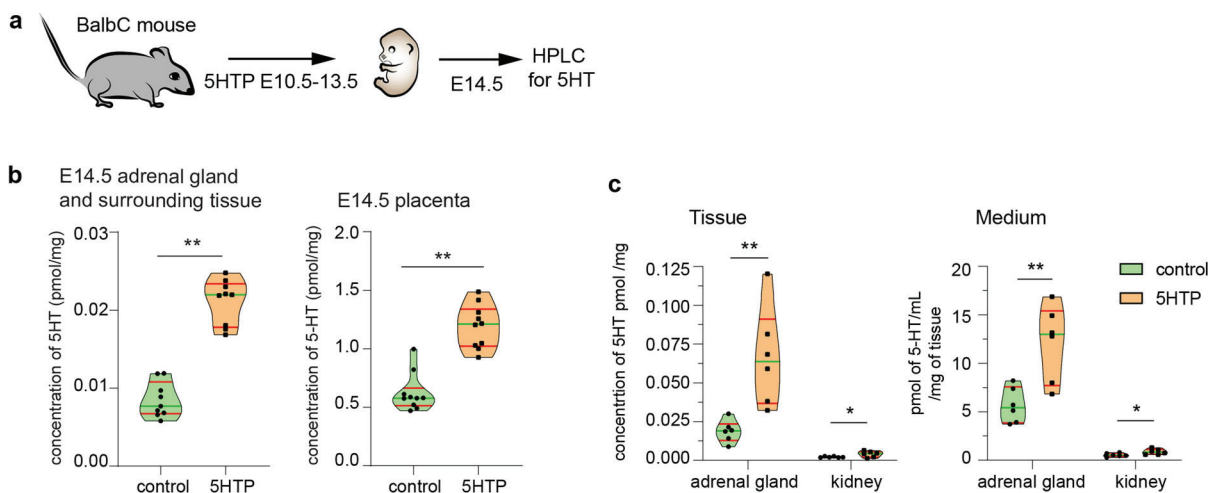
Adrenal medulae are smaller in 5HTP-treated embryos
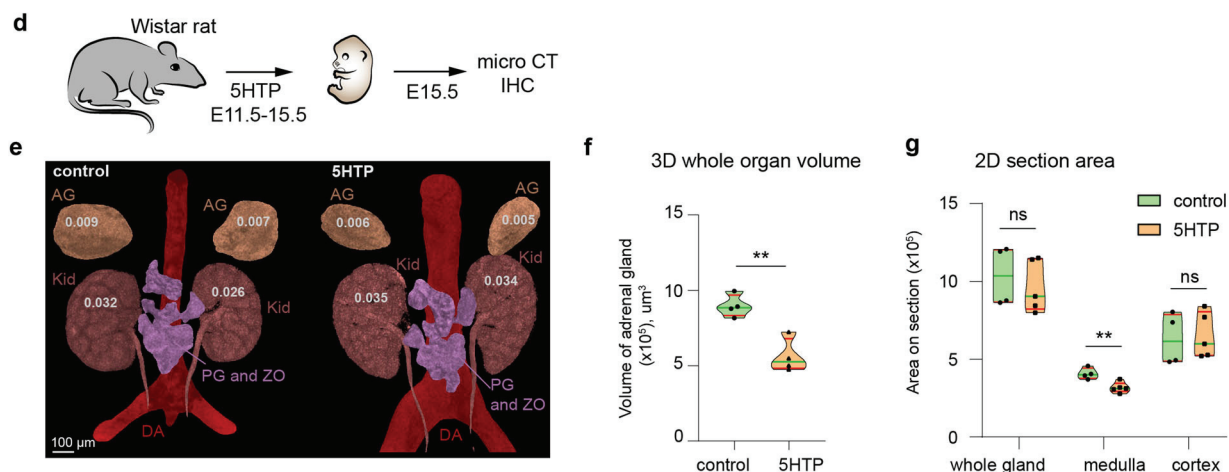
Reduction of adrenal medullae after 5HTP treatment

genes per cell on average). The general composition, cell type proportions, and the developmental sequence of cell types (SCPs, "bridge" cells, chromaffin cells, and sympathoblasts) (Fig. 5b, c) remained the same upon 5HTP treatment. At the same time, we detected a reliable change in expression of a gene responsible for

the regulation of splicing (*Cwc22*)[38,39] (Fig. 5d, e). In line with this, we detected changes in differential splicing of several long non-coding RNAs (*Uph*, *Uph.AS2*, *Uph.AS3*, *Uph.AS4*) (Fig. 5e) controlling the expression of *Hand2*[40], a transcription factor essential for the transition to the catecholaminergic program in

Fig. 2 Administration of 5HTP, the immediate precursor of 5HT, to pregnant rodents reduces adrenal medulla in the progeny. a 5HTP was administered to pregnant BalbC mice at E10.5–E13.5. The embryos are collected at E14.5 for the HPLC-based analysis of 5HT. **b** Concentration of 5HT in the adrenal glands and surrounding tissues (left) and placentas (right) at E14.5 after 5HTP administration at E10.5–E13.5 stage. Unpaired double-sided t-test p-value ** < 0.001, biological $n = 9$. **c** Adrenal glands from E14.5 embryos release 5HT into the surrounding medium measured by HPLC-ED. Note: kidneys, used as a control tissue, do not release 5HT. Unpaired double-sided *t*-test p-value * < 0.05, **= 0.005, biological $n = 6$. **d** 5HTP was administered to pregnant Wistar rats at E11.5–E15.5 followed by embryo collection at E15.5 and analysis by X-ray computed microtomography (microCT). **e** microCT X-ray reconstruction of adrenal glands and kidney volume from E15.5 rat embryos obtained from females in control and 5HTP-treated groups. Volumes of the organs in μm^3 (×10^5). **f** Adrenal gland volume normalized to the volume of adjacent kidneys. Biological $n = 4$. Unpaired double-sided t-test p-value ** < 0.005. **g** Section areas of adrenal gland, adrenal medulla and adrenal cortex based on immunohistochemistry analysis with anti-TH immunostaining. Unpaired double-sided *t*-test p-value ns > 0.05, * < 0.05, biological $n = 4$ (control), 5 (5HTP). **h** Prenatal 5HTP exposure at the time of "bridge" cell differentiation (E11.5–E15.5 in rats and E10.5–E14.5 in mice) causes the decrease of postnatal adrenal medulla size in P30 animals, which was greater than decreased induced by 5HTP exposure after the time of "bridge" cell differentiation (E15.5–E18.5 in rats and E14.5–E15.5 in mice). Green line in all violin plots—the median, red lines—quartiles. One-way ANOVA test with Dunnett's multiple comparison test **$p = 0.0017$, ***$p = 0.0002$, ****$p < 0.0001$, biological n (adrenal gland) = 24 (control male rat), 19 (E11.5–E15.5 male rat), 20 (E15.5–E18.5 male rat), 35 (control female mice), 16 (E11.5–E15.5 female rat), 20 (E15.5–E18.5 female rat), 40 (control male mice), 24 (E10.5–E14.5 male mice), 27 (E14.5–E15.5 male mice), 35 (control female mice), 18 (E10.5–E14.5 and E14.5–E15.5 female mice). For all experiments normality is checked with Shapiro–Wilk test. AG: adrenal gland, Kid: kidney, PG and ZO: paraganglia and organ of Zuckerkandl, DA: dorsal aorta.

chromaffin cells and sympathoblasts[41]. The other differentially spliced genes, *Apobec3* and long non-coding RNA *Cenpa.AS2*[42], might be involved in the control of a cell cycle length in "bridge" cells, where they are enriched.

The deficit of 5HT has no effect on chromaffin cells. As the elevated levels of 5HT lead to a decreased chromaffin cell numbers in vivo by delaying the cell cycle of precursor "bridge" cells, we expected to see the opposite effect in the case of reduced levels of 5HT. However, the previously reported genetic loss-of-function of the HTR3A receptor failed to show any abnormal phenotype in adrenal glands[43]. A potential explanation for these observations is that 5HT affects cell cycle progression in HTR3A$^+$ "bridge" cells only when 5HT levels reach a certain threshold. Furthermore, HTR3A-dependent paracrine regulation may not be critical for the development of the adrenal gland, but is an important controller of excessive chromaffin tissue growth and pre-malignant states.

To explore how the deficit of 5HT affects chromaffin development, we analyzed several mouse models with a reduction of embryonic and maternal 5HT. *Pet1*$^{-/-}$ embryos collected from *Pet1*$^{+/-}$ females, as well as *Tph2*$^{-/-}$ embryos collected from *Tph2*$^{+/-}$ females, lack 5HT derived from the central nervous system of the mutant embryos, although maternal 5HT remains unchanged. The numbers of TH$^+$ chromaffin cells did not differ in E15.5 *Pet1*$^{-/-}$ and *Tph2*$^{-/-}$ embryos in comparison with their *Pet1*$^{+/-}$ and *Tph2*$^{+/-}$ littermates serving as controls (Supplementary Fig. 8a, b). One of the major peripheral sources of 5HT in the embryo is represented by the enterochromaffin cells, which start to secrete 5HT at E15.5[10] and therefore cannot contribute to the developing adrenal glands at E12.5–E13.5. Thus, the reduction of embryonic sources of 5HT is not critical for the development of chromaffin cells, while the extraembryonic 5HT might be important.

To address how a complete removal of 5HT from both maternal and embryonic sources affects the development of chromaffin cells in an embryo, we took advantage of the *Tph1*$^{-/-}$;*Tph2*$^{-/-}$, *Tph1*$^{-/-}$;*Scl6a4*$^{-/-}$, and *Tph1*$^{-/-}$;*Tph2*$^{-/-}$;*Scl6a4*$^{-/-}$ mouse models, which lack the ability to produce central and peripheral 5HT and to selectively transport it into cells in both mothers and progeny. We analyzed E13.5 embryos from these mouse models for the number of chromaffin cells and 5HT$^+$ cells in adrenal glands. At E13.5, the number of 5HT$^+$ cells demonstrated 80% to 95% reduction in all knockout (KO) animals when compared with C57BL/6 controls (Supplementary Fig. 8c, d). The average number of TH$^+$ chromaffin cells also appeared reduced in KOs (in *Tph1*$^{-/-}$;*Tph2*$^{-/-}$ for 11.4%,

in *Tph1*$^{-/-}$;*Scl6a4*$^{-/-}$ for 27.1%, in *Tph1*$^{-/-}$;*Tph2*$^{-/-}$;*Scl6a4*$^{-/-}$ for 31.2%, based on the difference between mean values) (Supplementary Fig. 8d). To check whether the reduction of chromaffin cells was specific, we measured the number of cells in SCG. The number of TH$^+$ sympathoblasts in SCG was significantly lower in KO embryos in comparison with wild type embryos (in *Tph1*$^{-/-}$;*Tph2*$^{-/-}$ for 17.8%, in *Tph1*$^{-/-}$;*Scl6a4*$^{-/-}$ for 30.2%, in *Tph1*$^{-/-}$;*Tph2*$^{-/-}$;*Scl6a4*$^{-/-}$ for 48.6%, based on the difference between mean values) (Supplementary Fig. 8e), which indicated a general developmental delay and reduction of the embryonic growth, independently of cell origin and due to the lack of maternal 5HT. Therefore, the reduction of chromaffin cells in 5HT deficient models is not specific to the adrenal medulla. Of note, the numbers of SCPs, were not changed in AM and SCG in control and KO embryos (Supplemetary Fig. 8f), because SCPs depend on the local innervation coming from elsewhere. The expression of *Htr3a* mRNA was evident in *Tph1*$^{-/-}$;*Tph2*$^{-/-}$;*Scl6a4*$^{-/-}$ E13.5 adrenal glands, which indicated that "bridge" cells are still present in the KOs (Supplementary Fig. 8g). Overall, these experiments demonstrated that the reduction of maternal and embryonic 5HT has no specific effect on the number of chromaffin cells, contrary to the excess of 5HT during a critical developmental time window.

High expression of HTR3A in tumorigenic neuroblastoma cells. To investigate the possible action of 5HT on HTR3A in the progression of tumors originating from sympathoadrenal cells, we analyzed several clones of human-derived neuroblastoma for *HTR3A* expression and tumorigenicity using an immunodeficient mouse model. Based on mRNA (Fig. 6a) and protein expression levels (Fig. 6b, c), the examined neuroblastoma cell lines could be characterized as either *HTR3A*^{high} (SH-SY5Y, CHLA-15, and CHLA-20), expressing markedly high levels of *HTR3A*, or *HTR3A*^{low} (NBL-28, NBL-38, and NBL-40), with only weak *HTR3A* expression. While all cell lines were negative for *MYCN* amplification (two copies of gene in the genome), HTR3A protein expression was associated with expression of major drivers of aggressive neuroblastomas, N-MYC and c-MYC[44,45], or one of the core stemness factors SOX2 (Fig. 6b). Intriguingly, the same association was observed in NTERA-2 embryonal pluripotent carcinoma cells, which served as a positive control for HTR3A expression, and which are known to express high levels of N-MYC and share characteristics with early neural progenitors. To investigate the possible role of HTR3A receptor in regulation of proliferation in tumor cells, we treated the cells with the HTR3A agonists, N-methylquipazine dimaleate (NMQ) and SR57277, as well as antagonists, VUF10166 and granisetron HCl, in the
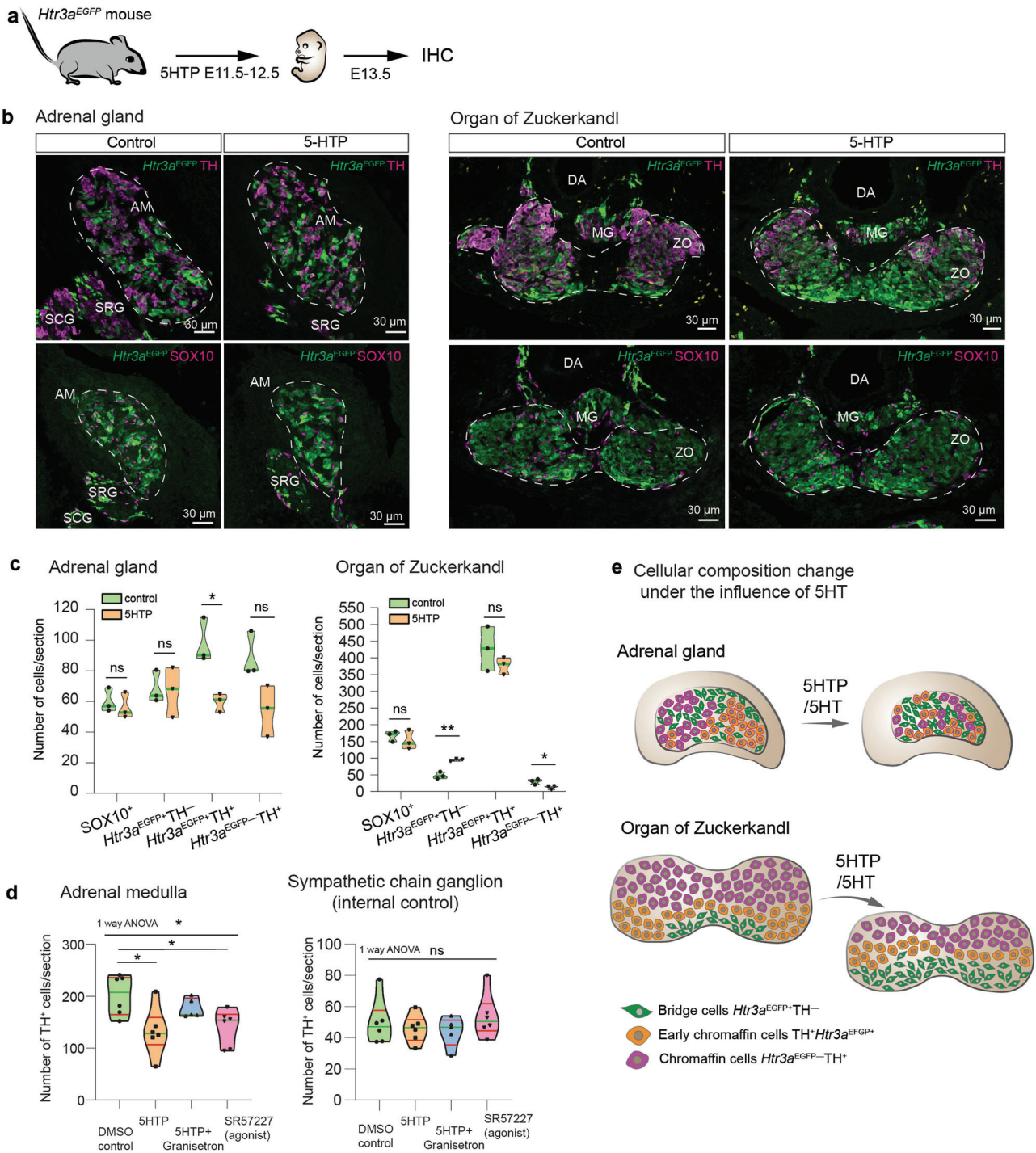
presence of 5HT. HTR3A agonists dramatically limited proliferation of HTR3A^high cell lines, whereas they did not affect HTR3A^low cell lines, or the effects were seen only at much higher doses (Fig. 6d, e). No cleaved caspase-3 was detected after the treatment with NMQ, indicating that such treatment does not induce apoptosis (Supplementary Fig. 9). In contrast, there was no significant effect of HTR3A antagonists on cell growth of both HTR3A^high SH-SY5Y and HTR3A^low NBL-28 cell lines (Fig. 6f, g).

We also tested the ability of cells to form spheres to check their stem cell-like properties (Fig. 6h). HTR3A^high cells formed spheres more frequently in comparison with HTR3A^low cell lines. Importantly, pre-treatment with 75 μM NMQ for 5 days did not reduce sphere-forming capacity of both HTR3A^high and HTR3A^low

cell lines. Therefore, the activation of HTR3A receptor does not compromise the stem-like state of neuroblastoma HTR3A^high cells, but only reduces their proliferation. When NMQ is removed the cells form spheres with the same or even increased efficiency (in case of NBL-38), as compared to vehicle-pretreated controls (Fig. 6i).

SH-SY5Y and CHLA-20 *HTR3A*^high cell lines formed large tumors in NOD/SCID gamma (NSG) mice, whereas *HTR3A*^low cells did not form xenograft tumors even in 4 months after injection (Fig. 6j, k). The tumor volume increase of the xenografts during the experiment (Fig. 6l) further demonstrated the association of *HTR3A* expression with the aggressive phenotype of neuroblastoma cells.

Fig. 3 Administration of 5HTP to pregnant females influences chromaffin and "bridge" cells in embryonic chromaffin organs. a 5HTP was administered to pregnant $Htr3a^{EGFP+/-}$ females, which was followed by the analysis of embryonic adrenals at E13.5 by immunohistochemistry. **b** Transversal section through the adrenal glands (left) and Organ of Zuckerkandl (right) immunostained for TH, EGFP (indicating expression of $Htr3a$), and SOX10. The sections were obtained from E13.5 embryos collected from $Htr3a^{EGFP+/-}$ females from control and 5HTP-treated groups. **c** Cell numbers in adrenal medulla (left) and Organ of Zuckerkandl (right) at E13.5 in control and treated groups. Note that early chromaffin cells ($HTR3A^{EGFP+}/TH^+$) and mature chromaffin cells ($HTR3A^{EGFP-}/TH^+$) decrease, whereas SCPs ($SOX10^+$) and "bridge" cells ($HTR3A^{EGFP+}/TH^-$) do not change in the treated group vs control in the adrenal medulla. At the same time, "bridge" cells ($HTR3A^{EGFP+}/TH^-$) accumulate and mature chromaffin cells ($HTR3A^{EGFP-}/TH^+$) decrease in the Organ of Zuckerkandl in the treated group. Cell number are presented as violin plots, where the green line indicates median, biological $n = 3$, Shapiro–Wilk test for normality and unpaired double-sided t-test p-value ns > 0.05, * < 0.05, ** < 0.002. **d** Cell number in adrenal medulla and sympathetic chain ganglia across four groups of E13.5 embryos treated during E11.5–E12.5 with: DMSO (control), 5HTP, 5HTP and Granisetron (HTR3A antagonist), SR57227 (HTR3A agonist). Note that cell numbers change in the adrenal medulla, but not in the sympathetic chain ganglion. Biological $n = 6$ (DMSO, 5HTP, SR57227), 5 (5HTP + Granisetron), one-way ANOVA AM p-value *0.0135, followed by Tukey multiple comparison test DMSO vs 5HTP p-value *0.0189, DMSO vs SR57227 p-value *0.0406; ANOVA SCG p-value ns 0.6265. **e** Changes in size and cellular composition in E13.5 adrenal medulla and Organ of Zuckerkandl in mice under the influence of increased 5HT (E11.5–E12.5). Cell numbers are presented as violin plots, the green line—median and the red lines—quartiles. Adrenal medulla (AM) and Organ of Zuckerkandl (ZO) are outlined by the dashed line in sections. SRG: suprarenal ganglion, SCG: sympathetic chain ganglion, MG: mesenteric ganglion.

High 5HT alters catecholamine-mediated behavior in progeny. To evaluate the long-term effect of elevated levels of 5HT during prenatal development in rodents, pregnant Wistar rats were administered 5HTP *per os* during E11.5–E15.5, a stage critical for the transition of "bridge" cells to chromaffin cells. The offspring of treated mothers was maintained until postnatal day 75 (P75), when the behavioral tests and measurements of respective catecholamine levels in blood and adrenal glands were performed (Fig. 7a).

The total body weight of P75 animals was similar in treated and control groups (Supplementary Fig. 10a, b), whereas the weight of adrenal glands was significantly reduced in males and females from the 5HTP-treated group (Fig. 7b). In embryonically-treated adult females, this reduction of adrenals correlated with significantly lower amounts of adrenaline, noradrenaline, and dopamine in the adrenal glands, and lower adrenaline in blood plasma (Fig. 7c). In males from the 5HTP-treated group, smaller adrenal glands contained respectively less adrenaline, but the levels of noradrenaline and dopamine did not show any significant difference (Fig. 7c). To ensure that the observed reduction of adrenaline in males and the reduction of adrenaline, noradrenaline, and dopamine in females were not associated with accelerated catabolism by catechol-O-methyltransferase in blood, we measured catecholamine metabolites: metanephrine and normetanephrine (Supplementary Fig. 10c). These measurements confirmed that the decrease in adrenaline supply from the adrenal glands in the 5HTP-treated group was not due to the acceleration of adrenaline catabolism (Supplementary Fig. 10c). On the other hand, the concentration of normetanephrine was significantly higher in 5HTP-treated males, suggesting an enhanced catabolism of noradrenaline that is typically observed in major pheochromocytoma subtypes in human[46,47]. The elevation of normetanephrine is not observed in females. Of note, high metanephrine levels might not always reflect high catecholamine synthesis and following catabolism, as inhibition of monoamine oxidase may also lead to elevated levels of catecholamines/metanephrines, which we cannot rule out even though we consider this scenario unlikely based on the previous literature[48–51]. The system of catecholamines and their metabolism is complex and stretches beyond the production of adrenaline and noradrenaline in chromaffin organs. Therefore, the observed differences in males and females, as well as the only partial correlations with behavioral data might be due to other systemic regulatory mechanisms, which are not covered by this study.

In the next line of behavioral experiments, we assessed how the prenatal exposure to enhanced 5HT during the critical time window of chromaffin cell generation shaped the adaptive capacity of the offspring. According to the resident-intruder test and foot shock-induced aggression test, the males from 5HTP-treated mothers were less aggressive and did not defend their territory, compared with control males (Fig. 7d). Moreover, the experimental animals were more adaptive and flexible, demonstrating less anxiety and reduced stress-induced behavior (Supplementary Fig. 10d). These results are in line with in vivo measurements of catecholamines in adult mice revealing lower levels of adrenaline supplied by smaller adrenal glands (evident when measured as ng/organ, Fig. 7c) in animals prenatally exposed to elevated 5HT levels.

Stress affects fetal 5HT, medulla size, and progeny behavior. The connection between embryonic 5HT levels and subsequent animal behavior allowed us to hypothesize a connection between the stress of a pregnant female, 5HT and the development of adrenals in progeny.

The following line of experiments based on the published method[52] revealed that mild stress induced by 1-h-restrain of pregnant mice (E10.5–E14.5) significantly enhanced 5HT level in both placenta and fetuses (Fig. 7e, f), causing decreased medulla size in a progeny (Fig. 7e, f), similarly to 5HTP exposure (Fig. 2b, h). The resulting experimental progeny demonstrated less aggressive behavior according to the standard resident-intruder test: they showed cooperative behavior and reduced number of attacks on the intruder (Fig. 7f). Overall, the prenatally 5HTP-treated animals and the progenies from stress-induced mothers showed consistency in adrenal medulla reduction and behavioral changes. Although our data from mice and rats appear to be consistent, we do not claim that the effects of maternal stress on postnatal behavior are only rooted in decreased adrenals and embryonic influence from the mother. However, mild stress and 5HTP treatment during the same embryonic period result in similar behavioral outcomes in postnatal progeny, and are associated with a decreased AM size. Overall, the prenatal effects and postnatal effect are likely connected and correlate via the reduced number of chromaffin cells in adrenal glands.

The ratio of medulla to cortex changes in migrating voles. As the experimentation on laboratory animals might not fully reflect the ecological and evolutionary situation, we committed to perform the analysis of adrenals in wild rodents with different well-documented intra-species modes of behavior. For this, we set out for an expedition to Yenisey Ecological Station "Mirnoe" (62.2 N; 89.0 W) in Siberia, to study the wild population of red-backed
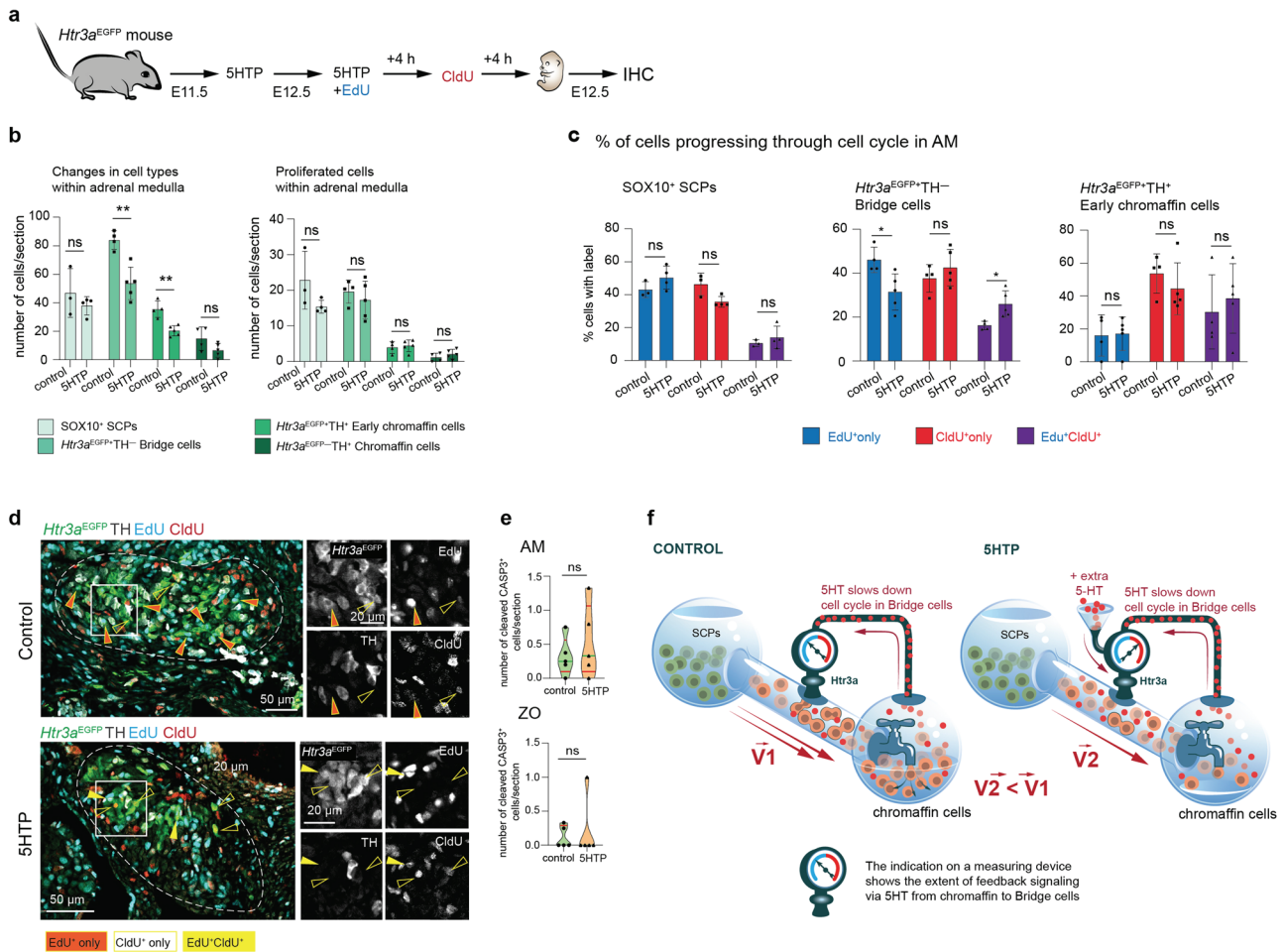
Fig. 4 Prenatal 5HT influences cell cycle length of the "bridge" progenitors in embryonic adrenal glands. a Pregnant $Htr3a^{EGFP+/-}$ females were administered 5HTP at E11.5; at E12.5, females received 5HTP together with 5-Ethynyl-2′-deoxyuridine (EdU); in 4 h females received 5-Chloro-2′-deoxyuridine (CldU); embryos were harvested in 4 h after CldU injection at E12.5. This allows identifying the proportions of cells, which incorporated EdU+ only, CldU+ only, or both thymidine analogues (EdU+CldU+). **b** Numbers of all cells (left) and numbers of proliferated cells (right) in populations of SCPs, "bridge" cells, early chromaffin cells, and mature chromaffin cells at E12.5 under the influence of 5HTP in adrenal medulla. Shapiro–Wilk test for normality and unpaired double-sided t-test p-value ns > 0.05, ** < 0.002, biological $n = 3$ (control SCPs), 4 (control other cell types), 4 (5HTP SCPs), 5 (5HTP other cell types). **c** Proportions of EdU+ only, CldU+ only, and EdU+CldU+ cells in populations of SCPs, "bridge" cells, and early chromaffin cells at E12.5 under the influence of 5HT in adrenal medulla. Note that the cell cycle lengthened in "bridge" cells in the treated condition, as there are more EdU+CldU+ "bridge" cells. Shapiro–Wilk test for normality and unpaired double-sided t-test p-value ns > 0.05, * < 0.05, biological $n = 3$ (control SCPs), 4 (control other cell types), 4 (5HTP SCPs), 5 (5HTP other cell types). **d** Transversal sections of adrenal glands from $Htr3a^{EGFP+/-}$ embryos immunostained for TH, EGFP (indicating the expression of $Htr3a$), EdU, and CldU. Arrowheads point at EdU+ only, CldU+ only, and EdU+CldU+ cells. **e** Numbers of cleaved CASP3+ cells in adrenal medulla and Organ of Zuckerkandl. Note that the number of cleaved CASP3+ cells is exceptionally low. Cell numbers are presented in violin plots, the green line indicates median and the red lines are quartiles. Shapiro–Wilk test for normality and unpaired double-sided t-test (AM) and Mann–Whitney test (ZO), p-value ns > 0.05, biological $n = 5$. **f** Proposed mechanism of the paracrine/autocrine regulation of a cell cycle length in HTR3A+ "bridge" precursors by 5HT-releasing chromaffin cells in the developing adrenal medulla.

voles (*Clethrionomys rutilus*). *C. rutilus* represent a "cycling" population with periods of expansion and migration, with well-defined residents and migrants triggered by the spiking increase of density[53–55]. To check if there is a correlation between the size of adrenal medulla and resident vs migrant profile in wild *C. rutilus*, we measured the medulla size in representatives of residents and migrants in the year of a peak population density accompanied by enhanced migration activity (2020). The results showed that the migrant animals of both sexes are characterized by reduced medulla size as compared to residents (Fig. 7g), which might be connected to the fact that the increase in population density is associated with increased chronic stress[56]. According to our experiments with laboratory animals and previously published results[52], increased level of stress in pregnant mothers elevates 5HT in the placenta and embryo. This, in turn, results in

reduced chromaffin organs in the offspring, altered hormonal profiles and more cooperative and flexible catecholamine-controlled behavior.

Discussion

Recent findings[6,8] have challenged the older paradigm about the immediate origin of chromaffin cells from ventrally migrating neural crest cells[57], and raised questions about how the numbers of chromaffin cells are established and controlled during embryonic and postnatal life. These findings introduced intermediate cell states intercalating into the trajectory from the neural crest to chromaffin cells. One state is represented by nerve-associated Schwann cell precursors[6,58] giving rise to "bridge" cells, which in turn transit into chromaffin cells[6].

a Overview of the experimental design
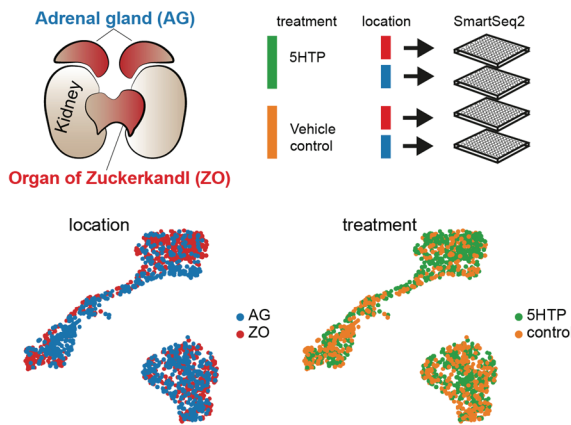
b Unbiased clustering and annotation
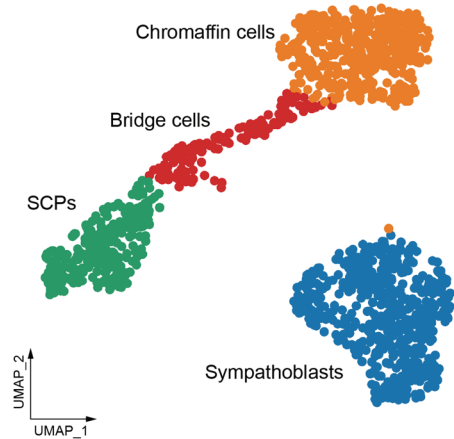
c Main markers for each clusters
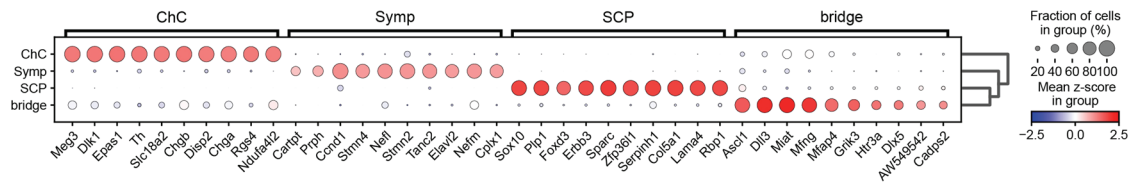
d Per cluster DE genes (5HTP vs control)
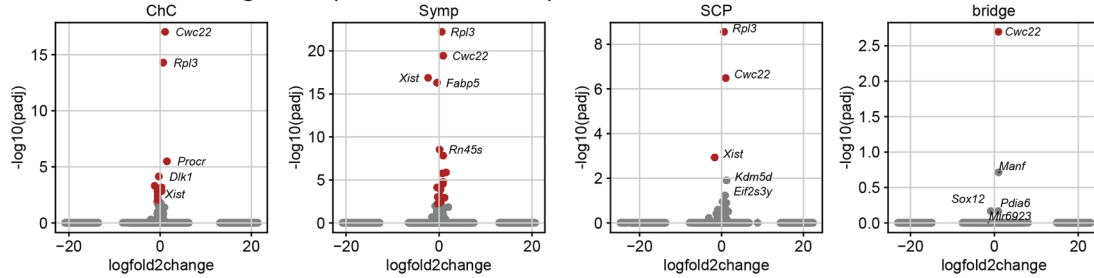
e Differentially spliced genes (5HTP vs control)
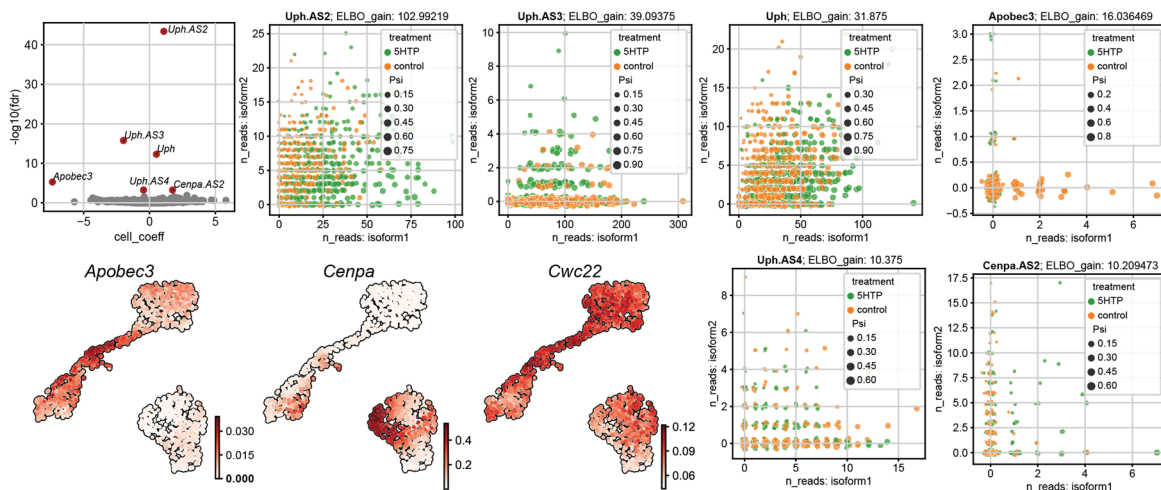
Here we investigated how these intermediate cell types regulate their numbers and define the future size of the chromaffin population. We found that 32% of the chromaffin cells are 5HT positive as soon as they emerge at E12.5 in mouse and this number goes up to 77.8% at E14.5. The 5HT, which is derived from chromaffin cells and a small population of "bridge" cells, signals to neighboring HTR3A+ "bridge" cells, lengthening their cell cycle. This causes a reduction of adrenal medulla because less "bridge" cells become available for differentiation into non-dividing chromaffin cells. Being 5HT-sensitive, "bridge" cells are a part of a negative feedback loop controlling the size of the 5HT-releasing chromaffin population. Similar modes of paracrine feedback loops were shown for retinoic acid signaling[59] or angiogenic growth factors[60] which are known to control

Fig. 5 Single-cell transcriptomics reveal differential changes in genes related to RNA splicing and cell cycle upon 5HTP treatment. a Adrenal glands (AG) and Organ of Zuckerkandl (ZO) were dissected from E13.5 *Wnt1-Cre*^{+/−};*R26R*[Tomato+]/wt embryos; the tissue was dissociated, and *Wnt1*[Tomato+] cells were sorted into 384-well plates for Smart-seq2 sequencing. Note the absence of statistically-tested compositional effects (see the "Methods" section) between 5HTP-treated and control conditions, shown as UMAPs (bottom panels). **b** Joint UMAP embedding of cells from AG and ZO from both treated and control groups. **c** Main marker genes defining each cluster. **d** Differential gene expression per cluster in 5HTP-treated vs control groups. **e** Statistically significant differential spliced genes in 5HTP-treated vs control groups. Note that at least four long non-coding RNAs responsible for regulation of *Hand2* activity appeared differentially spliced (*Uph, Uph.AS2, Uph.AS3, Uph.AS4*) and well as *Cenpa*-related long non-coding RNA. The bottom: UMAP plots showing meaningful differentially spliced and differentially expressed genes.

organogenesis. Overall, the paracrine and autocrine role of 5HT in developing chromaffin organs results in two important aspects related to health and survival: protection from chromaffin tissue overgrowth or neoplasia, and prevention of excessive catecholamines and catecholamine-controlled behavior. In humans, the sparse expression of *HTR3A* appeared in "bridge" population at weeks 5-to-7 according to RNAseq and at weeks 6 and 8 according to experimental validations with RNAscope. Despite the expression was detected in principle, it appeared low and at the border of detection, leaving a question about the role of *HTR3A* in human "bridge" cells open. Contrary to this, the expression of *HTR3A* in sympathoblasts showed a strong and consistent pattern, also in agreement with other studies[22]. Therefore, the human-specific role of the described paracrine regulation via 5HT and chromaffin progenitor-specific HTR3A is probable, although it requires further experimentation to be validated. Of note, avian chromaffin cells[29] and the cells of the oxygen sensory organ (carotid body) are 5HT-positive as well[61], and may employ the 5HT-dependent mechanism to control their numbers.

The single-cell transcriptomics analysis showed that elevated embryonic 5HT influences the expression of *Cwc22*—a key gene controlling splicing[38,39], and also changes the levels of differentially spliced proliferation—and differentiation-related genes expressed by a "bridge" population (*Apobec3*, long non-coding RNAs controlling *Hand2* and potentially *Cenpa*).

The proposed mechanism of chromaffin cell number control via 5HT-HTR3A-dependent paracrine regulation is unidirectional, as the complete elimination of 5HT and pharmacological blockage of HTR3A receptor do not result in overgrowth of chromaffin cell organs. This goes in line with previous reports showing that the excess of 5HT has stronger effects on brain development as compared to the lack of 5HT[62,63]. For example, *Sert*^{−/−} mice demonstrate elevated levels of extracellular 5HT in the brain, which causes a number of structural abnormalities related to the role of 5HT during brain development together with depressive- and anxiety-like behavior[64], with no changes in adrenal gland morphology and catecholamine release[65]. Conceptually similar results were obtained via inhibition of SERT with selective 5HT reuptake inhibitors at E8–E18 of mouse development[62,66]. On the other hand, *Pet1* KO and *Tph2* KO mice lack 5HT, but have structurally normal brains (although *Pet1* KO mice lack serotonergic neurons) with altered anxiety-related behavior[67,68]. These results are in line with our loss-of-function experiments, where the drastic decrease of embryonic and maternal 5HT did not yield any alteration of size of chromaffin organs, apart from the general reduction of an embryo size reported previously[11,12]. Thus, the 5HT-dependent control of chromaffin cell numbers protects only against the excessive growth and, potentially, tumor-permissive situations.

Consistent with this reasoning, chromaffin organs within the sympathoadrenal complex represent the sites of childhood tumor neuroblastoma, as well as pheochromocytoma and paraganglioma. The comparison of human *HTR3A*^{high} and *HTR3A*^{low} neuroblastoma cell lines revealed that cell lines with *HTR3A*^{high}

expression level have higher tumor-initiating potential. Those cell lines had key characteristics of cancer stem cells and appeared tumorigenic in a mouse xenograft model system as well as formed significantly more spheres in vitro. In line with the in vivo cell cycle progression experiments, we managed to inhibit the proliferation rate of *HTR3A*^{high} neuroblastoma cells with a specific HTR3A agonist, which might be developed into a potential therapeutic strategy, especially in a combination with differentiation-inducing drugs[69–71]. Still, it might be wise to keep in mind the potential difference between tumor and healthy *HTR3A*^{+} cells, as the tumor cells might have additional, unpredictable effects following from HTR3A activation, and the relevance of 5HT paracrine regulation within tumors remains to be elucidated. Moreover, the origin of neuroblastoma is highly debatable[9,22,72–75], and our results regarding the feedback loop mechanism involving 5HT and HTR3A in "bridge" cells in vivo and in cancer cell lines should be interpreted with great care.

Hypothetically, beyond the anticancer-related roles, the 5HT-dependent chromaffin tissue control might have important behavioral, ecological and evolutionary dimensions. Indeed, in addition to local chromaffin cells synthesizing 5HT from 5HTP directly within chromaffin organs, the other major source of embryonic 5HT are represented by the maternal blood[76] and placenta[14,77]. The biosynthetic enzymes TPH1 and DDC are produced in the syncytiotrophoblastic cell layer of the murine placenta, which is in line with previous observations of in vitro placental 5HT neo-synthesis at E10.5–E18.5 in mice. In line with this observation, human placental fetal villi demonstrated a similar biosynthetic capacity during early gestation[77]. The combination of different 5HT sources and the switch from systemic (extraembryonic) to the local source of 5HT were previously noticed during embryonic brain development in mice[14]. Similar to brain development, the presence of extraembryonic-derived 5HT in the embryonic circulation adds another variable to the equation of chromaffin cell number control. In fact, not only local paracrine/autocrine regulation might take place in developing chromaffin organs, but also systemic extraembryonic 5HT might influence the future size of the adrenal medulla. In turn, the intensity of 5HT synthesis in placenta depends on the availability of mother-derived biochemical precursor 5HTP and tryptophan. This opens a potential for a non-genetic control of adrenergic organ development in a progeny of mothers capable of tuning the levels of tryptophan and 5HTP. This tuning might depend on stress factors or health conditions[52,78,79]. Interestingly, chronic mild stress, excessive maternal inflammation, and hypoxia lead to the increased 5HT synthesis in the fetal placenta with increased output to the fetus, as was previously shown for rodents and humans[80]. In our experiments, prenatal mild stress in pregnant females resulted in elevated levels of 5HT in progeny, which reduced adrenal medulla and changed the offspring behavior similarly to the experiment with chemically (5HTP)-treated mothers. In this "chemical" in vivo experiment, we mimicked the maternal-dependent elevation of 5HT by introducing higher levels of 5HTP into pregnant females. As a result, we detected a reduced number of chromaffin cells, smaller adrenal medulla and
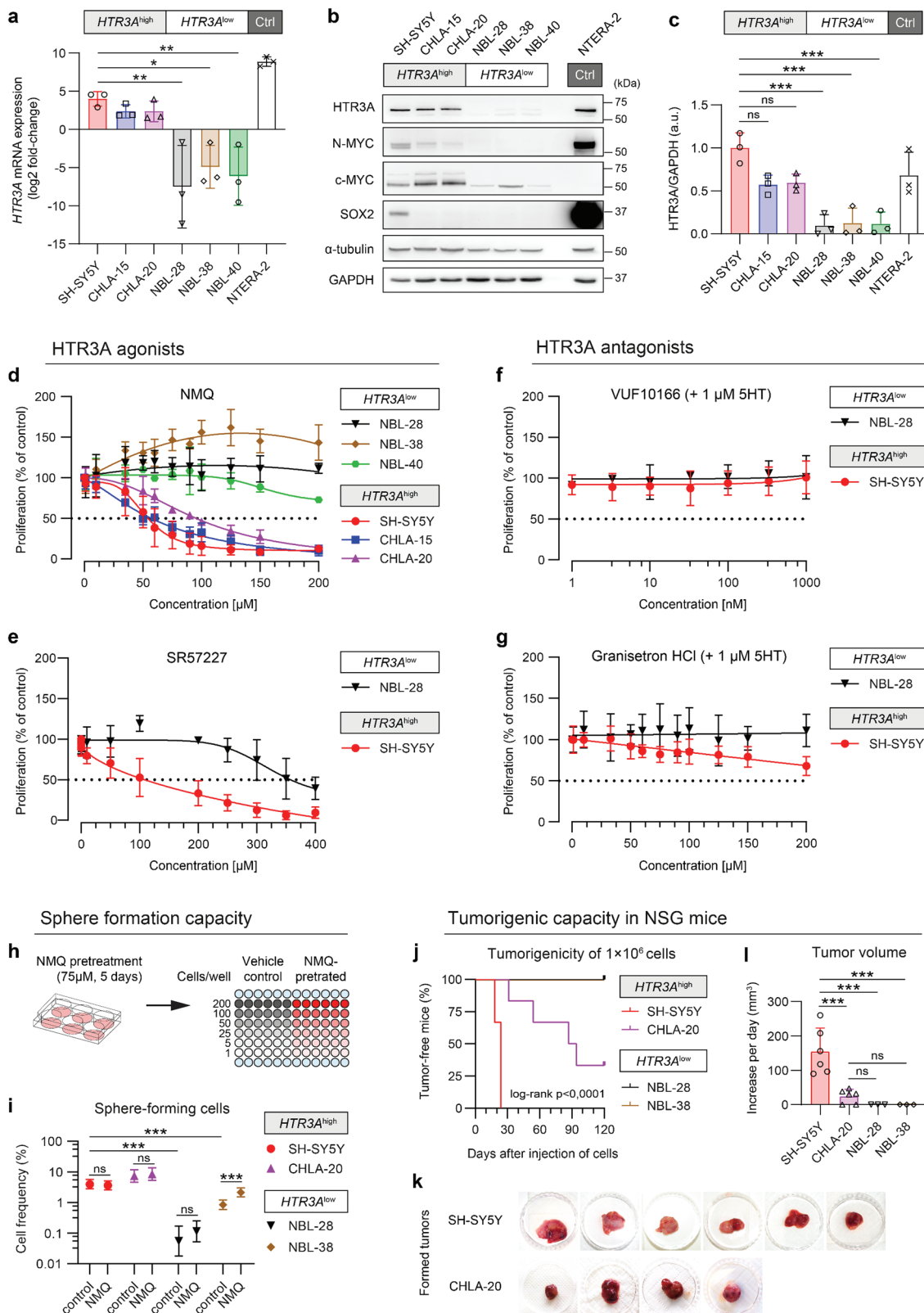
decreased levels of catecholamines associated with changes in the behavior of the adult offspring.

One can admit that the molecular mechanisms controlling the size of chromaffin tissues are important for natural and artificial selection. Although we do not provide direct data supporting this idea, the low aggressiveness, changes in 5HT synthesis and degradation, and reduction of chromaffin organs were previously reported as a part of the so-called "domestication syndrome", observed in a number of domesticated species[20,21]. In line with these domestication-associated behavioral patterns, our experimental rodents subjected to 5HT-driven reduction of adrenals showed less aggressive responses and altered levels of catecholamines. The individual levels of aggressive behavior are indeed related to how the animals react to a wide variety of

Fig. 6 HTR3A^high neuroblastoma cells are highly tumorigenic and reduce their proliferation under excessive HTR3A stimulation. a Gene expression analysis by qRT-PCR revealed marked differences in relative expression of *HTR3A* among individual human neuroblastoma cell lines. NTERA-2 pluripotent embryonal carcinoma cells served as a positive expression control (Ctrl). Data presented as mean ± SD, biological $n = 3$, technical $n = 3$; *$p < 0.05$, **$p < 0.01$ using one-way ANOVA followed by Tukey's post hoc test. **b** Western blotting showed differences in HTR3A protein levels, which also corresponded to the differences in expression of N-MYC, c-MYC, and SOX2 proteins between HTR3A^high and HTR3A^low groups. Blots are representative of three experiments. **c** Densitometric quantitation of the HTR3A protein expression confirms the defined HTR3A^high and HTR3A^low groups. Data presented as mean ± SD, biological $n = 3$; ***$p < 0.01$ using one-way ANOVA followed by Tukey's post hoc test. **d–g** MTT assay on cells treated with agonists of HTR3A receptor (**d, e**) revealed significant dose-response decrease in proliferation of *HTR3A*^high neuroblastoma cells after 5 days of treatment with either N-methylquipazine dimaleate (NMQ, **d**) or SR57227 (**e**); treatments with HTR3A antagonists (**f, g**) did not exert a significant effect on cell proliferation. Data presented as mean ± SD, biological $n = 3–5$, technical $n = 5$. **h** Schematic depiction of limiting dilution sphere formation assay: neuroblastoma cells were pretreated with 75 µM NMQ or vehicle (DMSO) for 5 days and serially diluted in fresh serum-free media w/o the drugs at indicated numbers per well. **i** The frequencies of sphere-forming cells significantly differed between HTR3A^high and HTR3A^low cell lines, while NMQ pretreatment did not reduced sphere formation capacity of the tested cells. Data are shown as mean ± 95% confidence interval, frequencies, and probability were computed using ELDA software[79]. ***$p < 0.01$, χ^2 pairwise test. **j–l** Only *HTR3A*^high neuroblastoma cell lines formed xenograft tumors in NOD/SCID gamma (NSG) mice (**k**). The higher levels of *HTR3A* expression in SH-SY5Y cells corresponded to the earlier onset of tumor formation (**j**) and increased tumor growth (**l**) when compared with CHLA-20 cells; ***$p < 0.01$ using one-way ANOVA followed by Tukey's post hoc test.

environmental challenges including two major coping strategies—proactive and reactive[81]. Aggressive males typically express a more proactive type of behavioral response demonstrating rigid, cue-independent, and impulsive reactions and a tendency to defend their home territory. At the same time, non-aggressive reactive males are rather flexible, cautious, and open to the external cues, which can assist in variable or unpredictable environments, such as during migration[81,82]. Our results demonstrated that prenatal exposure to enhanced 5HT during the critical time window (resulting from maternal mild stress or availability of 5HTP) leads to the birth of progeny with a preferentially reactive type of a coping strategy. This suggests a possible non-genetic information transmission from mother to progeny via the 5HT-dependent developmental control of chromaffin organ size. Conceptually, a similar 5HT-based mother-to-progeny information transmission was identified in invertebrates[13,83,84] and, given our results, might be a more general strategy in nature[85].

Furthermore, the mechanism of 5HT-based mother-to-progeny information transmission might be more evident in a wild population under critical environmental stress. The oscillating population density in red-backed voles (*C. rutilus*) periodically reaches exceptional values and causes unprecedented social stress to individual animals[56]. This, along with other factors, forces the voles to segregate into residents and migrants, shaping the population cycles[86]. The difference between the animals forced to migrate and those who stay might involve a behavioral control of aggression, which is affected by the different size of chromaffin organs. We tested this hypothesis and found an association of the adrenal medulla size with the type of the coping strategy (resident—proactive and migrants—reactive) in wild rodents. This association supports the connection between stress in pregnant mothers, 5HT concentrations and the resulting size of chromaffin organs in progeny. Overall, the described mechanism of chromaffin cell number control via 5HT-sensitive precursor cells may provide a regulatory 5HT-mediated pathway of prenatal programming for long-lasting changes in progeny underlying the behavior of domesticated species as well as wild animals with active and reactive types of coping strategy. Future research should establish the role of genetic factors responsible for the variation of the chromaffin organs in wild animals as compared to the power of the 5HT-based mother-to-progeny information transfer mechanisms.

Methods

Animals and corresponding ethics. All experiments involving laboratory animals were done in accordance with European Convention on the Protection of

Vertebrate Animals Used for Experimental and Other Scientific Purposes (Strasburg, 1986) and approved by the Ethics Committee for Animal Research of the Koltsov Institute of Developmental Biology (Russian Academy of Sciences, approval code: 22, approved on 15 March 2018) as well as in accordance with The Swedish Animal Agency's Provisions and Guidelines for Animal Experimentation recommendations and approved by Ethical Committee on Animal Experiments (Norra Djurförsöksetiska Nämd, ethical permit N226/15).

Laboratory animals were kept in standardized conditions (24 °C, 12:12 h light–dark cycle, 40–60% humidity, food, and water ad libitum).

Htr3a^EGFP transgenic animals are Tg(Htr3a-EGFP)DH30Gsat/Mmnc) were received from MMRRC and provided by the J. Hjerling-Leffler laboratory (Karolinska Institutet, Stockholm, Sweden) (https://www.mmrrc.org/catalog/sds.php?mmrrc_id=273). Animals were kept as heterozygotes for the EGFP transgene. *Wnt1-Cre* (The Jackson Laboratory, stock number 009107), full strain name B6.Cg-Tg(Wnt1-cre)11Rth Tg(Wnt1-GAL4)11Rth/J) and reporter mice line *R26R^Tomato* (The Jackson Laboratory stock number 007914) were used for the study. As wild type animals Wistar Rat, BalbC, and C57Bl6 mice were used.

For all experiments, a single embryo was considered as a biological n, and the embryos from 1 to 2 litters were used in experiment to comply with the 3R policy about the usage of animals in research. Furthermore, the exact timing of the embryonic development varies depending on the time of conception and embryo implantation, which can be up to 12 h apart. The developmental difference within this time-window can affect the results and introduce the unwanted noise into the assessment of developing organs at E8–E14.5 stages. Based on our previous experience with such variation, pulling several litters into one comparison can result in much greater variability within the overall group, which can hide the true differences. Selecting and aligning the perfectly comparable litters requires the unnecessary sacrifice of higher numbers of without much of necessity. With this in mind, and with the goal to minimize the number of animals used, we focused on the analysis of adequate numbers of individual embryos (3–6) serving as biological replicates for our studies. For the majority of the experiments, we utilized 1–2 litters per experimental condition.

NOD/ShiLtSz-*scid/Il2ry^null* mice were used as a NSG model. All NSG mouse experiments were conducted in accordance with a study (21379/2011-30) approved by the Institutional Animal Care and Use Committee of Masaryk University and registered by the Ministry of Agriculture of the Czech Republic as required by national legislation.

E15.5 embryos (gender was not identified) from *Pet1^−/−* knockout mice were received from Patricia Gaspar (INSERM: Paris, France). E15.5 embryos (gender was not identified) from *Tph2* knockout mice were received from Massimo Pasqualetti from (Dept of Biology, University of Pisa, Italy). E13.5 embryos (gender was not identified) from *Tph1;Tph2*, *Tph1;Scl6a4*, and *Tph1;Tph2;Scl6a4* knockout mice together with E13.5 embryos (gender was not identified) of C57BL/6 mice bred in the same facility were received from Natalia Alenina and Michael Bader (Max-Delbruck Center for Molecular Medicine (MDC), Berlin, Deutschland). Before shipment embryos were fixed in 4% paraformaldehyde in PBS (pH 7.4) at 4 °C 4–6 h depending on the embryonic stage. Samples were rinsed in PBS and placed in 30% sucrose in PBS for cryoprotection. Samples were sent in 30% sucrose in PBS solution incubated on ice and processed for immunohistochemical analysis after receipt.

All experiments involving wild animals red-backed voles *Clethrionomys rutilus* were approved by the Biomedical Ethics Commission of FSBI "Zakusov Institute of Pharmacology" (Russian Academy of Sciences, approval code: 01, dated 20 January 2017). Red-backed voles *C. rutilus* (Pallas, 1779) is not an endangered species. The wild representatives of red-backed voles *C. rutilus* were collected during August-September 2020 in the Yenisey ecological station "Mirnoe" (62.2 N; 89.0 W), Turukhansky region of Krasnoyarsk territory, within the Central Siberia Biosphere Reserve. The long-term population-ecological investigations demonstrated a 4-year
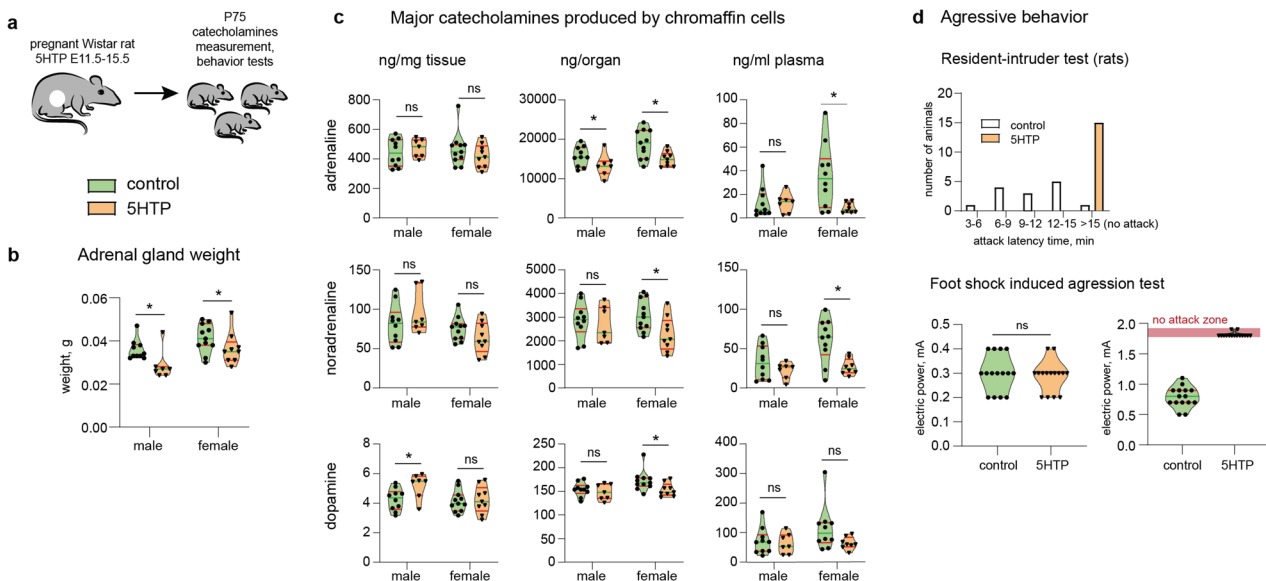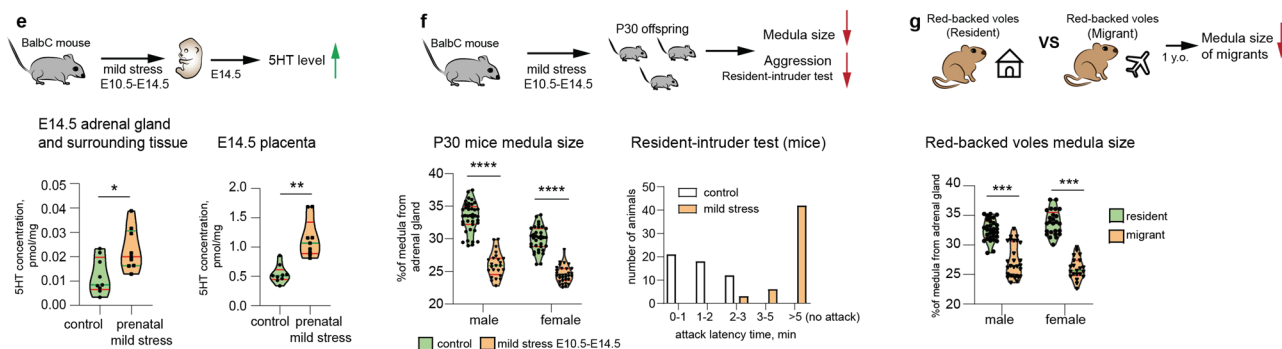
Fig. 7 Embryo-to-adult effects of prenatal 5HT on adult behavior and adrenals are similar to the effect of stress induced in pregnant mothers.
a Pregnant Wistar rats were administered 5HTP during E11.5–E15.5, and their offspring (P)75 was analyzed with the behavioral tests and catecholamine measurements. **b** The size of adrenal glands in animals from the 5HTP-treated females was significantly smaller then from control group. Mann–Whitney test, p-value * < 0.05, biological n = male: 11 (control), 8 (5HTP); female: 12 (control), 10 (5HTP). **c** Major catecholamines measured in ng/mg of tissue, ng/organ and ng/mL of plasma by HPLC-MS. Note: ng/mg of tissue reflects normal function of chromaffin cells, and does not change; ng/organ decreases in 5HTP-treated group. Mann–Whitney test, p-value ns > 0.05, * < 0.05, biological n = male: 11 (control), 8 (5HTP); female 12 (control), 10 (5HTP), for plasma n = male: 10 (control), 7 (5HTP); female 10 (female), 8 (female). **d** Aggression-assessing behavioral tests: "resident-intruder test" (top) and "foot shock-induced aggression test" (bottom) indicate the reduced aggression in the 5HTP-treated group. Mann–Whitney test, p-value ns > 0.05, biological n = 14 and 15 (control), 15 (5HTP group). **e** Pregnant BalbC mice were exposed to a mild stress (1 h restrain) at E10.5–E14.5, followed by 5HT measurements in the embryo trunks and placentas. Note: the 5HT levels were increased similarly to experiment with 5HTP-treatment (refer to Fig. 2a, b). Mann–Whitney test, p-value * <0.05, ** < 0.002, biological n = 9. **f** Pregnant BalbC mice were exposed to a mild stress (1 h restrain) at E10.5–E14.5, and their P30 offspring was tested for the size of adrenal medulla and aggression. Note: the proportion of adrenal medulla was significantly lower in the stress-induced group similarly to the 5HTP-treated group (refer to Fig. 2h). Shapiro–Wilk test for normality, unpaired double-sided t-test p-value, **** < 0.0001, n (adrenal gland) =40 (control male), 24 (1 h restrain male), 35 (control female), 32 (1 h restrain female). **g** The ratio of adrenal medulla of the adrenal gland in *C. rutilus*. Mann–Whitney test, p-value * < 0.05, *** < 0.001, biological n (adrenal gland) = male: 31 (resident), 29 (migrant); female: 25 (resident), 21 (migrant). In all violon plots the green line—median, the red lines—quartiles.

cycle of population dynamics of Micromammalia which is stable in the conditions of Yenisey Central Siberia. *C.rutilus* population dynamic peak occurred in Central Siberia in 2020 (mean 29,1 animals per 100 traps per day in 2020, compared to mean 13,8 animals per 100 traps per day in 2018. Year monitoring of ecological station "Mirnoe"), and the collection period at the late summer\autumn considered the most relevant to estimate the wave dynamics in cycling population[55]. Representatives of *C. rutilus* collected in Sherman traps (live traps) in taiga (dark coniferous forest consisting of Siberian cedar, fir, pine, and larch) were considered as settled individuals or residents. Representatives collected in pitfall traps in Yenisey River valley (meadows without tree communities) were considered as migrants. Trapped species were settled individually in plastic boxes for 2 h. The animals were weighed and adrenals were dissected under inhalant isoflurane anesthesia (SomnoSuite system, Kent Scientific, USA). The gender, pregnancy and

fertility status, approximate ages were determined visually after dissection. Altogether 24 females and 31 males of ~1 year old were used for the study.

5HTP administration to pregnant females and embryo collection. Three- to four-month-old females of Wistar rats, BalbC mice, and 2–4-month-old *Htr3aEGFP* mice were placed in time-controlled mating and the day of plug was considered as embryonic day (E) 0.5 for mice, day of conception was considered as embryonic day (E) 0.5 for rats. 5-hydroxy-L-tryptophan (Sigma-Aldrich H9772) was dissolved in saline and fed (1 mg/kg BW, once a day) to pregnant rats through gavage or intraperitoneally injected (40 mg/kg BW, once a day) to pregnant mice females. At the stage of embryo harvest, the females were sacrificed by cervical dislocation after

anesthesia with 2–3% isoflurane, embryos were eviscerated and placed in ice-cold PBS. The gender of embryos was not identified.

HTR3A agonist and antagonist treatment. Three- to four-month-old pregnant BalbC females received intraperitoneal (i.p.) injections of the selective agonist of the HTR3A receptor, SR57227 hydrochloride (2 mg/kg BW, once a day) at E11.5 and E12.5 stages. Another group of animals was i.p. administered with the HTR3A antagonist, granisetron hydrochloride (2 mg/kg BW, once a day) in combination with 5HTP (40 mg/kg BW, once a day) at E11.5 and E12.5 stages. Drugs were purchased from Tocris (UK), dissolved in DMSO, and then diluted in sterile physiological saline. In the control group, mice received identical volumes of iso-tonic saline with DMSO (DMSO control). E13.5 embryos were fixed in 4% par-aformaldehyde and processed for immunohistochemistry. The gender of embryos was not identified.

MicroCT tissue preparation and analysis. E15.5 rat embryos (gender was not identified) were fixed in 4% paraformaldehyde in PBS (pH 7.4) at 4 °C for 6 h. Samples were dehydrated by incubation in the ethanol gradient solutions in PBS (30%, 50%, 70%); incubation was done at 4 °C with agitation for 24 h in each concentration. For contrasting the samples were transferred to 1.0% PTA (Phos-photungstic acid, Sigma-Aldrich, P4006) in 90% methanol and incubated with rotation at 4 °C with agitation for 3 weeks; the PTA solution was changed weekly. After contrasting, the samples were rehydrated through a methanol gradient (90%, 75%, 50% and 30%). After that, rehydrated embryos were shipped on ice to Brno University of Technology, Czech Republic for microCT scanning.

Samples were placed in polypropylene tubes and embedded in 1% agarose gel to minimize movement during microCT measurement. MicroCT scanning was performed using system GE phoenix v|tome|x L 240, equipped with a 180 kV/15 W maximum power nanofocus X-ray tube and high flat panel dynamic 41|100 with 4000 × 4000 pixels and a pixel size of 100 × 100 μm. The exposure time was 900 ms in 2000 positions over 360°. The microCT scan was carried out at 60 kV acceleration voltage and with 200 μA X-ray tube current. The beam was filtered by a 0.2 mm-thick aluminum filter. The voxel size of obtained volumes was 2.2 μm for all samples. The tomographic reconstructions were performed using GE phoenix datos|x 2.0 3D computed tomography software. Segmentation of structures was performed manually by a combination of software Avizo (Thermo Fisher Scientific, USA) and VG Studio MAX 3.2 (Volume Graphics GmbH, Germany).

Thymidine analogues labeling during S-phase combined with 5HTP treatment. Double thymidine analogues labeling of cells in S-phase was based on the methods described previously[87]. 5-ethynyl-2′-deoxyuridine (EdU, Life Technologies, E10415) and 5-Chloro-2′-deoxyuridine (CldU, Sigma-Aldrich, C6891) were dissolved in PBS at stock concentrations 5 mg/ml and 5.2 mg/mL, respectively, intraperitoneally injected to 2–4-month-old $Htr3a^{EGFP}$ mice pregnant females in equimolar concentrations to 50 mg/kg body weight of EdU with 4-h interval. Females also received 2 injections of 5HTP 40 mg/kg or vehicle control at E11.5 and at E12.5. To minimize the number of 5HTP injections, at E12.5 and the EdU dose were combined in one injection solution. Embryos were harvested 4 h after CldU injection E12.5, gender of the embryos cannot be identified.

Tissue preparation for immunohistochemistry. Whole embryos, dissected sympathoadrenal complexes were fixed in 4% paraformaldehyde in PBS at 4 °C with agitation for 2–6 h followed by rinse in PBS. After fixation samples were cryoprotected in 30% sucrose in PBS at +4 °C with agitation for 24 h. Samples were embedded in OCT and frozen at −20 °C. 14 μm serial sections were produced from each sample, collected on SuperFrost microscopy slides (Thermo Scientific) and kept at −20 °C before staining.

Immunohistochemistry. Cryosections were brought to room temperature and dried for at least 2 h before antigen retrieval. Antigen retrieval was done by sub-merging the slides in 1× Target Retrieval Solution (Dako, S1699) in water, bringing the solution to boiling and letting it cool down for 40–60 min. Sections were washed three times for 10 min in PBS containing 0.1% Tween-20 (PBST), encircled by Super PAP Pen (Invitrogen, 008899), and incubated at room temperature overnight with primary antibodies diluted in PBST in a humidified chamber. Then, sections were washed in PBST three times for 10 min and incubated with secondary antibodies and DAPI (5 μg/mL) diluted in PBST at RT for 90 min, washed again three times in PBST and mounted using Mowiol (Merck, 81381) mounting med-ium, prepared according to manufacturer's instructions.

Detection of thymidine analogues in combinations with IHC. Antigen retrieval was done by submerging the slides in 1× Target Retrieval Solution (Dako, S1699) in water, bringing the solution to boiling point, and cooling it down for 40–60 min. Sections were washed three times for 10 min in PBS. Sections were further per-meabilized with 4% triton X-100 solution for 1 h followed by 3 washes 10 min in PBS.

EdU visualization was performed by click reactions. Sections were incubated in Click Buffer 1 (0.1 M Tris pH 7.5, 20 μL CuSO₄ 100 mM, 5 μM Alexa Fluor 647

azide (ThermoFisher, A10277) (stock 10 mM in DMSO), 100 mM ascorbic acid) for 15 min with gentle rocking. Washed three times for 5 min in PBS and incubated with Click Buffer 2 (20 μL CuSO₄ 100 mM, 40 mM ascorbic acid and 2 mM azidomethyl phenyl sulfide (Sigma-Aldrich) in PBS) for blocking of non-specific reactions of anti-BrdU (clone BU1/75) antibody with EdU[68]. The sections were incubated for 15 min with gentle rocking followed by 3 washes for 5 min in PBS. For CldU visualization with antibodies, a DNA denaturing step by 2N Hydrochloric acid (incubation at 37 °C for 40 min) is critical to allow the antibody to bind to DNA. The sections were neutralized by washing in 0.1 M borate buffer (pH 8.0) two times for 10 min followed by three washes in PBS for 5 min. Then sections were blocked in 5% normal donkey serum (Sigma-Aldrich), 0.1% Triton X-100 in PBS for 1 h. Primary antibodies were dissolved in 5% normal donkey serum (Sigma-Aldrich), 0.1% Triton X-100 in PBS and incubated with sections overnight at RT with gentle rocking. A combination of anti-BrdU (recognizes CldU) antibody and cell type-specific antibodies was applied. Next day, the sections were washed in PBS three times for 5 min and incubated with the solution of secondary antibodies and DAPI in PBS for 90 min at RT. After incubation, the samples were washed in PBS three times for 10 min at room temperature and mounted using Mowiol mounting medium, prepared according to manufacturer's instructions.

Primary and secondary antibodies. The following primary antibodies were used: rabbit anti-TH (1:1000, Pel-Freez Biologicals, #P40101-150), sheep anti-TH (1:2000, Novus Biologicals, #NB300-110), rabbit anti-serotonin (1:2000, Immu-noStar, #20080), chicken anti-GFP (1:600, Aves Labs Inc., #GFP-1020), goat anti-human SOX10 (1:800, R&D Systems, #AF2864), rabbit anti-KI67 (1:500, Thermo Scientific, #RM-9106), rabbit anti-Cleaved Caspase-3 (1:500, Cell signaling, Asp175), rat anti-BrdU (1:300, Abcam, BU1/75, also recognizes CldU). For detection of the primary antibodies, secondary antibodies raised in donkey and conjugated with Alexa-405, -488, -555, and -647 fluorophores were used (1:1000, Molecular Probes, ThermoFisher Scientific). Goat anti-chicken conjugated to Alexa fluor-488 (1:600, Jackson ImmunoResearch, 703-545-155).

RNA scope® in situ hybridization. Fluorescent in situ hybridization manual assay against *Pnmt* (probe 426421-C3) and *Htr3a* (probe 411141-C3) was performed using the RNAscope Fluorescent® Multiplex Assay kit according to manufacturer's instructions (Advanced Cell Diagnostics). Immunostaining following the hybridi-zation was performed as described above except for the antigen retrieval step.

Microscopy. Images were acquired using LSM700, LSM 710, and LSM 880 con-focal microscopes (Carl Zeiss, Germany) equipped with ×10, ×20, and ×40 objectives. Images were acquired in the .lsm format.

Cell counts and area measurements. Cell counts and area measurements were done manually using the Cell counter plugin and measurement functions of ImageJ (2.1.0/1.53c) software. The area of adrenal gland section was calculated by sur-rounding the area based on DAPI signal. The area of medulla was calculated based on TH⁺ signal within adrenal gland. The area of cortex was calculated by sub-traction of adrenal medulla area from the area of the whole gland per individual section. Three section per gland and 2 glands per embryo were evaluated.

Venn diagrams were built with https://www.meta-chart.com/venn#/your-charts free on-line platform and redrawn in Adobe Illustrator 25.2.1. The percentage of Sox10⁺$Htr3a^{EGFP+}$ cells was calculated as a fraction of Sox10⁺$Htr3a^{EGFP+}$ cells from the sum of all Sox10⁺ and all $Htr3a^{EGFP+}$ at E13.5 and E14.5 in adrenal medulla.

Measurements of relative medulla size in postnatal animals. The dissected adrenals of P30 BalbC mice and collected red-backed voles *Clethrionomys rutilus* were processed for whole-mount Benzyl alcohol/Benzyl benzoate tissue optical clearing method. The preparations were scanned using LSM 880 confocal micro-scope (Carl Zeiss, Germany) with a green channel determining the tissue auto-fluorescence. The optical section with maximal external volume was selected for relative medulla size analysis. The area of central medulla and the whole adrenal were measured using ImageJ software. Relative medulla size represented by the ratio: (medulla area/total area) × 100%.

Re-analysis of single-cell transcriptomic data published by Furlan et al., 2017. We re-analyzed single-cell RNA-seq data of mouse adrenal gland from Furlan et al.[6]. Gene counts were obtained from GEO database (GSE99933). Gene count matrix was analyzed with a standard Seurat (version 3.0.2) workflow[88]. We used the original embeddings and clustering from ref. [6] (Figs. 5B and 5G), downloaded from the published pagoda apps: http://pklab.med.harvard.edu/cgi-bin/R/rook/nc.SS2_16_249-2/pathcl.json and http://pklab.med.harvard.edu/cgi-bin/R/rook/nc.SS2_16_250-2/pathcl.json (json slots embedding/data for the embedding and col-cols/clusters/data for the cluster labels).

Seurat function FeaturePlot and DotPlot were used to plot gene expression in individual cells on the embedding and average gene expression in the clusters as dot plots, respectively.

Single-cell RNA sequencing of mouse tissue by SmartSeq2. *Wnt1-Cre*^{+/−}; *R26R*[Tomato+/wt] E13.5 embryos prenatally treated with 5HTP or vehicle for control at E11.5 and E12.5 were harvested in ice-cold PBS. Adrenal glands and Organ of Zuckerkandl were dissected under the stereoscope equipped with a fluorescent light source. Tissue was added to 500 μL of 0.05% Trypsin/0.02% EDTA (Sigma, 59417-C) and incubated at 37 °C for 10 min. The tissue was triturated slowly with a P-200 pipette until complete dissociation. Trypsin was deactivated by adding 500 μL of PBS containing 10% FBS. The cells were centrifuged at $500 \times g$ at 4 °C for 5 min. The cells were washed two times with PBS + 10% FBS followed by centrifugation. The non-single cell clusters of cells were removed by filtering through 40 μm-pore size cell strainers. Fluorescent cells were sorted in single cells mode into 384-well plates prefilled with lysis buffer according to a previously published protocol using a BD FACS Aria III Cell Sorter. One full 384-well plate was sorted and sequenced per organ and per treatment. Single-cell library preparation was done following Smartseq2 protocol[89].

Single-cell transcriptomics data analysis of SmartSeq2. First, generation of count matrices, QC and filtering was performed. The single-cell transcriptome data were generated at the Eukaryotic Single-cell Genomics facility at Science for Life Laboratory in Stockholm, Sweden. The samples were demultiplexing the .fastq files using deindexer (https://github.com/ws6/deindexer) using the NextEra index adapters and the 384-well plate layout. Individual .fastq files were then mapped to mm10_ERCC genome (https://www.ncbi.nlm.nih.gov/assembly/GCF_000001635.20/) using the STAR aligner version 2.7.5c using 2-pass alignment. Reads were filtered for only uniquely mapped and were saved in BAM file format; count matrices were subsequently produced. Estimated count matrices were gathered and converted to an anndata object. Cells with the following quantities were kept as high quality: having more than 10^5 and less than 5×10^5 transcripts, containing more than 4000 and less than 8000 detected genes and or less than 15% of ERCC reads. Cells with low number of reads, potential doublets, cells with high fraction of ribosomal and mitochondrial genes were removed from the analysis. The resulting filtered count matrix contained 1361 high-quality cells (out of 1528 total cells sequenced).

The preprocessing and initial analysis of the count matrix was performed without any batch correction, using scanpy python package v1.7.2, scFates python package v0.2.4, and scvelo python package v0.2.3. Highly variable genes were detected using pagoda2 approach (scFates.pp.find_overdispersed, default parameters). Cell cycle genes were removed from the list of high variable genes to remove their effect. PCA was performed on the scaled count matrix using the high variable genes (scanpy.pp.pca, default parameters). kNN graph (scanpy.pp.neighbors, n_neighbors = 30, n_pcs = 30, metric = "cosine") was generated from PCA space, followed by UMAP embedding generation (scanpy.tl.umap, default parameters) and leiden clustering (scanpy.tl.leiden, Resolution = 0.3)[90]. Differential gene expression analysis was performed per cluster between treated cells and control, using Wilcoxon rank-sum test.

To detect possible differentially spliced genes between the two conditions, BRIE2 algorithm was employed[91,92]. Counting of the isoform-specific reads in each splicing event was performed for BAM files of the QC filtered cells, using filtered mouse annotation provided by the package maintainers. The annotation has the following characteristics: from GENCODE mouse vM17, exon skipping events located on autosome and chrX, not overlapped by any other AS-exon, surrounding introns are no shorter than a fixed length 100 bp. Length of alternative exon regions, between 50 and 450 bp. With a minimum distance, 500 bp, from TSS or TTS. Specific splice sites: surrounded by AG-GT, i.e., AG-AS.exon-GT. Splicing isoform proportion and variable splicing detection was performed in mode 3, by including a design matrix containing the both treatment and location as columns, location effect was removed as potential cofounder.

Ethical aspects of procedures involving human tissue. Human pre-natal tissue was obtained from clinical routine abortions with oral and written consent from the patient. Swedish Ethical Research Authority and the National Board of Health and Welfare has approved the acquisition of human pre-natal tissue for research purposes (ethical reference is 2018/769-31 with the addendum EPN2019-04595). The material was donated for a general research purpose especially with the focus on neuronal and nervous system-related cell types. Measurement of crown-rump-length (CRL) and anatomical landmarks were used to determine the post-conception age.

Human fetal cell isolation, storage in methanol, and rehydration. The tissue was received in ice-cold PBS and enzymatically digested to obtain the single-cell suspension. For this, tissue cut into smaller pieces was incubated with 500 μl 0.05% Trypsin/0.02% EDTA (Sigma, 59417-C) for 15 min at 37 °C with gentle swirling every 5 min. Gentle pipetting up and down was used to mechanically dissociate bigger pieces if any. 500 μl 10% FBS in PBS was added to cell suspension and the cells were pelleted at $500 \times g$ for 5 min at 4 °C. Cells were washed two times with 1000 μL PBS, passed though the 35 μm cell strainer (Falcon, 352235), pelleted at $500 \times g$ for 5 min at 4 °C and re-suspended in 100 μl 0.04% BSA in PBS. Ice-cold methanol (400 μL was added for fixation of the cells and the cells were stored at −80 °C. For the preparation of the library the cells were brought to +4 °C and pelleted at $1000 \times g$ for 10 min at 4 °C. Cell pellet was re-suspended in 500 μL of

rehydration buffer (1X DPBS (Gibco 14190144) containing 1.0% BSA (Sigma, B4287) and 0.5 U/μl RNAse Out (ThermoFisher Scientific, 10777019) followed by two washes with 500 μL of rehydration buffer. The rehydrated cell suspension was sorted to remove debris with BD FACS Aria Fusion instrument (BD Biosciences, San Jose, CA) equipped with 100 μm nozzle. After FACS cells were pelleted to obtain concentrated cell suspension with 700–1200 cells/μL.

10x Genomics RNAseq library preparation and sequencing of human cells. 10x Genomics Chromium Single Cell 3′ protocol for Reagent Kits v3 was used for library preparation aiming to recover 5000–8000 cells. Sequencing was done on Illumina NovaSeq 6000 Sequencing System (NovaSeq 6000 S1 Reagent Kit or NovaSeq 6000 S2 Reagent Kit were used) with the standard recommended read set up for 10X Genomics libraries: Read 1: 28 cycles (Cell barcode and UMI), i7 index: 8 cycles (Sample index), Read 2: 91 cycles. The 10X single-cell transcriptome data were generated at the Eukaryotic Single-cell Genomics facility at Science for Life Laboratory in Stockholm, Sweden.

Human single-cell transcriptomics data analysis with 10x Genomics. The count matrix for each sample was produced by Cell Ranger version 3.1.0 that processed, mapped, and counted raw sequencing data to the Cell Ranger GRCh38-3.0.0 genome and its corresponding annotation. Seurat package pipeline (v.4.0.2)[93] was used for the downstream analysis. Genes expressed in fewer than ten cells in each dataset were removed from further analysis. To keep only high-quality cells, the cells with less than 2000 or more than 25,000 transcripts and the cells with less than 1500 detected genes per cell were omitted. The cells with high mitochondrial content (more than 10%) were also excluded from the analysis. The putative doublets were predicted by Scrublet[94]. The filtered datasets first were analyzed separately to extract the cells belonging to the neural crest-derived sympathoadrenal lineage and then integrated with Seurat function IntegrateData (2000 integration anchor features, 20 dims). The resulting integrated filtered dataset consisted of 3503 high-quality cells. The effects of cell cycle heterogeneity in gene expression were mitigated by regressing out the difference between G2M and S phase signatures by Seurat functions CellCycleScoring and ScaleData (vars.to.regress = "CC.Difference"). Then to perform a graph-based clustering and visualization by UMAP, the first 30 principal components and 30 nearest neighbors were used. Louvain clustering algorithm with resolution equal to 0.2 resulted into finding 13 clusters, two of them were removed due to containing the high doublet scores. The remaining clusters were re-analyzed using the same parameters except the resolution (30 PCs, 30 kNN, resolution = 0.1) and the resulting seven clusters were merged based on the expression of classical cell type-specific markers into four biologically meaningful clusters. To check whether the expression of *HTR3A* gene in the "bridge" cells is not noise-derived, the exact Fisher test was applied after removal of the sympathoblast clusters from the dataset.

Behavioral studies. The tests were performed on 21 male and 25 females P75 Wistar rats, weighing 180–200 g. Animals were acclimatized 15 min a day for 5 days before the tests[95].

Resident-intruder test was performed on rat and mice[81]. For the test on Wistar rats, each resident male was housed with the companion female in the resident cage (floor space of about half a square meter) for 1 week prior to testing. The companion females were sterilized 3 weeks before the test. The cages were not cleaned until the end of the experiment. Testing was performed once a day at 8:00 p.m. The companion female was removed from the cage and an unfamiliar male was introduced in the residential cage, followed by recording the behavior of the resident for 15 min. The time between the introductions of the intruder and the first clinch attack was considered as attack latency.

For the test on BalbC mice, male mice were singly housed for 1 week prior to testing. The cages were not cleaned until the end of the experiment. The male intruders were group-housed (five per cage) and matched with resident mice for approximate age and body weight. The unfamiliar male was introduced in the residential cage and behavior of resident mice was monitored during 5-min after exposure to male intruder. One trial per day was conducted at 8:00 p.m. The time between the introductions of the intruder and the first biting attack was considered as attack latency.

Foot-shock induced aggression test[96] was performed on rats. Two male rats were placed on the electrode floor of the test chamber for both, pain sensitivity and aggression, and then the current was gradually increased at a rate of 0.1 mA/s. The threshold of pain sensitivity was determined by the minimum current at which the animals made the first squealing. The minimum value of the current that causes the typical upright defensive postures (threat posture) in a rat was considered as the threshold of aggressiveness. The test was stopped at 1.8–1.9 mA/s.

Elevated Plus-maze (EPM) test was performed on rats. The apparatus for EPM test was constructed from 2 horizontal arms 50 cm long and 10 cm wide crossing each other in the middle at 90° angle. Two opposing parts of the maze have 40 cm high walls "closed arms". The maze was elevated 40 cm from the floor. The rat was placed in the middle of the apparatus facing one of the closed arms. The time the rat spent on the central part of the maze, in open and closed arms, and the number of entries to open and closed arms were recorded. The total time of one animal observation was 5 min[97].

Novelty-induced hypophagia test was performed on rats. The apparatus for Novelty-induced hypophagia test is a cylindrical platform 97 cm in diameter, with a 42 cm high wall made from white plastic. The floor of the platform has the marks of the central circle, 23 cm in diameter and the middle part, 18.5 cm wide, divided into 6 equal size sectors and the peripheral part 18.5 cm wide, divided into 12 equal size sectors. The source of light was 100 W lamp 1 m above the floor of the platform. In the center of the platform, the food was placed. During 10 min of the test the duration of food take latency was measured.

Extrapolation Escape Task was performed on rats. In this task animals need to find an escape solution from an acute stress situation. The apparatus consists of a basket with an internal cylinder 25 cm high and 10 cm in diameter. The basket is filled with 21–23 °C water up to 2 cm from the bottom of the internal cylinder. Rats were placed in the internal cylinder and their behavior was observed during 2 min. The dive latency and time to find the escape ladder was registered.

Catecholamine analysis. The catecholamine standards (norepinephrine (NE), epinephrine (E), and dopamine (DA)) and catecholamine metabolites (normetanephrine (NM), metanephrine (M)) were obtained from Sigma-Aldrich (USA). The catecholamine and catecholamine metabolites labeled internal standards (norepinephrine-d6, epinephrine-d3 and dopamine-d4, normetanephrine-d3, metanephrine-d3) were obtained from TRC (Canada). All reagents were of analytical grade. Methanol was obtained from Thermo Fisher Scientific (Fisher Scientific UK Ltd.). Ethyl ester was obtained from Panreac (Germany). 2-Aminoethyl diphenylborinate, Formic acid, Hydrochloric acid, Sodium hydroxide, Ammonium chloride were obtained from Sigma-Aldrich (USA). Water used in the entire analysis was prepared using Milli-Q water purification system from Millipore (UK).

A Shimadzu HPLC system (Japan) was used for chromatographic separation of analytes on an Eclipse XDB-C18 (150 mm, 4.6 mm, 5 mm) analytical column, maintained at 40 °C in a column oven. Gradient elution was used for the chromatographic separation of analytes. The mobile phase A: 0.1% formic acid in water, the mobile phase B: 0.1% formic acid in methanol.

A triple quadrupole mass spectrometer Shimadzu 8060 (Japan), equipped with electrospray ionization and operating in positive ionization mode was used for detection of analytes and ISs. For quantitation, multiple reaction monitoring (MRM) was used to monitor precursor-product ion transitions m/z 151.90 → 77.10 (norepinephrine), m/z 158.90 → 111.00 (norepinephrine-d6), m/z 183.90 → 107.00 (epinephrine), m/z 187.00 → 107.00 (epinephrine-d3), m/z 165.90 → 121.15 (normetanephrine), m/z 169.00 → 137.00 (normetanephrine-d3), m/z 153.90 → 91.10 (dopamine), m/z 157.00 → 94.00 (dopamine-d4), m/z 179.90 → 165.15 (metanephrine), m/z 183.00 → 168.00 (metanephrine-d3).

Calibration standards and quality control samples. Stock solutions of analytes (1 mg/mL) were prepared by dissolving accurately weighed reference standards in 0.1% HCl in water. Stock solutions of ISs (1 mg/mL) were prepared by dissolving accurately weighed reference standards in 0.1% formic acid in water. Calibration standards (CSs) and quality control (QC) samples were prepared by spiking blank sample (water) (10% of total volume of blank sample) with mixed stock solutions. CSs were made at concentration levels (Table 1).

QC samples were prepared at two concentration levels (Table 2).

All the solutions (standard stock, CSs and QC samples) were stored at −20°C until use.

To extract catecholamines, adrenal glands were weighed, homogenized in 0.9% NaCl, and frozen in liquid nitrogen. Heparinized blood samples were collected from the heart and centrifuged. Samples were kept at −80 °C until the mass spectrometric analysis of catecholamines and their metabolites.

Prior to analysis, all frozen samples, CSs and QC samples were thawed in RT. To each glass tube (16 × 100 mm) 0.5 ml CSs, QC or sample; 20 μL of the internal standards mix and 0.8 mL of buffer containing a complexing agent (0.2% DPBA-ethanolamine ester and 5 g/L EDTA in 2 mol/L NH₄ Cl–NH₄ OH buffer, pH 8.5) was added. After mixing, the pH of the complexed sample preparation was checked with a pH probe or narrow range pH paper. If the pH was <7.5, it was adjusted with concentrated ammonia to be between 7.5 and 9.5. Ethyl Ester (1500 μL) was added to extract the analytes and vortex-mixed (10 min), and the sample was then centrifuged for 10 min at 3000 × *g*. The Ethyl Ester layer was removed (800 μL) and placed into a recovery vial (Waters Corp., Elstree, UK). The vial solution was then evaporated to dryness using a centrifugal vacuum evaporator (Eppendorf, USA).

The samples were reconstituted in 200 μL (0.1% formic acid in water), and 2 μL was injected onto the column.

Quantification was performed using Shimadzu LabSolution software, version 5.3 (Japan) using the integration peak area ratio of analyte and labeled IS.

5HT measurement by high-performance liquid chromatography with electrochemical detection (HPLC-ED). 5HT concentration was determined after the following experiments: (1) Pregnant BalbC mice were subjected to mild stress based on a published method[52] for 1 h daily from E10.5 to E13.5. 5HT was measured at E14.5 in placenta and fetal tissues; (2) Pregnant BalbC mice received 5HTP from E10.5 to E13.5. 5HT was measured at E14.5 in placenta and fetal tissues; (3) Pregnant BalbC mice received 5HTP from E10.5 to E13.5. At E 14.5 fetal adrenals and kidneys were dissected and incubated for 1 h in DMEM medium at 37 °C in a humidified 5% CO₂/95% air atmosphere. About 16–20 adrenals and 10–12 kidneys were pooled per sample. After the incubation 5HT was measured in culture medium and fetal tissues.

A Shimadzu HPLC-ED LC-20ADsp (Japan) was used for chromatographic separation of analytes on a reversed-phase ReproSil-Pur column, ODS-3, 4 × 100 mm with pore diameter of 3 μm (Dr. Majsch GMBH, Germany) at a temperature of 30 °C and a flow rate of 1.0 mL/min. The mobile phase consisted of 0.1 M citrate–phosphate buffer containing 0.3 mM sodium octanesulfonate, 0.1 mM EDTA and 7% acetonitrile (all reagents purchased from Sigma) (pH 2.56). Decade II electrochemical detector (Antec Leyden, Netherlands) was equipped with a glassy carbon working electrode (+0.85 V) and an Ag/AgCl reference electrode. Collected tissues were homogenized in 10 volumes of 0.1 N HClO₄ containing 3,4-dihydroxybenzylamine hydrobromide (internal standard, Sigma, St. Louis, USA) (25–250 pmol/mL) by an ultrasonic homogenizer (Sonopuls HD 2000.2, Bandelin, Berlin, Germany), centrifuged at 16,500 × *g* for 20 min, and 5HT in the supernatant were measured. Peaks corresponding to 5HT were identified according to elution time of the standard solution, and the contents of substances were estimated as a ratio of the peak area of the internal standard solution to that of the specimen using software LabSolutions (Shimadzu, Japan).

Cell cultures. Patient-derived neuroblastoma cell lines NBL-28, NBL-38, and NBL-40 were established from tumor tissue samples[98,99], with written informed consent obtained for our previous research project (IGA MZCR NR/9125-4), approved by the Research Ethics Committee of the School of Medicine, Masaryk University, Brno, Czech Republic (Approval No. 23/2005). According to Czech legal and ethical regulations governing the use of human biological material for research purposes, a new ethical assessment of this study is not necessary. In brief, the tumor biopsy was disinfected, cut into ~2 mm pieces, and placed into T25 flask with 1 mL of complete medium based on DMEM (PAA Laboratories, Linz, Austria) supplemented with 20% fetal calf serum (PAA), 2 mM glutamine and 1× penicillin/streptomycin (BioWhittaker, Inc., Walkersville, MD, USA) under 37 °C and 5% CO₂. After specimen attachment, the volume of the medium was slowly brought up to 5 ml during 48 h. Once outgrowing cells reached 60% confluency, they were passaged and maintained. The SH-SY5Y neuroblastoma cell line was purchased from ECACC cat. # 94030304). CHLA-15 and CHLA-20 neuroblastoma cell lines were obtained from Alex's Lemonade Stand Foundation Childhood Cancer Repository (cccells.org) and kindly provided by Dr. Michael D. Hogarty (Children's Hospital of Philadelphia, PA, USA). Pluripotent embryonal carcinoma cell line NTERA-2 (clone D1) was purchased from ECACC (cat. # 01071221) and served as a control of HTR3A expression. Cells were cultured in DMEM/Ham's F-12 medium mixture (1:1; all neuroblastoma cells) or DMEM (NTERA-2) supplemented with 10% (CHLA-15, CHLA-20, and NTERA-2) or 20% fetal calf serum (FCS), 2 mM l-glutamine, 100 IU/mL penicillin, and 100 μg/mL streptomycin (all from Biosera, Nuaillé, France), at 37 °C with 5% CO₂. For all neuroblastoma cell lines, media were further supplemented with 1% of nonessential amino acids (Biosera) and in case of CHLA-15 and CHLA-20 also with 1× ITS-X (Gibco). All cell lines were routinely authenticated by STR profiling.

qRT-PCR. Total RNA was extracted with the GenElute™ Mammalian Total RNA Miniprep kit including genomic DNA elimination step using the On-Column DNase I Digestion Set (both Sigma-Aldrich, St. Louis, MO, USA). For all samples, equal amounts of RNA (25 ng of RNA/1 μL of total reaction content) were reverse transcribed into cDNA using M-MLV (Top-Bio, Prague, Czech Republic) and oligo-dT (Qiagen Inc., Valencia, CA, USA) priming. Quantitative PCR was performed in 10 μL reaction volumes using the KAPA SYBR® FAST qPCR Kit (Kapa Biosystems, Wilmington, MA, USA) and 7500 Fast Real-Time PCR System and 7500 Software v.2.0.6 (both Life Technologies, Carlsbad, CA, USA). The expression of individual genes was assessed using at least three technical replicates from three

Table 1 Composition of calibration standards.

№	Name	NM/D/E/M/NE concentration, ng/ml
1	Cal 1	1/50/5/1/5
2	Cal 2	10/100/25/10/25
3	Cal 3	50/250/50/50/50
4	Cal 4	100/500/100/100/100
5	Cal 5	500/750/250/500/250
6	Cal 6	1000/1000/500/1000/500

Table 2 Composition of quality control samples.

№	Name	NM/D/E/M/NE concentration, ng/ml
1	QCL	3/75/15/3/15
2	QCH	800/800/400/800/400

biological replicates of each cell line. The heat shock protein gene HSP90AB1 was used as the endogenous reference control. Following primers ($5' \rightarrow 3'$) were used for this study: *HTR3A* (5-hydroxytryptamine receptor 3A) forward—AGGAAGCCA ACCACCGTATC; *HTR3A* reverse—GTCCGTGGGGATGGACAACT; *HSP90AB1* (Heat shock protein 90 alpha family class B member 1) forward—CGCATGA AGGAGACACAGAA; *HSP90AB1* reverse—TCCCATCAAATTCCTTGAGC.

Western blotting. Whole-cell extracts were collected using RIPA buffer and 30 μg of total proteins were resolved on 10% polyacrylamide gels and blotted onto PVDF membranes (Bio-Rad Laboratories, Munich, Germany). The membranes were blocked with 5% non-fat dry milk in Tris-buffered saline with 0.05% Tween-20 (Sigma) and incubated overnight with primary antibodies. The following antibodies were used: rabbit anti-HTR3A (1:5000, Abcam, #ab13897), rabbit anti-c-MYC (1:1000, Cell Signaling Technology, CST, #5605), rabbit anti-N-MYC (1:1000, CST, #84406), rabbit anti-SOX2 (1:1000, CST, #3579), rabbit anti-cleaved caspase-3 (1:1000; CST, #9664), rabbit anti-GADPH (1:10,000, CST, #2118), and mouse anti-α-tubulin (1:10,000, Abcam, #ab7291). The next day, the membranes were incubated for 1 h with HRP-linked secondary antibodies: goat anti-rabbit IgG (1:5000, CST, #7074) or horse anti-mouse IgG (1:5000, CST, #7076). Chemiluminescent detection was performed using Amersham ECL Prime (Cytiva, Marlborough, MA, USA) and either Azure 600 imaging system (Azure Bio-systems, Dublin, CA, USA) or photosensitive film. GAPDH or α-tubulin served as loading controls. Protein band densities were quantified using ImageJ (Fiji) software (NIH, Bethesda, MD, USA), version 2.1.0/1.53c.

Neuroblastoma xenografts in NSG mice. Eight-week-old female NSG (NOD/ShiLtSz-*scid/Il2ry*[null]) mice were injected subcutaneously into the right flank with a suspension of 1×10^6 enzymatically dissociated cells in 100 μL of serum-free DMEM. The mice were examined every three days over the period of 4 months for the presence of subcutaneous tumors. After the development of a tumor or after 4 months, the mice were sacrificed and surgically examined. The xenograft tumors were excised and photographed, and the final tumor volume was measured using the following formula: tumor volume (mm^3) = length (mm) × width (mm) × width (mm) × 1/2.

MTT cell proliferation assay. Neuroblastoma cells were seeded in 96-well plates at a density of 10^3 cells/well in a defined serum-free medium: DMEM/F12 based medium (as detailed in Cell lines) w/o FCS, supplemented with 10 ng/mL EGF (Sigma-Aldrich), 20 ng/mL FGF2 (Sigma-Aldrich), and 1× B-27 supplement w/o vitamin A (Gibco). After 24 h, cells were treated by the addition of fresh medium with the selective HTR3A receptor agonists, N-methylquipazine dimaleate (NMQ; Tocris, cat. #0566) or SR57227 (Tocris, cat. #1205), or the HTR3A receptor antagonists, granisetron hydrochloride (Tocris, cat. #2903) and VUF 10166 (Tocris, cat. #10166). In case of HTR3A receptor antagonists, medium was further supplemented with 5HT (Merck, cat. #14927) to the final concentration of 1 μM to evaluate the effect of HTR3A receptor inhibition. The proliferation activity was analyzed after additional 5 days using 3-[4,5-dimethylthiazol-2-yl]-2,5-diphenyltetrazolium bromide (MTT) (Sigma) at a final concentration of 455 μg/ml[100]. The medium with MTT was replaced by 200 μL of DMSO per well after a 3 h incubation under standard conditions in order to solubilize the MTT product. The absorbance was measured at 570 nm with a reference absorbance at 620 nm wavelength using a Sunrise Absorbance Reader (Tecan).

Limiting dilution sphere formation assay. Prior to sphere formation assay, cells were treated for 5 days with 75 μM NMQ or an equivalent concentration of vehicle (DMSO). Cells were then harvested and dissociated into single-cell suspension by Accutase (Biosera), re-suspended in a defined serum-free medium (detailed above) and serially diluted into ultra-low attachment 96-well plates (Corning, cat. #3474) to reach final cell densities of 200, 100, 50, 25, 5, and 1 per well. At least four technical replicates of each cell density were included per cell line and treatment group. Every three days, growth factors were replenished by addition of fresh defined medium. After a week, for each cell density, the fraction of wells containing neurospheres ≥50 μm in diameter was determined using an Olympus CKX41 light microscope with Lumenera Infinity 2 CCD camera and QuickPhoto Camera 2.3 system (PROMICRA, Prague, Czech Republic). Frequencies of sphere-forming cells among experimental groups were calculated and compared using ELDA software[101].

Statistical analysis. Statistical analysis was done using GraphPad Prism 8.1.1 software. All datasets were checked for normality with Shapiro–Wilk test, as this test reliably works for small datasets. For datasets with normal distribution double-sided unpaired t-test was applied. For datasets which failed a test for normal distribution, Mann–Whitney test was applied. For comparisons between multiple groups for one variable the one-way ANOVA test was applied (Fig. 3d, Fig. 6a, c, l, Supplementary Fig. 7d, e, f). In case one-way ANOVA test was showing significant differences, Tukey's multiple comparison test was used for a robust pairwise comparison of groups with unequal size (every mean to every other mean) or Dunnet's multiple comparison test for a pairwise comparison of groups to a control group.

In the analyses of statistical significance in catecholamine measurement as well as in behavioral tests (Fig. 7, Supplementary Fig.8) we have chosen the pairwise comparison within genders. The reason for it is that the treatment with 5HTP or

1-h restrain was applied at the stage, when the sexual dimorphism is not established in the forming adrenal glands and, consequently, the treatment equally affects males and females. However, adrenal glands have sexual dimorphism at postnatal stages and therefore must be analyzed separately, since the combined analysis of these groups can mask the effects of our prenatal treatment. We do not report a quantitative difference in catecholamines and catecholamine metabolites concentration. We have calculated statistical significance with Mann–Whitney test within genders between treated and control animals as this test is applicable to small samples and can evaluate statistical significance regardless of the normality of data distribution and homoscedasticity of the data. For these experiments the analysis was performed in SigmaPlot 12.1.

One of the values of catecholamine content in plasma in female 5HTP-treated group was removed based on the τ-criterion (blunder detection techniques). The outlier value from one animal may be caused by an error when taking a blood sample. Indeed, catecholamine release from adrenals is known to be very sensitive to various factors (in particular, stressful ones, at the time of sampling).

For all violin plots, median and quartiles are shown as those values work equally good for normally and not normally distributed data points.

Data availability

The raw and processed data of single-cell transcriptomic experiments generated in this study have been deposited in the GEO database under accession codes: GSE180861 (mouse), GSE195929 (human). The single-cell RNA-seq data of mouse adrenal gland from Furlan et al. (2017) used in this study are available in the GEO database under accession code GSE99933, mm10_ERCC genome used in this study is available in the RefSeq database under accession code GCF_000001635.20. The data other than RNA-seq data generated in this study are provided in the Source data file.

Code availability

The code for reproducing the bioinformatic analysis can be found on the following GitHub repository: [https://github.com/LouisFaure/Adrenal5HTP_paper] (https://doi.org/10.5281/zenodo.6247197).

References

1. Kastriti, M. E., Kameneva, P. & Adameyko, I. Stem cells, evolutionary aspects and pathology of the adrenal medulla: a new developmental paradigm. *Mol. Cell. Endocrinol.* **518**, 110998 (2020).
2. Lin, V. T. G., Pruitt, H. C., Samant, R. S. & Shevde, L. A. Developing cures: targeting ontogenesis in cancer. *Trends Cancer* **3**, 126–136 (2017).
3. Tirosh, I. et al. Single-cell RNA-seq supports a developmental hierarchy in human oligodendroglioma. *Nature* **539**, 309–313 (2016).
4. Gojo, J. et al. Single-cell RNA-Seq reveals cellular hierarchies and impaired developmental trajectories in pediatric ependymoma. *Cancer Cell* **38**, 44–59.e49 (2020).
5. Couturier, C. P. et al. Single-cell RNA-seq reveals that glioblastoma recapitulates a normal neurodevelopmental hierarchy. *Nat. Commun.* **11**, 3406 (2020).
6. Furlan, A. et al. Multipotent peripheral glial cells generate neuroendocrine cells of the adrenal medulla. *Science* **357**, eaal3753 (2017).
7. La Manno, G. et al. RNA velocity of single cells. *Nature* **560**, 494–498 (2018).
8. Kastriti, M. E. et al. Schwann cell precursors generate the majority of chromaffin cells in Zuckerkandl organ and some sympathetic neurons in paraganglia. *Front. Mol. Neurosc.* **12**, https://doi.org/10.3389/fnmol.2019.00006 (2019).
9. Kameneva, P. et al. Single-cell transcriptomics of human embryos identifies multiple sympathoblast lineages with potential implications for neuroblastoma origin. *Nat. Genet.* **53**, 694-706 (2021).
10. Cote, F. et al. Maternal serotonin is crucial for murine embryonic development. *Proc. Natl Acad. Sci. USA* **104**, 329–334 (2007).
11. Alenina, N. et al. Growth retardation and altered autonomic control in mice lacking brain serotonin. *Proc. Natl Acad. Sci. USA* **106**, 10332–10337 (2009).
12. Narboux-Neme, N. et al. Postnatal growth defects in mice with constitutive depletion of central serotonin. *ACS Chem. Neurosci.* **4**, 171–181 (2013).
13. Ivashkin, E. et al. Serotonin mediates maternal effects and directs developmental and behavioral changes in the progeny of snails. *Cell Rep.* **12**, 1144–1158 (2015).

14. Bonnin, A. et al. A transient placental source of serotonin for the fetal forebrain. *Nature* **472**, 347–350 (2011).

15. Vitalis, T., Ansorge, M. S. & Dayer, A. G. Serotonin homeostasis and serotonin receptors as actors of cortical construction: special attention to the 5-HT3A and 5-HT6 receptor subtypes. *Front Cell Neurosci.* **7**, 93 (2013).

16. Migliarini, S., Pacini, G., Pelosi, B., Lunardi, G. & Pasqualetti, M. Lack of brain serotonin affects postnatal development and serotonergic neuronal circuitry formation. *Mol. Psychiatry* **18**, 1106–1118 (2013).

17. Lv, J & Liu, F. The role of serotonin beyond the central nervous system during embryogenesis. *Front Cell Neurosci.* **11**, 74 (2017).

18. Rauw, W. M., Johnson, A. K., Gomez-Raya, L. & Dekkers, J. C. M. A hypothesis and review of the relationship between selection for improved production efficiency, coping behavior, and domestication. *Front Genet.* **8**, 134 (2017).

19. Cagan, A. & Blass, T. Identification of genomic variants putatively targeted by selection during dog domestication. *BMC Evol. Biol.* **16**, 10 (2016).

20. Trut, L., Oskina, I. & Kharlamova, A. Animal evolution during domestication: the domesticated fox as a model. *BioEssays* **31**, 349–360 (2009).

21. Wilkins, A. S., Wrangham, R. W. & Fitch, W. T. The "domestication syndrome" in mammals: a unified explanation based on neural crest cell behavior and genetics. *Genetics* **197**, 795–808 (2014).

22. Jansky, S. et al. Single-cell transcriptomic analyses provide insights into the developmental origins of neuroblastoma. *Nat. Genet.* **53**, 683–693 (2021).

23. Munoz-Manchado, A. B. et al. Novel striatal gabaergic interneuron populations labeled in the 5HT3a(EGFP) mouse. *Cereb. Cortex* **26**, 96–105 (2016).

24. Finger, T. E., Bartel, D. L., Shultz, N., Goodson, N. B. & Greer, C. A. 5HTR3A-driven GFP labels immature olfactory sensory neurons. *J. Comp. Neurol.* **525**, 1743–1755 (2017).

25. Jessen, K. R. & Mirsky, R. The origin and development of glial cells in peripheral nerves. *Nat. Rev. Neurosci.* **6**, 671–682 (2005).

26. Schroeter, S., Levey, A. I. & Blakely, R. D. Polarized expression of the antidepressant-sensitive serotonin transporter in epinephrine-synthesizing chromaffin cells of the rat adrenal gland. *Mol. Cell Neurosci.* **9**, 170–184 (1997).

27. Brindley, R. L., Bauer, M. B., Blakely, R. D. & Currie, K. P. M. Serotonin and serotonin transporters in the adrenal medulla: a potential hub for modulation of the sympathetic stress response. *ACS Chem. Neurosci.* **8**, 943–954 (2017).

28. Delarue, C., Becquet, D., Idres, S., Hery, F. & Vaudry, H. Serotonin synthesis in adrenochromaffin cells. *Neuroscience* **46**, 495–500 (1992).

29. García-Arrarás, J. E. & Martínez, R. Developmental expression of serotonin-like immunoreactivity in the sympathoadrenal system of the chicken. *Cell Tissue Res.* **262**, 363–372 (1990).

30. Bondarenko, N. S. et al. Plasticity of central and peripheral sources of noradrenaline in rats during ontogenesis. *Biochemistry* **82**, 373–379 (2017).

31. Mitchell, J. A., Hammer, R. E. & Goldman, H. Serotonin induced disruption of implantation in rats: II. Suppression of decidualization. *Biol. Reprod.* **29**, 6 (1983).

32. Udenfriend, S., Weissbach, H. & Bordanski, D. Increase in tissue serotonin following administration of its precursor 5-hydroxytryptophan. *J. Bilogical Chem.* **224**, 7 (1957).

33. Bogdanski, D. F., Weissbach, H. & Udenfriend, S. Pharmacological studies with the serotonin precursor, 5-hydroxytryptophan. *J. Pharm. Exp. Ther.* **122**, 182–194 (1958).

34. Schneider, B. F. & Norton, S. Equivalent ages in rat, mouse and chick embryos. *Teratology* **19**, 273–278 (1979).

35. Le Douarin, N. M., Smith, J. & Le Lievre, C. S. From the neural crest to the ganglia of the peripheral nervous system. *Annu. Rev. Physiol.* **43**, 653–671 (1981).

36. Cheraghali, A. M., Knaus, E. E. & Wiebe, L. I. Bioavailability and pharmacokinetic parameters for 5-ethyl-2′-deoxyuridine. *Antivir. Res.* **25**, 259–267 (1994).

37. Chan, W. H. et al. Differences in CART expression and cell cycle behavior discriminate sympathetic neuroblast from chromaffin cell lineages in mouse sympathoadrenal cells. *Developmental Neurobiol.* **76**, 137–149 (2016).

38. Alexandrov, A., Colognori, D., Shu, M.-D. & Steitz, J. A. Human spliceosomal protein CWC22 plays a role in coupling splicing to exon junction complex deposition and nonsense-mediated decay. *Proc. Natl Acad. Sci. USA* **109**, 21313 (2012).

39. Steckelberg, A.-L., Boehm, V., Gromadzka, A. M. & Gehring, N. H. CWC22 connects pre-mRNA splicing and exon junction complex assembly. *Cell Rep.* **2**, 454–461 (2012).

40. Anderson, K. M. et al. Transcription of the non-coding RNA upperhand controls Hand2 expression and heart development. *Nature* **539**, 433–436 (2016).

41. Morikawa, Y., D'Autréaux, F., Gershon, M. D. & Cserjesi, P. Hand2 determines the noradrenergic phenotype in the mouse sympathetic nervous system. *Developmental Biol.* **307**, 114–126 (2007).

42. McCann, J. L. et al. The DNA deaminase APOBEC3B interacts with the cell-cycle protein CDK4 and disrupts CDK4-mediated nuclear import of Cyclin D1. *J. Biol. Chem.* **294**, 12099–12111 (2019).

43. Martin, V. et al. Response of Htr3a knockout mice to antidepressant treatment and chronic stress. *Br. J. Pharm.* **174**, 2471–2483 (2017).

44. Zimmerman, M. W. et al. MYC drives a subset of high-risk pediatric neuroblastomas and is activated through mechanisms including enhancer hijacking and focal enhancer amplification. *Cancer Discov.* **8**, 320 (2018).

45. Wang, L. L. et al. Augmented expression of MYC and/or MYCN protein defines highly aggressive MYC-driven neuroblastoma: a Children's Oncology Group study. *Br. J. Cancer* **113**, 57–63 (2015).

46. Eisenhofer, G. et al. Plasma normetanephrine and metanephrine for detecting pheochromocytoma in von Hippel–Lindau disease and multiple endocrine neoplasia type 2. *N. Engl. J. Med.* **340**, 1872–1879 (1999).

47. Raber, W. et al. Diagnostic efficacy of unconjugated plasma metanephrines for the detection of pheochromocytoma. *Arch. Intern. Med.* **160**, 2957–2963 (2000).

48. Axelrod, J. Metabolism of epinephrine and other sympathomimetic amines. *Physiological Rev.* **39**, 751–776 (1959).

49. Axelrod, J. Noradrenaline: fate and control of its biosynthesis. *Science* **173**, 598–606 (1971).

50. Kopin, I. J. Storage and metabolism of catecholamines: the role of monoamine oxidase. *Pharm. Rev.* **16**, 179–191 (1964).

51. Parvez, H., Ismahan, G., Parvez, S. & Youdim, M. B. Developmental changes in the activity of catechol-O-methyl transferase in rat and rabbit fetuses. *J. Neural Transm.* **44**, 65–75 (1979).

52. Chen, H. J. et al. Prenatal stress causes intrauterine inflammation and serotonergic dysfunction, and long-term behavioral deficits through microbe- and CCL2-dependent mechanisms. *Transl. Psychiatry* **10**, 191 (2020).

53. Dmitriev, S. G., Zakharov, V. M. & Sheftel, B. I. Cytogenetic homeostasis and population density in red-backed voles *Clethrionomys glareolus* and *C. rutilus* in central Siberia. *Acta Theriologica* **Suppl. 4**, 49–55 (1997).

54. Zakharov, V. M., Trofimov, I. E. & Sheftel, B. I. Fluctuating asymmetry and population dynamics of the common shrew, *Sorex araneus*, in Central Siberia under climate change conditions. *Symmetry* **12**, 1960 (2020).

55. Henttonen, H., McGuire, A. D. & Hansson, L. Comparisons of amplitudes and frequencies (spectral analyses) of density variations in long-term data sets of *Clethrionomys* species. *Annales Zoologici Fennici* **22**, 221–227 (1985).

56. Liu, J. et al. High housing density increases stress hormone- or disease-associated fecal microbiota in male Brandt's voles (Lasiopodomys brandtii). *Hormones Behav.* **126**, 104838 (2020).

57. Huber, K., Kalcheim, C. & Unsicker, K. The development of the chromaffin cell lineage from the neural crest. *Auton. Neurosci.* **151**, 10–16 (2009).

58. Furlan, A. & Adameyko, I. Schwann cell precursor: a neural crest cell in disguise? *Developmental Biol.* **444**, S25–S35 (2018).

59. Duester, G. Retinoic Acid synthesis and signaling during early organogenesis. *Cell* **134**, 921–931 (2008).

60. Nicosia, R. F., Zorzi, P., Ligresti, G., Morishita, A. & Aplin, A. C. Paracrine regulation of angiogenesis by different cell types in the aorta ring model. *Int. J. Dev. Biol.* **55**, 447–453 (2011).

61. Hockman, D. et al. Striking parallels between carotid body glomus cell and adrenal chromaffin cell development. *Dev. Biol.* **444**, S308–S324 (2018).

62. St-Pierre, J., Laurent, L., King, S. & Vaillancourt, C. Effects of prenatal maternal stress on serotonin and fetal development. *Placenta* **48**, S66–S71 (2016).

63. Nordquist, N. & Oreland, L. Serotonin, genetic variability, behaviour, and psychiatric disorders—a review. *Upsala J. Med. Sci.* **115**, 2–10 (2010).

64. Kalueff, A. V., Olivier, J. D. A., Nonkes, L. J. P. & Homberg, J. R. Conserved role for the serotonin transporter gene in rat and mouse neurobehavioral endophenotypes. *Neurosci. Biobehav. Rev.* **34**, 373–386 (2010).

65. Brindley, R. L. et al. Adrenal serotonin derives from accumulation by the antidepressant-sensitive serotonin transporter. *Pharmacol. Res.* **140**, 56–66 (2019).

66. Noorlander, C. W. et al. Modulation of serotonin transporter function during fetal development causes dilated heart cardiomyopathy and lifelong behavioral abnormalities. *PLoS ONE* **3**, e2782 (2008).

67. Gutknecht, L. et al. Impacts of brain serotonin deficiency following Tph2 inactivation on development and raphe neuron serotonergic specification. *PLoS ONE* **7**, e43157 (2012).

68. Schaefer, T. L., Vorhees, C. V. & Williams, M. T. Mouse plasmacytoma-expressed transcript 1 knock out induced 5-HT disruption results in a lack of cognitive deficits and an anxiety phenotype complicated by hypoactivity and defensiveness. *Neuroscience* **164**, 1431–1443 (2009).

69. Thiele, C. J., Reynolds, C. P. & Israel, M. A. Decreased expression of N-myc precedes retinoic acid-induced morphological differentiation of human neuroblastoma. *Nature* **313**, 404–406 (1985).

70. Hölzel, M. et al. NF1 is a tumor suppressor in neuroblastoma that determines retinoic acid response and disease outcome. *Cell* **142**, 218–229 (2010).

71. Bayeva, N., Coll, E. & Piskareva, O. Differentiating neuroblastoma: a systematic review of the retinoic acid, its derivatives, and synergistic interactions. *J. Pers. Med.* **11** (2021).

72. Dong, R. et al. Single-cell characterization of malignant phenotypes and developmental trajectories of adrenal neuroblastoma. *Cancer Cell* **38**, 716–733.e716 (2020).

73. Bedoya-Reina, O. C. et al. Single-nuclei transcriptomes from human adrenal gland reveal distinct cellular identities of low and high-risk neuroblastoma tumors. *Nat. Commun.* **12**, 5309 (2021).

74. Hanemaaijer, E. S. et al. Single-cell atlas of developing murine adrenal gland reveals relation of Schwann cell precursor signature to neuroblastoma phenotype. *Proc. Natl Acad. Sci. USA* **118**, e2022350118 (2021).

75. Kildisiute, G. et al. Tumor to normal single-cell mRNA comparisons reveal a pan-neuroblastoma cancer cell. *Sci. Adv.* **7**, eabd3311 (2021).

76. Kliman, H. J. et al. Pathway of maternal serotonin to the human embryo and fetus. *Endocrinology* **159**, 1609–1629 (2018).

77. Bonnin, A. & Levitt, P. Fetal, maternal, and placental sources of serotonin and new implications for developmental programming of the brain. *Neuroscience* **197**, 1–7 (2011).

78. Goeden, N. et al. Maternal inflammation disrupts fetal neurodevelopment via increased placental output of serotonin to the fetal brain. *J. Neurosci.* **36**, 6041–6049 (2016).

79. Williams, M. et al. Maternal inflammation results in altered tryptophan metabolism in rabbit placenta and fetal brain. *Dev. Neurosci.* **39**, 399–412 (2017).

80. Ranzil, S. et al. The relationship between the placental serotonin pathway and fetal growth restriction. *Biochimie* **161**, 80–87 (2019).

81. Koolhaas, J. M. et al. The resident-intruder paradigm: a standardized test for aggression, violence and social stress. *J. Vis. Exp.* e4367, https://doi.org/10.3791/4367 (2013).

82. de Boer, S. F., Buwalda, B. & Koolhaas, J. M. Untangling the neurobiology of coping styles in rodents: towards neural mechanisms underlying individual differences in disease susceptibility. *Neurosci. Biobehav. Rev.* **74**, 401–422 (2017).

83. Voronezhskaya, E. E., Khabarova, M. Y., Nezlin, L. P. & Ivashkin, E. G. Delayed action of serotonin in molluscan development. *Acta Biol. Hung.* **63**, 210–216 (2012).

84. Voronezhskaya, E. E. Maternal serotonin: shaping developmental patterns and behavioral strategy on progeny in molluscs. *Front. Ecol. Evol.* **9**, https://doi.org/10.3389/fevo.2021.739787 (2021).

85. Das, S. et al. Serotonin signaling by maternal neurons upon stress ensures progeny survival. *eLife* **9**, e55246 (2020).

86. Andreassen, H. P. et al. Population cycles and outbreaks of small rodents: ten essential questions we still need to solve. *Oecologia* **195**, 601–622 (2021).

87. Podgorny, O., Peunova, N., Park, J. H. & Enikolopov, G. Triple S-phase labeling of dividing stem cells. *Stem Cell Rep.* **10**, 615–626 (2018).

88. Stuart, T. et al. Comprehensive integration of single-cell data. *Cell* **177**, 1888–1902.e1821 (2019).

89. Picelli, S. et al. Full-length RNA-seq from single cells using Smart-seq2. *Nat. Protoc.* **9**, 171–181 (2014).

90. Becht, E. et al. Dimensionality reduction for visualizing single-cell data using UMAP. *Nat. Biotechnol.* **37**, 38–44 (2019).

91. Huang, Y. & Sanguinetti, G. BRIE: transcriptome-wide splicing quantification in single cells. *Genome Biol.* **18**, 123 (2017).

92. Huang, Y. & Sanguinetti, G. BRIE2: computational identification of splicing phenotypes from single-cell transcriptomic experiments. *Genome Biol.* **22**, 251 https://doi.org/10.1186/s13059-021-02461-5 (2021).

93. Hao, Y. et al. Integrated analysis of multimodal single-cell data. *Cell* **184**, 3573–3587.e3529 (2021).

94. Wolock, S. L., Lopez, R. & Klein, A. M. Scrublet: computational identification of cell doublets in single-cell transcriptomic data. *Cell Syst.* **8**, 281–291 e289 (2019).

95. Blasco-Serra, A., Gonzalez-Soler, E. M., Cervera-Ferri, A., Teruel-Marti, V. & Valverde-Navarro, A. A. A standardization of the novelty-suppressed feeding test protocol in rats. *Neurosci. Lett.* **658**, 73–78 (2017).

96. Bali, A. & Jaggi, A. Electric foot shock stress: a useful tool in neuropsychiatric studies. *Rev. Neurosci.* **26**, 655–677 (2015).

97. Wall, P. M. & Messier, C. Methodological and conceptual issues in the use of the elevated plus-maze as a psychological measurement instrument of animal anxiety-like behavior. *Neurosci. Behav. Rev.* **25**, 12 (2001).

98. Veselska, R. et al. Nestin expression in osteosarcomas and derivation of nestin/CD133 positive osteosarcoma cell lines. *BMC Cancer* **8**, 300 (2008).

99. Veselska, R. et al. Nestin expression in the cell lines derived from glioblastoma multiforme. *BMC Cancer* **6**, 32 (2006).

100. Dobrotkova, V. et al. Prediction of neuroblastoma cell response to treatment with natural or synthetic retinoids using selected protein biomarkers. *PLoS ONE* **14**, e0218269 (2019).

101. Hu, Y. & Smyth, G. K. ELDA: extreme limiting dilution analysis for comparing depleted and enriched populations in stem cell and other assays. *J. Immunol. Methods* **347**, 70–78 (2009).

Acknowledgements

Author contributions

Funding

Competing interests

The authors declare no competing interests.

Additional information

Supplementary information The online version contains supplementary material available at https://doi.org/10.1038/s41467-022-30438-w.

Correspondence and requests for materials should be addressed to Elena E. Voronezhskaya or Igor Adameyko.

Peer review information *Nature Communications* thanks Lukas Sommer and the other anonymous reviewers for their contribution to the peer review of this work. Peer reviewer reports are available.

Reprints and permission information is available at http://www.nature.com/reprints

Publisher's note Springer Nature remains neutral with regard to jurisdictional claims in published maps and institutional affiliations.

APPENDIX 5

Curylova L, Ramos H, Saraiva L, **Skoda J***. Noncanonical roles of p53 in cancer stemness and their implications in sarcomas. *Cancer Letters*. 2022;525:131-145. (JCR 2022, IF = 9.7; Q1 - Oncology)

APPENDIX 6

Krchniakova M, Paukovcekova S, Chlapek P, Neradil J, **Skoda J***, Veselska R. Thiosemicarbazones and selected tyrosine kinase inhibitors synergize in pediatric solid tumors: NDRG1 upregulation and impaired prosurvival signaling in neuroblastoma cells. *Frontiers in Pharmacology*. 2022;13:976955. (JCR 2022, IF = 5.6; Q1 - Pharmacology & Pharmacy)

Check for updates

Thiosemicarbazones and selected tyrosine kinase inhibitors synergize in pediatric solid tumors: NDRG1 upregulation and impaired prosurvival signaling in neuroblastoma cells

Maria Krchniakova[1,2], Silvia Paukovcekova[1], Petr Chlapek[1,2], Jakub Neradil[1,2], Jan Skoda[1,2]*† and Renata Veselska[1,2]*†

[1]Laboratory of Tumor Biology, Department of Experimental Biology, Faculty of Science, Masaryk University, Brno, Czechia, [2]International Clinical Research Center, St. Anne's University Hospital, Brno, Czechia

Tyrosine kinase inhibitors (TKIs) are frequently used in combined therapy to enhance treatment efficacy and overcome drug resistance. The present study analyzed the effects of three inhibitors, sunitinib, gefitinib, and lapatinib, combined with iron-chelating agents, di-2-pyridylketone-4,4-dimethyl-3-thiosemicarbazone (Dp44mT) or di-2-pyridylketone-4-cyclohexyl-4-methyl-3-thiosemicarbazone (DpC). Simultaneous administration of the drugs consistently resulted in synergistic and/or additive activities against the cell lines derived from the most frequent types of pediatric solid tumors. The results of a detailed analysis of cell signaling in the neuroblastoma cell lines revealed that TKIs inhibited the phosphorylation of the corresponding receptor tyrosine kinases, and thiosemicarbazones downregulated the expression of epidermal growth factor receptor, platelet-derived growth factor receptor, and insulin-like growth factor-1 receptor, leading to a strong induction of apoptosis. Marked upregulation of the metastasis suppressor N-myc downstream regulated gene-1 (NDRG1), which is known to be activated and upregulated by thiosemicarbazones in adult cancers, was also detected in

thiosemicarbazone-treated neuroblastoma cells. Importantly, these effects were more pronounced in the cells treated with drug combinations, especially with the combinations of lapatinib with thiosemicarbazones. Therefore, these results provide a rationale for novel strategies combining iron-chelating agents with TKIs in therapy of pediatric solid tumors.

1 Introduction

The overall 5-year survival rate of childhood cancer patients has considerably increased over the past decades, reaching approximately 85% (Miller et al., 2019). Despite improved outcomes, the development of therapy resistance remains a major obstacle for a wide variety of pediatric solid tumors, including neuroblastoma (Alisi et al., 2013), medulloblastoma (Othman et al., 2014), osteosarcoma (Brambilla et al., 2012), and rhabdomyosarcoma (Gallego et al., 2004). The management of pediatric cancers is aimed at eradicating the tumor and must also carefully consider organ toxicity and the development of chronic health conditions in young individuals (Oeffinger et al., 2007; Miller et al., 2019). Therefore, personalized medicine and drug combination strategies are being investigated to improve the efficacy of therapy while reducing short- and/ or long-term adverse effects in patients.

Tyrosine kinase inhibitors (TKIs) are a group of targeted therapeutics that attenuate the aberrant activity of tyrosine kinases in cancer; thus, TKIs are a promising approach in pediatric oncology (Yamaoka et al., 2018). We have previously identified receptor tyrosine kinases (RTKs) as druggable targets in relapsed or refractory childhood solid tumors (Mudry et al., 2017; Neradil et al., 2019). However, the use of TKIs as monotherapy is notoriously associated with the development of multidrug resistance (MDR) in patients (Jiao et al., 2018). Various mechanisms underlie MDR, including enhanced drug elimination by upregulated ABC transporters, which efflux the drugs out of the cells (Wu et al., 2011), or by lysosomal sequestration (Zhitomirsky and Assaraf, 2016). Particular physico-chemical properties of some drugs may be responsible for sequestration into the lysosomes where the drugs become charged and thus trapped, preventing the drugs from reaching their targets (Zhitomirsky and Assaraf, 2016). On the other hand, a combination of TKIs with standard chemotherapeutics has been shown to improve the clinical response, resulting in more efficient treatment of the tumors prevalent in adults (Krchniakova et al., 2020). Furthermore, new compounds with proven anticancer effects are emerging as the candidates to be tested in these combination therapies (Tong et al., 2017), and these new compounds include thiosemicarbazones (Paukovcekova et al., 2020).

Thiosemicarbazone iron chelators of the DpT class, including di-2-pyridylketone-4,4-dimethyl-3-thiosemicarbazone (Dp44mT) and its analog di-2-pyridylketone-4-cyclohexyl-4-methyl-3-thiosemicarbazone (DpC), have been shown to be effective and selective against a wide variety of tumors both *in vitro* and *in vivo* (Yu et al., 2009; Liu et al., 2012; Dixon et al., 2013; Potuckova et al., 2014; Jansson et al., 2015; Guo et al., 2016; Xu et al., 2018; Paukovcekova et al., 2020). In addition to chelation of iron and copper, which are critical for tumor cell proliferation (Lovejoy et al., 2011; Lane et al., 2015), these agents have been shown to potently induce the expression of the metastasis suppressor N-myc downstream regulated gene-1 (NDRG1) (Bae et al., 2013; Park et al., 2018) and to suppress the key oncogenic signaling pathways (Chen et al., 2012; Dixon et al., 2013; Liu et al., 2015; Kovacevic et al., 2016; Menezes et al., 2017, 2019b; Chekmarev et al., 2021; Geleta et al., 2021). Multiple reports have demonstrated that Dp44mT and DpC potentiate the effects of anticancer drugs both *in vitro* and *in vivo* (Lovejoy et al., 2012; Potuckova et al., 2014; Seebacher N. A. et al., 2016; Maqbool et al., 2020; Paukovcekova et al., 2020), and our previous study showed a promising synergy between thiosemicarbazones and celecoxib in pediatric cancer cells (Paukovcekova et al., 2020).

Both Dp44mT and DpC were suggested to accumulate in the lysosomes, where they form redox-active complexes with copper, which lead to the generation of reactive oxygen species (ROS) that permeabilize the lysosomal membrane and subsequently induce apoptosis (Yamagishi et al., 2013; Jansson et al., 2015). Hence, Dp44mT was shown to restore the sensitivity of carcinoma cells to doxorubicin that is otherwise trapped in the lysosomes (Jansson et al., 2015; Seebacher N. A. et al., 2016). Interestingly, lysosomal trapping was also shown to mediate resistance to several TKIs, including sunitinib (SUN), gefitinib (GEF), and lapatinib (LAP) (Gotink et al., 2011; Kazmi et al., 2013).

Based on these published findings, we decided to examine the potential anticancer interactions of Dp44mT and DpC with the three TKIs already in use in pediatric oncology: 1) GEF targeting epidermal growth factor receptor (EGFR) (Pollack et al., 2010), 2) LAP that targets EGFR and ErbB2 (Fouladi et al., 2013), and 3) a multikinase inhibitor SUN that primarily inhibits platelet-derived growth factor receptors (PDGFRs), vascular endothelial growth factor receptors (VEGFRs), c-Kit, or FLT3 (Mudry et al., 2017; Verschuur et al., 2019). The results of the

tests of multiple combination strategies in the cell lines derived from pediatric solid tumors performed in the present study demonstrated that Dp44mT and DpC significantly potentiated the activity of selected TKIs. The results of the present study also identified several targets that are synergistically affected by these drugs. These findings provide promising evidence for novel treatment strategies that combine TKIs with iron-chelating agents, such as Dp44mT or DpC, to treat pediatric solid tumors.

2 Materials and methods

2.1 Cell lines and cell culture

Five cancer cell lines derived from pediatric solid tumors were used in the present study. The neuroblastoma SH-SY5Y (ECACC 94030304), SK-N-BE(2) (ECACC 95011815), and rhabdomyosarcoma RD (ECACC 85111502) cell lines were purchased from the European Collection of Authenticated Cell Cultures (ECACC, Salisbury, United Kingdom). The medulloblastoma DAOY (ATCC HTB-186™) and osteosarcoma Saos-2 (ATCC HTB-85™) cell lines were obtained from the American Type Culture Collection (ATCC, Manassas, VA, United States). All cell lines were authenticated by STR profiling and routinely tested negative for mycoplasma contamination by PCR.

All reagents for cell culture were purchased from Biosera (Nuaille, France). DAOY and Saos-2 cells were cultured in Dulbecco's modified Eagle's medium (DMEM; low glucose, cat. no. LM-D1100) supplemented with 10% fetal calf serum (FCS; cat. no. FB-1101); RD cells were maintained in DMEM (high glucose, cat. no. LM-D1112) with 10% FCS, and SH-SY5Y and SK-N-BE(2) cells were cultured in a mixture of DMEM/F12 (1:1, cat no. LM-D1224) supplemented with 20% FCS. All media were further supplemented with 2 mM glutamine (cat. no. XC-T1715), penicillin (100 IU/ml), and streptomycin (100 μg/ml; cat. no. XC-A4122). The media used for DAOY, RD, SH-SY5Y, and SK-N-BE(2) cells also contained 1% nonessential amino acids (cat. no. XC-E1154). The cells were maintained under standard cell culture conditions at 37°C in a humidified atmosphere containing 5% CO_2 and were subcultured 1–2 times weekly.

2.2 Chemicals

The tyrosine kinase inhibitors SUN (cat. no. 12328), GEF (cat. no. 4765), and LAP (cat. no. 12121) were purchased from Cell Signaling Technology (Danvers, MA, United States). Thiosemicarbazones Dp44mT (cat. no. SML0186) and DpC (cat. no. SML0483) and Valspodar (VAL; cat. no. SML0572) were purchased from Sigma–Aldrich (St. Louis, MO, United States). All reagents were prepared as stock solutions in dimethyl sulfoxide (DMSO; purchased from Sigma–Aldrich)

at the concentrations of 10 mM (LAP), 75 mM (SUN) or 100 mM (GEF, Dp44mT, DpC, and VAL).

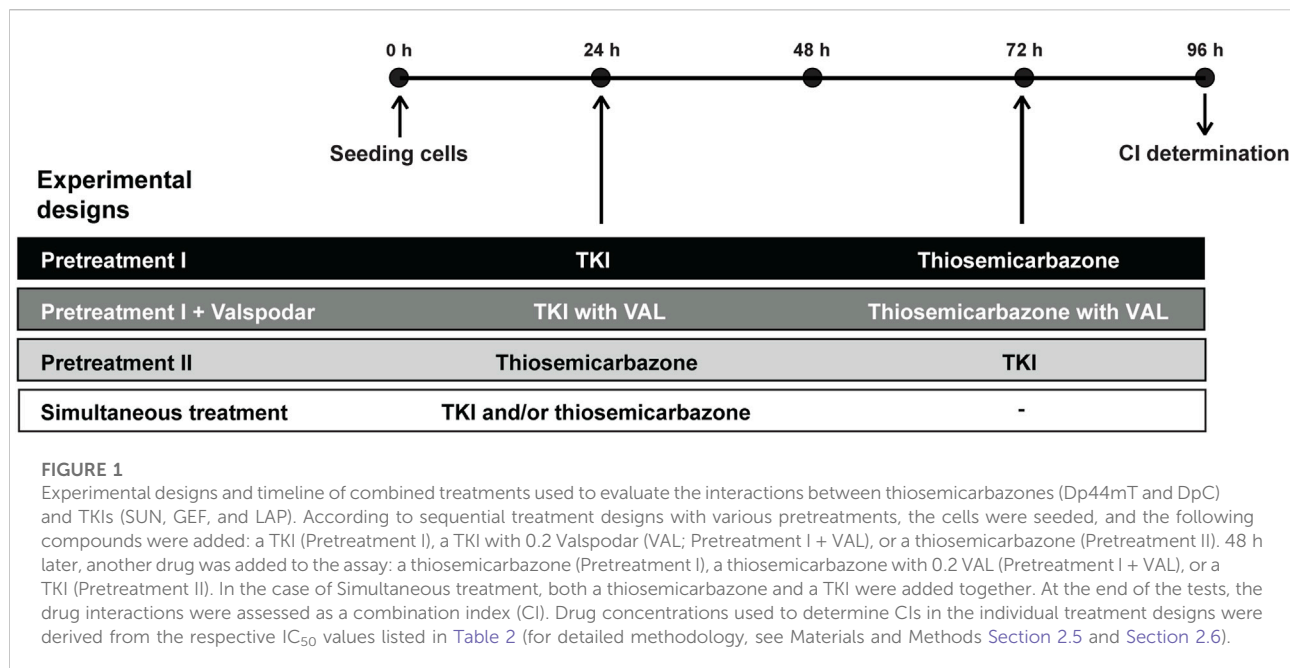## 2.3 Cell proliferation assays

Cell proliferation was evaluated after drug treatment using the 3-[4,5-dimethylthiazol-2-yl]-2,5-diphenyltetrazolium bromide (MTT) assays. The cells were seeded at variable densities to ensure that they remained in the log growth phase during the drug treatments. For 24-hour treatment, the cells were seeded in 96-well plates at a density of 2×10^4 cells/well (SH-SY5Y, SK-N-BE(2), Saos-2, and RD cells) or 5×10^3 cells/well (DAOY cells). For 72-hour treatment, the cells were seeded at a density of 5×10^3 cells/well (SH-SY5Y, SK-N-BE(2), Saos-2, and RD cells) or 8×10^2 cells/well (DAOY cells). After incubation with the drugs, the cells were incubated with MTT (0.5 mg/ml; cat. no. M2128, purchased from Sigma–Aldrich) for 3 h under standard cell culture conditions. Subsequently, the medium was removed, and formazan crystals were dissolved in 200 μl of DMSO. The absorbance was measured at 570 nm, and the reference absorbance was measured at 620 nm using a Sunrise absorbance reader (Tecan, Männedorf, Switzerland).

2.4 IC_{50} determination

The MTT assay was used to determine the IC_{50} values (concentration at which the cellular population was reduced by 50%) for each drug (SUN, GEF, LAP, Dp44mT, or DpC). 24 h after seeding, the medium was replaced with 200 μl of the fresh medium containing appropriate concentrations of the drugs alone. After incubation for 72 and/or 24 h under standard cell culture conditions, the cells were incubated with MTT and analyzed as described above. The IC_{50} value was assessed using CalcuSyn software (version 2.0, Biosoft, Cambridge, United Kingdom).

2.5 Combined treatment protocols

The MTT assay was used to quantify the synergy between thiosemicarbazones and TKIs. Based on the initially calculated IC_{50} values of each drug, the drug concentrations used in the combined treatment experiments corresponded to 1/8-, ¼-, ½-, 1-, 2-, 4-, and 8-fold of the IC_{50} using methodology as reported previously (Paukovcekova et al., 2020). The cells were seeded as described above. After 24 h, the medium was replaced, and the cells were incubated with the drugs alone or in combination under standard cell culture conditions. Different experimental designs were utilized to assess the effects of the

FIGURE 1
Experimental designs and timeline of combined treatments used to evaluate the interactions between thiosemicarbazones (Dp44mT and DpC) and TKIs (SUN, GEF, and LAP). According to sequential treatment designs with various pretreatments, the cells were seeded, and the following compounds were added: a TKI (Pretreatment I), a TKI with 0.2 Valspodar (VAL; Pretreatment I + VAL), or a thiosemicarbazone (Pretreatment II). 48 h later, another drug was added to the assay: a thiosemicarbazone (Pretreatment I), a thiosemicarbazone with 0.2 VAL (Pretreatment I + VAL), or a TKI (Pretreatment II). In the case of Simultaneous treatment, both a thiosemicarbazone and a TKI were added together. At the end of the tests, the drug interactions were assessed as a combination index (CI). Drug concentrations used to determine CIs in the individual treatment designs were derived from the respective IC$_{50}$ values listed in Table 2 (for detailed methodology, see Materials and Methods Section 2.5 and Section 2.6).

combinations of thiosemicarbazones Dp44mT and DpC with TKIs SUN, GEF, and LAP (Figure 1).

In the experiments with sequential administration of the drugs (Figure 1, Pretreatment designs), the cells were initially treated with an appropriate concentration of SUN, GEF, or LAP (Pretreatment I), SUN, GEF, or LAP with 0.2 μM VAL (Pretreatment I + VAL), or Dp44mT or DpC (Pretreatment II). After 48 h, 100 μl of the fresh medium was added, and the medium contained an appropriate concentration of Dp44mT or DpC (Pretreatment I), Dp44mT or DpC with 0.2 μM VAL (Pretreatment I + VAL), or SUN, GEF, or LAP (Pretreatment II). In the simultaneous treatment experiments (Figure 1, Simultaneous treatment), the cells were treated with an appropriate concentration of individual drugs or their combinations and incubated for another 72 h. After the drugs were incubated according to the corresponding experimental design, cell proliferation was analyzed by the MTT assays as described above.

To investigate the molecular effects of TKIs in combination with thiosemicarbazones, the cells were seeded in Petri dishes (90 mm in diameter) and allowed to adhere overnight. To reproduce the simultaneous treatment design (Figure 1), thiosemicarbazones and TKIs alone or in combination were added at the corresponding IC$_{50}$ concentrations. The cells were incubated under standard cell culture conditions in the presence or in the absence (control) of the indicated drugs for 72 h before being processed for immunoblotting.

2.6 Calculation of combination index

CalcuSyn software (version 2.0, Biosoft, Cambridge, United Kingdom) and the Chou Talalay method were used to calculate the combination index (CI) values as described previously (Paukovcekova et al., 2020). A 1:1 ratio of the drugs was used for combination treatments, and the CI values were calculated based on the growth inhibition curves. The dose-effect relationship for each drug alone was compared to the corresponding combination to identify the synergistic (CI < 0.9), additive (CI: 0.9–1.1), or antagonistic (CI > 1.1) interactions between thiosemicarbazones and TKIs (Chou, 2006).

2.7 Phospho-RTK arrays

The relative levels of phosphorylation of 49 RTKs (Supplementary Figure S1) were assayed using a Proteome Profiler™ human phospho-RTK array kit (cat. no. ARY001B) purchased from R&D Systems (Minneapolis, MN, United States). Treated and/or untreated control cells were lysed using lysis buffer 17 and processed according to the manufacturer's instructions. Each array was incubated with 300 μg of the whole-cell lysate. The relative levels of RTK phosphorylation were quantified using Fiji software (Schindelin et al., 2012), and analysis was performed as described previously (Neradil et al., 2019).

TABLE 1 Primary and secondary antibodies used in the experiments. All antibodies, except an anti-alpha tubulin antibody (Abcam, Cambridge, MA, United States), were purchased from Cell Signaling Technologies (Danvers, MA, United States). BSA, bovine serum albumin; HRP, horseradish peroxidase; Mo, mouse; Mono, monoclonal; NFDM, nonfat dry milk; Poly, polyclonal; Rb, rabbit.

Primary antibodies

Antigen	Type/Host	Clone	Cat. No.	Dilution	Blocking
AKT (pan)	Mono/Rb	C67E7	4691	1:1000	NFDM
Phospho-AKT (Ser473)	Mono/Rb	D9E	4060	1:1000	BSA
Alpha tubulin	Mono/Mo	DM1A	ab7291	1:10,000	NFDM
Cleaved Caspase 3 (Asp175)	Mono/Rb	5A1E	9664	1:1000	NFDM
EGFR	Mono/Rb	C74B9	2646	1:1000	NFDM
Phospho-EGFR (Tyr1068)	Mono/Mo	1H12	2236	1:1000	BSA
Phospho-EGFR (Tyr1148)	Poly/Rb	—	4404	1:1000	BSA
ERK1/2	Mono/Rb	137F5	4695	1:1000	NFDM
Phospho-ERK1/2 (Thr202/204)	Mono/Rb	D13.14.4E	4370	1:1000	BSA
GAPDH	Mono/Rb	14C10	2118	1:5000	NFDM
IGF-1Rβ	Mono/Rb	D23H3	9750	1:1000	NFDM
MEK1/2	Poly/Rb	—	9122	1:1000	NFDM
Phospho-MEK1/2 (Ser217/221)	Poly/Rb	—	9121	1:1000	BSA
NDRG1	Mono/Rb	D8G9	9485	1:1000	NFDM
Phospho-NDRG1 (Thr346)	Mono/Rb	D98G11	5482	1:1000	BSA
PDGFRβ	Mono/Rb	28E1	3168	1:1000	NFDM
Phospho-PDGFRβ (Tyr751)	Mono/Rb	C63G6	4549	1:1000	NFDM

Secondary Antibodies

Specificity	Host	Conjugate	Cat. No.	Dilution	Blocking
Anti-Mo IgG	Horse	HRP	7076	1:5000	NFDM
Anti-Rb IgG	Goat	HRP	7074	1:5000	NFDM

2.8 Western blotting and immunodetection

Whole-cell lysates of treated and untreated control cells were loaded on 10% polyacrylamide gels (10–20 μg/well), electrophoresed, and blotted on the polyvinylidene difluoride membranes (purchased from Bio–Rad Laboratories, Munich, Germany). Depending on the primary antibody, the membranes were blocked either with 5% nonfat dry milk or with bovine serum albumin (BSA; Sigma–Aldrich) in phosphate-buffered saline (PBS) containing 0.1% Tween-20 (Sigma–Aldrich) for 1 h at room temperature and then incubated at 4°C overnight with the corresponding primary antibodies listed in Table 1. Then, the membranes were incubated with the corresponding secondary antibodies (Table 1) for 1 h at room temperature. Chemiluminescence detection was performed using Amersham™ ECL™ Prime Western blotting detection reagent (purchased from GE Healthcare, Little Chalfont, United Kingdom) according to the manufacturer's instructions. Densitometry analyses were performed using Fiji software (Schindelin et al., 2012), and the densities of protein bands of interest were normalized to that of the loading control. Glyceraldehyde-3-phosphate dehydrogenase (GAPDH) and alpha tubulin were used as the loading controls. Biological replicates were normalized using the sum of all data points in a replicate as described by Degasperi et al. (2014).

2.9 Statistical analysis

Quantitative data are shown as the mean ± standard deviation (SD) of three independent experiments. The data of the MTT assays of the combination treatments and the results of densitometry were analyzed using one-way ANOVA followed by Dunnett's post-hoc test. All statistical analyses were performed using GraphPad Prism 8.0.2 software (GraphPad Software Inc., San Diego, CA, United States), and $p < 0.05$ was considered statistically significant.
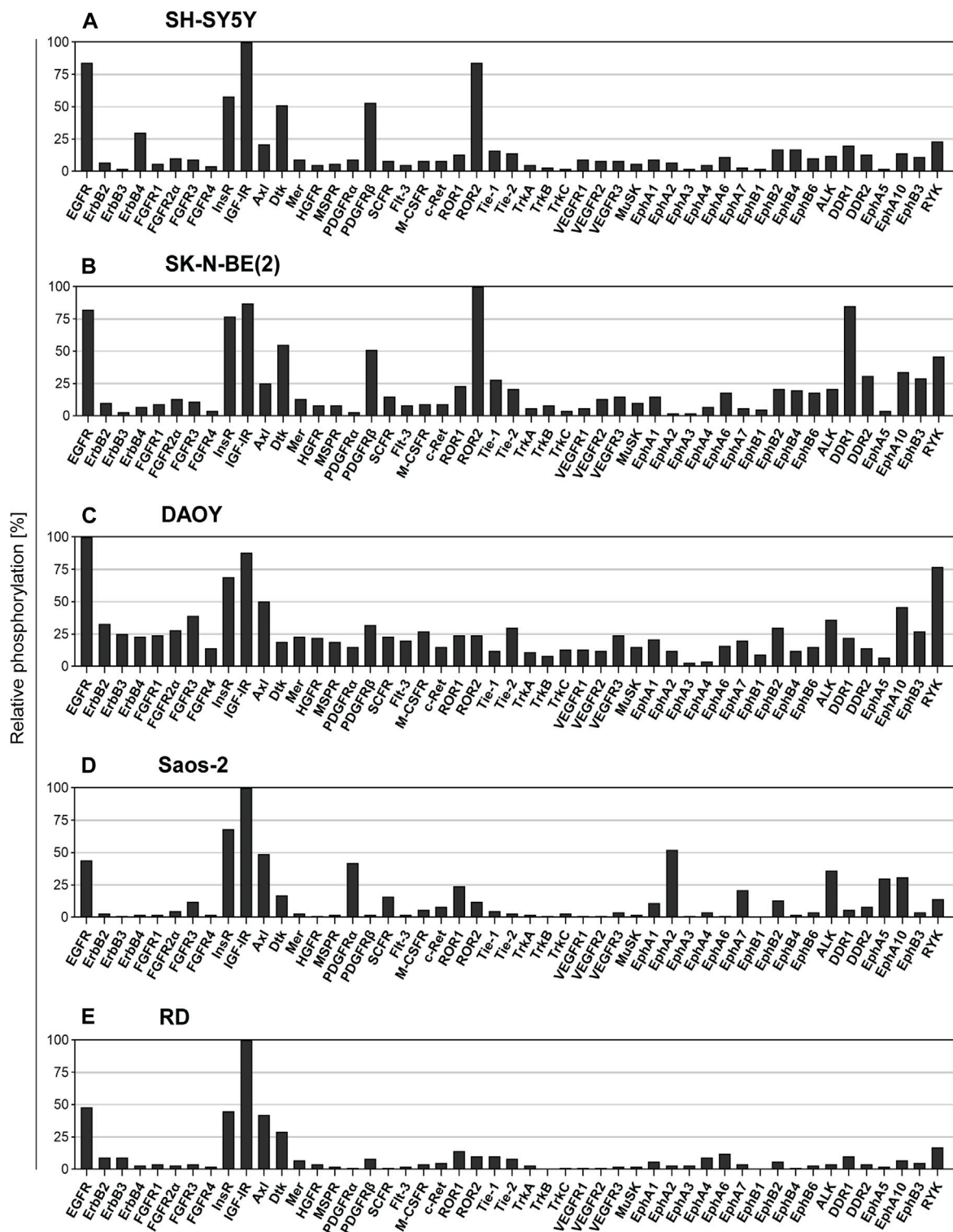
FIGURE 2
Screening of the levels of the RTK phosphorylation in untreated cell lines. The relative phosphorylation levels of 49 RTKs were assayed in the cell lines: **(A)** SH-SY5Y and **(B)** SK-N-BE (2) cells derived from neuroblastoma, **(C)** DAOY cells derived from medulloblastoma, **(D)** Saos-2 cells derived from osteosarcoma, and **(E)** RD cells derived from rhabdomyosarcoma. Columns represent the levels of relative phosphorylation of RTKs assessed as described in Materials and Methods. The corresponding array images are shown in Supplementary Figure S2.

TABLE 2 The IC_{50} values. The concentrations of the drugs corresponding to a reduction in cell proliferation by 50%. The IC_{50} values were determined for each cell line after incubation with TKIs (SUN, GEF, and LAP) and thiosemicarbazones (Dp44mT and DpC) alone for 72 and/or 24 h at 37°C. Bullets indicate drug concentrations used in different combined treatment designs in accordance with Figure 1 (black: Pretreatment I; dark grey: Pretreatment + Valspodar; light grey: Pretreatment II; white: Simultaneous treatment).

Drugs	Time (h)	IC_{50}				
		SH-SY5Y	SK-N-BE(2)	Daoy	Saos-2	RD
SUN	24 h	8.1 µM ●	9.8 µM ●	—	—	—
	72 h	4.5 µM ●●○	5.6 µM ●●○	3.7 µM ●●○	2.0 µM ●●○	2.4 µM ●●○
GEF	24 h	41.7 µM ●	86.7 µM ●	—	—	—
	72 h	15.8 µM ●●○	20.0 µM ●●○	14.0 µM ●●○	15.2 µM ●●○	15.5 µM ●●○
LAP	24 h	36.9 µM ●	27.2 µM ●	—	—	—
	72 h	9.7 µM ●●○	8.3 µM ●●○	10.0 µM ●●○	11.9 µM ●●○	8.7 µM ●●○
Dp44mT	24 h	28.6 µM ●●	47.6 µM ●●	0.6 µM ●●	101.8 µM ●●	105.7 µM ●●
	72 h	1.1 nM ●○	2.3 nM ●○	11.1 nM ○	15.3 nM ○	7.2 nM ○
DpC	24 h	10.7 µM ●●	31.0 µM ●●	1.6 µM ●●	30.8 µM ●●	24.9 µM ●●
	72 h	8.6 nM ●○	6.3 nM ●○	14.6 nM ○	21.5 nM ○	13.1 nM ○

Treatment designs in which the respective concentrations were used:

● Pretreatment I   ● Pretreatment II

● Pretreatment I + Valspodar   ○ Simultaneous treatment

3 Results

3.1 Active prosurvival RTK signaling and sensitivity to both thiosemicarbazones and TKIs is detected in pediatric solid tumor cells

The drugs investigated in the present study, including the TKIs SUN, GEF, and LAP and thiosemicarbazones Dp44mT and DpC, have been demonstrated to affect the critical oncogenic signaling pathways (Pollack et al., 2010; Chen et al., 2012; Dixon et al., 2013; Fouladi et al., 2013; Lui et al., 2015b; Kovacevic et al., 2016; Menezes et al., 2017; Mudry et al., 2017; Menezes et al., 2019a; Verschuur et al., 2019; Geleta et al., 2021). Therefore, we initially assayed the basal activity of 49 key RTKs in untreated cell lines derived from pediatric solid tumors, including the SH-SY5Y and SK-N-BE(2) neuroblastoma, Saos-2 osteosarcoma, RD rhabdomyosarcoma, and DAOY medulloblastoma cell lines (Figure 2; Supplementary Figure S2).

Overall, the results of screening using the human phosphoprotein arrays revealed high phosphorylation of multiple pro-oncogenic RTKs, several of which are known to be attenuated by the drugs used in the present study. The ErbB family of RTKs are known to be targeted by GEF, LAP, and both thiosemicarbazones (Pollack et al., 2010; Fouladi et al., 2013; Kovacevic et al., 2016; Menezes et al., 2017), and EGFR was consistently identified as one of the five most phosphorylated RTKs in all tested cell lines (Figure 2). In contrast, the activation of other ErbB family members was substantially lower (Figure 2). Regarding the targets of SUN (Mudry et al., 2017; Verschuur et al., 2019), we detected relatively active PDGFRα in Saos-2 cells (Figure 2D) and PDGFRβ in both SH-SY5Y and SK-N-BE(2) neuroblastoma cells (Figures 2A,B); however, the phosphorylation of other RTKs targeted by SUN, e.g., VEGFRs or FLT3, was minimal (Figure 2). Notably, IGF-1R signaling is modulated by thiosemicarbazones (Geleta et al., 2021). The levels of

FIGURE 3

Combined treatments using thiosemicarbazones (Dp44mT and DpC) and TKIs (SUN, GEF, and LAP) of the cells derived from pediatric solid tumors. Combined treatments were evaluated in following cell lines **(A)** SH-SY5Y, **(B)** SK-N-BE(2), **(C)** Saos-2, **(D)** RD, and **(E)** DAOY. The drug combinations were applied using **(i)** sequential (Pretreatment I, Pretreatment I + Valspodar (VAL), or Pretreatment II) or (ii) simultaneous experimental designs (see Materials and Methods). IC_{50} values that served to determine drug concentrations used in the respective combined treatment designs are listed in Table 2. The interactions between the corresponding drugs were evaluated as a combination index (CI) and were calculated based on the growth inhibition curves. A 1:1 ratio of the drugs and the Chou-Talalay method were used to identify the synergistic (green), nearly additive (yellow), or antagonistic activity (orange) using CalcuSyn Software. Columns represent the CI values $\pm$SD ($n = 3$). The data were analyzed using one-way ANOVA followed by Dunnett's post-hoc test. *$p < 0.05$, **$p < 0.01$ and ***$p < 0.0001$ indicate significant differences compared to the results obtained according to the Pretreatment I experimental design.

phosphorylation of IGF-1R, and insulin receptor (InsR) were very high in all cell types (Figure 2). These results indicated that the activation of prosurvival RTK signaling was shared among all pediatric tumor cell lines, further supporting the

rationale for the investigation of the interactions of selected RTK-targeting drugs in the present study.

Then, we determined the antiproliferative effect of thiosemicarbazones and selected TKIs used as single

treatment agents and calculated the concentrations of the drugs at which cell proliferation was reduced by 50% (IC_{50}). To determine the IC_{50} values needed for the subsequent combined treatment experiments, cell proliferation was evaluated after 24- and/or 72-hour incubation with individual drugs. In the case of TKI treatment, all tested cells were most sensitive to SUN and least sensitive to GEF after incubation for both 24 and 72 h (Table 2). Dp44mT and DpC administered for 24 h were most effective in DAOY medulloblastoma cells, whereas other cell lines showed ~6- to 170-fold lower sensitivity (Table 2). After 72 h of incubation, SH-SY5Y and SK-N-BE(2) neuroblastoma cells showed higher sensitivity to thiosemicarbazones than other cell types (Table 2). As expected, all examined drugs demonstrated higher efficacy (corresponding to lower IC_{50} values) after prolonged incubation. This phenomenon was particularly evident in the case of thiosemicarbazones; the corresponding IC_{50} values for these compounds shifted from a micromolar range after 24-hour treatments to a nanomolar range after 72-hour treatments (Table 2). Furthermore, after incubation for 72 h, both Dp44mT and DpC were significantly more effective than SUN, GEF, or LAP in all cell lines (Table 2).

Based on these data, we comprehensively evaluated the interactions between thiosemicarbazones and TKIs using several combined treatment designs (Figure 1): 1) sequential treatment protocols (Pretreatment I, Pretreatment I + VAL, and Pretreatment II) and 2) a simultaneous treatment protocol (Simultaneous treatment). The results of these experiments were recalculated as the CIs under various settings to assess the effects of the combinations of Dp44mT or DpC thiosemicarbazones with selected TKIs (Figure 3; Supplementary Table S1).

3.2 Variable effects of sequential treatments with thiosemicarbazones and TKIs on pediatric solid tumor cells

Based on the studies that have demonstrated that drug resistance to TKIs is mediated by lysosomal sequestration (Krchniakova et al., 2020) and on the ability of thiosemicarbazones to release the drugs, such as doxorubicin, sequestered into lysosomes (Jansson et al., 2015; Seebacher N. et al., 2016, Seebacher et al., 2016 N. A.), we hypothesized that the Pretreatment I strategy (Figure 1, Supplementary Table S1) may be a potent approach to enhance the anticancer effects of TKIs.

To test this hypothesis, the cells were initially treated with individual TKIs for 48 h and subsequently treated with Dp44mT or DpC for the next 24 h (Figure 1). However, the results of CI analyses revealed that this sequential treatment induced predominantly antagonistic drug interactions in all tested cell lines with the exception of DAOY medulloblastoma

cells (Figure 3). These results contradicted our initial hypothesis.

SH-SY5Y cells express P-glycoprotein (Pgp) (Dalzell et al., 2015), which is an extensively studied ABC transporter involved in drug resistance (Wu et al., 2011). In addition to the drug efflux activity of Pgp at the plasma membrane, Pgp at the lysosomal membranes has been implicated in trapping of TKIs (Krchniakova et al., 2020) and inducing the accumulation of thiosemicarbazones in the lysosomes (Jansson et al., 2015; Seebacher N. A. et al., 2016, Seebacher et al., 2016 N.). To determine whether Pgp activity plays a role in the effects of the tested drugs, the selective Pgp inhibitor VAL at a concentration of 0.2 μM (Jansson et al., 2015) was added to the assay (Pretreatment I + VAL design; Figure 1). The most pronounced differences between the VAL(−) and VAL(+) conditions were detected in case of LAP + Dp44mT or DpC combinations in Pgp-expressing SH-SY5Y cells, where moderate antagonistic interactions changed to synergy (Figure 3A). In other cell lines, no consistent trends in the changes in the CI values were detected in case of the VAL(−) and VAL(+) treatment strategies (Figure 3).

To further elaborate on these results, we compared effective concentrations of the tested drugs under VAL(−) and VAL(+) conditions in Pgp-expressing SH-SY5Y cells. Unlike SUN and GEF, which are able to inhibit Pgp (Kitazaki et al., 2005; Shukla et al., 2009), thiosemicarbazones are transported by Pgp (Jansson et al., 2015; Seebacher N. A. et al., 2016), and LAP has been described as both Pgp substrate and inhibitor (Dai et al., 2008; Radic-Sarikas et al., 2017). Despite reported differences in the interactions of these drugs with Pgp, no significant changes in the efficacy of the drugs were detected by comparison of VAL-treated and control SH-SY5Y cells (Supplementary Figure S3). However, Pgp is known to export a wide variety of xenobiotics, metabolites, and toxins (Aller et al., 2009), and blockade of these functions by VAL could have explained enhanced cytotoxic effects of combined treatments in SH-SY5Y cells with inhibited Pgp (Pretreatment I + VAL design; Figure 3A). The inhibition of Pgp has been shown to prevent the accumulation of Dp44mT or DpC in the lysosomes, leading to a significant reduction in the cytotoxicity of these drugs in carcinoma cells (Jansson et al., 2015); however, the results of the present study suggested that this Pgp-dependent mechanism of action was not present in pediatric tumor cells. The inhibition of Pgp did not reduce the sensitivity of the tested cells to combined treatments with thiosemicarbazones. In the case of Pgp-overexpressing SH-SY5Y cells, the blockade of the Pgp activity even potentiated the effects of the drug combinations (Figure 3). These findings in combination with the failure of thiosemicarbazones to improve the efficacy of TKIs in TKI-pretreated cells indicated that the anticancer activity of thiosemicarbazones in pediatric solid tumor cells is most likely not facilitated through a lysosomal burst.
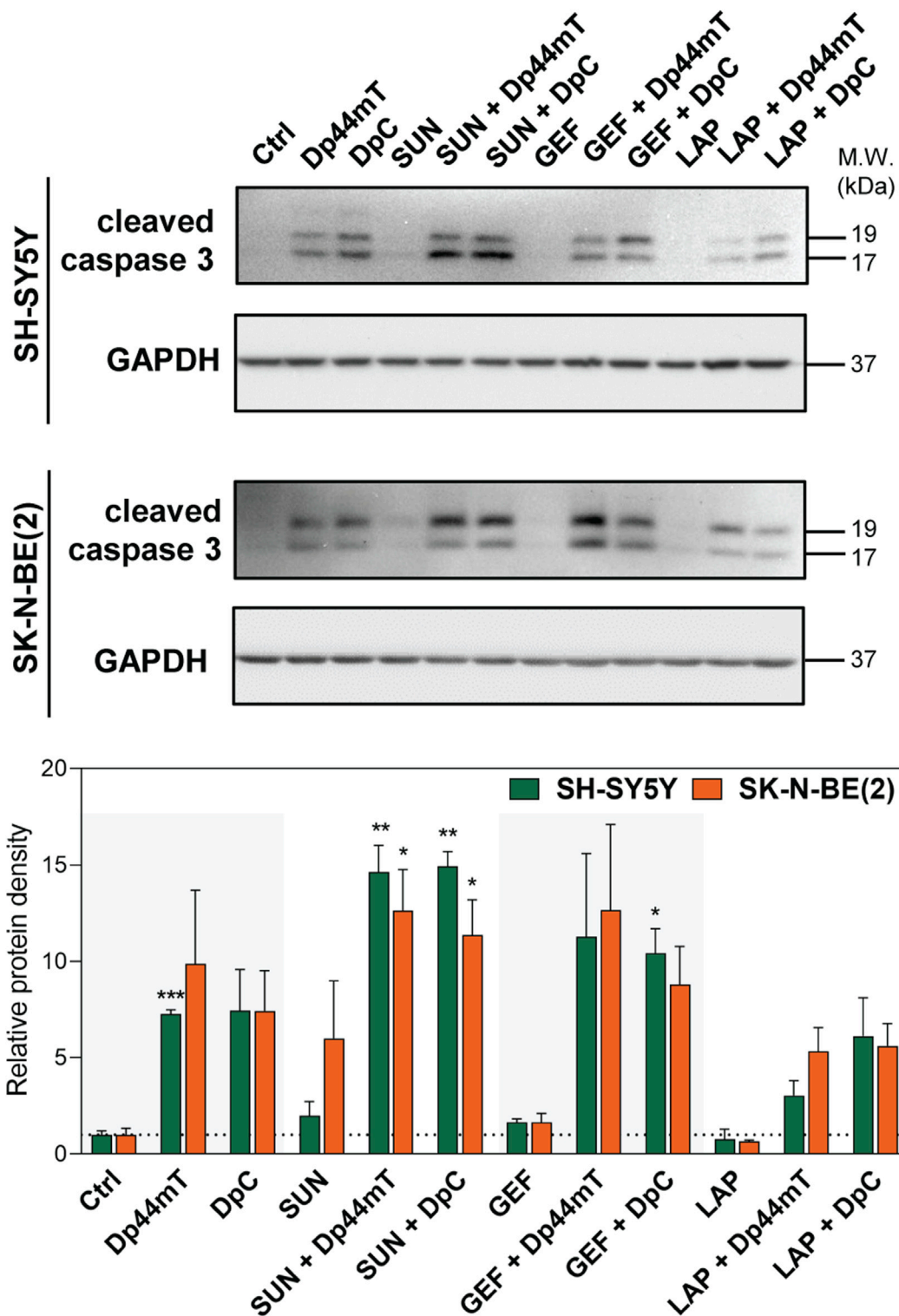
FIGURE 4
Western blotting of cleaved caspase-3, a marker of apoptosis, in SH-SY5Y and SK-N-BE(2) neuroblastoma cells. The changes in caspase-3 cleavage were detected after 72-hour incubation with either a control medium or a medium containing the drugs, including TKIs (SUN, GEF, or LAP) and thiosemicarbazones (Dp44mT or DpC) alone or in combination. The drugs were used at concentrations of IC_{50} for 72 h as listed in Table 2. Representative blots (left) and their densitometric quantification (right) of three independent experiments are shown. The data are presented as mean $\pm$ SD ($n = 3$) normalized to GAPDH that was used as the protein-loading control. *$p < 0.05$, **$p < 0.01$, ***$p < 0.001$ relative to the untreated control samples; the p values were evaluated using Welch's ANOVA followed by Dunnett's T3 multiple comparisons test. The dotted horizontal line in the graph represents the control levels of cleaved caspase-3.

Since the treatments with thiosemicarbazones following the TKI pretreatment (Pretreatment I design) did not result in synergistic interactions in most cell lines, we explored another sequential design, Pretreatment II (Figure 1; Supplementary Table S1). According to this strategy, the drugs were administrated sequentially in reverse order: the treatment with Dp44mT or DpC for 48 h was followed by the addition of a TKI for the next 24 h (Figure 1). Considering that the drugs used in the present study interact with Pgp (Seebacher N. A. et al., 2016; Krchniakova et al., 2020), the neuroblastoma cell lines with different levels of Pgp expression, including SH-SY5Y (high Pgp expression) and SK-N-BE(2) cells (low Pgp expression) (Bates et al., 1989; Dalzell et al., 2015), were selected for these analyses.

Interestingly, in SK-N-BE(2) cells, the treatment according to the Pretreatment II design induced a significant decrease in the CI values compared to Pretreatment I, resulting in the uniform synergistic interactions between the tested drug combinations (Figure 3B). Additive/synergistic effects were also observed in SH-SY5Y cells when SUN or GEF was combined with Dp44mT or DpC (Figure 3A). These results suggested that thiosemicarbazones apparently sensitized pediatric solid tumor cells to TKIs. However, the combinations of LAP and thiosemicarbazones remained antagonistic in SH-SY5Y cells (Figure 3A), further emphasizing the role of Pgp in drug resistance.

Overall, sequential treatment protocols induced variable and generally unsatisfactory interactions between thiosemicarbazones and TKIs across the pediatric cancer cell lines, thus excluding the therapeutic potential of this approach.

3.3 Simultaneous administration of thiosemicarbazones and TKIs induces evident synergistic effects in pediatric solid tumor cells and apoptosis in neuroblastoma cells

Our previous report demonstrated that Dp44mT and DpC added simultaneously with celecoxib produce synergistic effects on pediatric cancer cells (Paukovcekova et al., 2020). Therefore, we implemented a similar strategy to examine the interactions between thiosemicarbazones and TKIs in all tested cell lines. According to this Simultaneous treatment design, the drugs were added to the assay at the same time, and the cells were incubated for 72 h (Figure 1, Supplementary Table S1).

imultaneous treatment was the most effective combination strategy in all cell lines tested in the present study. The effects of thiosemicarbazones and TKIs on DAOY cells were uniformly synergistic, with minimal differences versus the effects observed in the experiments performed according to the Pretreatment I design protocol (Figure 3E). Importantly, a significant difference between the two strategies was observed in SH-SY5Y (Figure 3A), SK-N-BE(2)

(Figure 3B), and Saos-2 cells (Figure 3C), resulting in the uniformly synergistic and/or additive interactions in these cells in the experiments performed according to the Simultaneous treatment protocol. Furthermore, the synergy was achieved even after combining Dp44mT or DpC with LAP in SH-SY5Y cells; this drug combination produced antagonistic effects in the experiments performed according to the sequential treatment protocols (Figure 3A). The effects on RD cells were not as uniform as the effects on other cell lines; however, this Simultaneous approach produced a decrease in the CI values in most combinations (Figure 3D).

Since this treatment design was proven to represent the most effective approach, we further analyzed whether the synergistic interactions of the drugs are reflected by an increase in the induction of apoptosis. Due to higher sensitivity to the drugs and a substantial response to combined treatments, SH-SY5Y and SK-N-BE(2) neuroblastoma cells were selected as a model and were treated with thiosemicarbazones and TKIs alone or in combination using the concentrations corresponding to the IC_{50} values. We detected a prominent increase in caspase-3 cleavage in the cells treated with Dp44mT and DpC alone and in combination with TKIs, notably SUN or GEF (Figure 4).

Overall, the results of the experiments performed according to the Simultaneous combined treatment protocol indicated synergistic inhibition of the proliferation of pediatric cancer cells (Figure 3), and induction of apoptosis in tested neuroblastoma cells (Figure 4). Therefore, this treatment design and SH-SY5Y and SK-N-BE(2) neuroblastoma cell lines were selected to further examine the molecular mechanisms of the interactions between thiosemicarbazones and selected TKIs.

3.4 DpC downregulates the phosphorylation of the key RTKs in SK-N-BE(2) cells

Since thiosemicarbazones have been shown to affect various RTKs and the downstream signaling pathways in the cells derived from carcinomas (Dixon et al., 2013; Kovacevic et al., 2013; Lui et al., 2015a; Liu et al., 2015; Kovacevic et al., 2016; Park et al., 2020a; Lim et al., 2020), and in neuroblastoma cells (Guo et al., 2016; Paukovcekova et al., 2020; Macsek et al., 2022), we treated SK-N-BE(2) cells with DpC to identify the potential RTK targets. Human phosphoprotein arrays were used to determine the changes in the phosphorylation of RTKs in SK-N-BE(2) cells after 24-, 48-, and 72-hour incubation with DpC (Figure 5; Supplementary Figure S4).

Thiosemicarbazones have been reported to downregulate EGFR expression and phosphorylation in pancreatic and colon cancer cells (Kovacevic et al., 2016); however, we did not detect any alterations in EGFR activity after treatment with DpC. In contrast, the phosphorylation of IGF-1R and
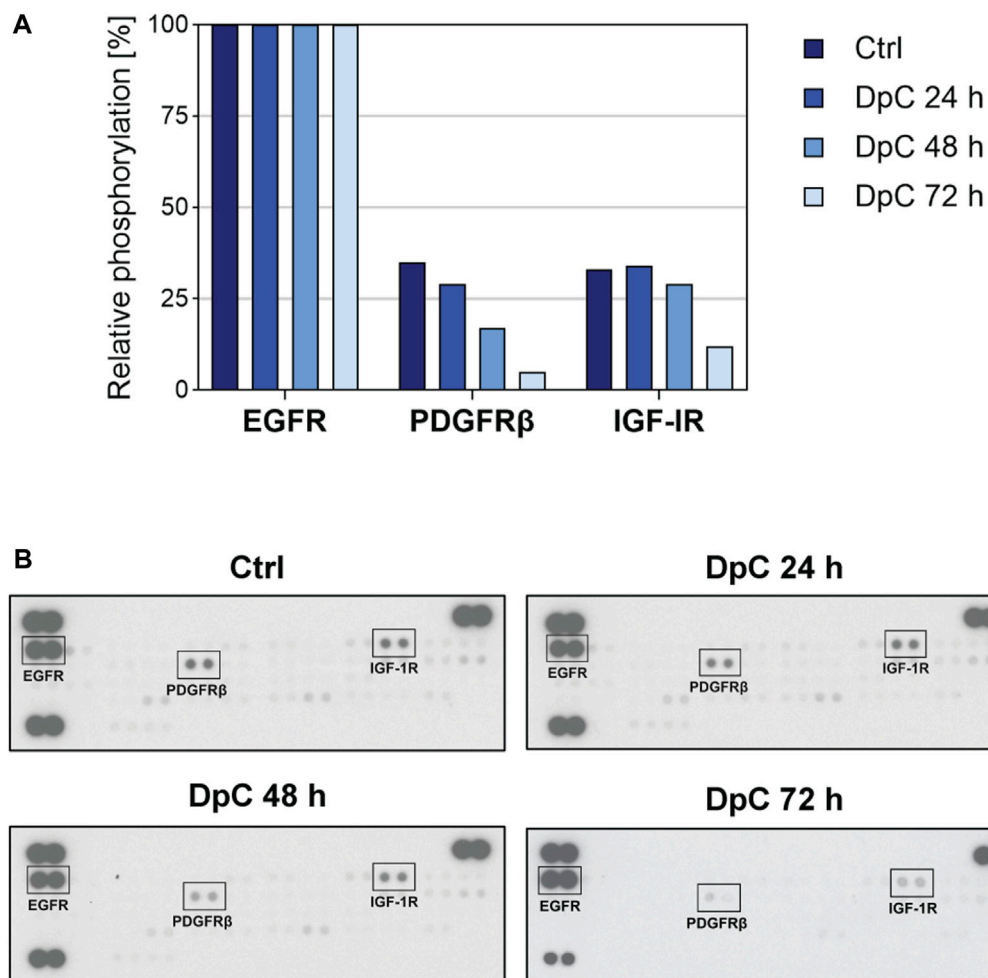
FIGURE 5

Phospho-RTK array screening in the SK-N-BE(2) neuroblastoma cell line after treatment with DpC. The cells were incubated with a control medium or a medium containing 6.3 nM DpC (the IC_{50} value obtained after 72 h) for 24, 48, and 72 h. **(A)** Evaluation of the relative phosphorylation of selected RTKs (EGFR, PDGFRβ, and IGF-1R). Columns represent the relative phosphorylation of RTKs assessed as described in Materials and Methods. **(B)** The images of the corresponding phospho-RTK arrays of untreated and treated cells were captured on an X-ray film at a constant exposure. Selected RTKs are marked by black rectangles. EGFR, epidermal growth factor receptor; IGF-1R, insulin-like growth factor-1 receptor; PDGFRβ, platelet-derived growth factor receptor β.

PDGFRβ, which were activated in untreated cells, was markedly decreased during the treatment, and was almost completely abrogated after 72-hour incubation with DpC (Figure 5). The relative phosphorylation levels of other tested RTKs of the panel are shown in Supplementary Figure S4.

Considering the data of the phosphoprotein array screening and previous studies, which have described the modulation of cell signaling by thiosemicarbazones (Dixon et al., 2013; Kovacevic et al., 2016; Paukovcekova et al., 2020; Geleta et al., 2021; Macsek et al., 2022), we further focused on the signaling pathways that could have been affected by both thiosemicarbazones and TKIs selected for the present study.

3.5 Combinations of thiosemicarbazones with TKIs reduce phosphorylation and downregulate the key RTKs in neuroblastoma cells

The next part of the present study examined the combined effects of thiosemicarbazones and TKIs on selected RTKs that were shown to be activated in both SH-SY5Y and SK-N-BE(2) cells. These effects included EGFR expression, major sites of EGFR phosphorylation (Tyr1068 and Tyr1148) relevant to EGFR activation, expression of PDGFRβ, Tyr751 phosphorylation of PDGFRβ needed for PI3K activation, and IGF-1R expression.

As expected, TKIs inhibited the phosphorylation of the corresponding RTKs in both neuroblastoma cell lines;
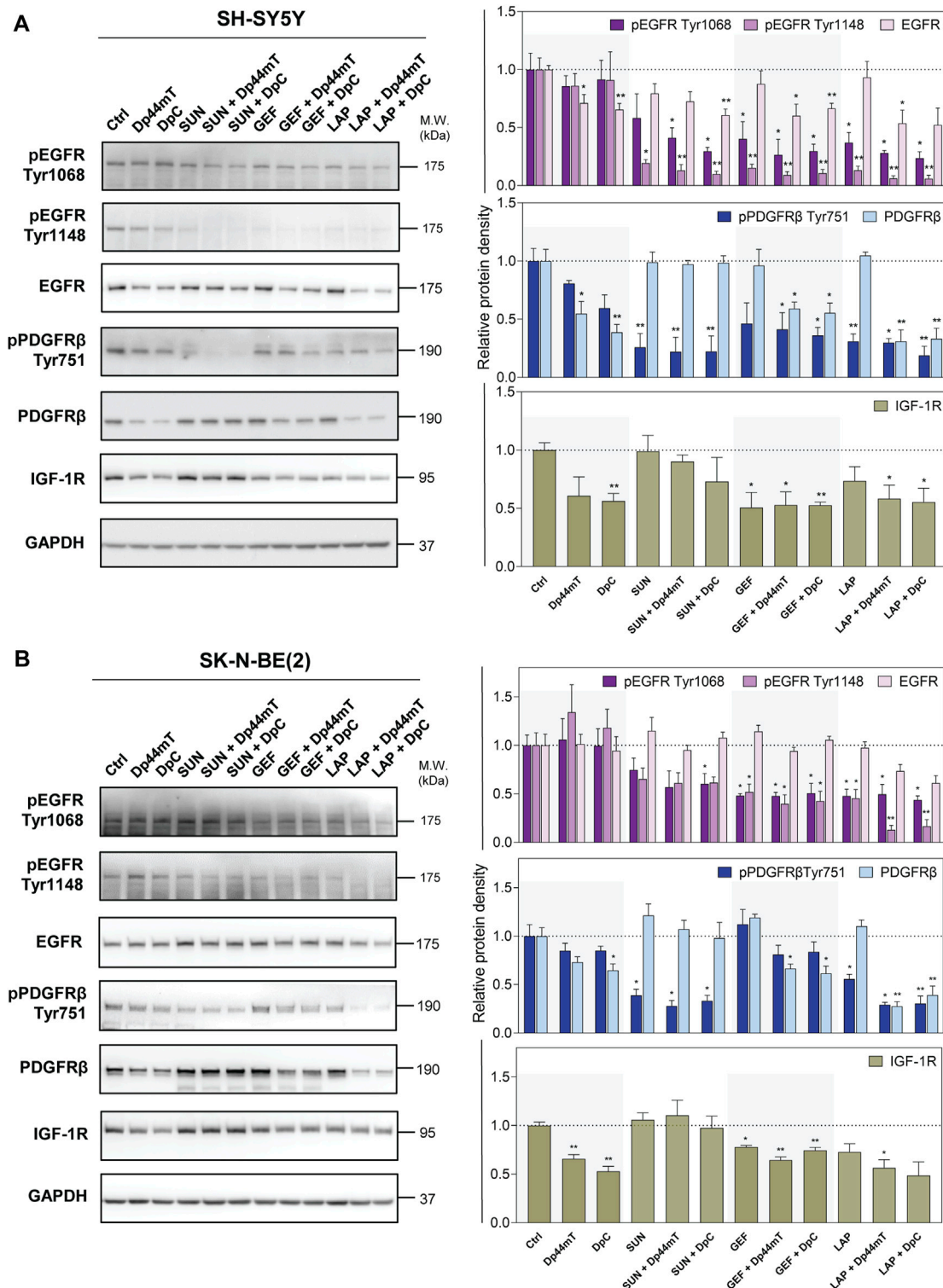
FIGURE 6
Western blotting of the levels of total and phosphorylated selected RTK proteins, including epidermal growth factor receptor (EGFR), platelet-derived growth factor receptor-β (PDGFRβ), and insulin-like growth factor receptor (IGF-1R). The changes in the levels of phosphorylated EGFR (Tyr1068 and Tyr1148) and PDGFRβ (Tyr751) and of total EGFR, PDGFRβ, and IGF-1R proteins were detected in SH-SY5Y **(A)** and SK-N-BE(2) **(B)** cells after a 72-hour incubation with either a control medium or a medium containing the drugs, including TKIs (SUN, GEF, or LAP) and thiosemicarbazones (Dp44mT or DpC) alone or in combination. The drugs were used at concentrations of IC$_{50}$ for 72 h as listed in Table 2.

(Continued)

FIGURE 6
Representative blots (left) and their densitometric quantification (right) of three independent experiments are shown. The data are presented as mean $\pm$ SD (n = 3) normalized to GAPDH that was used as the protein-loading control. *$p < 0.05$, **$p < 0.01$, ***$p < 0.001$ relative to the untreated control samples; the p values were evaluated using Welch's ANOVA followed by Dunnett's T3 multiple comparisons test. The dotted horizontal line in the graph represents the corresponding protein levels detected in the control cells.

however, we also detected significant off-target inhibitory activity in the case of other tested RTKs (Figure 6). In SH-SY5Y cells, SUN reduced EGFR activation at Tyr1148, and GEF and LAP alone targeted pPDGFRβ (Figure 6A). In SK-N-BE(2) cells, these effects were observed only after LAP treatment (Figure 6B). TKIs did not significantly alter the total EGFR or PDGFRβ levels; however, LAP and especially GEF downregulated IGF-1R in both cell lines (Figure 6).

In agreement with the data of phosphoprotein array analysis, EGFR phosphorylation was not significantly affected in DpC-treated SK-N-BE(2) cells (Figure 6B). The studies of other authors shown EGFR inhibition and/or downregulation by thiosemicarbazones (Liu et al., 2015; Kovacevic et al., 2016; Menezes et al., 2017; Macsek et al., 2022); however, the results of the present study demonstrated a Dp44mT- and DpC-induced decrease in total EGFR only in SH-SY5Y cells (Figure 6A). In contrast, Dp44mT and DpC consistently downregulated PDGFRβ and IGF-1R in both neuroblastoma cell lines (Figure 6).

In cells treated with the drug combinations, pEGFR (Tyr1068 and Tyr1148) was uniformly decreased in both cell lines, and this decrease was detected even in cells treated with the SUN + Dp44mT/DpC combinations (Figure 6). The combination of thiosemicarbazones and TKIs significantly downregulated EGFR expression in SH-SY5Y cells (Figure 6A); however, only a partial EGFR reduction was detected in LAP + Dp44mT/DpC-treated SK-N-BE(2) cells (Figure 6B).

Similarly, inhibition of pPDGFRβ (Tyr751) was detected across all drug combinations in both neuroblastoma cell lines (Figure 6) but was not detected in SK-N-BE(2) cells treated with GEF and thiosemicarbazones (Figure 6B). The levels of the PDGFRβ protein in the cells incubated with the combinations containing SUN remained comparable to the levels in the control cells, whereas the combination of GEF or LAP with thiosemicarbazones resulted in PDGFRβ downregulation in both cell lines (Figure 6). Furthermore, IGF-1R expression was significantly decreased in the cells treated with the latter combinations (Figure 6).

These data showed that the phosphorylation and/or expression of the key pro-oncogenic RTKs was activated in SH-SY5Y and SK-N-BE(2) neuroblastoma cells; specifically EGFR, PDGFRβ, and IGF-1R were inhibited by both thiosemicarbazones and TKIs. Importantly, these effects were more pronounced in the cells treated with the drug combinations, especially after simultaneous incubation with

LAP and Dp44mT/DpC, suggesting that the observed synergistic effects were at least to some extent mediated by the blockade of the activity of these crucial RTKs.

3.6 Thiosemicarbazones combined with TKIs modulate the signaling of the downstream kinases in neuroblastoma cells

Therefore, in the next step, we aimed to determine whether these changes impair the downstream signaling pathways. Since thiosemicarbazones alone have been shown to target PI3K/AKT and MAPK signaling in carcinoma cells (Dixon et al., 2013; Kovacevic et al., 2013, 2016; Lui et al., 2015a; Menezes et al., 2017; Macsek et al., 2022), we assessed the expression and phosphorylation of AKT (Ser473), ERK1/2 (Thr202/204), and MEK1/2 (Ser201/221) after combined treatments of neuroblastoma cells (Figure 7).

Unexpected activation of these downstream kinases was detected after the treatment of SH-SY5Y cells with thiosemicarbazones (Figure 7A). Similar activation of pAKT and pERK1/2 was observed in these cells after treatment with the combinations of thiosemicarbazones with GEF or LAP (Figure 7A). Thiosemicarbazones alone did not influence AKT activation in SK-N-BE(2) cells; however, an increase in pAKT was detected when thiosemicarbazones were combined with GEF or LAP (Figure 7B). Although activation of these kinases was unexpected, other authors have shown similar effects of Dp44mT in prostate cancer cells (Dixon et al., 2013), and we have previously demonstrated the activation of AKT and induction of a stress response in DpC-treated SH-SY5Y cells (Macsek et al., 2022).

In contrast, thiosemicarbazones alone inhibited pERK1/2 and pMEK1/2 in SK-N-BE(2) cells (Figure 7B). Furthermore, a decrease in pMEK1/2 was prominent after treatment of SK-N-BE(2) cells with all drug combinations (Figure 7B). In SH-SY5Y cells, this decrease was detected only after treatment with a combination of LAP and Dp44mT or DpC (Figure 7A).

In summary, combined treatments did not uniformly impair the kinases downstream of analyzed RTKs in the tested neuroblastoma cell lines. In fact, the activation of these kinases may be attributed to other upstream receptors, which
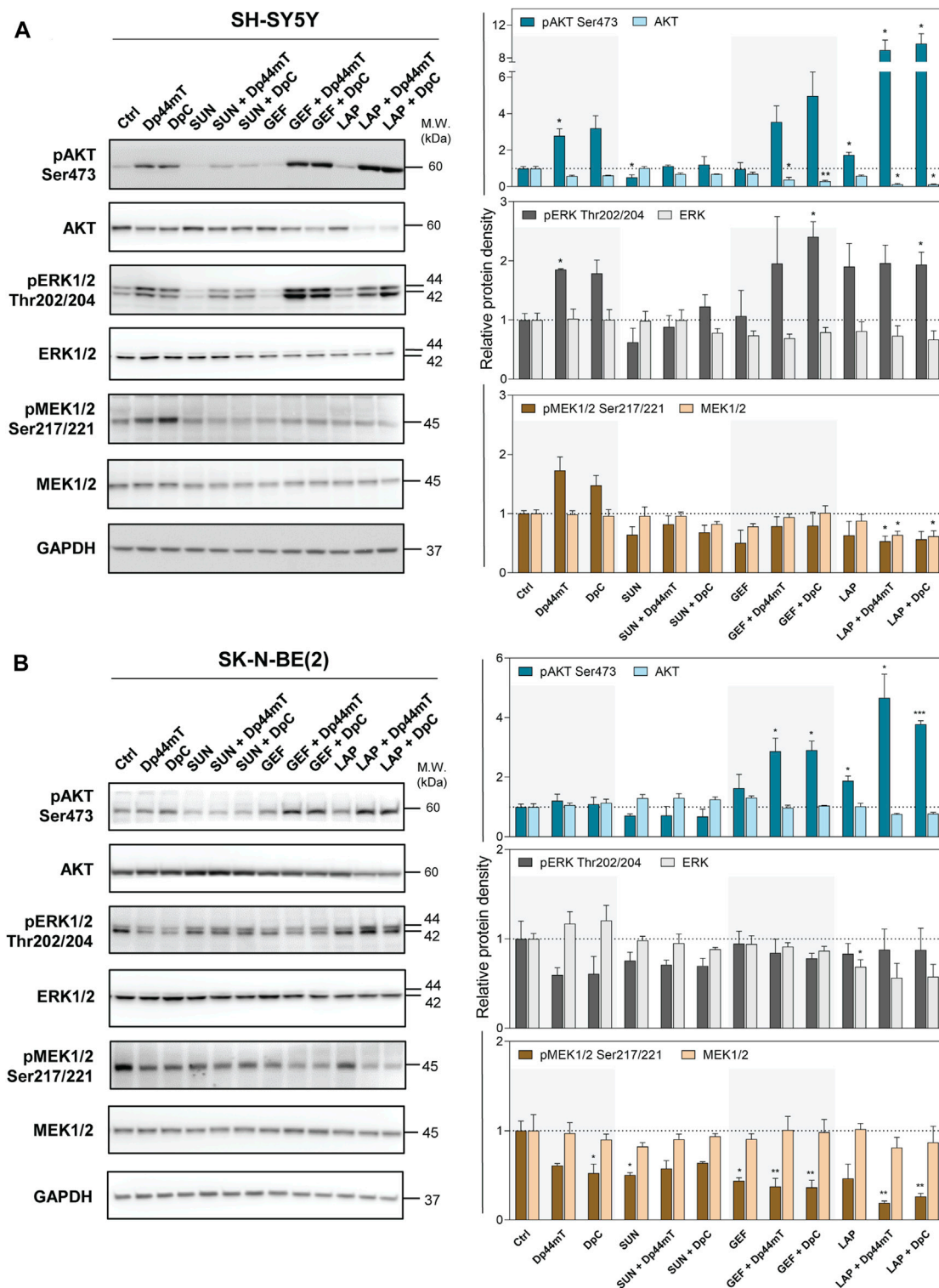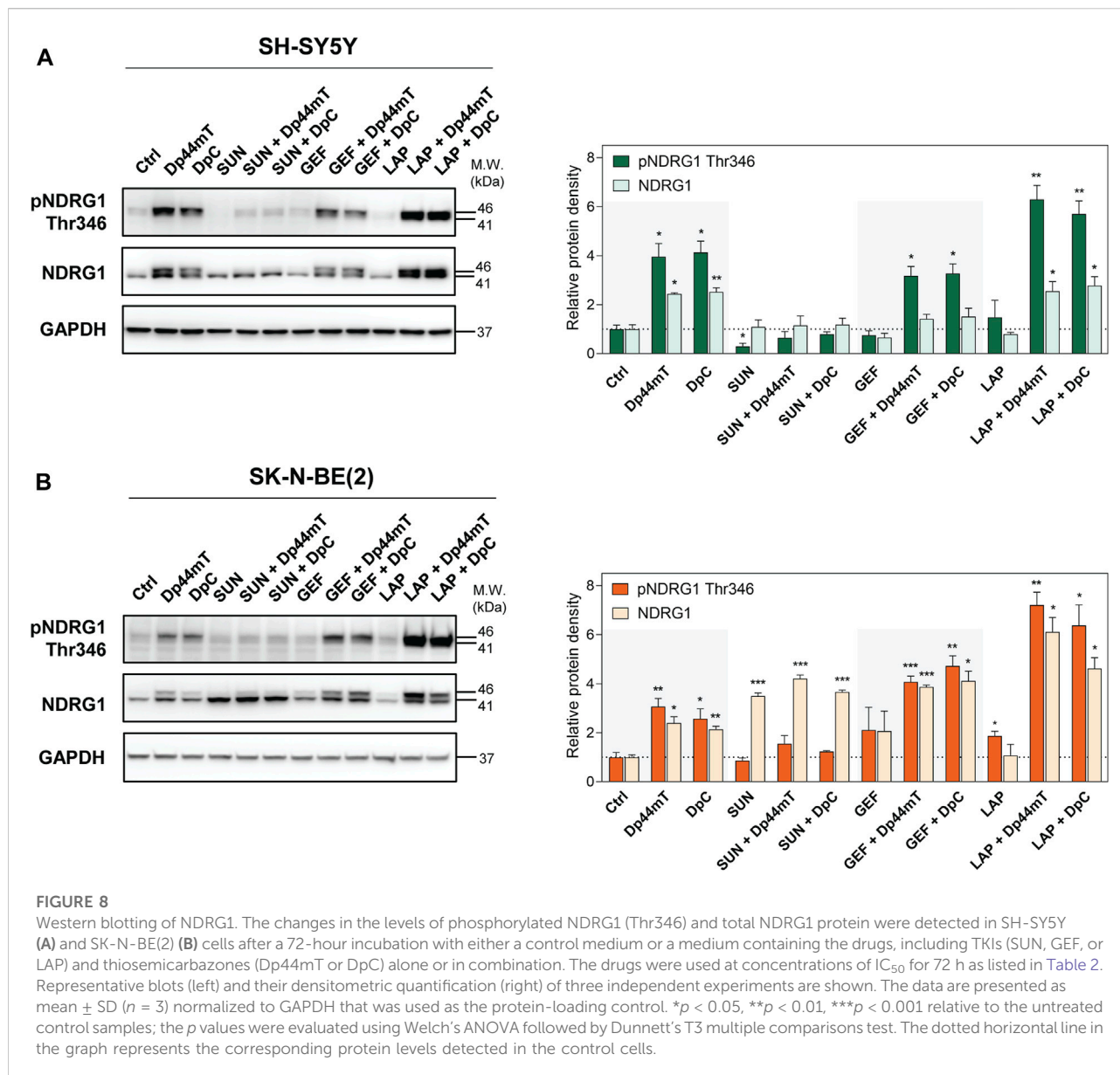
FIGURE 7

Western blotting of AKT, ERK1/2, and MEK1/2 protein kinases. The changes in the total protein levels and phosphorylation of AKT (Ser473), ERK1/2 (Thr202/204), and MEK1/2 (Ser 217/221) were detected in SH-SY5Y **(A)** and SK-N-BE(2) **(B)** cells after a 72-hour incubation with either a control medium or a medium containing the drugs, including TKIs (SUN, GEF, or LAP) and thiosemicarbazones (Dp44mT or DpC) alone or in combination. The drugs were used at concentrations of IC_{50} for 72 h as listed in Table 2. Representative blots (left) and their densitometric quantification (right) of three independent experiments are shown. The data are presented as mean $\pm$ SD ($n = 3$) normalized to GAPDH that was used as the protein-loading control. $*p < 0.05$, $**p < 0.01$, $***p < 0.001$ relative to the untreated control samples; the p values were evaluated using Welch's ANOVA followed by Dunnett's T3 multiple comparisons test. The dotted horizontal line in the graph represents the corresponding protein levels detected in the control cells.

FIGURE 8
Western blotting of NDRG1. The changes in the levels of phosphorylated NDRG1 (Thr346) and total NDRG1 protein were detected in SH-SY5Y
(A) and SK-N-BE(2) **(B)** cells after a 72-hour incubation with either a control medium or a medium containing the drugs, including TKIs (SUN, GEF, or
LAP) and thiosemicarbazones (Dp44mT or DpC) alone or in combination. The drugs were used at concentrations of IC_{50} for 72 h as listed in Table 2.
Representative blots (left) and their densitometric quantification (right) of three independent experiments are shown. The data are presented as
mean $\pm$ SD ($n = 3$) normalized to GAPDH that was used as the protein-loading control. *$p < 0.05$, **$p < 0.01$, ***$p < 0.001$ relative to the untreated
control samples; the p values were evaluated using Welch's ANOVA followed by Dunnett's T3 multiple comparisons test. The dotted horizontal line in
the graph represents the corresponding protein levels detected in the control cells.

were unaffected by the treatments and/or were triggered by a stress response of the cells.

3.7 NDRG1 is prominently activated and upregulated after treatment with the combinations of thiosemicarbazones with GEF and LAP in neuroblastoma cells

NDRG1 has been described as a potent metastasis suppressor in a number of tumors, e.g., colon, prostate, and breast cancers (Bae et al., 2013; Park et al., 2020b). NDRG1 is often upregulated

after stress-inducing stimuli (Bae et al., 2013), including cellular iron depletion (Chen et al., 2012; Lane et al., 2013; Lui et al., 2015a; Kovacevic et al., 2016). In fact, NDRG1 has been identified as a target of both Dp44mT and DpC in adult and pediatric tumors (Kovacevic et al., 2016; Menezes et al., 2017; Paukovcekova et al., 2020; Macsek et al., 2022) and implicated in the downregulation of the molecules involved in signal transduction, such as the ErbB family of RTKs and several downstream kinases (Liu et al., 2012; Dixon et al., 2013; Kovacevic et al., 2016; Menezes et al., 2017; Macsek et al., 2022). Our previous studies have shown a prominent upregulation of NDRG1 in the Dp44mT- and DpC-treated

cancer cell lines derived from pediatric solid tumors, including neuroblastomas (Paukovcekova et al., 2020; Macsek et al., 2022); thus, we evaluated the NDRG1 levels after combined treatments of SH-SY5Y and SK-N-BE(2) cells (Figure 8). NDRG1 was detected as two closely migrating bands at 41 and 46 kDa, as reported previously (Park et al., 2018, 2020b; Paukovcekova et al., 2020; Macsek et al., 2022).

Similar to other cell lines, Dp44mT and DpC markedly elevated NDRG1 phosphorylation and expression in both SH-SY5Y and SK-N-BE(2) neuroblastoma cells (Figure 8). SUN treatment induced pNDRG1 inhibition in SH-SY5Y cells (Figure 8A); however, it considerably increased total NDRG1 expression in SK-N-BE(2) cells. Moreover, only the lower band at 41 kDa was preferentially upregulated (Figure 8B). In contrast, LAP treatment tended to increase pNDRG1 (Figure 8), although this change was significant only in SK-N-BE(2) cells (Figure 8B).

In both cell lines, the combinations of thiosemicarbazones with SUN reduced NDRG1 phosphorylation compared with Dp44mT- and DpC-treated controls (Figure 8). However, these combined treatments induced the upregulation of total NDRG1 in SK-N-BE(2) cells, and the effect was specifically directed at the 41 kDa band (Figure 8B). In contrast, the combinations of thiosemicarbazones with LAP or GEF markedly elevated pNDRG1 in both cell lines or in SK-N-BE(2) cells, respectively (Figure 8). In SK-N-BE(2) cells, the synergy between thiosemicarbazones and both LAP and GEF was manifested as an apparent upregulation of total NDRG1 expression compared with the effects of these agents alone (Figure 8B).

These data demonstrated that the combinations of thiosemicarbazones, particularly with GEF or LAP, enhanced the efficacy of these agents in upregulating and activating the metastasis suppressor NDRG1 in neuroblastoma cells. These data were in agreement with our initial assessment that revealed strong synergistic interactions of these drugs not only in both neuroblastoma cell lines but also in the tested pediatric solid tumor cell lines in general (Figure 3).

4 Discussion

Approximately 30% of RTKs are mutated or overexpressed in malignant diseases, which makes RTKs the key regulators of malignancy in multiple tumor types, including tumors affecting children (Du and Lovly, 2018). The results of our initial screening showed the activation of the key RTKs in the cell lines derived from various pediatric solid tumors, including neuroblastoma, medulloblastoma, osteosarcoma, and rhabdomyosarcoma. Many of these RTKs are known oncoproteins that promote tumorigenesis and tumor progression, making them suitable targets for anticancer therapy (Crose and Linardic, 2010; Yamaoka et al., 2018). Thus, we selected TKIs used in

pediatric oncology, specifically SUN, GEF, and LAP, for the present study (Crose and Linardic, 2010; Pollack et al., 2010; Fouladi et al., 2013; Ségaliny et al., 2015).

These TKIs exhibit antiproliferative effects in cancer cells, and these observations were supported by the results of the present study; however, application of these TKIs as monotherapy for anticancer treatment often leads to the development of resistance (Jiao et al., 2018; Krchniakova et al., 2020). Thus, sequential or simultaneous applications of TKIs with other chemotherapeutics have been suggested as a promising approach to establish more effective therapies to overcome drug resistance (Krchniakova et al., 2020). An increase in antitumor efficacy and patient survival has been observed in multiple clinical trials, e.g., using a combination of GEF with carboplatin and pemetrexed in patients with non-small-cell lung carcinoma (Hosomi et al., 2020), of LAP with capecitabine (Cetin et al., 2014) or paclitaxel to treat breast carcinoma (Di Leo et al., 2008), or of SUN with docetaxel in breast carcinoma (Bergh et al., 2012) or gastric carcinoma patients (Yi et al., 2012).

Previous studies have shown that the thiosemicarbazone iron chelators Dp44mT and DpC are potent and selective against multiple adult cancer cell types (Liu et al., 2012; Lovejoy et al., 2012; Dixon et al., 2013; Jansson et al., 2015; Kovacevic et al., 2016; Xu et al., 2018) and cancer cell lines derived from pediatric solid tumors (Guo et al., 2016; Li et al., 2016; Paukovcekova et al., 2020; Macsek et al., 2022). Furthermore, Dp44mT and/or DpC enhance the effect of standard chemotherapeutics, e.g., doxorubicin in various carcinoma cells (Potuckova et al., 2014; Seebacher N. A. et al., 2016), tamoxifen, paclitaxel and 5-fluorouracil in breast carcinoma cells (Potuckova et al., 2014; Maqbool et al., 2020), gemcitabine and cisplatin in lung carcinoma cells (Lovejoy et al., 2012), or celecoxib in pediatric solid tumor cells in vitro (Paukovcekova et al., 2020). The present study expanded these findings by analyzing the interactions of Dp44mT and DpC with targeted therapeutics, i.e., TKIs SUN, GEF, and LAP, in the cell lines derived from the most frequent solid tumors in children.

The main goals of the combinational strategies are to achieve a higher efficacy of anticancer therapy while avoiding and/or overcoming drug resistance. The data of the present study suggested that sequential combination treatment designs failed to improve the effects of selected thiosemicarbazones and TKIs; however, simultaneous applications of these drugs resulted in consistent synergy and/or additivity independent of the cancer cell type. Furthermore, this design enabled the use of lower concentrations of these antiproliferative agents, notably Dp44mT and DpC. These results are particularly important because lowering the required drug doses while retaining anticancer efficacy is one of the major aims of combinational therapies (Mokhtari et al., 2017). Furthermore, this approach enables to reduce associated toxicity, which is a crucial aspect of the treatment of the pediatric population (Oeffinger et al., 2007).

TKIs have been developed to attenuate specific RTKs that are frequently dysregulated in cancer cells (Kannaiyan and Mahadevan, 2018). In addition to the inhibition of the corresponding targets, we also identified interesting off-target effects of GEF and LAP on PDGFRβ activation and the effect of SUN on EGFR phosphorylation (at the Tyr1148 residue) in both SH-SY5Y and SK-N-BE(2) neuroblastoma cell lines, which served as the models for detailed analyses of the molecular effects of combined treatments. There are no studies that have focused on this type of activity of GEF or LAP; however, the multikinase inhibitor SUN has been previously shown to target a number of unconventional RTKs, including EGFR, FGFR, TrkA, and TrkB, in neuroblastoma cells (Calero et al., 2014).

In contrast, thiosemicarbazones used in the present study target cancer cells via multiple mechanisms (Lui et al., 2015a). The antiproliferative activity of these derivates is attributed to iron depletion, which subsequently modulates the regulation of cell cycle (Dixon et al., 2013; Lui et al., 2015b), key signaling pathways (Dixon et al., 2013; Kovacevic et al., 2013, 2016; Menezes et al., 2017; Park et al., 2020a; Macsek et al., 2022), apoptosis (Zhou et al., 2020), and autophagy (Gutierrez et al., 2014). The results of the present study indicated that a combination of thiosemicarbazones with TKIs affected critical oncogenic RTKs and/or downstream targets, leading to the synergistic/additive interactions observed in the tested cell types.

Thiosemicarbazones have been demonstrated to inhibit the expression and activation of the ErbB family of receptors in response to EGF in pancreatic carcinoma cells *in vitro* and *in vivo* (Kovacevic et al., 2016; Menezes et al., 2017). A potent metastasis suppressor, NDRG1, has been proposed as the key regulator of these effects (Kovacevic et al., 2016; Menezes et al., 2017). Phosphorylation of NDRG1 is crucial for a number of physiological events, e.g., T-cell clonal anergy or cell division (Park et al., 2020b), and the anticancer effects of NDRG1 have been implicated in multiple cancers (Bae et al., 2013; Park et al., 2018, 2020b; Paukovcekova et al., 2020; Macsek et al., 2022). Furthermore, NDRG1 is modulated via cellular iron levels (Lui et al., 2015a) and is thus upregulated by the chelators, such as Dp44mT and DpC (Chen et al., 2012; Lane et al., 2013; Lui et al., 2015a; Kovacevic et al., 2016; Menezes et al., 2017). We have previously demonstrated the upregulation of NDRG1 by thiosemicarbazones and the anticancer effects of NDRG1 in cancer cells derived from pediatric solid tumors, including neuroblastomas (Paukovcekova et al., 2020; Macsek et al., 2022). As suggested for other cancer types (Kovacevic et al., 2016; Menezes et al., 2017; Macsek et al., 2022), a thiosemicarbazone-mediated decrease in EGFR observed in SH-SY5Y cells in the present study may be attributed to NDRG1 upregulation.

In addition to marked NDRG1 activation in the cells treated with thiosemicarbazones alone, these effects were also detected when thiosemicarbazones were combined with GEF or LAP in both neuroblastoma cell lines. Interestingly, a similar effect was not detected in SUN-treated cells (Figure 8), which may be due to the multikinase inhibitory activity of SUN (Calero et al., 2014). Of note, SUN has been shown to target AKT (Calero et al., 2014), which is one of the activators of NDRG1 (Park et al., 2020b).

In addition to EGFR downregulation, we observed intriguing effects of both Dp44mT and DpC on other tested RTKs, including PDGFRβ and IGF-1R (Figure 6). Although RTKs are presumed to form dimers with the partners of the same RTK family, the formation of the cross-family dimers has also been reported, especially in the case of EGFR (Kennedy et al., 2016). These dimers include EGFR-IGF-1R (Ahmad et al., 2004) or EGFR-PDGFRβ heterodimers (Saito et al., 2001), and their formation may lead to the concomitant degradation of both dimer components, potentially contributing to a decrease in these RTKs after thiosemicarbazone treatment demonstrated in the present study. Moreover, NDRG1 has been implicated in RTK degradation (Kovacevic et al., 2016; Menezes et al., 2019b; Park et al., 2020a). The activity and signaling of multiple growth factor receptors, including EGFR, PDGFRβ, and IGF-1R, is modulated via c-Src (Bromann et al., 2004; Amanchy et al., 2009; Liu et al., 2015), which is one of multiple NDRG1 targets (Liu et al., 2015). Similarly, NDRG1 has been recently shown to induce the expression of proteins involved in the degradation of IGF-1R. Multiubiquitination and subsequent degradation of IGF-1R upon ligand binding is mediated by E3 ubiquitin ligase NEDD4 in complex with the Grb10 adaptor protein, which acts as a bridge between NEDD4 and IGF-1R (Vecchione et al., 2003; Monami et al., 2008). Interestingly, NEDD4-like E3 ubiquitin ligase (NEDD4L) and Grb10 have been identified as the molecular targets of NDRG1 (Zhao et al., 2011; Kovacevic et al., 2013).

NDRG1 overexpression has also been shown to inhibit the downstream targets of EGFR signaling, e.g., MEK1/2 or ERK1/2, in pancreatic and prostate carcinoma cells (Dixon et al., 2013; Kovacevic et al., 2013, 2016). However, the data of the present study indicated that the treatment with thiosemicarbazones resulted in significantly upregulated phosphorylation of AKT, ERK1/2, and MEK1/2 kinases in SH-SY5Y cells. Enhanced kinase activation in the cells incubated with Dp44mT or DpC has been detected previously (Dixon et al., 2013; Macsek et al., 2022) and may be a result of a pro-survival response of the cells to stress stimuli induced by drug treatment (Dixon et al., 2013; Macsek et al., 2022). However, a different response of kinase signaling was detected in SK-N-BE(2) cells. Although both cell lines included in the present study are derived from neuroblastomas, each of these cell lines represent different neuroblastoma cell phenotypes (Ross et al., 2003). The heterogeneity of the cell populations is a distinctive feature of neuroblastomas, and this heterogeneity may be responsible for the discrepancies between the neuroblastoma cell lines detected in the present study. SH-SY5Y cells manifest the characteristics of N-type (neuroblastic/neuroendocrine precursors) neuroblastoma cells,

and SK-N-BE(2) cells manifest a stem cell phenotype of I-type cells (Ross et al., 2003). Furthermore, the amplification of *MYCN*, which is a major prognostic marker for neuroblastoma, was detected only in SK-N-BE(2) cells, and the N-myc protein is known to repress NDRG1 (Li and Kretzner, 2003). Despite these differences, a combination of thiosemicarbazones with TKIs induced uniformly synergistic and/or additive interactions in both neuroblastoma cell lines and increased apoptosis, especially after the combined treatments.

In conclusion, the combined treatments with thiosemicarbazones and TKIs have substantial synergistic potential for anticancer therapies of pediatric solid tumors. Simultaneous administration of the drugs was identified as the most potent approach for application of the combinations of thiosemicarbazones Dp44mT and DpC with TKIs SUN, GEF, and LAP in all tested cell lines. TKIs inhibited the activation of the corresponding RTKs; however, both thiosemicarbazones decreased the expression of RTKs, including EGFR and novel targets PDGFRβ and IGF-1R identified in the present study. The downregulation of NDRG1 mRNA expression has been shown to be associated with poor prognosis of neuroblastoma patients (Matsushita et al., 2013). Considering this finding and the data obtained in the present and previous studies (Paukovcekova et al., 2020; Macsek et al., 2022), we suggest that the upregulation of NDRG1, which is detected after combined treatment with thiosemicarbazones and GEF or LAP, presents a promising strategy for neuroblastoma treatment. The exact molecular functions of NDRG1 in the cells after combined treatment require further investigation; however, the present study provided a valid rationale for combined therapy of pediatric solid tumors using iron-chelating agents together with TKIs, especially with GEF or LAP.

Data availability statement

The data that support the findings of the present study are available from the corresponding authors upon reasonable request.

Author contributions

Study conceptualization: RV, JS, and MK. Development of methodology: MK, SP, JN, and PC. Investigation and data curation: MK and SP. Writing the original draft: MK. Writing, review and/or revision of the manuscript: MK, SP, JN, PC, JS, and RV. Visualization: MK. Statistical analysis: MK and JS. Study supervision: JS and RV. Funding acquisition: RV.

Funding

Acknowledgments

Conflict of interest

The authors declare that the research was conducted in the absence of any commercial or financial relationships that could be construed as a potential conflict of interest.

Publisher's note

All claims expressed in this article are solely those of the authors and do not necessarily represent those of their affiliated organizations, or those of the publisher, the editors and the reviewers. Any product that may be evaluated in this article, or claim that may be made by its manufacturer, is not guaranteed or endorsed by the publisher.

Supplementary material

The Supplementary Material for this article can be found online at: https://www.frontiersin.org/articles/10.3389/fphar.2022.976955/full#supplementary-material

References

Ahmad, T., Farnie, G., Bundred, N. J., and Anderson, N. G. (2004). The mitogenic action of insulin-like growth factor I in normal human mammary epithelial cells requires the epidermal growth factor receptor tyrosine kinase. *J. Biol. Chem.* 279, 1713–1719. doi:10.1074/jbc.M306156200

Alisi, A., Cho, W., Locatelli, F., and Fruci, D. (2013). Multidrug resistance and cancer stem cells in neuroblastoma and hepatoblastoma. *Int. J. Mol. Sci.* 14, 24706–24725. doi:10.3390/ijms141224706

Aller, S. G., Yu, J., Ward, A., Weng, Y., Chittaboina, S., Zhuo, R., et al. (2009). Structure of P-glycoprotein reveals a molecular basis for poly-specific drug binding. *Sci. 80.* 323, 1718–1722. doi:10.1126/science.1168750

Amanchy, R., Zhong, J., Hong, R., Kim, J. H., Gucek, M., Cole, R. N., et al. (2009). Identification of c-Src tyrosine kinase substrates in platelet-derived growth factor receptor signaling. *Mol. Oncol.* 3, 439–450. doi:10.1016/j.molonc.2009.07.001

Bae, D. H., Jansson, P. J., Huang, M. L., Kovacevic, Z., Kalinowski, D., Lee, C. S., et al. (2013). The role of NDRG1 in the pathology and potential treatment of human cancers. *J. Clin. Pathol.* 66, 911–917. doi:10.1136/jclinpath-2013-201692

Bates, S. E., Mickley, L. A., Chen, Y. N., Richert, N., Rudick, J., Biedler, J. L., et al. (1989). Expression of a drug resistance gene in human neuroblastoma cell lines: Modulation by retinoic acid-induced differentiation. *Mol. Cell. Biol.* 9, 4337–4344. doi:10.1128/mcb.9.10.4337

Bergh, J., Bondarenko, I. M., Lichinitser, M. R., Liljegren, A., Greil, R., Voytko, N. L., et al. (2012). First-line treatment of advanced breast cancer with sunitinib in combination with docetaxel versus docetaxel alone: Results of a prospective, randomized phase III study. *J. Clin. Oncol.* 30, 921–929. doi:10.1200/JCO.2011.35.7376

Brambilla, D., Zamboni, S., Federici, C., Lugini, L., Lozupone, F., Milito, A. D., et al. (2012). P-glycoprotein binds to ezrin at amino acid residues 149-242 in the FERM domain and plays a key role in the multidrug resistance of human osteosarcoma. *Int. J. Cancer* 130, 2824–2834. doi:10.1002/ijc.26285

Bromann, P. A., Korkaya, H., and Courtneidge, S. A. (2004). The interplay between Src family kinases and receptor tyrosine kinases. *Oncogene* 23, 7957–7968. doi:10.1038/sj.onc.1208079

Calero, R., Morchon, E., Johnsen, J. I., and Serrano, R. (2014). Sunitinib suppress neuroblastoma growth through degradation of MYCN and inhibition of angiogenesis. *PLoS One* 9, e95628. doi:10.1371/journal.pone.0095628

Cetin, B., Benekli, M., Turker, I., Koral, L., Ulas, A., Dane, F., et al. (2014). Lapatinib plus capecitabine for HER2-positive advanced breast cancer: A multicentre study of anatolian society of medical oncology (ASMO). *J. Chemother.* 26, 300–305. doi:10.1179/1973947813Y.0000000147

Chekmarev, J., Ayad, M. G., and Richardson, D. R. (2021). The oncogenic signaling disruptor, NDRG1: Molecular and cellular mechanisms of activity. *Cells* 10, 1–30. doi:10.3390/cells10092382

Chen, Z., Zhang, D., Yue, F., Zheng, M., Kovacevic, Z., and Richardson, D. R. (2012). The iron chelators Dp44mT and DFO inhibit TGF-β-induced epithelial-mesenchymal transition via up-regulation of N-Myc downstream-regulated gene 1 (NDRG1). *J. Biol. Chem.* 287, 17016–17028. doi:10.1074/jbc.M112.350470

Chou, T. C. (2006). Theoretical basis, experimental design, and computerized simulation of synergism and antagonism in drug combination studies. *Pharmacol. Rev.* 58, 621–681. doi:10.1124/pr.58.3.10

Crose, L. E. S., and Linardic, C. M. (2010). Receptor tyrosine kinases as therapeutic targets in rhabdomyosarcoma. *Sarcoma* 2011, 756982. doi:10.1155/2011/756982

Dai, C.-L., Tiwari, A. K., Wu, C.-P., Su, X., Wang, S.-R., Liu, D., et al. (2008). Lapatinib (tykerb, GW572016) reverses multidrug resistance in cancer cells by inhibiting the activity of ATP-binding cassette subfamily B member 1 and G member 2. *Cancer Res.* 68, 7905–7914. doi:10.1158/0008-5472.can-08-0499

Dalzell, A. M., Mistry, P., Wright, J., Williams, F. M., and Brown, C. D. A. (2015). Characterization of multidrug transporter-mediated efflux of avermectins in human and mouse neuroblastoma cell lines. *Toxicol. Lett.* 235, 189–198. doi:10.1016/j.toxlet.2015.04.005

Degasperi, A., Birtwistle, M. R., Volinsky, N., Rauch, J., Kolch, W., and Kholodenko, B. N. (2014). Evaluating strategies to normalise biological replicates of Western blot data. *PLoS One* 9, e87293. doi:10.1371/journal.pone.0087293

Di Leo, A., Gomez, H. L., Aziz, Z., Zvirbule, Z., Bines, J., Arbushites, M. C., et al. (2008). Phase III, double-blind, randomized study comparing lapatinib plus paclitaxel with placebo plus paclitaxel as first-line treatment for metastatic breast cancer. *J. Clin. Oncol.* 26, 5544–5552. doi:10.1200/JCO.2008.16.2578

Dixon, K. M., Lui, G. Y. L., Kovacevic, Z., Zhang, D., Yao, M., Chen, Z., et al. (2013). Dp44mT targets the AKT, TGF-β and ERK pathways via the metastasis suppressor NDRG1 in normal prostate epithelial cells and prostate cancer cells. *Br. J. Cancer* 108, 409–419. doi:10.1038/bjc.2012.582

Du, Z., and Lovly, C. M. (2018). Mechanisms of receptor tyrosine kinase activation in cancer. *Mol. Cancer* 17, 58–13. doi:10.1186/s12943-018-0782-4

Fouladi, M., Stewart, C. F., Blaney, S. M., Onar-Thomas, A., Schaiquevich, P., Packer, R. J., et al. (2013). A molecular biology and phase II trial of lapatinib in children with refractory CNS malignancies: A pediatric brain tumor consortium study. *J. Neurooncol.* 114, 173–179. doi:10.1007/s11060-013-1166-7

Gallego, S., Llort, A., Parareda, A., and Sanches de Toledo, J. (2004). Expression of multidrug resistance-1 and multidrug resistance-associated protein genes in pediatric rhabdomyosarcoma. *Oncol. Rep.* 11, 179–183. doi:10.3892/or.11.1.179

Geleta, B., Park, K. C., Jansson, P. J., Sahni, S., Maleki, S., Xu, Z., et al. (2021). Breaking the cycle: Targeting of NDRG1 to inhibit bi-directional oncogenic cross-talk between pancreatic cancer and stroma. *FASEB J.* 35, e21347. doi:10.1096/fj.202002279R

Gotink, K. J., Broxterman, H. J., Labots, M., De Haas, R. R., Dekker, H., Honeywell, R. J., et al. (2011). Lysosomal sequestration of sunitinib: A novel mechanism of drug resistance. *Clin. Cancer Res.* 17, 7337–7346. doi:10.1158/1078-0432.CCR-11-1667

Guo, Z.-L., Richardson, D. R., Kalinowski, D. S., Kovacevic, Z., Cheng Tan-Un, K., and Chi-Fung Chan, G. (2016). The novel thiosemicarbazone, di-2-pyridylketone 4-cyclohexyl-4-methyl-3-thiosemicarbazone (DpC), inhibits neuroblastoma growth *in vitro* and *in vivo* via multiple mechanisms. *J. Hematol. Oncol.* 9, 98–16. doi:10.1186/s13045-016-0330-x

Gutierrez, E., Richardson, D. R., and Jansson, P. J. (2014). The anticancer agent di-2-pyridylketone 4, 4-dimethyl-3-thiosemicarbazone (Dp44mT) overcomes prosurvival autophagy by two mechanisms: Persistent induction of autophagosome synthesis and impairment of lysosomal integrity. *J. Biol. Chem.* 289, 33568–33589. doi:10.1074/jbc.M114.599480

Hosomi, Y., Morita, S., Sugawara, S., Kato, T., Fukuhara, T., Gemma, A., et al. (2020). Gefitinib alone versus gefitinib plus chemotherapy for non-small-cell lung cancer with mutated epidermal growth factor receptor: NEJ009 study. *J. Clin. Oncol.* 38, 115–123. doi:10.1200/JCO.19.01488

Jansson, P. J., Yamagishi, T., Arvind, A., Seebacher, N., Gutierrez, E., Stacy, A., et al. (2015). Di-2-pyridylketone 4, 4-dimethyl-3-thiosemicarbazone (Dp44mT) overcomes multidrug resistance by a novel mechanism involving the hijacking of lysosomal P-glycoprotein (Pgp). *J. Biol. Chem.* 290, 9588–9603. doi:10.1074/jbc.M114.631283

Jiao, Q., Bi, L., Ren, Y., Song, S., Wang, Q., and Wang, Y.-S. (2018). Advances in studies of tyrosine kinase inhibitors and their acquired resistance. *Mol. Cancer* 17, 36. doi:10.1186/s12943-018-0801-5

Kannaiyan, R., and Mahadevan, D. (2018). A comprehensive review of protein kinase inhibitors for cancer therapy. *Expert Rev. Anticancer Ther.* 18, 1249–1270. doi:10.1080/14737140.2018.1527688

Kazmi, F., Hensley, T., Pope, C., Funk, R. S., Loewen, G. J., Buckley, D. B., et al. (2013). Lysosomal sequestration (trapping) of lipophilic amine (cationic amphiphilic) drugs in immortalized human hepatocytes (Fa2N-4 cells). *Drug Metab. Dispos.* 41, 897–905. doi:10.1124/DMD.112.050054

Kennedy, S. P., Hastings, J. F., Han, J. Z. R., and Croucher, D. R. (2016). The under-appreciated promiscuity of the epidermal growth factor receptor family. *Front. Cell Dev. Biol.* 4, 88–11. doi:10.3389/fcell.2016.00088

Kitazaki, T., Oka, M., Nakamura, Y., Tsurutani, J., Doi, S., Yasunaga, M., et al. (2005). Gefitinib, an EGFR tyrosine kinase inhibitor, directly inhibits the function of P-glycoprotein in multidrug resistant cancer cells. *Lung Cancer* 49, 337–343. doi:10.1016/J.LUNGCAN.2005.03.035

Kovacevic, Z., Chikhani, S., Lui, G. Y. L., Sivagurunathan, S., and Richardson, D. R. (2013). The iron-regulated metastasis suppressor NDRG1 targets NEDD4L, PTEN, and SMAD4 and inhibits the PI3K and ras signaling pathways. *Antioxid. Redox Signal.* 18, 874–887. doi:10.1089/ars.2011.4273

Kovacevic, Z., Menezes, S. V., Sahni, S., Kalinowski, D. S., Bae, D. H., Lane, D. J. R., et al. (2016). The metastasis suppressor, N-MYC downstream-regulated gene-1 (NDRG1), down-regulates the ErbB family of receptors to inhibit downstream oncogenic signaling pathways. *J. Biol. Chem.* 291, 1029–1052. doi:10.1074/jbc.M115.689653

Krchniakova, M., Skoda, J., Neradil, J., Chlapek, P., and Veselska, R. (2020). Repurposing tyrosine kinase inhibitors to overcome multidrug resistance in cancer: A focus on transporters and lysosomal sequestration. *Int. J. Mol. Sci.* 21, 3157. doi:10.3390/ijms21093157

Lane, D. J. R., Merlot, A. M., Huang, H., Bae, D.-H., Jansson, P. J., Sahni, S., et al. (2015). Cellular iron uptake, trafficking and metabolism: Key molecules and mechanisms and their roles in disease. *Biochim. Biophys. Acta* 1853, 1130–1144. doi:10.1016/j.bbamcr.2015.01.021

Lane, D. J. R., Saletta, F., Rahmanto, Y. S., Kovacevic, Z., and Richardson, D. R. (2013). N-Myc downstream regulated 1 (NDRG1) is regulated by eukaryotic initiation factor 3a (eIF3a) during cellular stress caused by iron depletion. *PLoS One* 8, e57273. doi:10.1371/journal.pone.0057273

Li, J., and Kretzner, L. (2003). The growth-inhibitory Ndrg1 gene is a Myc negative target in human neuroblastomas and other cell types with overexpressed N- or c-myc. *Mol. Cell. Biochem.* 250, 91–105. doi:10.1023/A:1024918328162

Li, P., Zheng, X., Shou, K., Niu, Y., Jian, C., Zhao, Y., et al. (2016). The iron chelator Dp44mT suppresses osteosarcoma's proliferation, invasion and migration: *In vitro* and *in vivo*. *Am. J. Transl. Res.* 8, 5370–5385.

Lim, S. C., Jansson, P. J., Assinder, S. J., Maleki, S., Richardson, D. R., and Kovacevic, Z. (2020). Unique targeting of androgen-dependent and -independent AR signaling in prostate cancer to overcome androgen resistance. *FASEB J.* 34, 11511–11528. doi:10.1096/fj.201903167R

Liu, W., Xing, F., Iizumi-Gairani, M., Okuda, H., Watabe, M., Pai, S. K., et al. (2012). N-myc downstream regulated gene 1 modulates Wnt-β-catenin signalling and

pleiotropically suppresses metastasis. *EMBO Mol. Med.* 4, 93–108. doi:10.1002/emmm.201100190

Liu, W., Yue, F., Zheng, M., Merlot, A., Bae, D. H., Huang, M., et al. (2015). The proto-oncogene c-Src and its downstream signaling pathways are inhibited by the metastasis suppressor, NDRG1. *Oncotarget* 6, 8851–8874. doi:10.18632/oncotarget.3316

Lovejoy, D. B., Jansson, P. J., Brunk, U. T., Wong, J., Ponka, P., and Richardson, D. R. (2011). Antitumor activity of metal-chelating compound Dp44mT is mediated by formation of a redox-active copper complex that accumulates in lysosomes. *Cancer Res.* 71, 5871–5880. doi:10.1158/0008-5472.CAN-11-1218

Lovejoy, D. B., Sharp, D. M., Seebacher, N., Obeidy, P., Prichard, T., Stefani, C., et al. (2012). Novel second-generation di-2-pyridylketone thiosemicarbazones show synergism with standard chemotherapeutics and demonstrate potent activity against lung cancer xenografts after oral and intravenous administration *in vivo. J. Med. Chem.* 55, 7230–7244. doi:10.1021/jm300768u

Lui, G. Y. L., Kovacevic, Z., Richardson, V., Merlot, A. M., Kalinowski, D. S., and Richardson, D. R. (2015a). Targeting cancer by binding iron: Dissecting cellular signaling pathways. *Oncotarget* 6, 18748–18779. doi:10.18632/oncotarget.4349

Lui, G. Y. L., Kovacevic, Z., Menezes, S., Kalinowski, D. S., Merlot, A. M., Sahni, S., et al. (2015b). Novel thiosemicarbazones regulate the signal transducer and activator of transcription 3 (STAT3) pathway: Inhibition of constitutive and interleukin 6–induced activation by iron depletion. *Mol. Pharmacol.* 87, 543–560. doi:10.1124/mol.114.096529

Macsek, P., Skoda, J., Krchniakova, M., Neradil, J., and Veselska, R. (2022). Iron-chelation treatment by novel thiosemicarbazone targets major signaling pathways in neuroblastoma. *Int. J. Mol. Sci.* 23, 376. doi:10.3390/ijms23010376

Maqbool, S. N., Lim, S. C., Park, K. C., Hanif, R., Richardson, D. R., Jansson, P. J., et al. (2020). Overcoming tamoxifen resistance in oestrogen receptor-positive breast cancer using the novel thiosemicarbazone anti-cancer agent, DpC. *Br. J. Pharmacol.* 177, 2365–2380. doi:10.1111/bph.14985

Matsushita, K., Uchida, K., Saigusa, S., Ide, S., Hashimoto, K., Koike, Y., et al. (2013). Low NDRG1 mRNA expression predicts a poor prognosis in neuroblastoma patients. *Pediatr. Surg. Int.* 29, 363–368. doi:10.1007/s00383-012-3248-6

Menezes, S. V., Fouani, L., Huang, M. L. H., Geleta, B., Maleki, S., Richardson, A., et al. (2019a). The metastasis suppressor, NDRG1, attenuates oncogenic TGF-β and NF-κB signaling to enhance membrane E-cadherin expression in pancreatic cancer cells. *Carcinogenesis* 40, 805–818. doi:10.1093/carcin/bgy178

Menezes, S. V., Kovacevic, Z., and Richardson, D. R. (2019b). The metastasis suppressor NDRG1 down-regulates the epidermal growth factor receptor via a lysosomal mechanism by up-regulating mitogen-inducible gene 6. *J. Biol. Chem.* 294, 4045–4064. doi:10.1074/jbc.RA118.006279

Menezes, S. V., Sahni, S., Kovacevic, Z., and Richardson, D. R. (2017). Interplay of the iron-regulated metastasis suppressor NDRG1 with epidermal growth factor receptor (EGFR) and oncogenic signaling. *J. Biol. Chem.* 292, 12772–12782. doi:10.1074/jbc.R117.776393

Miller, K. D., Nogueira, L., Mariotto, A. B., Rowland, J. H., Yabroff, K. R., Alfano, C. M., et al. (2019). Cancer treatment and survivorship statistics, 2019. *Ca. Cancer J. Clin.* 69, 363–385. doi:10.3322/caac.21565

Mokhtari, R. B., Homayouni, T. S., Baluch, N., Morgatskaya, E., Kumar, S., Das, B., et al. (2017). Combination therapy in combating cancer. *Oncotarget* 8, 38022–38043. doi:10.18632/oncotarget.16723

Monami, G., Emiliozzi, V., and Morrione, A. (2008). Grb10/Nedd4-mediated multiubiquitination of the insulin-like growth factor receptor regulates receptor internalization. *J. Cell. Physiol.* 216, 426–437. doi:10.1002/jcp.21405

Mudry, P., Slaby, O., Neradil, J., Soukalova, J., Melicharkova, K., Rohleder, O., et al. (2017). Case report: Rapid and durable response to PDGFR targeted therapy in a child with refractory multiple infantile myofibromatosis and a heterozygous germline mutation of the PDGFRB gene. *BMC Cancer* 17, 119. doi:10.1186/s12885-017-3115-x

Neradil, J., Kyr, M., Polaskova, K., Kren, L., Macigova, P., Skoda, J., et al. (2019). Phospho-protein arrays as effective tools for screening possible targets for kinase inhibitors and their use in precision pediatric oncology. *Front. Oncol.* 9, 930. doi:10.3389/fonc.2019.00930

Oeffinger, K. C., Mertens, A. C., and Sklar, C. A. (2007). Chronic health conditions in adult survivors of childhood cancer. *Oncol. Times* 29, 26. doi:10.1097/01.COT.0000265629.30194.8e

Othman, R. T., Kimishi, I., Bradshaw, T. D., Storer, L. C., Korshunov, A., Pfister, S. M., et al. (2014). Overcoming multiple drug resistance mechanisms in medulloblastoma. *Acta Neuropathol. Commun.* 2, 57–14. doi:10.1186/2051-5960-2-57

Park, K. C., Geleta, B., Leck, L. Y. W., Paluncic, J., Chiang, S., Jansson, P. J., et al. (2020a). Thiosemicarbazones suppress expression of the c-Met oncogene by mechanisms involving lysosomal degradation and intracellular shedding. *J. Biol. Chem.* 295, 481–503. doi:10.1074/jbc.RA119.011341

Park, K. C., Menezes, S. V., Kalinowski, D. S., Sahni, S., Jansson, P. J., Kovacevic, Z., et al. (2018). Identification of differential phosphorylation and sub-cellular localization of the metastasis suppressor, NDRG1. *Biochim. Biophys. Acta. Mol. Basis Dis.* 1864, 2644–2663. doi:10.1016/j.bbadis.2018.04.011

Park, K. C., Paluncic, J., Kovacevic, Z., and Richardson, D. R. (2020b). Pharmacological targeting and the diverse functions of the metastasis suppressor, NDRG1, in cancer. *Free Radic. Biol. Med.* 157, 154–175. doi:10.1016/j.freeradbiomed.2019.05.020

Paukovcekova, S., Skoda, J., Neradil, J., Mikulenkova, E., Chlapek, P., Sterba, J., et al. (2020). Novel thiosemicarbazones sensitize pediatric solid tumor cell-types to conventional chemotherapeutics through multiple molecular mechanisms. *Cancers (Basel)* 12, 3781. doi:10.3390/cancers12123781

Pollack, I. F., Steward, C. F., Kocak, M., Young Poussaint, T., Broniccer, A., Banerjee, A., et al. (2010). A phase II study of gefitinib and irradiation in children with newly diagnosed brainstem gliomas: A report from the pediatric brain tumor consortium. *Neuro. Oncol.* 12, 116–121.

Potuckova, E., Jansova, H., Machacek, M., Vavrova, A., Haskova, P., Tichotova, L., et al. (2014). Quantitative analysis of the anti-proliferative activity of combinations of selected iron-chelating agents and clinically used anti-neoplastic drugs. *PLoS One* 9, e88754. doi:10.1371/journal.pone.0088754

Radic-Sarikas, B., Halasz, M., Huber, K. V. M., Winter, G. E., Tsafou, K. P., Papamarkou, T., et al. (2017). Lapatinib potentiates cytotoxicity of YM155 in neuroblastoma via inhibition of the ABCB1 efflux transporter. *Sci. Rep.* 7, 3091–3098. doi:10.1038/s41598-017-03129-6

Ross, R. A., Biedler, J. L., and Spengler, B. A. (2003). A role for distinct cell types in determining malignancy in human neuroblastoma cell lines and tumors. *Cancer Lett.* 197, 35–39. doi:10.1016/S0304-3835(03)00079-X

Saito, Y., Haendeler, J., Hojo, Y., Yamamoto, K., and Berk, B. C. (2001). Receptor heterodimerization: Essential mechanism for platelet-derived growth factor-induced epidermal growth factor receptor transactivation. *Mol. Cell. Biol.* 21, 6387–6394. doi:10.1128/mcb.21.19.6387-6394.2001

Schindelin, J., Arganda-Carreras, I., Frise, E., Kaynig, V., Longair, M., Pietzsch, T., et al. (2012). Fiji: An open-source platform for biological-image analysis. *Nat. Methods* 9, 676–682. doi:10.1038/nmeth.2019

Seebacher, N. A., Richardson, D. R., and Jansson, P. J. (2016a). A mechanism for overcoming P-glycoprotein-mediated drug resistance: Novel combination therapy that releases stored doxorubicin from lysosomes via lysosomal permeabilization using Dp44mT or DpC. *Cell Death Dis.* 7, e2510. doi:10.1038/cddis.2016.381

Seebacher, N., Lane, D. J. R., Richardson, D. R., and Jansson, P. J. (2016b). Turning the gun on cancer: Utilizing lysosomal P-glycoprotein as a new strategy to overcome multi-drug resistance. *Free Radic. Biol. Med.* 96, 432–445. doi:10.1016/j.freeradbiomed.2016.04.201

Ségaliny, A. I., Tellez-Gabriel, M., Heymann, M. F., and Heymann, D. (2015). Receptor tyrosine kinases: Characterisation, mechanism of action and therapeutic interests for bone cancers. *J. Bone Oncol.* 4, 1–12. doi:10.1016/j.jbo.2015.01.001

Shukla, S., Robey, R. W., Bates, S. E., and Ambudkar, S. V. (2009). Sunitinib (Sutent, SU11248), a small-molecule receptor tyrosine kinase inhibitor, blocks function of the ATP-binding cassette (ABC) transporters P-glycoprotein (ABCB1) and ABCG2. *Drug Metab. Dispos.* 37, 359–365. doi:10.1124/dmd.108.024612

Tong, C. W. S., Wu, W. K. K., Loong, H. H. F., Cho, W. C. S., and To, K. K. W. (2017). Drug combination approach to overcome resistance to EGFR tyrosine kinase inhibitors in lung cancer. *Cancer Lett.* 405, 100–110. doi:10.1016/j.canlet.2017.07.023

Vecchione, A., Marchese, A., Henry, P., Rotin, D., and Morrione, A. (2003). The Grb10/Nedd4 complex regulates ligand-induced ubiquitination and stability of the insulin-like growth factor I receptor. *Mol. Cell. Biol.* 23, 3363–3372. doi:10.1128/mcb.23.9.3363-3372.2003

Verschuur, A. C., Bajčiová, V., Mascarenhas, L., Khosravan, R., Lin, X., Ingrosso, A., et al. (2019). Sunitinib in pediatric patients with advanced gastrointestinal stromal tumor: Results from a phase I/II trial. *Cancer Chemother. Pharmacol.* 84, 41–50. doi:10.1007/s00280-019-03814-5

Wu, C.-P., Hsieh, C.-H., and Wu, Y.-S. (2011). The emergence of drug transporter-mediated multidrug resistance to cancer chemotherapy. *Mol. Pharm.* 8, 1996–2011. doi:10.1021/mp200261n

Xu, Y. X., Zeng, M. L., Yu, D., Ren, J., Li, F., Zheng, A., et al. (2018). *In vitro* assessment of the role of DpC in the treatment of head and neck squamous cell carcinoma. *Oncol. Lett.* 15, 7999–8004. doi:10.3892/ol.2018.8279

Yamagishi, T., Sahni, S., Sharp, D. M., Arvind, A., Jansson, P. J., and Richardson, D. R. (2013). P-glycoprotein mediates drug resistance via a novel mechanism involving lysosomal sequestration. *J. Biol. Chem.* 288, 31761–31771. doi:10.1074/jbc.M113.514091

Yamaoka, T., Kusumoto, S., Ando, K., Ohba, M., and Ohmori, T. (2018). Receptor tyrosine kinase-targeted cancer therapy. *Int. J. Mol. Sci.* 19, 3491. doi:10.3390/ijms19113491

Yi, J. H., Lee, J., Lee, J., Park, S. H., Park, J. O., Yim, D.-S., et al. (2012). Randomised phase II trial of docetaxel and sunitinib in patients with metastatic gastric cancer who were previously treated with fluoropyrimidine and platinum. *Br. J. Cancer* 106, 1469–1474. doi:10.1038/bjc.2012.100

Yu, Y., Kalinowski, D. S., Kovacevic, Z., Siafakas, A. R., Jansson, P. J., Stefani, C., et al. (2009). Thiosemicarbazones from the old to new: Iron chelators that are more than just ribonucleotide reductase inhibitors. *J. Med. Chem.* 52, 5271–5294. doi:10.1021/jm900552r

Zhao, G., Chen, J., Deng, Y., Gao, F., Zhu, J., Feng, Z., et al. (2011). Identification of NDRG1-regulated genes associated with invasive potential in cervical and ovarian cancer cells. *Biochem. Biophys. Res. Commun.* 408, 154–159. doi:10.1016/j.bbrc.2011.03.140

Zhitomirsky, B., and Assaraf, Y. G. (2016). Lysosomes as mediators of drug resistance in cancer. *Drug resist. updat.* 24, 23–33. doi:10.1016/J.DRUP.2015.11.004

Zhou, J., Jiang, Y., Zhao, J., Zhang, H., Fu, J., Luo, P., et al. (2020). Dp44mT, an iron chelator, suppresses growth and induces apoptosis via RORA-mediated NDRG2-IL6/JAK2/STAT3 signaling in glioma. *Cell. Oncol.* 43, 461–475. doi:10.1007/s13402-020-00502-y

APPENDIX 7

Paukovcekova S, Krchniakova M, Chlapek P, Neradil J, **Skoda J***, Veselska R. Thiosemicarbazones Can Act Synergistically with Anthracyclines to Downregulate CHEK1 Expression and Induce DNA Damage in Cell Lines Derived from Pediatric Solid Tumors. *International Journal of Molecular Sciences.* 2022;23(15):8549. (JCR 2022; IF = 5.6, Q1 - Biochemistry & Molecular Biology)

Article

Thiosemicarbazones Can Act Synergistically with Anthracyclines to Downregulate CHEK1 Expression and Induce DNA Damage in Cell Lines Derived from Pediatric Solid Tumors

Silvia Paukovcekova [1], Maria Krchniakova [1,2], Petr Chlapek [1,2], Jakub Neradil [1,2], Jan Skoda [1,2,*,†] and Renata Veselska [1,2,*,†]

1   Department of Experimental Biology, Faculty of Science, Masaryk University, 61137 Brno, Czech Republic; silvia.paukovcekova@mail.muni.cz (S.P.); maria.krchniakova@mail.muni.cz (M.K.); chlapek@sci.muni.cz (P.C.); jneradil@sci.muni.cz (J.N.)
2   International Clinical Research Center, St. Anne's University Hospital, 65691 Brno, Czech Republic
*   Correspondence: jan.skoda@sci.muni.cz (J.S.); veselska@mail.muni.cz (R.V.)
†   These authors contributed equally to this work.

Abstract: Anticancer therapy by anthracyclines often leads to the development of multidrug resistance (MDR), with subsequent treatment failure. Thiosemicarbazones have been previously suggested as suitable anthracycline partners due to their ability to overcome drug resistance through dual Pgp-dependent cytotoxicity-inducing effects. Here, we focused on combining anthracyclines (doxorubicin, daunorubicin, and mitoxantrone) and two thiosemicarbazones (DpC and Dp44mT) for treating cell types derived from the most frequent pediatric solid tumors. Our results showed synergistic effects for all combinations of treatments in all tested cell types. Nevertheless, further experiments revealed that this synergism was independent of Pgp expression but rather resulted from impaired DNA repair control leading to cell death via mitotic catastrophe. The downregulation of checkpoint kinase 1 (CHEK1) expression by thiosemicarbazones and the ability of both types of agents to induce double-strand breaks in DNA may explain the Pgp-independent synergism between anthracyclines and thiosemicarbazones. Moreover, the concomitant application of these agents was found to be the most efficient approach, achieving the strongest synergistic effect with lower concentrations of these drugs. Overall, our study identified a new mechanism that offers an avenue for combining thiosemicarbazones with anthracyclines to treat tumors regardless the Pgp status.

Keywords: thiosemicarbazones; anthracyclines; anthracenedione; pediatric solid tumors; combined anticancer treatment; checkpoint kinase 1; double strand breaks in DNA

1. Introduction

Anthracyclines belong to a class of natural cytotoxic antibiotics and represent highly potent antineoplastic agents widely used to treat a variety of tumor types [1]. Since the early 1970s, when the first compounds from the anthracycline class—doxorubicin (DOX) and daunorubicin (DAU)—were approved for clinical use, anthracyclines have been therapeutically used as potent anticancer drugs [1–3]. Their cytotoxic and cytostatic effects result from the combination of different mechanisms, i.e., intercalation into DNA, induction of oxidative stress, and poisoning of the topoisomerase II enzyme (TOP2) [4,5]. In general, DOX is usually indicated for treating lymphomas, sarcomas, and other solid tumors (bone tumors, lung carcinoma, bladder carcinoma, breast carcinoma, and cervical carcinoma), whereas DAU is more active on lymphoblastic and acute myeloblastic leukemia [1].

Despite its efficacy, anthracycline therapy is associated with cumulative dose-dependent cardiotoxic side effects, such as ventricular contractility and cardiomyopathy, leading to heart failure [6]. The other common side effects include acute nausea and vomiting, stomatitis, gastrointestinal disturbances, baldness, alopecia, neurologic disturbances (dizziness, hallucinations, and vertigo), and bone marrow aplasia [7]. Because of this toxicity,

anthracyclines are often used in lower concentrations as a component in combination therapies [3]. To improve the therapeutic profile of anthracyclines, a synthetic anthracenedione—mitoxantrone (MIT)—was developed. This drug is routinely used in the treatment of lymphomas, leukemias, breast carcinoma, and prostate carcinoma [8].

In addition to the cardiotoxicity of anthracyclines, chemoresistance is a major reason for the failure of anthracycline therapy [9]. In general, the emergence of resistance to anthracyclines in malignant cells is a multifactorial process [9]. One of the main mechanisms is often associated with the acquisition of multidrug resistance (MDR) conferred by overexpression of permeability glycoprotein-1 (Pgp) [10–12]. Pgp is an efflux pump induced by drugs, heat shock, some natural products, environmental stress, and other nonspecific stress factors [9]. To date, several approaches have been explored to overcome MDR induced by Pgp [9], e.g., formulation of nanodelivery systems for anthracyclines [13–15], anthracycline derivatives with improved properties [16–21], and gene-targeted downregulation or pharmacological inhibition of Pgp [22–26].

Another promising strategy for overcoming Pgp-mediated drug resistance is based on combining DOX with thiosemicarbazones—di-2-pyridylketone 4-cyclohexyl-4-methyl-3-thiosemicarbazone (DpC) and di-2-pyridylketone 4,4-dimethyl-3-thiosemicarbazone (Dp44mT)—to directly leverage lysosomal Pgp transport activity [27,28]. Previously, Pgp was shown to be topologically inverted during the endocytic process, thus facing into lysosomes, leading to lysosomal loading of Pgp substrates [29–31]. Therefore, in cells with high Pgp expression, Pgp mediates not only drug efflux through the plasma membrane [32], but also increased drug trapping within lysosomes, creating drug "safe houses", which can be observed [29]. DOX, DAU, and MIT were defined as lysosomotropic drugs on the basis of their pKa values, i.e., at acidic pH, these compounds are protonated and trapped in lysosomes, preventing their distribution to major targets in the nucleus [29]. DpC and Dp44mT are also Pgp substrates, and, in cells with MDR, they are transported via Pgp into lysosomes, where they are trapped due to protonation in a manner identical to anthracycline trapping [30,33–35]. However, positively charged thiosemicarbazones can bind copper and enter redox cycles to generate reactive oxygen species (ROS) that induce lysosomal membrane permeabilization (LMP) and subsequent proapoptotic signaling [27,30,33–35]. Moreover, LMP enables the release of stored anthracyclines from lysosomes, leading to restoration of their cytotoxic activity [27]. According to this mechanism, synergistic interactions between anthracyclines and thiosemicarbazones are expected to be beneficial predominantly in MDR malignant cells with typically high Pgp expression.

In this study, we focused for the first time on the combination of anthracyclines with thiosemicarbazones in pediatric solid tumors. Due to the improvement of therapeutic strategies, from aggressive surgical approaches to multimodal approaches with neoadjuvant chemotherapeutic treatments, almost 83% of children with a diagnosis of cancer become long-term survivors [36,37]. However, the use of new drugs has led to malignant acquisition of MDR, which is currently the leading cause of treatment failure in pediatric oncology [37]. Here, we aimed to address this problem and we present results that revealed a previously unrecognized mode of synergistic interaction between anthracyclines and thiosemicarbazones in model cell lines derived from pediatric solid tumors.

2. Results

2.1. SH-SY5Y Cells: The Only Tested Cell Line with High Pgp Expression

The first step in our study was to determine Pgp expression in untreated cell lines. For correct evaluation, two cervical carcinoma cell lines were used: KB-V1 cells with typical high Pgp expression were used as positive controls and KB-3-1 cells with minimal Pgp expression were used as negative controls. Analysis by qPCR revealed high *ABCB1* (the gene encoding Pgp) expression only in the SH-SY5Y neuroblastoma cells (Figure 1A). ABCB1 mRNA level in the SK-N-BE(2) neuroblastoma, Saos-2 osteosarcoma, and Daoy medulloblastoma cells was lower than it was in the SH-SY5Y cells, whereas ABCB1 expression in the RD rhabdomyosarcoma cell line was comparable with that in the negative

control cells (Figure 1A). The results obtained using immunoblotting proved that the Pgp level was high only in the SH-SY5Y cells (Figure 1B, Supplementary Figure S1). Moreover, to verify the obtained results, Pgp immunofluorescence staining was performed, and the results confirmed that Pgp signals were high only in the positive control and SH-SY5Y cells (Figure 2).
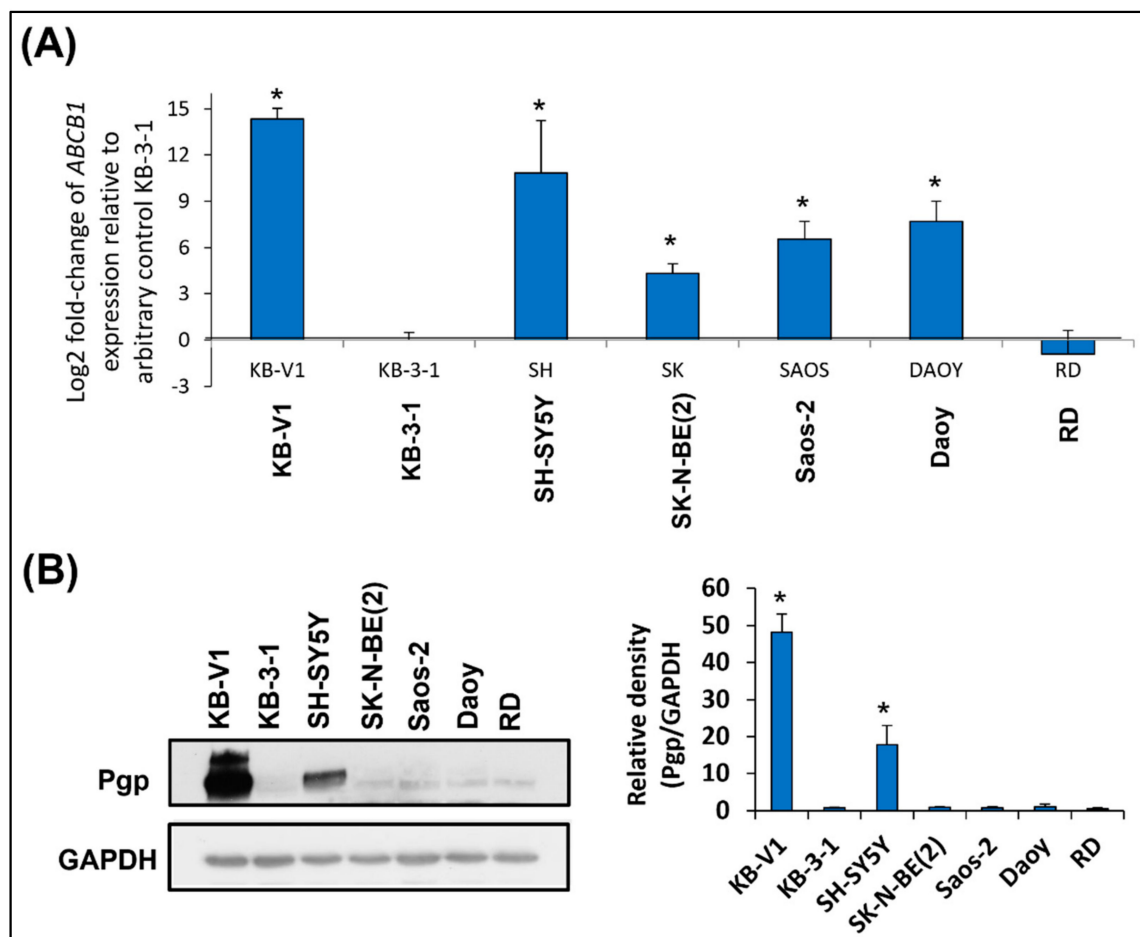
Figure 1. Measuring Pgp in the selected cell lines. KB-V1 cells were used as positive controls for *ABCB1* (gene encoding Pgp) expression, whereas KB-3-1 cells were used as negative controls. All experiments were performed in biological triplicates. (**A**) The graph shows the mRNA expression of *ABCB1* (the gene encoding Pgp) in untreated cell lines. The data were obtained using RT-qPCR. The levels of ABCB1 expression are presented as a log2-fold change based on mRNA expression relative to that of the negative control (y = 0). GAPDH served as the reference control. The data were analyzed by one sample *t*-test: * $p < 0.05$ indicates significant differences compared to the respective control group. (**B**) Immunoblot analysis of the endogenous Pgp level in untreated cell lines. GAPDH served as the loading control. The data are presented as the means $\pm$ SD and they were analyzed by unpaired *t*-test with Welch's correction: * $p < 0.05$ indicates significant differences compared to the respective control group.

2.2. Thiosemicarbazones Acted Mainly Synergistically with Anthracyclines

The investigation continued with the quantification of the synergy between the thiosemicarbazones (DpC and Dp44mT) and anthracyclines (DOX, DAU, and MIT) using MTT assays with a subsequent analysis performed using Calcusyn software (Figure 3). The hypothesis on the synergy between these compounds was based on previously published findings [27,28] that described the synergistic effect of thiosemicarbazones and anthracyclines in overcoming Pgp-mediated multidrug resistance.
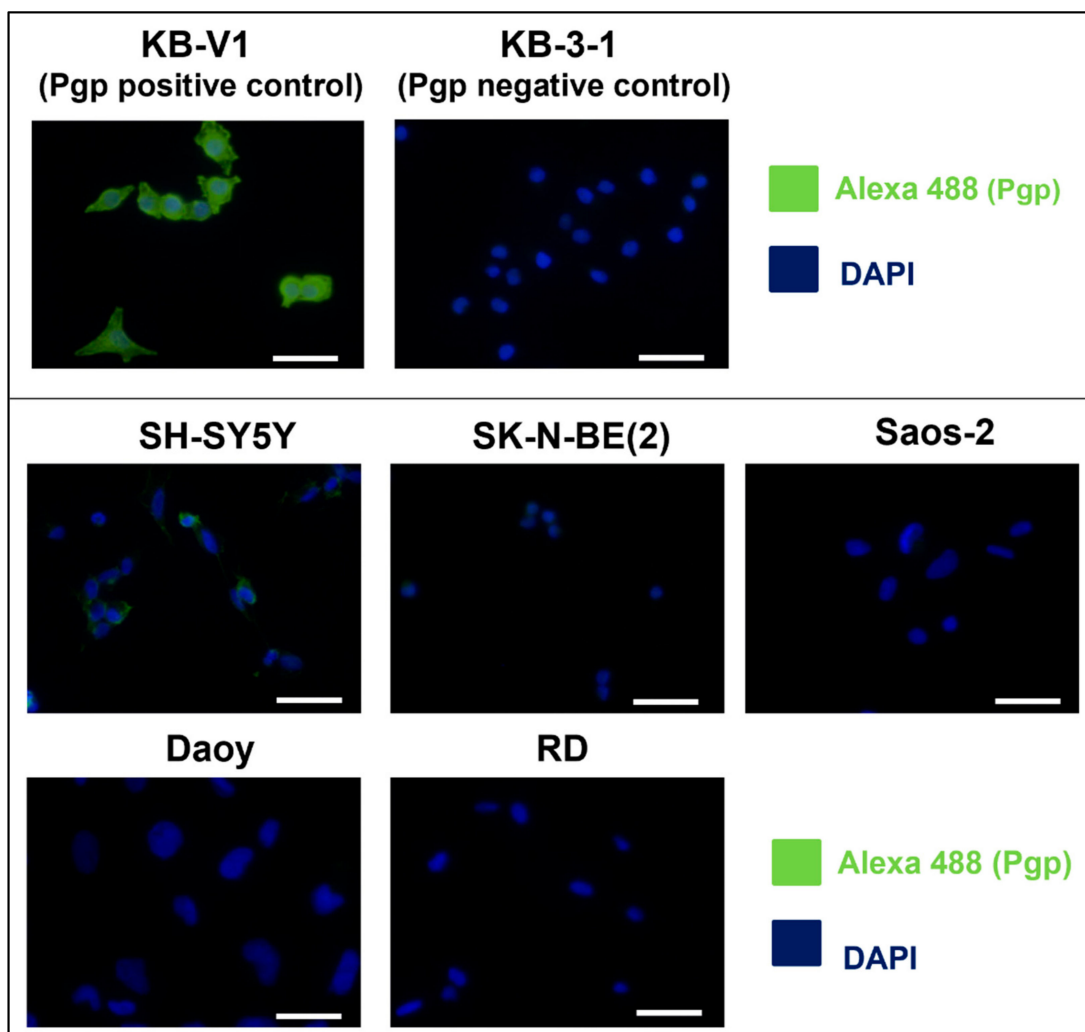
Figure 2. Pgp expression in the untreated cell lines. The expression of Pgp analyzed in the untreated cell lines was visualized by indirect immunofluorescence using an anti-Pgp primary antibody and an Alexa-488-conjugated secondary antibody (green signal). Nuclei were labeled by DAPI (blue signal). KB-V1 cells served as positive controls for Pgp expression, whereas KB-3-1 cells served as negative controls. The scale bars represent 50 μm.

First, the treatment was applied in the consecutive design treatment (Figure 3A). IC_{50} dose of DpC and Dp44mT (for 24 h) was determined according to the micromolar concentration (Table 1), whereas the IC_{50} dose of all the anthracyclines (used for 72 h) varied according to the nanomolar concentrations (Table 1).

Table 1. IC_{50} values used for subsequent experiments.

Cell Line	DOX [nM] 3D	DAU [nM] 3D	MIT [nM] 3D	DpC [nM] 3D	Dp44m [nM] 3D	DpC [μM] 1D	Dp44mT [μM] 1D
SH-SY5Y	29.7 ± 4.9	40.2 ± 13.9	20.1 ± 3.6	3.8 ± 0.3	1.9 ± 0.8	11.1 ± 2.2	30.1 ± 1.5
SK-N-BE(2)	40.8 ± 8.1	31.9 ± 8.7	27.0 ± 1.7	7.2 ± 1.2	4.2 ± 1.1	14.8 ± 2.3	31.1 ± 5.2
Saos-2	23.9 ± 2.8	20.8 ± 0.9	6.1 ± 0.6	4.4 ± 0.9	6.6 ± 0.9	20.0 ± 4.2	61.6 ± 14.9
Daoy	9.8 ± 2.0	17.6 ± 3.3	7.5 ± 0.2	17.0 ± 3.4	7.9 ± 1.9	3.9 ± 0.6	0.9 ± 0.1
RD	18.2 ± 3.8	15.7 ± 1.0	26.3 ± 4.4	13.8 ± 2.4	9.4 ± 0.8	11.5 ± 1.5	55.8 ± 7.7

3D indicates cultivation with the respective compound for 3 days (72 h), 1D indicates cultivation for 1 day (24 h).
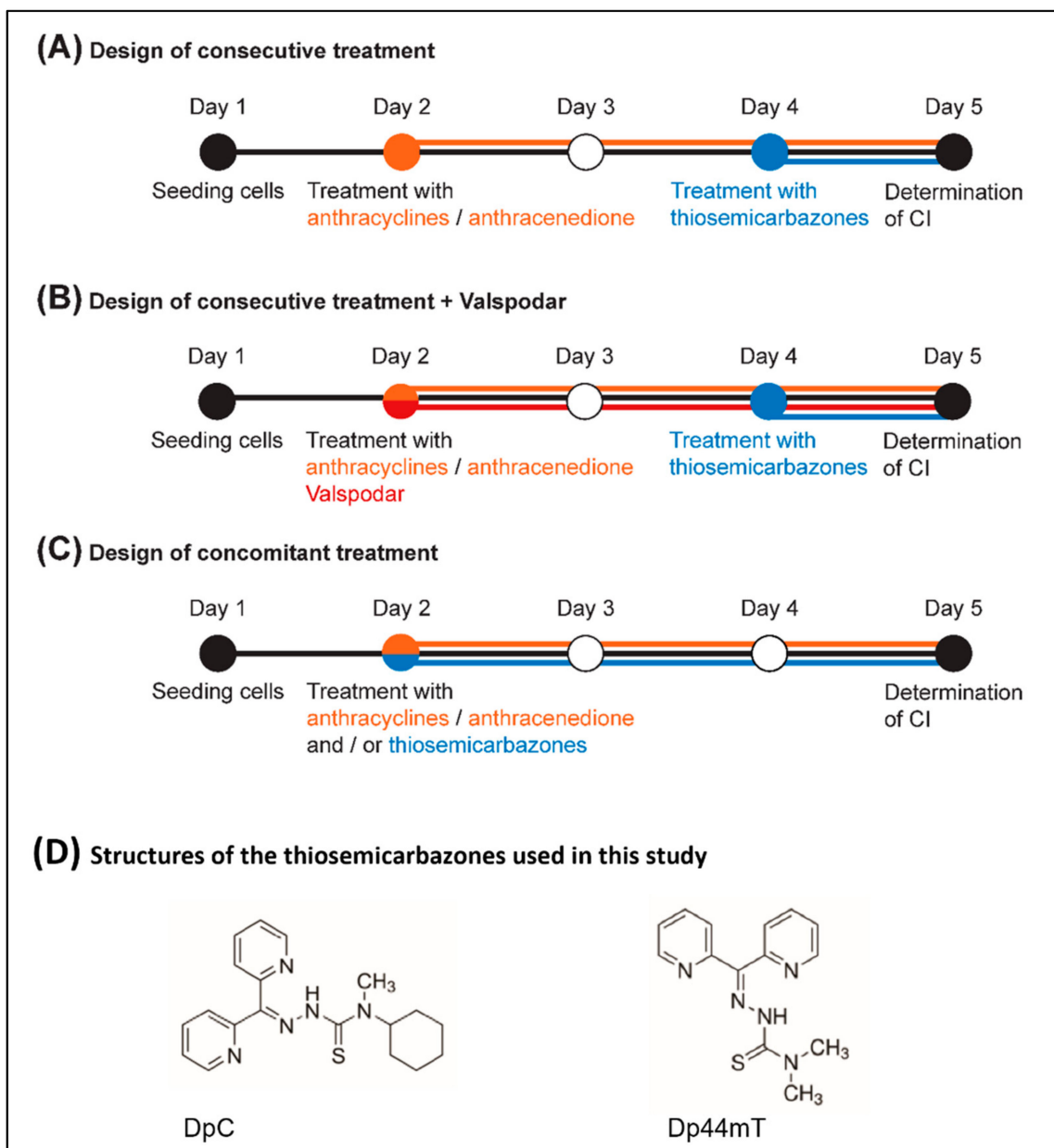
Figure 3. The three different combination treatment designs used in this study. (**A**) The design of consecutive treatment included the pretreatment of cells for 48 h with an anthracycline/anthracenedione (either DOX, DAU, or MIT), and then either DpC or Dp44mT was added to the cells undergoing anthracycline/anthracenedione treatment for a period of 24 h. (**B**) To examine whether the mechanism of synergy was based on Pgp transport activity, Valspodar, a selective inhibitor of Pgp, was added to the design of consecutive treatment. (**C**) In the design of concomitant treatment, both anthracycline/anthracenedione (either DOX, DAU, or MIT) and thiosemicarbazones (either DpC or Dp44mT) were added in combination to the cells and proliferation was evaluated after 72 h. (**D**) Structure of di-2-pyridylketone 4-cyclohexyl-4-methyl-3-thiosemicarbazone (DpC) and di-2-pyridylketone 4,4-dimethyl-3-thiosemicarbazone (Dp44mT).

The computational analyses of synergy showed that the combination of a thiosemicarbazone and anthracycline acted synergistically in four cell lines: SH-SY5Y, SK-N-BE(2), Daoy, and RD cells (Table 2). In the Saos-2 cell line, the analysis revealed moderate antagonism for each compound combination (Table 2).

Table 2. Quantitative assessment of the interactions between drugs.

Cell Line	Drug Combination		Treatment Design					
			Consecutive		Consecutive + Valspodar		Concomitant	
			CI	SD	CI	SD	CI	SD
SH-SY5Y	DOX	Dp44mT	0.739	0.064	0.795	0.062	0.779	0.079
		DpC	0.793	0.127	0.492	0.068	0.684	0.062
	DAU	Dp44mT	0.655	0.174	0.828	0.066	0.842	0.124
		DpC	0.599	0.077	0.588	0.051	0.647	0.161
	MIT	Dp44mT	0.507	0.099	0.758	0.121	0.921	0.091
		DpC	0.527	0.081	0.898	0.054	0.620	0.222
SK-N-BE(2)	DOX	Dp44mT	0.722	0.053	0.567	0.117	0.712	0175
		DpC	0.974	0.050	0.635	0.062	0.795	0,161
	DAU	Dp44mT	0.562	0.118	0.534	0.117	0.732	0.202
		DpC	0.640	0.140	0.409	0.074	0.638	0.154
	MIT	Dp44mT	0.304	0.107	0.524	0.049	0.458	0.157
		DpC	0.590	0.137	0.531	0.133	0.569	0.177
Saos-2	DOX	Dp44mT	1.105	0.102	0.710	0.125	0.657	0.051
		DpC	1.205	0.066	0.596	0.057	0.831	0.101
	DAU	Dp44mT	1.244	0.289	0.712	0.149	0.813	0.135
		DpC	1.422	0.085	0.611	0.172	0.672	0.177
	MIT	Dp44mT	1.108	0.182	0.610	0.056	0.828	0.112
		DpC	1.439	0.255	0.723	0.160	0.527	0.108
Daoy	DOX	Dp44mT	0.720	0.210	0.591	0.078	1.055	0.081
		DpC	0.578	0.138	0.611	0.015	0.637	0.113
	DAU	Dp44mT	0.474	0.033	0.602	0.118	1.275	0.280
		DpC	0.789	0.167	0.788	0.157	0.854	0.103
	MIT	Dp44mT	0.663	0.277	0.564	0.137	0.501	0.238
		DpC	0.439	0.029	0.746	0.035	0.700	0.175
RD	DOX	Dp44mT	0.807	0.126	0.472	0.108	0.648	0.043
		DpC	0.770	0.008	0.830	0.057	0.712	0.312
	DAU	Dp44mT	0.458	0.143	0.383	0.059	0.773	0.211
		DpC	0.609	0.097	0.671	0.173	0.764	0.118
	MIT	Dp44mT	0.501	0.099	0.366	0.031	0.493	0.108
		DpC	0.641	0.081	0.541	0.134	0.638	0.127

Categories of Interactions

0.31–0.70	synergism		0.91–1.10	nearly additive	
0.71–0.85	moderate synergism		1.11–1.20	slight antagonism	
0.86–0.90	slight synergism		1.21–1.45	moderate antagonism	

Computational analysis of the interaction of doxorubicin (DOX), daunorubicin (DAU), or mitoxantrone (MIT) with thiosemicarbazones (DpC or Dp44mT) was performed using Calcusyn software. The combination index (CI) was calculated from the growth inhibition curves of the compounds alone or their combinations. A ratio of 1:1 was maintained between the drugs added in combination. The method of Chou and Talalay was employed to define synergism, additive effects, or antagonism. The experiments were performed in biological triplicates.

In the next step, 200 nM Valspodar (VAL), a selective inhibitor of Pgp, was added to the consecutive design treatment to verify whether the mechanism of synergy was based on lysosomal sequestration of the compounds via Pgp (Figure 3B). We expected to observe a change in the compound interactions because of a synergistic, an additive, or even an antagonistic effect. The results did not confirm this expectation—synergistic effects were observed even after Pgp inhibition (Table 2). Moreover, treatment with VAL changed the moderate antagonistic effect of all compound groups in Saos-2 cells to a synergistic effect (Table 2).

As an additional analysis of anthracycline sequestration into lysosomes, fluorescence microscopy was performed. DOX is an autofluorescent compound, which allowed us to observe its effect on cells 2 h after its addition to the culture medium. For this purpose, the DOX concentration was increased to 10 μM. The lysosomes were visualized by indirect

staining using an anti-LAMP-2 antibody. KB-V1 cells served as positive controls for the expected lysosomal sequestration of DOX (Figure 4A, Supplementary Figure S2A), whereas KB-3-1 cells served as negative controls (Figure 4B, Supplementary Figure S2B).
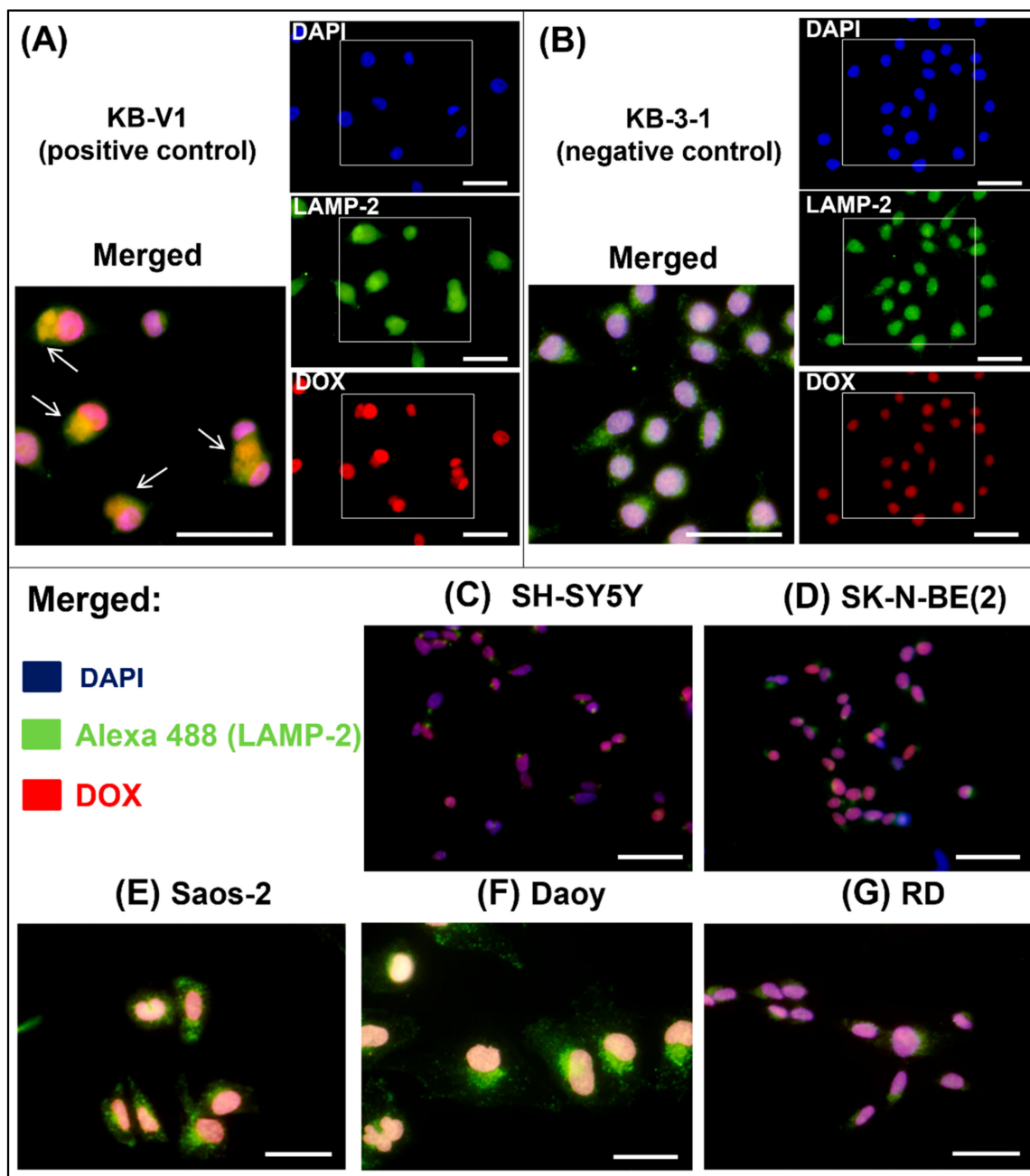
Figure 4. DOX localization in cells. All cell lines were treated with 10 μM doxorubicin (DOX). The localization of DOX (red fluorescence) within cells after 2 h of treatment was observed using fluorescence microscopy. Additionally, the target organelles, lysosomes, and nuclei were stained. The lysosomes were visualized by indirect immunofluorescence using an anti-LAMP-2 primary antibody and an Alexa-488-conjugated secondary antibody (green fluorescence). The nuclei were labeled with DAPI (blue fluorescence). The KB-V1 cell line (**A**) served as a positive control for the lysosomal sequestration of DOX (indicated by arrows: yellow fluorescence—overlap of green and red fluorescence emissions). In contrast, the KB-3-1 cells served as a negative control (**B**). The analyses were performed with all five selected cell lines: SH-SY5Y (**C**), SK-N-BE(2) (**D**), Saos-2 (**E**), Daoy (**F**), and RD (**G**) cells. The scale bars represent 50 μm.

In general, this analysis showed that DOX did not colocalize with LAMP-2 but was primarily localized to the nucleus in all five tested cell types (Figure 4C–G, Supplementary Figure S2C–G). Therefore, we rejected the hypothesis that lysosomal sequestration of anthracyclines via Pgp played a major role in the synergistic effect of thiosemicarbazones and anthracyclines in the tested cell types derived from pediatric solid tumors.

Because the initial hypothesis explaining the mechanism of synergy was rejected, we changed the design to the concomitant treatment (Figure 3C), which allowed us to use markedly lower concentrations of thiosemicarbazones necessary to achieve the same effects as those achieved with micromolar concentrations in the consecutive design. The IC50 dose (for 72 h) for both DpC and Dp44mT varied in the nanomolar range (Table 1). Moreover, synergistic interactions between thiosemicarbazones and anthracyclines after concomitant treatment were observed in all five tested cell types (Table 2). Overall, the obtained data suggested that the concomitant design of treatment was more effective, enabling usage of lower drug doses than the consecutive design of treatment. Given the serious side effects associated with anthracycline therapy, approaches that would minimize concentrations of anthracyclines while maintaining their anticancer activity are needed. Therefore, in the subsequent analyses, we focused solely on the effects of the concomitant drug application given its apparent potential to reduce nonselective toxicity of the drugs.

2.3. Thiosemicarbazones Downregulated CHEK1 Expression, Leading to Mitotic Catastrophe after These Drugs Were Combined with Anthracyclines

As synergy between both thiosemicarbazones (DpC and Dp44mT) and all three anthracyclines (DOX, DAU, and MIT) was observed in all evaluated cell lines (SH-SY5Y, SK-N-BE(2), Saos-2, Daoy, and RD cells) after both combined treatments (consecutive and concomitant designs), the possible mechanism of synergistic interaction between these compounds seemed to be universal. Therefore, we predominantly focused on the common mechanisms of action of both types of compounds used.

The first of the main effects of anthracyclines is the production of double-strand breaks (DSBs) in DNA molecules, which are associated with cell cycle arrest in the G_2/M phase. To confirm this effect in our tested cell lines, propidium iodide staining with subsequent flow cytometry analysis was performed to identify the changes in the cell cycle after 3 days of treatment with IC_{50} doses of DOX, DAU, and MIT. Cell cycle arrest in the G_2/M phase was detected in four of the tested cell lines: SK-N-BE(2), Saos-2, Daoy, and RD cells (Figure 5, Supplementary Table S1). For the SH-SY5Y cells, only an increased proportion of cells in the sub-G_1 phase, which is associated with formation of apoptotic bodies, was detected (Figure 5, Supplementary Table S1). Arrest in the G_2/M phase would likely have been observed in an earlier phase of treatment, i.e., after 24 or 48 h.

For apoptosis induction based on the production of DSBs in DNA, it is essential to force cells with damaged DNA to bypass cell cycle arrest in the S/G_2 phase and enter mitosis, which can lead to mitotic catastrophe [38,39]. Therefore, we investigated the ability of thiosemicarbazones, DOX, or their combinations to downregulate the expression of checkpoint kinase 1 and 2 (CHEK1 and CHEK2) at IC_{50} doses after 3 days. Immunoblotting revealed that both thiosemicarbazones effectively decreased CHEK1 levels in the SH-SY5Y, Saos-2, and Daoy cell lines, and a slight decrease in CHEK1 levels was also observed in the SK-N-BE(2) and RD cells (Figure 6A–E, Supplementary Figure S3A–E). DOX reduced the levels of CHEK1 less effectively than the thiosemicarbazones in all of the tested cell lines, and combined treatment caused a greater decrease in CHEK1 levels compared with single-compound treatments only in the SH-SY5Y cells (Figure 6A, Supplementary Figure S3A). In contrast, CHEK2 levels were almost completely abrogated in all the tested cell lines after treatment with DOX (Figure 6A–E, Supplementary Figure S3A–E). DpC and Dp44mT also decreased the CHEK2 levels in SH-SY5Y, SK-N-BE(2), Saos-2, and Daoy cells but less effectively than DOX (Figure 6A–D, Supplementary Figure S3A–D). The combined treatment did not achieve any enhanced effects considering the very strong inhibitory effect of DOX (Figure 6A–E, Supplementary Figure S3A–E). Regarding the obtained results, we

can assume that downregulation of both checkpoint kinases by combined treatment with thiosemicarbazones and DOX can lead to the effective abrogation of the cell cycle checkpoint and the subsequent induction of mitotic catastrophe in cancer cells with damaged DNA.
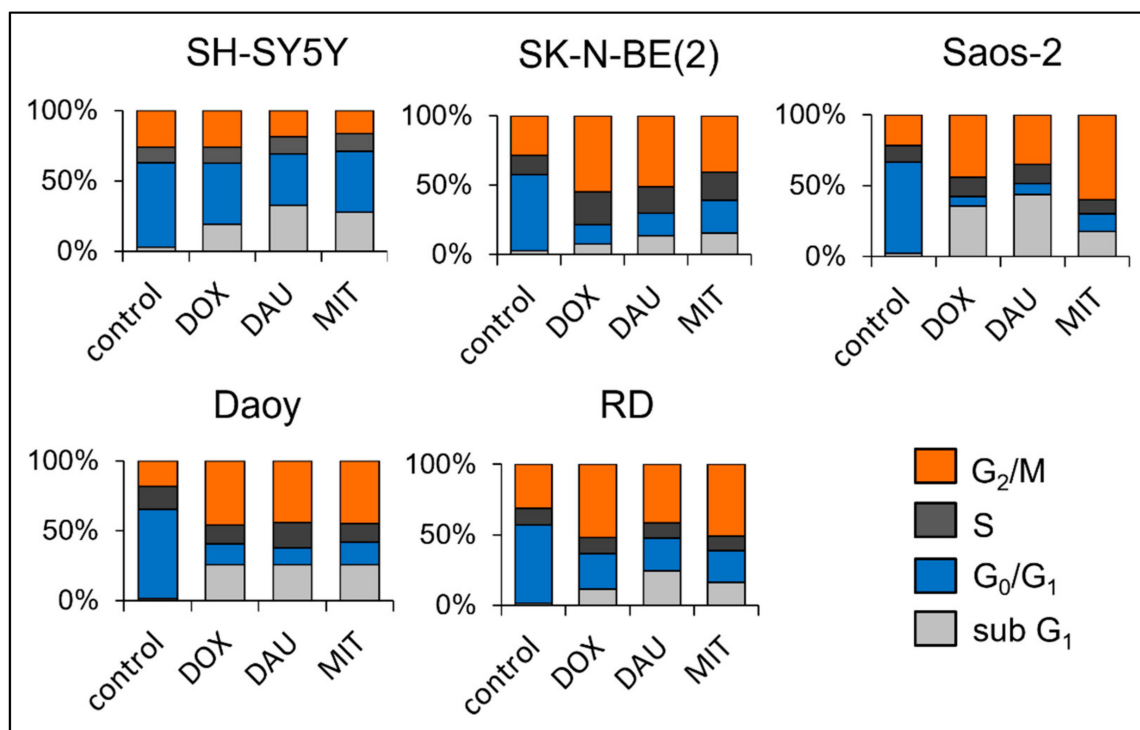
Figure 5. Analysis of the cell cycle using propidium iodide staining. Cell cycle analysis of selected cell lines (SH-SY5Y, SK-N-BE(2), Saos-2, Daoy, and RD cells) was performed by quantification of the DNA content with propidium iodide staining and subsequent flow cytometry detection. Changes in the cell cycle were obtained after 72 h of treatment with IC_{50} doses of doxorubicin (DOX), daunorubicin (DAU), or mitoxantrone (MIT). The graphs show the mean proportion of cells (%) in the cell cycle phases: sub G_1, G_0/G_1, S, and G_2/M. The detailed table showing the means $\pm$ SD is provided in Supplementary Table S1. All experiments were performed in biological triplicates.

2.4. Thiosemicarbazones Can Induce DSBs in DNA

In addition, the ability of thiosemicarbazones to produce DSBs in DNA (similar to anthracyclines) was investigated as a possible mechanism contributing to combination treatment synergy. The generation of DSBs after the selected treatment was verified by indirect immunofluorescence staining of the phosphorylated γ-H2AX protein, which is considered a biomarker of DSBs [40]. Staining was performed after 2 days of treatment with DpC, Dp44mT, or DOX alone and with their combinations (DpC + DOX or Dp44mT + DOX). The results obtained after 2 days showed that the IC_{50} doses of thiosemicarbazones caused γ-H2AX activation in all tested cell lines (Figure 7A–E, Supplementary Figure S4A–E). In general, the rate of DNA damage was apparently more intense after DOX treatment than after thiosemicarbazone treatment (Figure 7A–E, Supplementary Figure S4A–E). Enhanced DNA damage after administration of the DpC + DOX and Dp44mT + DOX combinations, compared to that after each compound was administered alone, was observed only in the Saos-2 cells (Figure 7C, Supplementary Figure S4C). Nevertheless, this method demonstrated that even nanomolar concentrations of DpC and Dp44mT induce DSBs in DNA.
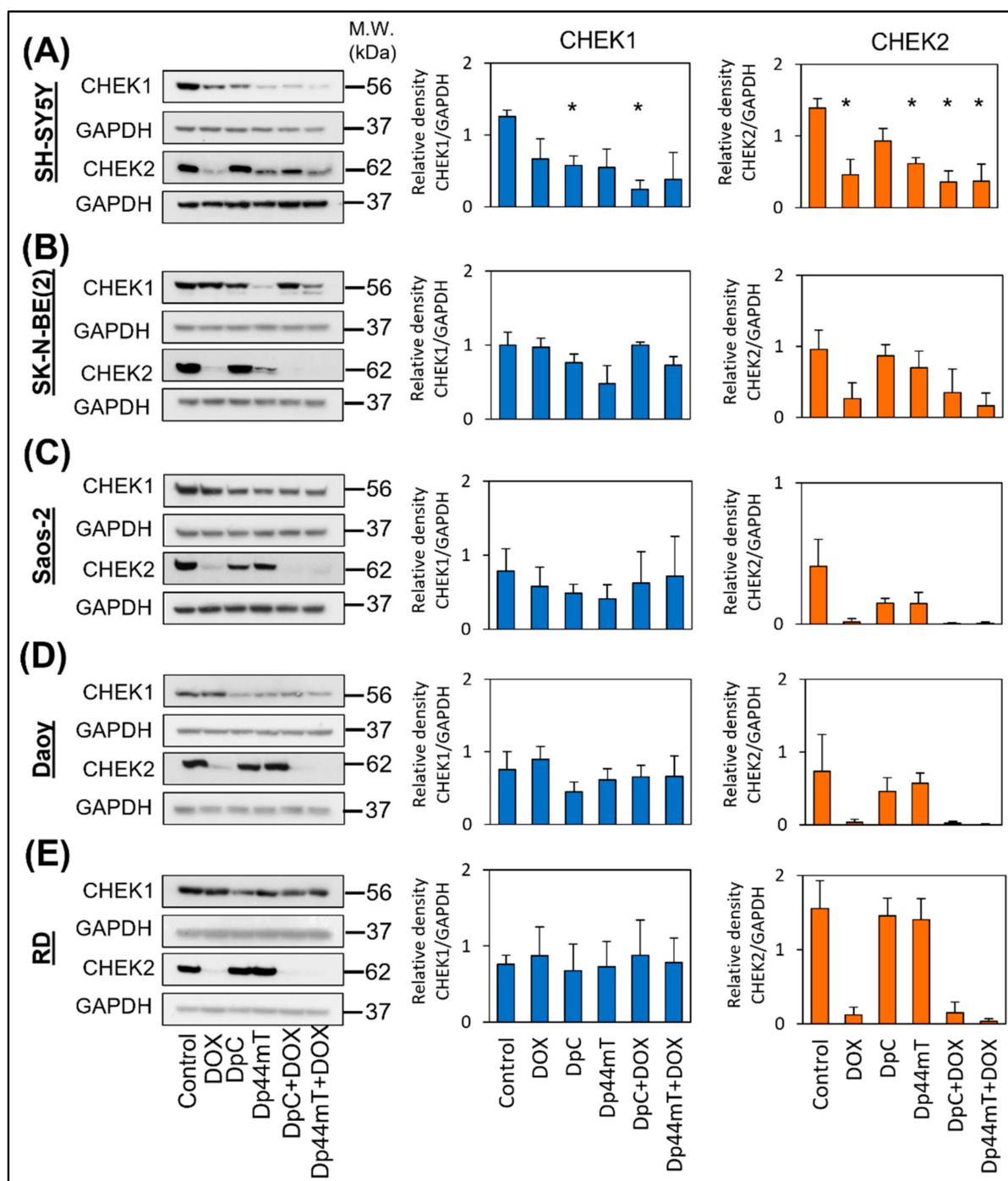
Figure 6. Immunoblotting to determine CHEK1 and CHEK2 levels in selected cell lines. CHEK1 and CHEK2 expression was evaluated in the SH-SY5Y (**A**), SK-N-BE(2) (**B**), Saos-2 (**C**), Daoy (**D**), and RD (**E**) cell lines after 3 days of incubation with IC_{50} doses of DOX, DpC, Dp44mT, or their combinations. GAPDH served as the loading control. The experiments were performed in biological triplicates. The obtained data were analyzed by unpaired Welch's *t*-test followed by Games–Howell post hoc test. * $p < 0.05$ indicates significant differences compared to the respective control group.
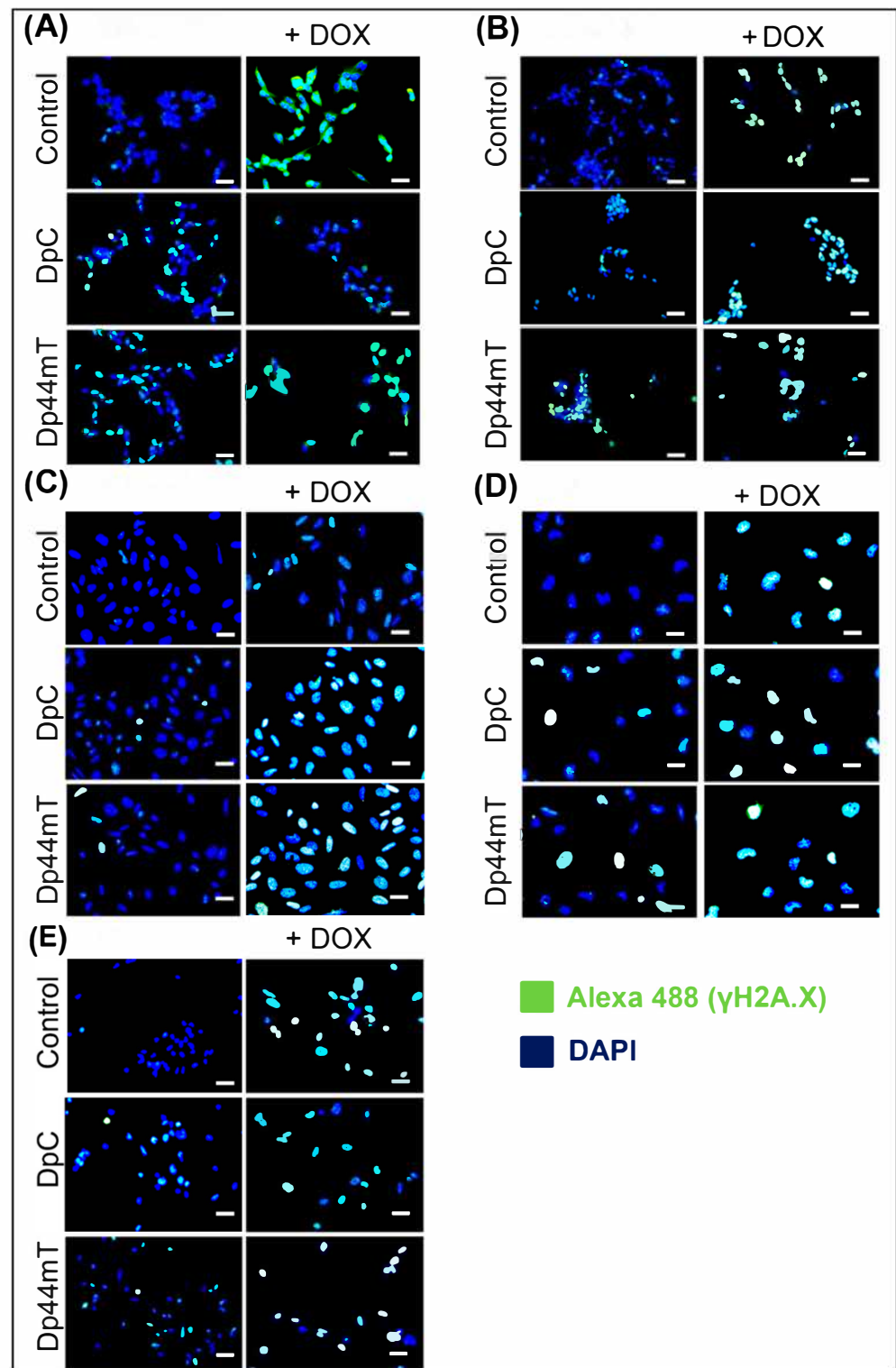
Figure 7. Detection of double-strand breaks (DSBs) in DNA using immunofluorescence staining of phosphorylated γ-H2AX protein. Detection of DSBs in SH-SY5Y (**A**), SK-N-BE(2) (**B**), Saos-2 (**C**), Daoy (**D**), and RD (**E**) cells after 48 h of treatment with IC$_{50}$ doses of DpC, Dp44mT, DOX, or their combination was performed by fluorescence microscopy. Phosphorylated γ-H2AX protein (a DSB marker) was visualized by indirect immunofluorescence using an anti-γ-H2AX primary antibody and Alexa-488-conjugated secondary antibody (green fluorescence). The nuclei were labeled by DAPI (blue fluorescence). The scale bars represent 50 μm.

3. Discussion

The obtained results proved the synergism of the combined thiosemicarbazone and anthracycline treatments in all chosen cell lines derived from pediatric solid tumors but also demonstrated that overcoming drug resistance mediated by Pgp is not the main mechanism of the observed synergism, as initially hypothesized. Accordingly, another synergistic mechanism based on enhanced DNA damage and the inhibition of checkpoint kinases was suggested.

Considering previous studies that demonstrated a positive correlation between Pgp expression and the synergistic action of thiosemicarbazones in combination with DOX [27,30,33,41], we started the investigation with Pgp screening in the chosen cell lines derived from childhood tumors. High Pgp expression at the mRNA and protein levels was found only in the SH-SY5Y cells. In the other cell lines, Pgp expression was very similar to that in the negative control cells. Therefore, the synergy of anthracycline and thiosemicarbazone treatments was expected only in SH-SY5Y cells.

To evaluate interactions between compound combinations, we first used a consecutive design of treatment, which was reported as effective in the literature [27]. Contrary to the predictions, synergistic action of thiosemicarbazones and anthracyclines in combination was found for four of the five cell lines. Therefore, to verify the main role of Pgp in the synergistic mechanism, VAL, a selective inhibitor of Pgp, was added to the consecutive design of treatment. In this regimen for compound application, we expected to see a change from synergistic action to an additive effect or even antagonism. Interestingly, the synergy between the thiosemicarbazones and anthracyclines was found in all five cell lines. Moreover, the analysis using fluorescence microscopy demonstrating primary localization of DOX to the nucleus in all cell lines contributed to the definitive rejection of the initial hypothesis stating that the main synergistic mechanism in chosen cell lines is based on lysosomal sequestration of Pgp.

To explore the least toxic regimen of treatment, we decided to change the combined treatment design from a consecutive to concomitant application of the drugs. With this change, we were not only able to reduce the thiosemicarbazone IC_{50} doses from the micromolar to nanomolar level, but were also able to observe synergistic action of the compound treatments in all five cell lines. Therefore, it can be concluded that concomitant application is the most convenient administration regimen for the combined treatment of anthracyclines and thiosemicarbazones in the tested cell lines.

Since the suitable application of the selected compounds was determined, the next objective was to describe the possible mechanism of the observed synergy. The mechanism seemed to be universal because all the combinations of DpC or Dp44mT with DOX, DAU, or MIT acted synergistically in four different cell types (neuroblastoma, medulloblastoma, osteosarcoma, and rhabdomyosarcoma cells). Therefore, we focused on the common features of thiosemicarbazone and anthracycline mechanisms of action.

The cytotoxic activity of anthracyclines is exerted through several mechanisms. In addition to their ability to intercalate between base pairs of DNA and induce ROS generation, anthracyclines can inhibit TOP2 activity by covalently binding to the DNA–TOP2 complex [5]. The potential lethality of stabilized DNA–TOP2 complexes is markedly increased during DNA replication, when the replication fork attempts to traverse this structure and convert transient single- or double-strand breaks into permanent double-stranded fractures [42]. Stalled DNA replication activates ataxia telangiectasia, Rad3-related (ATR) kinase, and, subsequently, CHEK1, which leads to cell cycle arrest mediated by cyclin A-Cdk2 inhibition [43,44].

In addition, ROS generated by anthracyclines cause DSBs in DNA and activate ATM-dependent pathways [45]. ATM kinase phosphorylates CHEK2, resulting in the inhibition of cyclin E-Cdk2 complexes and subsequent cell cycle arrest [46].

There is evidence of cross-talk and functional redundancy between ATR-CHEK1 and ATM-CHEK2 after anthracycline treatment. It was proven that DNA damage caused by DOX elicits both check kinase pathways [47].

The stabilization of the DNA–TOP2 complex, manifesting as DNA breaks, was observed after treatment with Dp44mT in a breast cancer cell type [48]. According to the observed expression of γH2A.X—a specific reporter of DSBs [49–51], our results indicate that both DpC and Dp44mT caused DNA damage in the neuroblastoma, medulloblastoma, osteosarcoma, and rhabdomyosarcoma cell types. This analysis revealed that both thiosemicarbazones can induce DSBs but with much less efficiency than DOX.

One promising strategy for enhancing the effect of anthracyclines is based on their combined application with drugs targeting cell cycle checkpoints (CHEK1 and CHEK2). In general, cell cycle arrest is a major mechanism of cellular resistance to drugs that cause DNA damage [52,53]. Therefore, TOP2 inhibitors can be combined with drugs inhibiting the checkpoint kinase pathways and administered to force cancer cells to bypass cell cycle arrest and enter mitosis with DNA damage, which leads to mitotic catastrophe [38,39]. For drug combinations with DOX, it was previously demonstrated that the double inhibition of CHEK1 and CHEK2 did not achieve better efficacy than inhibition of CHEK1 alone. Thus, only inhibition of CHEK1 abolishes DOX-induced cell cycle arrest followed by mitotic catastrophe [54]. Our investigations proved that both DpC and Dp44mT can downregulate CHEK1 in all tested cell lines derived from the most frequent pediatric solid tumors.

Regarding the obtained results, we can assume that the observed synergy between the selected thiosemicarbazones and anthracyclines is based on the following mechanism. Both types of compounds, thiosemicarbazones and anthracyclines, cause DNA damage by inducing replication fork stalling and ROS production. Therefore, their combined treatment leads to an increase in DSB induction. Moreover, thiosemicarbazones decrease CHEK1 expression and, thus, help cells with damaged bypass arrest, increasing the rate of cells undergoing mitotic catastrophe. Together, our results suggest a new mechanism of synergism between thiosemicarbazones and anthracyclines that is effective in tumor cells regardless of the Pgp expression.

4. Materials and Methods

4.1. Chemicals

The selected thiosemicarbazones Dp44mT (Cat. No. SML0186) and DpC (Cat. No. SML0483), the DOX (Cat. No. D2975000), DAU (Cat. No. D0125000), and MIT (Cat. No. M2305000), and Pgp inhibitor VAL (Cat. No. SML0572) were obtained from Sigma-Aldrich (St. Louis, MO, USA). All chemicals were prepared as stock solutions in DMSO (Cat. No. D8418, Sigma-Aldrich) and then diluted in cell culture medium to achieve a DMSO concentration < 0.5% (v/v), which has been shown to have no effect on cell proliferation relative to the control medium [55]. To prepare the stock solution, DpC, Dp44mT, MIT, and VAL were dissolved to reach a concentration of 100 mM; similarly, the DOX and DAU concentrations were each 10 mM.

4.2. Cell Culture

RD rhabdomyosarcoma cell line (Cat. No. 85111502), SH-SY5Y (Cat. No. 94030304), and the SK-N-BE(2) (Cat. No. 95011815) neuroblastoma cell lines were purchased from the European Collection of Authenticated Cell Cultures (Salisbury, UK). The Daoy medulloblastoma cell line (Cat. No. HTB-186) and Saos-2 osteosarcoma cell line (Cat. No. HTB-85) were purchased from the American Type Culture Collection (Manassas, VA, USA). The KB-3-1 and KB-V1 cervical carcinoma cell lines were gifts from Prof. Nóra Kucsma (Szakács Gergely's Laboratory, Budapest, Hungary). The selected cell lines were cultured in various culture media, as shown in Table 3, and maintained under standard cell culture conditions: 37 °C in an atmosphere of 95% air and 5% CO_2. All reagents for cell culture were purchased from Biosera (Nuaille, France).

Table 3. Composition of culture media used for culturing the selected cell lines.

Cell Line	Type of Medium	Glucose	FCS	Atb	Glu	NEAA
Daoy	DMEM	Low	10%	+	+	+
KB-3-1	DMEM	High	10%	+	+	-
KB-V1	DMEM + VBL	High	10%	+	+	+
RD	DMEM	High	10%	+	+	+
Saos-2	DMEM	Low	10%	+	+	-
SH-SY5Y	DMEM:F12 (1:1)	High	20%	+	+	+
SK-N-BE(2)	DMEM:F12 (1:1)	High	20%	+	+	+

DMEM—Dulbecco's modified Eagle's medium; low glucose—1000 mg/L; high glucose—4500 mg/L; HVBL—vinblastine 1 µg/mL; FCS—fetal calf serum; Atb—streptomycin (100 µg/mL) and penicillin (100 IU/mL); Glu—2 mM L-glutamine; NEAA—1% nonessential amino acids.

4.3. Treatment Protocol

MTT proliferation assays were used to determine the IC_{50} values for the anthracyclines and thiosemicarbazones in the SH-SY5Y, SK-N-BE(2), Saos-2, Daoy, and RD cell lines. The cells were seeded in 96-well plates at a density of 5×10^3 cells/well (SH-SY5Y, SK-N-BE(2), Saos-2, and RD cells) or 2×10^3 cells/well (Daoy cells) in 100 µL of complete DMEM, and then allowed to adhere overnight. Different seeding densities for the cell lines were chosen to ensure that the cells remained in the log phase of growth during all 3 days of treatment. The IC_{50} values for the individual compounds were calculated from the growth inhibition curves obtained after treatment with increasing compound concentrations based on the initial estimated IC_{50} values ($1/8$-, $1/4$-, $1/2$-, 1-, 2-, 4-, and 8-fold of the estimated initial IC_{50}). The IC_{50} values for both anthracyclines and thiosemicarbazones were obtained after 3 days of treatment. For thiosemicarbazones only, the IC_{50} values were also obtained after 1 day of treatment.

To determine the combination index (CI) value, three different experimental designs of compound application were chosen (Figure 3). The "consecutive design" (Figure 3A) included the pretreatment of cells with an anthracycline (DOX, DAU, or MIT) only. After 48 h, DpC or Dp44mT was added to the cells undergoing anthracycline treatment. Proliferation was evaluated after 24 h using MTT assay. The second experimental design, labeled "+ Valspodar" (Figure 3B), was the same as the "consecutive design" with the addition of 200 nM VAL along with the anthracycline in the first treatment step. In the "concomitant design" (Figure 3C), both anthracyclines and thiosemicarbazones were added in combination to the cells. Proliferation was evaluated using MTT assay after 72 h of culture. Growth inhibition curves for compound combinations were constructed for increasing drug concentrations based on previously determined IC_{50} values ($1/8$-, $1/4$-, $1/2$-, 1-, 2-, 4-, and 8-fold of the previously determined IC_{50}).

For direct observation of DOX administration in cells, the cells were seeded onto coverslips in Petri dishes (35 mm in diameter) and allowed to grow to 80% confluence at 37 °C. All the cell lines were then treated with 10 µM DOX and observed after 2 h of incubation at 37 °C.

An indirect immunofluorescence assay was employed to reveal DSBs in DNA by staining for phosphorylated histone γH2AX. The cells were seeded onto coverslips and allowed to grow to 80% confluence as described above. The cell lines were then treated with the respective IC_{50} doses of DOX, DpC, Dp44mT, or with their combinations (DOX + DpC or DOX + Dp44mT) and incubated at 37 °C for 2 days.

To analyze the cell cycle using propidium iodide staining, all the tested cell lines were seeded in Petri dishes (90 mm in diameter) at a density of 1×10^5/dish. The cells were then treated with the respective IC_{50} doses of DOX, DAU, and MIT and incubated at 37 °C for 3 days.

Immunoblotting was performed to determine the levels of CHEK1 and CHEK2. The cells were seeded in the same manner as in the cell cycle analysis described above. The cells were then treated with the respective IC$_{50}$ doses of DOX, DpC, Dp44mT, or with their combinations DOX + DpC or DOX + Dp44mT and incubated at 37 °C for 3 days.

4.4. Cell Proliferation

A colorimetric MTT assay was performed to evaluate the cell proliferation rate as previously described [56]. Briefly, the treated cells were incubated with MTT (0.5 mg/mL; Sigma-Aldrich) at 37 °C for 3 h. The formed formazan crystals were dissolved in 200 µL of DMSO. The absorbance was read at 570 nm with a reference absorbance of 620 nm using a Sunrise Absorbance Reader (Tecan, Männedorf, Switzerland).

4.5. Calculation of the CI

The CI values for the compound combinations were calculated to quantitatively compare the dose–effect relationship of each compound individually and in combination to determine whether a selected combination acts synergistically. CI values were obtained from growth inhibition curves using the constant ratio of the compounds in combination (1:1) as previously described [57]. The CI values were calculated using CalcuSyn software (version 2.0, Biosoft, Cambridge, UK). The Chou Talalay method was adopted to identify antagonism (CI > 1.1), additive effects (CI = 0.9–1.1), or synergism (CI < 0.9) [58].

4.6. RT-qPCR

The relative expression of selected genes was determined using RT-qPCR. Total RNA was isolated using a GenElute Mammalian Total RNA Miniprep Kit (Sigma-Aldrich) and reverse transcribed into cDNA as described previously [56]. qPCR was performed in a 10-µL volume using a Kapa Biosystems Quantitative Real-Time PCR kit (Kapa Biosystems, Wilmington, MA, USA) and analyzed using a 7500 Fast Real-Time PCR System and 7500 Software v. 2.0.6 (both obtained from Life Technologies, Carlsbad, CA, USA). To detect differences in the transcript levels among the cell types or after the treatment, Cq values normalized to the endogenous reference control (the GAPDH gene) were compared. The primer sequences used for the ABCB1 and GAPDH genes are provided in Table 4.

Table 4. Sequences of the primers used for RT-qPCR.

Gene	Primer Sequence	Product Length (bp)
ABCB1	F: 5′-CTTTAGTGGAAAGACCACAGATGA-3′ R: 5′-CTTTAGTGGAAAGACCACAGATGA-3′	228
GAPDH	F: 5′-AGC CAC ATC GCT CAG ACA CC-3′ R: 5′-GTA CTC AGC GCC AGC ATC G-3′	302

F—forward; R—reverse.

4.7. Immunoblotting

Protein extracts were obtained using LB1 lysis buffer (50 mM HEPES-KOH, pH 7.5; 140 mM NaCl; 1 mM EDTA; 10% glycerol; 0.5% NP-40; and 0.25% Triton X-100). Total proteins (25 µg/well) were loaded onto 8% (for Pgp analysis) or 10% (for CHEK1 and CHEK2 analysis) polyacrylamide gels and electrophoresed. The separated proteins were then blotted onto PVDF membranes (Bio-Rad Laboratories, Munich, Germany). The membranes were blocked with 5% nonfat dry milk in PBS with 0.1% Tween-20 at RT for 1 h. Subsequently, the blocked membranes were incubated overnight with primary monoclonal antibodies. The following day, the membranes were washed in TBS-Tween and incubated with secondary antibodies at RT for 1 h. The primary and secondary antibodies are listed in Table 5. ECL-Plus detection was performed according to the manufacturer's instructions (GE Healthcare, Little Chalfont, UK). The obtained protein bands were analyzed using ImageJ software (NIH, MD, USA).

Table 5. Primary and secondary antibodies used for immunoblotting.

Primary antibodies					
Antigen	**Type/Host**	**Clone**	**Catalog No.**	**Manufacturer**	**Dilution**
GAPDH	Mono/Rb	14C10	2118S	CST	1:10,000
CHEK1	Mono/Mo	2G1D5	2360S	CST	1:1000
CHEK2	Mono/Rb	D9C6	6334S	CST	1:1000
Pgp	Mono/Mo	F4	P7965	Sigma-Aldrich	1:5000
Secondary antibodies					
Host	**Specificity**	**Conjugate**	**Catalog No.**	**Manufacturer**	**Dilution**
Goat	Anti-Rb IgG	HRP	7074	CST	1:5000
Horse	Anti-Mo IgG	HRP	7076	CST	1:5000

Mono—monoclonal; Rb—rabbit; Mo—mouse; CST—Cell Signaling Technology Inc.; Bioss—Bioss Antibodies, Inc.

4.8. Indirect Immunofluorescence

Indirect fluorescence analysis was performed as described previously [59]. The cells on coverslips were fixed with 3% paraformaldehyde (Sigma-Aldrich) at RT for 20 min. The samples were then permeabilized with 0.2% Triton X-100 (Sigma-Aldrich) in PBS at RT for 1 min. For the DOX and LAMP-2 colocalization analysis, 0.2% Triton was replaced with 100 µM digitonin (Sigma-Aldrich), and the cells were permeabilized at RT for 10 min. The primary and secondary antibodies used for indirect fluorescence staining are listed in Table 6. Coverslips used as negative controls were prepared by omitting the primary antibody. The cell nuclei were counterstained with 0.05% Hoechst 33342 (Life Technologies, Carlsbad, CA, USA). The coverslips with stained cells were mounted using ProLong Diamond Antifade Mountant (Thermo Fisher Scientific, Waltham, MA, USA). For fluorescence evaluation, an Olympus BX-51 microscope was used; the micrographs were captured using an Olympus DP72 CCD camera and analyzed using a Cell^P imaging system (Olympus, Tokyo, Japan).

Table 6. Primary and secondary antibodies used for indirect immunofluorescence staining.

Primary antibodies					
Antigen	**Type/Host**	**Clone**	**Catalog No.**	**Manufacturer**	**Dilution**
Pgp	Mono/Mo	F4	P7965	Sigma-Aldrich	1:100
LAMP-2	Mono/Mo	H4B4	ab25631	Abcam	1:100
Phospho-γH2A.X	Mono/Mo	3F2	MA1-2022	Invitrogen	1:100
Secondary antibodies					
Host	**Specificity**	**Conjugate**	**Catalog No.**	**Manufacturer**	**Dilution**
Donkey	Anti-Mo IgG	AF-488	A21202	Invitrogen	1:200

Mono—monoclonal; Mo—mouse.

4.9. Cell Cycle Analysis Using Propidium Iodide Staining

The treated cells were harvested from Petri dishes using Accutase (Biosera, Nuaille, France) and fixed in cold 70% ethanol (Sigma-Aldrich) at 4 °C for 30 min. The fixed cells were washed with PBS, and the pellets were carefully resuspended in 100 µL of Vindelov's staining solution (1 M Tris pH 8 (Sigma-Aldrich); 10 mM NaCl (Sigma-Aldrich); 5 µM ribonuclease A (Sigma-Aldrich); and 75 µM PI) [60]. After 30 min of incubation in Vindelov's solution at 37 °C, the stained cells were analyzed in a FACSCanto TMII flow cytometer using BD FACS DIVA Software (Beckton Dickinson, CA, USA). The fluorescence of 10,000 cells in each sample was evaluated.

4.10. Statistical Analyses

All experiments were performed in biological triplicates (unless otherwise specified). Numerical data are presented as the means $\pm$ standard deviation (SD). The data obtained by qPCR or immunoblotting were analyzed using SPSS Statistics software (version 25.0, IBM, New York, NY, USA) by unpaired Welch's *t*-test followed by the Games–Howell post hoc test. * $p < 0.05$ indicates significant differences compared with the respective control group.

References

1. Martins-Teixeira, M.B.; Carvalho, I. Antitumour Anthracyclines: Progress and Perspectives. *Chem. Med. Chem.* **2020**, *15*, 933–948. [CrossRef] [PubMed]
2. Nadas, J.; Sun, D. Anthracyclines as effective anticancer drugs. *Expert Opin. Drug Discov.* **2006**, *1*, 549–568. [CrossRef] [PubMed]
3. Cortés-Funes, H.; Coronado, C. Role of anthracyclines in the era of targeted therapy. *Cardiovasc. Toxicol.* **2007**, *7*, 56–60. [CrossRef]
4. Gewirtz, D.A. A critical evaluation of the mechanisms of action proposed for the antitumor effects of the anthracycline antibiotics adriamycin and daunorubicin. *Biochem. Pharmacol.* **1999**, *57*, 727–741. [CrossRef]
5. Marinello, J.; Delcuratolo, M.; Capranico, G. Anthracyclines as Topoisomerase II Poisons: From Early Studies to New Perspectives. *Int. J. Mol. Sci.* **2018**, *19*, 3480. [CrossRef] [PubMed]
6. Menna, P.; Paz, O.G.; Chello, M.; Covino, E.; Salvatorelli, E.; Minotti, G. Anthracycline cardiotoxicity. *Expert Opin. Drug Saf.* **2012**, *11* (Suppl. S1), S21–S36. [CrossRef] [PubMed]
7. Carvalho, C.; Santos, R.X.; Cardoso, S.; Correia, S.; Oliveira, P.J.; Santos, M.S.; Moreira, P.I. Doxorubicin: The good, the bad and the ugly effect. *Curr. Med. Chem.* **2009**, *16*, 3267–3285. [CrossRef]
8. Evison, B.J.; Sleebs, B.E.; Watson, K.G.; Phillips, D.R.; Cutts, S.M. Mitoxantrone, More than Just Another Topoisomerase II Poison. *Med. Res. Rev.* **2016**, *36*, 248–299. [CrossRef] [PubMed]
9. Capelôa, T.; Benyahia, Z.; Zampieri, L.X.; Blackman, M.C.N.M.; Sonveaux, P. Metabolic and non-metabolic pathways that control cancer resistance to anthracyclines. *Semin. Cell Dev. Biol.* **2020**, *98*, 181–191. [CrossRef]
10. Raviv, Y.; Pollard, H.B.; Bruggemann, E.P.; Pastan, I.; Gottesman, M.M. Photosensitized labeling of a functional multidrug transporter in living drug–resistant tumor cells. *J. Biol. Chem.* **1990**, *265*, 3975–3980. [CrossRef]
11. Nielsen, D.; Maare, C.; Poulsen, F.; Lauridsen, S.T.; Skovsgaard, T. Relationship between resistance, P-glycoprotein content and steady-state accumulation in five series of Ehrlich ascites tumour cell lines selected for resistance to daunorubicin. *Cell Pharmacol.* **1994**, *1*, 127–135.
12. Nielsen, D.; Maare, C.; Skovsgaard, T. Kinetics of daunorubicin transport in Ehrlich ascites tumor cells with different expression of P-glycoprotein. *Biochem. Pharmacol.* **1994**, *47*, 2125–2135. [CrossRef]
13. Shieh, M.J.; Hsu, C.Y.; Huang, L.Y.; Chen, H.Y.; Huang, F.H.; Lai, P.S. Reversal of doxorubicin-resistance by multifunctional nanoparticles in MCF-7/ADR cells. *J. Control Release* **2011**, *152*, 418–425. [CrossRef] [PubMed]

14. Cheah, H.Y.; Šarenac, O.; Arroyo, J.J.; Vasić, M.; Lozić, M.; Glumac, S.; Hoe, S.Z.; Hindmarch, C.C.; Murphy, D.; Kiew, L.V.; et al. Hemodynamic effects of HPMA copolymer based doxorubicin conjugate: A randomized controlled and comparative spectral study in conscious rats. *Nanotoxicology* **2017**, *11*, 210–222. [CrossRef]

15. Ma, P.; Mumper, R.J. Anthracycline Nano-Delivery Systems to Overcome Multiple Drug Resistance: A Comprehensive Review. *Nano Today* **2013**, *8*, 313–331. [CrossRef] [PubMed]

16. Akasov, R.; Drozdova, M.; Zaytseva-Zotova, D.; Leko, M.; Chelushkin, P.; Marc, A.; Chevalot, I.; Burov, S.; Klyachko, N.; Vandamme, T.; et al. Novel Doxorubicin Derivatives: Synthesis and Cytotoxicity Study in 2D and 3D in Vitro Models. *Adv. Pharm. Bull.* **2017**, *7*, 593–601. [CrossRef]

17. Weiss, R.B. The anthracyclines: Will we ever find a better doxorubicin? *Semin. Oncol.* **1992**, *19*, 670–686.

18. Chhikara, B.S.; Mandal, D.; Parang, K. Synthesis, anticancer activities, and cellular uptake studies of lipophilic derivatives of doxorubicin succinate. *J. Med. Chem.* **2012**, *55*, 1500–1510. [CrossRef]

19. Yu, S.; Zhang, G.; Zhang, W.; Luo, H.; Qiu, L.; Liu, Q.; Sun, D.; Wang, P.G.; Wang, F. Synthesis and biological activities of a 3′-azido analogue of Doxorubicin against drug-resistant cancer cells. *Int. J. Mol. Sci.* **2012**, *13*, 3671–3684. [CrossRef]

20. Piorecka, K.; Stanczyk, W.; Florczak, M. NMR analysis of antitumor drugs: Doxorubicin, daunorubicin and their functionalized derivatives. *Tetrahedron Lett.* **2017**, *58*, 152–155. [CrossRef]

21. Kratz, F.; Beyer, U.; Roth, T.; Tarasova, N.; Collery, P.; Lechenault, F.; Cazabat, A.; Schumacher, P.; Unger, C.; Falken, U. Transferrin conjugates of doxorubicin: Synthesis, characterization, cellular uptake, and in vitro efficacy. *J. Pharm. Sci.* **1998**, *87*, 338–346. [CrossRef] [PubMed]

22. Callaghan, R.; Luk, F.; Bebawy, M. Inhibition of the multidrug resistance P-glycoprotein: Time for a change of strategy? *Drug Metab. Dispos.* **2014**, *42*, 623–631. [CrossRef] [PubMed]

23. Ozols, R.F.; Cunnion, R.E.; Klecker, R.W., Jr.; Hamilton, T.C.; Ostchega, Y.; Parrillo, J.E.; Young, R.C. Verapamil and adriamycin in the treatment of drug-resistant ovarian cancer patients. *J. Clin. Oncol.* **1987**, *5*, 641–647. [CrossRef] [PubMed]

24. List, A.F.; Kopecky, K.J.; Willman, C.L.; Head, D.R.; Persons, D.L.; Slovak, M.L.; Dorr, R.; Karanes, C.; Hynes, H.E.; Doroshow, J.H.; et al. Benefit of cyclosporine modulation of drug resistance in patients with poor-risk acute myeloid leukemia: A Southwest Oncology Group study. *Blood* **2011**, *98*, 3212–3220. [CrossRef] [PubMed]

25. Dalton, W.S.; Grogan, T.M.; Meltzer, P.S.; Scheper, R.J.; Durie, B.G.; Taylor, C.W.; Miller, T.P.; Salmon, S.E. Drug-resistance in multiple myeloma and non-Hodgkin's lymphoma: Detection of P-glycoprotein and potential circumvention by addition of verapamil to chemotherapy. *J. Clin. Oncol.* **1989**, *7*, 415–424. [CrossRef]

26. Kim, H.G.; Hien, T.T.; Han, E.H.; Hwang, Y.P.; Choi, J.H.; Kang, K.W.; Kwon, K.I.; Kim, B.H.; Kim, S.K.; Song, G.Y.; et al. Metformin inhibits P-glycoprotein expression via the NF-κB pathway and CRE transcriptional activity through AMPK activation. *Br. J. Pharmacol.* **2011**, *162*, 1096–1108. [CrossRef]

27. Seebacher, N.A.; Richardson, D.R.; Jansson, P.J. A mechanism for overcoming P-glycoprotein-mediated drug resistance: Novel combination therapy that releases stored doxorubicin from lysosomes via lysosomal permeabilization using Dp44mT or DpC. *Cell Death Dis.* **2016**, *7*, e2510. [CrossRef]

28. Seebacher, N.; Lane, D.J.R.; Richardson, D.R.; Jansson, P.J. Turning the gun on cancer: Utilizing lysosomal P-glycoprotein as a new strategy to overcome multi-drug resistance. *Free Radic. Biol. Med.* **2016**, *96*, 432–445. [CrossRef]

29. Yamagishi, T.; Sahni, S.; Sharp, D.M.; Arvind, A.; Jansson, P.J.; Richardson, D.R. P-glycoprotein mediates drug resistance via a novel mechanism involving lysosomal sequestration. *J. Biol. Chem.* **2013**, *288*, 31761–31771. [CrossRef]

30. Jansson, P.J.; Yamagishi, T.; Arvind, A.; Seebacher, N.; Gutierrez, E.; Stacy, A.; Maleki, S.; Sharp, D.; Sahni, S.; Richardson, D.R. Di-2-pyridylketone 4,4-dimethyl-3-thiosemicarbazone (Dp44mT) overcomes multidrug-resistance by a novel mechanism involving the hijacking of lysosomal P-glycoprotein (Pgp). *J. Biol. Chem.* **2015**, *290*, 9588–9603. [CrossRef]

31. Seebacher, N.A.; Lane, D.J.R.; Jansson, P.J.; Richardson, D.R. Glucose modulation induces lysosome formation and increases lysosomotropic drug sequestration via the P-glycoprotein drug transporter. *J. Biol. Chem.* **2016**, *291*, 3796–3820. [CrossRef] [PubMed]

32. Gottesman, M.M. Multidrug resistance in cancer: Role of ATP-dependent transporters. *Nat. Rev. Cancer* **2002**, *2*, 48–58. [CrossRef] [PubMed]

33. Lovejoy, D.B.; Jansson, P.J.; Brunk, U.T.; Wong, J.; Ponka, P.; Richardson, D.R. Antitumor Activity of Metal-Chelating Compound Dp44mT Is Mediated by Formation of a Redox-Active Copper Complex That Accumulates in Lysosomes. *Cancer Res.* **2011**, *71*, 5871–5880. [CrossRef] [PubMed]

34. Gutierrez, E.M.; Seebacher, N.A.; Arzuman, L.; Kovacevic, Z.; Lane, D.J.; Richardson, V.; Merlot, A.M.; Lok, H.; Kalinowski, D.S.; Sahni, S.; et al. Lysosomal membrane stability plays a major role in the cytotoxic activity of the anti-agent, di-2-pyridylketone 4,4-dimethyl-3-thiosemicarbazone (Dp44mT). *Biochim. Biophys. Acta* **2016**, *1863*, 1665–1681. [CrossRef] [PubMed]

35. Stacy, A.E.; Palanimuthu, D.; Bernhardt, P.V.; Kalinowski, D.S.; Jansson, P.J.; Richardson, D.R. Zinc(II)-thiosemicarbazone complexes are localized to the lysosomal compartment where they transmetallate with copper ions to induce cytotoxicity. *J. Med. Chem.* **2016**, *59*, 4965–4984. [CrossRef] [PubMed]

36. Siegel, R.L.; Miller, K.D.; Jemal, A. Cancer statistics, 2016. *CA Cancer J. Clin.* **2016**, *66*, 7–30. [CrossRef] [PubMed]

37. Fruci, D.; Cho, W.C.S.; Nobili, V.; Locatelli, F.; Alisi, A. Drug Transporters and Multiple Drug Resistance in Pediatric Solid Tumors. *Curr. Drug Metab.* **2016**, *17*, 308–316. [CrossRef]

38. Vitale, I.; Galluzzi, L.; Castedo, M.; Kroemer, G. Mitotic catastrophe: A mechanism for avoiding genomic instability. *Nat. Rev. Mol. Cell Biol.* **2011**, *12*, 385–392. [CrossRef] [PubMed]

39. Chen, Z.; Zhang, D.; Yue, F.; Zheng, M.; Kovacevic, Z.; Richardson, D.R. The Iron Chelators Dp44mT and DFO Inhibit TGF-β-induced Epithelial-Mesenchymal Transition via Up-Regulation of N-Myc Downstream-regulated Gene 1 (NDRG1). *J. Biol. Chem.* **2012**, *287*, 17016–17028. [CrossRef]

40. Kuo, L.J.; Yang, L.X. Gamma-H2AX—A novel biomarker for DNA double-strand breaks. *In Vivo* **2008**, *22*, 305–309.

41. Stacy, A.E.; Palanimuthu, D.; Bernhardt, P.V.; Kalinowski, D.S.; Jansson, P.J.; Richardson, D.R. Structure-activity relationships of di-2-pyridylketone, 2-benzoylpyridine and 2-acetylpyridine thiosemicarbazones for overcoming Pgp-mediated drug resistance. *J. Med. Chem.* **2016**, *59*, 8601–8620. [CrossRef] [PubMed]

42. Hande, K.R. Etoposide: Four decades of development of a topoisomerase II inhibitor. *Eur. J. Cancer* **1998**, *34*, 1514–1521. [CrossRef]

43. Kastan, M.B.; Bartek, J. Cell-cycle checkpoints and cancer. *Nature* **2004**, *432*, 316–323. [CrossRef] [PubMed]

44. Visconti, R.; Della Monica, R.; Grieco, D. Cell cycle checkpoint in cancer: A therapeutically targetable double-edged sword. *J. Exp. Clin. Cancer Res.* **2016**, *35*, 153. [CrossRef] [PubMed]

45. Kurz, E.U.; Douglas, P.; Lees-Miller, S.P. Doxorubicin activates ATM-dependent phosphorylation of multiple downstream targets in part through the generation of reactive oxygen species. *J. Biol. Chem.* **2004**, *279*, 53272–53281. [CrossRef]

46. Bartek, J.; Lukas, J. Pathways governing G1/S transition and their response to DNA damage. *FEBS Lett.* **2001**, *490*, 117–122. [CrossRef]

47. Mustofa, M.K.; Tanoue, Y.; Tateishi, C.; Vaziri, C.; Tateishi, S. Roles of CHEK2/CHEK2 in guarding against environmentally induced DNA damage and replication-stress. *Environ. Mol. Mutagenes.* **2020**, *61*, 730–735. [CrossRef] [PubMed]

48. Rao, V.A.; Klein, S.R.; Agama, K.K.; Toyoda, E.; Adachi, N.; Pommier, Y.; Shacter, E.B. The Iron Chelator Dp44mT Causes DNA Damage and Selective Inhibition of Topoisomerase IIα in Breast Cells. *Cancer Res.* **2009**, *69*, 948–957. [CrossRef] [PubMed]

49. Banáth, J.P.; Olive, P.L. Expression of phosphorylated histone H2AX as a surrogate of cell killing by drugs that create DNA double-strand breaks. *Cancer Res.* **2003**, *63*, 4347–4350.

50. Olive, P.L. Detection of DNA damage in individual cells by analysis of histone H2AX phosphorylation. *Methods Cell Biol.* **2004**, *75*, 355–373. [CrossRef]

51. Takahashi, A.; Ohnishi, T. Does gammaH2AX foci formation depend on the presence of DNA double strand breaks? *Cancer Lett.* **2005**, *229*, 171–179. [CrossRef] [PubMed]

52. Hartwell, L.H.; Kastan, M.B. Cell cycle control and cancer. *Science* **1994**, *266*, 1821–1828. [CrossRef] [PubMed]

53. Zhou, B.B.; Elledge, S.J. The DNA damage response: Putting checkpoints in perspective. *Nature* **2000**, *408*, 433–439. [CrossRef] [PubMed]

54. Xiao, Z.; Xue, J.; Sowin, T.J.; Rosenberg, S.H.; Zhang, H. A novel mechanism of checkpoint abrogation conferred by CHEK1 downregulation. *Oncogene* **2005**, *24*, 1403–1411. [CrossRef] [PubMed]

55. Richardson, D.R.; Tran, E.H.; Ponka, P. The potential of iron chelators of the pyridoxal isonicotinoyl hydrazone class as effective antiproliferative agents. *Blood* **1995**, *86*, 4295–4306. [CrossRef]

56. Krzyzankova, M.; Chovanova, S.; Chlapek, P.; Radsetoulal, M.; Neradil, J.; Zitterbart, K.; Sterba, J.; Veselska, R. LOX/COX inhibitors enhance the antineoplastic effects of all-trans retinoic acid in osteosarcoma cell lines. *Tumor Biol.* **2014**, *35*, 7617–7627. [CrossRef]

57. Lovejoy, D.B.; Sharp, D.M.; Seebacher, N.; Obeidy, P.; Prichard, T.; Stefani, C.; Basha, M.T.; Sharpe, P.C.; Jansson, P.J.; Kalinowski, D.S.; et al. Novel Second-Generation Di-2-Pyridylketone Thiosemicarbazones Show Synergism with Standard Chemotherapeutics and Demonstrate Potent Activity against Lung Cancer Xenografts after Oral and Intravenous Administration in Vivo. *J. Med. Chem.* **2012**, *55*, 7230–7244. [CrossRef]

58. Chou, T.C. Theoretical basis, experimental design, and computerized simulation of synergism and antagonism in drug combination studies. *Pharmacol. Rev.* **2006**, *58*, 621–681. [CrossRef]

59. Mikulenkova, E.; Neradil, J.; Zitterbart, K.; Sterba, J.; Veselska, R. Overexpression of the ΔNp73 isoform is associated with centrosome amplification in brain tumor cell lines. *Tumor. Biol.* **2015**, *36*, 7483–7491. [CrossRef]

60. Vindeløv, L.L.; Christensen, I.J.; Nissen, N.I. A detergent-trypsin method for the preparation of nuclei for flow cytometric DNA analysis. *Cytometry* **1983**, *3*, 323–327. [CrossRef] [PubMed]

APPENDIX 8

Macsek P, **Skoda J**, Krchniakova M, Neradil J, Veselska R. Iron-Chelation Treatment by Novel Thiosemicarbazone Targets Major Signaling Pathways in Neuroblastoma. *International Journal of Molecular Sciences*. 2022;23(1):376. (JCR 2022; IF = 5.6, Q1 - Biochemistry & Molecular Biology)

Iron-Chelation Treatment by Novel Thiosemicarbazone Targets Major Signaling Pathways in Neuroblastoma

Peter Macsek [1,2], Jan Skoda [1,2], Maria Krchniakova [1], Jakub Neradil [1,2,3,*,†] and Renata Veselska [1,2,3,†]

1 Laboratory of Tumor Biology, Department of Experimental Biology, Faculty of Science, Masaryk University, 601 77 Brno, Czech Republic; macsek@mail.muni.cz (P.M.); janskoda@sci.muni.cz (J.S.); maria.krchniakova@mail.muni.cz (M.K.); veselska@sci.muni.cz (R.V.)
2 International Clinical Research Center, St. Anne's University Hospital, 656 91 Brno, Czech Republic
3 Department of Pediatric Oncology, Faculty of Medicine, University Hospital Brno, Masaryk University, 662 63 Brno, Czech Republic
* Correspondence: jneradil@sci.muni.cz; Tel.: +420-549-49-6003
† These authors contributed equally to this work.

Abstract: Despite constant advances in the field of pediatric oncology, the survival rate of high-risk neuroblastoma patients remains poor. The molecular and genetic features of neuroblastoma, such as *MYCN* amplification and stemness status, have established themselves not only as potent prognostic and predictive factors but also as intriguing targets for personalized therapy. Novel thiosemicarbazones target both total level and activity of a number of proteins involved in some of the most important signaling pathways in neuroblastoma. In this study, we found that di-2-pyridylketone 4-cyclohexyl-4-methyl-3-thiosemicarbazone (DpC) potently decreases N-MYC in *MYCN*-amplified and c-MYC in *MYCN*-nonamplified neuroblastoma cell lines. Furthermore, DpC succeeded in downregulating total EGFR and phosphorylation of its most prominent tyrosine residues through the involvement of NDRG1, a positive prognostic marker in neuroblastoma, which was markedly upregulated after thiosemicarbazone treatment. These findings could provide useful knowledge for the treatment of MYC-driven neuroblastomas that are unresponsive to conventional therapies.

Keywords: thiosemicarbazone; DpC; neuroblastoma; MYC; EGFR; NDRG1; lipid droplet

1. Introduction

Neuroblastoma is a rare solid neuroendocrine tumor arising from neural crest derivates in the developing sympathetic nervous system. Subsequently, the adrenal medulla and sympathetic ganglia are the most common sites of the primary disease. Generally affecting infants aged 18 months or younger, neuroblastoma is traditionally categorized into three risk groups [1]. Low-risk neuroblastomas (50% of cases) often undergo spontaneous regression without the need for surgical intervention [2]. Intermediate-risk group patients, while likely to undergo surgical and chemotherapeutic intervention (usually containing carboplatin, cyclophosphamide, doxorubicin, and etoposide), still have a high 5-year overall survival (OS) rate of ~90% [1,3,4]. Treatment of high-risk patients usually involves surgical resection, chemo- and radiotherapy, differentiation therapy by isotretinoin, myeloablative therapy followed by stem cell transplantation, or additional procedures, such as immunotherapy [5]. However, the survival rate of high-risk neuroblastoma patients remains low and the 5-year OS rate has plateaued at only 50% [4].

Along with age at diagnosis, histology status, and chromosomal aberrations (1p and/or 11q deletion), *MYCN* amplification ranks as one of the most important prognostic factors in neuroblastoma [6–8]. Along with its structural homologs c-MYC and L-MYC, N-MYC represents one of the most potent master regulators of cell fate, proliferation, and metabolism, affecting the expression of more than 15% of all human genes [9]. Being established as one of the most prominent stem cell factors, elevated expression of MYC was

linked not only to sustaining but also to inducing undifferentiated phenotype in various cell types [10]. Indeed, their reprogramming potential further signifies the oncogenic role of *MYC* genes, explaining their dysregulation in up to 70% of human cancers [11]. *MYCN* amplification is of particular interest as it accounts for approximately 20% of neuroblastoma cases and is strongly associated with a malignant course of disease and poor survival, even in localized disease. This makes N-MYC an intriguing molecular target for the treatment of *MYCN*-amplified neuroblastomas. In *MYCN*-nonamplified neuroblastomas, high c-MYC levels indicate an identical clinical outcome to that of *MYCN*-amplified, further proving their functional overlap [12] and establishing c-MYC as a hallmark of an unfavorable course of this cancer type [13]. The importance of MYC oncoproteins in cancer pathogenesis cannot be overstated as dysregulation of these transcription factors alone is sufficient to promote genome instability and initiate malignant transformation [14]. Conversely, downregulation of MYC oncoproteins leads to the induction of transient [15] or even sustained [16] loss of the neoplastic phenotype. However, given the largely "undruggable" properties of MYC, clinically applicable MYC-directed therapies remain elusive and the focus has shifted to targeting proteins regulating the stability of MYC oncoproteins, disrupting protein–protein interactions with MYC cofactors or exploiting dependencies of MYC-addicted tumor cells [17].

Thiosemicarbazone-based chelators have been the subject of study for over 15 years. These low-molecular-weight, metal-binding compounds have been shown to have promising pharmacological effects on cancer cells through a variety of mechanisms [18]. By generating oxidative stress inside lysosomes, to which they are sequestered by P-glycoprotein, novel thiosemicarbazones were reported to contribute to overcoming multidrug resistance. This is caused by the formation of redox-active complexes, which results in the induction of lysosomal membrane permeabilization [19]. On a physiological level, thiosemicarbazones were found to regulate various cancer hallmarks, such as proliferation, epithelial–mesenchymal transition, and migration, many of which are credited to thiosemicarbazones' ability to induce N-myc downstream regulated gene 1 (NDRG1) expression [20–22]. NDRG1-mediated effects are particularly intriguing, since NDRG1 has proved to be a promising positive prognostic factor in neuroblastoma [23].

NDRG1 is a structural gene encoding the regulatory protein NDRG1, which belongs to the four-member NDRG family of the alpha/beta hydrolase superfamily. NDRG1, however, does not elicit hydrolytic function, and its exact mechanism of action remains largely elusive. As its name suggests, NDRG1 is suppressed by N-MYC at the transcriptional level. N-MYC binds to the NDRG1 promoter in an MIZ-1-dependent manner and effectively downregulates the expression of NDRG1 [24,25]. Importantly, NDRG1 was found to be a positive prognostic factor in neuroblastoma, regardless of the *MYCN* amplification status, which suggests a functional role of NDRG1 on its own in addition to its role as a marker of N-MYC dysregulation in neuroblastoma [23]. NDRG1 has been reported to exert both oncogenic and tumor-suppressive properties in different tumor types. NDRG1 inhibited cell proliferation and migration in endometrial carcinoma [26]; sensitized cells to TRAIL-mediated apoptosis in colorectal carcinoma [27]; and reduced EGFR and HER2 levels, dimer formation, and subsequent signalization in ovarian carcinoma [28]. In contrast, NDRG1 was linked with poor differentiation and prognosis in hepatocellular carcinoma [29] and mediated chemoresistance to alkylating agents in glioblastoma [30]. However, its correlation with better prognoses and overall patient survival in neuroblastoma makes NDRG1 a target worth investigating in this pediatric malignancy.

NDRG1 has been reported to exert broad antitumor activity by downregulating various proto-oncogenic signaling molecules, notably RAS, ERK, PI3K, AKT, and SRC [31–33]. Such a broad effect indicates that NDRG1 is a master regulator of a more upstream signaling protein. Consequently, the role of NDRG1 in receptor tyrosine kinase (RTK) regulation was investigated. NDRG1 was found to regulate several members of the ERBB receptor tyrosine kinase family, namely EGFR. In human pancreatic (PANC-1) and colorectal (HT-29) adenocarcinoma cell lines, NDRG1 markedly reduced total EGFR levels, inhibited EGFR

dimerization and activation, and lowered EGFR phosphorylation even in the presence of EGF [34]. The tumor-suppressive functions of NDRG1 were further elucidated in pancreatic carcinoma. In the PANC-1 cell line, NDRG1 promoted EGFR downregulation by facilitating its lysosomal/endosomal degradation. This interaction was mediated by a negative EGFR regulator, MIG-6, which was in turn upregulated by increased NDRG1 levels [35].

Thiosemicarbazones have been already proved efficient against neuroblastoma cells by our group and others [22,36], which makes neuroblastoma an intriguing target for the study of the molecular effects of novel thiosemicarbazones. Our initial results in a single neuroblastoma cell line also suggest that di-2-pyridylketone 4-cyclohexyl-4-methyl-3-thiosemicarbazone (DpC) can potently induce NDRG1 expression in these cells. Here, we therefore aimed to investigate the molecular effects of DpC on a panel of neuroblastoma cell lines to evaluate its impact on some of the most prominent molecules (MYC oncoproteins, NDRG1, and EGFR) in neuroblastoma.

2. Results

2.1. DpC Inhibits EGFR and Its Phosphorylated Forms through NDRG1

Initially, we evaluated the dose-dependent potency of DpC to induce cell death in various neuroblastoma cell lines and found that 20 µM DpC induces a similar response in both the *MYCN*-nonamplified cell line SH-SY5Y and the *MYCN*-amplified cell line SK-N-BE(2), killing half of the cells within 24 h (Figures S1 and S2). However, CHLA-15 and CHLA-20 were treated with only 2 µM DpC, as the former concentration killed nearly all the cells by the end of the first day of treatment. The 2 µM concentration was chosen as it succeeded in inducing a comparable effect on proliferation in these cell lines (Figure S2).

After establishing the potency of DpC in inducing cell death, we focused on investigating its potency in upregulating NDRG1, a positive prognostic factor in neuroblastoma. Cells were exposed to DpC in the medium for 24 and 48 h, and the changes in NDRG1 protein levels were analyzed by Western blotting. DpC efficiently induced marked NDRG1 expression across all tested cell lines (Figure 1A), as well as phosphorylated NDRG1, whose increase mimicked that of NDRG1 (Figures S3 and S4).
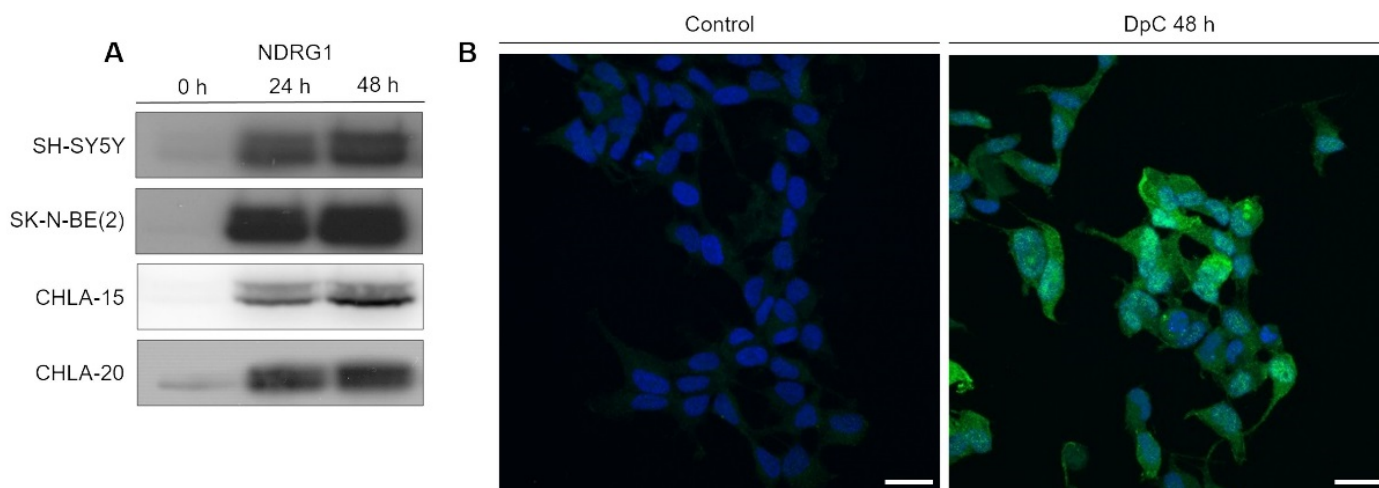
Figure 1. NDRG1 is upregulated in neuroblastoma cells in response to iron-chelation therapy by DpC. (**A**) Immunoblotting of NDRG1 protein levels in neuroblastoma cell lines treated with 20 µM (SH-SY5Y, SK-N-BE(2)) or 2 µM (CHLA-15, CHLA-20) DpC. Representative images of three independent experiments. Source data are provided in Figure S1. (**B**) Massive increase of NDRG1 (green) expression in DpC-treated cells in comparison to control. Immunofluorescence micrographs of SH-SY5Y cells treated with 20 µM DpC for 48 h. Nuclei counterstained with Hoechst 33342 (blue). Scale bar: 20 µm.

To determine NDRG1′s subcellular localization and validate the change in its expression in response to DpC treatment, immunofluorescence analysis was performed in SH-SY5Y neuroblastoma cells. The results were in accordance with the Western blot analysis, and highly upregulated expression of NDRG1 was observed in DpC-treated SH-SY5Y cells that exhibited both cytoplasmic and nuclear patterns of NDRG1 signal (Figure 1B).

Having confirmed the potency of DpC in inducing NDRG1, we tested its effect on EGFR signaling, as was previously reported in carcinoma models [34]. Indeed, DpC succeeded in moderately decreasing the levels of total EGFR over the course of 2 days in all tested neuroblastoma cell lines (Figure 2 and Figure S3).
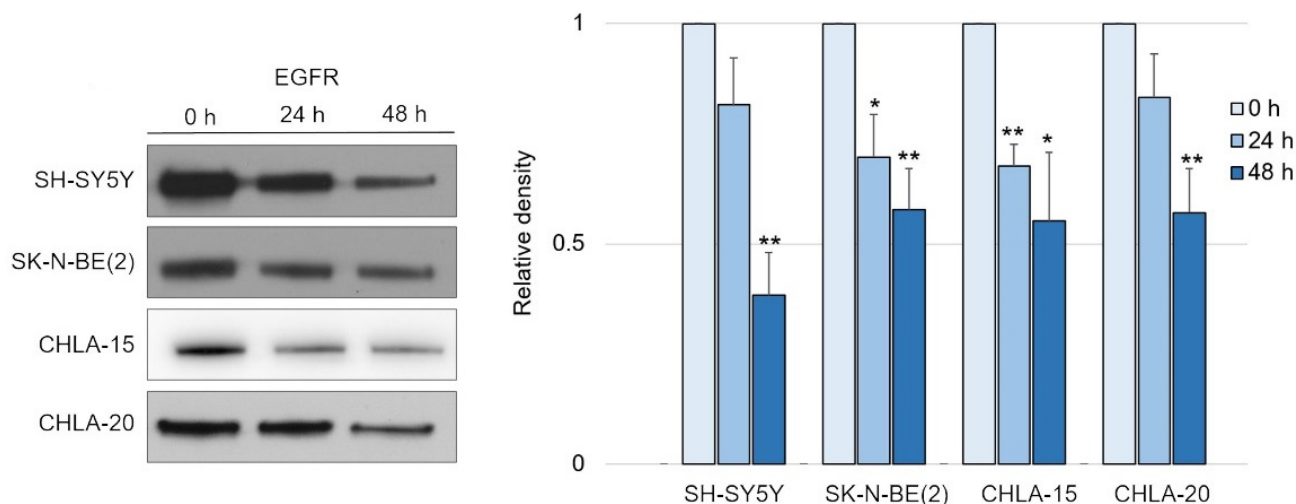
Figure 2. EGFR is downregulated in response to iron-chelation therapy by DpC. Immunoblotting of EGFR protein levels in neuroblastoma cell lines treated with 20 μM (SH-SY5Y, SK-N-BE(2)) or 2 μM (CHLA-15, CHLA-20) DpC. Representative images (**left**) and relative optical density values (**right**) of three independent experiments. Source data are provided in Figure S1. Densitometry data are shown as the mean ± SD normalized to 0 h values. * $p < 0.05$; ** $p < 0.01$, two-tailed unpaired *t*-test.

Following this finding, it was crucial to determine whether the decrease in EGFR levels was mediated by NDRG1 induced after treatment with DpC. To study the role of NDRG1 in EGFR inhibition, siRNA-mediated silencing of NDRG1 expression was performed. Transfection with NDRG1-targeted siRNAs potently decreased NDRG1 protein levels in SH-SY5Y cells (Figure 3A), whereas only a moderate decrease was observed in SK-N-BE(2) cells (Figure 3B). In accordance with these observations, silencing NDRG1 in SH-SY5Y cells rescued the EGFR downregulation induced by DpC, thus confirming the role of NDRG1 in the regulation of EGFR expression (Figure 3A). However, this effect was not observed in SK-N-BE(2) cells, which showed only moderate NDRG1 silencing (Figure 3B), which suggests that the decrease in NDRG1 levels might have been insufficient to rescue EGFR expression. Alternatively, DpC could regulate EGFR through a different mechanism in this cell line. One such possibility was explored by Hossain et al. [37], elucidating mutual regulation between EGFR and N-MYC in *MYCN*-amplified neuroblastoma cell lines such as SK-N-BE(2).

Aside from the inhibitory effect of DpC on total EGFR protein levels, phosphorylated forms of the receptor were also of interest, as they confer the transduction of signals downstream of their molecular targets. Five phosphorylation sites at EGFR were selected, and the levels of their phosphorylation were determined in regard to DpC treatment in the SH-SY5Y cell line. Selected phosphotyrosine residues facilitate the transduction of signals toward some of the most prominent signaling pathways regulated by EGFR activation (Y845: SRC–FAK axis, Y992: PLC-γ–PKC axis, Y1045: c-CBL, Y1068 and Y1148: AKT-bound and RAS-bound signaling pathways) [38]. Similar to the total EGFR protein level, all examined phosphotyrosine forms were also downregulated by DpC treatment (Figure 4A).

EGFR phosphorylated at residues Y845 (pY845-EGFR) and Y1148 (pY1148-EGFR) was decreased most significantly ($p < 0.01$), while the downregulation at Y1045 (pY1045-EGFR, responsible for the negative feedback loop pathway of EGFR via c-CBL) was the least prominent, albeit still significant ($p < 0.05$) (Figure 4A). Importantly, EGFR phosphorylated at Y1068 (one of the most significant phosphotyrosine residues playing a pivotal role in EGFR-mediated activation of RAS) was downregulated even when stimulated by EGF (40 ng/mL; 15 min; 37 °C). Immunofluorescence analysis showed the expected receptor internalization after its stimulation with EGF and confirmed the inhibitory effect of DpC on pY1068-EGFR in cells both unstimulated and stimulated by EGF ligand; a marked decrease in the pEGFR signal was detected, and its localization shifted from predominantly membranous to the form of a single perinuclear cluster, presumably a stress granule (Figure 4B). To quantify the effect of DpC on pEGFR (Y1068), flow cytometry analysis was performed, which confirmed a significant decrease in Y1068 phosphorylation ($p < 0.05$) (Figure 4C).
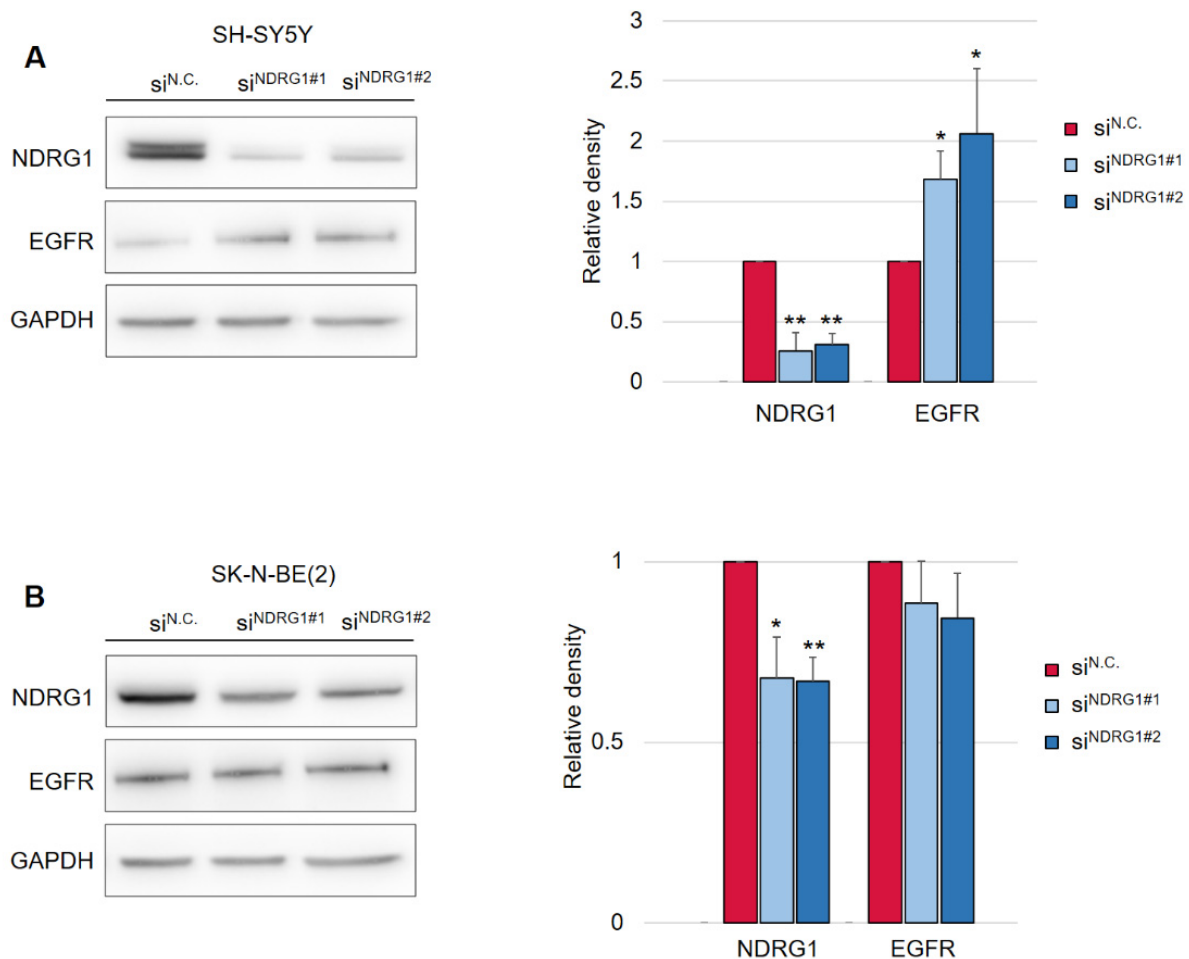
Figure 3. Silencing of NDRG1 rescues the effect of DpC on total levels of EGFR in the SH-SY5Y cell line but not in SK-N-BE(2). (**A**) Immunoblotting of NDRG1 and EGFR protein levels in SH-SY5Y cells treated with 20 μM DpC for 48 h and specific siRNAs for NDRG1 (siNDRG1#1 and siNDRG1#2) or negative silencer control (siN.C.). (**B**) Immunoblotting of NDRG1 and EGFR protein levels in SK-N-BE(2) cells treated with 20 μM DpC for 48 h and specific siRNAs for NDRG1 (siNDRG1#1 and siNDRG1#2) or negative silencer control (siN.C.). Representative images (**left**) and relative optical density values (**right**) of three independent experiments. Densitometry data are shown as the mean ± SD normalized to siN.C. values. * $p < 0.05$; ** $p < 0.01$; two-tailed unpaired *t*-test.
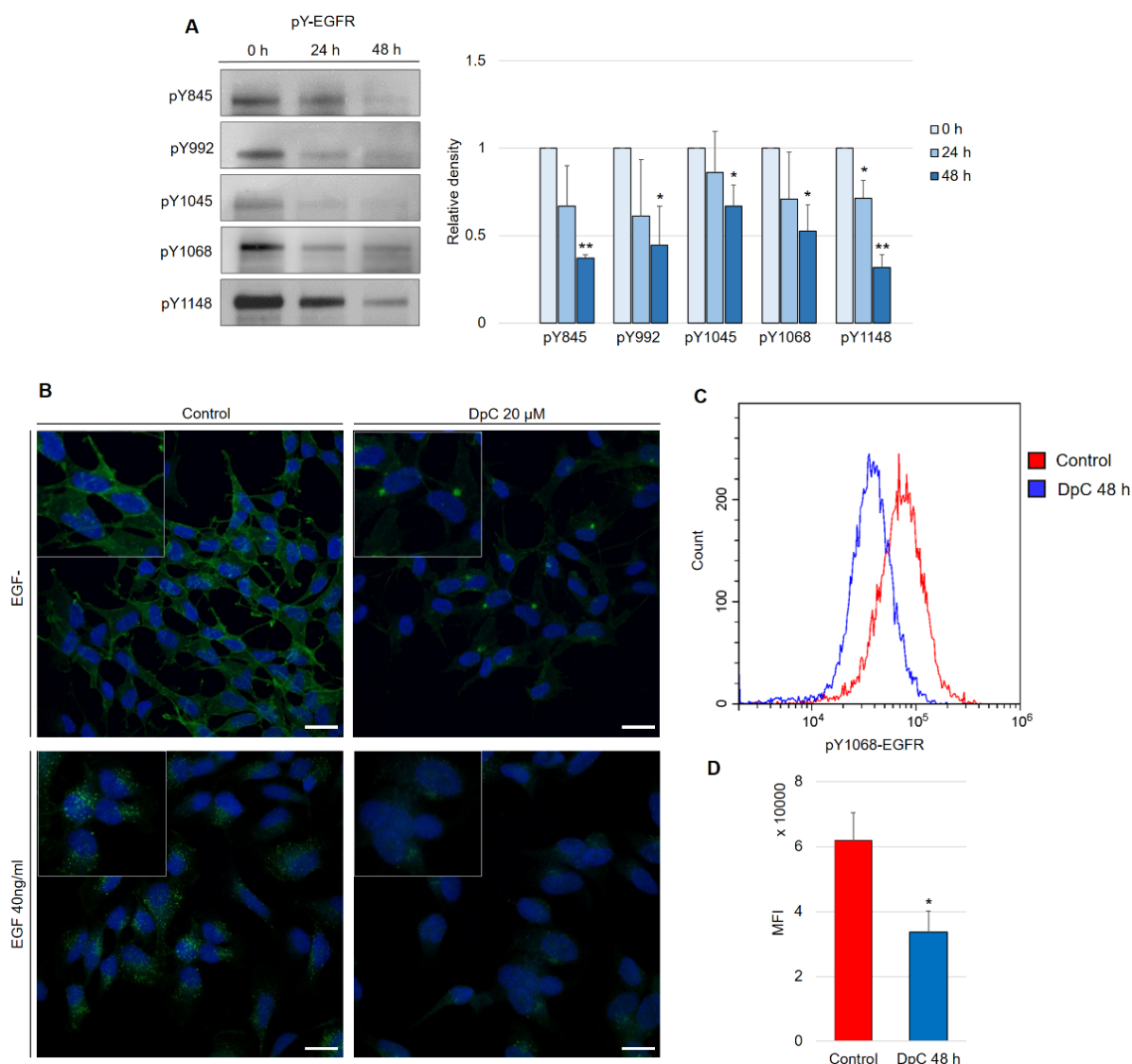
Figure 4. DpC downregulates the levels of phosphotyrosine-EGFR. (**A**) Immunoblotting of phosphorylated forms of EGFR in the SH-SY5Y neuroblastoma cell line treated with 20 μM DpC. Representative images (**left**) and relative optical density values (**right**) of three independent experiments. Source data are provided in Figure S1. Densitometry data are shown as the mean ± SD normalized to 0 h values. * $p < 0.05$; ** $p < 0.01$; two-tailed unpaired t-test. (**B**) Immunofluorescence micrographs of EGFR (green) in SH-SY5Y cells treated with 20 μM DpC and EGF (40 ng/mL; 10 min; 37 °C). Nuclei counterstained with Hoechst 33342 (blue). Scale bar: 20 μm. (**C,D**) Quantification of pY1068-EGFR protein levels in response to DpC treatment (20 μM; 48 h) in SH-SY5Y cells. Median fluorescence intensity (MFI) ± SD comprised of three independent experiments. * $p < 0.05$; ** $p < 0.01$; two-tailed unpaired t-test.

2.2. DpC Induces a Stress Response and the Activation of AKT Effectors

Having established the effects of DpC treatment on EGFR, a molecular target known for its broad range of effectors, proteome profiler arrays were used to identify downstream targets most affected by DpC treatment.

First, to evaluate the nature of the stress response elicited on 24 and 48 h of treatment with 20 μM DpC in the SH-SY5Y reference cell line, the Proteome Profiler Human Cell Stress Kit was used (Figure 5A). As expected, a sharp increase in HIF1A was detected due to DpC's iron-chelation activity, reaffirming its role in NDRG1 activation, as well as the activation of other hypoxia-regulated proteins, such as carbonic anhydrase. This

was further confirmed by immunofluorescence assay, reporting a sharp increase in HIF1A nuclear localization (Figure S5), supporting the previous studies reporting that HIF1 drives the expression of NDRG1 [39,40]. Furthermore, the response exhibited a distinct temporal variation (Figure 5B): increases in p27, SOD2, NFκB, and SIRT2 were characteristic of the early phases of the cell stress response (Figure 5A, 24 h), the latter three being particularly attributed to the oxidative stress response [41,42]. Gradual upregulation of HSP60, HIF2A, and Cited-2 as well as phosphorylated HSP27 (S78/S82), p38 (T180/Y182), and p53 (S46) defined the later stages of the stress response to 48 h DpC treatment (Figure 5A, 48 h).
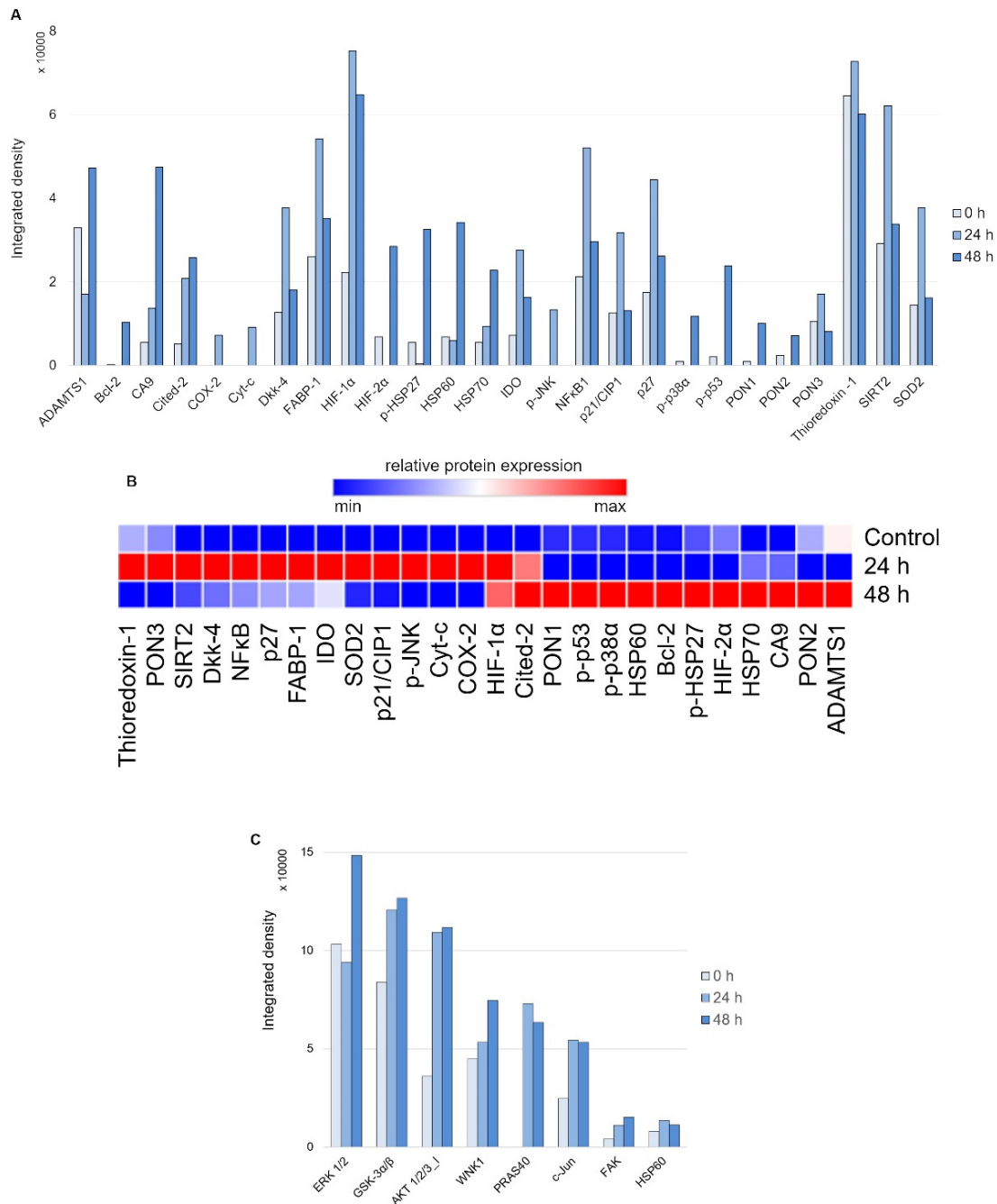
Figure 5. Array profiling of stress response proteins and kinase phosphorylation in response to DpC in the SH-SY5Y cell line. (**A**) Stress response protein profile of cells treated with 20 μM DpC for 24 and 48 h. (**B**) Hierarchical clustering of relative stress protein expression. (**C**) Phospho-kinase protein profile of cells treated with 20 μM DpC for 24 and 48 h.

Second, to examine the differential phosphorylation rate of proteins that might be regulated downstream of RTKs (including EGFR) in response to DpC treatment, the Proteome Profiler Human Phospho-Kinase Array Kit was used (Figure 5C). Interestingly, the results indicated an upregulated mode of the AKT signaling pathway. DpC treatment led to an increase in activating phosphorylation of AKT 1/2/3 (S473) together with phosphorylation of its downstream effectors and an increase in AKT-mediated activating phosphorylation of PRAS40 (T246), inhibitory phosphorylation of GSK3α/β (S21/S9), and activating phosphorylation of WNK1 (T60). WNK1 activation is of particular interest as it is reported to play a role in oxidative stress response [43]. Similarly, upregulation of c-JUN phosphorylation has been noted as a response to ROS-generating, iron-chelation treatment [44], which suggests that different iron chelators indeed elicit a similar stress response.

In contrast to what was expected after observing EGFR downregulation, the activation of the AKT pathway in general led us to further investigate the manner of AKT activity in response to DpC treatment. Interestingly, a consistent pattern of regulation was detected across all neuroblastoma cell lines, with little variation among them. While the total AKT levels decreased by approximately 25% in response to DpC treatment (Figure 6A), the levels of phosphorylated AKT (S473) showed a marked increase (Figure 6B), consistent with the previous results from phospho-kinase array analysis. While the increase in AKT phosphorylation was significant only after the first 24 h of DpC application, the levels of pAKT remained elevated throughout the 48 h treatment in all studied cell lines, with the exception of the CHLA-15 cell line.
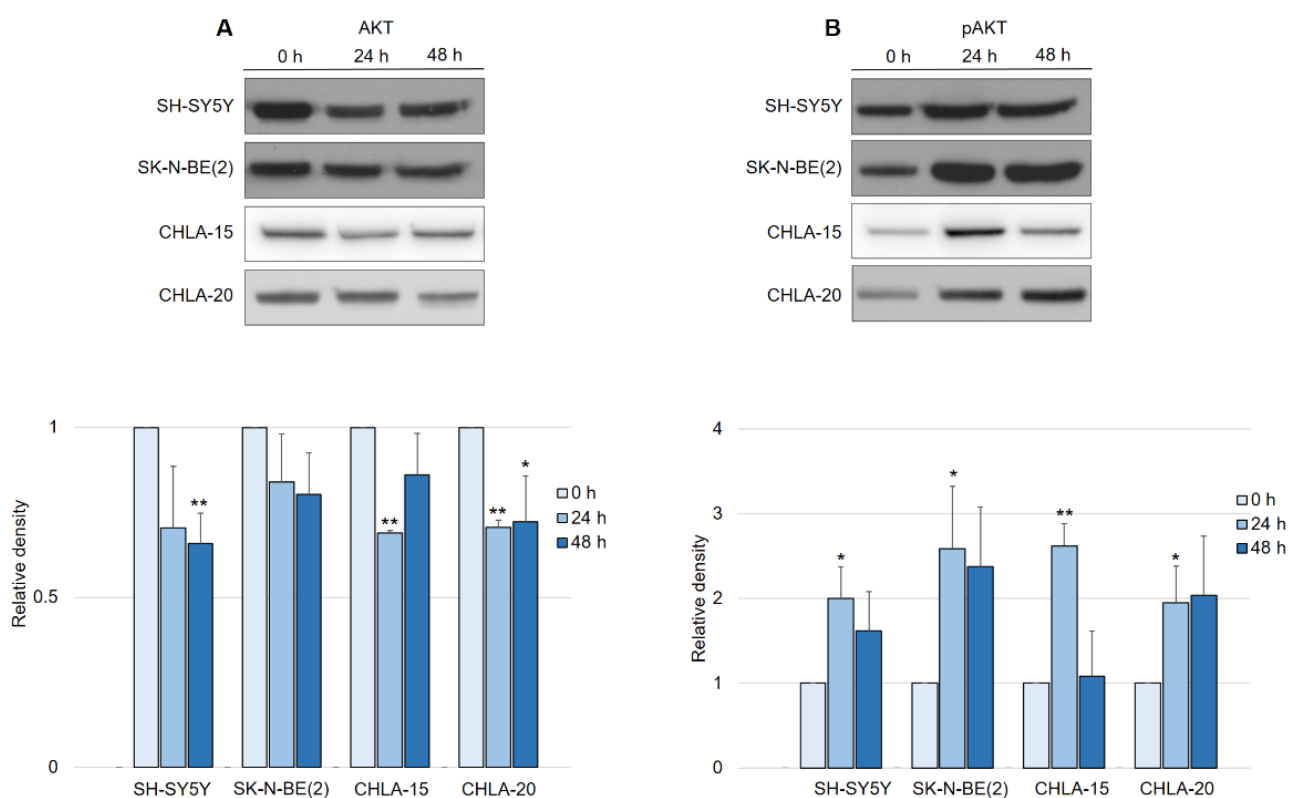
Figure 6. DpC regulates total and phosphorylated AKT protein levels in neuroblastoma cell lines. (**A**) Immunoblotting of AKT and (**B**) immunoblotting of pAKT (S473) protein levels in neuroblastoma cells treated with 20 μM (SH-SY5Y, SK-N-BE(2)) or 2 μM (CHLA-15, CHLA-20) DpC. Representative images (**up**) and relative optical density values (**down**) of three independent experiments. Source data are provided in Figure S1. Densitometry data are shown as the mean ± SD normalized to 0 h values. * $p < 0.05$; ** $p < 0.01$; two-tailed unpaired *t*-test.

2.3. DpC Inhibits MYC Proteins Regardless of the MYCN Amplification Status

Although DpC-induced, HIF1-mediated expression of NDRG1 has already been elucidated, it appears that this is not the only mode of NDRG1 activation [45]. We report that DpC markedly decreases the levels of the well-established NDRG1 suppressor N-MYC [46] and its structural and functional homolog c-MYC [47,48]. Inhibition of N-MYC/c-MYC alleviated the suppression of the NDRG1 promoter and further enhanced the HIF1-mediated expression of NDRG1. Indeed, DpC treatment dramatically reduced the N-MYC oncoprotein *MYCN*-amplified SK-N-BE(2) cell line, as well as c-MYC in all other *MYCN*-nonamplified cell lines, SH-SY5Y, CHLA-15, and CHLA-20 (Figure 7A; Figure S3). In the SH-SY5Y cell line, the nuclear localization of c-MYC was markedly decreased after treatment, thus validating the results obtained from immunoblotting analysis (Figure 7B).
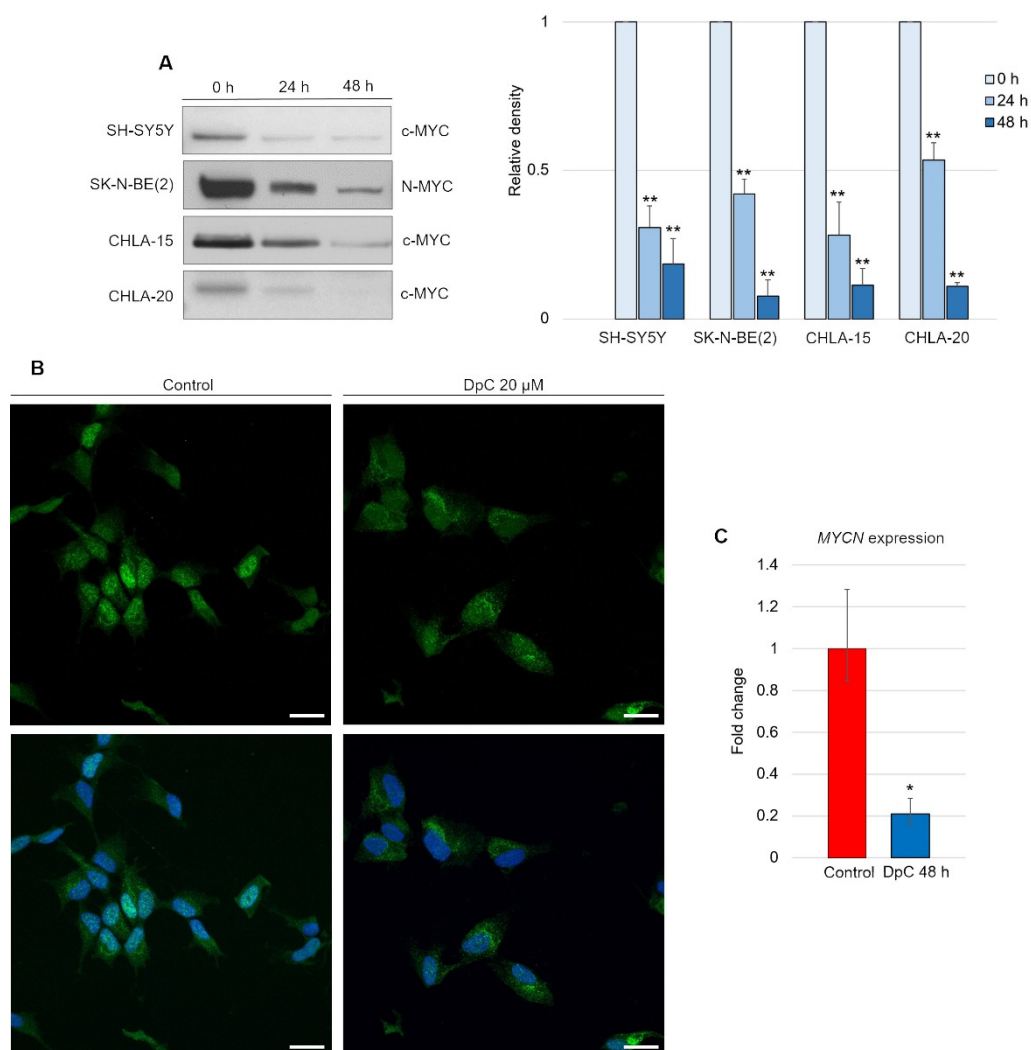
Figure 7. DpC downregulates MYC proteins in neuroblastoma cell lines. (**A**) Immunoblotting of c-MYC (SH-SY5Y, CHLA-15, CHLA-20) and N-MYC (SK-N-BE(2)) protein levels in neuroblastoma cells treated with 20 μM (SH-SY5Y) or 2 μM (CHLA-15, CHLA-20) DpC. Representative images (**left**) and relative optical density values (**right**) of three independent experiments. Source data are provided in Figure S1. Densitometry data are shown as the mean ± SD normalized to 0 h values. * $p < 0.05$; ** $p < 0.01$; two-tailed unpaired *t*-test. (**B**) Immunofluorescence micrographs of c-MYC (green) in SH-SY5Y cells treated with 20 μM DpC and EGF (40 ng/mL; 10 min; 37 °C). Nuclei counterstained with Hoechst 33342 (blue). Scale bar = 20 μm. (**C**) qRT–PCR analysis of the effect of 20 μM DpC on the expression of *MYCN* in the SK-N-BE(2) cell line. Fold change ± SD comprised of three independent experiments. * $p < 0.05$; ** $p < 0.01$; two-tailed unpaired *t*-test.

To elucidate whether DpC downregulates N-MYC at the transcriptional level, qRT–PCR was performed. Significant downregulation of *MYCN* transcripts ($p < 0.05$) was detected in DpC-treated SK-N-BE(2) cells (Figure 7C), which suggests that DpC might exert its activity against neuroblastoma cells via transcriptional inhibition of MYC oncoproteins, which are major drivers of aggressive neuroblastoma.

2.4. DpC Induces Morphological Changes and Lipid Accumulation in Neuroblastoma Cells

An intriguing morphological change was detected during routine microscopic analysis of DpC-treated neuroblastoma cells. The cytoplasm of these cells contained large spherical bodies (Figure 8A), which were identified as neutral lipid droplets and confirmed by bright-field imaging after staining with lipophilic Oil Red O and through fluorescence imaging after staining with LipidTOX™ Green (Figure 8B). Interestingly, the accumulation of neutral lipid droplets has already been reported by Zirath et al. [49] in SK-N-BE(2) neuroblastoma cells treated with N-MYC inhibitors. Here, we observed an identical phenotype in yet another neuroblastoma cell line: *MYCN*-nonamplified SH-SY5Y (Figure 8A). When quantified by flow cytometry after neutral lipid staining by LipidTOX™ Green, DpC treatment resulted in a significant (approximately 6-fold) increase in lipid accumulation (Figure 8C). This shows that various modes of MYC protein inhibition result in identical phenotypes and suggests a common role of MYC proteins in lipid metabolism/trafficking.
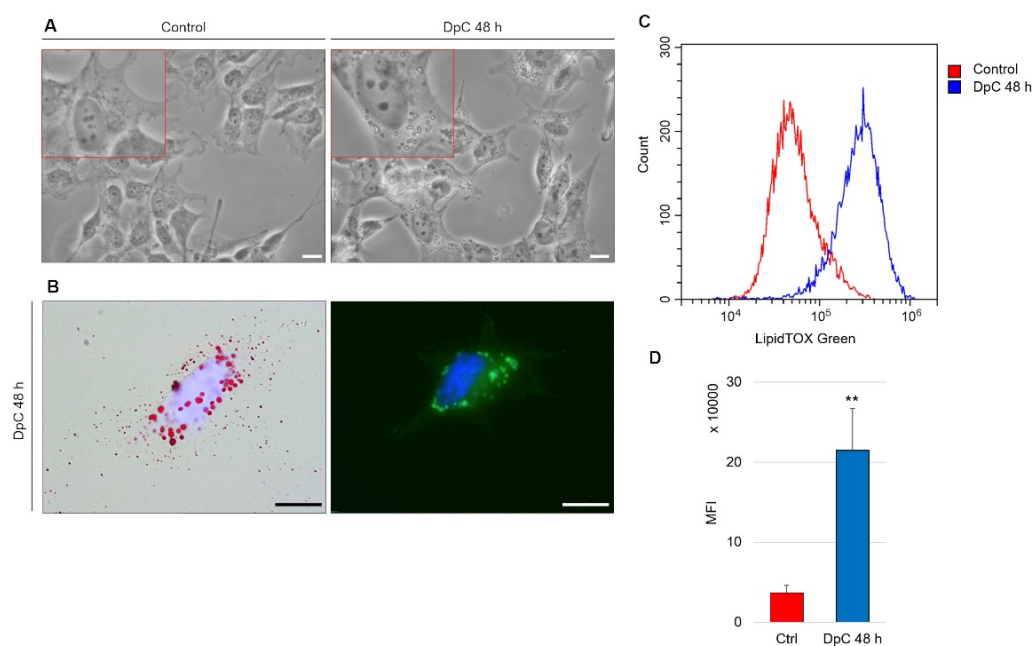
Figure 8. Lipid accumulation in SH-SY5Y neuroblastoma cells in response to DpC treatment. (**A**) Light-microscopy micrograms revealing spherical bodies in the cytoplasm of SH-SY5Y cells. (**B**) Neutral lipid staining of DpC-treated cells by Oil Red O (red, **left**) and LipidTOX™ Green (green, **right**). Nuclei counterstained with Hoechst 33342 (blue). Scale bar: 20 μm. (**C**,**D**) Increase in the median fluorescence intensity (MFI) of LipidTOX™ Green emission after DpC treatment. MFI ± SD comprised of three independent experiments. ** $p < 0.01$.

3. Discussion

Elucidating the role of thiosemicarbazone treatment in neuroblastoma cell lines at the molecular level proved to be a natural continuation of several previous observations: DpC succeeded in inhibiting growth as well as inducing cell death in neuroblastoma cells and increasing the levels of caspase 3 and 9 as well as phosphorylated JNK [22]. Moreover, thiosemicarbazone treatment greatly increases NDRG1 levels [50], a positive prognostic factor in neuroblastoma [23]. DpC sequesters cellular iron, which drives cells into a hypoxia-like state, and subsequently activates HIF1, as previously described [40],

which was in concordance with our observation in the SH-SY5Y cell line (Figure S2). However, HIF1-mediated induction of NDRG1 expression (i.e., HIF1 binding to the HIF1-responsive element of the NDRG1 promoter) does not seem to be the only mode of NDRG1 upregulation by thiosemicarbazone treatment [45]. Iron-chelation treatment by DFO was reported to inhibit the expression of a well-known NDRG1 suppressor, N-MYC [51].

For the first time, we hereby report that DpC also markedly decreases the levels of N-MYC, as well as its structural and functional homolog c-MYC, both of which are known to bind to the core promoter of NDRG1 in an MIZ-1-dependent manner [25]. Our results indicate that DpC-mediated inhibition of MYC proteins alleviated the suppression of NDRG1 expression and further enhanced the expression of NDRG1. In the *MYCN*-amplified SK-N-BE(2) cell line, the level of the N-MYC oncoprotein decreased greatly, as did c-MYC in all other *MYCN*-nonamplified cell lines (SH-SY5Y, CHLA-15, CHLA-20). On a subcellular level, nuclear c-MYC localization decreased greatly, which further confirms the effect of DpC on this transcription factor. Generally, iron chelators are known for their ability to induce cell arrest and inhibit the function of iron-dependent enzymes, such as ribonucleotide reductase and DNA polymerase α [52,53]. However, the inhibition of these enzymes was reportedly not responsible for the decrease in N-MYC levels in response to iron-chelation treatment [51]. The decrease in MYC proteins by DpC thus seems to be facilitated through a different mechanism.

Downregulation of MYC proteins bears significance beyond facilitating the liberation of NDRG1 expression. Deregulated in over half of all human cancers [54] and established as one of the prominent cancer stem cell markers in neuroblastoma [55], MYC oncoproteins represent an intriguing target for cancer therapy. DpC treatment significantly decreased MYC protein levels across all neuroblastoma cell lines, which suggests promising new therapy strategies, especially in *MYCN*-amplified neuroblastomas, which account for approximately 20% of cases and rank among those with the most difficult course of the disease [1]. DpC suppressed *MYCN* expression and total protein levels, which proves its multimodal effect on one of the most prominent prognostic factors in neuroblastoma.

DpC succeeded in downregulating the levels of EGFR in all four studied neuroblastoma cell lines; thus we identified another shared effect of thiosemicarbazone treatment in this type of cancer. Moreover, in the SH-SY5Y neuroblastoma cell line, DpC was found to inhibit EGFR through NDRG1 in accordance with Menezes et al. [35], who partially elucidated the role of NDRG1 in EGFR regulation in pancreatic carcinoma cell lines. A decrease in the phosphorylated forms of EGFR (pY845, pY992, pY1045, pY1068, and pY1148) suggests inhibition of downstream signal transduction at multiple levels. However, we were unable to detect MIG-6, which has been reported to be responsible for NDRG1-mediated EGFR downregulation in pancreatic carcinoma cell lines (data not shown), which illustrates the need for further study of the means of action. Additionally, in the SK-N-BE(2) neuroblastoma cell line, silencing NDRG1 did not rescue EGFR downregulation, thus suggesting a different mechanism than via NDRG1.

Following downstream of EGFR, we explored two of the most important EGFR-mediated signaling pathways: the PI3K–AKT and the RAF–MEK–ERK axes. While the overall decrease in total AKT protein levels across all studied cell lines would suggest the downregulation of this pathway, the levels of its phosphorylated/active form increased in all reference cell lines. The upregulation of the pro-survival AKT pathway is indeed in stark contrast to what would be expected, considering the cytotoxic effect that the DpC treatment exerted on neuroblastoma cells. Two possible explanations emerge to clarify such observation: (1) the cytotoxic effects of DpC could be responsible for cell death in spite of the up-regulated pro-survival AKT pathway. In this scenario, pAKT upregulation would work against the intended effect of DpC and thus elevated pAKT signaling would actually confer resistance to the genotoxic treatment [56]. However, a study by Lui et al. [57] elucidated that while there was an increase in pAKT following thiosemicarbazone treatment, the activation of its downstream effectors (mTOR, Cyclin D) expression was not observed. (2) Overly up-regulated AKT signaling could induce cell death by sensitizing neuroblastoma cells to ROS,

which are generated in the process of DpC treatment. While some reports can be found to support this claim [58,59], the elucidation of AKT dynamic in response to treatment by thiosemicarbazones in neuroblastoma requires further research. As for ERK-bound signalization, the unhindered levels of total and phosphorylated ERK (Figure S1) strongly suggest its lateral activation, which compensates for the loss of EGFR signaling [60].

The induction of lipid accumulation in response to chelation therapy proved to be an unexpected discovery that warrants further research for multiple reasons.

First, it coincides with the identical phenotype that was observed by Zirath et al. [49], who used a specific N-MYC inhibitor in the SK-N-BE(2) neuroblastoma cell line. We expanded this by observing lipid accumulation in yet another neuroblastoma cell line, SH-SY5Y. Even though this cell line is *MYCN*-nonamplified, its structural and functional homolog, c-MYC, is downregulated in response to DpC treatment. Therefore, direct inhibition of c-MYC in SH-SY5Y cells would not only further confirm the functional overlap in MYC proteins but also further establish their role in lipid accumulation in neuroblastoma.

Second, since MYC proteins are direct transcriptional inhibitors of NDRG1, any inhibition of MYC protein expression (whether through DpC application, knockout, or direct small-molecule inhibitors) likely results in NDRG1 expression liberation and upregulation. Stacking evidence across cell/tissue types indicates that NDRG1 could play a major role in facilitating lipid accumulation in the following ways. (i) In oligodendrocytes, NDRG1 confers LDL uptake by regulating endosomal trafficking of LDL-R. Silencing NDRG1 indeed resulted in a reduction in lipid uptake by cells [61]. (ii) In Schwann cells, NDRG1 mutation manifests as a rare demyelinating neuropathy (Charcot–Marie–Tooth disease type 4D) characteristic of progressive hypomyelination and axonal loss [62]. Schwann cells share a neural crest origin with neuroblastoma cells, thus indicating that NDRG1 could play a similar role in lipid metabolism in these cell types. (iii) In adipocytes, silencing NDRG1 results in decreased lipidogenesis in differentiated cells [63]. While these findings indicate that NDRG1 plays a pivotal role in cellular lipid uptake in neuroblastoma, further investigation is needed to fully explain the exact mechanism of NDRG1 action.

Overall, iron chelators treatment by the novel thiosemicarbazone DpC induces potent cell death of neuroblastoma cells, while targeting some of the major drivers of aggressive neuroblastomas, regardless of their *MYCN* status (Figure ??). DpC could thus be a useful addition in the treatment of MYC-driven neuroblastomas.
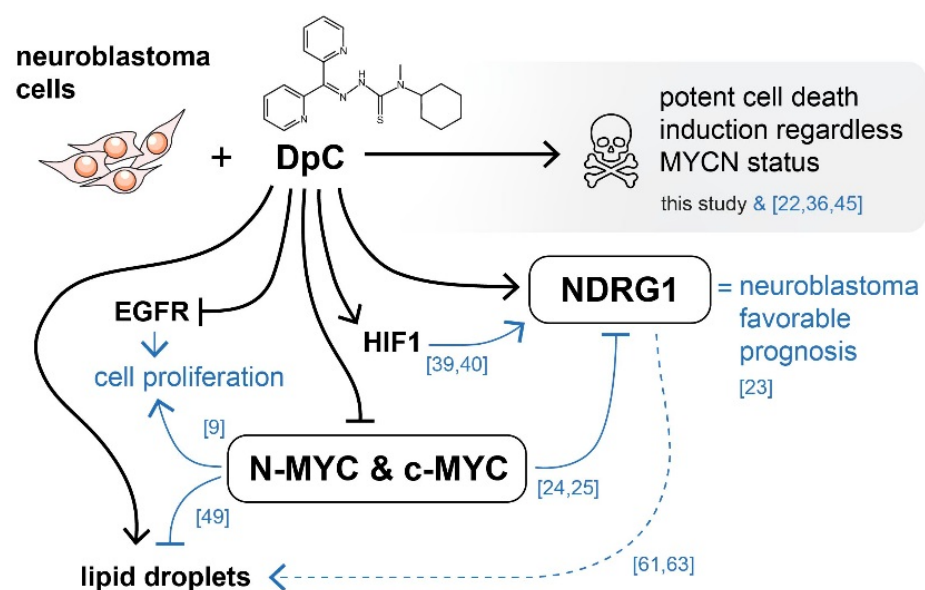
Figure 9. Graphical overview of the major molecular targets affected by DpC treatment in neuroblastoma. Black arrows indicate findings of this study. Blue arrows represent existing knowledge (see

references), providing a mechanistic insight into the effects of thiosemicarbazones in the context of neuroblastoma cells. DpC suppressed the expression of EGFR and MYC proteins in all studied neuroblastoma cell lines. Additionally, the treatment induced a massive increase in NDRG1 levels, as well as lipid droplet accumulation. Although the involvement of NDRG1 in lipid accumulation has been suggested in neuroblastoma [61] and other cell types [62,63], the underlying mechanism is still unclear (dashed line).

4. Materials and Methods

4.1. Cell Culture

Four neuroblastoma cell lines used in this study were selected based on their genetic background or treatment status to better cover the heterogeneity observed among neuroblastomas. The *MYCN*-nonamplified SH-SY5Y (No. 94030304) and *MYCN*-amplified SK-N-BE(2) (No. 95011815) cell lines were obtained from ECACC (Salisbury, UK). To analyze postrelapse changes in neuroblastoma pathophysiology, the CHLA-15 cell line was derived from initial surgical biopsy and the CHLA-20 cell line was derived from the posttreatment relapse resection of neuroblastoma in the same patient. Both of these cell lines were obtained from Alex's Lemonade Stand Foundation Childhood Cancer Repository (cccells.org) and kindly provided by Dr. Michael D. Hogarty (Children's Hospital of Philadelphia, Philadelphia, PA, USA).

Cells were grown in Dulbecco's modified Eagle's medium-F12 medium mixture (DMEM-F12, GE Healthcare, Chicago, IL, USA) supplemented with 10% (CHLA 15, CHLA 20) or 20% (SH-SY5Y, SK-N-BE(2)) fetal bovine serum (FBS), 100 IU/mL penicillin, 100 IU/mL streptomycin, 2 mM glutamine, and 1% MEM amino acid solution (all from Biosera, Nuaillé, France). The medium for the CHLA-15 and CHLA-20 cell lines was further supplemented with $1\times$ ITSX (insulin–transferrin–selenium) solution (Thermo Fisher Scientific, Waltham, MA, USA). Cell culture was performed under standard conditions at 37 °C and 95% humidity in 5% CO_2.

4.2. DpC Treatment

Di-2-pyridylketone 4-cyclohexyl-4-methyl-3-thiosemicarbazone (DpC) was obtained from Sigma–Aldrich (St. Louis, MO, USA, Cat. No. SML0483), diluted with DMSO (Sigma–Aldrich) to a 100 mM stock solution, aliquoted, and stored at 20 °C. For all experiments, cells were treated with DpC 24 h after being seeded onto Petri dishes so that the confluence reached 70%. Diluting DpC from the 100 mM stock solution resulted in a final DpC concentration of 20 µM (SH-SY5Y, SK-N-BE(2)) or 2 µM (CHLA 15, CHLA 20), while the concentration of DMSO did not exceed 0.02% or 0.002%, respectively.

4.3. Western Blot Analysis

Protein extracts were isolated from cell lysates and stored at −80 °C. Prior to loading, the protein concentration was determined using the DC™ Protein Assay Kit (Bio–Rad Laboratories, Hercules, CA, USA) as per the manufacturer's protocol. Protein samples were loaded into 10% polyacrylamide gels, electrophoresed, and blotted onto PVDF membranes. Following membrane blocking (with either 5% bovine serum albumin or 5% nonfat dry milk solution in a TBS–Tween buffer), the membranes were incubated with primary antibodies overnight at 4 °C (Table S1). Mouse or rabbit IgG horseradish peroxidase-conjugated antibodies served as secondary antibodies (Table S1). Chemiluminescence was induced by an ECL-Plus detection kit (GE Healthcare), detected by an Azure c600 imaging system (Azure Biosystems, Dublin, CA, USA) or AGFA CP-BU X-ray films (AGFA, Mortsel, Belgium) and quantified using ImageJ software v1.52a (U. S. National Institutes of Health, Bethesda, MD, USA) [64]. All experiments were performed in biological triplicate.

4.4. siRNA Silencing Assay

Cells were cultivated in 60 mm Petri dishes in a complete DMEM-F12 medium and transfected using a Lipofectamine® RNAiMAX and Silencer™ Pre-Designed siRNA mixture

in Gibco™ Opti-MEM™ Medium (Thermo Fisher Scientific) according to the manufacturer's instructions. Two distinct siRNAs (Thermo Fisher Scientific; siRNA1 ID: 135611; siRNA2 ID: 135612) and one scramble negative control siRNA (Thermo Fisher Scientific; ID: 4390843) were used in the assay. Cells were harvested 72 h after transfection, followed by lysate preparation and protein extraction.

4.5. Immunofluorescence Staining

To perform the immunofluorescence assay, cells were seeded onto coverslips in 35 mm Petri dishes and cultured for 24 h so that the confluence reached 70%. At this confluence, treatment was added to the medium for 48 h. The cells were then washed with PBS, fixed with 3% paraformaldehyde (Sigma–Aldrich), and permeabilized with 0.2% Triton X-100 (Sigma–Aldrich). Afterward, the cells were rinsed with PBS and blocked with 3% bovine serum albumin solution in PBS. The cells were incubated with either primary or fluorophore-conjugated antibodies in a humidified chamber for 60 min at 37 °C (Table S1). After the cells were thoroughly rinsed with PBS, secondary antibodies were added to the corresponding primary antibody for another 45 min at 37 °C in a humidified chamber (Table S1). Cell nuclei were counterstained with 0.05% Hoechst 33342 (Life Technologies, Carlsbad, CA, USA). The coverslips were mounted onto microscope slides with ProLong™ Diamond Antifade Mountant (Thermo Fisher Scientific). Negative controls were prepared by either using a fluorophore-conjugated isotype control antibody or omitting the primary antibodies. An Olympus BX-51 microscope with an Olympus DP72 CCD camera was used to capture micrographs, which were then analyzed by CellˆP v2.3 imaging software (Olympus, Tokyo, Japan). Additionally, confocal microscopy was employed to acquire high-resolution micrographs using a Leica SP8 confocal microscope (Leica Microsystems, Wetzlar, Germany). LAS X v5.0.3 imaging software (Leica Microsystems) was used for the subsequent graphic analysis of micrographs.

4.6. qRT–PCR

Total RNA was extracted and transcribed into cDNA as described by Skoda et al. [65]. The expression of *MYCN* (F: 5′-AGAGGACACCCTGAGCGATT-3′; R: 5′-GGTGAATGTGGT GACAGCCT-3′) in response to DpC treatment was performed in technical and biological triplicates (i.e., different cell passages in vitro). The heat shock protein gene HSP90AB1 (F: 5′-CGCATGAAGGAGACACAGAA-3′; R: 5′-TCCCATCAAATTCCTTGAGC-3′) was used as the endogenous reference control.

4.7. Neutral Lipid Staining

For bright-field microscopy analysis, cells were fixed with 3% paraformaldehyde, rinsed with PBS, stained with lipophilic Oil Red O for 20 min, washed with PBS, and mounted onto slides. For immunofluorescence analysis, cells were fixed with 3% paraformaldehyde, rinsed with PBS, and treated with a 1:500 solution of LipidTOX™ Green for 30 min at room temperature, followed by another wash with PBS. For flow cytometry analysis, the cell suspension was fixed with 3% paraformaldehyde, washed with PBS, and treated with a 1:1000 solution of LipidTOX™ Green for 30 min, followed by another wash with PBS.

4.8. Immunostaining for Flow Cytometry

Cell suspensions were fixed with 3% paraformaldehyde for 20 min, permeabilized with 0.1% Triton X-100 (Sigma–Aldrich) for 1 min, blocked with 3% bovine serum albumin, and incubated with fluorophore-conjugated antibodies or their respective isotype control for 1 h at 37 °C (Table S1). The cell suspension was rinsed with PBS between each step. Cytometric analysis was performed using CytoFLEX S (Beckmann Coulter, Brea, CA, USA), and 1×10^4 valid events were evaluated by CytExpert v2.4 software (Beckmann Coulter).

4.9. Phospho-Protein and Cell Stress Protein Array Analysis

Relative total and/or phosphorylation levels of selected target proteins involved in signal transduction and the cell stress response were analyzed using the following protein array kits: Proteome Profiler™ Human Cell Stress Array Kit (Table S2) and Proteome Profiler™ Human Phospho-Kinase Array Kit (Table S3) (both R&D Systems, Minneapolis, MN, USA). The samples were processed according to the manufacturer's protocol, and the chemiluminescence signal was quantified using ImageJ software v1.52a (U. S. National Institutes of Health) [64] and analyzed in concordance with our previous study [66].

4.10. Statistical Analysis

Relative density analyses of immunoblotting were normalized with regard to their respective GAPDH loading control. Relative pixel density (Western blot), fold change (qRT-PCR), as well as median fluorescence intensity (flow cytometry) were evaluated using two-tailed unpaired t-test: * $p < 0.05$ and ** $p < 0.01$ were considered statistically significant.

5. Conclusions

This study built upon the previous findings of thiosemicarbazone treatment in neuroblastoma and elucidated its effect on some of the important signaling molecules in this cancer type, namely MYC proteins, EGFR and its downstream targets, or NDRG1, whose exact mechanism of action remains largely elusive. As it entered Phase I clinical trials, DpC held promise to become a new addition to certain oncotherapy protocols. Despite DpC exhibiting superior pharmacokinetic properties (e.g., increased half-life and resistance against inactivation by N-demethylation) over its predecessor Dp44mT [67], clinical trials have reported myalgia in patients treated with DpC [68]. Nevertheless, iron chelators still show promising results in potentially treating certain types of neuroblastoma, particularly those with upregulated expression of N-MYC.

Specifically, treatment with DpC proved to target some of the major molecular targets in neuroblastoma, namely the MYC proteins and both total and phosphorylated levels of EGFR. Regulation of EGFR is at least partially mediated by NDRG1, which is in accordance with the results observed in pancreatic carcinoma. Furthermore, the formation of lipid droplets after DpC treatment (and subsequent MYC downregulation) in the SH-SY5Y cell line expanded upon the induction of an identical phenotype in the SK-N-BE(2) cell line in response to N-MYC inhibition.

References

1. Matthay, K.K.; Maris, J.M.; Schleiermacher, G.; Nakagawara, A.; Mackall, C.L.; Diller, L.; Weiss, W.A. Neuroblastoma. *Nat. Rev. Dis. Prim.* **2016**, *2*, 1–21. [CrossRef]
2. Nuchtern, J.G.; London, W.B.; Barnewolt, C.E.; Naranjo, A.; McGrady, P.W.; Geiger, J.D.; Diller, L.; Schmidt, M.; Lou Maris, J.M.; Cohn, S.L. A prospective study of expectant observation as primary therapy for neuroblastoma in young infants: A children's oncology group study. *Ann. Surg.* **2012**, *256*, 573. [CrossRef]
3. Baker, D.L.; Schmidt, M.L.; Cohn, S.L.; Maris, J.M.; London, W.B.; Buxton, A.; Stram, D.; Castleberry, R.P.; Shimada, H.; Sandler, A.; et al. Outcome after Reduced Chemotherapy for Intermediate-Risk Neuroblastoma. *N. Engl. J. Med.* **2010**, *363*, 1313–1323. [CrossRef]
4. Johnsen, J.I.; Dyberg, C.; Wickström, M. Neuroblastoma—A Neural Crest Derived Embryonal Malignancy. *Front. Mol. Neurosci.* **2019**, *12*, 9. [CrossRef]
5. Park, J.R.; Bagatell, R.; London, W.B.; Maris, J.M.; Cohn, S.L.; Mattay, K.M.; Hogarty, M. Children's Oncology Group's 2013 blueprint for research: Neuroblastoma. *Pediatr. Blood Cancer* **2013**, *60*, 985–993. [CrossRef]
6. Brodeur, G.M.; Seeger, R.C.; Schwab, M.; Varmus, H.E.; Michael Bishop, J. Amplification of N-myc in untreated human neuroblastomas correlates with advanced disease stage. *Science* **1984**, *224*, 1121–1124. [CrossRef] [PubMed]
7. London, W.B.; Castleberry, R.P.; Matthay, K.K.; Look, A.T.; Seeger, R.C.; Shimada, H.; Thorner, P.; Brodeur, G.; Maris, J.M.; Reynolds, C.P.; et al. Evidence for an age cutoff greater than 365 days for neuroblastoma risk group stratification in the Children's Oncology Group. *J. Clin. Oncol.* **2005**, *23*, 6459–6465. [CrossRef]
8. Thompson, D.; Vo, K.T.; London, W.B.; Fischer, M.; Ambros, P.F.; Nakagawara, A.; Brodeur, G.M.; Matthay, K.K.; DuBois, S.G. Identification of patient subgroups with markedly disparate rates of MYCN amplification in neuroblastoma: A report from the International Neuroblastoma Risk Group project. *Cancer* **2016**, *122*, 935–945. [CrossRef] [PubMed]
9. Otte, J.; Dyberg, C.; Pepich, A.; Johnsen, J.I. MYCN Function in Neuroblastoma Development. *Front. Oncol.* **2021**, *27*, 624079. [CrossRef] [PubMed]
10. Takahashi, K.; Yamanaka, S. Induction of pluripotent stem cells from mouse embryonic and adult fibroblast cultures by defined factors. *Cell* **2006**, *126*, 663–676. [CrossRef]
11. Dang, C.V. MYC on the path to cancer. *Cell* **2012**, *149*, 22–35. [CrossRef] [PubMed]
12. Zimmerman, M.W.; Liu, Y.; He, S.; Durbin, A.D.; Abraham, B.J.; Easton, J.; Shao, Y.; Xu, B.; Zhu, S.; Zhang, X.; et al. MYC Drives a Subset of High-Risk Pediatric Neuroblastomas and Is Activated through Mechanisms Including Enhancer Hijacking and Focal Enhancer Amplification. *Cancer Discov.* **2018**, *8*, 320–335. [CrossRef] [PubMed]
13. Westermann, F.; Muth, D.; Benner, A.; Bauer, T.; Henrich, K.O.; Oberthuer, A.; Brors, B.; Beissbarth, T.; Vandesompele, J.; Pattyn, F.; et al. Distinct transcriptional MYCN/c-MYC activities are associated with spontaneous regression or malignant progression in neuroblastomas. *Genome Biol.* **2008**, *9*, R150. [CrossRef]
14. Dominguez-Sola, D.; Ying, C.Y.; Grandori, C.; Ruggiero, L.; Chen, B.; Li, M.; Galloway, D.A.; Gu, W.; Gautier, J.; Dalla-Favera, R. Non-transcriptional control of DNA replication by c-Myc. *Nature* **2007**, *448*, 445–451. [CrossRef] [PubMed]
15. Shachaf, C.M.; Kopelman, A.M.; Arvanitis, C.; Karlsson, Å.; Beer, S.; Mandl, S.; Bachmann, M.H.; Borowsky, A.D.; Ruebner, B.; Cardiff, R.D.; et al. MYC inactivation uncovers pluripotent differentiation and tumour dormancy in hepatocellular cancer. *Nature* **2004**, *431*, 1112–1117. [CrossRef] [PubMed]
16. Jain, M.; Arvanitis, C.; Chu, K.; Dewey, W.; Leonhardt, E.; Trinh, M.; Sundberg, C.D.; Bishop, J.M.; Felsher, D.W. Sustained loss of a neoplastic phenotype by brief inactivation of MYC. *Science* **2002**, *297*, 102–104. [CrossRef]
17. Wolf, E.; Eilers, M. Targeting MYC Proteins for Tumor Therapy. *Annu. Rev. Cancer Biol.* **2020**, *4*, 61–75. [CrossRef]
18. Serda, M.; Kalinowski, D.S.; Rasko, N.; Potůčková, E.; Mrozek-Wilczkiewicz, A.; Musiol, R.; Małecki, J.G.; Sajewicz, M.; Ratuszna, A.; Muchowicz, A.; et al. Exploring the Anti-Cancer Activity of Novel Thiosemicarbazones Generated through the Combination of Retro-Fragments: Dissection of Critical Structure-Activity Relationships. *PLoS ONE* **2014**, *9*, e110291. [CrossRef]
19. Jansson, P.J.; Yamagishi, T.; Arvind, A.; Seebacher, N.; Gutierrez, E.; Stacy, A.; Maleki, S.; Sharp, D.; Sahni, S.; Richardson, D.R. Di-2-pyridylketone 4,4-dimethyl-3-thiosemicarbazone (Dp44mT) overcomes multidrug resistance by a novel mechanism involving the hijacking of lysosomal P-Glycoprotein (Pgp). *J. Biol. Chem.* **2015**, *290*, 9588–9603. [CrossRef]
20. Chen, Z.; Zhang, D.; Yue, F.; Zheng, M.; Kovacevic, Z.; Richardson, D.R. The iron chelators Dp44mT and DFO inhibit TGF-β-induced epithelial-mesenchymal transition via up-regulation of N-Myc downstream-regulated gene 1 (NDRG1). *J. Biol. Chem.* **2012**, *287*, 17016–17028. [CrossRef]
21. Wangpu, X.; Lu, J.; Xi, R.; Yue, F.; Sahni, S.; Park, K.C.; Menezes, S.; Huang, M.L.H.; Zheng, M.; Kovacevic, Z.; et al. Targeting the metastasis suppressor, n-myc downstream regulated gene-1, with novel di-2-pyridylketone thiosemicarbazones: Suppression of tumor cell migration and cell-collagen adhesion by inhibiting focal adhesion kinase/paxillin signaling. *Mol. Pharmacol.* **2016**, *89*, 521–540. [CrossRef]

22. Guo, Z.L.; Richardson, D.R.; Kalinowski, D.S.; Kovacevic, Z.; Tan-Un, K.C.; Chan, G.C.F. The novel thiosemicarbazone, di-2-pyridylketone 4-cyclohexyl-4-methyl-3-thiosemicarbazone (DpC), inhibits neuroblastoma growth in vitro and in vivo via multiple mechanisms. *J. Hematol. Oncol.* **2016**, *9*, 98. [CrossRef]

23. Matsushita, K.; Uchida, K.; Saigusa, S.; Ide, S.; Hashimoto, K.; Koike, Y.; Otake, K.; Inoue, M.; Tanaka, K.; Kusunoki, M. Low NDRG1 mRNA expression predicts a poor prognosis in neuroblastoma patients. *Pediatr. Surg. Int.* **2013**, *29*, 363–368. [CrossRef]

24. Li, J.; Kretzner, L. The growth-inhibitory Ndrg1 gene is a Myc negative target in human neuroblastomas and other cell types with overexpressed N- or c-myc. *Mol. Cell. Biochem.* **2003**, *250*, 91–105. [CrossRef]

25. Zhang Jian Chen, S.; Zhang, W.; Zhang Jing Liu, X.; Shi, H.; Che, H.; Wang, W.; Li, F.; Yao, L. Human differentiation-related gene NDRG1 is a Myc downstream-regulated gene that is repressed by Myc on the core promoter region. *Gene* **2008**, *417*, 5–12. [CrossRef] [PubMed]

26. Lv, X.H.; Chen, J.W.; Zhao, G.; Feng, Z.Z.; Yang, D.H.; Sun, W.W.; Fan, J.S.; Zhu, G.H. N-myc downstream-regulated gene 1/Cap43 may function as tumor suppressor in endometrial cancer. *J. Cancer Res. Clin. Oncol.* **2012**, *138*, 1703–1715. [CrossRef]

27. Zhang, X.; Feng, B.; Zhu, F.; Yu, C.; Lu, J.; Pan, M.; He, Z.; Wangpu, X.; Sun, J.; Yang, X. N-myc downstream-regulated gene 1 promotes apoptosis in colorectal cancer via up-regulating death receptor 4. *Oncotarget* **2017**, *8*, 82593–82608. [CrossRef]

28. Yang, Y.; Liu, Y.; Guo, R.; Fu, Y.; Zhang, Z.; Zhang, P.; Zhou, P.; Wang, T.; Huang, T.; Li, X.; et al. The novel dithiocarbamate, DpdtC suppresses HER2-overexpressed cancer cells by up-regulating NDRG1 via inactivation of HER2-ERK 1/2 signaling. *Sci. Rep.* **2018**, *8*, 3398. [CrossRef]

29. Chua, M.S.; Sun, H.; Cheung, S.T.; Mason, V.; Higgins, J.; Ross, D.T.; Fan, S.T.; So, S. Overexpression of NDRG1 is an indicator of poor prognosis in hepatocellular carcinoma. *Mod. Pathol.* **2007**, *20*, 76–83. [CrossRef] [PubMed]

30. Weiler, M.; Blaes, J.; Pusch, S.; Sahm, F.; Czabanka, M.; Luger, S.; Bunse, L.; Solecki, G.; Eichwald, V.; Jugold, M.; et al. MTOR target NDRG1 confers MGMT-dependent resistance to alkylating chemotherapy. *Proc. Natl. Acad. Sci. USA* **2014**, *111*, 409–414. [CrossRef] [PubMed]

31. Dixon, K.M.; Lui, G.Y.L.; Kovacevic, Z.; Zhang, D.; Yao, M.; Chen, Z.; Dong, Q.; Assinder, S.J.; Richardson, D.R. Dp44mT targets the AKT, TGF-β and ERK pathways via the metastasis suppressor NDRG1 in normal prostate epithelial cells and prostate cancer cells. *Br. J. Cancer* **2013**, *108*, 409–419. [CrossRef]

32. Kovacevic, Z.; Chikhani, S.; Lui, G.Y.L.; Sivagurunathan, S.; Richardson, D.R. The iron-regulated metastasis suppressor NDRG1 targets NEDD4L, PTEN, and SMAD4 and inhibits the PI3K and ras signaling pathways. *Antioxid. Redox Signal.* **2013**, *18*, 874–887. [CrossRef]

33. Liu, W.; Yue, F.; Zheng, M.; Merlot, A.; Bae, D.H.; Huang, M.; Lane, D.; Jansson, P.; Liu, G.; Richardson, V.; et al. The proto-oncogene c-Src and its downstream signaling pathways are inhibited by the metastasis suppressor, NDRG1. *Oncotarget* **2015**, *6*, 8851–8874. [CrossRef]

34. Kovacevic, Z.; Menezes, S.V.; Sahni, S.; Kalinowski, D.S.; Bae, D.H.; Lane, D.J.R.; Richardson, D.R. The metastasis suppressor, N-MYC downstream-regulated gene-1 (NDRG1), down-regulates the ErbB family of receptors to inhibit downstream oncogenic signaling pathways. *J. Biol. Chem.* **2016**, *291*, 1029–1052. [CrossRef] [PubMed]

35. Menezes, S.V.; Kovacevic, Z.; Richardson, D.R. The metastasis suppressor NDRG1 down-regulates the epidermal growth factor receptor via a lysosomal mechanism by up-regulating mitogen-inducible gene 6. *J. Biol. Chem.* **2019**, *294*, 4045–4064. [CrossRef] [PubMed]

36. Paukovcekova, S.; Skoda, J.; Neradil, J.; Mikulenkova, E.; Chlapek, P.; Sterba, J.; Richardson, D.R.; Veselska, R. Novel Thiosemicar-bazones Sensitize Pediatric Solid Tumor Cell-Types to Conventional Chemotherapeutics through Multiple Molecular Mechanisms. *Cancers* **2020**, *12*, 3781. [CrossRef] [PubMed]

37. Hossain, S.; Takatori, A.; Nakamura, Y.; Suenaga, Y.; Kamijo, T.; Nakagawara, A. NLRR1 enhances EGF-mediated MYCN induction in neuroblastoma and accelerates tumor growth in vivo. *Cancer Res.* **2012**, *72*, 4587–4596. [CrossRef]

38. Wee, P.; Wang, Z. Epidermal growth factor receptor cell proliferation signaling pathways. *Cancers* **2017**, *9*, 52. [CrossRef] [PubMed]

39. Salnikow, K.; Blagosklonny, M.V.; Ryan, H.; Johnson, R.; Costa, M. Carcinogenic nickel induces genes involved with hypoxic stress. *Cancer Res.* **2000**, *60*, 38–41.

40. Cangul, H. Hypoxia upregulates the expression of the NDRG1 gene leading to its overexpression in various human cancers. *BMC Genet.* **2004**, *5*, 27. [CrossRef]

41. Lingappan, K. NF-κB in Oxidative Stress. *Curr. Opin. Toxicol.* **2018**, *7*, 81. [CrossRef]

42. Zhang, H.; Park, S.-H.; Pantazides, B.G.; Karpiuk, O.; Warren, M.D.; Hardy, C.W.; Duong, D.M.; Park, S.-J.; Kim, H.-S.; Vassilopoulos, A.; et al. SIRT2 directs the replication stress response through CDK9 deacetylation. *Proc. Natl. Acad. Sci. USA* **2013**, *110*, 13546. [CrossRef]

43. Kankanamalage, S.G.; Karra, A.S.; Cobb, M.H. WNK pathways in cancer signaling networks. *Cell Commun. Signal.* **2018**, *16*, 1–6. [CrossRef]

44. Kim, J.L.; Lee, D.-H.; Na, Y.J.; Kim, B.R.; Jeong, Y.A.; Lee, S.I.; Kang, S.; Joung, S.Y.; Lee, S.-Y.; Oh, S.C.; et al. Iron chelator-induced apoptosis via the ER stress pathway in gastric cancer cells. *Tumor Biol.* **2016**, *377*, 9709–9719. [CrossRef] [PubMed]

45. Le, N.T.V.; Richardson, D.R. Iron chelators with high antiproliferative activity up-regulate the expression of a growth inhibitory and metastasis suppressor gene: A link between iron metabolism and proliferation. *Blood* **2004**, *104*, 2967–2975. [CrossRef]

46. Shimono, A.; Okuda, T.; Kondoh, H. N-myc-dependent repression of Ndr1, a gene identified by direct subtraction of whole mouse embryo cDNAs between wild type and N-myc mutant. *Mech. Dev.* **1999**, *83*, 39–52. [CrossRef]

47. Malynn, B.A.; Alboran IM de O'Hagan, R.C.; Bronson, R.; Davidson, L.; DePinho, R.A.; Alt, F.W. N-myc can functionally replace c-myc in murine development, cellular growth, and differentiation. *Genes Dev.* **2000**, *14*, 1390. [CrossRef]

48. Beltran, H. The N-myc Oncogene: Maximizing its Targets, Regulation, and Therapeutic Potential. *Mol. Cancer Res.* **2014**, *12*, 815–822. [CrossRef]

49. Zirath, H.; Frenzel, A.; Oliynyk, G.; Segerström, L.; Westermark, U.K.; Larsson, K.; Persson, M.M.; Hultenby, K.; Lehtiö, J.; Einvik, C.; et al. MYC inhibition induces metabolic changes leading to accumulation of lipid droplets in tumor cells. *Proc. Natl. Acad. Sci. USA* **2013**, *110*, 10258–10263. [CrossRef] [PubMed]

50. Bae, D.-H.; Jansson, P.J.; Huang, M.L.; Kovacevic, Z.; Kalinowski, D.; Lee, C.S.; Sahni, S.; Richardson, D.R. The role of NDRG1 in the pathology and potential treatment of human cancers. *J. Clin. Pathol.* **2013**, *66*, 911–917. [CrossRef]

51. Fan, L.; Iyer, J.; Zhu, S.; Frick, K.K.; Wada, R.K.; Eskenazi, A.E.; Berg, P.E.; Ikegaki, N.; Kennett, R.H.; Frantz, C.N. Inhibition of N-myc Expression and Induction of Apoptosis by Iron Chelation in Human Neuroblastoma Cells 1. *Cancer Res.* **2001**, *61*, 1073–1079.

52. Siriwardana, G.; Seligman, P.A. Two cell cycle blocks caused by iron chelation of neuroblastoma cells: Separating cell cycle events associated with each block. *Physiol. Rep.* **2013**, *1*, 176. [CrossRef] [PubMed]

53. Zhang, C. Essential functions of iron-requiring proteins in DNA replication, repair and cell cycle control. *Protein Cell* **2014**, *5*, 750. [CrossRef] [PubMed]

54. Chen, H.; Liu, H.; Qing, G. Targeting oncogenic Myc as a strategy for cancer treatment. *Signal Transduct. Target. Ther.* **2018**, *3*, 1–7. [CrossRef] [PubMed]

55. Yang, X.H.; Tang, F.; Shin, J.; Cunningham, J.M. A c-Myc-regulated stem cell-like signature in high-risk neuroblastoma: A systematic discovery (Target neuroblastoma ESC-like signature). *Sci. Rep.* **2017**, *7*, 41. [CrossRef]

56. Liu, Q.; Turner, K.M.; Yung, W.K.A.; Chen, K.; Zhang, W. Role of AKT signaling in DNA repair and clinical response to cancer therapy. *Neuro. Oncol.* **2014**, *16*, 1313–1323. [CrossRef]

57. Lui, G.Y.; Kovacevic, Z.; Richardson, V.; Merlot, A.M.; Kalinowski, D.S.; Richardson, D.R. Targeting cancer by binding iron: Dissecting cellular signaling pathways. *Oncotarget* **2015**, *6*, 18748–18779. [CrossRef]

58. Nogueira, V.; Park, Y.; Chen, C.C.; Xu, P.Z.; Chen, M.L.; Tonic, I.; Unterman, T.; Hay, N. Akt Determines Replicative Senescence and Oxidative or Oncogenic Premature Senescence and Sensitizes Cells to Oxidative Apoptosis. *Cancer Cell* **2008**, *14*, 458–470. [CrossRef]

59. Los, M.; Maddika, S.; Erb, B.; Schulze-Osthoff, K. Switching Akt: From survival signaling to deadly response. *BioEssays* **2009**, *31*, 492–495. [CrossRef]

60. Liu, Q.; Yu, S.; Zhao, W.; Qin, S.; Chu, Q.; Wu, K. EGFR-TKIs resistance via EGFR-independent signaling pathways. *Mol. Cancer* **2018**, *17*, 53. [CrossRef]

61. Pietiäinen, V.; Vassilev, B.; Blom, T.; Wang, W.; Nelson, J.; Bittman, R.; Bäck, N.; Zelcer, N.; Ikonen, E. NDRG1 functions in LDL receptor trafficking by regulating endosomal recycling and degradation. *J. Cell Sci.* **2013**, *126*, 3961–3971. [CrossRef] [PubMed]

62. Kalaydjieva, L.; Gresham, D.; Gooding, R.; Heather, L.; Baas, F.; Jonge, R.; de Blechschmidt, K.; Angelicheva, D.; Chandler, D.; Worsley, P.; et al. N-myc Downstream-Regulated Gene 1 Is Mutated in Hereditary Motor and Sensory Neuropathy–Lom. *Am. J. Hum. Genet.* **2000**, *67*, 47–58. [CrossRef] [PubMed]

63. Cai, K.; El-Merahbi, R.; Loeffler, M.; Mayer, A.E.; Sumara, G. Ndrg1 promotes adipocyte differentiation and sustains their function. *Sci. Rep.* **2017**, *71*, 7191. [CrossRef] [PubMed]

64. Schneider, C.A.; Rasband, W.S.; Eliceiri, K.W. NIH Image to ImageJ: 25 years of image analysis. *Nat. Methods* **2012**, *9*, 671–675. [CrossRef]

65. Skoda, J.; Hermanova, M.; Loja, T.; Nemec, P.; Neradil, J.; Karasek, P.; Veselska, R. Co-Expression of Cancer Stem Cell Markers Corresponds to a Pro-Tumorigenic Expression Profile in Pancreatic Adenocarcinoma. *PLoS ONE* **2016**, *11*, e0159255. [CrossRef]

66. Neradil, J.; Kyr, M.; Polaskova, K.; Kren, L.; Macigova, P.; Skoda, J.; Sterba, J.; Veselska, R. Phospho-Protein Arrays as Effective Tools for Screening Possible Targets for Kinase Inhibitors and Their Use in Precision Pediatric Oncology. *Front. Oncol.* **2019**, *9*, 930. [CrossRef]

67. Sestak, V.; Stariat, J.; Cermanova, J.; Potuckova, E.; Chladek, J.; Roh, J.; Bures, J.; Jansova, H.; Prusa, P.; Sterba, M.; et al. Novel and potent anti-tumor and anti-metastatic di-2-pyridylketone thiosemicarbazones demonstrate marked differences in pharmacology between the first and second generation lead agents. *Oncotarget* **2015**, *6*, 42411–42428. [CrossRef]

68. Wijesinghe, T.P.; Dharmasivam, M.; Dai, C.C.; Richardson, D.R. Innovative Therapies for Neuroblastoma: The Surprisingly Potent Role of Iron Chelation in Up-Regulating Metastasis and Tumor Suppressors and Down-Regulating the Key Oncogene, N-myc. *Pharmacol. Res.* **2021**, *173*, 105889. [CrossRef] [PubMed]

APPENDIX 9

Mikulenkova E, Neradil J, Vymazal O, **Skoda J***, Veselska R. NANOG/NANOGP8 Localizes at the Centrosome and is Spatiotemporally Associated with Centriole Maturation. *Cells*. 2020;9:692. (JCR 2020, IF = 6.600; Q2 – Cell Biology)

NANOG/NANOGP8 Localizes at the Centrosome and is Spatiotemporally Associated with Centriole Maturation

Erika Mikulenkova [1,2], **Jakub Neradil** [1,2], **Ondrej Vymazal** [1], **Jan Skoda** [1,2,*,†] and **Renata Veselska** [1,2,3,†]

1   Department of Experimental Biology, Faculty of Science, Masaryk University, 61137 Brno, Czech Republic; mikulenkova@mail.muni.cz (E.M.); jneradil@sci.muni.cz (J.N.); ovymazal@mail.muni.cz (O.V.); veselska@sci.muni.cz (R.V.)
2   International Clinical Research Center, St. Anne's University Hospital, 65691 Brno, Czech Republic
3   Department of Pediatric Oncology, University Hospital Brno and Faculty of Medicine, Masaryk University, 62500 Brno, Czech Republic
*   Correspondence: janskoda@sci.muni.cz; Tel.: +420-549-49-8021
†   These authors contributed equally to this work.

Abstract: NANOG is a transcription factor involved in the regulation of pluripotency and stemness. The functional paralog of NANOG, NANOGP8, differs from NANOG in only three amino acids and exhibits similar reprogramming activity. Given the transcriptional regulatory role played by NANOG, the nuclear localization of NANOG/NANOGP8 has primarily been considered to date. In this study, we investigated the intriguing extranuclear localization of NANOG and demonstrated that a substantial pool of NANOG/NANOGP8 is localized at the centrosome. Using double immunofluorescence, the colocalization of NANOG protein with pericentrin was identified by two independent anti-NANOG antibodies among 11 tumor and non-tumor cell lines. The validity of these observations was confirmed by transient expression of GFP-tagged NANOG, which also colocalized with pericentrin. Mass spectrometry of the anti-NANOG immunoprecipitated samples verified the antibody specificity and revealed the expression of both NANOG and NANOGP8, which was further confirmed by real-time PCR. Using cell fractionation, we show that a considerable amount of NANOG protein is present in the cytoplasm of RD and NTERA-2 cells. Importantly, cytoplasmic NANOG was unevenly distributed at the centrosome pair during the cell cycle and colocalized with the distal region of the mother centriole, and its presence was markedly associated with centriole maturation. Along with the finding that the centrosomal localization of NANOG/NANOGP8 was detected in various tumor and non-tumor cell types, these results provide the first evidence suggesting a common centrosome-specific role of NANOG.

Keywords: NANOG; NANOGP8; human; localization; centrosome; mother centriole

1. Introduction

NANOG is a homeodomain transcription factor involved in embryonic stem cell (ESC) self-renewal and pluripotency [1–3]. NANOG has been identified as a common stem cell marker and is crucial for the regulation of the cancer stem cell phenotype in several types of solid tumors [4–10]. Together with SOX2 and OCT4, NANOG plays a key role in maintaining the features of ESCs [11–13]. NANOG is highly expressed in pluripotent cells, such as ESCs and embryonal carcinoma cells, and its expression is downregulated upon differentiation [1,14].

Human NANOG is encoded by the *NANOG* gene, which is located in chromosomal region 12p13.31 [15]. Two NANOG isoforms, NANOG and NANOG-delta 48, resulting from alternative splicing [15], and 11 pseudogenes, NANOGP1 to NANOGP11, have been described in humans [16]. Based on the NCBI protein database, while the human NANOG protein (NP_079141.2) consists of 305 amino acids, the NANOG-delta 48 isoform (NP_001284627.1) lacks amino acids 167–182. The *NANOGP8* pseudogene represents a transcribed retrogene that has 99% homology with NANOG. Thus, *NANOGP8* can potentially code for a 305 amino acid protein (NP_001342210.1) that differs from NANOG by only three amino acids. A study focused on the expression of NANOG paralogs found that human ESCs express large amounts of NANOG [17]. In contrast, most human cancer cells express NANOGP8 [18], although its expression is not restricted solely to transformed cells [17–19].

NANOG is a homeobox-containing protein that is typically localized in the cell nucleus [20,21]. However, the cytoplasmic localization of this protein has also been described [22,23], even though the role of cytoplasmic NANOG has not been fully elucidated. During our ongoing study on rhabdomyosarcoma, we unexpectedly noticed an atypical cytoplasmic localization of NANOG, which resembled the perinuclear localization of centrosomes. Given these surprising results, we sought to examine NANOG protein localization across a panel of various tumor and non-tumor cell types. In this report, we present our comprehensive analysis of this phenomenon and provide the first evidence for an intriguing centrosomal localization of NANOG/NANOGP8, which was detected as common among several cell types.

2. Materials and Methods

2.1. Cell Lines and Cell Culture

Nine tumor cell lines of different origins and two non-tumor cell lines were used in this study; a brief description of these cell lines is provided in Table 1. NSTS-34 and NSTS-35 tumor samples were obtained from patients undergoing rhabdomyosarcoma resection surgery. Written informed consent was obtained from each patient or patient's legal guardian prior to participation in this study. The study was conducted in compliance with the Declaration of Helsinki, and the study protocol (#12/Si/2011) was approved by the Research Ethics Committee of the School of Science (Masaryk University). The paraformaldehyde-fixed CCTL14 human embryonal stem cells were a gift from Dr. Hampl [24]. RD and NTERA-2 cells were cultured in high glucose DMEM supplemented with 10% fetal calf serum (FCS), NSTS-11, NSTS-34, NSTS-35, GM7, HGG-02, and KF1 cells were maintained in DMEM with 20% FCS, Daoy cells in DMEM with 10% FCS, and SH-SY5Y cells were cultured in DMEM/Ham's F12 medium supplemented with 20% FCS. All media were supplemented with 2 mM glutamine, 100 IU/mL penicillin, and 100 µg/mL streptomycin; the addition of 1% non-essential amino acids (all from Biosera, Nuaillé, France) was used for RD, SH-SY5Y, and Daoy culture media. Cells were maintained at 37 °C in a humidified atmosphere containing 5% CO_2.

Table 1. Description of cell lines.

Cell Line	Tissue Type	Source
Tumor Cell Lines		
RD	Embryonal rhabdomyosarcoma	ECACC, Cat. No. 85111502
NSTS-11	Rhabdomyosarcoma	[25]
NSTS-34	Rhabdomyosarcoma	Established in the laboratory
NSTS-35	Rhabdomyosarcoma	Established in the laboratory
GM7	Glioblastoma multiforme	[26]
HGG-02	Glioblastoma multiforme	[27]
Daoy	Medulloblastoma	ATCC, HTB-186[TM]
SH-SY5Y	Neuroblastoma	ECACC, Cat. No. 94030304
NTERA-2	Embryonal carcinoma	ECACC, Cat. No. 01071221
Non-Tumor Cell Lines		
CCTL14	Human embryonal stem cells	[24]
KF1	Normal fibroblasts	[28]

2.2. Immunofluorescence

For indirect immunofluorescence (IF), cells were cultivated on coverslips in Petri dishes for 1–2 days (grown to 80–90% confluence), depending on the cell proliferation rate. IF was performed as previously described [29]. The primary and secondary antibodies used in these experiments are listed in Table 2. Anti-CP110 antibody was a gift from Dr. Cajanek [30]. Negative controls were prepared by omitting the primary antibody. After a final wash with PBS, the coverslips were mounted using ProLong™ Diamond Antifade Mountant (Thermo Fisher Scientific, Waltham, MA, USA). An Olympus BX-51 microscope was used for sample evaluation; micrographs were captured using an Olympus DP72 CCD camera and analyzed using the Cell^P imaging system (Olympus, Tokyo, Japan).

Table 2. Antibodies used in the study.

Primary Antibodies					
Antigen	**Isotype**	**Clone (Cat. No.)**	**Manufacturer**	**Dilution**	
				IF	**WB**
Nanog	Rb IgG	D73G4 (4903)	CST	1:200	1:2000
Nanog	Rb IgG	EPR2027(2) (ab109250)	Abcam	1:200	1:2000
Pericentrin	Rb IgG	- (ab4448)	Abcam	1:400	-
CP110	Mo	-	-	1:5	-
Ninein	Mo IgG2a	79.160-7 (41-3400)	Thermo Fisher	1:800	-
α-Tubulin	Mo IgG1	DM1A (ab7291)	Abcam	-	1:10,000
Lamin B2	Rb IgG	D8P3U (12255)	CST	-	1:400
Secondary Antibodies					
Host	**Specificity**	**Conjugate**	**Manufacturer**	**Dilution**	
				IF	**WB**
Donkey	anti-Mo IgG	Alexa Fluor 488	Life Technologies	1:200	-
Donkey	anti-Rb IgG	Alexa Fluor 488	Life Technologies	1:200	-
Donkey	anti-Mo IgG	Alexa Fluor 568	Life Technologies	1:200	-
Donkey	anti-Rb IgG	Alexa Fluor 568	Life Technologies	1:200	-
Horse	anti-Mo IgG	HRP	CST	-	1:5000
Goat	anti-Rb IgG	HRP	CST	-	1:5000

Mo mouse, *Rb* rabbit, *HRP* horseradish peroxidase, *IF* immunofluorescence, *WB* Western blotting, *CST* Cell Signaling Technology.

2.3. Western Blotting

Fifty micrograms of whole-cell extracts were loaded onto 10% sodium dodecyl sulfate (SDS)-polyacrylamide gels, electrophoresed, and blotted onto polyvinylidene difluoride membranes (Bio-Rad Laboratories GmbH, Feldkirchen, Germany). The membranes were blocked with 5% nonfat milk in PBS with 0.05% Tween 20 (PBS-Tween) and then incubated with primary antibody diluted in blocking solution at 4 °C overnight. After rinsing with PBS-Tween, the membranes were incubated with the corresponding secondary antibody at room temperature for 60 min. After rinsing with PBS-Tween, chemiluminescent detection using Amersham™ ECL™ Prime Western Blotting Detection Reagent (GE Healthcare, Little Chalfont, UK) was performed according to the manufacturer's instructions. To analyze the nuclear and cytoplasmic fractions separately, a Nuclear Protein Extraction kit (Thermo Fisher Scientific) was used according to the manufacturer's instructions. Forty-five microliters of protein extract was loaded onto 10% (SDS)-polyacrylamide gels. The primary and secondary antibodies used in the experiments are listed in Table 2. Anti-Lamin B2 and anti-α-tubulin antibodies served as the controls for the purity of the nuclear and cytoplasmic cell fractions, respectively. Three biological replicates were analyzed for each sample.

2.4. Transient Transfection

RD and NTERA-2 cells were transiently transfected with 2 μg of pCMV6-AC-GFP vector encoding NANOG (OriGene, Rockville, MD, USA). The cells were cultured on coverslips in Petri dishes with complete growth medium overnight and then transfected using TurboFectinTM 8.0 (OriGene) according to the manufacturer's protocol. The transient transfection experiments were repeated twice.

2.5. Immunoprecipitation and Protein Digestion

Cells were overlaid with lysis buffer (10 mM Tris-HCl pH 7.9, 420 mM NaCl, 0.1% NP-40) with the addition of a protease inhibitor cocktail (Sigma-Aldrich, St. Louis, MO, USA). Cell lysates were frozen and thawed three times and then sonicated 12 times (1 s on/2 s off) with 50% amplitude. Lysates were centrifuged, and supernatants were incubated with Ab precoated Dynabeads[TM] protein G beads (Thermo Fisher Scientific) prepared according to the manufacturer's protocol at room temperature for 60 min. Beads were washed with washing buffer (50 mM Tris-HCl pH 7.5, 150 mM NaCl) and transferred into clean tubes. Bound protein elution was performed by adding 100 μl of 8 M urea followed by 15 min incubation. Elution was repeated two times, and yields were combined.

Urea-eluted samples were loaded on a 10 kDa Amicon® MWCO filter and processed by the FASP method [31]. Briefly, proteins were washed with 8 M urea followed by centrifugation. The reduction of the disulfide bonds was performed with 10 mM dithiothreitol at room temperature for 15 min. Acetylation was performed with 50 mM iodoacetamide at room temperature for 15 min. After washing with 25 mM triethylammonium bicarbonate, Pierce[TM] Trypsin Protease (Thermo Fisher Scientific) was added at a 1:50 ratio, and the digestion proceeded overnight at 37 °C.

2.6. Mass Spectrometry and Data Processing

LC-MS/MS analysis of tryptic peptides was performed using a Dionex UltiMate 3000 RSLCnano liquid chromatograph connected to a micrOTOF-Q II mass spectrometer (Bruker, Billerica, MA, USA). Samples were separated on a C18 Acclaim PepmapRSLC separation column (25 cm, I.D. 75 μm, particles 2 μm) using a flow rate of 300 nl/min of solvent A (0.1% formic acid) and solvent B (0.1% formic acid in 20/80 H_2O/ACN (vol/vol)) mixed in a 90 min-long linear gradient from 4% to 55% of solvent B. The mass spectrometer was operated at a scanning frequency of 4 Hz and in a data-dependent mode. The five most intensive precursor ions were fragmented using CID fragmentation using an isolation width of 1.2 Th. The collision energy was adjusted between 27 and 48 eV as a function of the m/z value. Dynamic exclusion of the fragmented precursor was enabled for 30 s.

Raw LC-MS/MS data were converted into mzML format using ProteoWizard [32] and further processed by the Crux pipeline [33]. MS/MS spectra identification was performed by the Tide search engine using the *Homo sapiens* protein fasta file as a database (SwissProt sequences obtained from UniProt protein database), 40 ppm and 0.05 Da as parent and fragment tolerances (respectively) and oxidation and carbamidomethylation as potential and fixed modifications (respectively). Percolator [34] was then employed to validate spectral matches, perform protein inference, and calculate false discovery rates (FDR). Only those proteins passing 5% FDR were retained. FlashLFQ [35] was used for chromatographic peak area estimation using 10 ppm precursor tolerance and list of identified peptide features as input. For each protein, its peptide areas were combined into single values by averaging the areas of the three most intensive peptides (TOP3 approach) [36].

2.7. RT-qPCR

Total RNA was extracted using the GenElute[TM] Mammalian Total RNA Miniprep kit (Sigma-Aldrich), and RNA concentration and purity were determined spectrophotometrically. For all samples, equal amounts of RNA were reverse transcribed into cDNA using M-MLV reverse transcriptase (Top-Bio, Prague, Czech Republic) and oligo-dT priming (Qiagen Inc., Valencia, CA, USA). Quantitative PCR was performed in 10 μL reaction volumes using the KAPA SYBR® FAST qPCR Kit (Kapa

Biosystems, Wilmington, MA, USA) and analyzed using the 7500 Fast Real-Time PCR System and 7500 Software v. 2.0.6 (both Life Technologies, Carlsbad, CA, USA). Technical triplicates were analyzed for each of the three biological replicates and relative gene expression levels were determined using the $2^{-\Delta\Delta CT}$ method [37]. The housekeeping gene *HSP90AB1* was used as an endogenous reference control. The primer sequences used in this study are summarized in Table 3. NANOG primers were designed as previously published [38].

Table 3. Primers used in the study.

Gene	Gene Symbol	Primer Sequence
Nanog homeobox	*NANOG*	F: 5′-TTCATTATAAATCTAGAGACTCCAGGA-3′ R: 5′-CTTTGGGACTGGTGGAAGAATC-3′
Nanog homeobox/Nanog homeobox retrogene P8 *	*NANOG/P8*	F: 5′-GCAGAGAAGAGTGTCG-3′ R: 5′-AGCTGGGTGGAAGAGAACACAG-3′
Heat shock protein 90 alpha family class B member 1	*HSP90AB1*	F: 5′-CGCATGAAGGAGACACAGAA-3′ R: 5′-TCCCATCAAATTCCTTGAGC-3′

F forward primer, *R* reverse primer; * Indicates that this set of primers matches to both NANOG and NANOGP8 sequences.

3. Results

3.1. Centrosomal Localization of the NANOG Protein

During our ongoing study aimed at the analysis of established and patient-derived rhabdomyosarcoma cell lines, we revealed an intriguing extranuclear localization of NANOG protein. Using anti-NANOG commercial antibody (#4903, Cell Signaling Technology (CST)) (Figure 1a), the NANOG signal was detected in the form of one or two punctae located in the cytoplasm near the cell nucleus (Figure 1b and Figure S1). The apparent perinuclear NANOG localization was confirmed using another anti-NANOG commercial antibody (#ab109250, Abcam) (Figure 1a,b and Figure S1).

Surprisingly, the NANOG cytoplasmic signal resembled centrosomes in their localization and quantity. To investigate whether extranuclear NANOG colocalizes with centrosomes, we performed double indirect immunofluorescence using an anti-pericentrin antibody specific for the detection of centrosomes (Figure 2) combined with each of the two independent anti-NANOG commercial antibodies (Figure 3a–c). In addition to rhabdomyosarcoma cell lines, we also examined established and patient-derived tumor cell lines of neurogenic origin, as well as the NTERA-2 human pluripotent embryonal carcinoma cell line, which served as a positive control of nuclear NANOG expression [39]. Indeed, the localization of the fluorescence signal for NANOG colocalized with centrosomes in each of the nine examined tumor cell lines (Figure 3a–c). While rhabdomyosarcoma cell lines (Figure 3a and Figure S2) and tumor cell lines of neurogenic origin (Figure 3b and Figure S3) showed primarily centrosomal and rarely weak nuclear (indicated by asterisks) localization of NANOG, strong NANOG expression was observed both in the cell nucleus (indicated by asterisks) and at the centrosomes of the control NTERA-2 cell line (Figure 3c and Figure S4).

Validation of the results achieved through indirect immunofluorescence was carried out by immunoblot analysis of the nuclear and cytoplasmic fractions of RD and NTERA-2 cells that differed in the nuclear expression of NANOG (Figure 3d). In agreement with the indirect immunofluorescence results, the presence of NANOG-specific bands was detected not only in the whole-cell lysate and the nuclear fraction but also in the cytoplasmic fraction of both RD and NTERA-2 cell lines. The weaker intensity of the NANOG-specific band detected in the nuclear fraction of RD cells compared with that of NTERA-2 cells is also completely in accordance with our findings obtained by indirect immunofluorescence, as reported above.
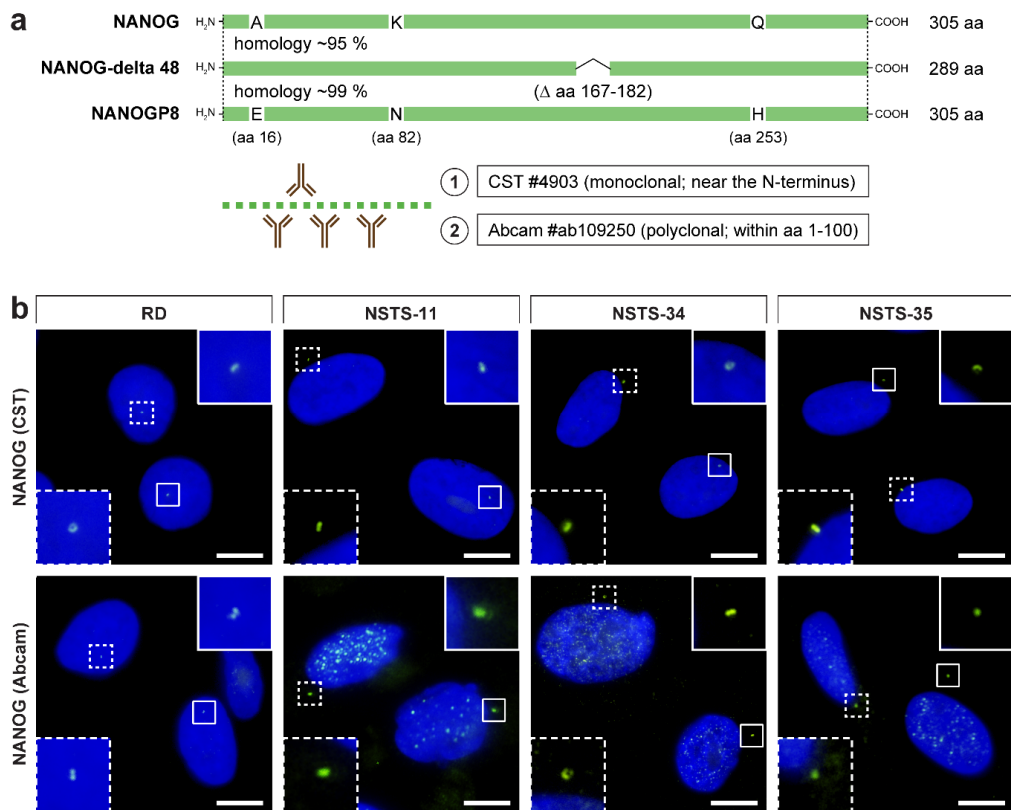
Figure 1. Overview of epitopes of the anti-NANOG antibodies used in this study and their detection of the perinuclear localization of NANOG in rhabdomyosarcoma cell lines. (**a**) Schematic illustration of NANOG isoforms and the NANOGP8 paralog and overview of epitopes of the anti-NANOG antibodies used in the study: (1) #4903, Cell Signaling Technology (CST) and (2) #ab109250, Abcam. Note the marked homology of the NANOG and NANOGP8 protein sequences in the protein region, which served as the immunogen for producing the anti-NANOG antibodies. (**b**) NANOG protein (green) was detected in the cytoplasm near the cell nucleus in the form of one or two punctae using two anti-NANOG commercial antibodies (#4903, Cell Signaling Technology (CST) and #ab109250, Abcam). The nuclei were counterstained with Hoechst 33342 (blue). For each image, regions of interest and the respective close-ups are indicated by the dashed and solid boxes. Scale bars, 10 μm.
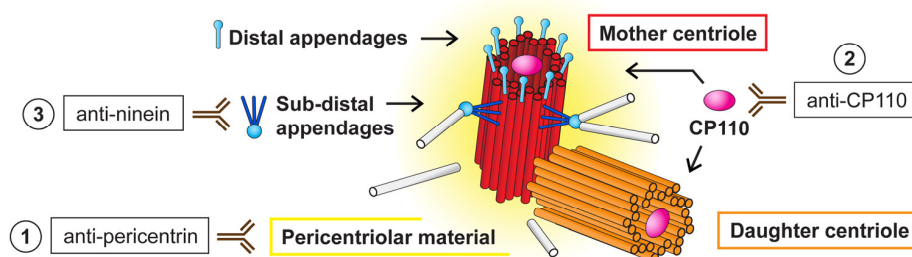
Figure 2. Schematic overview of the different centriolar structures and centrosome-specific antibodies used in this study. The centrosome is a microtubule organizing center (MTOC) composed of two centrioles—older mother centriole (red) and younger daughter centriole (orange). These two centrioles differ structurally [40–42]. The mother centriole has distal and subdistal appendages (blue) [43], which promote membrane docking during cilia initiation [44] and microtubule anchoring [45,46], respectively. Both centrioles are surrounded by pericentriolar material (yellow). Binding of the antibodies used in the study to distinguish specific centrosomal parts is depicted: (1) anti-pericentrin antibody is suitable to detect the whole centrosome, (2) anti-CP110 antibody recognizes distal ends of individual centrioles, and (3) anti-ninein is specific for subdistal appendages of the mother centriole.
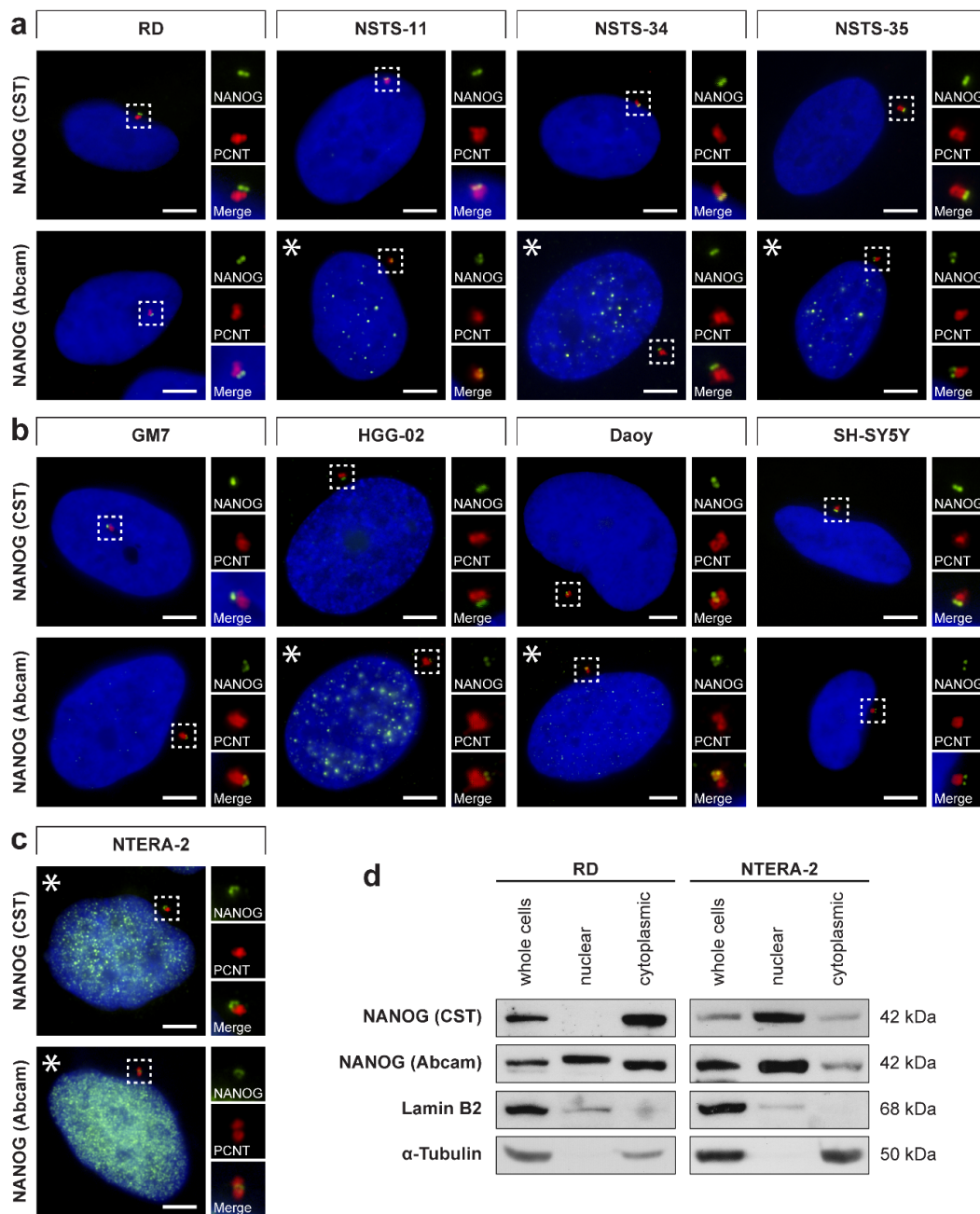
Figure 3. Centrosomal localization of NANOG in tumor cell lines and Western blotting of the nuclear and cytoplasmic fractions. The centrosomal localization of NANOG (green) was detected in (**a**) rhabdomyosarcoma cell lines, (**b**) cell lines of neurogenic origin, and (**c**) NTERA-2 pluripotent embryonal carcinoma cell line using two anti-NANOG antibodies (#4903, Cell Signaling Technology (CST) and #ab109250, Abcam) and anti-pericentrin antibody (PCNT; red). NANOG was also detected in the cell nucleus in the NTERA-2 cell line and some other tumor cell lines (indicated by asterisks). The nuclei were counterstained with Hoechst 33342 (blue). For each image, a region of interest is indicated by the dashed box, and the respective close-ups are provided on the right. Scale bars, 5 μm. (**d**) Western blot analysis revealed the presence of a substantial pool of cytoplasmic NANOG in both RD and NTERA-2 cell lines. Nuclear/cytoplasmic fractionation followed by immunoblotting was performed using two independent anti-NANOG commercial antibodies (#4903, Cell Signaling Technology (CST) and #ab109250, Abcam). Lamin B2 and α-tubulin served as controls of the nuclear fraction and cytoplasmic fraction purity, respectively. Western blots of biological replicates are provided in Figure S5.

Our results in nine tumor cell lines indicated that the centrosomal localization of NANOG might be common among tumor cells of various origins. To further investigate whether NANOG may also be present in centrosomes of non-cancerous cell types, we employed double indirect immunofluorescence of pluripotent CCTL14 hESCs and the KF1 normal skin fibroblast cell line using both anti-NANOG commercial antibodies and anti-pericentrin antibody (Figure 4 and Figure S4). Again, the colocalization of NANOG and pericentrin was observed in both cell lines. As expected, NANOG was also detected in the nucleus (indicated by asterisks) in CCTL14 hESCs but rarely in KF1 fibroblasts.
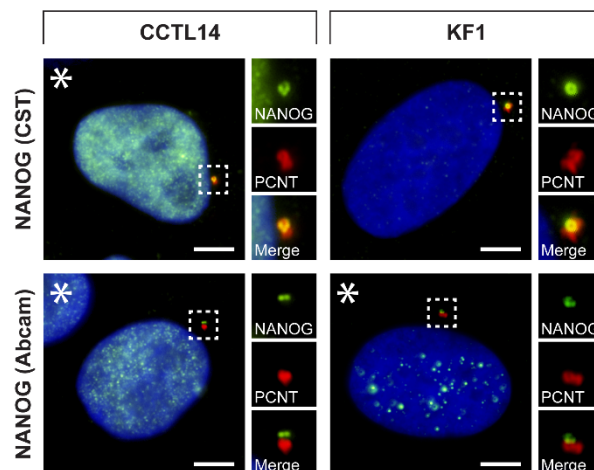
Figure 4. Centrosomal localization of NANOG in hESCs and normal fibroblast cells. The centrosomal localization of NANOG (green) was detected in CCTL14 hESCs and KF1 normal fibroblast cells using two anti-NANOG commercial antibodies (#4903, Cell Signaling Technology (CST) and #ab109250, Abcam) and anti-pericentrin antibody (PCNT; red). NANOG was also detected in the cell nucleus in the CCTL14 cell line and rarely in the KF1 cell line (indicated by asterisks). The nuclei were counterstained with Hoechst 33342 (blue). For each image, a region of interest is indicated by the dashed box, and the respective close-ups are provided on the right. Scale bars, 5 μm.

3.2. Validation of NANOG Centrosomal Signal Specificity and Anti-NANOG Antibodies

Given the intriguing centrosomal localization of NANOG protein detected among various cell types, we wanted to rule out the possibility that our observations were caused by a nonspecific binding of both independent anti-NANOG antibodies used for this study. To avoid the need for antibodies for NANOG protein visualization, RD and NTERA-2 cells were transiently transfected with a GFP-tagged NANOG (NANOG-GFP) expression vector. Subsequently, the detection of NANOG-GFP protein fluorescence was used to evaluate the colocalization of NANOG with centrosomes immunostained using anti-pericentrin antibody. As apparent from the immunofluorescence images, the NANOG-GFP signal was undoubtedly localized within the centrosome (Figure 5), which strongly supports the results obtained using anti-NANOG antibodies. However, in cases where two centrosomes were detected due to centrosome duplication, the NANOG-GFP signal was only present at one of the centrosomes in the cell.

In addition, the specificity of the anti-NANOG antibodies was further examined by two complementary approaches. First, the immunogen sequence of the #ab109250 antibody was compared with the sequences of centrosomal proteins using the Blast® (https://blast.ncbi.nlm.nih.gov/Blast.cgi) and UniProt (https://www.UniProt.org/align/) protein databases. Although the immunogen sequence of both antibodies is proprietary, we received information about the #ab109250 antibody on request from the Abcam manufacturer. Nevertheless, no identity with centrosomal proteins sequences was found. To validate the binding specificity of the anti-NANOG antibody, NTERA-2 cell lysate was immunoprecipitated using #ab109250 antibody, and the bound proteins were analyzed by mass spectrometry. The NANOGP8 (Q6NSW7) peptide was identified as the most prominent, although a

sequence identical for all NANOGP8, NANOG (Q9H9S0), and NANOGP1 (Q8N7R0) was also found (Table S1). These results confirmed the binding specificity of the anti-NANOG #ab109250 antibody and pointed to the expression of NANOGP8 protein along with NANOG and/or NANOGP1 in NTERA-2 cells. Notably, #4903 antibody is not suitable for immunoprecipitation; therefore, this antibody was not tested by mass spectrometry.
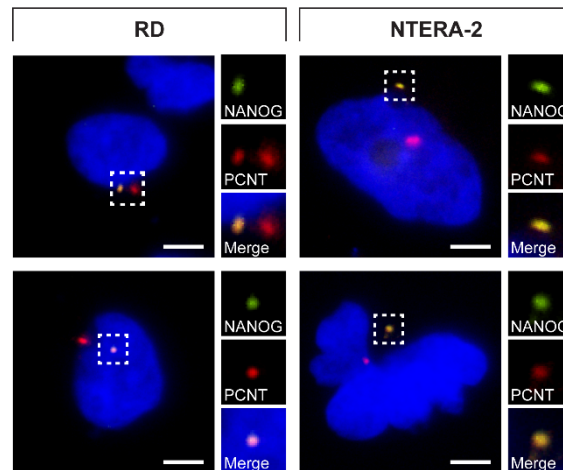
Figure 5. NANOG-GFP colocalization with centrosomes. NANOG-GFP (green) was detected in colocalization with the centrosomes stained by anti-pericentrin antibody (PCNT; red). The nuclei were counterstained with Hoechst 33342 (blue). For each image, a region of interest is indicated by the dashed box, and the respective close-ups are provided on the right. Scale bars, 5 μm.

3.3. Analysis of NANOG and NANOGP8 Gene Expression

Based on the mass spectrometry results, we next investigated the relative expression levels of *NANOG* and *NANOGP8* genes using RT-qPCR. While *NANOG*-specific primers revealed *NANOG* gene expression only in the NTERA-2 cell line, data obtained using *NANOGP8* primers, which may also amplify *NANOG* gene transcripts, indicated that *NANOGP8* is expressed in both NTERA-2 and RD cell lines (Figure 6). The results further showed that *NANOGP8* is abundantly expressed in RD cells. Together with mass spectrometry, these data suggest that the protein might in fact be the NANOGP8 protein, which is localized at the centrosomes.
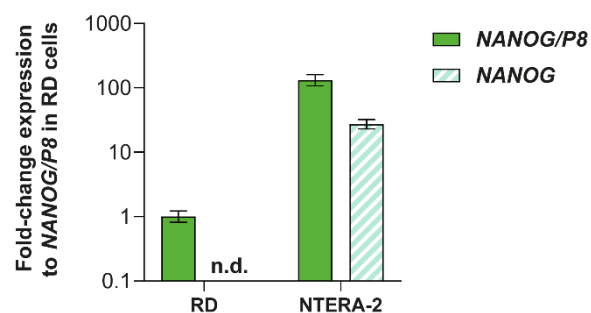
Figure 6. Expression levels of *NANOG* and *NANOGP8* in RD and NTERA-2 cell lines. The relative expression was analyzed by RT-qPCR using *NANOG*-specific primers (*NANOG*) and primers, which detect both *NANOGP8* and *NANOG* transcripts (*NANOG/P8*). Expression was normalized to the endogenous control, *HSP90AB1*, and the fold-change expression values are presented as the mean ± SD from three biological replicates.

3.4. NANOG Colocalizes with the Mother Centriole

As briefly noted above (Figure 5), during the immunofluorescence analysis, we noted an apparent association of the NANOG signal with only one centrosome from the centrosome pair present in

interphase cells (Figure 7a). These results led us to perform a detailed analysis of the interaction of NANOG with centrosomal components. First, we employed double indirect immunofluorescence of anti-CP110 specific for the detection of distal end of the centriole (Figure 2) together with each of the anti-NANOG antibodies used in this study (Figure 7b). Regardless of the anti-NANOG antibody used, in both examined RD and NTERA-2 cell lines, the extranuclear signal of NANOG was localized to only one of the centrioles within individual interphase cells. Therefore, the next step of this study was to determine which centriole the NANOG protein associates with.
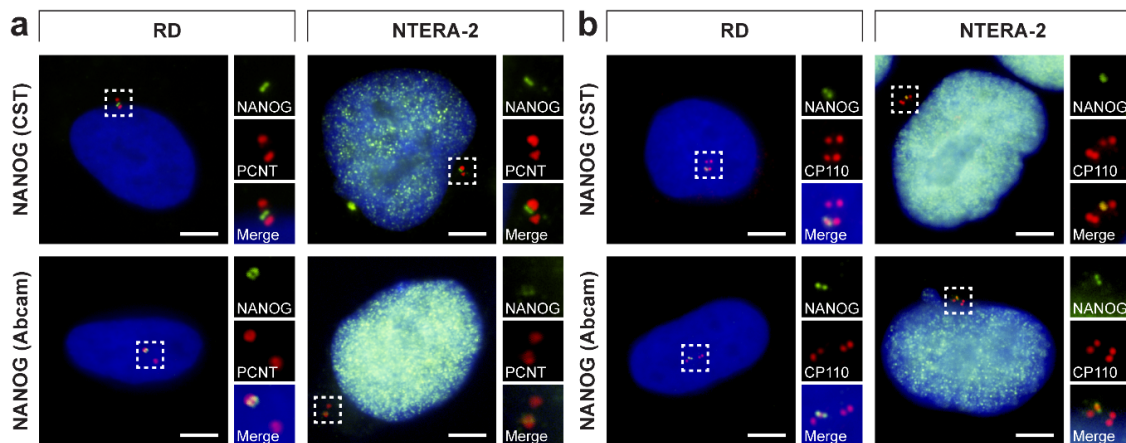
Figure 7. Interaction of NANOG with only one centriole within a cell. NANOG (green; #4903, Cell Signaling Technology (CST) and #ab109250, Abcam) was detected in only (**a**) one centrosome (pericentrin, PCNT; red) and (**b**) one centriole (CP110; red) during the interphase of RD and NTERA-2 cells. The nuclei were counterstained with Hoechst 33342 (blue). For each image, a region of interest is indicated by the dashed box, and the respective close-ups are provided on the right. Scale bars, 5 μm.

Centrosome duplication is coordinated with cell cycle progression [47–50] and results in two daughter cells: one with the mother centrosome and one with the daughter centrosome (Figure 8b) [51]. Thus, we focused on the presence or absence of the NANOG signal during the cell cycle (Figure 8a,c) to determine whether the centrosomal localization of NANOG is also coordinated with cell cycle progression. In interphase cells, NANOG was detected in only one centrosome (Figure 8a). However, the fluorescence signal of NANOG on the second centrosome was established in mitosis (Figure 8c and Figure S6). Considering the centrosome duplication cycle (Figure 8b) and the differences in the structure of mother and daughter centrioles (Figure 2), these results suggested that appearance of NANOG labelling at the second mitotic spindle pole correlated with centrosome maturation. This led us to conclusion that during interphase, NANOG localized in the centrosome which contains the mother centriole.
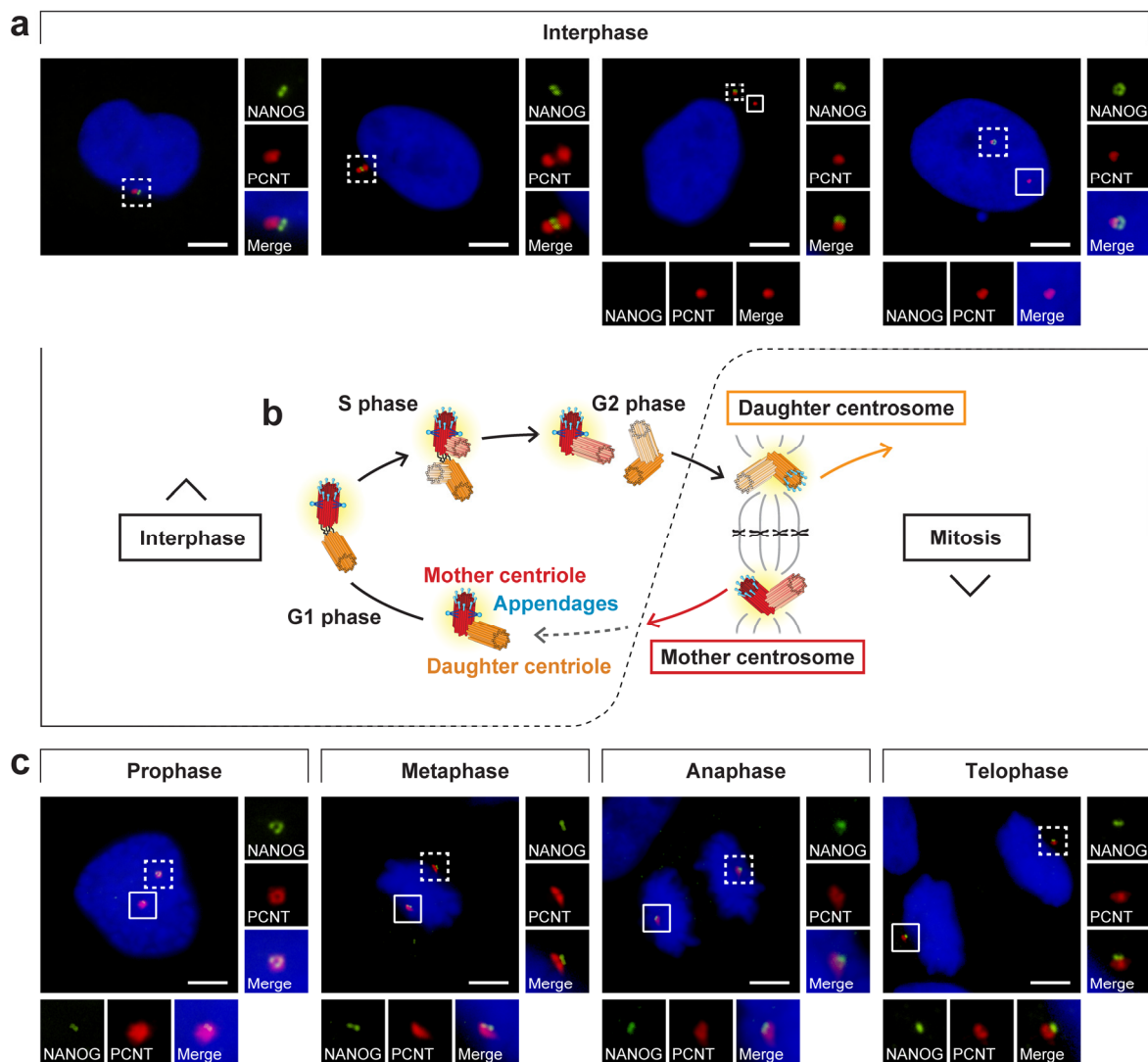
Figure 8. NANOG localization during the cell cycle. (**a**,**c**) Analysis of NANOG during the cell cycle by double indirect immunofluorescence. NANOG (green; #4903, Cell Signaling Technology (CST)) colocalized with one centrosome (pericentrin, PCNT; red) only during interphase (**a**) but with both centrosomes (pericentrin, PCNT; red) during mitosis (**c**). The nuclei were counterstained with Hoechst 33342 (blue). For each image, regions of interest are indicated by the dashed and solid boxes, and the close-ups are provided on the right and below, respectively. Scale bars, 5 μm. (**b**) Schematic visualization of the centrosome duplication cycle: The centrosome is copied only once per cell cycle following cytokinesis. The centrosome duplication cycle results in two daughter cells with different ages of centrosomes: one that keeps the mother centrosome with the old mother centriole and the other cell that inherits the daughter centrosome, which comprises the young mother centriole [51,52]. Distal appendages (light blue) remain on the mother centriole during the whole cell cycle and appear during mitosis or shortly after mitosis on the older centriole of the daughter centrosome [43,53]. After mitosis, the newly formed mother centriole assembles subdistal appendages (blue) [43,53].

To examine whether NANOG interacts with the mother centriole, we performed double indirect immunofluorescence of both anti-NANOG commercial antibodies together with the detection of ninein (Figure 9), which is a mother centriole–specific protein predominantly localized at subdistal appendages of the mother centriole (Figure 2) [54–57]. These experiments revealed a close spatial proximity of fluorescence signals for NANOG and ninein (Figure 9), which clearly confirms the interaction of NANOG with the mother centriole. Several studies have shown that when a centrosome is imaged

from the side view, the immunofluorescence signals of ninein at the mother centriole mostly appear as three foci: an individual spot, which marks the proximal part of the mother centriole, and two closer spots (sometimes merged in a larger signal), which are located at the subdistal appendages of the mother centriole [58–60]. Given the observed spatial distribution of NANOG relative to signals of ninein (Figure 9b) and CP110 (Figure 7b), which caps the distal ends of centrioles [30,61], we conclude that NANOG localizes at the distal region of the mother centriole.
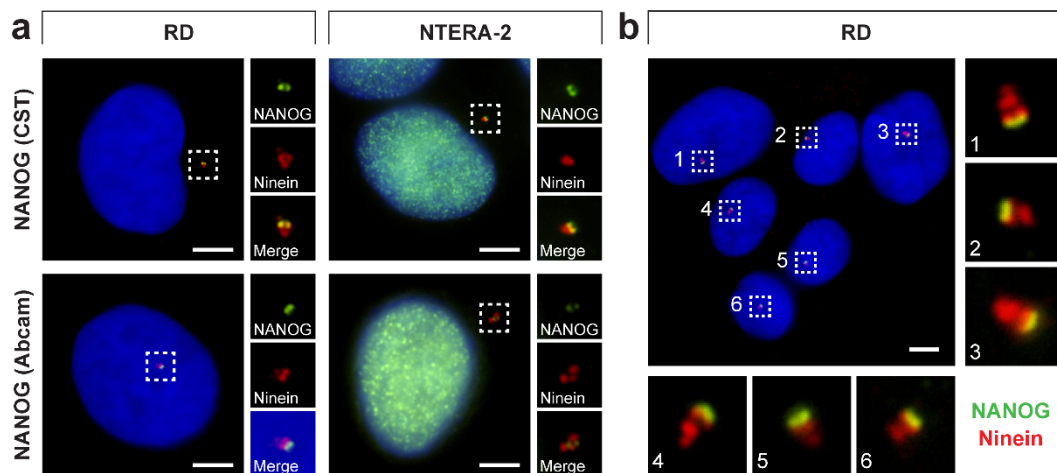
Figure 9. NANOG colocalization with the mother centriole. (**a**) A colocalization of NANOG (green; #4903, Cell Signaling Technology (CST) and #ab109250, Abcam) with the mother centriole was detected using anti-ninein antibody (red), recognizing a protein of the mother centriole subdistal appendages. The nuclei were counterstained with Hoechst 33342 (blue). For each image, regions of interest and the respective close-ups are indicated by the dashed boxes. (**b**) NANOG signal (green; #4903, Cell Signaling Technology) partially colocalized with the "double-spot" signal of ninein (red). The nuclei were counterstained with Hoechst 33342 (blue). Respective close-ups of NANOG and ninein colocalization are indicated by numbers. Scale bars, 5 μm.

4. Discussion

Taken together, our results clearly demonstrate the presence of NANOG protein at the centrosomes and indicate that its spatiotemporal localization associates with the mother centriole. This interesting phenomenon was proven in tumor cell lines, as well as non-cancerous hESCs and normal fibroblast cells. Considering the mass spectrometry and RT-qPCR results, this protein was most likely the NANOG paralog NANOGP8, which was localized in centrosomes and might be the cause of the NANOG signal detected within these organelles. Whether this phenomenon is common remains speculative, and further investigation will be needed to distinguish the subcellular localization of NANOG and NANOGP8 proteins, which have nearly 100% homology and have been demonstrated to possess similar reprogramming activity [17].

To date, the atypical centrosomal localization of NANOG was only briefly noted in a study focused on induced pluripotent stem cells [62]. By using the same #4903 Cell Signaling Technology anti-NANOG antibody, the authors observed a perinuclear signal of NANOG in HEK293 cells and amniotic cell-derived iPSCs. However, the study lacks validation of the suggested centrosomal localization of NANOG by any centrosome-specific antibody, and the anti-NANOG antibody specificity has not been examined by proper controls and additional experiments [62]. In this report, we present the first systematic analysis of NANOG colocalization with centrosomes using two independent anti-NANOG commercial antibodies together with antibodies recognizing different centrosomal proteins.

Indeed, our immunofluorescence results undeniably demonstrate the colocalization of NANOG with centrosomes, as visualized by anti-pericentrin, anti-CP110, and anti-ninein antibodies. Importantly, the authenticity of the NANOG signal in centrosomes was independently proven by NANOG-GFP

transfection experiments. Surprisingly, cell fractionation further revealed that RD cells, which exhibit only weak nuclear staining of NANOG compared with NTERA-2 cells, contained a substantial amount of NANOG protein present in the cytoplasmic fraction. Given the specific cytoplasmic distribution of NANOG in RD cells, the amount of protein detected in the cytoplasmic fraction generally reflected the centrosome-localized pool of NANOG. Along with the finding that the centrosomal localization of NANOG was observed among various tumor and non-tumor cell types, these results provide the first evidence suggesting a common centrosome-specific role of NANOG. We hypothesize that this function might be maintained even in cells with low/basal levels of NANOG protein.

Several transcription factors have been previously described to be present at the centrosome [63,64], including recently reported ATF5 [64]. Independent of its role as a transcription factor, ATF5 was demonstrated to be indispensable for proper centrosome assembly and maintenance [64]. To exert its function in the process of pericentriolar material accumulation, ATF5 localizes at the mother centriole in a cell cycle- and centriole age-dependent manner [64]. Interestingly, the reported spatial and temporal profile of ATF5 [64] is in keeping with our observations with NANOG.

In our study, NANOG was identified at only one centrosome in interphase cells, even after centrosome separation before mitosis. In contrast, the fluorescence signal of NANOG was also detected at the other centrosome of the centrosome pair during mitosis. The presence/absence of NANOG signal at the centrosome during the cell cycle corresponded with the centriole maturation, which is accompanied by the formation of centriole appendages. The association of NANOG protein with the mother centriole was experimentally confirmed by immunofluorescence staining using anti-ninein antibody, which is specific for the mother centriole subdistal appendages. Taken together, these results suggest an intricate centriole maturation-dependent interaction of NANOG with the mother centriole. The main observations of our study regarding NANOG occurrence at the centrosome during the cell cycle are schematically summarized in Figure 10.
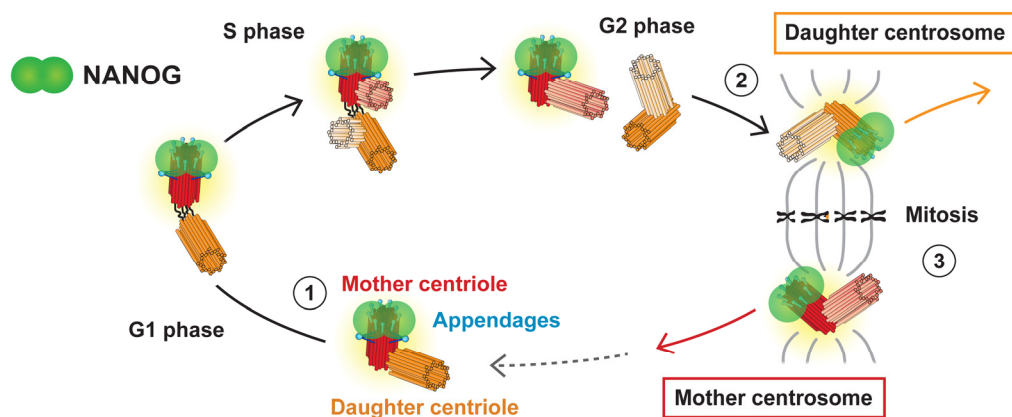
Figure 10. Schematic summarizing the observed spatiotemporal localization of NANOG/NANOGP8 at centrosome during the cell cycle. NANOG (green) is present at the same time as mother centriole appendages: (1) During interphase, NANOG protein colocalizes with the distal region of the mother centriole (red), which carries distal and subdistal appendages (blue). (2) NANOG signal as well as the distal appendages also later appear on the initially daughter centriole (orange) during the G2/mitosis transition. (3) The centrosome duplication cycle results in two daughter cells with different ages of centrosomes, mother and daughter centrosomes, both having the older, mother centriole marked with NANOG protein.

A question remains regarding the exact role of NANOG and/or NANOGP8 in centrosomes and why its presence appears to be dependent on the age of centrosomes. Centrosome duplication is an elaborate process in which many proteins are involved [48–50]. Duplication of centrosomes begins by separation of mother and daughter centrioles and formation of a procentriole adjacent to both centrioles during the G1 phase [65,66]. Procentrioles elongate through S and G2 phases followed by

maturation of centrioles. The final step of centriole maturation is the building of distal and subdistal appendages on their distal ends. The presence of distal appendages depends on ODF1 [50,67] and C2cd3 [68] followed by Cep83, which then recruits other proteins, including Cep89, SCLT1, FBF1, and Cep164 [44,50]. The formation of subdistal appendages is initiated by two groups of proteins. The first group is led by ODF2 [50,58,69,70] followed by the recruitment of various proteins, including CCDC120, CCDC68, trichoplein [50,59], CEP128, and centriolin [69]. The second group is led by ninein, followed by Kif2a, p150^{Glued} and CEP170 [59,69,70], centriolin, and ε-tubulin [71].

The formation of distal and subdistal appendages is a highly complicated and still poorly understood process. Nevertheless, the newly formed mother centriole lacks distal and subdistal appendages until the G2/M phase transition and G1 phase of the next cell cycle, respectively [43,53]. Corroborating the functional differences between the mother and daughter centrosomes, a strong correlation between centrosome age and cell fate has been demonstrated during the cell division of stem cells [72,73]. In addition, proper orientation of centrosomes and thus mitotic spindle orientation also appear to be strictly orchestrated for the maintenance of stemness [72,74]. Our results describing the presence/absence of the NANOG signal during the cell cycle (Figure 8a,c) correspond with the occurrence of centriole appendages. Therefore, all these results indicate the association of NANOG protein or its NANOGP8 paralog with the process of centriole maturation. Such connections have never been described or functionally explored. The hypothesis that NANOG, a protein crucially involved in the regulation of pluripotency and stemness, might be directly involved in the regulation of centrosome and/or mitotic spindle assembly provokes many scientific questions that should be pursued in future studies. For this reason, our further research will investigate the possible function of NANOG/NANOGP8 associated with centrosomes.

References

1. Chambers, I.; Colby, D.; Robertson, M.; Nichols, J.; Lee, S.; Tweedie, S.; Smith, A. Functional Expression Cloning of Nanog, a Pluripotency Sustaining Factor in Embryonic Stem Cells. *Cell* **2003**, *113*, 643–655. [CrossRef]
2. Mitsui, K.; Tokuzawa, Y.; Itoh, H.; Segawa, K.; Murakami, M.; Takahashi, K.; Maruyama, M.; Maeda, M.; Yamanaka, S. The Homeoprotein Nanog Is Required for Maintenance of Pluripotency in Mouse Epiblast and ES Cells. *Cell* **2003**, *113*, 631–642. [CrossRef]
3. Silva, J.; Nichols, J.; Theunissen, T.W.; Guo, G.; van Oosten, A.L.; Barrandon, O.; Wray, J.; Yamanaka, S.; Chambers, I.; Smith, A. Nanog is the gateway to the pluripotent ground state. *Cell* **2009**, *138*, 722–737. [CrossRef] [PubMed]

4.   Hart, A.H.; Hartley, L.; Parker, K.; Ibrahim, M.; Looijenga, L.H.J.; Pauchnik, M.; Chow, C.W.; Robb, L. The pluripotency homeobox gene NANOG is expressed in human germ cell tumors. *Cancer* **2005**, *104*, 2092–2098. [CrossRef] [PubMed]

5.   Zbinden, M.; Duquet, A.; Lorente-Trigos, A.; Ngwabyt, S.-N.; Borges, I.; Ruiz i Altaba, A. NANOG regulates glioma stem cells and is essential in vivo acting in a cross-functional network with GLI1 and p53. *EMBO J.* **2010**, *29*, 2659–2674. [CrossRef] [PubMed]

6.   Nagata, T.; Shimada, Y.; Sekine, S.; Hori, R.; Matsui, K.; Okumura, T.; Sawada, S.; Fukuoka, J.; Tsukada, K. Prognostic significance of NANOG and KLF4 for breast cancer. *Breast Cancer* **2014**, *21*, 96–101. [CrossRef]

7.   Santaliz-Ruiz, L.E.; Xie, X.; Old, M.; Teknos, T.N.; Pan, Q. Emerging Role of Nanog in Tumorigenesis and Cancer Stem Cells. *Int. J. Cancer J. Int. Cancer* **2014**, *135*, 2741–2748. [CrossRef]

8.   Fan, Z.; Li, M.; Chen, X.; Wang, J.; Liang, X.; Wang, H.; Wang, Z.; Cheng, B.; Xia, J. Prognostic Value of Cancer Stem Cell Markers in Head and Neck Squamous Cell Carcinoma: A Meta-analysis. *Sci. Rep.* **2017**, *7*, 43008. [CrossRef]

9.   Freitag, D.; McLean, A.L.; Simon, M.; Koch, A.; Grube, S.; Walter, J.; Kalff, R.; Ewald, C. NANOG overexpression and its correlation with stem cell and differentiation markers in meningiomas of different WHO grades. *Mol. Carcinog.* **2017**, *56*, 1953–1964. [CrossRef]

10.   Rasti, A.; Mehrazma, M.; Madjd, Z.; Abolhasani, M.; Zanjani, L.S.; Asgari, M. Co-expression of Cancer Stem Cell Markers OCT4 and NANOG Predicts Poor Prognosis in Renal Cell Carcinomas. *Sci. Rep.* **2018**, *8*, 1–11. [CrossRef]

11.   Nichols, J.; Zevnik, B.; Anastassiadis, K.; Niwa, H.; Klewe-Nebenius, D.; Chambers, I.; Schöler, H.; Smith, A. Formation of pluripotent stem cells in the mammalian embryo depends on the POU transcription factor Oct4. *Cell* **1998**, *95*, 379–391. [CrossRef]

12.   Avilion, A.A.; Nicolis, S.K.; Pevny, L.H.; Perez, L.; Vivian, N.; Lovell-Badge, R. Multipotent cell lineages in early mouse development depend on SOX2 function. *Genes Dev.* **2003**, *17*, 126–140. [CrossRef] [PubMed]

13.   Pan, G.; Thomson, J.A. Nanog and transcriptional networks in embryonic stem cell pluripotency. *Cell Res.* **2007**, *17*, 42–49. [CrossRef] [PubMed]

14.   Hyslop, L.; Stojkovic, M.; Armstrong, L.; Walter, T.; Stojkovic, P.; Przyborski, S.; Herbert, M.; Murdoch, A.; Strachan, T.; Lako, M. Downregulation of NANOG induces differentiation of human embryonic stem cells to extraembryonic lineages. *Stem Cells Dayt. Ohio* **2005**, *23*, 1035–1043. [CrossRef] [PubMed]

15.   Schorle, H.; Nettersheim, D. NANOG (Nanog homeobox). *Atlas Genet. Cytogenet. Oncol. Haematol.* **2012**. [CrossRef]

16.   Booth, H.A.F.; Holland, P.W.H. Eleven daughters of NANOG. *Genomics* **2004**, *84*, 229–238. [CrossRef]

17.   Palla, A.R.; Piazzolla, D.; Abad, M.; Li, H.; Dominguez, O.; Schonthaler, H.B.; Wagner, E.F.; Serrano, M. Reprogramming activity of NANOGP8, a NANOG family member widely expressed in cancer. *Oncogene* **2014**, *33*, 2513–2519. [CrossRef]

18.   Zhang, J.; Wang, X.; Li, M.; Han, J.; Chen, B.; Wang, B.; Dai, J. NANOGP8 is a retrogene expressed in cancers. *FEBS J.* **2006**, *273*, 1723–1730. [CrossRef]

19.   Ambady, S.; Malcuit, C.; Kashpur, O.; Kole, D.; Holmes, W.F.; Hedblom, E.; Page, R.L.; Dominko, T. Expression of NANOG and NANOGP8 in a variety of undifferentiated and differentiated human cells. *Int. J. Dev. Biol.* **2010**, *54*, 1743–1754. [CrossRef]

20.   Do, H.-J.; Lim, H.-Y.; Kim, J.-H.; Song, H.; Chung, H.-M.; Kim, J.-H. An intact homeobox domain is required for complete nuclear localization of human Nanog. *Biochem. Biophys. Res. Commun.* **2007**, *353*, 770–775. [CrossRef]

21.   Chang, D.F.; Tsai, S.C.; Wang, X.C.; Xia, P.; Senadheera, D.; Lutzko, C. Molecular Characterization of the Human NANOG Protein. *Stem Cells* **2009**, *27*, 812–821. [CrossRef] [PubMed]

22.   Gu, T.-T.; Liu, S.-Y.; Zheng, P.-S. Cytoplasmic NANOG-Positive Stromal Cells Promote Human Cervical Cancer Progression. *Am. J. Pathol.* **2012**, *181*, 652–661. [CrossRef] [PubMed]

23.   van Schaijik, B.; Davis, P.F.; Wickremesekera, A.C.; Tan, S.T.; Itinteang, T. Subcellular localisation of the stem cell markers OCT4, SOX2, NANOG, KLF4 and c-MYC in cancer: A review. *J. Clin. Pathol.* **2018**, *71*, 88–91. [CrossRef] [PubMed]

24.   Dvorak, P.; Dvorakova, D.; Koskova, S.; Vodinska, M.; Najvirtova, M.; Krekac, D.; Hampl, A. Expression and Potential Role of Fibroblast Growth Factor 2 and Its Receptors in Human Embryonic Stem Cells. *STEM CELLS* **2005**, *23*, 1200–1211. [CrossRef]

25. Sana, J.; Zambo, I.; Skoda, J.; Neradil, J.; Chlapek, P.; Hermanova, M.; Mudry, P.; Vasikova, A.; Zitterbart, K.; Hampl, A.; et al. CD133 Expression and Identification of CD133/nestin Positive Cells in Rhabdomyosarcomas and Rhabdomyosarcoma Cell Lines. *Anal. Cell. Pathol. Amst.* **2011**, *34*, 303–318. [CrossRef]

26. Loja, T.; Chlapek, P.; Kuglik, P.; Pesakova, M.; Oltova, A.; Cejpek, P.; Veselska, R. Characterization of a GM7 glioblastoma cell line showing CD133 positivity and both cytoplasmic and nuclear localization of nestin. *Oncol. Rep.* **2009**, *21*, 119–127.

27. Veselska, R.; Skoda, J.; Loja, T.; Zitterbart, K.; Pavelka, Z.; Smardova, J.; Valaskova, I.; Hermanova, M.; Sterba, J. An unusual loss of EGFR gene copy in glioblastoma multiforme in a child: A case report and analysis of a successfully derived HGG-02 cell line. *Childs Nerv. Syst. ChNS Off. J. Int. Soc. Pediatr. Neurosurg.* **2010**, *26*, 841–846. [CrossRef]

28. Veselska, R.; Janisch, R. Reaction of the Skin Fibroblast Cytoskeleton to Micromanipulation Interventions–ScienceDirect. Available online: https://www.sciencedirect.com/science/article/pii/S1047847701944326 (accessed on 2 August 2019).

29. Mikulenkova, E.; Neradil, J.; Zitterbart, K.; Sterba, J.; Veselska, R. Overexpression of the ΔNp73 isoform is associated with centrosome amplification in brain tumor cell lines. *Tumour Biol. J. Int. Soc. Oncodevelopmental Biol. Med.* **2015**, *36*, 7483–7491. [CrossRef]

30. Kleylein-Sohn, J.; Westendorf, J.; Le Clech, M.; Habedanck, R.; Stierhof, Y.-D.; Nigg, E.A. Plk4-induced centriole biogenesis in human cells. *Dev. Cell* **2007**, *13*, 190–202. [CrossRef]

31. Wiśniewski, J.R.; Zougman, A.; Nagaraj, N.; Mann, M. Universal sample preparation method for proteome analysis. *Nat. Methods* **2009**, *6*, 359–362. [CrossRef]

32. Holman, J.D.; Tabb, D.L.; Mallick, P. Employing ProteoWizard to Convert Raw Mass Spectrometry Data. *Curr. Protoc. Bioinforma.* **2014**, *46*, 13–24. [CrossRef] [PubMed]

33. McIlwain, S.; Tamura, K.; Kertesz-Farkas, A.; Grant, C.E.; Diament, B.; Frewen, B.; Howbert, J.J.; Hoopmann, M.R.; Käll, L.; Eng, J.K.; et al. Crux: Rapid open source protein tandem mass spectrometry analysis. *J. Proteome Res.* **2014**, *13*, 4488–4491. [CrossRef] [PubMed]

34. The, M.; MacCoss, M.J.; Noble, W.S.; Käll, L. Fast and Accurate Protein False Discovery Rates on Large-Scale Proteomics Data Sets with Percolator 3.0. *J. Am. Soc. Mass Spectrom.* **2016**, *27*, 1719–1727. [CrossRef] [PubMed]

35. Millikin, R.J.; Solntsev, S.K.; Shortreed, M.R.; Smith, L.M. Ultrafast Peptide Label-Free Quantification with FlashLFQ. *J. Proteome Res.* **2018**, *17*, 386–391. [CrossRef] [PubMed]

36. Silva, J.C.; Gorenstein, M.V.; Li, G.-Z.; Vissers, J.P.C.; Geromanos, S.J. Absolute quantification of proteins by LCMSE: A virtue of parallel MS acquisition. *Mol. Cell. Proteomics MCP* **2006**, *5*, 144–156. [CrossRef]

37. Livak, K.J.; Schmittgen, T.D. Analysis of relative gene expression data using real-time quantitative PCR and the 2(-Delta Delta C(T)) Method. *Methods San Diego Calif* **2001**, *25*, 402–408. [CrossRef]

38. Ma, X.; Wang, B.; Wang, X.; Luo, Y.; Fan, W. NANOGP8 is the key regulator of stemness, EMT, Wnt pathway, chemoresistance, and other malignant phenotypes in gastric cancer cells. *PLoS ONE* **2018**, *13*, e0192436. [CrossRef]

39. Hu, Q.; Khanna, P.; Ee Wong, B.S.; Lin Heng, Z.S.; Subhramanyam, C.S.; Thanga, L.Z.; Sing Tan, S.W.; Baeg, G.H. Oxidative stress promotes exit from the stem cell state and spontaneous neuronal differentiation. *Oncotarget* **2018**, *9*, 4223–4238. [CrossRef]

40. Paintrand, M.; Moudjou, M.; Delacroix, H.; Bornens, M. Centrosome organization and centriole architecture: Their sensitivity to divalent cations. *J. Struct. Biol.* **1992**, *108*, 107–128. [CrossRef]

41. Sonnen, K.F.; Schermelleh, L.; Leonhardt, H.; Nigg, E.A. 3D-structured illumination microscopy provides novel insight into architecture of human centrosomes. *Biol. Open* **2012**, *1*, 965–976. [CrossRef]

42. Nigg, E.A.; Holland, A.J. Once and only once: Mechanisms of centriole duplication and their deregulation in disease. *Nat. Rev. Mol. Cell Biol.* **2018**, *19*, 297–312. [CrossRef] [PubMed]

43. Uzbekov, R.; Alieva, I. Who are you, subdistal appendages of centriole? *Open Biol.* **2018**, *8*, 180062. [CrossRef] [PubMed]

44. Tanos, B.E.; Yang, H.-J.; Soni, R.; Wang, W.-J.; Macaluso, F.P.; Asara, J.M.; Tsou, M.-F.B. Centriole distal appendages promote membrane docking, leading to cilia initiation. *Genes Dev.* **2013**, *27*, 163–168. [CrossRef] [PubMed]

45. Vorobjev, I.A.; Nadezhdina, E.S. The centrosome and its role in the organization of microtubules. *Int. Rev. Cytol.* **1987**, *106*, 227–293. [PubMed]

46. Bornens, M. Centrosome composition and microtubule anchoring mechanisms. *Curr. Opin. Cell Biol.* **2002**, *14*, 25–34. [CrossRef]

47. Hinchcliffe, E.H. "It Takes Two to Tango": Understanding how centrosome duplication is regulated throughout the cell cycle. *Genes Dev.* **2001**, *15*, 1167–1181. [CrossRef]

48. Loncarek, J.; Khodjakov, A. Ab ovo or de novo? Mechanisms of centriole duplication. *Mol. Cells* **2009**, *27*, 135–142. [CrossRef]

49. Fujita, H.; Yoshino, Y.; Chiba, N. Regulation of the centrosome cycle. *Mol. Cell. Oncol.* **2015**, *3*, e1075643. [CrossRef]

50. Loncarek, J.; Bettencourt-Dias, M. Building the right centriole for each cell type. *J. Cell Biol.* **2018**, *217*, 823–835. [CrossRef]

51. Stearns, T. Centrosome duplication. A centriolar pas de deux. *Cell* **2001**, *105*, 417–420. [CrossRef]

52. Reina, J.; Gonzalez, C. When fate follows age: Unequal centrosomes in asymmetric cell division. *Philos. Trans. R. Soc. Lond. B. Biol. Sci.* **2014**, *369*. [CrossRef] [PubMed]

53. Vorobjev, I.A.; Chentsov, Y.S. Centrioles in the cell cycle. I. Epithelial cells. *J. Cell Biol.* **1982**, *93*, 938–949. [CrossRef] [PubMed]

54. Piel, M.; Meyer, P.; Khodjakov, A.; Rieder, C.L.; Bornens, M. The respective contributions of the mother and daughter centrioles to centrosome activity and behavior in vertebrate cells. *J. Cell Biol.* **2000**, *149*, 317–330. [CrossRef] [PubMed]

55. Mogensen, M.M.; Malik, A.; Piel, M.; Bouckson-Castaing, V.; Bornens, M. Microtubule minus-end anchorage at centrosomal and non-centrosomal sites: The role of ninein. *J. Cell Sci.* **2000**, *113*, 3013–3023. [PubMed]

56. Ou, Y.Y.; Mack, G.J.; Zhang, M.; Rattner, J.B. CEP110 and ninein are located in a specific domain of the centrosome associated with centrosome maturation. *J. Cell Sci.* **2002**, *115*, 1825–1835.

57. Lee, M.; Rhee, K. Determination of Mother Centriole Maturation in CPAP-Depleted Cells Using the Ninein Antibody. *Endocrinol. Metab. Seoul Korea* **2015**, *30*, 53–57. [CrossRef]

58. Tateishi, K.; Yamazaki, Y.; Nishida, T.; Watanabe, S.; Kunimoto, K.; Ishikawa, H.; Tsukita, S. Two appendages homologous between basal bodies and centrioles are formed using distinct Odf2 domains. *J. Cell Biol.* **2013**, *203*, 417–425. [CrossRef]

59. Huang, N.; Xia, Y.; Zhang, D.; Wang, S.; Bao, Y.; He, R.; Teng, J.; Chen, J. Hierarchical assembly of centriole subdistal appendages via centrosome binding proteins CCDC120 and CCDC68. *Nat. Commun.* **2017**, *8*, 1–14. [CrossRef]

60. Kashihara, H.; Chiba, S.; Kanno, S.; Suzuki, K.; Yano, T.; Tsukita, S. Cep128 associates with Odf2 to form the subdistal appendage of the centriole. *Genes Cells* **2019**, *24*, 231–243. [CrossRef]

61. Fu, J.; Glover, D.M. Structured illumination of the interface between centriole and peri-centriolar material. *Open Biol.* **2012**, *2*, 120104. [CrossRef]

62. Wilson, P.G.; Payne, T. Genetic reprogramming of human amniotic cells with episomal vectors: Neural rosettes as sentinels in candidate selection for validation assays. *PeerJ* **2014**, *2*, e668. [CrossRef] [PubMed]

63. Chuang, L.S.H.; Lai, S.K.; Murata-Hori, M.; Yamada, A.; Li, H.-Y.; Gunaratne, J.; Ito, Y. RUNX3 interactome reveals novel centrosomal targeting of RUNX family of transcription factors. *Cell Cycle Georget. Tex* **2012**, *11*, 1938–1947. [CrossRef] [PubMed]

64. Madarampalli, B.; Yuan, Y.; Liu, D.; Lengel, K.; Xu, Y.; Li, G.; Yang, J.; Liu, X.; Lu, Z.; Liu, D.X. ATF5 Connects the Pericentriolar Materials to the Proximal End of the Mother Centriole. *Cell* **2015**, *162*, 580–592. [CrossRef] [PubMed]

65. Uzbekov, R.E. Centriole duplication in PE (SPEV) cells starts before the beginning of the DNA replication. *Biochem. Mosc. Suppl. Ser. Membr. Cell Biol.* **2007**, *1*, 206–211. [CrossRef]

66. Gupta, A.; Tsuchiya, Y.; Ohta, M.; Shiratsuchi, G.; Kitagawa, D. NEK7 is required for G1 progression and procentriole formation. *Mol. Biol. Cell* **2017**, *28*, 2123–2134. [CrossRef]

67. Singla, V.; Romaguera-Ros, M.; Garcia-Verdugo, J.M.; Reiter, J.F. Ofd1, a human disease gene, regulates the length and distal structure of centrioles. *Dev. Cell* **2010**, *18*, 410–424. [CrossRef]

68. Ye, X.; Zeng, H.; Ning, G.; Reiter, J.F.; Liu, A. C2cd3 is critical for centriolar distal appendage assembly and ciliary vesicle docking in mammals. *Proc. Natl. Acad. Sci. USA* **2014**, *111*, 2164–2169. [CrossRef]

69. Galati, D.F.; Mitchell, B.J.; Pearson, C.G. Subdistal Appendages Stabilize the Ups and Downs of Ciliary Life. *Dev. Cell* **2016**, *39*, 387–389. [CrossRef]

70. Mazo, G.; Soplop, N.; Wang, W.-J.; Uryu, K.; Tsou, M.-F.B. Spatial Control of Primary Ciliogenesis by Subdistal Appendages Alters Sensation-Associated Properties of Cilia. *Dev. Cell* **2016**, *39*, 424–437. [CrossRef]

71. Chang, P.; Giddings, T.H.; Winey, M.; Stearns, T. Epsilon-tubulin is required for centriole duplication and microtubule organization. *Nat. Cell Biol.* **2003**, *5*, 71–76. [CrossRef]

72. Yamashita, Y.M.; Mahowald, A.P.; Perlin, J.R.; Fuller, M.T. Asymmetric Inheritance of Mother Versus Daughter Centrosome in Stem Cell Division. *Science* **2007**, *315*, 518–521. [CrossRef] [PubMed]

73. Pelletier, L.; Yamashita, Y.M. Centrosome asymmetry and inheritance during animal development. *Curr. Opin. Cell Biol.* **2012**, *24*, 541–546. [CrossRef] [PubMed]

74. Yamashita, Y.M.; Jones, D.L.; Fuller, M.T. Orientation of asymmetric stem cell division by the APC tumor suppressor and centrosome. *Science* **2003**, *301*, 1547–1550. [CrossRef] [PubMed]

Skoda J*, Neradil J, Staniczkova Zambo I, Nunukova A, Macsek P, Borankova K, Dobrotkova V, Nemec P, Sterba J, Veselska R. Serial Xenotransplantation in NSG Mice Promotes a Hybrid Epithelial/Mesenchymal Gene Expression Signature and Stemness in Rhabdomyosarcoma Cells. *Cancers*. 2020;12:196. (JCR 2020, IF = 6.639; Q1 – Oncology)

Serial Xenotransplantation in NSG Mice Promotes a Hybrid Epithelial/Mesenchymal Gene Expression Signature and Stemness in Rhabdomyosarcoma Cells

Jan Skoda [1,2,*,†], Jakub Neradil [1,2], Iva Staniczkova Zambo [2,3], Alena Nunukova [1], Peter Macsek [1], Karolina Borankova [1], Viera Dobrotkova [1], Pavel Nemec [1], Jaroslav Sterba [2,4] and Renata Veselska [1,2,4,*,†]

[1] Department of Experimental Biology, Faculty of Science, Masaryk University, 61137 Brno, Czech Republic; jneradil@sci.muni.cz (J.N.); 416784@mail.muni.cz (A.N.); macsek@mail.muni.cz (P.M.); karolina.borankova@mail.muni.cz (K.B.); 380342@mail.muni.cz (V.D.); 78094@mail.muni.cz (P.N.)

[2] International Clinical Research Center, St. Anne's University Hospital, 65691 Brno, Czech Republic; iva.zambo@fnusa.cz (I.S.Z.); sterba.jaroslav@fnbrno.cz (J.S.)

[3] 1st Department of Pathological Anatomy, St. Anne's University Hospital and Faculty of Medicine, Masaryk University, 65691 Brno, Czech Republic

[4] Department of Pediatric Oncology, University Hospital Brno and Faculty of Medicine, Masaryk University, 62500 Brno, Czech Republic

* Correspondence: janskoda@sci.muni.cz (J.S.); veselska@sci.muni.cz (R.V.); Tel.: +420-549-49-7905 (R.V.)

† The two authors contributed equally as senior authors.

Abstract: Serial xenotransplantation of sorted cancer cells in immunodeficient mice remains the most complex test of cancer stem cell (CSC) phenotype. However, we have demonstrated in various sarcomas that putative CSC surface markers fail to identify CSCs, thereby impeding the isolation of CSCs for subsequent analyses. Here, we utilized serial xenotransplantation of unsorted rhabdomyosarcoma cells in NOD/SCID gamma (NSG) mice as a proof-of-principle platform to investigate the molecular signature of CSCs. Indeed, serial xenotransplantation steadily enriched for rhabdomyosarcoma stem-like cells characterized by enhanced aldehyde dehydrogenase activity and increased colony and sphere formation capacity in vitro. Although the expression of core pluripotency factors (SOX2, OCT4, NANOG) and common CSC markers (CD133, ABCG2, nestin) was maintained over the passages in mice, gene expression profiling revealed gradual changes in several stemness regulators and genes linked with undifferentiated myogenic precursors, e.g., *SOX4*, *PAX3*, *MIR145*, and *CDH15*. Moreover, we identified the induction of a hybrid epithelial/mesenchymal gene expression signature that was associated with the increase in CSC number. In total, 60 genes related to epithelial or mesenchymal traits were significantly altered upon serial xenotransplantation. In silico survival analysis based on the identified potential stemness-associated genes demonstrated that serial xenotransplantation of unsorted rhabdomyosarcoma cells in NSG mice might be a useful tool for the unbiased enrichment of CSCs and the identification of novel CSC-specific targets. Using this approach, we provide evidence for a recently proposed link between the hybrid epithelial/mesenchymal phenotype and cancer stemness.

Keywords: rhabdomyosarcoma; cancer stem cells; stemness; stem-like state; serial xenotransplantation; in vivo tumorigenicity assay; epithelial/mesenchymal phenotype

1. Introduction

Rhabdomyosarcoma is the most common malignant mesenchymal tumor in children, with a peak incidence in patients younger than 5 years old [1]. The embryonal subtype represents ~70% of all rhabdomyosarcoma cases and is associated with a good prognosis. Yet approximately one-third of embryonal rhabdomyosarcoma patients die, mostly from metastatic disease [1,2]. Despite the significant improvement in the survival of rhabdomyosarcoma patients, the prognosis of children with relapsed or metastatic disease has not changed over the last 30 years [2].

As in other cancers, cancer stem cells (CSCs) have been implicated in the recurrence and progression of rhabdomyosarcoma. Although the first studies suggested prominin-1 (CD133) [3,4] or nestin [3] as rhabdomyosarcoma CSC markers, our recent study showed that, regardless of these proteins, only sarcoma cell lines that express high levels of the transcription factor SOX2 form tumors in immunodeficient NOD/SCID gamma (NSG) mice [5]. An in vivo tumorigenicity assay remains a gold-standard functional assay of the CSC phenotype because it enables us to test (directly in an animal model) the ability of cancer cells to self-renew and form a tumor that exhibits the cellular heterogeneity of the primary tumor [6]. Commonly, this assay has been used to determine the tumorigenicity of different cell populations sorted based on prospective CSC surface markers (e.g., CD133, ABCG2, CD24, CD44 [7,8]). Ideally, when a xenograft tumor forms, cells are sorted again and transplanted into secondary recipient mice. This serial xenotransplantation should validate the specificity of a studied marker and verify that the sorted population of cells retains its CSC characteristics [6]. Although it may provide some important evidence, such an approach is to a large extent limited because it assumes sustained levels of marker proteins on the cell surface of CSCs. However, it is becoming evident that the subcellular localization of these putative CSC markers, e.g., CD133 [5,9,10] or CD24 [10,11], is dictated by a complex dynamic process, which presumably reflects cellular needs under different conditions and impairs the use of such proteins as surface markers to distinguish between CSC and non-CSC states [8].

A growing body of evidence shows that enhanced cell plasticity, one of the intrinsic characteristics of CSCs, may provide another explanation for the contradictory results reported regarding the validity of CSC surface markers [7,8,12]. Many of the previously suggested markers have been recently demonstrated as being non-specific, either because both marker-positive and marker-negative cell populations exhibited the same tumorigenic capacities or because marker-positive cells did not form tumors in mice [8]. Thus, recent CSC studies have focused on proteins that are functionally involved in the regulation of stemness and cellular plasticity, such as SOX2, OCT4, or NANOG [8,13]. Indeed, many studies clearly demonstrated a crucial role for these stemness regulators in the induction and maintenance of CSCs in various cancers [8,13,14]. However, because most of these proteins are intracellular, cells must be genetically manipulated to enable their sorting and enrichment according to these markers [13].

Here, we present another approach to study CSCs utilizing an in vivo tumorigenicity assay. It has been previously reported that serial xenotransplantation of cancer cells in immunodeficient mice (passaging in vivo) selects highly tumorigenic cells that generate more aggressive tumors [15–17]. Similarly, the acquisition of stemness has been linked with cancer progression and more advanced disease [15]. Thus, we employed serial xenotransplantation of unsorted rhabdomyosarcoma cells as a platform for an unbiased screening of molecular targets that are relevant for the acquisition and maintenance of a CSC phenotype. Our results demonstrate that serial xenotransplantation in NSG mice might be a useful tool for CSC enrichment, allowing subsequent analyses to identify prospective CSC markers and potential therapeutic targets. Using serial xenotransplantation of embryonal rhabdomyosarcoma cells, we revealed an upregulation of several genes associated with stemness and early myogenic precursors. More importantly, this approach allowed us to unveil complex molecular changes that may underlie the induction of stemness in rhabdomyosarcoma, such as a hybrid epithelial/mesenchymal signature, which was recently linked with CSCs in other cancers.

2. Results

2.1. Tumorigenicity of NSTS-11 Rhabdomyosarcoma Cells Is Maintained during Serial Xenotransplantation in NSG Mice

The long-term capacity of NSTS-11 cells to form tumors in NSG mice was tested by three subsequent xenotransplantations (passages in vivo; for the experimental design, see Figure 1a). In each passage in vivo, NSTS-11 cells and xenograft tumor-derived cells formed tumors with high efficiency (Table 1). These results confirmed the presence of rhabdomyosarcoma CSCs in the NSTS-11 cell line and demonstrated that these CSCs are maintained during long-term passaging, which included both xenotransplantation in NSG mice and in vitro culture (refer to the experimental design in Figure 1a). The tumorigenicity of 9 cell lines derived from the secondary xenograft tumors was 100%, as revealed in the third, and last, passage in vivo (27 of 27 mice had tumors; Table 1). More importantly, the later in vivo passages resulted in markedly aggressive growth and larger xenografts, as evident from the statistically significant 1.95-fold higher daily increase of the tumor volume in the third passage in vivo compared with the first passage in vivo (2.89 ± 0.74 versus 5.66 ± 0.72 mm^3/day; Table 1). Hence, tumor growth parameters and tumorigenic efficiency in the third passage in vivo suggested a selection of aggressive tumorigenic cells, i.e., CSCs, during serial xenotransplantation.
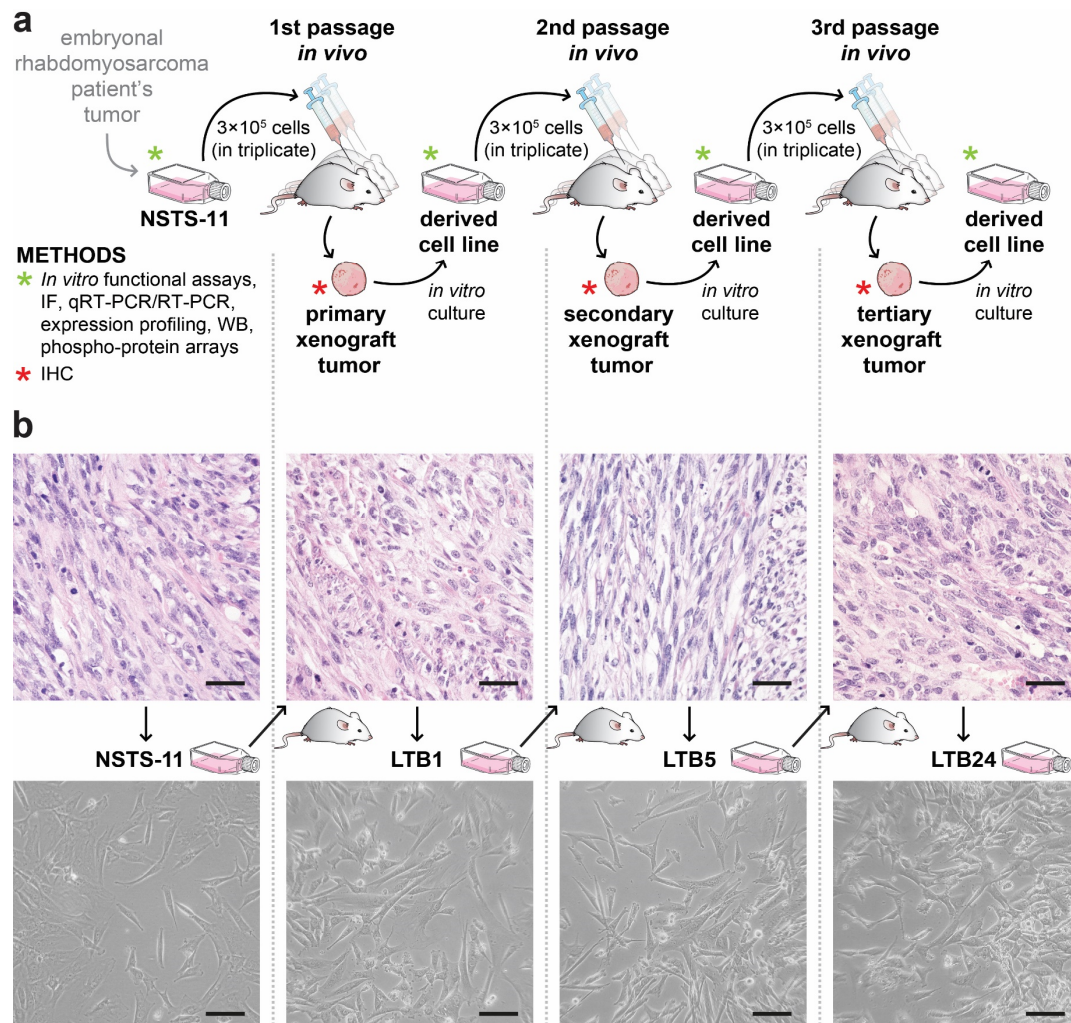
Figure 1. (**a**) Schematic overview of the experimental design. NSTS-11 cells derived from the embryonal rhabdomyosarcoma were injected subcutaneously into three NOD/SCID gamma (NSG) mice (in vivo

passage). After the appearance of a tumor, the mouse was sacrificed, and the xenograft tumor was excised and divided into equal parts. One part of the xenograft tumor was used to prepare formalin-fixed paraffin-embedded (FFPE) tissue sections. The second part was processed for primary culture, and the derived cell line was used in a subsequent passage in vivo. This procedure was repeated twice to achieve three in vivo passages. Methods used to analyze tumor tissues or cell lines are indicated. IF, immunofluorescence; qRT-PCR/RT-PCR, real-time/reverse transcription polymerase chain reaction; WB, Western blotting; IHC, immunohistochemistry. (**b**) Representative hematoxylin-eosin images of the tumor tissues (upper panel) and phase contrast microscopy images of the parental NSTS-11 cells and the cells derived from the primary (LTB1), secondary (LTB5), and tertiary (LTB24) xenograft tumors (lower panel). Scale bars, 50 μm (upper panel), 100 μm (lower panel).

Table 1. Serial xenotransplantation of NSTS-11 cells in NSG mice. A total of 3×10^5 parental NSTS-11 cells or cultured cells derived from the xenograft tumors obtained in a previous in vivo passage were subcutaneously injected into the mice.

In Vivo Passage Number	Tumorigenic Efficiency		Mean Tumor Volume Increase (mm³/Day ± SEM)
	Mice with Tumors/Mice Injected	Tumors Formed in Total [1]	
First	3 of 3 (100%)	3	2.89 ± 0.74 (*n* = 3)
Second	6 of 9 (67%)	9	4.37 ± 1.83 (*n* = 9)
Third	27 of 27 (100%)	33	5.66 ± 0.72 (*n* = 27) *

[1] In several mice, subcutaneously injected cells formed two spatially separated tumors within the site of injection and these tumors were handled separately in subsequent experiments. SEM, standard error of the mean; n, number of mice evaluated. * Statistically significant compared with the first in vivo passage ($p < 0.05$; Welch's *t*-test).

To investigate the differences at the cellular and molecular levels that might reflect the selection of CSCs, we decided to analyze three xenograft-derived cell lines and respective tumors that represent one arm of subsequent passages in vivo (Figure 1b). LTB1 (first passage in vivo), LTB5 (second passage in vivo), and LTB24 (third passage in vivo) cell lines and respective tumors were included for further analyses; NSTS-11 cells and the primary tumor served as a parental control.

2.2. The Colony Formation and Sphere Formation Capacity of NSTS-11 Cells Is Enhanced after In Vivo Passages

To evaluate how the serial xenotransplantation of NSTS-11 cells affects their CSC characteristics in vitro, we first assayed the capacity of LTB1, LTB5, and LTB24 cells to form colonies and spheres compared with that of parental NSTS-11 cells (Figure 2). The results of these in vitro functional assays of CSCs revealed an increase in both colony and sphere formation capacity over in vivo passages, which indicates an enrichment of CSCs. Tertiary xenograft tumor-derived LTB24 cells formed significantly more colonies (Figure 2a,b) and rhabdospheres (Figure 2c,d) in vitro than parental NSTS-11 cells. The upward trend in the number of colonies and increased sphere formation capacity supported our in vivo observations and implied that CSCs are enriched during serial xenotransplantation. Importantly, together with the in vivo tumorigenicity assay, the colony formation assay and sphere formation assay confirmed that CSCs are maintained in low passages of xenograft-derived cell lines cultured in vitro.
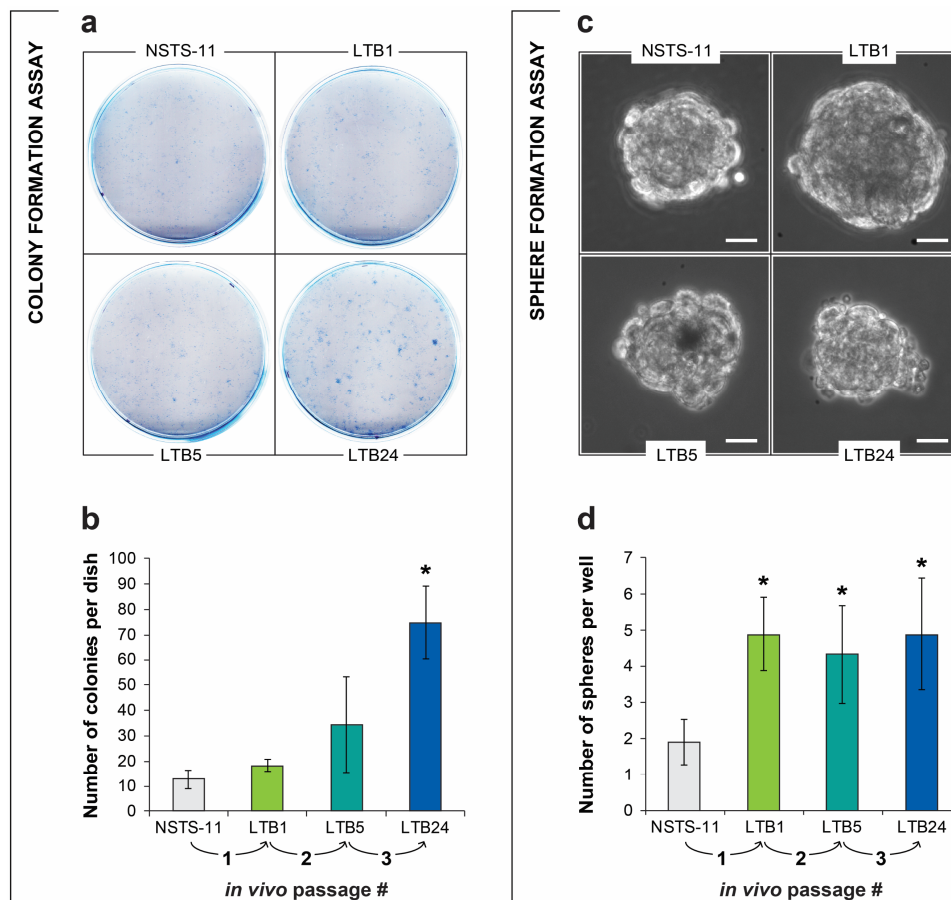
Figure 2. In vitro functional assays revealed an enrichment of cancer stem cells (CSCs) over in vivo passages. (**a**) Representative images of the colony formation assay. A total of 1000 cells were plated per culture dish and cultured for 8 days. (**b**) Quantification of the colonies (>50 cells per colony) formed by the parental NSTS-11 cells and the cells derived from the primary (LTB1), secondary (LTB5), and tertiary (LTB24) xenograft tumors. Data are presented as the mean ± SD of three independent experiments. (**c**) Representative images of rhabdospheres formed by the respective cell lines. Scale bars, 25 μm. (**d**) More than a two-fold increase in sphere formation capacity over in vivo passages. The number of spheres is presented as the mean ± SD of three independent experiments. * Significantly higher compared with the parental NSTS-11 cells ($p < 0.05$).

2.3. Serial Xenotransplantation in NSG Mice Increases Aldehyde Dehydrogenase Activity In Vitro

High aldehyde dehydrogenase (ALDH) activity has been attributed to CSCs in many cancers, including rhabdomyosarcoma [18]. Therefore, we employed an Aldefluor™ assay to functionally characterize changes in ALDHs during in vivo passaging. In agreement with the previous in vitro assays of CSCs, the Aldefluor™ assay demonstrated a significant increase in ALDH activity in LTB24 cells and revealed a trend of gradually increasing ALDH activity over in vivo passages (Figure 3a). Surprisingly, analysis of the ALDH1 enzyme showed its downregulated expression in later xenograft-derived cell lines (Figure 3b and Figure S1). Similarly, RT-PCR demonstrated downregulated expression of the *ALDH1A1* gene (Figure 3c), which encodes one of the prominent ALDH1 isoforms commonly associated with CSCs [19]. We therefore analyzed expression profiling data and compared the expression levels of each of the 19 ALDH gene variants (Figure 3d). Expression profiling confirmed the downregulation of several members of the ALDH1 family, mainly *ALDH1A1* and *ALDH1A3*. However, the analysis revealed upregulated expression of some ALDH gene variants, especially *ALDH6A1*, which may account for the Aldefluor™ assay results, as discussed later. The significant upregulation of ALDH6A1 variant was further confirmed also at protein levels (Figure 3e and Figure S2).
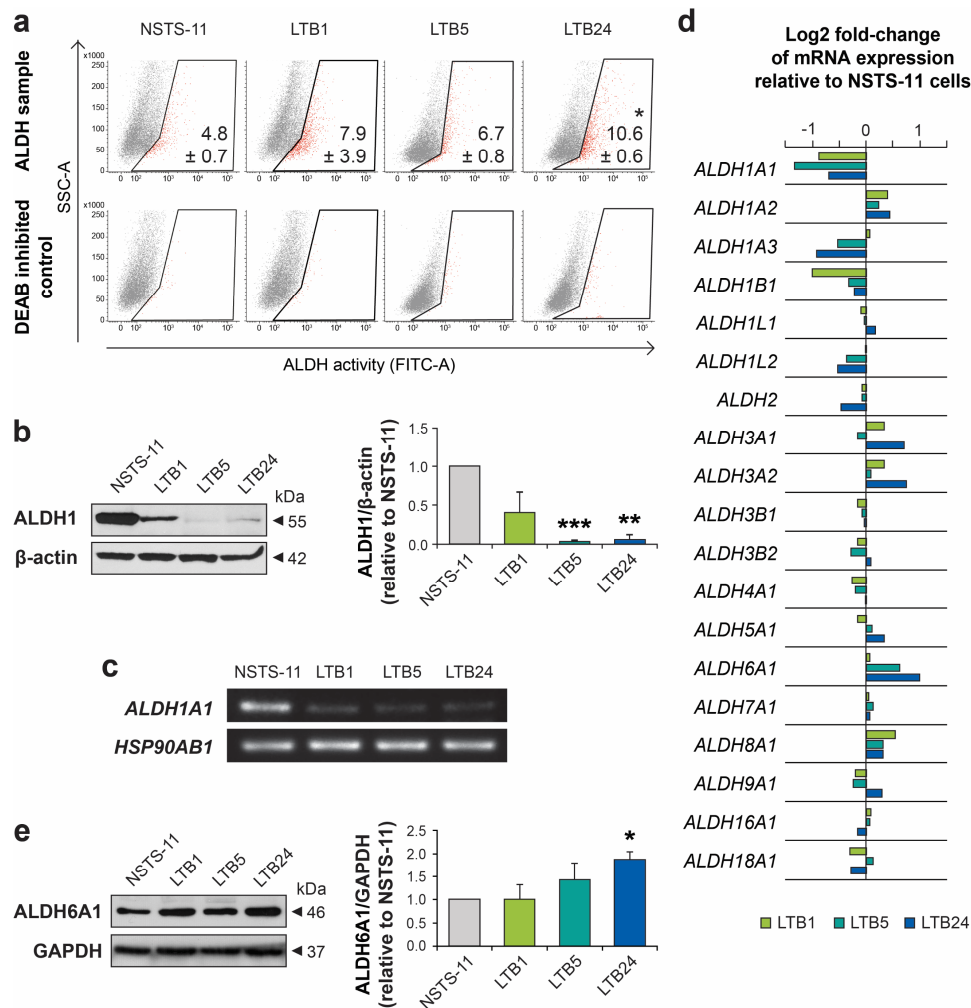
Figure 3. Aldehyde dehydrogenase activity and expression analysis. (**a**) Aldefluor™ assay showed an increase in aldehyde dehydrogenase (ALDH) activity over in vivo passages. Representative dot plots are shown. The percentage of ALDH-positive cells is presented as the mean ± SD of three independent experiments. * Statistically significant difference from parental NSTS-11 cells ($p < 0.05$). (**b**) Western blot analysis of ALDH1 expression. β-actin served as a loading control. Representative image (left) and mean relative optical density values ± SD (right) of three independent experiments. ** $p < 0.01$, *** $p < 0.001$. (**c**) Expression of the *ALDH1A1* gene as detected by RT-PCR. *HSP90AB1* served as a control. (**d**) Microarray gene expression analysis of ALDH gene variants. (**e**) Western blot analysis confirmed upregulation of ALDH6A1 protein over in vivo passages. Glyceraldehyde-3-phosphate dehydrogenase (GAPDH) served as a loading control. Representative image (**left**) and mean relative optical density values ± SD (**right**) of three independent experiments. * $p < 0.05$.

2.4. Expression Levels of Core Pluripotency Factors and Common CSC Markers Are Preserved Over the Passages In Vivo

Our previous study showed the key role of the pluripotency factor SOX2 in sarcoma tumorigenesis [5]; thus, we aimed to investigate whether the enrichment of CSCs during serial xenotransplantation was accompanied by changes in expression of the core pluripotency factors (SOX2, OCT4, and NANOG) or commonly used CSC markers (nestin, CD133, and ABCG2). Immunohistochemistry (IHC) of tumor tissues did not show any evidence of gradual selection for any of the evaluated proteins (Table 2, Figures S3 and S4). The expression levels of these proteins were maintained in the tumor tissues over the passages in vivo, except for minor changes in SOX2 and CD133 expression.

In agreement with the IHC results, immunofluorescence analysis did not show any significant difference in expression of SOX2, OCT4, NANOG, nestin, CD133, or ABCG2 among the derived cell lines (Figure 4a, Figures S5 and S6). In addition, no clear trend in the expression of these proteins at the mRNA level was identified using gene expression profiling (Figure 4b) and further validated using RT-PCR (Figure S7). Together, these results suggested that the expression of the six investigated proteins did not account for the enhanced stemness observed during serial xenotransplantation in NSG mice and that other genes or mechanisms were involved. However, a sustained expression of most of these proteins confirms their important roles in rhabdomyosarcoma tumorigenesis.
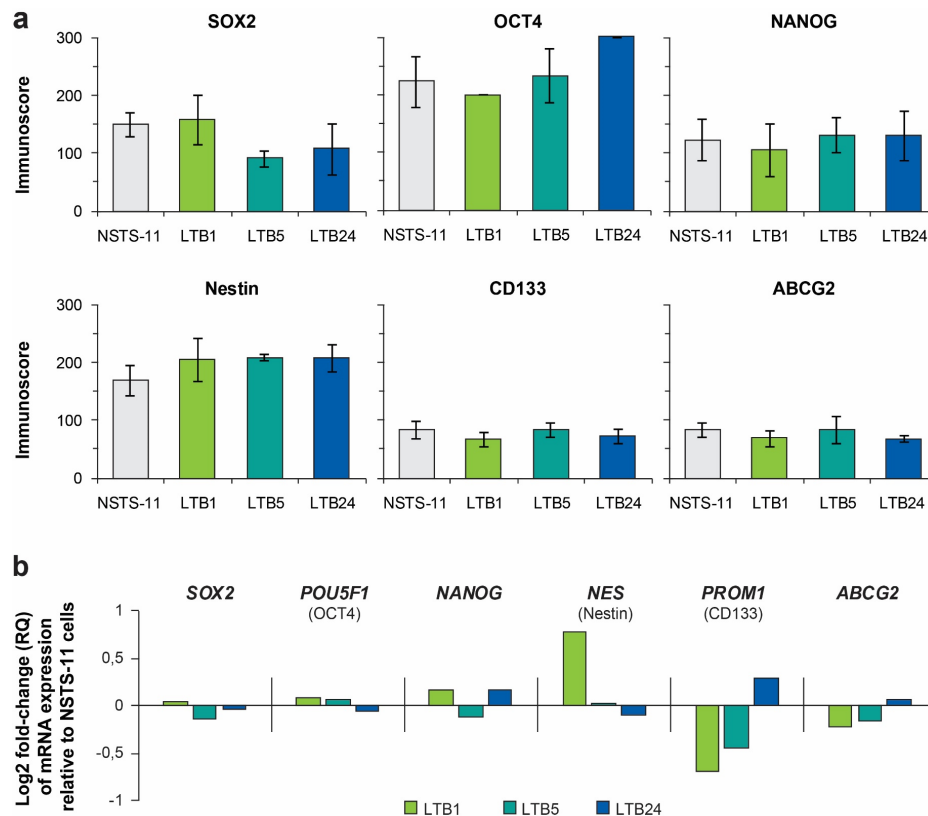
Figure 4. (**a**) Immunofluorescence analysis of core pluripotency factors (upper panel) and commonly used CSC markers (lower panel). Immunoscores were determined by multiplying the percentage of positive cells by the respective immunoreactivity. Data are presented as the mean ± SD of at least three independent experiments. (**b**) Expression profiling data of genes encoding the investigated proteins. Where necessary, the protein name is noted under the official gene symbol.

Table 2. Immunohistochemical analysis of primary tumor tissue and xenograft tumor tissues.

Antigen	Primary Tumor		Primary Xenografts [1]		Secondary Xenografts [1]		Tertiary Xenografts [1]	
	%TC	IR	%TC	IR	%TC	IR	%TC	IR
SOX2	2	+++	3	+++	3	++	3	++
OCT4	1	+	1	+	1	+	1	+
NANOG	0	-	0	-	0	-	0	-
Nestin	4	+++	4	+++	4	+++	4	+++
CD133	3	+	1	+	1	+	1	+
ABCG2	1	++	1	++	1	+	1	+

The percentage of positive tumor cells (%TC) was categorized into five levels: 0 (0%), 1 (1–5%), 2 (6–20%), 3 (21–50%), and 4 (51–100%). The immunoreactivity of tumor cells (IR) was graded as - (none), + (weak), ++ (medium), and +++ (strong). [1] Data are presented as the mean of three independent xenograft tumor tissues representing the three arms of the serial xenotransplantation of NSTS-11 cells derived from the primary tumor.

2.5. Serial Xenotransplantation of Rhabdomyosarcoma Cells Promotes an Expression Profile Associated with Muscle Progenitor Cells and a Hybrid Epithelial/Mesenchymal Phenotype

To identify genes that may account for the observed enrichment of cells with CSC characteristics during serial passaging in vivo, we performed gene expression profiling of NSTS-11, LTB1, LTB5, and LTB24 cell lines. First, we defined two groups of differentially expressed genes (refer to Section 4 for the detailed procedure; Table S1). The group of upregulated genes (n = 544) included only genes that were significantly upregulated after the third in vivo passage and exhibited an upward trend in expression during serial xenotransplantation (Figure 5a). Conversely, the group of downregulated genes (n = 696) comprised only significantly downregulated genes that followed a downward trend of expression (Figure 5a). Analysis of these two groups of genes allowed us to determine the expression profile that was gradually selected over the passages in vivo and might be associated with CSCs in embryonal rhabdomyosarcoma.
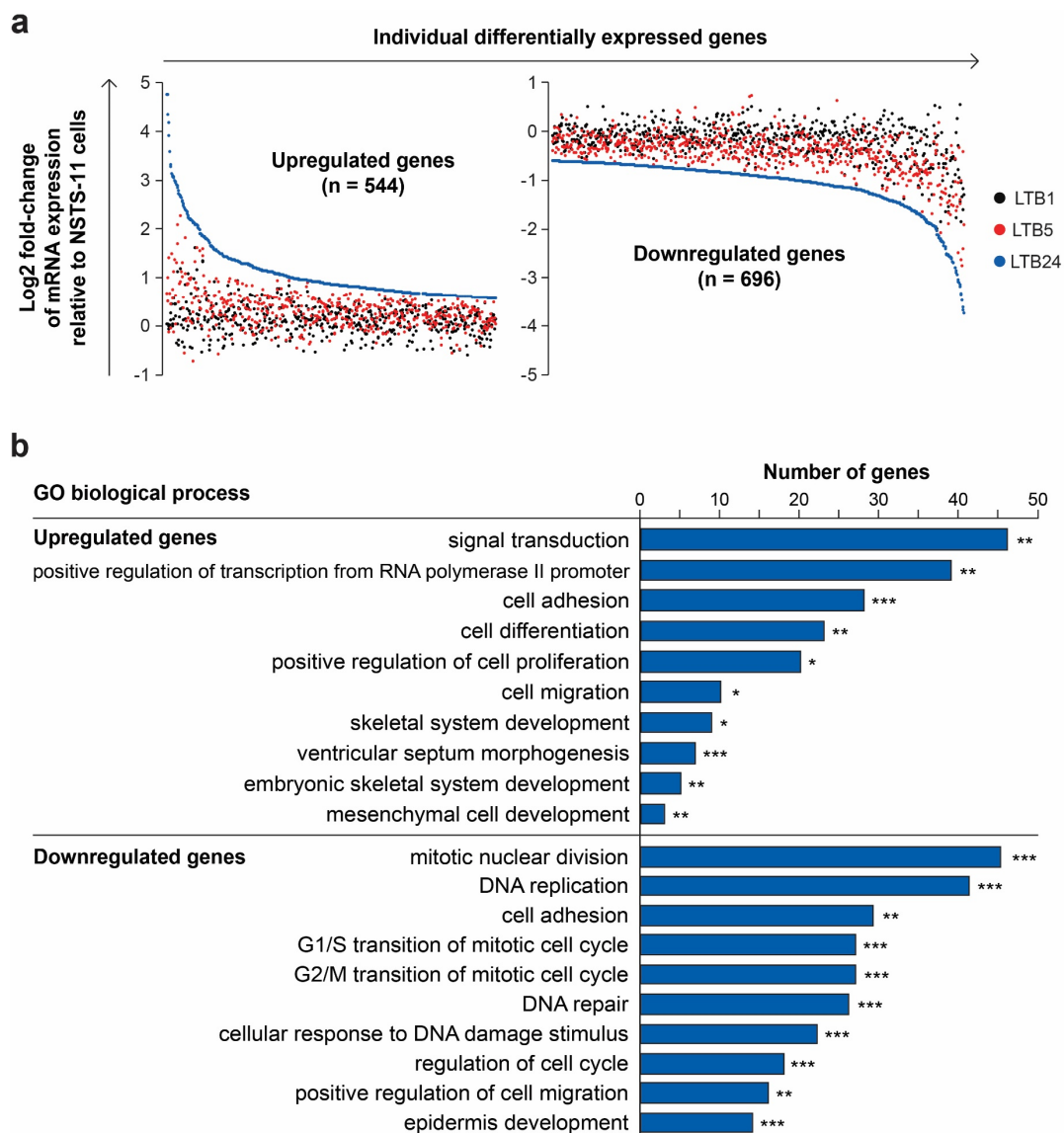
Figure 5. Analysis of the differentially expressed genes. (**a**) Expression levels of differentially expressed genes identified by their upward (upregulated genes; left plot) or downward (downregulated genes; right plot) trend of expression over passages in vivo; (**b**) Gene ontology (GO) analysis of biological processes. The DAVID annotation tool with the GOTERM_BP_DIRECT database was used. Modified Fisher's exact test, * $p < 0.05$, ** $p < 0.01$, and *** $p < 0.001$.

Gene Ontology term enrichment analysis (Table S1) showed that upregulated genes were involved in biological processes comprising signal transduction, cell adhesion, and migration, positive regulation of transcription and cell proliferation, and several developmental processes (Figure 5b). Downregulated genes were enriched in processes such as cell cycle and DNA repair regulation, cell adhesion and migration, and epidermis development (Figure 5b). Many of the downregulated genes, which were included in the epidermis development term, encoded keratins (Table S1), therefore we hypothesized that serial xenotransplantation induced epithelial-mesenchymal transition (EMT) program in NSTS-11 cells. A significant enrichment of "cell migration" and "cell adhesion" ontology terms among both downregulated and upregulated genes (Figure 5b) further encouraged our hypothesis.

To test this hypothesis, we created a list of EMT-related genes by combining two published gene sets that were identified based on a review of the literature [20] and a meta-analysis of gene expression studies [21] (Table S1). The list contains a set of genes associated with mesenchymal traits (mesenchymal genes) and a set of genes commonly associated with epithelial traits (epithelial genes). This list allowed us to categorize the differentially expressed genes accordingly (Figure 6a). Of the mesenchymal genes (n = 126), 15 genes, including *ZEB1*, *MME*, *LAMC2*, or *COL3A1*, were found to be upregulated, whereas 19 genes, including *CDH2* (N-cadherin), *SNAI1*, *FGF2*, *AOX1*, or *ANKRD1*, were downregulated (Figure 6a). Of the epithelial genes (n = 137), 16 genes, including *CDH1* (E-cadherin), *CDH3* (P-cadherin), *KRT14*, *KRT17*, or *KRT18*, were downregulated over the passages in vivo, whereas 10 genes, such as *KRT5*, *LAMA3*, or *ANK3,* were upregulated (Figure 6a). In total, the expression of 60 genes (22.8%) out of 263 EMT-related genes was significantly and gradually shifted during serial xenotransplantation. However, the functional distribution of these genes equally indicated a transition to both mesenchymal (31 genes) and epithelial (29 genes) phenotypes (Figure 6a). These results suggest that the acquisition of aggressive stem-like traits was associated with the selection of cells that exhibit a hybrid epithelial/mesenchymal phenotype (mixed epithelial and mesenchymal gene expression signature).

According to the gene ontology analysis, several developmental processes were enriched for upregulated genes that encode transcription factors, such as *SOX4*, *HEYL*, *HEY2*, or *PITX2*, and genes involved in TGFβ and BMP signaling, i.e., *TGFBR3* and *NOG* (Table S1). Based on a review of the literature, we focused on genes related to stemness and muscle progenitor cells (satellite cells). Indeed, we identified several upregulated myogenic transcription factors that are associated with quiescent/undifferentiated muscle precursors (Figure 6b). *PAX3* [22], *HEYL*, *HEY2*, and *PITX2* [23] were identified among the most prominent differentially expressed genes. Furthermore, markers of satellite cells, CDH15 (M-cadherin), and of the myogenic cell lineage, *MYOD1*, were also upregulated. Importantly, the expression pattern of several stemness regulators provided further evidence for the progressive dedifferentiation and/or enhanced stemness of NSTS-11 cells over the passages in vivo. In addition to the upregulation of *SOX4* and *EYA1*, we identified the downregulation of two microRNA genes, *MIR29A* and a well-known stemness inhibitor *MIR145* [8,24] (Figure 6b). Further analysis of 18 genes that correlate with mesenchymal stem cell senescence [25] revealed a remarkably significant downregulation of 10 genes (*ANKRD1*, *KRT34*, *KRT19*, *SERPINB2*, *KRTAP1-5*, *LOC730755*, *PLCB4*, *THBS1*, *OXTR*, *MRVI1*), while none of the analyzed genes was significantly upregulated during serial xenotransplantation (Figure 6c). Overall, these results clearly suggest that serial xenotransplantation in NSG mice selected for rhabdomyosarcoma cells (presumably CSCs), which acquire an expression signature of primitive undifferentiated cells that resemble non-senescent myogenic precursors/mesenchymal stem cells.

To validate the gene expression profiling results, we performed qRT-PCR of 11 genes associated with EMT, stemness, or muscle progenitor cells, as described above (Figure 6d). Indeed, qRT-PCR using three biological replicates (different cell passages in vitro) confirmed the trends in expression of all the examined genes previously identified by gene expression profiling. This result demonstrates the validity of the gene expression profiling data in our study and underpins the stability of gene expression signatures during in vitro culture.
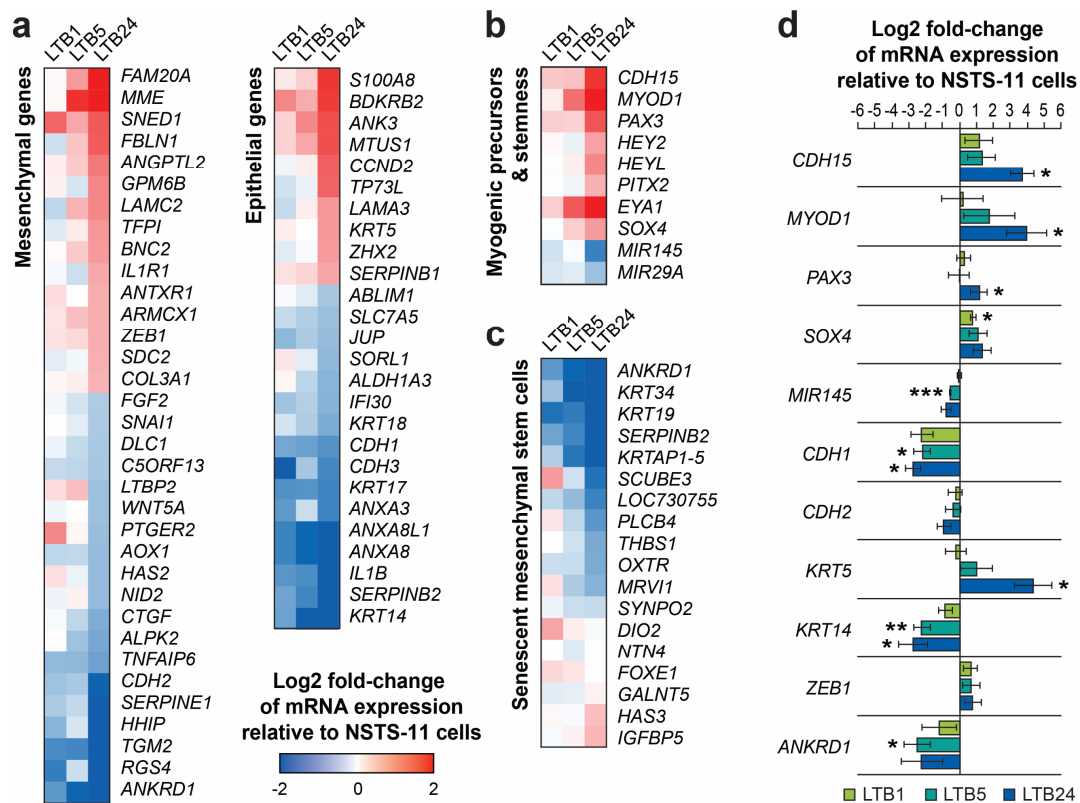
Figure 6. (**a**) Expression levels of differentially expressed genes categorized based on their association with a mesenchymal or an epithelial phenotype. (**b**) Expression profile signature suggesting enhanced stemness and impaired myogenic differentiation. (**c**) Expression profile of the genes that are associated with senescence of mesenchymal stem cells [25]. (**d**) qRT-PCR validation of the gene expression profiling data. The expression of all 11 genes tightly reflected the expression profile detected by microarray analysis (see **a**,**b**). Data are presented as the mean ± SD of three biological replicates. * $p < 0.05$, ** $p < 0.01$, and *** $p < 0.001$ relative to parental NSTS-11 cells.

2.6. Serial Passaging In Vivo Enhanced the Phosphorylation of the Wnt Coreceptor RYK

As gene expression profiling revealed a gradual upregulation of several genes involved in cell signaling and signal transduction (e.g., *PDGFRB*, *ROR2*, or *FGF18*; Figure 5b and Table S1), we next investigated whether this led to the activation of receptor tyrosine kinases (RTKs) and their downstream signaling pathways. To assess the levels of phosphorylation of various RTKs, we performed a phospho-RTK antibody array using cells cultured for 24 h in either serum-free or complete media. Unexpectedly, regardless of the culture conditions, the phosphorylation of most of the RTKs did not differ among NSTS-11 and xenograft tumor-derived cell lines (Figure S8). However, one of the most abundantly phosphorylated RTKs in our study, receptor like tyrosine kinase (RYK), showed a gradual increase (>2.5-fold) in phosphorylation during serial xenotransplantation of NSTS-11 cells in NSG mice (Figure S8). This increase in the level of phosphorylated RYK was not caused by upregulated gene expression, as *RYK* mRNA levels remained unchanged (Table S1).

RYK is an atypical RTK with impaired kinase activity [26,27] but functions as a coreceptor in Wnt signaling, which is implicated in self-renewal and stemness [28]. Notably, RYK has also been demonstrated to activate mitogen-activated protein kinases (MAPKs), i.e., ERK1/2 [26]. In line with these findings, we detected an apparent upregulation of phosphorylated ERK1 using phospho-MAPK antibody arrays (Figure S9). Compared with parental NSTS-11 cells in both serum- and serum-free conditions, the levels of phosphorylated ERK1 were upregulated in LTB5 and LTB24 cells derived from secondary and tertiary xenografts, respectively (Figure S9). These results suggest positive regulation of the MAPK/ERK1 cascade via enhanced Wnt/RYK signaling. Gene expression profiling of the

xenograft-derived cell lines further revealed upregulated mRNA levels of several Wnt receptors and coreceptors, including *FZD3*, *FZD4*, *FZD8*, and *ROR2*, and identified a significant increase in the expression of the Wnt downstream target gene *WISP2/CCN5* (Table S1). High expression levels of *WISP2* were reported in undifferentiated mesenchymal stem cells, and Wisp2 was shown to increase mesenchymal precursor cell proliferation in vitro [29,30]. Wisp2 also induces a dedifferentiated state in adipose cells favoring the myofibroblast phenotype [30]. Together, the antibody arrays and gene expression profiling identified a marked modulation of Wnt signaling during serial xenotransplantation and suggested RYK as a prospective target in rhabdomyosarcoma CSCs.

2.7. Expression of Several Identified Prospective CSC-Specific Target Genes Predicts Survival in Soft-Tissue Sarcomas

Using serial xenotransplantation in conjunction with gene expression profiling and antibody arrays, we identified several prospective targets that might be associated with the progression of rhabdomyosarcoma and the acquisition of a CSC phenotype. Hence, we applied in silico analysis of publicly available gene expression data to test the relevance of our model.

First, we performed an analysis of Gene Expression Omnibus GSE51130 dataset, which comprises expression profiles of primary rhabdomyosarcoma and xenograft tumors obtained during serial propagation of patient-derived xenograft (PDX) in mice treated with standard chemotherapy (Figure 7). Supporting our model, gene expression profiles of the refractory chemoresistant rhabdomyosarcoma PDXs strikingly corresponds with the stemness-associated gene expression signature identified in our study, including significant upregulation of *ALDH6A1*, *SOX4*, *CDH15*, and *MYOD1* expression as well as downregulation of *ALDH1A1* and *ALDH1A3* (Figure 7).
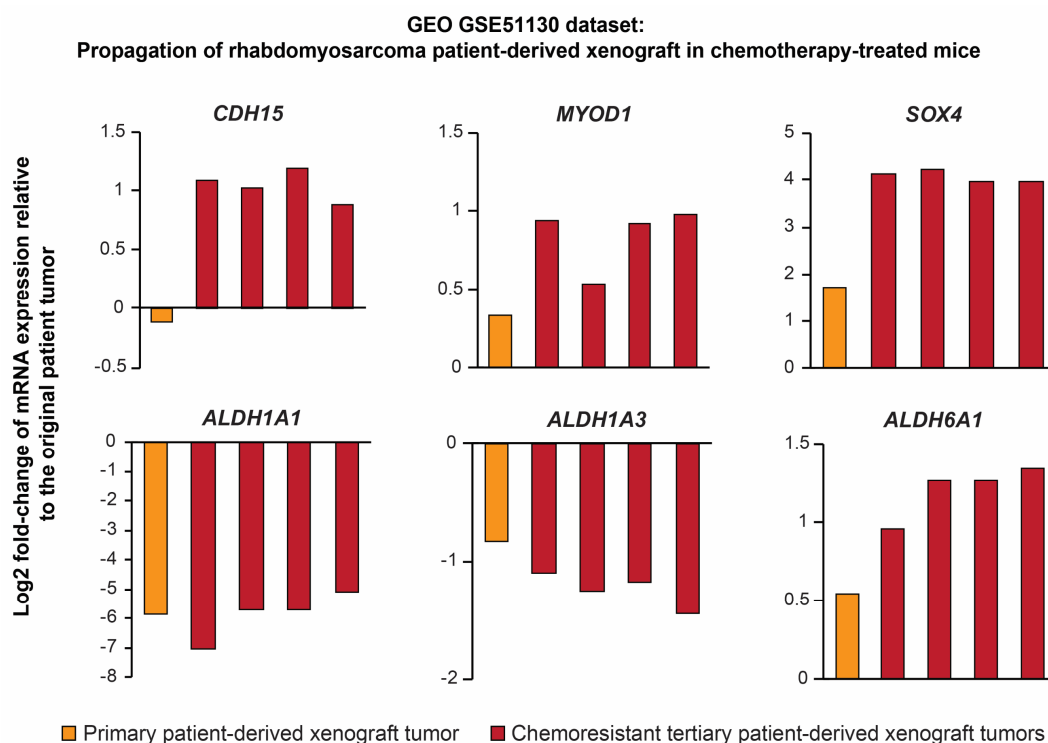
Figure 7. Gene expression profiles of aggressive chemotherapy-resistant rhabdomyosarcoma patient-derived xenografts (Gene Expression Omnibus (GEO) GSE51130 dataset) resemble the stemness-associated gene expression signature identified using our approach. Note the marked downregulation of *ALDH1A1* and upregulation of *ALDH6A1* in refractory chemoresistant xenografts (red bars; expression for individual biological replicates) compared with the original patient tumor.

To the best of our knowledge, no rhabdomyosarcoma-specific gene expression dataset paired with clinical follow-up data was available at the time of the analysis. Thus, we utilized The Cancer Genome Atlas Sarcoma (TCGA-SARC) dataset, which includes various soft-tissue sarcomas, to evaluate the clinical relevance and prognostic significance of the prospective rhabdomyosarcoma CSC-associated genes identified in our model.

In line with our previous results [5], survival analysis revealed that among *SOX2*, *POU5F1* (encoding OCT4), *NANOG*, *PROM1* (encoding CD133), *NES* (encoding nestin), and *ABCG2* genes, only *SOX2* expression was significantly ($p < 0.05$) associated with the survival of sarcoma patients and predicted poor prognosis (Figure S10). In the present study, we also observed a slight increase in the number of SOX2-positive cells in the xenograft tissues (Table 2; Figure S3), which further supports that SOX2 plays a major role in sarcoma tumorigenesis and the maintenance of CSCs [8].

More importantly, TCGA-SARC analysis revealed a marked prognostic potential of several identified target genes, which were gradually modulated during serial xenotransplantation and associated with the increased stemness of rhabdomyosarcoma cells. In agreement with the downregulation of *ALDH1A1* detected in the xenograft-derived cell lines (Figure 3c,d), low levels of *ALDH1A1* expression are strongly correlated ($p < 0.0001$) with short overall survival among patients with soft-tissue sarcomas (Figure 8a). These striking results suggest that ALDH1A1 may play different roles in the tumorigenesis and stemness of sarcomas than were commonly reported in carcinomas [19]. In contrast, the expression of *ALDH1A3* (Figure 8b) or *ALDH6A1* (Figure 8c) alone cannot predict survival in soft-tissue sarcoma patients, but the differential expression of these genes might be specific for rhabdomyosarcoma as indicated by PDX expression profiling data (Figure 7) and by a previous study that reported *ALDH6A1* to be associated with worse survival in rhabdomyosarcoma patients [31].

Of the highly expressed myogenic precursor and stemness-related genes, *CDH15* (Figure 8d) was identified as a significant ($p < 0.05$) predictor of poor prognosis in soft-tissue sarcomas along with *MYOD1* (Figure 8e) and SOX4 (Figure 8f), which, however, did not reach the level of statistical significance ($p = 0.053$ and $p = 0.054$, respectively). Among the identified genes linked with mesenchymal traits, expression of the *ARMCX1* gene, which encodes mitochondria-localized armadillo repeat-containing X-linked protein 1, was revealed as a very strong predictor of poor outcome in soft-tissue sarcomas (Figure 8g). Conversely, the expression of another mesenchymal gene, *AOX1*, which was downregulated during serial xenotransplantation (see Figure 6a), significantly correlates with a better prognosis in sarcoma patients (Figure 8h). These results provide exemplary evidence that sarcoma progression may not be driven by an enhanced mesenchymal gene expression but rather by a hybrid epithelial/mesenchymal expression signature that reflects the activation of both epithelial and mesenchymal programs.

In agreement with the results of phospho-RTK arrays, the upregulated expression of *RYK* tends to correspond with worse prognosis (Figure 8i). However, the prognostic power of *RYK* expression is fully pronounced when analyzed in combination with the expression of other prospective CSC-related genes that nearly reached statistical significance in the survival analysis. In fact, the expression signature of six genes, including *CDH15*, *MYOD1*, *SOX4*, *ARMCX1*, *RYK*, and *ALDH6A1*, was identified as a strong predictor of poor survival ($p < 0.001$) that markedly overcomes statistical significance of the individual genes (Figure 8j). On the contrary, gene signatures comprising *ALDH1A1* or *ALDH1A3* instead of *ALDH6A1* failed to predict survival (Figure 8j). These results suggest that it is the *ALDH6A1* gene (not *ALDH1A1* or *ALDH1A3*) that is more likely upregulated together with *CDH15*, *MYOD1*, *SOX4*, *ARMCX1*, and *RYK* in aggressive soft-tissue sarcomas.

It is important to note, that TCGA-SARC soft-tissue sarcoma dataset does not contain rhabdomyosarcoma samples, which poses some limitations for the interpretation of the survival data in regard to this tumor type. However, the marked level of agreement between our experimental results and the survival data of various soft-tissue sarcomas suggests that our approach for CSC enrichment could be a useful tool for the unbiased identification of molecular targets that might be associated with enhanced stemness and poor prognosis in rare cancers, such as embryonal rhabdomyosarcoma.
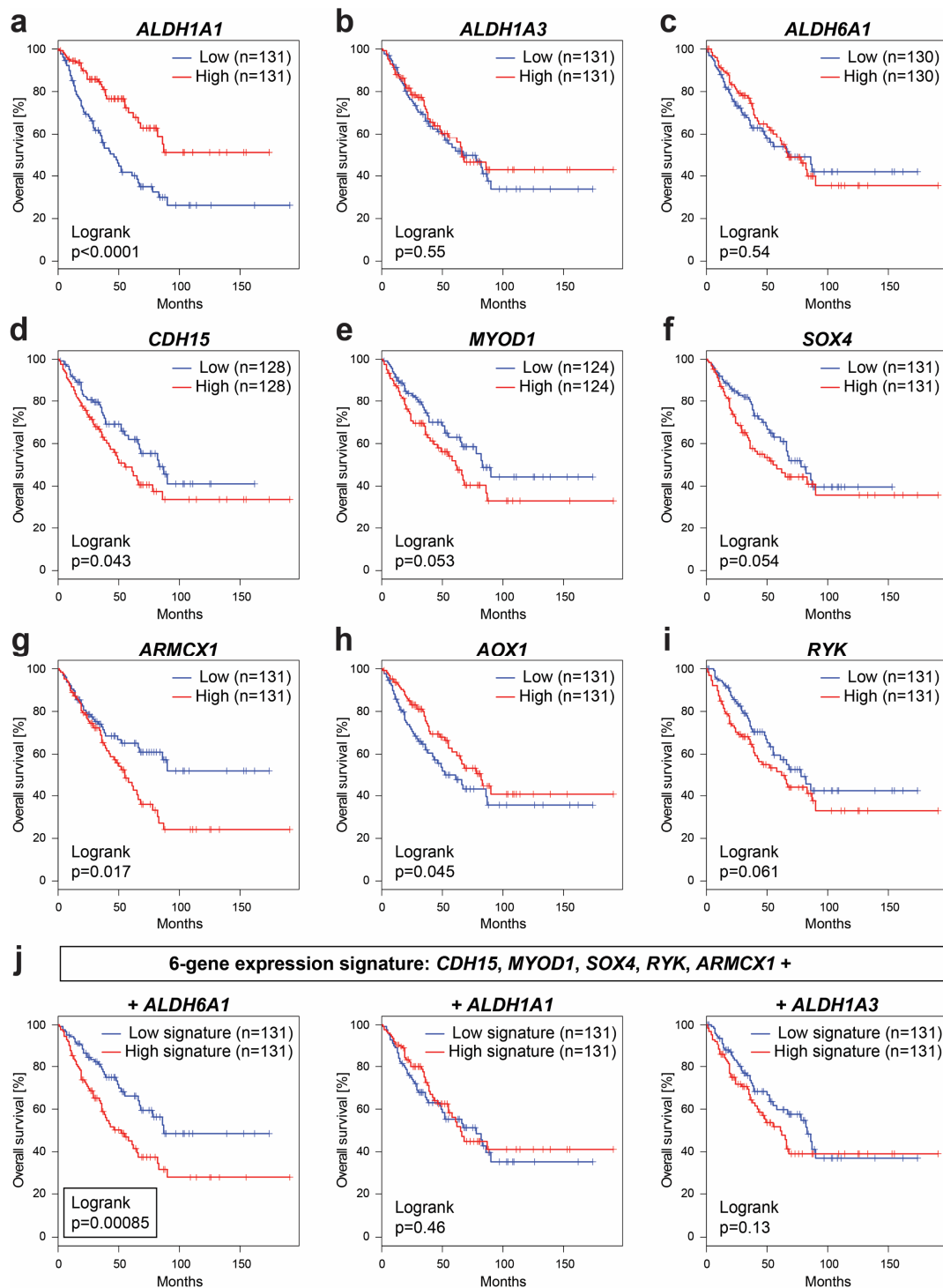
Figure 8. Overall survival in soft-tissue sarcomas (The Cancer Genome Atlas Sarcoma (TCGA-SARC) dataset) based on the gene expression levels of (**a**) *ALDH1A1*, (**b**) *ALDH1A3*, (**c**) *ALDH6A1*, (**d**) *CDH15*, (**e**) *MYOD1*, (**f**) *SOX4*, (**g**) *ARMCX1*, (**h**) *AOX1*, and (**i**) *RYK*. (**j**) Significant prognostic value of 6-gene expression signature comprising *ALDH6A1* (**left**) but not *ALDH1A1* (**middle**) and *ALDH1A3* gene (**right**). The analysis was performed using the GEPIA 2 online tool [32].

3. Discussion

Bottom-up approaches that would enrich for CSCs based on their functional characteristics and might allow the objective screening of CSC-specific markers and therapeutic targets are currently of broad interest to many cancer researchers. Here, we report a proof-of-principle platform to study

rhabdomyosarcoma CSCs that successfully combines serial xenotransplantation in vivo with short-term culture of xenograft-derived cells in vitro.

A fundamental observation made while testing our approach is that rhabdomyosarcoma CSCs are maintained during short-term in vitro culture of xenograft-derived cell lines, which was confirmed by the high tumorigenicity of primary and secondary xenograft-derived cells. In fact, as serial xenotransplantation selected for CSCs, their numbers in xenograft-derived cell lines increased, which resulted in a statistically significant difference between the parental cell line NSTS-11 and the tertiary xenograft-derived cell line LTB24. This increase in CSC number was documented by the enhanced ALDH activity as well as high colony and sphere formation capacity of LTB24 cells. As these functional assays for CSC phenotype were performed using biological replicates from different passages in vitro, the obtained data also underpinned the stability of CSC numbers during short-term in vitro culture. Such stability was further demonstrated by similar expression patterns detected by immunofluorescence and qRT-PCR among different in vitro passages of each of the examined cell lines. Thus, the major advantage of our approach resides in the continuous supply of xenograft-derived cell lines that (i) may serve as a cost-effective model for the selection of CSCs for comparative studies, (ii) may be stored for future studies, and (iii) provide enough material for subsequent analyses and assays.

One of the intriguing changes detected in our model was the increase in ALDH activity despite the decrease in ALDH1 level detected over the passages in vivo. It has only recently come to light that ALDH activity but not necessarily ALDH1 expression marks CSCs [33]. Indeed, it has been demonstrated in hematopoietic cells that ALDH1A1 deficiency does not affect Aldefluor staining [34]. Similarly, although Aldefluor positivity was associated with breast CSCs, ALDH1A1 did not correlate with Aldefluor positivity and performed poorly as a predictor of breast carcinoma progression [35]. In agreement with our results, the latter study showed that increased expression of other ALDH isoforms, e.g., ALDH6A1, correlated with high ALDH activity and was associated with metastatic disease in breast carcinoma [35]. Recently, proteomic analysis of primary and metastatic prostate cancer has also demonstrated that ALDH6A1 is highly specific to progressive metastatic disease [36]. Using our model of gradual selection of rhabdomyosarcoma CSCs, we revealed an apparent upregulation of ALDH6A1 at mRNA and protein level, which was associated with Aldefluor positivity and increased stemness, while *ALDH1A1* gene expression was markedly downregulated. Importantly, the survival analysis performed using TCGA-SARC database supported the observed decrease in *ALDH1A1* expression. We show here that it is in fact the downregulation (not upregulation) of *ALDH1A1* gene expression that is associated with aggressive tumors and strongly predicts ($p < 0.0001$) poor prognosis among various sarcomas. Notably, these results contradict the previous report by Martinez-Cruzado et al., whom used artificially transformed mesenchymal stem cells as an experimental model of sarcomagenesis and proposed that ALDH1 expression is enhanced in xenograft-derived cells and associates with sarcoma CSCs [37]. In contrast, our model utilizing primary tumor-derived cells suggests ALDH6A1 as a candidate molecule that plays a role in rhabdomyosarcoma CSCs. Indeed, the expression of *ALDH6A1* has already been identified among the genes that correlate with poor outcome in rhabdomyosarcoma patients [31]. This is in agreement with our survival analysis on soft-tissue sarcomas demonstrating that upregulated expression of *ALDH6A1* but not *ALDH1A1* or *ALDH3A1* significantly correlates with poor survival when combined with other genes identified in our model, i.e., *CDH15*, *MYOD1*, *SOX4*, *ARMCX1*, and *RYK*.

Comparing the gene expression profiles of parental NSTS-11 cells and three subsequent xenograft-derived cell lines, we were able to identify gradual changes in the expression of several genes that confer stemness and/or are linked with undifferentiated myogenic precursors. For instance, our data showed an apparent increase in the expression of the *CDH15* gene, which encodes M-cadherin. In a model of RAS-driven rhabdomyosarcoma tumorigenesis, expression of *KRAS* under the *CDH15* promoter resulted in less differentiated and more aggressive tumors [38]. Cells isolated from such rhabdomyosarcoma tumor were enriched for tumor-initiating activity and expressed markers of early myoblasts and adult muscle stem cells, i.e., satellite cells [38]. Indeed, M-cadherin expression has been

clearly demonstrated to be a marker of satellite cells [39], which share many similarities with the gene expression signature of embryonal rhabdomyosarcoma [40].

Although embryonal rhabdomyosarcoma most likely arises from myoblasts, both markers of quiescent satellite cells [39,41], e.g., PAX3, PAX7, or HEYL, and markers of activated satellite cells, including MYOD1 [40], are frequently expressed. Notably, *MYOD1* was one of the most upregulated genes (>8-fold in tertiary xenograft-derived LTB24 cells) in our study. MYOD1 is a transcriptional activator expressed in early muscle progenitors and is required for and regulates muscle progenitor specification [38]. In rhabdomyosarcoma, MYOD1 is expressed in small, primitive tumor cells, whereas cells that exhibit morphological evidence of skeletal muscle differentiation generally lack MYOD1 expression [42]. Recently, it has been suggested that MYOD1 regulates common gene programs that lock cells in an arrested myogenic fate and is required for the self-renewal of rhabdomyosarcoma cells and sustained tumor growth [43]. Corroborating the increase in the expression of *CDH15* along with *MYOD1* in our model of rhabdomyosarcoma CSCs, *MYOD1* knockdown has been demonstrated to significantly downregulate *CDH15* expression [43].

MYOD1 may also maintain pre-myogenic mesoderm expression by upregulating PAX3, PAX7, and EYA2 [44]. PAX3 has been shown to prevent the differentiation of myoblasts and satellite cells [22]. PAX3 also acts as an upstream regulator maintaining stemness in neural crest cells [22], which suggests its general impact on cell fate. Thus, upregulated expression of *PAX3* might explain the increased stemness of LTB24 rhabdomyosarcoma cells in our study. The gradual increase in rhabdomyosarcoma stemness could be further substantiated by the detected downregulation of 10 out of 18 genes that are associated with mesenchymal stem cell senescence [25] and by the upregulation of genes involved in early mesenchymal development and maintenance of myogenic precursors, i.e., *SOX4* [45,46] and PITX2 [23]. *SOX4* has been previously demonstrated to contribute to tumor progression by promoting cancer stemness [46]. Importantly, SOX4 is highly expressed in embryonal rhabdomyosarcoma compared with normal muscle and knockdown of SOX4 leads to a significant decrease in MYOD1 levels and impaired rhabdomyosarcoma cell survival [47]. Conversely, we have identified downregulation of *MIR29A* and *MIR145* genes encoding microRNAs that are crucial for induction of myogenic differentiation [48] and repression of pluripotency [8,25], respectively. Although downregulation of microRNA 145 (miR-145) has been suggested in tumorigenesis of Ewing's sarcoma [8,49], our study provides the first evidence that miR-145 might be involved in regulation of CSC phenotype in rhabdomyosarcoma. Together, the gene expression profiling data indicate that serial xenotransplantation in NSG mice resulted in the progressive dedifferentiation of NSTS-11 rhabdomyosarcoma cells and their reprogramming towards the expression signature of non-senescent myogenic precursors, which was associated with enhanced rhabdomyosarcoma stemness both in vivo and in vitro.

Finally, the induction of stemness through serial xenotransplantation in NSG mice was also associated with the modulated expression of many genes involved in the EMT program. Intriguingly, functional analysis of these genes suggested an acquisition of an equilibrium between EMT and its reverse process, mesenchymal-epithelial transition (MET). Moreover, some of the typical markers of an epithelial phenotype (*CDH1*) or a mesenchymal phenotype (*CDH2*) were downregulated, which suggests a loss of differentiation and a shift towards an undifferentiated metastable phenotype that combines partial mesenchymal and epithelial traits. In carcinomas, recent accumulating evidence has shaped a widely accepted view that EMT generates CSCs, which appear to reside at an intermediate state along the epithelial-mesenchymal spectrum of phenotypes [49,50]. Carcinoma CSCs thus most likely undergo EMT only partially, attaining a hybrid epithelial/mesenchymal phenotype, which confers plasticity, invasiveness and tumor-initiating capacity [49,50]. In fact, hybrid epithelial/mesenchymal cells can integrate various epithelial and mesenchymal traits that facilitate collective cell migration and promote metastasis [51]. Corroborating these observations, excessive activation of the EMT program leading to a highly mesenchymal phenotype has been shown to be detrimental to the tumorigenic activity of CSCs [52,53]. In parallel to the results obtained in carcinomas, partial MET has been discussed

as a process contributing to the metastasis and stemness of sarcomas, although this mechanism remains elusive [54–56].

Here, we report novel evidence for the prospective role of MET in tumors of mesenchymal origin. Notably, some of the identified rhabdomyosarcoma CSC-specific targets have already been linked with MET. For instance, it has been demonstrated that overexpression of PAX3 induces MET in mesenchymal cells [57]. Importantly, MET has also been established as a key cellular mechanism in the process of reprogramming mesenchymal somatic cells, fibroblasts, towards pluripotency induced by transcription factors, including SOX2 [58,59]. These results suggest that enhanced expression of these stemness-related factors may, in the context of embryonal rhabdomyosarcoma, result in a partial loss of mesenchymal phenotype, as indicated here by the progressive downregulation of a prominent EMT inducer, *SNAI1*, and *CDH2*, which encodes N-cadherin.

Among sarcomas, osteosarcoma tumor tissues have been shown to exhibit extremely low expression levels of N-cadherin [60]. Furthermore, several cadherins, including P-cadherin, E-cadherin, and N-cadherin, are markedly downregulated in osteosarcoma cell lines in vitro [61], which is in line with the gene expression signature associated with the enhanced rhabdomyosarcoma stemness in our study. Mechanistically, N-cadherin overexpression has been demonstrated to significantly impair osteosarcoma migration in vitro and metastasis in vivo [61]. Experimental re-expression of N-cadherin also restores cell-cell contacts and inhibits cell migration in glioma, another highly aggressive non-epithelial tumor, which is frequently characterized by low levels of N-cadherin [62]. Similarly, metastatic dissemination of neuroblastoma is strongly correlated with low N-cadherin expression [63]. Notably, N-cadherin downregulation is crucial for the migration of neural crest cells [64] and smooth muscle cells [65], which offers an explanation for how partial MET, i.e., a loss of the typical mesenchymal marker, N-cadherin, may promote the progression of sarcomas towards a more aggressive phenotype.

Although epithelial differentiation has been reported in various sarcomas, it has never been associated with a full transition of sarcoma cells to the epithelial state and rather presents a hallmark of phenotypic plasticity resulting from the active MET program [54]. In fact, the combined presence of epithelial and mesenchymal features has been proposed to contribute to aggressive sarcomas [55]. From this perspective, EMT-related signaling that would counteract complete MET is crucial for the maintenance of mesenchymal traits. Indeed, such activation of the EMT program has been identified in the present study. In addition to the MET-related gene expression signature, the increase in rhabdomyosarcoma CSC number during serial xenotransplantation correlated with the upregulation of a typical EMT-inducing gene, *ZEB1*, and a stemness-associated gene, *SOX4*, which has recently been identified as a master inducer of EMT, controlling several EMT-relevant genes [46,66]. Based on the results reported here, we hypothesize that it is the activation of both MET and EMT signaling that sets the rhabdomyosarcoma cells in a "ready-to-act" stem-like state in which they can easily exploit various microenvironmental cues to promote their survival, proliferation, and/or migration. Remarkably, another evidence supporting this hypothesis has been recently reported in a mouse model demonstrating that rhabdomyosarcoma CSCs arise from genomically instable satellite cells, which undergo MET-like process [67]. Further mechanistic studies to examine the prospective link between the hybrid epithelial/mesenchymal phenotype and rhabdomyosarcoma progression are therefore needed to advance our understanding of this rare but aggressive disease.

4. Materials and Methods

4.1. Cell Lines and Tumor Samples

The NSTS-11 cell line derived from a primary embryonal rhabdomyosarcoma was originally described in our previous studies [3,5]. Written informed consent was obtained from the patient or patient's parents, and the primary tumor tissue was collected in accordance with the study protocol (#12/Si/2011) approved by The Research Ethics Committee of the School of Science (Masaryk University).

During the serial xenotransplantation of NSTS-11 cells in vivo, 45 xenograft tumors were collected, and 45 cell lines were successfully established from these xenografts (one cell line from each xenograft tumor). Three cell lines, LTB1, LTB5, and LTB24, derived from respective xenograft tumors after each of the three subsequent passages in vivo were included for detailed in vitro analyses. All cell lines were maintained in DMEM supplemented with 20% fetal calf serum under standard conditions as described previously [3]. For the in vivo tumorigenicity assay, cell passage numbers 8–12 were used according to the growth characteristics of the respective cell line. Cell passage numbers 10–15 were used in other experiments; NSTS-11 cells were used up to passage 20 for some biological replicates.

4.2. In Vivo Tumorigenicity Assay

For each cell line, three 8-week-old female NSG (NOD/ShiLtSz-*scid*/*Il2rγ*^{null}) mice were injected subcutaneously in the neck region with a suspension of 3×10^5 enzymatically dissociated cells in 100 μL of serum-free DMEM. The mice were examined every three days for the presence of subcutaneous tumors. After the appearance of a tumor, the mice were sacrificed, and the tumors were excised. All animal experiments were conducted in accordance with a study (21379/2011-30) approved by the Institutional Animal Care and Use Committee of Masaryk University and registered by the Ministry of Agriculture of the Czech Republic as required by national legislation. The tumors were photographed, and the final tumor volume was measured using the following formula:

$$\text{tumor volume (mm}^3) = \text{length (mm)} \times \text{width (mm)} \times \text{width (mm)} \times 1/2$$

Each tumor was divided into two equal portions: one portion was processed for primary culture [3], and the second portion was fixed in 10% buffered formalin for 24 h, routinely processed for histological examination and embedded in paraffin. FFPE samples were stained with hematoxylin-eosin and examined using an Olympus BX51 microscope. IHC was performed as described below.

4.3. Colony Formation Assay

Cells cultured in vitro were harvested, enzymatically dissociated with Accutase® (Gibco, Thermo Fisher Scientific, Waltham, MA, USA) to obtain single-cell suspension, and seeded at a density of 1000 cells per 10-cm culture dish (Sarstedt AG &Co, Numbrecht, Germany). Colonies were monitored to ensure they were derived from single cells. After 8 days of culture under standard conditions (see Section 4.1), cells were fixed with methanol and stained using Coomassie Brilliant Blue R-250 (Sigma-Aldrich, St. Louis, MO, USA) [68]. The whole culture dish was examined under a phase contrast Olympus CKX41 light microscope and the number of cells within individual colonies was determined by manual counting the nuclei of Coomassie-stained cells under a 20× objective. Only colonies that contained a minimum of 50 cells were considered for further analysis.

4.4. Sphere Formation Assay

For the sphere formation assay, cells were harvested and enzymatically dissociated with Accutase® (Gibco) to obtain a single-cell suspension. Cells were resuspended in a defined serum-free medium (DMEM/F12 (GE Healthcare Europe GmbH, Freiburg, Germany) supplemented with 10 ng/mL EGF (Sigma-Aldrich), 20 ng/mL FGF2 (Sigma-Aldrich), and B-27 supplement w/o vitamin A (Gibco)) and plated in triplicates into ultra-low attachment 6-well plates (Corning, Corning, NY, USA) at a density of 2000 cells/well. Every three days, growth factors were replenished with fresh culture medium. After two weeks, rhabdospheres were counted under an Olympus CKX41 light microscope.

4.5. Aldefluor Assay

The Aldefluor™ assay was performed according to the kit manufacturer's instructions (Stem Cell Technologies, Grenoble, France). Briefly, cells were suspended in Aldefluor™ assay buffer (1×10^4 cells/mL) containing ALDH substrate (BODIPY-aminoacetaldehyde) and incubated at 37 °C

for 45 min. Control samples were incubated in a buffer containing a specific ALDH inhibitor, diethylaminobenzaldehyde (DEAB). The fluorescence signal was measured using a BD FACS Verse flow cytometer, and ALDH activity was analyzed with BD FACSuite software (both BD Biosciences, San Diego, CA, USA).

4.6. Immunohistochemistry

For immunohistochemical analysis, primary tumor tissue and three sets of xenograft tumor tissues collected during subsequent xenotransplantations in NSG mice were used. Four-micron-thick tissue sections were first deparaffinized with xylene and rehydrated through a graded alcohol series. Endogenous peroxidase activity was quenched with 3% hydrogen peroxide for 10 min. For the detection of OCT4, CD133, SOX2, nestin, and NANOG, heat-induced epitope retrieval was performed in a Decloaking Chamber NxGen (Biocare Medical, Pacheco, CA, USA) at 95 °C for 40 min using citrate (pH 6.0) or Tris/EDTA (pH 9.0) buffer (Dako, Glostrup, Denmark) (Table S2). For ABCG2 staining, the sections were not pretreated. Next, the slides were incubated with the indicated primary antibody at room temperature for 60 min. Subsequently, a streptavidin-biotin horseradish peroxidase complex (Vectastain Elite ABC Kit; Vector Laboratories, Burlingame, CA, USA) or a two-step detection system without avidin and biotin (EnVision+ Dual Link system-HRP; Dako) was applied. All slides were immersed in 3,3'-diaminobenzidine (DAB; Dako) and counterstained with Gill's hematoxylin. Negative controls were prepared by incubating samples without primary antibody. Antibody specifications, dilutions, pretreatments, detection systems and positive controls are listed in Table S2.

All immunostained slides were evaluated using a compact research microscope (Nikon ECLIPSE Ci-E). At least five discrete foci of neoplastic infiltration were selected, and the proportion of positive tumor cells was scored as follows: 0 (0%), 1 (1–5%), 2 (6–20%), 3 (21–50%), and 4 (51–100%). The immunoreactivity of tumor cells was graded as - (none), + (weak), ++ (medium), and +++ (strong).

4.7. Immunofluorescence

Indirect immunofluorescence (IF) was performed as previously described [3]. The primary and secondary antibodies that were used in these experiments are listed in Table S3; mouse monoclonal anti-α-tubulin served as the positive control. An Olympus BX-51 microscope was used for sample evaluation; images were captured using an Olympus DP72 CCD camera and were analyzed using the CellˆP imaging system (Olympus, Tokyo, Japan). The samples were prepared from at least three independent passages of all examined cell lines, and at least 200 cells were evaluated in each sample. The immunoreactivity and the percentage of cells showing positivity for the examined antigen were determined. Finally, for each cell line, the total immunoscores were calculated for individual antigens by multiplying the percentage of positive cells by the respective immunoreactivity as described previously [69].

4.8. Western Blotting

ALDH1 and ALDH6A1 protein expression was analyzed per our standard procedure [3]. The primary and secondary antibodies used are listed in Table S3; mouse monoclonal anti-β-actin and rabbit monoclonal anti-glyceraldehyde-3-phosphate dehydrogenase (GAPDH) served as loading controls. Densitometry was performed using Fiji software [70]. Band densities for protein of interest were normalized to that of the band for β-actin or GAPDH in the same sample.

4.9. RT-PCR and qRT-PCR

For both RT-PCR and qRT-PCR, total RNA was extracted and reverse transcribed as previously described [71]. For end point PCR, the reaction mixture (25 μL) contained 100 μM of deoxynucleoside triphosphate (dNTP) mixture, 1 U of Taq polymerase (Top-Bio, Vestec, Czech Republic), 0.25 μM of each primer and 10 μL of cDNA. The amplification was performed for 35 cycles of 94 °C for 30 s, 60 °C for 30 s, and 72 °C for 45 s.

For microarray validation experiments, qPCR was performed using the KAPA SYBR® FAST qPCR Kit (Kapa Biosystems, Wilmington, MA, USA) and 7500 Fast Real-Time PCR System (Applied Biosystems, Foster City, CA, USA) as previously described [10]. The expression of individual genes was assessed using at least three technical replicates from three biological replicates (different cell passages in vitro) of each cell line. The heat shock protein gene *HSP90AB1* was used as the endogenous reference control, and the level of gene expression was normalized to that in parental NSTS-11 cells. The primer sequences used are listed in Table S4.

4.10. Expression Profiling

Total RNA was extracted and processed through an Affymetrix workflow as previously described [10]. Raw microarray data are available in the ArrayExpress database (www.ebi.ac.uk/arrayexpress) under accession number E-MTAB-7664. Affymetrix power tools were used to normalize raw CEL files at the gene level. Robust multiarray averaging (RMA) normalization and complete annotation files were selected.

Gene expression fold changes (FCs) were calculated for each xenograft-derived cell line using the parental NSTS-11 cell line as a reference control. Thus, gene expression FCs represent the differences in gene expression after each passage in vivo: first passage (LTB1/NSTS-11), second passage (LTB5/NSTS-11), and third passage (LTB24/NSTS-11).

To identify genes that exhibited a downward or an upward trend of expression during serial xenotransplantation, the following approach was used. First, reference fold-change values, which reflected a mean decrease or increase in gene expression after each passage in vivo, were calculated based on a set of significantly downregulated genes ($n = 55$) or a set of significantly upregulated genes ($n = 55$), respectively (Table S1). The set of significantly downregulated genes was identified using the following parameters: FC $\leq$ 0.25 after the third passage in vivo and FC $\leq$ 1.5 after any passage in vivo. Conversely, significantly upregulated genes were defined as follows: FC $\geq$ 4 after the third passage in vivo and FC $\geq$ 0.66 after any passage in vivo.

The calculated reference fold-change values were then used to determine the Pearson's correlation coefficient of each gene. Only differentially expressed genes ($\geq$1.5-fold after the third passage in vivo) with a strong correlation coefficient (>0.8) were included in further analyses (Table S1). Genes with FC >1.5 or FC <0.66 after the first passage in vivo were excluded from the group of downregulated or upregulated genes, respectively. The DAVID annotation tool [72] was used for gene ontology analysis, and expression heat maps were prepared using the visualization and analysis software Morpheus (https://software.broadinstitute.org/morpheus).

4.11. Phospho-Protein Arrays

The relative phosphorylation levels of 49 RTKs and 26 downstream kinases, including 9 MAPKs, were analyzed using the Human Phospho-RTK Array kit and the Human Phospho-MAPK Array kit (both R&D Systems, Minneapolis, MN, USA), respectively, according to the manufacturer's protocol. Each array was incubated with 250 µg of protein lysate. The levels of phosphorylation were quantified using Fiji software [70]. Pixel densities of duplicated spots were averaged, and the value of background was subtracted. The analysis was performed as previously described [71].

4.12. Statistical Analysis

The colony formation assay and sphere assay were analyzed using Mann-Whitney test (one-tailed), mean tumor volume increase, Aldefluor™ assay data and Western blot densitometry data were analyzed using unpaired Welch's *t*-test (two-tailed) in GraphPad Prism 8.0.2 software (GraphPad Software Inc., San Diego, CA, USA). $p < 0.05$ was considered statistically significant.

5. Conclusions

In this study, we demonstrate that serial xenotransplantation in NSG mice in conjunction with short-term culture of xenograft-derived cells is an effective tool to screen for molecular targets in rhabdomyosarcoma CSCs. This approach enabled us to identify several novel and promising rhabdomyosarcoma CSC-specific targets, e.g., *ALDH6A1*, *SOX4*, *PAX3*, *CDH15*, downregulated *MIR145*, or phosphorylated RYK, which warrant validation in subsequent mechanistic studies. Most importantly, the presented model of the progressive selection of CSCs has provided the first evidence that the recently emerged link between the hybrid epithelial/mesenchymal phenotype and cancer stemness may also account for embryonal rhabdomyosarcoma. Identification of the hybrid epithelial/mesenchymal gene expression signature associated with the rhabdomyosarcoma CSC phenotype demonstrates the ability of the reported approach to unveil complex molecular changes. Deciphering these complex molecular traits might be essential to achieving a better understanding of the mechanisms underlying the induction and maintenance of stemness in cancer.

References

1. Yang, L.; Takimoto, T.; Fujimoto, J. Prognostic model for predicting overall survival in children and adolescents with rhabdomyosarcoma. *BMC Cancer* **2014**, *14*, 654. [CrossRef]

2. Winter, S.; Fasola, S.; Brisse, H.; Mosseri, V.; Orbach, D. Relapse after localized rhabdomyosarcoma: Evaluation of the efficacy of second-line chemotherapy. *Pediatr. Blood Cancer* **2015**, *62*, 1935–1941. [CrossRef]

3. Sana, J.; Zambo, I.; Skoda, J.; Neradil, J.; Chlapek, P.; Hermanova, M.; Mudry, P.; Vasikova, A.; Zitterbart, K.; Hampl, A.; et al. CD133 expression and identification of CD133/nestin positive cells in rhabdomyosarcomas and rhabdomyosarcoma cell lines. *Anal. Cell. Pathol.* **2011**, *34*, 303–318. [CrossRef]

4. Walter, D.; Satheesha, S.; Albrecht, P.; Bornhauser, B.C.; D'Alessandro, V.; Oesch, S.M.; Rehrauer, H.; Leuschner, I.; Koscielniak, E.; Gengler, C.; et al. CD133 positive embryonal rhabdomyosarcoma stem-like cell population is enriched in rhabdospheres. *PLoS ONE* **2011**, *6*, e19506. [CrossRef] [PubMed]

5. Skoda, J.; Nunukova, A.; Loja, T.; Zambo, I.; Neradil, J.; Mudry, P.; Zitterbart, K.; Hermanova, M.; Hampl, A.; Sterba, J.; et al. Cancer stem cell markers in pediatric sarcomas: Sox2 is associated with tumorigenicity in immunodeficient mice. *Tumor Biol.* **2016**, *37*, 9535–9548. [CrossRef] [PubMed]

6. Clarke, M.F.; Dick, J.E.; Dirks, P.B.; Eaves, C.J.; Jamieson, C.H.; Jones, D.L.; Visvader, J.; Weissman, I.L.; Wahl, G.M. Cancer stem cells–perspectives on current status and future directions: AACR Workshop on cancer stem cells. *Cancer Res.* **2006**, *66*, 9339–9344. [CrossRef]

7. Kim, W.T.; Ryu, C.J. Cancer stem cell surface markers on normal stem cells. *BMB Rep.* **2017**, *50*, 285–298. [CrossRef]

8. Skoda, J.; Veselska, R. Cancer stem cells in sarcomas: Getting to the stemness core. *Biochim. Biophys. Acta Gen. Subj.* **2018**, *1862*, 2134–2139. [CrossRef]

9. Nunukova, A.; Neradil, J.; Skoda, J.; Jaros, J.; Hampl, A.; Sterba, J.; Veselska, R. Atypical nuclear localization of CD133 plasma membrane glycoprotein in rhabdomyosarcoma cell lines. *Int. J. Mol. Med.* **2015**, *36*, 65–72. [CrossRef]

10. Skoda, J.; Hermanova, M.; Loja, T.; Nemec, P.; Neradil, J.; Karasek, P.; Veselska, R. Co-Expression of Cancer Stem Cell Markers Corresponds to a Pro-Tumorigenic Expression Profile in Pancreatic Adenocarcinoma. *PLoS ONE* **2016**, *11*. [CrossRef]

11. Duex, J.E.; Owens, C.; Chauca-Diaz, A.; Dancik, G.M.; Vanderlinden, L.A.; Ghosh, D.; Leivo, M.Z.; Hansel, D.E.; Theodorescu, D. Nuclear CD24 Drives Tumor Growth and Is Predictive of Poor Patient Prognosis. *Cancer Res.* **2017**, *77*, 4858–4867. [CrossRef] [PubMed]

12. Agliano, A.; Calvo, A.; Box, C. The challenge of targeting cancer stem cells to halt metastasis. *Semin. Cancer Biol.* **2017**, *44*, 25–42. [CrossRef] [PubMed]

13. Iglesias, J.M.; Gumuzio, J.; Martin, A.G. Linking Pluripotency Reprogramming and Cancer. *Stem Cells Transl. Med.* **2017**, *6*, 335–339. [CrossRef] [PubMed]

14. Malta, T.M.; Sokolov, A.; Gentles, A.J.; Burzykowski, T.; Poisson, L.; Weinstein, J.N.; Kaminska, B.; Huelsken, J.; Omberg, L.; Gevaert, O.; et al. Machine Learning Identifies Stemness Features Associated with Oncogenic Dedifferentiation. *Cell* **2018**, *173*, 338–354. [CrossRef]

15. Ricci-Vitiani, L.; Lombardi, D.G.; Pilozzi, E.; Biffoni, M.; Todaro, M.; Peschle, C.; De Maria, R. Identification and expansion of human colon-cancer-initiating cells. *Nature* **2007**, *445*, 111–115. [CrossRef]

16. Ying, M.; Liu, G.; Shimada, H.; Ding, W.; May, W.A.; He, Q.; Adams, G.B.; Wu, L. Human osteosarcoma CD49f−CD133+ cells: Impaired in osteogenic fate while gain of tumorigenicity. *Oncogene* **2013**, *32*, 4252–4263. [CrossRef]

17. Golan, H.; Shukrun, R.; Caspi, R.; Vax, E.; Pode-Shakked, N.; Goldberg, S.; Pleniceanu, O.; Bar-Lev, D.D.; Mark-Danieli, M.; Pri-Chen, S.; et al. In Vivo Expansion of Cancer Stemness Affords Novel Cancer Stem Cell Targets: Malignant Rhabdoid Tumor as an Example. *Stem Cell Rep.* **2018**, *11*, 795–810. [CrossRef]

18. Nakahata, K.; Uehara, S.; Nishikawa, S.; Kawatsu, M.; Zenitani, M.; Oue, T.; Okuyama, H. Aldehyde Dehydrogenase 1 (ALDH1) Is a Potential Marker for Cancer Stem Cells in Embryonal Rhabdomyosarcoma. *PLoS ONE* **2015**, *10*, e0125454. [CrossRef]

19. Tomita, H.; Tanaka, K.; Tanaka, T.; Hara, A. Aldehyde dehydrogenase 1A1 in stem cells and cancer. *Oncotarget* **2016**, *7*, 11018–11032. [CrossRef]

20. George, J.T.; Jolly, M.K.; Xu, S.; Somarelli, J.A.; Levine, H. Survival Outcomes in Cancer Patients Predicted by a Partial EMT Gene Expression Scoring Metric. *Cancer Res.* **2017**, *77*, 6415–6428. [CrossRef]

21. Groger, C.J.; Grubinger, M.; Waldhor, T.; Vierlinger, K.; Mikulits, W. Meta-analysis of gene expression signatures defining the epithelial to mesenchymal transition during cancer progression. *PLoS ONE* **2012**, *7*, e51136. [CrossRef] [PubMed]

22. Wachtel, M.; Schafer, B.W. Unpeaceful roles of mutant PAX proteins in cancer. *Semin. Cell Dev. Biol.* **2015**, *44*, 126–134. [CrossRef]

23. Buckingham, M. Gene regulatory networks and cell lineages that underlie the formation of skeletal muscle. *Proc. Natl. Acad. Sci. USA* **2017**, *114*, 5830–5837. [CrossRef]

24. Xu, N.; Papagiannakopoulos, T.; Pan, G.; Thomson, J.A.; Kosik, K.S. MicroRNA-145 regulates OCT4, SOX2, and KLF4 and represses pluripotency in human embryonic stem cells. *Cell* **2009**, *137*, 647–658. [CrossRef] [PubMed]

25. Medeiros Tavares Marques, J.C.; Cornelio, D.A.; Nogueira Silbiger, V.; Ducati Luchessi, A.; de Souza, S.; Batistuzzo de Medeiros, S.R. Identification of new genes associated to senescent and tumorigenic phenotypes in mesenchymal stem cells. *Sci. Rep.* **2017**, *7*, 17837. [CrossRef] [PubMed]

26. Katso, R.M.; Russell, R.B.; Ganesan, T.S. Functional analysis of H-Ryk, an atypical member of the receptor tyrosine kinase family. *Mol. Cell. Biol.* **1999**, *19*, 6427–6440. [CrossRef] [PubMed]

27. Roy, J.P.; Halford, M.M.; Stacker, S.A. The biochemistry, signalling and disease relevance of RYK and other WNT-binding receptor tyrosine kinases. *Growth Factors* **2018**, *36*, 15–40. [CrossRef]

28. Cheyette, B.N. Ryk: Another heretical Wnt receptor defies the canon. *Sci. STKE* **2004**, *2004*, 54. [CrossRef]

29. Grunberg, J.R.; Hoffmann, J.M.; Hedjazifar, S.; Nerstedt, A.; Jenndahl, L.; Elvin, J.; Castellot, J.; Wei, L.; Moverare-Skrtic, S.; Ohlsson, C.; et al. Overexpressing the novel autocrine/endocrine adipokine WISP2 induces hyperplasia of the heart, white and brown adipose tissues and prevents insulin resistance. *Sci. Rep.* **2017**, *7*, 43515. [CrossRef]

30. Grunberg, J.R.; Hammarstedt, A.; Hedjazifar, S.; Smith, U. The Novel Secreted Adipokine WNT1-inducible Signaling Pathway Protein 2 (WISP2) Is a Mesenchymal Cell Activator of Canonical WNT. *J. Biol. Chem.* **2014**, *289*, 6899–6907. [CrossRef] [PubMed]

31. Davicioni, E.; Anderson, J.R.; Buckley, J.D.; Meyer, W.H.; Triche, T.J. Gene expression profiling for survival prediction in pediatric rhabdomyosarcomas: A report from the children's oncology group. *J. Clin. Oncol.* **2010**, *28*, 1240–1246. [CrossRef]

32. Tang, Z.; Kang, B.; Li, C.; Chen, T.; Zhang, Z. GEPIA2: An enhanced web server for large-scale expression profiling and interactive analysis. *Nucleic Acids Res.* **2019**, *47*, W556–W560. [CrossRef] [PubMed]

33. Zhou, L.; Sheng, D.; Wang, D.; Ma, W.; Deng, Q.; Deng, L.; Liu, S. Identification of cancer-type specific expression patterns for active aldehyde dehydrogenase (ALDH) isoforms in ALDEFLUOR assay. *Cell Biol. Toxicol.* **2018**. [CrossRef] [PubMed]

34. Levi, B.P.; Yilmaz, O.H.; Duester, G.; Morrison, S.J. Aldehyde dehydrogenase 1a1 is dispensable for stem cell function in the mouse hematopoietic and nervous systems. *Blood* **2009**, *113*, 1670–1680. [CrossRef] [PubMed]

35. Marcato, P.; Dean, C.A.; Pan, D.; Araslanova, R.; Gillis, M.; Joshi, M.; Helyer, L.; Pan, L.; Leidal, A.; Gujar, S.; et al. Aldehyde dehydrogenase activity of breast cancer stem cells is primarily due to isoform ALDH1A3 and its expression is predictive of metastasis. *Stem Cells* **2011**, *29*, 32–45. [CrossRef]

36. Cho, S.Y.; Kang, S.; Kim, D.S.; Na, H.J.; Kim, Y.J.; Choi, Y.D.; Cho, N.H. HSP27, ALDH6A1 and Prohibitin Act as a Trio-biomarker to Predict Survival in Late Metastatic Prostate Cancer. *Anticancer Res.* **2018**, *38*, 6551–6560. [CrossRef]

37. Martinez-Cruzado, L.; Tornin, J.; Santos, L.; Rodriguez, A.; Garcia-Castro, J.; Moris, F.; Rodriguez, R. Aldh1 Expression and Activity Increase During Tumor Evolution in Sarcoma Cancer Stem Cell Populations. *Sci. Rep.* **2016**, *6*, 27878. [CrossRef]

38. Storer, N.Y.; White, R.M.; Uong, A.; Price, E.; Nielsen, G.P.; Langenau, D.M.; Zon, L.I. Zebrafish rhabdomyosarcoma reflects the developmental stage of oncogene expression during myogenesis. *Development* **2013**, *140*, 3040–3050. [CrossRef]

39. Fukada, S.; Ma, Y.; Ohtani, T.; Watanabe, Y.; Murakami, S.; Yamaguchi, M. Isolation, characterization and molecular regulation of muscle stem cells. *Front. Physiol.* **2013**, *4*, 317. [CrossRef]

40. Rubin, B.P.; Nishijo, K.; Chen, H.I.; Yi, X.; Schuetze, D.P.; Pal, R.; Prajapati, S.I.; Abraham, J.; Arenkiel, B.R.; Chen, Q.R.; et al. Evidence for an unanticipated relationship between undifferentiated pleomorphic sarcoma and embryonal rhabdomyosarcoma. *Cancer Cell* **2011**, *19*, 177–191. [CrossRef]

41. Fukada, S.; Uezumi, A.; Ikemoto, M.; Masuda, S.; Segawa, M.; Tanimura, N.; Yamamoto, H.; Miyagoe-Suzuki, Y.; Takeda, S. Molecular signature of quiescent satellite cells in adult skeletal muscle. *Stem Cells* **2007**, *25*, 2448–2459. [CrossRef] [PubMed]

42. Cui, S.; Hano, H.; Harada, T.; Takai, S.; Masui, F.; Ushigome, S. Evaluation of new monoclonal anti-MyoD1 and anti-myogenin antibodies for the diagnosis of rhabdomyosarcoma. *Pathol. Int.* **1999**, *49*, 62–68. [CrossRef]

43. Tenente, I.M.; Hayes, M.N.; Ignatius, M.S.; McCarthy, K.; Yohe, M.; Sindiri, S.; Gryder, B.; Oliveira, M.L.; Ramakrishnan, A.; Tang, Q.; et al. Myogenic regulatory transcription factors regulate growth in rhabdomyosarcoma. *Elife* **2017**, *6*, e19214. [CrossRef]

44. Gianakopoulos, P.J.; Mehta, V.; Voronova, A.; Cao, Y.; Yao, Z.; Coutu, J.; Wang, X.; Waddington, M.S.; Tapscott, S.J.; Skerjanc, I.S. MyoD directly up-regulates premyogenic mesoderm factors during induction of skeletal myogenesis in stem cells. *J. Biol. Chem.* **2011**, *286*, 2517–2525. [CrossRef]

45. Bhattaram, P.; Penzo-Mendez, A.; Sock, E.; Colmenares, C.; Kaneko, K.J.; Vassilev, A.; Depamphilis, M.L.; Wegner, M.; Lefebvre, V. Organogenesis relies on SoxC transcription factors for the survival of neural and mesenchymal progenitors. *Nat. Commun.* **2010**, *1*, 9. [CrossRef]

46. Lourenco, A.R.; Coffer, P.J. SOX4: Joining the Master Regulators of Epithelial-to-Mesenchymal Transition? *Trends Cancer* **2017**, *3*, 571–582. [CrossRef]

47. Rajurkar, M.; Huang, H.; Cotton, J.L.; Brooks, J.K.; Sicklick, J.; McMahon, A.P.; Mao, J. Distinct cellular origin and genetic requirement of Hedgehog-Gli in postnatal rhabdomyosarcoma genesis. *Oncogene* **2014**, *33*, 5370–5378. [CrossRef]

48. Wang, H.; Garzon, R.; Sun, H.; Ladner, K.J.; Singh, R.; Dahlman, J.; Cheng, A.; Hall, B.M.; Qualman, S.J.; Chandler, D.S.; et al. NF-kappaB-YY1-miR-29 regulatory circuitry in skeletal myogenesis and rhabdomyosarcoma. *Cancer Cell* **2008**, *14*, 369–381. [CrossRef]

49. Shibue, T.; Weinberg, R.A. EMT, CSCs, and drug resistance: The mechanistic link and clinical implications. *Nat. Rev. Clin. Oncol.* **2017**, *14*, 611–629. [CrossRef]

50. Dongre, A.; Weinberg, R.A. New insights into the mechanisms of epithelial-mesenchymal transition and implications for cancer. *Nat. Rev. Mol. Cell Biol.* **2018**, *20*, 69–84. [CrossRef]

51. Jolly, M.K.; Somarelli, J.A.; Sheth, M.; Biddle, A.; Tripathi, S.C.; Armstrong, A.J.; Hanash, S.M.; Bapat, S.A.; Rangarajan, A.; Levine, H. Hybrid epithelial/mesenchymal phenotypes promote metastasis and therapy resistance across carcinomas. *Pharmacol. Ther.* **2018**, *194*, 161–184. [CrossRef]

52. Jolly, M.K.; Jia, D.; Boareto, M.; Mani, S.A.; Pienta, K.J.; Ben-Jacob, E.; Levine, H. Coupling the modules of EMT and stemness: A tunable stemness window model. *Oncotarget* **2015**, *6*, 25161–25174. [CrossRef]

53. Bierie, B.; Pierce, S.E.; Kroeger, C.; Stover, D.G.; Pattabiraman, D.R.; Thiru, P.; Liu Donaher, J.; Reinhardt, F.; Chaffer, C.L.; Keckesova, Z.; et al. Integrin-beta4 identifies cancer stem cell-enriched populations of partially mesenchymal carcinoma cells. *Proc. Natl. Acad. Sci. USA* **2017**, *114*, E2337–E2346. [CrossRef]

54. Yang, J.; Du, X.; Wang, G.; Sun, Y.; Chen, K.; Zhu, X.; Lazar, A.J.; Hunt, K.K.; Pollock, R.E.; Zhang, W. Mesenchymal to epithelial transition in sarcomas. *Eur. J. Cancer* **2014**, *50*, 593–601. [CrossRef]

55. Sannino, G.; Marchetto, A.; Kirchner, T.; Grunewald, T.G.P. Epithelial-to-Mesenchymal and Mesenchymal-to-Epithelial Transition in Mesenchymal Tumors: A Paradox in Sarcomas? *Cancer Res.* **2017**, *77*, 4556–4561. [CrossRef]

56. Kahlert, U.D.; Joseph, J.V.; Kruyt, F.A.E. EMT- and MET-related processes in nonepithelial tumors: Importance for disease progression, prognosis, and therapeutic opportunities. *Mol. Oncol.* **2017**, *11*, 860–877. [CrossRef]

57. Wiggan, O.; Fadel, M.P.; Hamel, P.A. Pax3 induces cell aggregation and regulates phenotypic mesenchymal-epithelial interconversion. *J. Cell Sci.* **2002**, *115*, 517–529.

58. Li, R.; Liang, J.; Ni, S.; Zhou, T.; Qing, X.; Li, H.; He, W.; Chen, J.; Li, F.; Zhuang, Q.; et al. A mesenchymal-to-epithelial transition initiates and is required for the nuclear reprogramming of mouse fibroblasts. *Cell Stem Cell* **2010**, *7*, 51–63. [CrossRef]

59. Hoffding, M.K.; Hyttel, P. Ultrastructural visualization of the Mesenchymal-to-Epithelial Transition during reprogramming of human fibroblasts to induced pluripotent stem cells. *Stem Cell Res.* **2015**, *14*, 39–53. [CrossRef]

60. Kashima, T.; Kawaguchi, J.; Takeshita, S.; Kuroda, M.; Takanashi, M.; Horiuchi, H.; Imamura, T.; Ishikawa, Y.; Ishida, T.; Mori, S.; et al. Anomalous cadherin expression in osteosarcoma. Possible relationships to metastasis and morphogenesis. *Am. J. Pathol.* **1999**, *155*, 1549–1555. [CrossRef]

61. Kashima, T.; Nakamura, K.; Kawaguchi, J.; Takanashi, M.; Ishida, T.; Aburatani, H.; Kudo, A.; Fukayama, M.; Grigoriadis, A.E. Overexpression of cadherins suppresses pulmonary metastasis of osteosarcoma in vivo. *Int. J. Cancer* **2003**, *104*, 147–154. [CrossRef] [PubMed]

62. Camand, E.; Peglion, F.; Osmani, N.; Sanson, M.; Etienne-Manneville, S. N-cadherin expression level modulates integrin-mediated polarity and strongly impacts on the speed and directionality of glial cell migration. *J. Cell Sci.* **2012**, *125*, 844–857. [CrossRef] [PubMed]

63. Lammens, T.; Swerts, K.; Derycke, L.; De Craemer, A.; De Brouwer, S.; De Preter, K.; Van Roy, N.; Vandesompele, J.; Speleman, F.; Philippe, J.; et al. N-cadherin in neuroblastoma disease: Expression and clinical significance. *PLoS ONE* **2012**, *7*, e31206. [CrossRef] [PubMed]

64. Nakagawa, S.; Takeichi, M. Neural crest emigration from the neural tube depends on regulated cadherin expression. *Development* **1998**, *125*, 2963–2971.

65. Blindt, R.; Bosserhoff, A.K.; Dammers, J.; Krott, N.; Demircan, L.; Hoffmann, R.; Hanrath, P.; Weber, C.; Vogt, F. Downregulation of N-cadherin in the neointima stimulates migration of smooth muscle cells by RhoA deactivation. *Cardiovasc. Res.* **2004**, *62*, 212–222. [CrossRef]

66. Tiwari, N.; Tiwari, V.K.; Waldmeier, L.; Balwierz, P.J.; Arnold, P.; Pachkov, M.; Meyer-Schaller, N.; Schubeler, D.; van Nimwegen, E.; Christofori, G. Sox4 is a master regulator of epithelial-mesenchymal transition by controlling Ezh2 expression and epigenetic reprogramming. *Cancer Cell* **2013**, *23*, 768–783. [CrossRef]

67. Preussner, J.; Zhong, J.; Sreenivasan, K.; Gunther, S.; Engleitner, T.; Kunne, C.; Glatzel, M.; Rad, R.; Looso, M.; Braun, T.; et al. Oncogenic Amplification of Zygotic Dux Factors in Regenerating p53-Deficient Muscle Stem Cells Defines a Molecular Cancer Subtype. *Cell Stem Cell* **2018**, *23*, 794–805. [CrossRef]

68. Mochizuki, Y.; Furukawa, K. Application of coomassie brilliant blue staining to cultured hepatocytes. *Cell Biol. Int. Rep.* **1987**, *11*, 367–371. [CrossRef]

69. Mikulenkova, E.; Neradil, J.; Zitterbart, K.; Sterba, J.; Veselska, R. Overexpression of the Np73 isoform is associated with centrosome amplification in brain tumor cell lines. *Tumor Biol.* **2015**, *36*, 7483–7491. [CrossRef]

70. Schindelin, J.; Arganda-Carreras, I.; Frise, E.; Kaynig, V.; Longair, M.; Pietzsch, T.; Preibisch, S.; Rueden, C.; Saalfeld, S.; Schmid, B.; et al. Fiji: An open-source platform for biological-image analysis. *Nat. Methods* **2012**, *9*, 676–682. [CrossRef]

71. Skoda, J.; Neradil, J.; Zitterbart, K.; Sterba, J.; Veselska, R. EGFR signaling in the HGG-02 glioblastoma cell line with an unusual loss of EGFR gene copy. *Oncol. Rep.* **2014**, *31*, 480–487. [CrossRef] [PubMed]

72. Huang da, W.; Sherman, B.T.; Lempicki, R.A. Systematic and integrative analysis of large gene lists using DAVID bioinformatics resources. *Nat. Protoc.* **2009**, *4*, 44–57. [CrossRef] [PubMed]

Paukovcekova S, **Skoda J**, Neradil J, Mikulenkova E, Chlapek P, Sterba J, Richardson DR, Veselska R. Novel Thiosemicarbazones Sensitize Pediatric Solid Tumor Cell-Types to Conventional Chemotherapeutics through Multiple Molecular Mechanisms. *Cancers*. 2020;12:3781. (JCR 2020, IF = 6.639; Q1 – Oncology)

Novel Thiosemicarbazones Sensitize Pediatric Solid Tumor Cell-Types to Conventional Chemotherapeutics through Multiple Molecular Mechanisms

Silvia Paukovcekova [1], Jan Skoda [1,2] , Jakub Neradil [1,2] , Erika Mikulenkova [1,2] , Petr Chlapek [1,2], Jaroslav Sterba [2,3], Des R. Richardson [1,4,†] and Renata Veselska [1,2,3,*,†]

[1] Department of Experimental Biology, Faculty of Science, Masaryk University, 61137 Brno, Czech Republic; silvia.paukovcekova@mail.muni.cz (S.P.); jan.skoda@sci.muni.cz (J.S.); jneradil@sci.muni.cz (J.N.); mikulenkova@mail.muni.cz (E.M.); chlapek@sci.muni.cz (P.C.)

[2] International Clinical Research Center, St. Anne's University Hospital, 65691 Brno, Czech Republic

[3] Department of Pediatric Oncology, University Hospital Brno and Faculty of Medicine, Masaryk University, 66263 Brno, Czech Republic; Sterba.Jaroslav@fnbrno.cz

[4] Griffith Institute for Drug Discovery, Centre for Cancer Cell Biology and Drug Discovery, Griffith University, Brisbane, Queensland 4111, Australia; d.richardson@griffith.edu.au

* Correspondence: veselska@sci.muni.cz

† These authors contributed equally to this paper as co-senior authors.

Simple Summary: Combination of chemotherapeutics for the treatment of childhood cancer can lead to the use of lower cytotoxic drug doses and better therapeutic tolerability (i.e., lower side effects) for patients. We discovered novel molecular targets of two lead thiosemicarbazone agents of the di-2-pyridylketone thiosemicarbazone class. These molecular targets include: cyclooxygenase, the DNA repair protein, O6-methylguanine DNA methyltransferase, mismatch repair proteins, and topoisomerase 2α. This research also identifies promising synergistic interactions of these thiosemicarbazones particularly with the standard chemotherapeutic, celecoxib.

Abstract: Combining low-dose chemotherapies is a strategy for designing less toxic and more potent childhood cancer treatments. We examined the effects of combining the novel thiosemicarbazones, di-2-pyridylketone 4-cyclohexyl-4-methyl-3-thiosemicarbazone (DpC), or its analog, di-2-pyridylketone-4, 4-dimethyl-3-thiosemicarbazone (Dp44mT), with the standard chemotherapies, celecoxib (CX), etoposide (ETO), or temozolomide (TMZ). These combinations were analyzed for synergism to inhibit proliferation of three pediatric tumor cell-types, namely osteosarcoma (Saos-2), medulloblastoma (Daoy) and neuroblastoma (SH-SY5Y). In terms of mechanistic dissection, this study discovered novel thiosemicarbazone targets not previously identified and which are important for considering possible drug combinations. In this case, DpC and Dp44mT caused: (1) up-regulation of a major protein target of CX, namely cyclooxygenase-2 (COX-2); (2) down-regulation of the DNA repair protein, O^6-methylguanine DNA methyltransferase (MGMT), which is known to affect TMZ resistance; (3) down-regulation of mismatch repair (MMR) proteins, MSH2 and MSH6, in Daoy and SH-SY5Y cells; and (4) down-regulation in all three cell-types of the MMR repair protein, MLH1, and also topoisomerase 2α (Topo2α), the latter of which is an ETO target. While thiosemicarbazones up-regulate the metastasis suppressor, NDRG1, in adult cancers, it is demonstrated herein for the first time that they induce NDRG1 in all three pediatric tumor cell-types, validating its role as a potential target. In fact, siRNA studies indicated that NDRG1 was responsible for MGMT down-regulation that may prevent TMZ resistance. Examining the effects of combining thiosemicarbazones with CX, ETO, or TMZ, the most promising synergism was obtained using CX. Of interest, a positive relationship was observed between NDRG1 expression of the cell-type

---

and the synergistic activity observed in the combination of thiosemicarbazones and CX. These studies identify novel thiosemicarbazone targets relevant to childhood cancer combination chemotherapy.

1. Introduction

As a result of therapeutic advances in pediatric oncology, almost 83% of patients survive long term [1]. Nevertheless, aggressive treatments used for tumors in children may result in several off-target effects, including increased risks of subsequent neoplasms and serious cardiomyopathies [2,3]. Therefore, it is critical to develop effective combinatory therapeutic regimens with lower toxicity.

The clinical protocol combined oral metronomic, bio-differentiating, anti-angiogenic treatment (COMBAT) is a low-toxicity regimen for the treatment of childhood cancers and was originally designed for pediatric patients with relapsed and/or high-risk solid tumors [4]. The therapy is based on a combination of low doses of anti-angiogenic (celecoxib (CX)) and cytotoxic (etoposide (ETO) and temozolomide (TMZ)) agents with differentiation inducers (retinoids, calcitriol and its derivatives) that are administered in a metronomic regimen [5]. In general, this treatment is well tolerated and has a low acute toxicity profile [5].

The aim of the current investigation was to: (1) determine novel molecular targets of two thiosemicarbazones of the di-2-pyridylketone (DpT) class [6,7] that could be important for combinatory studies with standard chemotherapies in the COMBAT protocol for pediatric cancers; and (2) to analyze the synergy between selected chemotherapeutics used in the COMBAT protocol (CX, ETO and TMZ) and these thiosemicarbazones. The DpT class of agents has been carefully optimized over a 10-year period of structure–activity relationship analysis. These compounds were derived from aroylhydrazone ligands [8,9] and are superior to other classical thiosemicarbazones such as Triapine® [6,7].

The DpT class of agents has been demonstrated by several international laboratories to possess potent and selective anti-tumor activity against a broad range of tumors in vitro and in vivo, with the compounds also being able to overcome P-glycoprotein-mediated resistance [6,7,10–14]. The two lead DpT agents of this class are di-2-pyridylketone-4-cyclohexyl-4-methyl-3-thiosemicarbazone (DpC) and the well-characterized parent analog, di-2-pyridylketone-4,4-dimethyl-3-thiosemicarbazone (Dp44mT) [6,7,10–16].

The molecular mechanism of action of DpT thiosemicarbazones involves the chelation of iron and copper within cancer cells, which is critical for proliferation and the induction of the expression of the potent metastasis suppressor N-myc downstream regulated gene-1 (NDRG1) [15,17]. These agents have been demonstrated to be effective even at very low concentrations in vitro and low doses in vivo [16,18].

The important properties of DpC and Dp44mT are their appropriate lipophilic balance, which allows facile permeation of cell membranes, and their lysosomotropic character, which results in their ability to overcome P-glycoprotein-mediated drug resistance [6,19–21]. Dp44mT binds iron and copper in lysosomes to form redox-active complexes that generate cytotoxic reactive oxygen species [18–20], which leads to permeabilization of the lysosomal membrane and the induction of apoptosis [19,21].

Moreover, many studies have demonstrated that these agents can down-regulate the key oncogenic tyrosine kinases EGFR, HER2, HER3 [22,23], and c-Met [24]. Both DpC and Dp44mT markedly suppress the activity of a variety of pro-oncogenic signaling pathways downstream of these tyrosine kinases, including the AKT, PI3K and RAS pathways [25], as well as other pathways, including the STAT3 [26], TGF-β [25,27,28], Wnt [10,27,29] and autophagic pathways [30]. As such, they subsequently inhibit proliferation, migration, the epithelial-mesenchymal transition [27], and metastasis in vivo [10].

Significantly, these novel thiosemicarbazones also synergistically increase the anti-neoplastic activity of several chemotherapeutic drugs, including gemcitabine or cisplatin [16], doxorubicin [21], paclitaxel, 5-fluorouracyl, methotrexate, 4-hydroper-oxycyclophosphamide and tamoxifen [31,32].

Considering the exciting anti-oncogenic properties of DpC and Dp44mT, three chemotherapeutics included in the COMBAT protocol, namely, CX, TMZ and ETO, were tested for their possible synergistic effects with these thiosemicarbazones.

The non-steroidal anti-inflammatory drug, CX, acts as a selective low-molecular-weight inhibitor of the heme-containing enzyme, cyclooxygenase-2 (COX-2) [33]. TMZ is a lipophilic alkylating agent that is hydrolyzed at neutral and alkaline pH values to the 5-(3-methyltriazen-1-yl)imidazole-4-carboxamide intermediate [34]. This active compound then methylates DNA bases, and thus introduces O6-methylguanine (O6-meG)/cytosine (O6-meG:C) pairs, which can result in DNA mismatches after the first round of replication [34].

Of note, ETO is often used at low doses as part of combination therapies because of its myelotoxic and leukemogenic actions, which limit its use at sufficiently high doses [35]. The primary cellular target of ETO is topoisomerase II alpha (TOP2α), which helps DNA maintain its appropriate conformation during semi-conservative DNA replication, transcription, recombination, and chromosome condensation and decondensation [36].

In this investigation, we discovered novel molecular targets of Dp44mT and DpC that could be important in terms of synergy with standard chemotherapeutics in the COMBAT protocol for pediatric tumors (CX, ETO and TMZ). This was done to better define the conditions necessary to rationally achieve synergy and develop safe and effective drug combinations. Studies were also performed to analyze for synergy between the thiosemicarbazones and these agents. These results demonstrate several novel molecular targets of thiosemicarbazones in pediatric tumor cells and identifies promising synergistic interactions particularly with CX.

2. Results

2.1. Synergism between Thiosemicarbazones and Established Chemotherapeutics Is Marked with CX

Our initial studies examined the anti-proliferative activity of the selected drugs and the interactions between thiosemicarbazones and the selected chemotherapeutics in SH-SY5Y neuroblastoma, Daoy medulloblastoma and Saos-2 osteosarcoma cells. The interactions of the tested drugs were evaluated in terms of changes in cellular proliferation after a 72-h incubation period. From these data, the concentration at which cellular proliferation was reduced by half (IC$_{50}$; Table 1) and combination index (CI; Table 2) values were calculated.

Table 1. IC$_{50}$ values. The IC$_{50}$ values of the individual drugs were determined in each cell-type after incubation with each drug alone for 72 h/37 °C. The results are presented as the mean ± SD (3 experiments).

Cell Line	IC$_{50}$ Values				
	CX [μM]	TMZ [μM]	ETO [μM]	DpC [nM]	Dp44mT [nM]
Saos-2	75.6 ± 7.1	116.5 ± 3.0	11.5 ± 0.7	8.8 ± 0.2	9.3 ± 0.6
Daoy	90.6 ± 6.7	212.9 ± 38.4	6.8 ± 2.0	8.5 ± 2.2	5.4 ± 0.8
SH-SY5Y	73.7 ± 9.1	112.4 ± 3.8	2.8 ± 0.3	3.7 ± 0.6	0.8 ± 0.1

Table 2. Quantitative assessment of drug interactions—combination index (CI) values. Analysis of the interaction between CX, TMZ, or ETO, and the thiosemicarbazones (DpC and Dp44mT) was performed using CalcuSyn software. The data were obtained after a 72 h/37 °C incubation with each agent alone or in combination. The CIs were calculated from growth inhibition curves. A 1:1 ratio of drugs was used for combination treatments. The Chou Talalay method was adopted to identify synergistic, additive and antagonistic activity. These results are mean ± SD (three experiments).

| Cell Line | Combination Index (CI) ± SD | | | | | |
| | CX | | TMZ | | ETO | |
	+DpC	+Dp44mT	+DpC	+Dp44mT	+DpC	+Dp44mT
Saos-2	0.29 ± 0.19	0.33 ± 0.15	0.48 ± 0.07	0.92 ± 0.37	1.55 ± 0.44	2.19 ± 0.70
Daoy	0.52 ± 0.03	0.39 ± 0.05	0.89 ± 0.11	1.59 ± 0.31	0.45 ± 0.12	0.64 ± 0.12
SH-SY5Y	1.56 ± 0.08	0.84 ± 0.11	1.62 ± 0.32	1.38 ± 0.25	1.66 ± 0.66	1.67 ± 0.25
Categories of Interactions						
0.10–0.30	strong synergism		0.91–1.10	nearly additive		
0.31–0.70	synergism		1.11–1.20	slight antagonism		
0.71–0.85	moderate synergism		1.21–1.45	moderate antagonism		
0.86–0.90	slight synergism		1.46–3.30	antagonism		

Generally, based on the IC_{50} values identified for all three cell-types, both the thiosemicarbazones, DpC and Dp44mT, demonstrated potent activity (0.8 nM–9.3 nM; Table 1). The anti-proliferative activity of each of these compounds was markedly and significantly ($p < 0.001$) greater than that of CX (73.7–90.6 μM), TMZ (112.4–212.9 μM) and ETO (2.8–11.5 μM; Table 1). Of all the agents tested, Dp44mT demonstrated on average the greatest anti-proliferative activity in all three cell-types, while TMZ was the least effective. The sensitivity of all cell-types to CX was similar, while SH-SY-5Y cells were consistently the most sensitive to the anti-proliferative activity of all agents (Table 1).

CI analysis revealed synergistic interactions between CX and either DpC or Dp44mT in all cell-types, except the combination of DpC and CX in SH-SY5Y cells, which was antagonistic (Table 2). Of note, the strongest synergistic interaction (i.e., strong synergy) observed in this study was between CX and DpC in Saos-2 cells. Synergism was observed for the combination of TMZ and DpC in Saos-2 cells (Table 2). Slight synergy was detected for TMZ and DpC in Daoy cells, while Dp44mT and TMZ had antagonistic effects in these cells (Table 2). Antagonism and moderate antagonism were observed when TMZ was used in combination with DpC and Dp44mT, respectively, in SH-SY5Y cells (Table 2). A nearly additive effect was observed with the combination of TMZ and Dp44mT in Saos-2 cells. A synergistic effect was observed when either thiosemicarbazone was combined with ETO in Daoy cells (Table 2). On the other hand, incubation of Saos-2 or SH-SY5Y cells with either thiosemicarbazone or ETO induced antagonistic effects (Table 2).

Due to the differential effects observed in the selected cell-types and for the different combinations of drugs (Table 2); in the next part of the study, we examined the molecular mechanisms of the interactions between the thiosemicarbazones and chemotherapeutics.

2.2. DpC and Dp44mT Up-Regulate COX-2 Expression

The studies described above demonstrated that the combination of CX with either thiosemicarbazone resulted in a mostly synergistic interactions in all three cell-types (Table 2). Considering that COX-2 activity is a primary target of CX [33], we hypothesized that the synergy observed between CX and the thiosemicarbazones may have been due to the ability of the latter to deplete cells of iron [6,16]. Iron is essential for the biosynthesis of the heme prosthetic group of COX-2, which is critical for its enzymatic activity [37]. Iron is also required for the prosthetic groups of other proteins, and once incorporated, is known to increase protein stability [38,39]. Thus, thiosemicarbazone-mediated iron depletion could decrease COX-2 protein levels, and this effect could potentially synergize with the inhibitory effect of CX on COX-2. To examine whether the thiosemicarbazones affected COX-2 expression, immunoblotting

studies were performed to first assess their effect on endogenous COX-2 protein levels in all three cell-types (Figure 1).
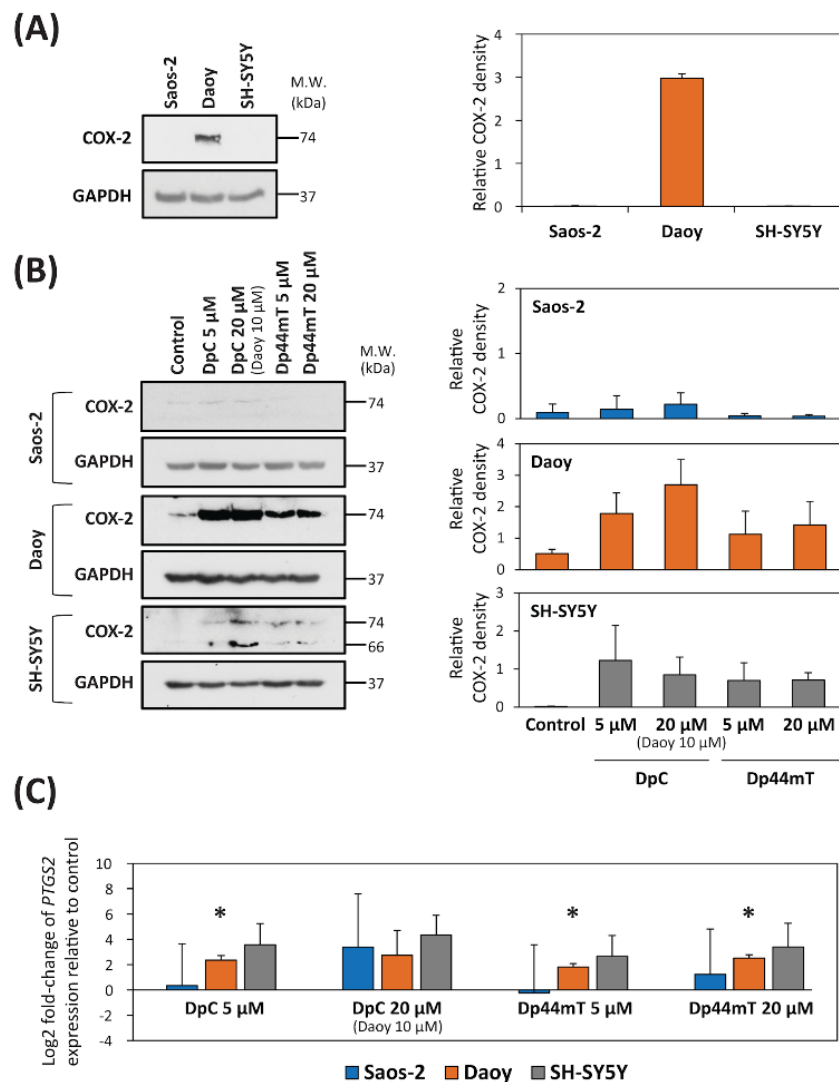

Figure 1. COX-2 expression is up-regulated at the (**A**,**B**) protein and (**C**) mRNA levels after incubation with DpC or Dp44mT for 24 h. (**A**) Western blot analysis of endogenous COX-2 levels in untreated (control) cells. GAPDH served as a protein loading control. (**B**) Western blot analysis of COX-2 levels in Saos-2, Daoy and SH-SY5Y cells after 24 h of incubation with either control medium, DpC (5 or 20 μM; 10 μM for Daoy cells—due to cytotoxicity) or Dp44mT (5 or 20 μM). GAPDH served as a loading control. (**C**) The graph shows changes in the mRNA expression of *PTGS2* in Saos-2, Daoy, or SH-SY5Y cells after 24 h of incubation with DpC or Dp44mT using the concentrations in (**B**). These data were obtained by RT-qPCR. The levels of mRNA expression after thiosemicarbazone treatment are presented as the $\log_2$ fold change in mRNA levels relative to that of the untreated controls. *GAPDH* served as a reference control. For all experiments, expression was assessed in at least three biological replicates. Western blots are typical of three experiments, while the quantitation of the blots is presented as mean ± SD (3 experiments). These data were analyzed using an unpaired Welch's *t*-test followed by the Games-Howell post hoc test. * $p < 0.05$ indicates significant differences compared to the respective control group.

Under control conditions, COX-2 expression was demonstrated to be pronounced in Daoy cells, where it was identified as a single 74-kDa band, while its expression was negligible in both Saos-2 and SH-SY5Y cells (Figure 1A; Figure S1A). The effect of the thiosemicarbazones on COX-2

expression in each cell-type was then examined after a 24 h incubation of cells with either control medium, DpC (5 or 20 μM; 10 μM for Daoy cells—due to cytotoxicity), or Dp44mT (5 or 20 μM). As shown in Figure 1A, examining Saos-2 cells, COX-2 expression was negligible and was not markedly affected by the thiosemicarbazones (Figure 1B, Figure S1B). On the other hand, examining both Daoy and SH-SY5Y cells, there was a marked increase in COX-2 expression in cells incubated with the thiosemicarbazones (especially DpC) relative to the control cells (Figure 1B, Figure S1B). Examining SH-SY5Y cells, incubation with thiosemicarbazones resulted in up-regulation of both the 74-kDa band and another 66-kDa band relative to the control, while again COX-2 expression in the control was negligible. This alteration suggested that incubation with the thiosemicarbazones changed the metabolic processing of COX-2 in SH-SY5Y cells. Interestingly, it has been reported that under other experimental conditions, COX-2 can be demonstrated as a 72-kDa *N*-glycosylated protein, as well as an unglycosylated form of the protein at 66 kDa [40].

Considering that COX-2 protein expression was up-regulated in both Daoy and SH-SY5Y cells after incubation with the thiosemicarbazones, alterations in the mRNA level of *PTGS2* (the gene encoding COX-2) were also investigated (Figure 1C). In Saos-2 cells, both thiosemicarbazones had little effect on its expression at a concentration of 5 μM relative to the control, while *PTGS2* mRNA expression was slightly, but not significantly increased at a thiosemicarbazone concentration of 20 μM (Figure 1C). In contrast, assessing Daoy cells, incubation with 5 μM DpC, or 5 and 20 μM Dp44mT, resulted in a significant ($p < 0.05$) increase in *PTGS2* mRNA relative to the control (Figure 1C). Examining SH-SY5Y cells, both DpC and Dp44mT caused up-regulation of *PTGS2* mRNA, with DpC being slightly more effective than Dp44mT (Figure 1C).

Collectively, these results in Figure 1 suggest the observed synergy in the three cell-types was not based on the ability of thiosemicarbazones to influence COX-2 expression, because the strongest synergistic effect was observed in COX-2-negative Saos-2 cells. Therefore, we focused on another common target of thiosemicarbazones and CX, namely protein kinase B (AKT) [41]. It was reported that CX suppresses tumor growth without apparent involvement of COX-2 via inhibition of PI3K/AKT signaling [41]. The PI3K/AKT signaling pathway is also known to be inhibited by the metastasis suppressor, NDRG1 [25], the expression of which is up-regulated by thiosemicarbazones [15,17,27].

To first test the influence of thiosemicarbazones on NDRG1 expression, endogenous NDRG1 protein levels were assessed in all three cell-types (Figure 2A). Under control conditions, the highest NDRG1 levels were demonstrated in Saos-2 cells, while NDRG1 levels in Daoy cells were significantly ($p < 0.05$) lower than those in Saos-2 cells (Figure 2A; Figure S2A). Assessing SH-SY5Y cells, NDRG1 expression under control conditions was almost undetectable by immunoblotting (Figure 2A; Figure S2A). Subsequently, studies then analyzed NDRG1 expression after a 24 h incubation of cells with either control medium, Dp44mT (20 μM), or DpC (20 μM; 10 μM for Daoy cells). These data confirmed that NDRG1 was markedly up-regulated by both DpC and Dp44mT in all tested cell-types, resulting in two closely migrating bands at 41- and 46-kDa (Figure 2B, Figure S2B), as reported previously [42,43].

Next, studies focused directly on p-AKT (Ser473) levels and total AKT protein expression in the three cell-types (Figure 3, Figure S3) incubated after 2 h of treatment with IC_{50} doses of CX, DpC, Dp44mT alone or combinations of DpC or Dp44mT and CX at their IC_{50} doses (Figure 3, Figure S3). The immunoblotting analyses demonstrated that CX alone resulted in a slight increase in the p-AKT levels in Saos-2 and SH-SY5Y cells relative to the control (Figure 3, Figure S3). In contrast, p-AKT levels were slightly decreased in all tested cell-types after treatment with the thiosemicarbazones alone relative to the respective controls (Figure 3, Figure S3). In fact, examining Saos-2 cells, the p-AKT level was reduced to 65% and 70% of the control level after incubation with Dp44mT and DpC, respectively (Figure 3, Figure S3). Assessing SH-SY5Y and Daoy cells, p-AKT levels were inhibited by only approximately 10% relative to the control by thiosemicarbazones (Figure 3). Combinations of CX and the thiosemicarbazones did not have a greater effect on p-AKT and AKT levels than the agents alone (Figure 3, Figure S3).

Total AKT levels in all three cell-types were either generally slightly decreased, or not altered relative to the control level after treatment with either CX, DpC, or Dp44mT alone (Figure 3, Figure S3). The combinations of CX and the thiosemicarbazones did not lead to any substantial alterations in total AKT levels relative to the control (Figure 3, Figure S3).

Collectively, these data in Figure 3 suggested that although both thiosemicarbazones alone were able to slightly decrease AKT phosphorylation, the combination treatments were no more effective than CX or the thiosemicarbazones alone.
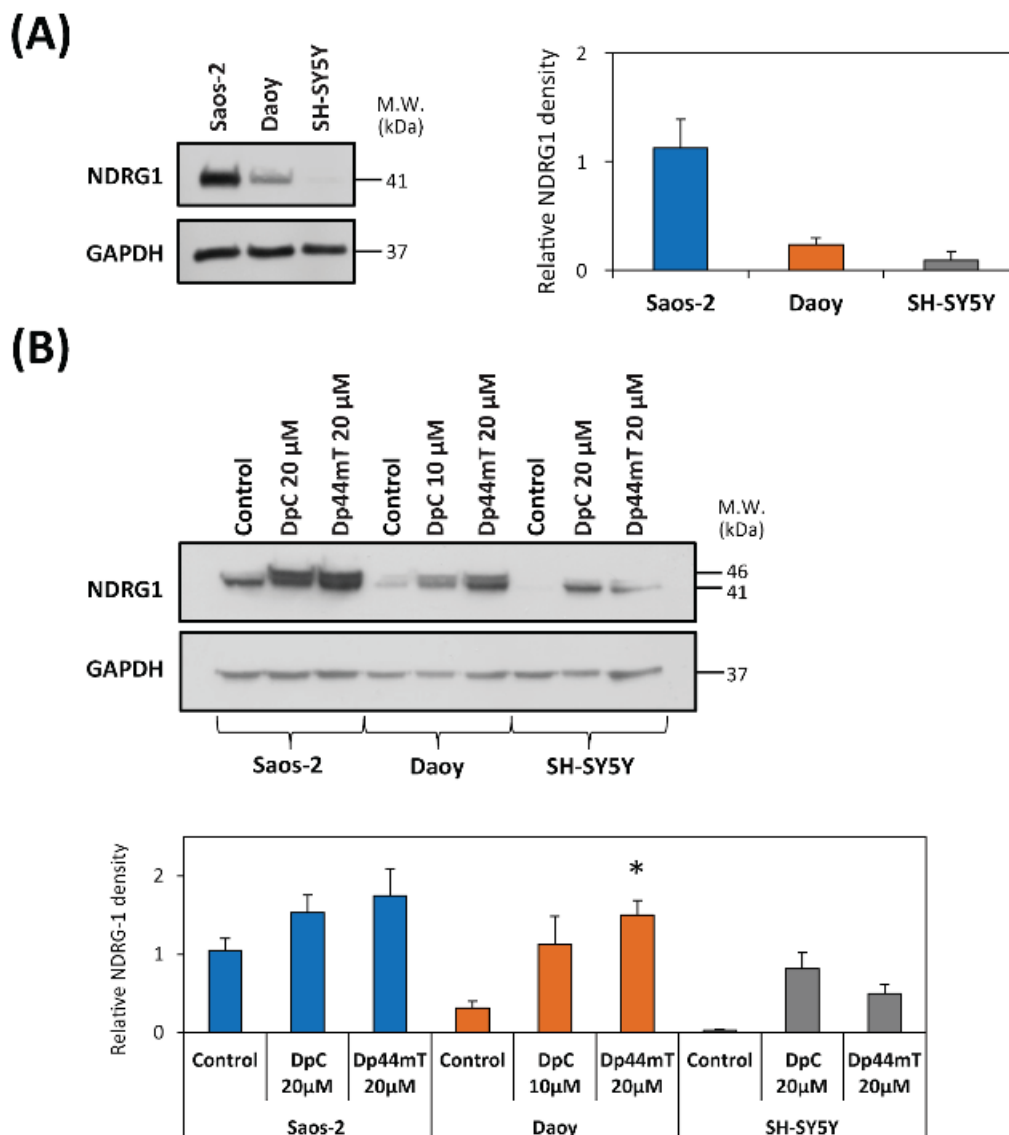
Figure 2. NDRG1 expression is markedly up-regulated relative to the control after a 24 h/37 °C incubation with DpC or Dp44mT. (**A**) Western blot analysis of endogenous NDRG1 levels in untreated cells. GAPDH served as a loading control. (**B**) Western blot analysis of NDRG1 levels in Saos-2, Daoy and SH-SY5Y cells after 24 h/37 °C of incubation with either control medium, DpC (20 μM; 10 μM for Daoy), or Dp44mT (20 μM). GAPDH served as a protein loading control. All experiments were repeated at least three times. Western blots are typical of three experiments, while the quantitation of the blots is presented as mean ± SD (3 experiments). These data were analyzed by unpaired Welch's *t*-test followed by the Games-Howell post hoc test. * $p < 0.05$ indicates significant differences compared to the respective control group.
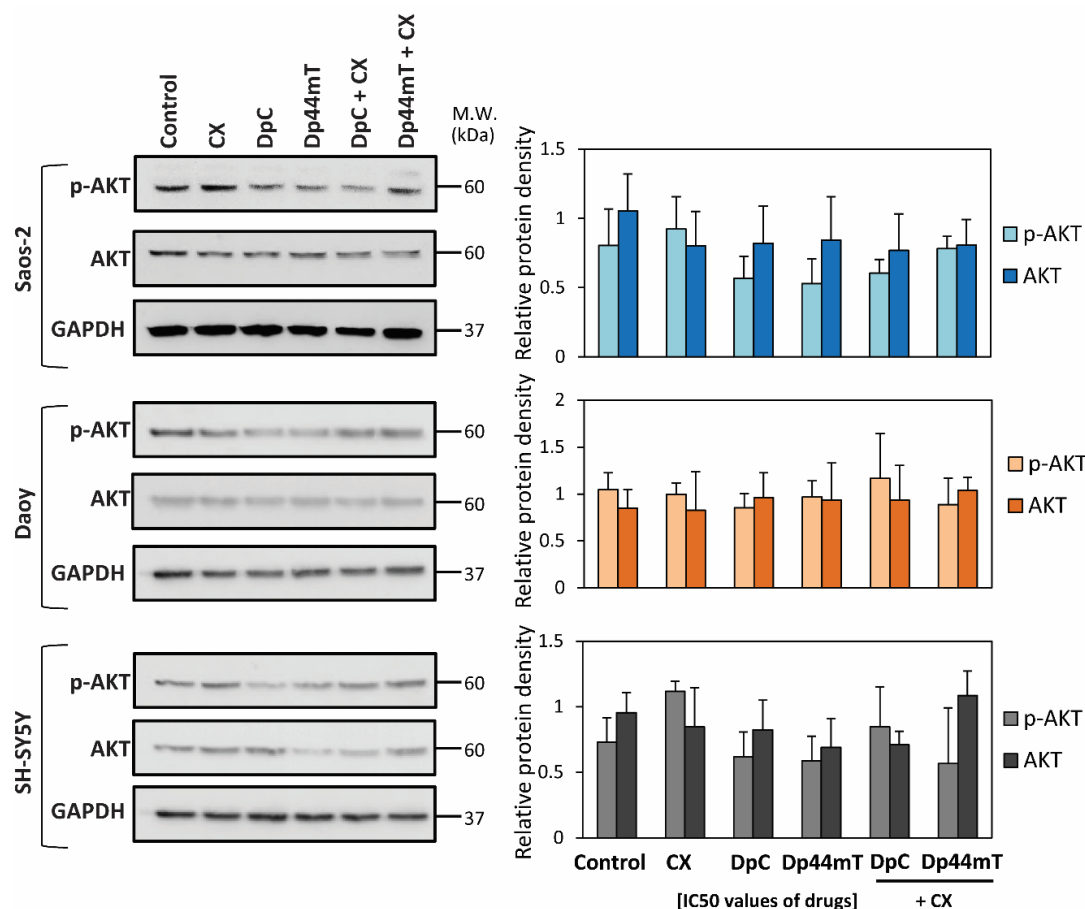
Figure 3. Changes in p-AKT (Ser473) level and total AKT protein expression after a 2 h/37 °C incubation of DpC, Dp44mT, CX alone, or the combinations of DpC and CX, or Dp44mT and CX (concentrations at IC_{50} levels; Table 1). Western blot analysis of p-AKT and total AKT using Saos-2, Daoy or SH-SY5Y cells incubated with control medium or this medium containing CX, thiosemicarbazones, or thiosemicarbazones combined with CX. GAPDH served as a loading control. The experiments were repeated at least three times with quantitation being the results. Western blots are typical of three experiments, while the quantitation of the blots is presented as mean ± SD (3 experiments). These data were analyzed using an unpaired Welch's *t*-test followed by the Games-Howell post hoc test.

2.3. DpC and Dp44mT Down-Regulate MGMT Expression

It is well known that the DNA repair enzyme, MGMT, inhibits TMZ activity within cells and induces resistance to TMZ therapy [44]. Therefore, to explain the differences in the anti-proliferative effects of thiosemicarbazones combined with TMZ between cell-types (see Table 2), we focused on the possible interactions between the thiosemicarbazones and MGMT expression (Figure 4). First, substantial differences in endogenous MGMT levels were found by immunoblotting between the three cell-types (Figure 4A, Figure S4A). Considering this, while no appreciable MGMT expression was detected in Saos-2 cells, SH-SY5Y cells exhibited two-fold higher MGMT levels than Daoy cells.

We then evaluated changes in MGMT levels after treatment with DpC or Dp44mT alone in the three cell-types (Figure 4B, Figure S4B). Immunoblotting revealed no appreciable MGMT expression in Saos-2 cells after treatment with thiosemicarbazones (Figure 4B, Figure S4B). This result is consistent with the almost undetectable endogenous levels of MGMT observed in this cell-type (Figure 4A, Figure S4A). On the other hand, both thiosemicarbazones alone decreased MGMT levels in Daoy and SH-SY5Y cells (Figure 4B, Figure S4B).
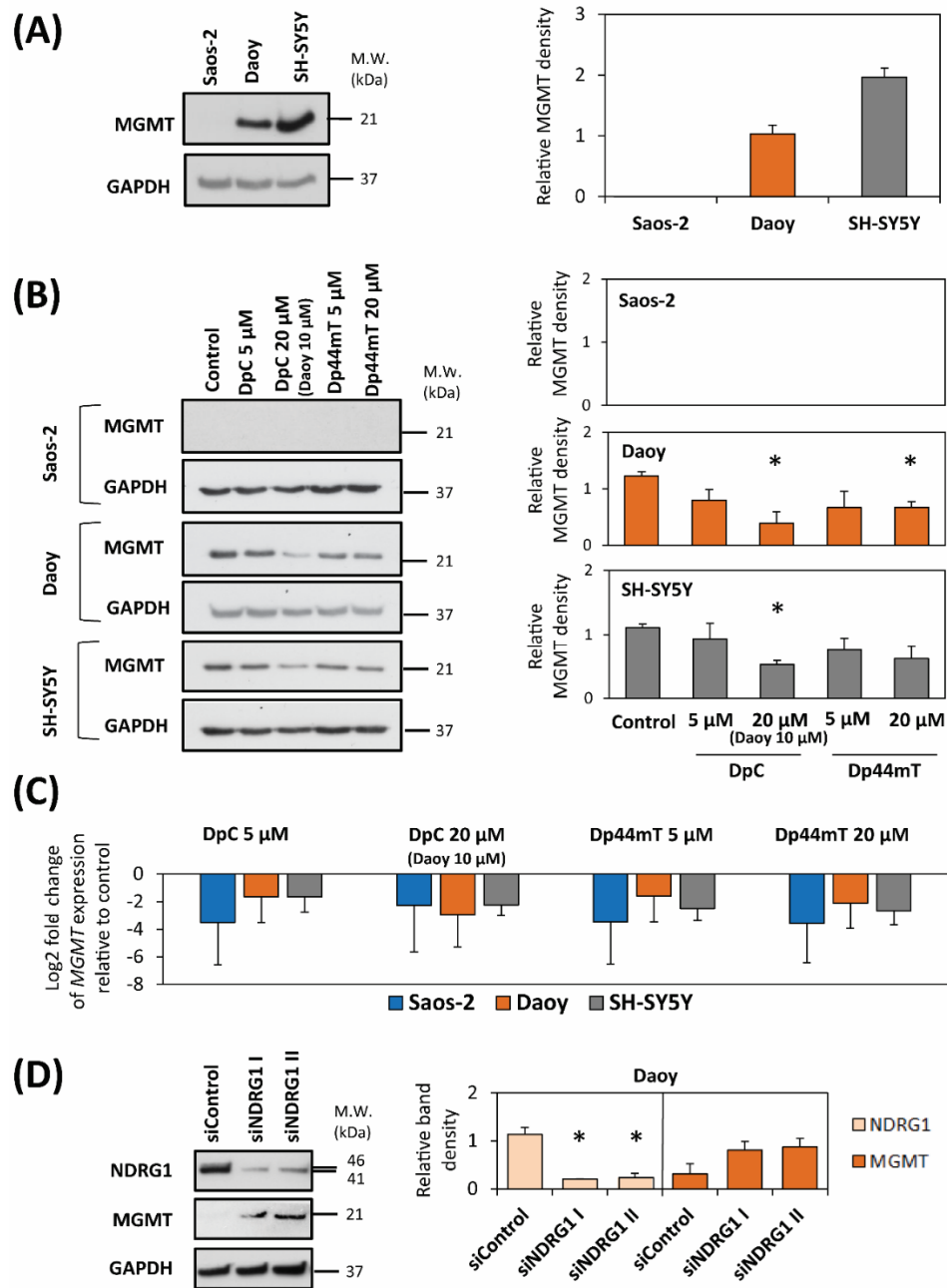
Figure 4. *MGMT* mRNA and protein expression was markedly down-regulated in cells after incubation with either control medium, DpC (20 µM; 10 µM for Daoy), or Dp44mT (20 µM) for 24 h/37 °C. (**A**) Western blot analysis of the endogenous MGMT level in untreated control cells. GAPDH served as a loading control. (**B**) Western blot analysis of the MGMT level in Saos-2, Daoy and SH-SY5Y cells after a 24 h/37 °C of incubation with DpC or Dp44mT. GAPDH served as a loading control. (**C**) The graph shows changes in mRNA expression of *MGMT* in Saos-2, Daoy and SH-SY5Y cells after 24 h of incubation with DpC or Dp44mT. These data were obtained by RT-qPCR. The levels of gene expression after thiosemicarbazone treatment are presented as the $\log_2$ fold change in mRNA expression relative to the untreated control. *GAPDH* served as a reference control. (**D**) Western blot analysis of NDRG1 and MGMT levels after *NDRG1* silencing. Two specific siRNAs for *NDRG1* were transiently transfected into Daoy cells with subsequent 48 h incubation. The cells were then transfected with a non-targeting, negative control siRNA as a relevant control. GAPDH served as a protein loading control. The western blots presented are from a typical experiment of three performed, while the quantitation of the blots is presented as mean ± SD (three experiments). These data were analyzed by the unpaired Welch's *t*-test followed by the Games-Howell post hoc test. * ($p < 0.05$) indicates significant differences compared to the respective control group.

Reverse transcription quantitative real-time PCR (RT-qPCR) confirmed that in all three cell-types, the relative expression of the *MGMT* gene was down-regulated relative to the control after a 24 h treatment with each of the thiosemicarbazones alone at 5- or 20-µM (Daoy 10 µM DpC; Figure 4C).

To investigate the potential role of NDRG1 in the decrease of MGMT expression by thiosemicarbazones, siRNA silencing of *NDRG1* was adopted (Figure 4D, Figure S4C). For this analysis, Daoy cells were chosen as the only cell-type with detectable endogenous NDRG1 and MGMT protein levels (Figures 2A and 4A). The immunoblotting revealed that the silencing of *NDRG1* by two different siRNA constructs resulted in up-regulation of MGMT levels (Figure 4D, Figure S4C). Hence, considering these results, the up-regulation of NDRG1 expression after DpC and Dp44mT treatment relative to the control (Figure 2B, Figure S2B), could lead to the down-regulation of MGMT induced by these agents, at least in Daoy cells (Figure 4B; Figure S4B).

2.4. DpC and Dp44mT Generally Down-Regulate the Mismatch Repair (MMR) Proteins, MSH2, MSH6 and MLH1, Which May Also Affect Cellular Sensitivity to TMZ

To further understand the molecular mechanisms involved in the effects of combining TMZ with the thiosemicarbazones, studies then examined the expression of mismatch repair (MMR) proteins, which may also affect sensitivity of tumor cells to TMZ [44–46] (Figure 5A, Figure S5A). We compared the endogenous levels of the most important MMR proteins, namely, MSH2, MSH6, and MLH1 [47], in the three cell-types. MSH2, MSH6 and MLH1 levels were comparable in Saos-2 and Daoy cells, while for SH-SY5Y cells approximately 2-fold higher levels of each protein relative to the other two cell-types were observed (Figure 5A, Figure S5A).

Additional analyses demonstrated that a 24 h incubation with either DpC (20 µM; 10 µM for Daoy cells) or Dp44mT (20 µM), down-regulated MLH1 levels in all three cell-types (Figure 5B, Figure S5B). Decreased expression of MSH2 and MSH6 levels were also apparent in Daoy and SH-SY5Y cells after a 24 h incubation with Dp44mT or DpC, while no marked change in their expression was observed for Saos-2 cells (Figure 5B, Figure S5C). While this general decrease in MLH1, MSH2 and MSH6 after incubation with Dp44mT or DpC could be expected to aid synergistic activity with TMZ, synergism was only observed for DpC with Saos-2 and to a lesser extent with Daoy cells.

2.5. DpC and Dp44mT Down-Regulate TOP2α Expression

To explore the possible interaction between the thiosemicarbazones and ETO, we tested the hypothesis that DpC and Dp44mT can modulate the level of TOP2α, which is the primary target of ETO [48]. Analysis of endogenous TOP2α expression revealed that the levels of TOP2α were almost two-fold higher in Daoy cells than in SH-SY5Y and Saos-2 cells (Figure 6A, Figure S6A).

Subsequently, studies analyzed TOP2α levels after 24 h of treatment with two different concentrations of the thiosemicarbazones to determine if their effects were concentration-dependent. In general, and relative to the control, down-regulation of TOP2α levels was observed at 20 µM of either thiosemicarbazone using all three cell-types, with less effect being observed at 5 µM, especially for SH-SY5Y cells where no decrease was apparent (Figure 6B, Figure S6B). Examining *TOP2A* mRNA levels, both concentrations of the thiosemicarbazone decreased its expression in all three cell-types (Figure 6C).
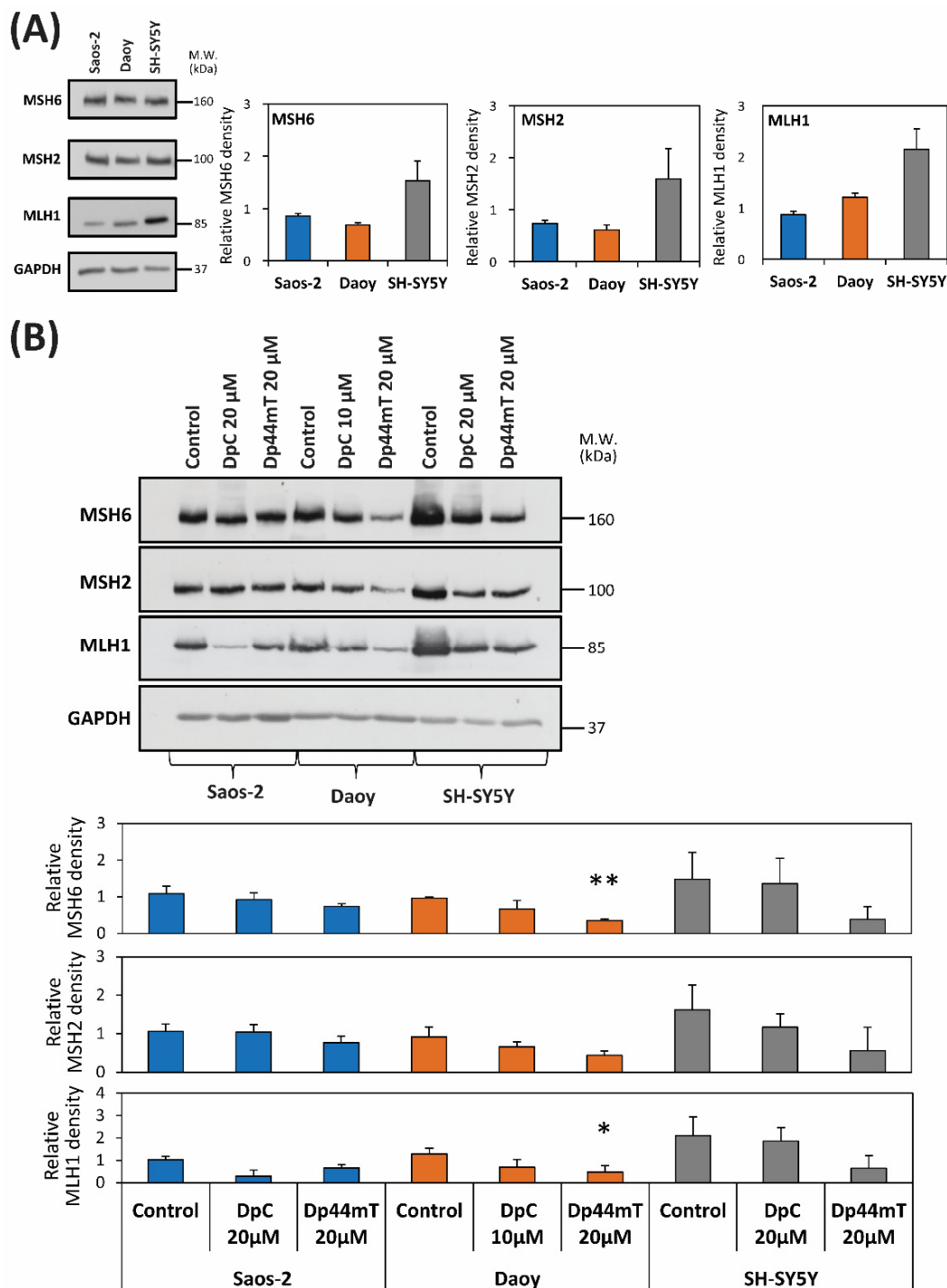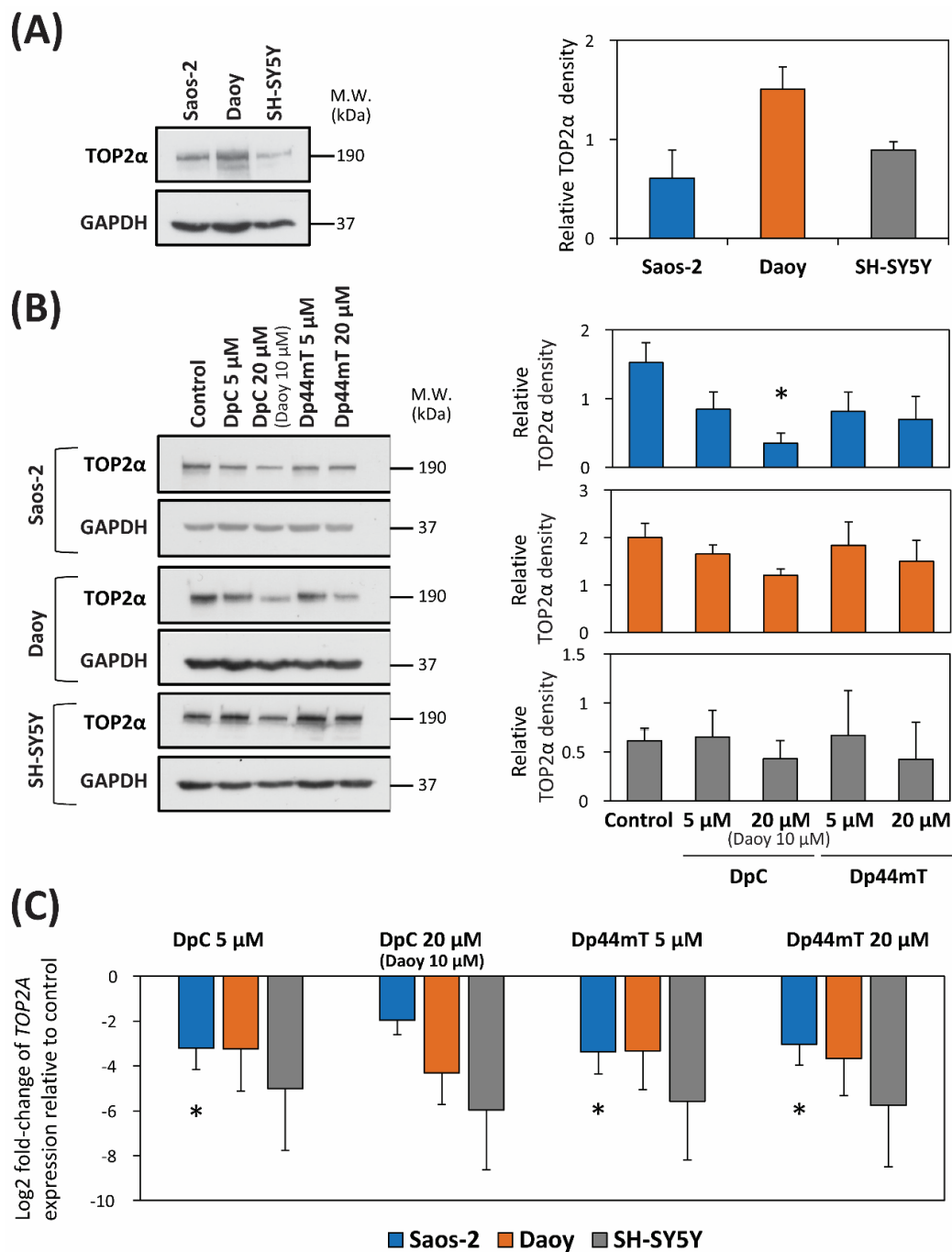
Figure 5. Changes in the expression of MMR proteins after incubation with either control medium, DpC (20 μM; 10 μM for Daoy), or Dp44mT (20 μM) for 24 h/37 °C. (**A**) Western blot analysis of endogenous MSH6, MSH2 and MLH1 levels in untreated cells. (**B**) MSH6, MSH2 and MLH1 levels in Saos-2, Daoy and SH-SY5Y cells after incubation with DpC or Dp44mT for 24 h. GAPDH served as a protein-loading control. The western blots presented are from a typical experiment of three performed, while the quantitation of the blots is presented as mean ± SD (3 experiments). These data were analyzed using the unpaired Welch's *t*-test followed by the Games-Howell post hoc test. * ($p < 0.05$) and ** ($p < 0.001$) indicate significant differences compared to the respective control group.

Figure 6. TOP2α expression is down-regulated at the (**A,B**) protein and (**C**) mRNA levels after incubation with either control medium, DpC (20 μM; 10 μM for Daoy), or Dp44mT (20 μM) for 24 h/37 °C. (**A**) Western blot analysis of the TOP2α level in untreated Saos-2, Daoy and SH-SY5Y cells. GAPDH served as a protein-loading control. (**B**) Western blot analysis of the TOP2α level in Saos-2, Daoy and SH-SY5Y cells after incubation with DpC or Dp44mT for 24 h. GAPDH served as a protein-loading control. (**C**) The graph shows changes in the mRNA expression of *TOP2A* in Saos-2, Daoy and SH-SY5Y cells after 24 h of incubation with DpC or Dp44mT. These data were obtained by RT-qPCR. The levels of gene expression after thiosemicarbazone treatment are presented as the $\log_2$ fold change in mRNA expression relative to that in the untreated control. *GAPDH* served as a reference control. For all experiments, expression was assessed in three biological replicates. The Western blots presented are from a typical experiment of three performed, while the quantitation of the blots is presented as mean ± SD (three experiments). These data were analyzed using the unpaired Welch's *t*-test followed by the Games-Howell post hoc test. * ($p < 0.05$) indicates significant differences compared to the respective control group.

3. Discussion

Combination therapy remains a cornerstone of cancer treatment, and as such, it is essential to investigate the synergistic activities of novel agents. The novel DpT class of thiosemicarbazones demonstrate: (1) potent and selective anti-tumor activity; (2) the ability to overcome P-glycoprotein-mediated resistance [11,21]; and (3) can inhibit metastasis via up-regulating NDRG1 [10,17,24,25,27,49,50]. In fact, our extensive previous studies, and subsequently those of others, have demonstrated that both Dp44mT [6,7,10–14,22,51,52] and DpC [12,15,16,22,52,53] show selective and potent anti-cancer efficacy in vitro and in vivo against a broad variety of tumor cell-types and tumors (e.g., lung cancer, melanoma, neuroblastoma, neuroepithelioma ovarian carcinoma) [6,7,10–32]. Due to the marked and selective activity and excellent safety and tolerability of DpC, the agent was examined in multi-centre, Phase I clinical trials in humans [54].

As a pertinent example of their utility in pediatric oncology, our previous studies in vitro have demonstrated that both DpC and Dp44mT (at 2.5 μM) showed no pronounced anti-proliferative activity against the non-tumorigenic, immortalized cell lines (i.e., MSC, H9C2, MIHA, and HK2), but demonstrated marked anti-tumor efficacy against neuroblastoma cells [12]. This led to studies using orthotopic neuroblastoma xenografts, which demonstrated that DpC significantly inhibited tumor growth and was well tolerated [12]. Considering these results collectively, which demonstrate potent and safe anti-cancer activity, it was important to investigate the ability of these thiosemicarbazones to synergize with established chemotherapies for the treatment of childhood cancers.

As shown in the current investigation, both thiosemicarbazones (DpC and Dp44mT) potentiated the cytotoxic activity of CX in particular, and to a much lesser extent, TMZ and ETO (Table 2). The synergistic interactions of the thiosemicarbazones with each chemotherapeutic drug assessed probably resulted from different pharmacological interactions.

3.1. Combination of the Novel Thiosemicarbazones and CX

The combination of DpC or Dp44mT and CX exhibited enhanced anti-proliferative activity and acted generally synergistically in all three cell-types, except for DpC treated SH-SY5Y cells. We hypothesized that COX-2 activity can be modulated by both CX and thiosemicarbazones, as the catalytic domain of CX contains an iron-dependent heme prosthetic group that is necessary for its activity [55]. Due to the well-known iron chelation activity of DpC and Dp44mT [6,16], it can be hypothesized that thiosemicarbazones chelate cellular iron necessary for heme biosynthesis, which is critical for COX-2 function.

To examine the effect of DpC or Dp44mT on COX-2 expression, their effects were assessed using Western blot analysis and qRT-PCR, with these studies demonstrating up-regulation of COX-2 expression at the mRNA and protein levels in Daoy and SH-SY5Y, while Saos2 cells did not express appreciable COX-2 protein levels. The observed increase in COX-2 expression after incubation with thiosemicarbazones can be speculated to be a "rescue" attempt by the cells to compensate for the loss of COX-2 function.

Assessing the mechanism of synergy between the thiosemicarbazones and CX, it is of interest that the strongest synergy for this combination was observed in COX-2 negative Saos-2 cells (Table 2). These data indicated that the mechanism of synergy in this cell-type was independent of COX-2 and suggested the existence of another molecular target. Other molecular targets of CX include AKT, its upstream kinase 3-phosphoinositide-dependent kinase-1 [41], cyclin-dependent kinase inhibitors and cyclins [52], the anti-apoptotic proteins survivin, Bcl-2 and Mcl-1 [56], and the sarcoplasmic/endoplasmic reticulum calcium ATPase [57]. Considering this, thiosemicarbazones have been demonstrated to target AKT and cyclin-dependent kinase inhibitors, e.g., p21 and p27, with many of their effects being mediated by the up-regulation of the metastasis suppressor, NDRG1 [25,51,58–60].

As such, to examine whether NDRG1 could be involved in the synergistic activity of thiosemicarbazones with CX (Table 2), the expression of endogenous NDRG1 was examined. These studies demonstrated that NDRG1 expression was up-regulated in all three cell-types by both thiosemicarbazones. Examining Saos-2 cells, which exhibited the highest NDRG1 expression (Figure 2A,B), it was demonstrated

that both thiosemicarbazones exhibited strong synergy with CX. Assessing SH-SY5Y cells, which expressed the lowest NDRG1 level, Dp44mT and CX exhibited only moderate synergy, while DpC and CX had an antagonistic effect. Thus, it can be suggested that the synergistic activity of the thiosemicarbazones and CX could be associated with high endogenous NDRG1 levels.

3.2. Combination of Novel Thiosemicarbazones and TMZ

A synergistic effect of the novel thiosemicarbazones in combination with TMZ was only observed for DpC-treated Saos-2 cells, with slight synergism being identified in Daoy cells (Table 2). In the other cell-types the combination of thiosemicarbazones and TMZ had additive or antagonistic effects. Given the mechanism of action of TMZ, we hypothesized that the observed differences in the effects of the different drug combinations among the cell-types could be due to different expression of either: (1) MGMT, whose repair activity inhibits TMZ activity and induces resistance to this drug [61,62]; or (2) proteins belonging to the MMR system (MSH2, MSH6, and MLH1) of DNA repair, which may also influence to TMZ sensitivity [63]. Of note, it has been demonstrated that binding of Zn^{2+} is necessary for the proper function of MGMT [64]. As DpC and Dp44mT chelate Zn(II) [20], we hypothesized that DpC and Dp44mT decrease MGMT activity by this mechanism and may potentiate TMZ anti-tumor activity.

Our results demonstrated that thiosemicarbazones down-regulate MGMT protein expression in all tested cell-types except Saos-2 cells, which did not express appreciable MGMT protein levels (Figure 4A,B). As the strongest synergism was observed in Saos-2 cells incubated with DpC (Table 2), it was unlikely that MGMT expression was a major molecular target that led to this response. Additionally, while thiosemicarbazones down-regulate MGMT in Daoy and SH-SY5Y cells, antagonism or slight synergism was observed for the combination of thiosemicarbazones and TMZ (Table 2). Again, this indicated MGMT down-regulation by thiosemicarbazones did not lead to marked synergism.

Because MGMT is a significant molecular target, and since the thiosemicarbazones down-regulate its protein levels in Daoy and SH-SY5Y cells, it was of interest to understand the mechanism of this activity, which could be beneficial for understanding the efficacy of these agents. One of the important effectors of DpC and Dp44mT anti-tumor activity is NDRG1 expression [7,10,15,17,22,23,25,27–29]. It is well known that thiosemicarbazones and NDRG1 can inhibit Wnt signaling and effects [10,27,29], with inhibition of Wnt activity being reported to down-regulate MGMT expression that restored chemosensitivity to TMZ [65].

Based on the relationship between the marked increase in NDRG1 expression (Figure 2B) and decreased MGMT protein levels after thiosemicarbazone treatment (Figure 4B), we hypothesized that NDRG1 up-regulation by thiosemicarbazones down-regulated MGMT. This premise was confirmed by *NDRG1* silencing using two different siRNA constructs, where inhibition of NDRG1 expression resulted in increased MGMT levels in Daoy cells (Figure 4D).

NDRG1 is a metastasis suppressor that acts through an impressive array of anti-oncogenic effectors in addition to MGMT [7,10,15,17,22,23,25,27–29]. As such, the ability of thiosemicarbazones to up-regulate NDRG1 may relate to the synergistic activity observed between TMZ and DpC in Saos2 and Daoy cells, although further studies are essential to demonstrate this. From these studies, and also the correlation between NDRG1 expression and synergism with CX discussed above, it can be concluded than NDRG1 up-regulation by thiosemicarbazones is an important factor for their synergistic activity upon combination with other drugs in pediatric tumor cell-types.

The proteins MSH6, MSH2 and MLH1 are necessary for the coordinated, multi-step process of excision and replacement of nucleic acid bases to ensure DNA repair [66]. Considering that the thiosemicarbazones down-regulated MMR protein expression particularly in Daoy and SH-SY5Y cells (Figure 5B), this would presumably aid the DNA alkylating activity of TMZ, and may explain the synergistic or additive interactions of thiosemicarbazones with TMZ in Saos-2 and Daoy cells (Table 2). However, the general down-regulation of MMR expression by the thiosemicarbazones does not explain the antagonism or moderate antagonism observed after their combination with TMZ in other cell-types. These data suggest more complex interactions that need to be further assessed.

3.3. Combination of Novel Thiosemicarbazones and ETO

The combination of DpC or Dp44mT and ETO only had synergistic effects in Daoy cells, whereas for SH-SY5Y and Saos-2 cells, antagonism was observed. When analyzing the possible drug interactions, we focused on the fact that the thiosemicarbazone, Dp44mT, and ETO inhibit the activity of TOP2α [36,67]. However, while Dp44mT was reported in one study to inhibit TOP2α [67], a subsequent investigation did not confirm this result and demonstrated Dp44mT did not affect TOP2α activity [68]. For both these studies by others, the effect of neither DpC nor Dp44mT was assessed directly on the basis of mRNA or protein levels of TOP2α. In contrast, the current investigation demonstrated DpC and Dp44mT down-regulated TOP2α mRNA and protein expression of TOP2α in all three cell-types.

Based on these latter results, we expected synergism between thiosemicarbazones and ETO. This was predicted because ETO is a TOP2α poison, which is well known to inhibit tumor cell growth [36,69]. Thus, having two pharmacologically different types of agents (thiosemicarbazones and ETO) acting on the same molecular target by different mechanisms (i.e., expression and enzymatic activity) would potentially be beneficial, leading to synergism. On the other hand, previous studies have demonstrated that an important determinant of sensitivity to TOP2α poisons is the overall endogenous level of TOP2α, with low TOP2 levels showing resistance to ETO [69,70]. As such, antagonism between thiosemicarbazones that decrease TOP2α expression and ETO could also be theoretically envisioned.

The Daoy cell-type expressed the highest endogenous level of TOP2α of the three cell-types and demonstrated synergistic activity with the combination of the thiosemicarbazones and ETO. In contrast, lower levels of TOP2α were observed in Saos-2 and SH-SY5Y cells where antagonism was identified. In all cell types, there was a decrease in TOP2α expression after incubation with either of the thiosemicarbazones. Considering these facts, it can be speculated that the relative levels of TOP2α could be important in terms of whether synergism or antagonism is observed. However, further studies are required to definitely determine the molecular mechanism involved.

In summary, the collective results of this investigation identified novel molecular targets of thiosemicarbazones in pediatric cancer cell-types. Moreover, the work provides new mechanistic insight into the alterations in anti-tumor efficacy of CX, ETO and TMZ upon combination with DpC or Dp44mT. As DpC has entered clinical trials [11], these data are useful for guiding future combinatory studies.

4. Materials and Methods

4.1. Chemicals

DpC and Dp44mT were synthesized and characterized as described previously [16,18]. Both thiosemicarbazones were prepared as stock solutions in DMSO at a concentration of 100 mM (Sigma-Aldrich, St. Louis, MO, USA) and then diluted in cell culture medium to achieve a DMSO concentration <0.5% (*v/v*). At this concentration of DMSO there was no effect on cellular proliferation relative to control medium [8]. The clinically used chemotherapeutics, namely ETO (Cat. No. E1383), CX (Cat. No. PZ0008) and TMZ (Cat. No. T2577), were obtained from Sigma-Aldrich, prepared as stock solutions in DMSO at a concentration of 100 mM, and then diluted as described above.

4.2. Cell Culture

Saos-2 osteosarcoma cells (Cat. No. HTB-85) and Daoy medulloblastoma cells (Cat. No. HTB-186™) were purchased from the American Type Culture Collection (Manassas, VA, USA). SH-SY5Y neuroblastoma cells (Cat. No. 94030304) were purchased from The European Collection of Authenticated Cell Cultures (Salisbury, UK).

The Daoy and Saos-2 cells were cultured in Dulbecco's modified Eagle's medium (DMEM) supplemented with 10% fetal calf serum (FCS), 2 mM glutamine, and the antibiotics, penicillin (100 IU/mL) and streptomycin (100 μg/mL) (all from GE Healthcare Europe GmbH, Freiburg, Germany). The medium used for Daoy cells was supplemented with 1% non-essential amino acids (Biosera, Nuaille, France).

SH-SY5Y cells were cultured in a mixture of DMEM/F12 (1:1) supplemented with 20% FCS, 2 mM glutamine and the antibiotics, penicillin (100 IU/mL) and streptomycin (100 µg/mL) (all from GE Healthcare), and 1% nonessential amino acids (Biosera).

All cells were maintained under standard cell culture conditions at 37 °C in an atmosphere of 95% air, 5% CO_2.

4.3. siRNA

Two specific siRNAs for *NDRG1* were used, namely siNDRG1 I (Cat. No. AM16708, ID: 135611; ThermoFisher Scientific, Waltham, MA, USA) and siNDRG1 II (Cat. No. AM16708, ID 135612; ThermoFisher Scientific). These were compared with non-targeting negative control siRNA (Cat. No. 4390846, ThermoFisher Scientific). The siRNA was transiently transfected into Daoy cells using Lipofectamine RNAiMAX (ThermoFisher Scientific) and incubated for 48 h/37 °C.

4.4. Treatment Protocol

The 3-[4,5-dimethylthiazol-2-yl]-2,5-diphenyltetrazolium bromide (MTT) proliferation assay (see Section 4.5, below) was employed to quantify synergy between the selected drugs and thiosemicarbazones. Cells were seeded in 96-well plates at a density of 5×10^3 cells/well (SH-SY5Y and Saos-2 cells) or 2×10^3 cells/well (Daoy cells) in 100 µL of complete DMEM. Different seeding densities were used to ensure that the cells remained in the log phase of growth during drug incubation.

The cells were allowed to adhere overnight, and the medium was then removed and replaced with fresh medium containing the appropriate concentrations of either of the drugs (DpC, Dp44mT, CX, ETO, or TMZ) alone or in appropriate combinations. The drug concentrations used for combination treatments were based on the initial IC_{50} values (⅛-, ¼-, ½-, 1-, 2-, 4-, and 8-fold of IC_{50}) of each drug, and therefore, they were specific for each cell line examined. The plates were incubated for 3 days at 37 °C.

To investigate the molecular effects of the thiosemicarbazones in combined treatments, samples were prepared for immunoblotting and RT-qPCR. Cells were seeded in Petri dishes (90 mm diameter) at a density of at 5×10^5/dish and allowed to adhere overnight. The next day, the cells were treated with the individual thiosemicarbazones at concentrations higher than the IC_{50} value for 24 h at 37 °C, and the expression changes then examined.

This shorter incubation period of 24 h prevented cytotoxicity, which would confound data interpretation. Therefore, the following concentrations were chosen: DpC: 5 µM and 20 µM; Dp44mT: 5 µM and 20 µM. Of note, due to the high cytotoxicity of 20 µM DpC in Daoy cells, DpC was used in these cells at concentrations of 5 µM and 10 µM. Treated cells and untreated controls were incubated under standard conditions for 24 h/37 °C.

In addition, the effects of combination treatment with the thiosemicarbazones and CX were analyzed in more detail. For this purpose, cells plated in Petri dishes (90 mm diameter) were treated with the IC_{50} doses of DpC, Dp44mT, CX, or the combinations of DpC and CX, or Dp44mT and CX. The cells were then incubated under standard conditions for 2 h/37 °C before being processed for immunoblotting.

4.5. Cell Proliferation

The MTT assay was used to evaluate cell proliferation and was performed as described [71]. As shown previously, the number of cells was demonstrated to be a linear function of MTT absorbance [8]. Briefly, the cells were treated and incubated for 3 days (see Section 4.3). Subsequently, they were then incubated with MTT (0.5 mg/mL; Sigma-Aldrich) for 3 h/37 °C. Then, the formazan crystals were dissolved in 200 µL of DMSO. The absorbance was measured at 570 nm with a reference absorbance of 620 nm using a Sunrise Absorbance Reader (Tecan, Männedorf, Switzerland).

4.6. Calculation of CI

CIs were calculated to quantitatively compare the dose-effect relationship of each drug alone or in combination to determine whether a given combination acts synergistically. CIs were calculated from growth inhibition curves, as previously described [16]. A 1:1 ratio of drugs was used for combination treatments. The CI values were determined using CalcuSyn software (version 2.0, Biosoft, Cambridge, UK). The Chou Talalay method was adopted to identify synergism (CI < 0.9), additive effect (CI = 0.9–1.1) or antagonism (CI > 1.1) [72].

4.7. RT-qPCR

The relative expression of selected genes was analyzed using RT-qPCR. Total RNA was isolated and reverse transcribed into cDNA by established methods [63]. RT-qPCR was performed in a 10-μL reaction using a Kapa Biosystems Quantitative Real-Time PCR kit (Kapa Biosystems, Wilmington, MA, USA) and analyzed using a 7500 Fast Real-Time PCR System and 7500 Software v. 2.0.6 (both Life Technologies, Carlsbad, CA, USA). Changes in transcript levels were examined using Cq values normalized to the housekeeping gene, GAPDH. The primer sequences used for TOP2A, PTGS2, MGMT and the GAPDH genes are provided in Table 3.

Table 3. Sequences of the primers used for RT-qPCR.

Gene	Primer Sequence	Product Length (bp)
GAPDH	F: 5′-AGC CAC ATC GCT CAG ACA CC-3′ R: 5′-GTA CTC AGC GCC AGC ATC G-3′	302
MGMT	F: 5′-CCGTTTGCGACTTGGTACTTG-3′ R: 5′-TGGTGAACGACTCTTGCTGG-3′	312
PTGS2	F: 5′-GATGATTGCCCGACTCCCTT-3′ R: 5′-TGAAAAGGCGCAGTTTACGC-3′	273
TOP2A	F: 5′-ACCATTGCAGCCTGTAAATGA-3′ R: 5′-GGGCGGAGCAAAATATGTTCC-3′	129

Abbreviations: F, forward; R, reverse.

4.8. Immunoblotting Assay

Protein extracts were collected using LB1 lysis buffer (50 mM Hepes-KOH, pH 7.5, 140 mM NaCl, 1 mM EDTA, 10% glycerol, 0.5% NP-40, and 0.25% Triton X-100). Total proteins (50 μg/well) were loaded onto 10% polyacrylamide gels and electrophoresed. Subsequently, the separated proteins were blotted onto PVDF membranes (Bio-Rad Laboratories, Munich, Germany).

The membranes were blocked for 1 h/20 °C with 5% BSA (Sigma-Aldrich) in PBS with 0.1% Tween-20 (Sigma-Aldrich) to detect p-AKT, or with 5% non-fat dry milk in PBS with 0.1% Tween-20 to detect all other proteins.

The blocked membranes were incubated overnight with the primary monoclonal antibodies listed in Table 4. The next day, the membranes were incubated with secondary antibodies for 1 h/20 °C (Table 4). ECL-Plus detection was carried out according to the manufacturer's instructions (GE Healthcare, Little Chalfont, UK). Quantification of the protein bands on western blots was performed using ImageJ software (NIH, Bethesda, MD, USA).

Table 4. Primary and secondary antibodies used in this study.

Primary Antibodies					
Antigen	**Type/Host**	**Clone**	**Catalog No.**	**Manufacturer**	**Dilution**
AKT (pan)	* Mono/Rb	C67E7	4691S	CST	1:2000
p-AKT (Ser473)	Mono/Rb	D9E	4060S	CST	1:2000
COX-2	Mono/Rb	D5H5	12282S	CST	1:1000
GAPDH	Mono/Rb	14C10	2118S	CST	1:10,000
MGMT	Mono/Mo	-	51234M	Bioss	1:1000
MLH1	Mono/Mo	4C9C7	3515S	CST	1:1000
MSH2	Mono/Rb	D24B5	2017S	CST	1:2500
MSH6	Mono/Rb	D60G2	5424S	CST	1:2500
NDRG1	Mono/Rb	-	9485	CST	1:2000
TOP2α	Mono/Rb	D10G9	12286	CST	1:1000
Secondary Antibodies					
Host	**Specificity**	**Conjugate**	**Catalog No.**	**Manufacturer**	**Dilution**
Goat	Anti-Rb IgG	HRP	7074	CST	1:5000
Horse	Anti-Mo IgG	HRP	7076	CST	1:5000

* Abbreviations: Mono, monoclonal; Rb, rabbit; Mo, mouse; CST, Cell Signaling Technology Inc., Danvers, MA, USA; Bioss, Bioss Antibodies Inc., Woburn, MA, USA.

4.9. Statistics

SPSS Statistics software (version 25.0, IBM, New York, NY, USA) was used for statistical analysis. Numerical data are presented as the mean ± standard deviation (of three independent experiments). Statistical comparisons of the RT-PCR and immunoblotting results were performed using an unpaired Welch's *t*-test. $p < 0.05$ (*) indicates significant differences compared to the respective control group. In all studies, experiments were independently performed at least three times.

5. Conclusions

In conclusion, the current investigation clearly demonstrated that DpC and Dp44mT potentiate the cytotoxic effects of selected chemotherapeutics used in metronomic regimens in pediatric oncology. The most marked synergism of the thiosemicarbazones was observed with CX, while synergism or slight synergism was only found for TMZ with DpC in two cell-types. Etoposide demonstrated largely antagonistic effects with the thiosemicarbazones, while nearly additive activity was found for Daoy cells.

In terms of mechanistic dissection, this study discovered several novel targets of thiosemicarbazones that had not been identified previously. These new targets could be important to consider when assessing possible drug combinations. For instance, this study demonstrated that both DpC and Dp44mT caused: (1) substantial up-regulation of COX-2 protein expression, but only in Daoy and SH-SY5Y cells; (2) down-regulation of the DNA repair protein MGMT in Daoy and SH-SY5Y cells; (3) down-regulation of MMR repair proteins, MSH2 and MSH6, in Daoy and SH-SY5Y cells; and (4) down-regulation of the MMR repair protein, MLH1, and Topo-2α in all three cell-types.

Additionally, as demonstrated previously in a variety of adult cancer cell-types, the thiosemicarbazones demonstrated strong activity at up-regulating NDRG1 in all three pediatric tumor cell lines. The up-regulation of NDRG1 was responsible for the down-regulation of MGMT in Daoy cells, which is important for preventing drug resistance to agents such as TMZ. Furthermore, a positive relationship was observed between NDRG1 levels of the cell-type and the synergistic activity observed in the combination of thiosemicarbazone and CX.

Of the combinations examined, the most promising was that using CX and either DpC or Dp44mT. This may be related to the ability of the thiosemicarbazones to up-regulate COX2 expression, although further studies are required to validate this.

In conclusion, the results herein provide new insight into the alterations in anti-neoplastic activity of CX, ETO and TMZ upon combination with DpC or Dp44mT. As DpC has entered clinical trials [11],

these data could be important for guiding future combinatory studies in vivo in animal models and eventually in human trials.

References

1. Miller, K.D.; Siegel, R.L.; Lin, C.C.; Mariotto, A.B.; Kramer, J.L.; Rowland, J.H.; Stein, K.D.; Alteri, R.; Jemal, A. Cancer treatment and survivorship statistics, 2016. *CA. Cancer J. Clin.* **2016**, *66*, 271–289. [CrossRef] [PubMed]

2. Richardson, D.R.; Persson, L.; Xu, X. Molecular pharmacology of the interaction of anthracyclines with iron. *Mol. Pharmacol.* **2005**, *68*, 1–11. [CrossRef]

3. Oeffinger, K.C.; Mertens, A.C.; Sklar, C.A. Chronic health conditions in adult survivors of childhood cancer. *Oncol. Times* **2007**, *29*, 26. [CrossRef]

4. Sterba, J.; Valik, D.; Mudry, P.; Kepak, T.; Pavelka, Z.; Bajciova, V.; Zitterbart, K.; Kadlecova, V.; Mazanek, P. Combined biodifferentiating and antiangiogenic oral metronomic therapy is feasible and effective in relapsed solid tumors in children: Single-center pilot study. *Onkologie* **2006**, *29*, 308–313. [CrossRef] [PubMed]

5. Zapletalova, D.; André, N.; Deak, L.; Kyr, M.; Bajciova, V.; Mudry, P.; Dubska, L.; Demlova, R.; Pavelka, Z.; Zitterbart, K.; et al. Metronomic chemotherapy with the COMBAT regimen in advanced pediatric malignancies: A multicenter experience. *Oncology* **2012**, *82*, 249–260. [CrossRef] [PubMed]

6. Yuan, J.; Lovejoy, D.B.; Richardson, D.R. Novel di-2-pyridyl-derived iron chelators with marked and selective antitumor activity: In vitro and in vivo assessment. *Blood* **2004**, *104*, 1450–1458. [CrossRef]

7. Whitnall, M.; Howard, J.; Ponka, P.; Richardson, D.R. A class of iron chelators with a wide spectrum of potent antitumor activity that overcomes resistance to chemotherapeutics. *Proc. Natl. Acad. Sci. USA* **2006**, *103*, 14901–14906. [CrossRef]

8. Richardson, D.R.; Tran, E.H.; Ponka, P. The potential of iron chelators of the pyridoxal isonicotinoyl hydrazone class as effective antiproliferative agents. *Blood* **1995**, *86*, 4295–4306. [CrossRef]

9. Lovejoy, D.B.; Richardson, D.R. Novel "hybrid" iron chelators derived from aroylhydrazones and thiosemicarbazones demonstrate selective antiproliferative activity against tumor cells. *Blood* **2002**, *100*, 666–676. [CrossRef]

10. Liu, W.; Xing, F.; Iiizumi-Gairani, M.; Okuda, H.; Watabe, M.; Pai, S.K.; Pandey, P.R.; Hirota, S.; Kobayashi, A.; Mo, Y.-Y.; et al. N-myc downstream regulated gene 1 modulates Wnt-β-catenin signalling and pleiotropically suppresses metastasis. *EMBO Mol. Med.* **2012**, *4*, 93–108. [CrossRef]

11. Jansson, P.J.; Yamagishi, T.; Arvind, A.; Seebacher, N.; Gutierrez, E.; Stacy, A.; Maleki, S.; Sharp, D.; Sahni, S.; Richardson, D.R. Di-2-pyridylketone 4,4-dimethyl-3-thiosemicarbazone (Dp44mT) overcomes multidrug resistance by a novel mechanism involving the hijacking of lysosomal P-glycoprotein (Pgp). *J. Biol. Chem.* **2015**, *290*, 9588–9603. [CrossRef]

12. Guo, Z.-L.; Richardson, D.R.; Kalinowski, D.S.; Kovacevic, Z.; Tan-Un, K.C.; Chan, G.C.-F. The novel thiosemicarbazone, di-2-pyridylketone 4-cyclohexyl-4-methyl-3-thiosemicarbazone (DpC), inhibits neuroblastoma growth in vitro and in vivo via multiple mechanisms. *J. Hematol. Oncol. J. Hematol. Oncol.* **2016**, *9*, 98. [CrossRef] [PubMed]

13. Lee, J.-C.; Chiang, K.-C.; Feng, T.-H.; Chen, Y.-J.; Chuang, S.-T.; Tsui, K.-H.; Chung, L.-C.; Juang, H.-H. The iron chelator, Dp44mT, effectively inhibits human oral squamous cell carcinoma cell growth in vitro and in vivo. *Int. J. Mol. Sci.* **2016**, *17*, 1435. [CrossRef] [PubMed]

14. Li, P.; Zheng, X.; Shou, K.; Niu, Y.; Jian, C.; Zhao, Y.; Yi, W.; Hu, X.; Yu, A. The iron chelator Dp44mT suppresses osteosarcoma's proliferation, invasion and migration: In vitro and in vivo. *Am. J. Transl. Res.* **2016**, *8*, 5370–5385. [PubMed]

15. Kovacevic, Z.; Chikhani, S.; Lovejoy, D.B.; Richardson, D.R. Novel thiosemicarbazone iron chelators induce up-regulation and phosphorylation of the metastasis suppressor N-myc down-stream regulated gene 1: A new strategy for the treatment of pancreatic cancer. *Mol. Pharmacol.* **2011**, *80*, 598–609. [CrossRef]

16. Lovejoy, D.B.; Sharp, D.M.; Seebacher, N.; Obeidy, P.; Prichard, T.; Stefani, C.; Basha, M.T.; Sharpe, P.C.; Jansson, P.J.; Kalinowski, D.S.; et al. Novel second-generation di-2-pyridylketone thiosemicarbazones show synergism with standard chemotherapeutics and demonstrate potent activity against lung cancer xenografts after oral and intravenous administration in vivo. *J. Med. Chem.* **2012**, *55*, 7230–7244. [CrossRef]

17. Le, N.T.V.; Richardson, D.R. Iron chelators with high antiproliferative activity up-regulate the expression of a growth inhibitory and metastasis suppressor gene: A link between iron metabolism and proliferation. *Blood* **2004**, *104*, 2967–2975. [CrossRef]

18. Richardson, D.R.; Sharpe, P.C.; Lovejoy, D.B.; Senaratne, D.; Kalinowski, D.S.; Islam, M.; Bernhardt, P.V. Dipyridyl thiosemicarbazone chelators with potent and selective antitumor activity form iron complexes with redox activity. *J. Med. Chem.* **2006**, *49*, 6510–6521. [CrossRef]

19. Lovejoy, D.B.; Jansson, P.J.; Brunk, U.T.; Wong, J.; Ponka, P.; Richardson, D.R. Antitumor activity of metal-chelating compound Dp44mT is mediated by formation of a redox-active copper complex that accumulates in lysosomes. *Cancer Res.* **2011**, *71*, 5871–5880. [CrossRef]

20. Stacy, A.E.; Palanimuthu, D.; Bernhardt, P.V.; Kalinowski, D.S.; Jansson, P.J.; Richardson, D.R. Zinc(II)–thiosemicarbazone complexes are localized to the lysosomal compartment where they transmetallate with copper ions to induce cytotoxicity. *J. Med. Chem.* **2016**, *59*, 4965–4984. [CrossRef]

21. Seebacher, N.A.; Richardson, D.R.; Jansson, P.J. A mechanism for overcoming P-glycoprotein-mediated drug resistance: Novel combination therapy that releases stored doxorubicin from lysosomes via lysosomal permeabilization using Dp44mT or DpC. *Cell Death Dis.* **2016**, *7*, e2510. [CrossRef] [PubMed]

22. Kovacevic, Z.; Menezes, S.V.; Sahni, S.; Kalinowski, D.S.; Bae, D.-H.; Lane, D.J.R.; Richardson, D.R. The metastasis suppressor, N-MYC downstream-regulated gene-1 (NDRG1), down-regulates the ErbB family of receptors to inhibit downstream oncogenic signaling pathways. *J. Biol. Chem.* **2016**, *291*, 1029–1052. [CrossRef] [PubMed]

23. Menezes, S.V.; Kovacevic, Z.; Richardson, D.R. The metastasis suppressor NDRG1 down-regulates the epidermal growth factor receptor via a lysosomal mechanism by up-regulating mitogen-inducible gene 6. *J. Biol. Chem.* **2019**, *294*, 4045–4064. [CrossRef] [PubMed]

24. Park, K.C.; Geleta, B.; Leck, L.Y.W.; Paluncic, J.; Chiang, S.; Jansson, P.J.; Kovacevic, Z.; Richardson, D.R. Thiosemicarbazones suppress expression of the c-Met oncogene by mechanisms involving lysosomal degradation and intracellular shedding. *J. Biol. Chem.* **2020**, *295*, 481–503. [CrossRef]

25. Kovacevic, Z.; Chikhani, S.; Lui, G.Y.L.; Sivagurunathan, S.; Richardson, D.R. The iron-regulated metastasis suppressor NDRG1 targets NEDD4L, PTEN, and SMAD4 and inhibits the PI3K and Ras signaling pathways. *Antioxid. Redox Signal.* **2013**, *18*, 874–887. [CrossRef]

26. Lui, G.Y.L.; Kovacevic, Z.; Menezes, S.; Kalinowski, D.S.; Merlot, A.M.; Sahni, S.; Richardson, D.R. Novel thiosemicarbazones regulate the signal transducer and activator of transcription 3 (STAT3) pathway: Inhibition of constitutive and interleukin 6 (IL6)-induced activation by iron depletion. *Mol. Pharmacol.* **2015**. [CrossRef]

27. Chen, Z.; Zhang, D.; Yue, F.; Zheng, M.; Kovacevic, Z.; Richardson, D.R. The iron chelators Dp44mT and DFO inhibit TGF-β-induced epithelial-mesenchymal transition via up-regulation of N-Myc downstream-regulated gene 1 (NDRG1). *J. Biol. Chem.* **2012**, *287*, 17016–17028. [CrossRef]

28. Menezes, S.V.; Fouani, L.; Huang, M.L.H.; Geleta, B.; Maleki, S.; Richardson, A.; Richardson, D.R.; Kovacevic, Z. The metastasis suppressor, NDRG1, attenuates oncogenic TGF-β and NF-κB signaling to enhance membrane E-cadherin expression in pancreatic cancer cells. *Carcinogenesis* **2019**, *40*, 805–818. [CrossRef]

29. Jin, R.; Liu, W.; Menezes, S.; Yue, F.; Zheng, M.; Kovacevic, Z.; Richardson, D.R. The metastasis suppressor NDRG1 modulates the phosphorylation and nuclear translocation of β-catenin through mechanisms involving FRAT1 and PAK4. *J. Cell Sci.* **2014**, *127*, 3116–3130. [CrossRef]

30. Gutierrez, E.; Richardson, D.R.; Jansson, P.J. The anticancer agent di-2-pyridylketone 4,4-dimethyl-3-thiosemicarbazone (Dp44mT) overcomes prosurvival autophagy by two mechanisms: Persistent induction of autophagosome synthesis and impairment of lysosomal integrity. *J. Biol. Chem.* **2014**, *289*, 33568–33589. [CrossRef]

31. Potuckova, E.; Jansova, H.; Machacek, M.; Vavrova, A.; Haskova, P.; Tichotova, L.; Richardson, V.; Kalinowski, D.S.; Richardson, D.R.; Simunek, T. Quantitative analysis of the anti-proliferative activity of combinations of selected iron-chelating agents and clinically used anti-neoplastic drugs. *PLoS ONE* **2014**, *9*, e88754. [CrossRef] [PubMed]

32. Maqbool, S.N.; Lim, S.C.; Park, K.C.; Hanif, R.; Richardson, D.R.; Jansson, P.J.; Kovacevic, Z. Overcoming tamoxifen resistance in oestrogen receptor-positive breast cancer using the novel thiosemicarbazone anti-cancer agent, DpC. *Br. J. Pharmacol.* **2020**, *177*, 2365–2380. [CrossRef] [PubMed]

33. Jendrossek, V. Targeting apoptosis pathways by celecoxib in cancer. *Cancer Lett.* **2013**, *332*, 313–324. [CrossRef] [PubMed]

34. Thomas, A.; Tanaka, M.; Trepel, J.; Reinhold, W.C.; Rajapakse, V.N.; Pommier, Y. Temozolomide in the era of precision medicine. *Cancer Res.* **2017**, *77*, 823–826. [CrossRef]

35. Relling, M.V.; Boyett, J.M.; Blanco, J.G.; Raimondi, S.; Behm, F.G.; Sandlund, J.T.; Rivera, G.K.; Kun, L.E.; Evans, W.E.; Pui, C.-H. Granulocyte colony-stimulating factor and the risk of secondary myeloid malignancy after etoposide treatment. *Blood* **2003**, *101*, 3862–3867. [CrossRef]

36. Walker, J.V.; Nitiss, J.L. DNA topoisomerase II as a target for cancer chemotherapy. *Cancer Investig.* **2002**, *20*, 570–589. [CrossRef]

37. Schwartzman, M.L.; Bonazzi, A.; Mieyal, P.; Mezentsev, A.; Abraham, N.G.; Dunn, M.W. COX-2 lack of function in hypoxia-induced ocular surface inflammation. *Thromb. Res.* **2003**, *110*, 293–298. [CrossRef]

38. Hausmann, A.; Lee, J.; Pantopoulos, K. Redox control of iron regulatory protein 2 stability. *FEBS Lett.* **2011**, *585*, 687–692. [CrossRef]

39. Saxena, N.; Maio, N.; Crooks, D.R.; Ricketts, C.J.; Yang, Y.; Wei, M.-H.; Fan, T.W.-M.; Lane, A.N.; Sourbier, C.; Singh, A.; et al. SDHB-deficient cancers: The role of mutations that impair iron sulfur cluster delivery. *JNCI J. Natl. Cancer Inst.* **2016**, *108*. [CrossRef]

40. Park, Y.-K.; Hong, H.; Jang, B.-C. Transcriptional and translational regulation of COX-2 expression by cadmium in C6 glioma cells. *Int. J. Mol. Med.* **2012**, *30*, 960–966. [CrossRef]

41. Arico, S.; Pattingre, S.; Bauvy, C.; Gane, P.; Barbat, A.; Codogno, P.; Ogier-Denis, E. Celecoxib induces apoptosis by inhibiting 3-phosphoinositide-dependent protein kinase-1 activity in the human colon cancer HT-29 cell line. *J. Biol. Chem.* **2002**, *277*, 27613–27621. [CrossRef] [PubMed]

42. Park, K.C.; Menezes, S.V.; Kalinowski, D.S.; Sahni, S.; Jansson, P.J.; Kovacevic, Z.; Richardson, D.R. Identification of differential phosphorylation and sub-cellular localization of the metastasis suppressor, NDRG1. *Biochim. Biophys. Acta Mol. Basis Dis.* **2018**, *1864*, 2644–2663. [CrossRef] [PubMed]

43. Sahni, S.; Park, K.C.; Kovacevic, Z.; Richardson, D.R. Two mechanisms involving the autophagic and proteasomal pathways process the metastasis suppressor protein, N-myc downstream regulated gene 1. *Biochim. Biophys. Acta Mol. Basis Dis.* **2019**, *1865*, 1361–1378. [CrossRef] [PubMed]

44. Happold, C.; Roth, P.; Wick, W.; Schmidt, N.; Florea, A.-M.; Silginer, M.; Reifenberger, G.; Weller, M. Distinct molecular mechanisms of acquired resistance to temozolomide in glioblastoma cells. *J. Neurochem.* **2012**, *122*, 444–455. [CrossRef]

45. Yip, S.; Miao, J.; Cahill, D.P.; Iafrate, A.J.; Aldape, K.; Nutt, C.L.; Louis, D.N. MSH6 mutations arise in glioblastomas during temozolomide therapy and mediate temozolomide resistance. *Clin. Cancer Res. Off. J. Am. Assoc. Cancer Res.* **2009**, *15*, 4622–4629. [CrossRef]

46. Liu, L.; Markowitz, S.; Gerson, S.L. Mismatch repair mutations override alkyltransferase in conferring resistance to temozolomide but not to 1,3-bis(2-chloroethyl)nitrosourea. *Cancer Res.* **1996**, *56*, 5375–5379.

47. Kunkel, T.A.; Erie, D.A. DNA mismatch repair. *Annu. Rev. Biochem.* **2005**, *74*, 681–710. [CrossRef]

48.   Montecucco, A.; Biamonti, G. Cellular response to etoposide treatment. *Cancer Lett.* **2007**, *252*, 9–18. [CrossRef]

49.   Merlot, A.M.; Kalinowski, D.S.; Kovacevic, Z.; Jansson, P.J.; Sahni, S.; Huang, M.L.-H.; Lane, D.J.R.; Lok, H.; Richardson, D.R. Exploiting cancer metal metabolism using anti-cancer metal-binding agents. *Curr. Med. Chem.* **2019**, *26*, 302–322. [CrossRef]

50.   Park, K.C.; Paluncic, J.; Kovacevic, Z.; Richardson, D.R. Pharmacological targeting and the diverse functions of the metastasis suppressor, NDRG1, in cancer. *Free Radic. Biol. Med.* **2020**, *157*, 154–175. [CrossRef]

51.   Dixon, K.M.; Lui, G.Y.L.; Kovacevic, Z.; Zhang, D.; Yao, M.; Chen, Z.; Dong, Q.; Assinder, S.J.; Richardson, D.R. Dp44mT targets the AKT, TGF-β and ERK pathways via the metastasis suppressor NDRG1 in normal prostate epithelial cells and prostate cancer cells. *Br. J. Cancer* **2013**, *108*, 409–419. [CrossRef] [PubMed]

52.   Lim, S.C.; Jansson, P.J.; Assinder, S.J.; Maleki, S.; Richardson, D.R.; Kovacevic, Z. Unique targeting of androgen-dependent and -independent AR signaling in prostate cancer to overcome androgen resistance. *FASEB J.* **2020**. [CrossRef] [PubMed]

53.   Xu, Y.-X.; Zeng, M.-L.; Yu, D.; Ren, J.; Li, F.; Zheng, A.; Wang, Y.-P.; Chen, C.; Tao, Z.-Z. In vitro assessment of the role of DpC in the treatment of head and neck squamous cell carcinoma. *Oncol. Lett.* **2018**, *15*, 7999–8004. [CrossRef] [PubMed]

54.   Jansson, P.J.; Kalinowski, D.S.; Lane, D.J.R.; Kovacevic, Z.; Seebacher, N.A.; Fouani, L.; Sahni, S.; Merlot, A.M.; Richardson, D.R. The renaissance of polypharmacology in the development of anti-cancer therapeutics: Inhibition of the "Triad of Death" in cancer by Di-2-pyridylketone thiosemicarbazones. *Pharmacol. Res.* **2015**, *100*, 255–260. [CrossRef] [PubMed]

55.   Zarghi, A.; Arfaei, S. Selective COX-2 inhibitors: A review of their structure-activity relationships. *Iran. J. Pharm. Res. IJPR* **2011**, *10*, 655–683. [PubMed]

56.   Rudner, J.; Elsaesser, S.J.; Müller, A.-C.; Belka, C.; Jendrossek, V. Differential effects of anti-apoptotic Bcl-2 family members Mcl-1, Bcl-2, and Bcl-xL on celecoxib-induced apoptosis. *Biochem. Pharmacol.* **2010**, *79*, 10–20. [CrossRef]

57.   Johnson, A.J.; Hsu, A.-L.; Lin, H.-P.; Song, X.; Chen, C.-S. The cyclo-oxygenase-2 inhibitor celecoxib perturbs intracellular calcium by inhibiting endoplasmic reticulum Ca^{2+}-ATPases: A plausible link with its anti-tumour effect and cardiovascular risks. *Biochem. J.* **2002**, *366*, 831–837. [CrossRef]

58.   Kovacevic, Z.; Sivagurunathan, S.; Mangs, H.; Chikhani, S.; Zhang, D.; Richardson, D.R. The metastasis suppressor, N-myc downstream regulated gene 1 (NDRG1), upregulates p21 via p53-independent mechanisms. *Carcinogenesis* **2011**, *32*, 732–740. [CrossRef]

59.   Sun, J.; Zhang, D.; Bae, D.-H.; Sahni, S.; Jansson, P.; Zheng, Y.; Zhao, Q.; Yue, F.; Zheng, M.; Kovacevic, Z.; et al. Metastasis suppressor, NDRG1, mediates its activity through signaling pathways and molecular motors. *Carcinogenesis* **2013**, *34*, 1943–1954. [CrossRef]

60.   Ma, W.; Na, M.; Tang, C.; Wang, H.; Lin, Z. Overexpression of N-myc downstream-regulated gene 1 inhibits human glioma proliferation and invasion via phosphoinositide 3-kinase/AKT pathways. *Mol. Med. Rep.* **2015**, *12*, 1050–1058. [CrossRef]

61.   Kaina, B.; Christmann, M.; Naumann, S.; Roos, W.P. MGMT: Key node in the battle against genotoxicity, carcinogenicity and apoptosis induced by alkylating agents. *DNA Repair* **2007**, *6*, 1079–1099. [CrossRef] [PubMed]

62.   Gerson, S.L. Clinical relevance of MGMT in the treatment of cancer. *J. Clin. Oncol.* **2002**, *20*, 2388–2399. [CrossRef]

63.   Woo, P.Y.M.; Li, Y.; Chan, A.H.Y.; Ng, S.C.P.; Loong, H.H.F.; Chan, D.T.M.; Wong, G.K.C.; Poon, W.-S. A multifaceted review of temozolomide resistance mechanisms in glioblastoma beyond O-6-methylguanine-DNA methyltransferase. *Glioma* **2019**, *2*, 68. [CrossRef]

64.   Duguid, E.M.; Rice, P.A.; He, C. The structure of the human AGT protein bound to DNA and its implications for damage detection. *J. Mol. Biol.* **2005**, *350*, 657–666. [CrossRef] [PubMed]

65.   Wickström, M.; Dyberg, C.; Milosevic, J.; Einvik, C.; Calero, R.; Sveinbjörnsson, B.; Sandén, E.; Darabi, A.; Siesjö, P.; Kool, M.; et al. Wnt/β-catenin pathway regulates MGMT gene expression in cancer and inhibition of Wnt signalling prevents chemoresistance. *Nat. Commun.* **2015**, *6*, 8904. [CrossRef]

66.   Alexander, B.M.; Pinnell, N.; Wen, P.Y.; D'Andrea, A. Targeting DNA repair and the cell cycle in glioblastoma. *J. Neurooncol.* **2012**, *107*, 463–477. [CrossRef]

67. Rao, V.A.; Klein, S.R.; Agama, K.K.; Toyoda, E.; Adachi, N.; Pommier, Y.; Shacter, E.B. The iron chelator Dp44mT causes DNA damage and selective inhibition of topoisomerase IIalpha in breast cancer cells. *Cancer Res.* **2009**, *69*, 948–957. [CrossRef]

68. Yalowich, J.C.; Wu, X.; Zhang, R.; Kanagasabai, R.; Hornbaker, M.; Hasinoff, B.B. The anticancer thiosemicarbazones Dp44mT and triapine lack inhibitory effects as catalytic inhibitors or poisons of DNA topoisomerase IIα. *Biochem. Pharmacol.* **2012**, *84*, 52–58. [CrossRef]

69. Nitiss, J.L. Targeting DNA topoisomerase II in cancer chemotherapy. *Nat. Rev. Cancer* **2009**, *9*, 338–350. [CrossRef]

70. Emanuelli, A.; Borroni, A.P.; Apel-Sarid, L.; Shah, P.A.; Ayyathan, D.M.; Koganti, P.; Levy-Cohen, G.; Blank, M. Smurf2-mediated stabilization of DNA topoisomerase IIα controls genomic integrity. *Cancer Res.* **2017**, *77*, 4217–4227. [CrossRef]

71. Krzyzankova, M.; Chovanova, S.; Chlapek, P.; Radsetoulal, M.; Neradil, J.; Zitterbart, K.; Sterba, J.; Veselska, R. LOX/COX inhibitors enhance the antineoplastic effects of all-trans retinoic acid in osteosarcoma cell lines. *Tumour Biol. J. Int. Soc. Oncodev. Biol. Med.* **2014**, *35*, 7617–7627. [CrossRef] [PubMed]

72. Chou, T.-C. Theoretical basis, experimental design, and computerized simulation of synergism and antagonism in drug combination studies. *Pharmacol. Rev.* **2006**, *58*, 621–681. [CrossRef] [PubMed]

APPENDIX 12

Skoda J*, Borankova K, Jansson PJ, Huang ML, Veselska R, Richardson DR. Pharmacological targeting of mitochondria in cancer stem cells: An ancient organelle at the crossroad of novel anti-cancer therapies. *Pharmacological Research*. 2019;139:298-313. (JCR 2019, IF = 5.893; T10 - Pharmacology & Pharmacy)

APPENDIX 13

Neradil J, Kyr M, Polaskova K, Kren L, Macigova P, **Skoda J**, Sterba J, Veselska R. Phospho-Protein Arrays as Effective Tools for Screening Possible Targets for Kinase Inhibitors and Their Use in Precision Pediatric Oncology. *Frontiers in Oncology*. 2019;9:930. (JCR 2019, IF = 4.848; Q2 – Oncology)

Phospho-Protein Arrays as Effective Tools for Screening Possible Targets for Kinase Inhibitors and Their Use in Precision Pediatric Oncology

Jakub Neradil [1,2], Michal Kyr [2], Kristyna Polaskova [2], Leos Kren [3], Petra Macigova [1,2], Jan Skoda [1,2], Jaroslav Sterba [2] and Renata Veselska [1,2]*

[1] *Laboratory of Tumor Biology, Department of Experimental Biology, Faculty of Science, Masaryk University, Brno, Czechia,*
[2] *Department of Pediatric Oncology, Faculty of Medicine, University Hospital Brno, Masaryk University, Brno, Czechia,*
[3] *Department of Pathology, Faculty of Medicine, University Hospital Brno, Masaryk University, Brno, Czechia*

The specific targeting of signal transduction by low-molecular-weight inhibitors or monoclonal antibodies represents a very promising personalized treatment strategy in pediatric oncology. In this study, we present the successful and clinically relevant use of commercially available phospho-protein arrays for analyses of the phosphorylation profiles of a broad spectrum of receptor tyrosine kinases and their downstream signaling proteins in tumor tissue samples. Although these arrays were made for research purposes on human biological samples, they have already been used by several authors to profile various tumor types. Our study performed a systematic analysis of the advantages and pitfalls of the use of this method for personalized clinical medicine. In certain clinical cases and their series, we demonstrated the important aspects of data processing and evaluation, the use of phospho-protein arrays for single sample and serial sample analyses, and the validation of obtained results by immunohistochemistry, as well as the possibilities of this method for the hierarchical clustering of pediatric solid tumors. Our results clearly show that phospho-protein arrays are apparently useful for the clinical consideration of druggable molecular targets within a specific tumor. Thus, their potential validation for diagnostic purposes may substantially improve the personalized approach in the treatment of relapsed or refractory solid tumors.

Keywords: phospho-protein arrays, receptor tyrosin kinases, signal transduction, low-molecular-weight inhibitors, pediatric solid tumors, phosphorylation profiling

INTRODUCTION

Current curative treatment regimens for high-risk pediatric solid tumors consist of surgery, sometimes radiotherapy (to achieve adequate local control) and different intensive chemotherapeutic schedules, with a highly limited role of targeted agents thus far. Despite this multimodal approach, the rate of survival in patients suffering from refractory or relapsed solid tumors is still disappointing, and treatment is accompanied by many early and late side effects. This finding supports the need for more effective therapeutic approaches that are based on the principle of personalized medicine (1).

The personalized treatment of malignant diseases is defined as evidence-based, individualized medicine that delivers the right care to the right cancer patient at the right time (2). This personalized approach leads to measurable improvements in patient outcomes and thus to a rational distribution of health care costs (3). Therefore, such molecular individualized medicine has recently prevailed in traditional "one size fits all" medicine (2).

One very promising strategy involves the specific targeting of signal transduction by small molecule inhibitors or monoclonal antibodies; some of these medications have recently been tested in phase I and phase II clinical trials (4, 5). However, the basic step for this personalized approach includes the precise characterization of the individual tumor regarding the receptor tyrosine kinase (RTK) pattern—both the expression and phosphorylation correlating with activation—as well as of downstream signaling pathways. In the majority of published studies on this topic, total protein expression levels were usually considered, mostly on archival formalin-fixed paraffin-embedded (FFPE) tumor samples (6–8).

Nevertheless, a specific screening approach for activated, i.e., phosphorylated, RTKs and/or downstream signaling molecules should provide more accurate data concerning the dependency of tumor cells on a particular pathway and may provide a better guide for treatment choice (4, 9). In this article, we report the experimental use of commercially available phospho-protein arrays designed for the rapid screening of phosphorylated RTKs and other signaling molecules in several types of pediatric solid tumors. Although these arrays were made for research purposes on human biological samples, they have already been used for the characterization of certain tumors in adults (10, 11) and sporadically for the characterization of pediatric tumors (12–14). Nevertheless, no systematic analysis of the advantages and pitfalls of the possible use of this method for personalized clinical medicine is available. Thus, we hope that our results on the experimental use of this method may help validate its potential for clinical practice.

MATERIALS AND METHODS

Tumor Samples

Tumor samples obtained from patients suffering from various types of relapsed or refractory pediatric solid tumors were included in this study. Written informed consent on the use of these samples and corresponding clinical data for research purposes were obtained from each patient or from the patient's parents/guardians. The Research Ethics Committee of the School of Medicine, Masaryk University (Brno, Czech Republic) approved the study protocol (certificate No. 29/2015). A description of the individual patients included in this study is given in **Table 1**. After surgery, the excised tumor tissue was examined macroscopically by pathologist and cut into two parts: one of them was designated for further microscopic examinations, and the second one was immediately frozen in liquid nitrogen. These frozen tumor samples were then processed for analyses using phospho-protein arrays. For immunohistochemistry (IHC) analyses, FFPE tumor samples

TABLE 1 | Overview of patients and their samples included in this study.

Sample No.	Sample type	Patient age range (months)	Tumor histology
1	Primary tumor	85–90	Malignant perivascular epitheliod cell tumor (PEComa)
2a	Primary tumor	185–190	Anaplastic ependymoma
2b	Relapsed primary tumor	215–220	
3	Relapsed primary tumor	35–40	Anaplastic ependymoma
4	Primary tumor	0–5	Infantile myofibromatosis
5	Primary tumor	20–25	Fibrodysplasia ossificans proggressiva
6	Lung metastasis	200–2005	Osteosarcoma
7	Primary tumor	95–100	Osteosarcoma
8a	Primary tumor	35–40	Alveolar rhabdomyosarcoma
8b	Relapsed primary tumor	45–50	
8c	Lymph node metastasis	45–50	
8d	Lymph node metastasis	80–85	
9	Primary tumor	20–25	Neuroblastoma
10	Primary tumor	30–35	Neuroblastoma
11	Orbital metastasis	15–20	Neuroblastoma
12	Hip metastasis	60–65	Neuroblastoma
13	Mediastinal metastasis	125–130	Neuroblastoma
14	Relapsed primary tumor	185–190	Pilocytic astrocytoma
15	Relapsed primary tumor	60–65	Pilocytic astrocytoma
16	Primary tumor	10–15	Pilomyxoid astrocytoma
17	Primary tumor	180–185	Glioblastoma
18	Relapsed primary tumor	140–145	Glioblastoma
19	Spinal cord metastasis	240–245	Medulloblastoma

were retrieved from files of the Department of Pathology, University Hospital Brno, Czech Republic.

Phospho-Protein Array Analysis

The relative phosphorylation levels of the selected target molecules involved in signal transduction pathways in human cells were analyzed using two types of commercially available phospho-protein arrays (R&D Systems, Minneapolis, MN, USA). The Proteome Profiler™ Human Phospho-RTK Array Kit (R&D Systems, Cat. No. ARY001B) was designed for the parallel detection of the activities of 49 RTKs (**Supplementary Table 1**), and the Proteome Profiler™ Human Phospho-MAPK Array Kit (R&D Systems, Cat. No. ARY002B) was designed for the parallel detection of 26 downstream signaling molecules, including 9 MAPKs (**Supplementary Table 2**). Deeply frozen tumor tissue samples were cut with a scalpel in 400 μl of appropriate lysis buffer on ice. Lysis Buffer 17 and Lysis Buffer 6 (both R&D Systems) were used for Phospho-RTK and Phospho-MAPK array kit, respectively. After complete homogenization,

TABLE 2 | Overview of antibodies used in this study.

Antigen	Type/host	Cat. No. (all Abcam)	Dilution	Positive control
EGFR (total)	Monoclonal/Rb	ab52894	1:200	Endometrial carcinoma
EGFR (anti-pTyr^{1092})	Monoclonal/Rb	ab40815	1:400	Papillary carcinoma of thyroid glad
PDGFRβ (total)	Monoclonal/Rb	ab32570	1:100	Breast and spleen
PDGFRβ (anti-pTyr^{751})	Polyclonal/Rb	ab51046	1:100	Brain
InsRβ (total)	Polyclonal/Rb	ab5500	1:200	Breast carcinoma
InsRβ (anti-pTyr^{1185})	Polyclonal/Rb	ab203278	1:150	Lung
Akt1/2/3 (total)	Monoclonal/Rb	ab32505	1:100	Prostate carcinoma
Akt1/2/3 (anti-pSer^{473})	Monoclonal/Rb	ab81283	1:50	Cervical carcinoma
ERK1/2 (total)	Monoclonal/Mo	ab54230	1:100	Stomach
ERK1/2 (anti-pThr^{202}/pTyr^{204}//pThr^{185}/pTyr^{187})	Monoclonal/Mo	ab50011	1:100	Brain

the whole suspension was centrifuged for 5 min at 14,000 g. The supernatants were used as whole-tissue lysates and then processed according to the manufacturer's protocol. The levels of phosphorylation were quantified using ImageJ software (15). The detailed procedure of data acquisition and processing is described below in the relevant part of the Results.

Immunohistochemical Analysis

Representative sections from relevant FFPE tumor samples were analyzed by IHC to determine the total and phosphorylated levels of the protein of interest. All of the antibodies used in this protocol are described in **Table 2**. The 4-μm-thick sections from FFPE blocks were deparaffinized with pure xylene for 3 × 5 min, washed in 96% alcohol for 3 × 5 min and then rinsed with distilled water. In the next step, endogenous peroxidase was inactivated by 3% H_2O_2 in methanol for 10 min, and the samples were washed in distilled water. Antigen retrieval was then performed by incubation in citrate buffer (pH 6.0) at 98°C for 20 min followed by cooling for 20 min and rinsing with PBS for 3 × 5 min. The incubation with primary antibodies was performed in a wet chamber at room temperature for 1 h, and samples were then rinsed with PBS for 3 × 5 min. The EnVision+System streptavidin-biotin peroxidase detection system (Dako, Glostrup, Denmark) was used according to the manufacturer's protocol in the wet chamber at room temperature for 45 min followed by washing in PBS and visualization using 3,3'diaminobenzidine as a substrate (Sigma-Aldrich, St. Louis, MO, USA). Nuclei were counterstained with Gill's hematoxylin for 1 min followed by bluing in water for 2–3 min for optimal results. Finally, the samples were dehydrated in a series of upconcentrated ethanol baths, cleared in xylene and mounted onto Entelan^{TM} slides (Entelan Microscopy, Karlsruhe, Germany). Positive and negative controls were evaluated in each IHC run. Positive controls for each protein are listed in **Table 2**. Negative controls consisted of slides run without the primary antibodies. An Olympus BX45 microscope (Olympus Optical, Tokyo, Japan) equipped with an Olympus DP50 digital camera was used for the evaluation of IHC staining and to capture the micrographs. Olympus Viewfinder Lite^{TM} software was used to process the images.

Statistical Analysis

Hierarchical clustering was used for multidimensional kinase phosphorylation data analysis to identify possible characteristic patterns of the kinase phosphorylation status for different diagnostic groups. Data preprocessing was performed as follows. Digitalized density levels were logarithmically transformed, and normalization and scaling of the data matrix were performed to enable comparison among samples. After filtering significantly different kinases, supervised clustering was applied. Hierarchical clustering using a Ward method with correlation distance metrics was performed. Data are presented using heatmap plots. Analyses were performed using R 3.4.3 (16) with gplots (17).
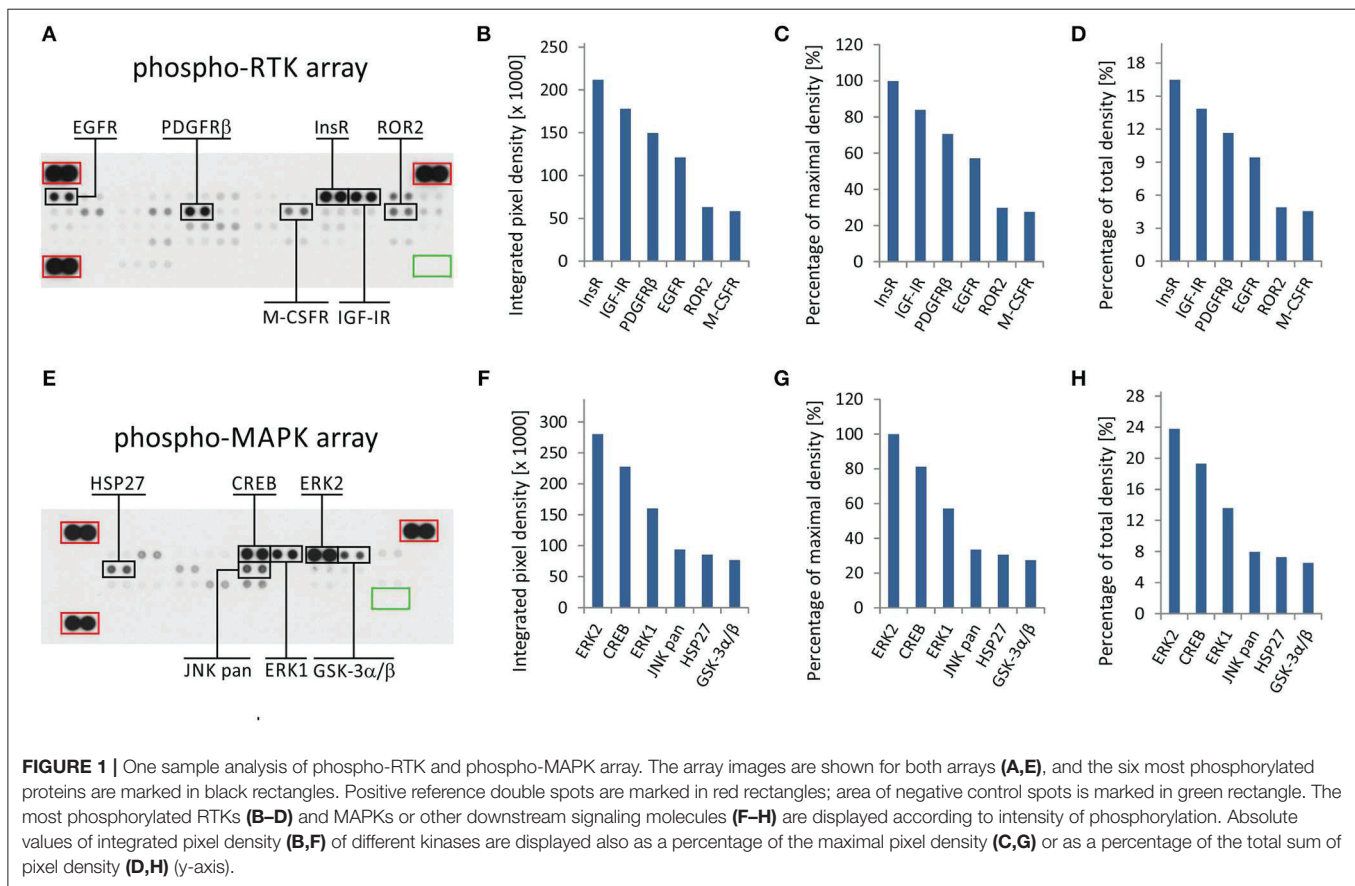
RESULTS

Although the phospho-protein arrays employed in this study were designed and produced by the manufacturer for research purposes only, our experimental results showed that they may also be successfully used for the rapid screening of active signal transducers as potential therapeutic targets in tumor tissue samples obtained from individual patients. Furthermore, we also showed that these arrays are also very suitable for comparative analyses of respective phospho-protein profiles among and/or within different tumor types, as described below in detail. Nevertheless, the use of phospho-protein arrays for these purposes encompasses several important aspects that must be carefully considered in the view of the correct interpretation of obtained results.

Data Acquisition and Processing

The phospho-protein arrays used in our experiments are based on analysis of tissue samples on nitrocellulose membranes, where specific antibodies against selected kinases are spotted in duplicate. In addition to these antibodies, each membrane contains three positive reference double spots and one negative control containing PBS only, which is also spotted in duplicate (**Figures 1A,E**). Tissue lysates are applied to this membrane, and both phosphorylated and unphosphorylated proteins are bound to the respective antibodies at an equimolar ratio.

In the phospho-RTK array, the phosphorylated proteins are distinguished only by a pan-anti-phospho-tyrosine antibody

FIGURE 1 | One sample analysis of phospho-RTK and phospho-MAPK array. The array images are shown for both arrays **(A,E)**, and the six most phosphorylated proteins are marked in black rectangles. Positive reference double spots are marked in red rectangles; area of negative control spots is marked in green rectangle. The most phosphorylated RTKs **(B–D)** and MAPKs or other downstream signaling molecules **(F–H)** are displayed according to intensity of phosphorylation. Absolute values of integrated pixel density **(B,F)** of different kinases are displayed also as a percentage of the maximal pixel density **(C,G)** or as a percentage of the total sum of pixel density **(D,H)** (y-axis).

conjugated with horseradish peroxidase. This allows us to detect all phosphorylated tyrosines that are predominantly located on the cytoplasmic part of the RTK molecule and thus reflect the overall activity of the receptor in question.

In the phospho-MAPK array, a mixture of biotinylated anti-phospho-kinase antibodies followed by streptavidin conjugated with horseradish peroxidase is used to distinguish between phosphorylated and unphosphorylated proteins. Each individual antibody in this antibody mixture is designed to detect a specific phosphorylation site (or sites) of each particular signaling protein included in the array. A table containing the overview of phosphorylation sites for all detected proteins is given in the manufacturer's manual.

Finally, the luminescence induced by the addition of a chemiluminescent substrate is captured on X-ray film in both arrays (**Figures 1A,E**). As described in our previous studies, the levels of phosphorylation were quantified using ImageJ software (15) and subsequently normalized to the positive control spots (18). Although the experimental use of a phospho-protein array is usually based on the comparison of acquired data with a reference cell line (18) or with untreated control cells (19), the employment of these arrays in clinical practice apparently requires a different approach.

We presumed that highly phosphorylated proteins, as detected by these arrays, are highly activated within the tumor tissue and thus represent the most suitable targets for treatment with available small-molecule inhibitors or monoclonal antibodies (20). To evaluate the results of one sample analysis, it is possible to use the absolute values of integrated density as obtained by the employment of image analysis software (**Figures 1B,F**). Alternatively, the data can be normalized to the maximal integrated density achieved in each individual array, i.e., the highest value indicates 100% phosphorylation (**Figures 1C,G**). The third method by which to process the obtained data is recommended by ImageJ software documentation (15): the integrated densities of each kinase are displayed as a percentage of the total sum of density (**Figures 1D,H**). The resulting phosphorylation profiles obtained by these three processing modes are identical to each other, and they show the same differences in the phosphorylation of kinases included in the respective array (**Figures 1B–D,F–H**).

From the clinical viewpoint, the results described above (**Figure 1**) are those obtained by the analysis of tumor tissue obtained from patient No. 1 (**Table 1**). This sample was obtained by surgical resection of the tumor mass from the supravesical space. According to the results from molecular biology analyses, including these phospho-profiles, the patient was treated with low-molecular-weight inhibitors (everolimus and sunitinib), and complete remission was achieved.

The results from RTK phospho-protein arrays showed that two members of the insulin receptor family (InsR and IGF-1R) displayed the highest phosphorylation. Slightly reduced positivity was also observed for PDGFRβ and EGFR (**Figures 1A–D**). The analysis of MAPKs revealed the high phosphorylation of ERK1 and ERK2 on activation loop residues Thr^{202}/Tyr^{204} and Thr^{185}/Tyr^{187}, respectively. Among the other downstream signaling molecules, CREB was substantially phosphorylated on residue Ser^{133}. Lower but still detectable levels of phosphorylation were found for JNK kinases on Thr^{183}/Tyr^{185} and Thr^{221}/Tyr^{223}, for Hsp27 (also known as HSPB1) on Ser^{78}/Ser^{82} residues, and for GSK-3 kinases on Ser^9/Ser^{21} (**Figures 1E–H**).

Verification of Druggable Targets in Tumor Tissue

The main advantage of the use of phospho-protein arrays for the identification of active signal transducers within tumor tissue is the promptness of such a screening method and the relatively high number of signaling molecules covered by these arrays. Nevertheless, as these arrays are still available for experimental

purposes only and not for routine laboratory diagnostics, the results obtained from these arrays should be verified by other independent methods.

Thus, we employed a standard IHC method for the independent detection of active signal transducers as already identified by the phospho-protein array. As an example of this approach, the results from both types of phospho-protein arrays were compared with results from the IHC analysis of paired FFPE samples from the same biopsies in a group of 6 patients: patients No. 2–7 (**Table 1**) were included in this part of the study.

For RTKs, the levels of phospho-EGFR, phospho-PDGFRβ, and phospho-InsR were compared with the presence of these phosphorylated RTKs as identified using specific anti-phospho antibodies (**Table 2**) against these three selected target molecules (**Figure 2**).

To verify EGFR phosphorylation, a specific anti-phospho-EGFR antibody against phosphorylated Tyr^{1092}, which is equivalent to Tyr^{1068} of mature EGFR, was used. All analyzed samples showed relatively high levels of phosphorylation as detected using both phospho-arrays, with ∼60–100% of maximal density, and the immunoreactivity was predominantly medium
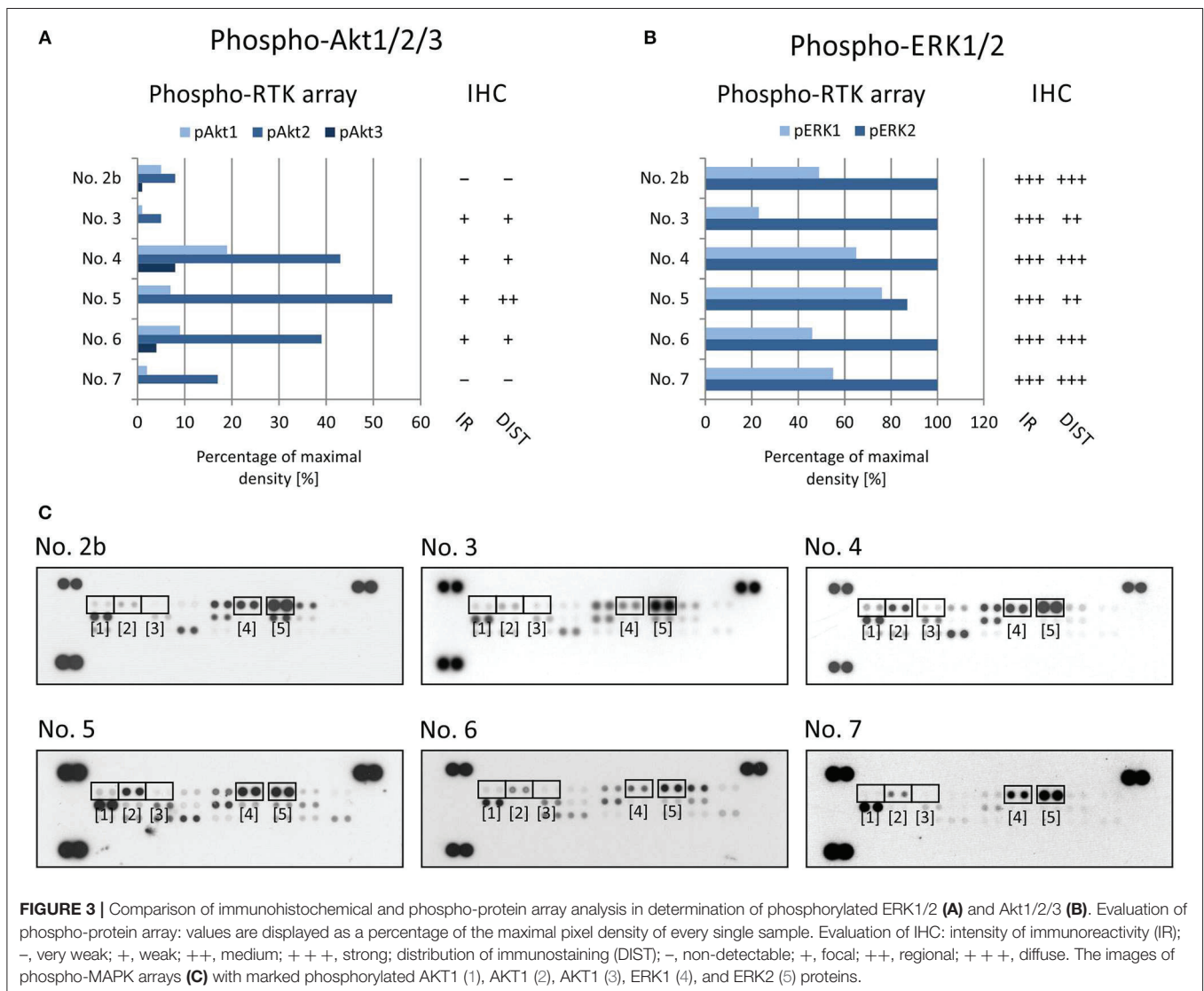

FIGURE 2 | Comparison of immunohistochemical and phospho-protein array analysis in determination of phosphorylated EGFR **(A)**, PDGFRβ **(B)**, and InsR **(C)**. Evaluation of phospho-protein array: values are displayed as a percentage of the maximal pixel density of every single sample. Evaluation of IHC: intensity of immunoreactivity (IR); −, very weak; +, weak; ++, medium; +++, strong; distribution of immunostaining (DIST); −, non-detectable; +, focal; ++, regional; +++, diffuse. The images of phospho-RTK arrays **(D)** with marked phosphorylated EGFR (1), PDGFRβ (2), and InsR (3) proteins.

to strong except in sample No. 6 (**Figure 2A**). The anti-phospho-PDGFRβ antibody against phosphorylated Tyr[751] also showed a very good match with PDGFRβ phosphorylation as detected by the phospho-protein array in all six samples (**Figures 2B,D**): strong or medium immunoreactivity corresponded to the highest density from the phospho-protein arrays and vice versa; and very weak immunoreactivity was in accordance with very low phosphorylation—up to 10% of maximal density—in sample Nos. 2 and 3 (**Figures 2B,D**). The anti-InsR antibody against phosphorylated Tyr[1185] in the beta chain of the InsR molecule showed strong or medium positivity in the same tumor tissues in which at least 50% of maximal density was detected by the phospho-array (**Figures 2C,D**). Nevertheless, for InsR activities up to 50% of maximal density, accordance with the IHC results was not obvious (**Figures 2C,D**).

To evaluate the two most prominent downstream signaling pathways, i.e., PI3K/AKT and RAS/RAF/MEK/ERK, antibodies designed to detect both phosphorylated forms of ERK kinase and all three phosphorylated forms of AKT kinase, respectively, were chosen. The phosphorylation of AKT kinases in FFPE tumor samples was evaluated using an anti-AKT1 antibody that detects phosphorylation at Ser[473] within the C-terminus. Due to the high degree of similarity to the corresponding regions in the AKT2 and AKT3 molecules, this antibody may cross-react with these isoforms at Ser[474] and Ser[472], respectively. The phospho-protein array can detect the relative phosphorylation of all three AKT isoforms at the same phospho-sites as the antibody employed for IHC. Anyway, the phosphorylation of AKT2 reached only ∼50% of the maximal density in sample Nos. 4, 5, and 6 (**Figures 3A,C**). The relative phosphorylation of AKT1 and AKT3 was close to the detection limit of this array in all tested samples, and the IHC method also showed very poor results for phosphorylated AKT1/2/3 molecules (**Figures 3A,C**). The anti-ERK1/2 antibody was designed against the epitopes with the same phospho-sites as those detected by the phospho-array. All FFPE samples showed strong immunoreactivity for ERK1/2, with diffuse or regional

FIGURE 3 | Comparison of immunohistochemical and phospho-protein array analysis in determination of phosphorylated ERK1/2 **(A)** and Akt1/2/3 **(B)**. Evaluation of phospho-protein array: values are displayed as a percentage of the maximal pixel density of every single sample. Evaluation of IHC: intensity of immunoreactivity (IR); −, very weak; +, weak; ++, medium; +++, strong; distribution of immunostaining (DIST); −, non-detectable; +, focal; ++, regional; +++, diffuse. The images of phospho-MAPK arrays **(C)** with marked phosphorylated AKT1 (1), AKT1 (2), AKT1 (3), ERK1 (4), and ERK2 (5) proteins.

positivity, and these results were in accordance with the very high relative phosphorylation of ERK2 as detected by the phospho-protein array (**Figures 3B,C**).

Taken together, these results indicate that the IHC method using compatible anti-phospho antibodies can serve as a useful tool for final detection or rather confirmation of the phosphorylation of the possible therapeutic target previously identified in the tumor tissue by rapid screening using phospho-protein arrays.

Example of Serial Sample Analysis During Clinical Progression of the Disease

As described above, the analysis of one individual tumor sample provides us with information concerning the phosphorylation profile of RTKs and/or downstream signaling molecules just at the time of tissue sample acquisition. A typical clinical reason for a one sample analysis is the rapid screening of suitable (and druggable) targets for personalized treatment during the phase of initial diagnostics. Nevertheless, especially in cases of refractory or relapsed tumors, we are also able to analyze and compare a series of tumor samples taken from the same patient at different phases of the disease.

Here, we describe the employment of phospho-protein arrays in the profiling of cell signaling pathways in four serial tumor samples taken from a child suffering from PAX3/FKHR-positive alveolar rhabdomyosarcoma of the ala of nose. The child was diagnosed at the age of 19 months, staged as T1aN1M0 and classified into a very-high-risk group (IRS st. IIIa) according to the European Pediatric Soft Tissue Sarcoma Study Group (EpSSG). First, complete remission was achieved after 3 cycles of chemotherapy (EpSSG RMS2005 protocol) and adjuvant radiotherapy; however, the tumor relapsed after 16 months. Second, complete remission was achieved after 6 cycles of chemotherapy (vincristine, irinotecan, and temozolomide). The patient was treated with individualized metronomic chemotherapy, but metastatic relapse was diagnosed 3 months later. Despite intensive individualized therapy, the child died within 7 months. The complete overview of this case is given (**Figure 4A**).

Step-by-step, we analyzed using both phospho-protein arrays the samples taken from the primary tumor before the treatment using both phospho-protein arrays, from the relapsed primary tumor and from two metastatic lymph nodes at different times during the disease (**Table 1**, **Figure 4A**). Changes in the phospho-profiles of RTKs (**Figure 4B**) are described in the context of personalized therapy with small molecule inhibitors used in this patient; the phospho-profiles of downstream signaling pathways (**Figure 4C**), as well as examples of target validation by IHC (**Figures 4D,E**), are also given.

Based on the obtained data, specific small molecule inhibitors were incorporated into the treatment protocol. Although pazopanib showed partial effect in terms of RTK activity, the subsequent treatment with erlotinib and sunitinib markedly diminished the activities of the target RTKs in the tumor tissue (**Figure 4B**). Unfortunately, despite this very clear response at the molecular level, no encouraging effects of this targeted therapy were observed at the clinical level, probably because of the advanced stage of metastatic disease. Nevertheless, this case markedly illustrates the importance and usefulness of the rapid screening of the possible molecular targets for personalized therapy.

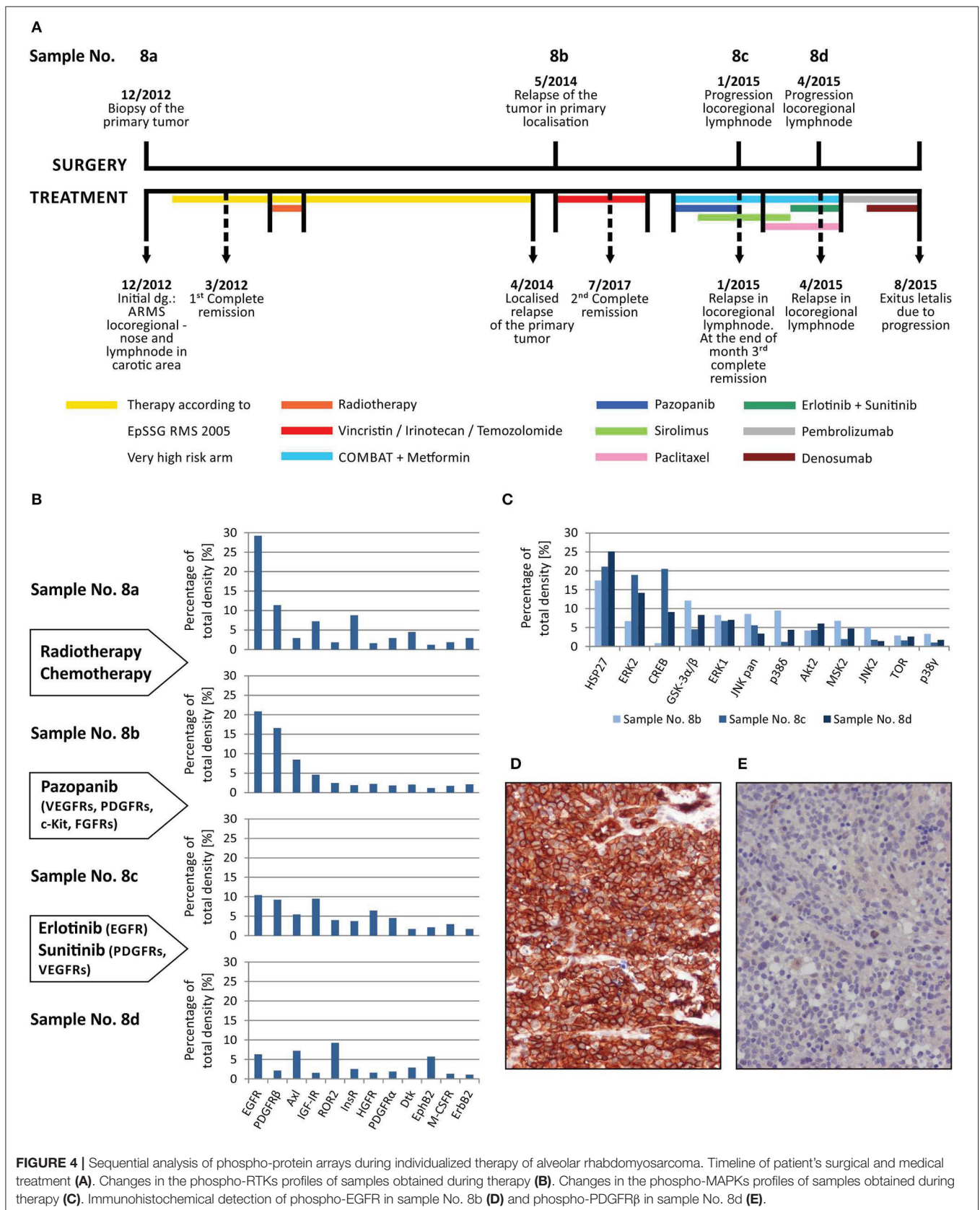## Multidimensional Analysis of Kinase Profiles in Specific Tumor Types

In addition to the individual and serial sample analyses described above, information regarding the phosphorylation profiles as obtained by the phospho-protein arrays can also be used for the hierarchical clustering of selected tumor samples. Here, we demonstrate the performance of such a classical multidimensional analysis using supervised hierarchical clustering on a small cohort ($n = 12$) of 5 neuroblastoma and 7 central nervous system (CNS) tumor samples: 3 astrocytomas, 2 glioblastomas, 1 ependymoma, and 1 medulloblastoma. The patients' detailed information is given in **Table 1**. This analysis performed on the data from the RTK phospho-protein arrays showed two distinct clusters of strongly and weakly phosphorylated RTK kinases in neuroblastoma and CNS tumors (**Figure 5A**). In contrast, even supervised clustering based on the data from the MAPK phospho-protein arrays did not result in distinct clusters of diagnostic groups in the same cohort (**Figure 5B**).
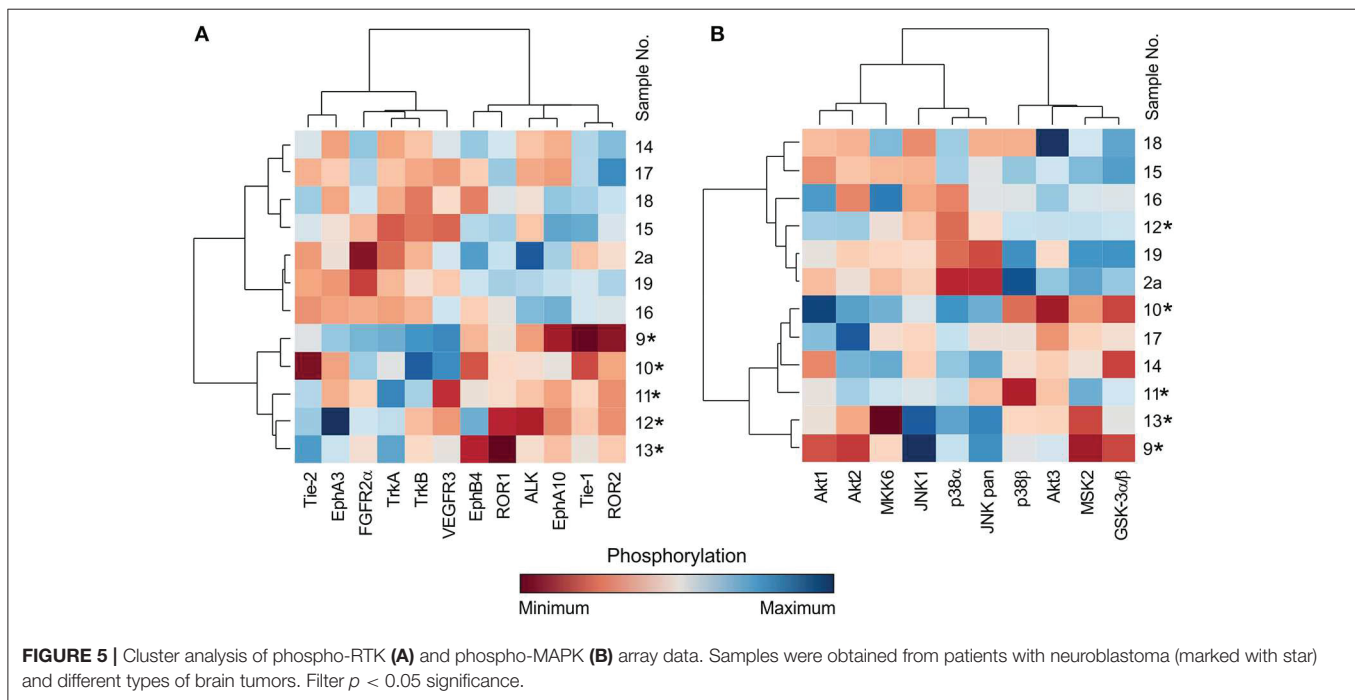
DISCUSSION

An antibody array is one of the simplest methods for measuring the relative levels of expression or phosphorylation of several proteins in a single sample. In this study, we present the successful and clinically relevant use of the Human Phospho-RTK Array Kit and the Human Phospho-MAPK Array Kit (both by R&D Systems) for the analyses of the phosphorylation profiles of a broad spectrum of RTKs and their downstream signaling proteins.

According to the manufacturer's instructions, the analysis of raw data obtained from these arrays includes determining the average signal of the pair of duplicate spots and subtracting the background signal. However, the subsequent analysis of these data is neither unified nor standardized and thus depends on the researcher's choice.

The results of one sample analysis can be presented as a specific profile with differently phosphorylated proteins, in which high levels of the detected signal, i.e., high density of spots in the phospho-protein arrays, correspond to high phosphorylation. Consequently, these highly phosphorylated signaling molecules can be considered potential therapeutic targets for low-molecular-weight kinase inhibitors or monoclonal antibodies. Moreover, the stability of phosphorylation profiles of frozen samples throughout long-term storing was proven (**Supplementary Figure 1**). The utility of commercially available phospho-protein arrays has already been demonstrated in other studies on various types of human solid tumors in adults (10, 11, 21–23).

FIGURE 4 | Sequential analysis of phospho-protein arrays during individualized therapy of alveolar rhabdomyosarcoma. Timeline of patient's surgical and medical treatment (A). Changes in the phospho-RTKs profiles of samples obtained during therapy (B). Changes in the phospho-MAPKs profiles of samples obtained during therapy (C). Immunohistochemical detection of phospho-EGFR in sample No. 8b (D) and phospho-PDGFRβ in sample No. 8d (E).

FIGURE 5 | Cluster analysis of phospho-RTK **(A)** and phospho-MAPK **(B)** array data. Samples were obtained from patients with neuroblastoma (marked with star) and different types of brain tumors. Filter $p < 0.05$ significance.

This experimental approach was also successfully used by our team in describing molecular targets and the subsequent effective treatment of several pediatric malignancies, such as Maffucci syndrome, which is characterized by multiple hemangiomas and enchondromas with a tendency to progress into malignancy (12), infantile myofibromatosis, in which PDGFR beta hyperphosphorylation is detected (13), or fibrodysplasia ossificans progressiva (14).

In addition to these individual cases, in this article, we summarize our experience with determining kinase phosphorylation profiles for single sample (**Figures 1**, **2**) and serial sample (**Figure 4**) analyses. The promising clinical response of patient No. 1 to sunitinib administration and the changes in serial kinase profiles after treatment with targeted low-molecular weight inhibitors (**Figure 4**) are other positive examples of the rational use of this experimental approach as a rapid screening method for the identification of druggable targets, which is a key part of personalized therapy. Nevertheless, as this method is not certified for diagnostic purposes, it is of high importance to employ another validation method to confirm the data from phospho-protein arrays independently.

Our data from the IHC validation showed good consistency in the levels of the phosphorylated forms of all three selected RTKs, i.e., phospho-EGFR, phospho-PDGFRβ, and phospho-InsR, as determined independently by IHC and the phospho-protein array (**Figure 2**). Similarly, data on the downstream signal transducers ERK and AKT showed moderate accordance (**Figure 3**), although the pan-phospho-ERK and pan-phospho-AKT antibodies were used for IHC detection, whereas isoform-specific antibodies against ERK1/2 or AKT1/2/3 were spotted onto the MAPK phospho-protein array. The same strategy, i.e., the validation of phosphorylated signal transducers as

suitable targets by IHC, was successfully used for personalized treatment with low-molecular-weight inhibitors in malignant mesothelioma (24).

The most interesting finding from our study is the example of a cluster analysis performed in a cohort of 12 patients suffering from neuroblastomas or CNS tumors. In general, for the graphical presentation of results on differences among individual samples and their clusters, a heat map is the best choice (**Figure 5**). For the heat map display, data normalization is required, and the values range from −3 to 3 (23, 25). The same approach was used, and the hierarchical clustering of data from the MAPK phospho-protein arrays showed no distinct clusters for these tumor types (**Figure 5B**), whereas the same clustering method revealed significantly different patterns of the selected 12 RTKs in neuroblastomas and in the group of CNS tumors (**Figure 5A**). These interesting data will be reanalyzed in our forthcoming study on a large cohort of patients with neurogenic tumors; however, these results suggest another useful approach to employ the phospho-protein arrays in personalized therapy.

As apparent from all results presented in the current study as well as those from previously published data obtained by the same type of phospho-protein arrays, the key step in the use of these arrays for the identification of druggable molecular targets is the manner of data processing and interpretation. Comparative analyses of phosphorylation profiles in various tumor tissue samples are typically used in these studies: the analysis of 20 glioma cell lines and 14 tissue samples of primary glioblastoma multiforme can be used as an example (26). The categorization of achieved data into several groups according to the signal intensity is also a frequently used approach (21, 22, 27). Some of these groups are distinguished by different levels of positive signals, and the last one is considered negative. The

definition of a particular group can be described by specific categorization terms such as "strongly activated," "moderately activated," "activated to a lower extent," and "poorly activated" (22) or by a grading system similar to the IHC evaluation (27). A simplified binary view is able to distinguish positive or negative signals only, and thus activated and non-activated proteins can be described by this approach (10, 11, 24). In the first of these studies, all intensity values of the probes and the local background of the probes were $\log_2$ transformed (to obtain a more symmetrical distribution) and subtracted. In the next step, the mean of all obtained values was calculated for the individual array, and only the probes with values higher than the mean plus standard deviation (SD) were considered significantly activated (10). In the second study, the cut-off level for activated proteins was calculated as triple that of the highest negative control (24). In the last study, the cut-off level was not described (11).

In conclusion, our study showed the usefulness of phospho-protein arrays for the personalized treatment of patients suffering from relapsed/refractory solid tumors. From the clinical point of view, these arrays are especially suitable for the rapid screening of targets for treatment with low-molecular-weight inhibitors or monoclonal antibodies, although they can also be used for deep analyses of the differences in phosphorylation profiles among selected tumor types. These phospho-protein arrays are available for research use only, and they are not designated for *in vitro* diagnostic purposes. However, their apparent usefulness in the clinical consideration of druggable molecular targets within a specific tumor brings forward a demand for their validation also for diagnostic purposes.

DATA AVAILABILITY STATEMENT

The datasets generated for this study are available on request to the corresponding author.

REFERENCES

1. Forrest SJ, Geoerger B, Janeway KA. Precision medicine in pediatric oncology. *Curr Opin Pediatr.* (2018) 30:17–24. doi: 10.1097/MOP.0000000000000570
2. Kalia M. Personalized oncology: recent advances and future challenges. *Metabolism.* (2013) 62:S11–4. doi: 10.1016/j.metabol.2012.08.016
3. Jackson SE, Chester JD. Personalised cancer medicine. *Int J Cancer.* (2015) 137:262–6. doi: 10.1002/ijc.28940
4. Fleuren ED, Versleijen-Jonkers YM, Heskamp S, van Herpen CM, Oyen WJ, van der Graaf WT, et al. Theranostic applications of antibodies in oncology. *Mol Oncol.* (2014) 8:799–812. doi: 10.1016/j.molonc.2014.03.010
5. Kalia M. Biomarkers for personalized oncology: recent advances and future challenges. *Metabolism.* (2015) 64:S16–21. doi: 10.1016/j.metabol.2014.10.027
6. Cossu-Rocca P, Contini M, Uras MG, Muroni MR, Pili F, Carru C, et al. Tyrosine kinase receptor status in endometrial stromal sarcoma: an immunohistochemical and genetic-molecular analysis. *Int J Gynecol Pathol.* (2012) 31:570–9. doi: 10.1097/PGP.0b013e31824fe289
7. Corbo V, Beghelli S, Bersani S, Antonello D, Talamini G, Brunelli M, et al. Pancreatic endocrine tumours: mutational and immunohistochemical survey of protein kinases reveals alterations in targetable kinases in cancer cell lines and rare primaries. *Ann Oncol.* (2012) 23:127–34. doi: 10.1093/annonc/mdr048

ETHICS STATEMENT

This study was reviewed and approved by The Research Ethics Committee of the School of Medicine, Masaryk University (Brno, Czech Republic). Written informed consent was obtained from the minor(s)' legal guardian/next of kin for use of the biological samples and corresponding clinical data for research purposes, as well as for the publication of any potentially identifiable images or data included in this article.

AUTHOR CONTRIBUTIONS

JN, JSt, and RV designed the study. KP and JSt provided tumor samples and relevant clinical data. JN and PM performed phospho-protein arrays. LK performed immunohistochemical analyses. MK performed statistical analyses. JN and RV composed the manuscript. MK and JSk participated in data analyses and manuscript preparation. All authors reviewed and approved the final version of the manuscript.

FUNDING

ACKNOWLEDGMENTS

SUPPLEMENTARY MATERIAL

The Supplementary Material for this article can be found online at: https://www.frontiersin.org/articles/10.3389/fonc.2019.00930/full#supplementary-material

8. Matsumura Y, Umemura S, Ishii G, Tsuta K, Matsumoto S, Aokage K, et al. Expression profiling of receptor tyrosine kinases in high-grade neuroendocrine carcinoma of the lung: a comparative analysis with adenocarcinoma and squamous cell carcinoma. *J Cancer Res Clin Oncol.* (2015) 141:2159–70. doi: 10.1007/s00432-015-1989-z
9. Sun X, Song Q, He L, Yan L, Liu J, Zhang Q, et al. Receptor tyrosine kinase phosphorylation pattern-based multidrug combination is an effective approach for personalized cancer treatment. *Mol Cancer Ther.* (2016) 15:2508–20. doi: 10.1158/1535-7163.MCT-15-0735
10. Dewaele B, Floris G, Finalet-Ferreiro J, Fletcher CD, Coindre JM, Guillou L, et al. Coactivated platelet-derived growth factor receptor {alpha} and epidermal growth factor receptor are potential therapeutic targets in intimal sarcoma. *Cancer Res.* (2010) 70:7304–14. doi: 10.1158/0008-5472.CAN-10-1543
11. Montero JC, Esparís-Ogando A, Re-Louhau MF, Seoane S, Abad M, Calero R, et al. Active kinase profiling, genetic and pharmacological data define mTOR as an important common target in triple-negative breast cancer. *Oncogene.* (2014) 33:148–56. doi: 10.1038/onc.2012.572
12. Melicharkova K, Neradil J, Mudry P, Zitterbart K, Obermannova R, Skotakova J, et al. Profile of activation of tyrosine kinases and MAP kinases in therapy of maffucci syndrome. *Klin Onkol.* (2015) 28:2S47–51. doi: 10.14735/amko20152S47
13. Mudry P, Slaby O, Neradil J, Soukalova J, Melicharkova K, Rohleder O, et al. Case report: rapid and durable response to PDGFR targeted

therapy in a child with refractory multiple infantile myofibromatosis and a heterozygous germline mutation of the PDGFRB gene. *BMC Cancer.* (2017) 17:119. doi: 10.1186/s12885-017-3115-x

14. Rohleder O, Mudry P, Neradil J, Noskova H, Slaby O, Sterba J. et al., Early clinical observations on the use of imatinibmesylate in FOP: a report of seven cases. *Bone.* (2018) 116:171. doi: 10.1016/j.bone.2018.08.003

15. Schneider CA, Rasband WS, Eliceiri KW. NIH Image to ImageJ: 25 years of image analysis. *Nat Methods.* (2012) 9:671–5. doi: 10.1038/nmeth.2089

16. R Core Team. *R: A Language and Environment for Statistical Computing.* Vienna: R Foundation for Statistical Computing (2017). Available online at: https://www.r-project.org/ (accessed September 12, 2019).

17. Warnes GR, Bolker B, Bonebakker L, Gentleman R, Liaw WHA, Lumley T, et al. *Gplots: Various R Programming Tools for Plotting Data. R Package Version 3.0.1.* (2016). Available online at: https://cran.r-project.org/web/packages/gplots/index.html (accessed September 12, 2019).

18. Skoda J, Neradil J, Zitterbart K, Sterba J, Veselska R. EGFR signaling in the HGG-02 glioblastoma cell line with an unusual loss of EGFR gene copy. *Oncol Rep.* (2014) 31:480–7. doi: 10.3892/or.2013.2864

19. Patwardhan PP, Musi E, Schwartz GK. Preclinical evaluation of nintedanib, a triple angiokinase inhibitor, in soft-tissue sarcoma: potential therapeutic implication for synovial sarcoma. *Mol Cancer Ther.* (2018) 17:2329–40. doi: 10.1158/1535-7163.MCT-18-0319

20. Regad T. Targeting RTK signaling pathways in cancer. *Cancers.* (2015) 7:1758–84. doi: 10.3390/cancers7030860

21. Stacchiotti S, Tamborini E, Marrari A, Brich S, Rota SA, Orsenigo M, et al. Response to sunitinib malate in advanced alveolar soft part sarcoma. *Clin Cancer Res.* (2009) 15:1096–104. doi: 10.1158/1078-0432.CCR-08-2050

22. Stacchiotti S, Negri T, Palassini E, Conca E, Gronchi A, Morosi C, et al. Sunitinib malate and figitumumab in solitary fibrous tumor: patterns and molecular bases of tumor response. *Mol Cancer Ther.* (2010) 9:1286–97. doi: 10.1158/1535-7163.MCT-09-1205

23. Guo T, Lee SS, Ng WH, Zhu Y, Gan CS, Zhu J, et al. Global molecular dysfunctions in gastric cancer revealed by an integrated analysis of the phosphoproteome and transcriptome. *Cell Mol Life Sci.* (2011) 68:1983–2002. doi: 10.1007/s00018-010-0545-x

24. Kawaguchi K, Murakami H, Taniguchi T, Fujii M, Kawata S, Fukui T, et al. Combined inhibition of MET and EGFR suppresses proliferation of malignant mesothelioma cells. *Carcinogenesis.* (2009) 30:1097–105. doi: 10.1093/carcin/bgp097

25. Lee H, Bennett AM. Receptor protein tyrosine phosphatase-receptor tyrosine kinase substrate screen identifies EphA2 as a target for LAR in cell migration. *Mol Cell Biol.* (2013) 33:1430–41. doi: 10.1128/MCB.01708-12

26. Stommel JM, Kimmelman AC, Ying H, Nabioullin R, Ponugoti AH, Wiedemeyer R, et al. Coactivation of receptor tyrosine kinases affects the response of tumor cells to targeted therapies. *Science.* (2007) 318:287–90. doi: 10.1126/science.1142946

27. Zhang YX, van Oosterwijk JG, Sicinska E, Moss S, Remillard SP, van Wezel T, et al. Functional profiling of receptor tyrosine kinases and downstream signaling in human chondrosarcomas identifies pathways for rational targeted therapy. *Clin Cancer Res.* (2013) 19:3796–807. doi: 10.1158/1078-0432.CCR-12-3647

Skoda J, Nunukova A, Loja T, Zambo I, Neradil J, Mudry P, Zitterbart K, Hermanova M, Hampl A, Sterba J, Veselska R. Cancer stem cell markers in pediatric sarcomas: Sox2 is associated with tumorigenicity in immunodeficient mice. *Tumor Biology*. 2016;37:9535-48. (JCR 2016, IF = 3.650; Q2 – Oncology)

APPENDIX 15

Skoda J, Hermanova M, Loja T, Nemec P, Neradil J, Karasek P, Veselska R. Co-Expression of Cancer Stem Cell Markers Corresponds to a Pro-Tumorigenic Expression Profile in Pancreatic Adenocarcinoma. *PLOS One*. 2016;11:e0159255. (JCR 2016, IF = 2.806; Q1 – Multidisciplinary Sciences)

RESEARCH ARTICLE

Co-Expression of Cancer Stem Cell Markers Corresponds to a Pro-Tumorigenic Expression Profile in Pancreatic Adenocarcinoma

Jan Skoda[1,2,3], Marketa Hermanova[4], Tomas Loja[1], Pavel Nemec[1], Jakub Neradil[1,2,3], Petr Karasek[5], Renata Veselska[1,2,3] *

1 Laboratory of Tumor Biology, Department of Experimental Biology, Faculty of Science, Masaryk University, Brno, Czech Republic, 2 Department of Pediatric Oncology, University Hospital Brno and Faculty of Medicine, Masaryk University, Brno, Czech Republic, 3 International Clinical Research Center, St. Anne's University Hospital and Faculty of Medicine, Masaryk University, Brno, Czech Republic, 4 1st Department of Pathological Anatomy, St. Anne's University Hospital and Faculty of Medicine, Masaryk University, Brno, Czech Republic, 5 Department of Complex Oncology Care, Masaryk Memorial Cancer Institute, Brno, Czech Republic

* veselska@sci.muni.cz

Abstract

Pancreatic ductal adenocarcinoma (PDAC) remains one of the most lethal malignancies. Its dismal prognosis is often attributed to the presence of cancer stem cells (CSCs) that have been identified in PDAC using various markers. However, the co-expression of all of these markers has not yet been evaluated. Furthermore, studies that compare the expression levels of CSC markers in PDAC tumor samples and in cell lines derived directly from those tumors are lacking. Here, we analyzed the expression of putative CSC markers—CD24, CD44, epithelial cell adhesion molecule (EpCAM), CD133, and nestin—by immunofluorescence, flow cytometry and quantitative PCR in 3 PDAC-derived cell lines and by immunohistochemistry in 3 corresponding tumor samples. We showed high expression of the examined CSC markers among all of the cell lines and tumor samples, with the exception of CD24 and CD44, which were enriched under *in vitro* conditions compared with tumor tissues. The proportions of cells positive for the remaining markers were comparable to those detected in the corresponding tumors. Co-expression analysis using flow cytometry revealed that CD24+/CD44+/EpCAM+/CD133+ cells represented a significant population of the cells (range, 43 to 72%) among the cell lines. The highest proportion of CD24+/CD44+/EpCAM+/CD133+ cells was detected in the cell line derived from the tumor of a patient with the shortest survival. Using gene expression profiling, we further identified the specific pro-tumorigenic expression profile of this cell line compared with the profiles of the other two cell lines. Together, CD24+/CD44+/EpCAM+/CD133+ cells are present in PDAC cell lines derived from primary tumors, and their increased proportion corresponds with a pro-tumorigenic gene expression profile.

Introduction

Pancreatic ductal adenocarcinoma (PDAC) is a highly lethal malignancy that represents the fourth leading cause of cancer-related deaths in Western countries [1]. PDAC has no early warning signs or symptoms; therefore, most patients present with advanced disease. The dismal prognosis of PDAC is primarily due to its late diagnosis, which is often accompanied by metastatic disease and high resistance of the primary tumor to chemotherapy and radiotherapy [2]. Despite recent advances in the diagnosis and treatment of pancreatic cancer, its incidence almost equals its mortality rate, and the 5-year survival rate does not generally reach 5% [1].

PDAC is a type of solid tumor in which transformed cells with stemness properties, termed cancer stem cells (CSCs), have been identified [3–5]. CSCs represent a subpopulation of tumor cells that can self-renew and undergo multilineage differentiation and that possess high tumorigenic potential *in vivo*. CSCs are highly resistant to conventional chemotherapy and radiotherapy and are considered a cause of tumor relapse after eradication of the tumor bulk.

The first evidence for the existence of CSCs in PDAC was reported by two groups in 2007 [3,4]. First, Li *et al.* demonstrated that the combination of cell surface markers CD44, CD24, and epithelial cell adhesion molecule (EpCAM; epithelial-specific antigen, ESA) identified a highly tumorigenic subpopulation of PDAC cells with stem cell properties [3]. Later, Hermann *et al.* reported pancreatic CSCs that were defined by the expression of prominin-1 (CD133) [4]. Since then, other putative markers of pancreatic CSCs have been found, including nestin, CXCR4, c-Met, and aldehyde dehydrogenase 1 [1, 6]. Some of these putative markers were also tested in combination with those first described. For example, c-Met^{high} cells were found to be more tumorigenic if they co-expressed CD44 [7]. CD133$^+$/CXCR4$^+$ cells were reported to have increased migration ability *in vitro*, and they also demonstrated metastatic potential in a mouse model [4]. However, a comprehensive study that has evaluated the co-expression of CD44, CD24, EpCAM and CD133 has not yet been conducted. Although Hermann *et al.* noted a 14% overlap among CD44$^+$/CD24$^+$/EpCAM$^+$ and CD133$^+$ cell populations in their pioneering study, this result was obtained in only one pancreatic cell line that was derived from a metastatic tumor and not from a primary tumor [4]. Similar to other combinations of CSC markers, the CD24$^+$/CD44$^+$/EpCAM$^+$/CD133$^+$ phenotype might more accurately identify true pancreatic CSCs. Thus, in the first step, the possible overlap among CD24$^+$/CD44$^+$/EpCAM$^+$ and CD133$^+$ cell populations in cell lines derived from primary PDAC should be determined. Additionally, it remains unknown to what extent the expression levels of CSC markers change under *in vitro* conditions because no study has compared the expression levels of CSC markers in PDAC tumor samples and in cell lines derived directly from those tumors.

Therefore, we performed a detailed expression analysis of the most frequently discussed putative markers of CSCs in PDAC (i.e., CD24, CD44, EpCAM, CD133, and nestin) in both human primary tumor samples and in the respective cell lines derived from those tumors. For the first time, we also examined the co-expression of CD24, CD44, EpCAM, and CD133 in cell lines derived from primary PDACs. Furthermore, these cell lines were subjected to expression profiling analysis to identify genes, the functions of which may correlate with the presence of CSC markers. We found that CD24$^+$/CD44$^+$/EpCAM$^+$/CD133$^+$ cells represented a significant subpopulation in these cell lines, and their increased proportion corresponded to a pro-tumorigenic gene expression profile.

Materials and Methods

Primary cell lines and tumor samples

Three PDAC primary cell lines were included in this study: P6B, P28B and P34B. These cell lines were derived from tissue samples of corresponding primary tumors. These tumor samples

Table 1. Description of patient cohort and derived cell lines.

Tumor sample	Gender	Age	Diagnosis	Localization	Grade	Stage	OS	PFS	Cell line
P6	M	66	PDAC	Head	3	pT3N1M0	33	21	P6B
P28	M	49	PDAC	Head	3	pT3N0M0	9	9	P28B
P34	F	62	PDAC	Body	2	pT3N1M0	21	11	P34B

Gender: M, male; F, female. Age at the time of diagnosis: years. Localization: Head, head of the pancreas; Body, body of the pancreas. Grade: 2, moderately differentiated; 3, poorly differentiated. OS, overall-free survival: months. PFS, progression free survival: months.

doi:10.1371/journal.pone.0159255.t001

were obtained from patients undergoing pancreatic resection surgery as a part of standard diagnostic therapeutic procedures for PDAC, and they were de-identified to comply with the Czech legal and ethical regulations governing the use of human biological material for research purposes (Act No. 372/2011 Coll. on Health Services, paragraph 81, article 4, letter a). The patients signed a written consent containing information on this issue. Resection specimens were routinely processed at the department of pathology and during the gross inspection, the pathologist (MH) obtained the tumor tissue samples for a derivation of cell lines. For immuno-histochemical (IHC) analysis, formalin-fixed, paraffin-embedded (FFPE) tumor tissue samples primarily taken for diagnostic purposes were used and selected by the pathologist (MH) who also performed the standard histopathological diagnostic procedures. A previously described protocol was used to generate the primary cultures [8]. A description of the cohort is provided in Table 1.

Cell cultures

The cell lines were cultured in DMEM supplemented with 20% fetal calf serum, 2 mM gluta-mine, 100 IU/ml penicillin, and 100 μg/ml streptomycin (all purchased from GE Healthcare Europe GmbH, Freiburg, Germany). The cells were maintained under standard conditions at 37°C in an atmosphere containing 5% CO_2 and were subcultured one or two times per week.

Immunohistochemistry

IHC detection was performed on FFPE samples of primary tumors, as mentioned above. Sections that were cut at a thickness of 4 μm were applied to positively charged slides, deparaffinized in xylene and rehydrated through a graded alcohol series. Antigen retrieval was performed in a calibrated pressure chamber Pascal (Dako, Glostrup, Denmark) for each antibody as follows: for nestin and CD133, the sections were heated in Tris/EDTA buffer (Dako) at pH 9.0 for 40 min at 97°C; for CD24, CD44 and EpCAM, the sections were heated in citrate buffer (Dako) at pH 6.1 for 4 min at 117°C. Endogenous peroxidase activity was quenched with 3% hydrogen peroxide in methanol for 20 min, followed by incubation at room temperature (RT) with the primary antibody (S1 Table). For nestin, the Vectastain Elite ABC kit using a streptavidin-biotin horseradish peroxidase (HRP) detection method was used (Vector Laboratories, Burlingame, CA, USA). For CD133 and EpCAM, the EnVision+ Dual Link system-HRP without avidin or biotin was used for detection (Dako). The expression of CD44 was visualized using an EXPOSE Rabbit-specific HRP/DAB detection kit (Abcam, Cambridge, UK), while the expression of CD24 was visualized using an ImmunoCruz ABC Staining system (Santa Cruz Biotechnology, Inc., Dallas, TX, USA). 3,3′-diaminobenzidine (DAB) (Dako) was used as the chromogen. Samples that were incubated without the primary antibodies served as negative controls. CD133- and nestin-positive endothelial cells in the tumor tissue samples served as internal positive controls, while glioblastoma multiforme tissue served as an external

positive control for nestin. For EpCAM, CD44 and CD24, colon carcinoma, urinary bladder tissue and lymph node tissue, respectively, served as the positive controls. An evaluation of all IHC results was performed using an Olympus BX51 microscope and an Olympus DP72 camera with uniform settings. All immunostained slides were evaluated at 400× magnification.

Immunofluorescence

Indirect immunofluorescence (IF) was performed as previously described [9]. The primary and secondary antibodies that were used in these experiments are listed in S1 Table; a mouse monoclonal anti-α-tubulin served as the positive control. An Olympus BX-51 microscope was used for sample evaluation; micrographs were captured using an Olympus DP72 CCD camera and were analyzed using the Cell^P imaging system (Olympus, Tokyo, Japan).

Flow cytometry

Flow cytometry was performed on either fixed or live cells. Briefly, cells were detached from the culture flask with Accutase (Life Technologies, Carlsbad, CA, USA) and were washed in PBS. Regarding cell surface labeling, live cells were incubated in 3% BSA for 10 minutes. For both cell surface and intracellular labeling, cells were fixed in 3% paraformaldehyde (Sigma) for 30 minutes, washed twice in PBS and incubated in 3% BSA for 10 minutes. All subsequent labeling was performed at 37°C for fixed cells or at 4°C for live cells. Each sample was divided into two, and in the parallel sample, the respective isotype controls were used instead of the primary antibodies. A list of antibodies used in this study is provided in S1 Table. Briefly, the sample was washed twice with 3% BSA, incubated with the mouse monoclonal CD133 antibody for 30 minutes, and washed twice in 3% BSA. A secondary donkey anti-mouse Alexa488-conjugated antibody was applied in the same manner. After two additional washes, primary conjugated antibodies against CD24, CD44 and EpCAM were added to the sample and incubated for 30 minutes. Finally, the sample was washed four times with PBS and was subjected to analysis using FACSVerse (BD Biosciences, San Jose, CA, USA). Side scatter and forward scatter profiles were used to eliminate cell doublets. At least 10,000 events were collected per sample, and the data were analyzed using FlowJo X software (Tree Star, Inc., Ashland, OR, USA). Positive cells were evaluated relative to the respective isotype control; Boolean gating was applied to determine the cells that co-expressed the CSC markers.

Real-Time Quantitative Reverse Transcription PCR (qRT-PCR)

Regarding qRT-PCR of PDAC cell lines, total RNA was extracted and reverse transcribed as previously described [10]. Quantitative PCR was performed in a volume of 10 μl using the KAPA SYBR® FAST qPCR Kit (Kapa Biosystems, Wilmington, MA, USA) and 7500 Fast Real-Time PCR System (Applied Biosystems, Foster City, CA, USA). At least three technical replicates were analyzed for each sample. For microarray validation experiments, three biological replicates (different cell passages) of each cell line were used. The data were analyzed by 7500 Software v. 2.0.6 (Applied Biosystems) and relative quantification (RQ) of gene expression was calculated using $2^{-\Delta\Delta CT}$ method [11]; heat shock protein gene (*HSP90AB1*) was used as the endogenous reference control. The primer sequences used are listed in S2 Table.

Gene expression profiling

Total RNA was extracted using the GenElute™ Mammalian Total RNA Miniprep Kit (Sigma-Aldrich; St. Louis, MO, USA). Total RNA with a purity ratio of 260/280>1.7 and an integrity (RIN)>7.5 (as measured by an Agilent 2010 Bioanalyzer; Agilent Technologies, Santa Clara,

CA, USA) was transcribed into cDNA (Ambion WT Expression Kit), labeled and hybridized to the Affymetrix GeneChip® Human Gene ST 1.0 array and processed through a complete Affymetrix workflow (all from Affymetrix, Santa Clara, CA, USA). Raw microarray data are available in the ArrayExpress database (www.ebi.ac.uk/arrayexpress) under accession number E-MTAB-4055. Affymetrix power tools were used to normalize raw CEL files at the gene level. Robust multiarray averaging (RMA) normalization and complete annotation files were selected. Gene ontology analysis was performed using the GOTERM_BP_FAT database in the DAVID functional annotation tool [12, 13]. Cytoscape v. 3.1.1 [14] with the Reactome Functional Interaction (FI) plug-in was used for functional protein interaction network analysis. The Reactome FI plug-in gene set analysis tool was selected to include interactions from the Reactome FI network 2013 version and FI annotations.

Statistical analysis

The qRT-PCR validation data were analyzed using one-tailed Mann-Whitney U test. $P < 0.01$ was considered statistically significant.

Results

CSC markers were highly expressed in PDAC-derived cell lines compared with PDAC tumor tissues

To address the expression of the putative CSC markers CD24, CD44, EpCAM, CD133, and nestin in pancreatic cancer, we used three cell lines (P6B, P28B, and P34B) derived from PDAC tumor tissues and three corresponding FFPE tumor samples (Table 1). Initially, the expression of individual CSC markers in the cell lines was assessed by IF (Fig 1). Using this method, the expression of all of the examined CSC markers was determined in all three cell lines. The observed pattern of expression of each marker was in accordance with the expected cellular localization of these molecules (Fig 1). Subsequently, the exact quantification of the proportion of cells that were positive for these markers was performed solely by flow cytometry (see below), with the exception of nestin. This was because approximately 95% of the cells in all
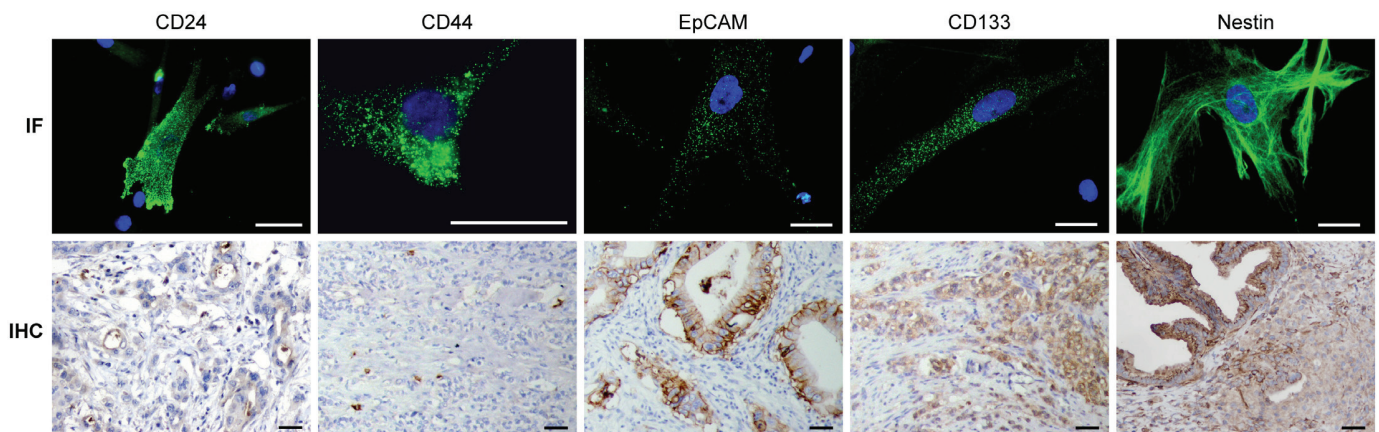
Fig 1. IF and IHC analysis of CSC marker expression in PDAC cell lines and corresponding tumors. Representative images of immunofluorescence (IF) and immunohistochemical (IHC) detection of CD24, CD44, EpCAM, CD133, and nestin expression are shown. For IF analysis, the cells of each PDAC cell line were stained with the appropriate antibodies against the CSC markers (green) and were counterstained with DAPI (blue) to visualize the nuclei. IHC was performed on tumor samples with antibodies that recognize specific markers; positive cells were visualized by DAB staining. Scale bars, 40 μm.

doi:10.1371/journal.pone.0159255.g001

Table 2. IHC analysis of CSC marker expression in PDAC tumor samples.

	Positive cells[a]			Localization of marker expression		
	P6	P28	P34	P6	P28	P34
CD24	++	+	-	apical cytoplasmic, luminal	apical cytoplasmic	–
CD44	-	+/-	-	–	poorly differentiated component	–
EpCAM	+++	+++	+++	membranous	membranous	membranous
Nestin	+++	+++	+++	cytoplasmic	cytoplasmic	cytoplasmic
CD133	++	+++	+	cytoplasmic	cytoplasmic, rarely membranous	cytoplasmic

[a]The percentage of positive tumor cells was categorized into five levels:—(0%), +/- (1–5%), + (6–20%), ++ (21–60%), and +++ (61–100%).

three cell lines were nestin-positive as detected by IF; thus, nestin was omitted from the flow cytometric analysis. IHC was used to evaluate the expression levels of the CSC markers in the corresponding FFPE tumor samples (Fig 1; Table 2). IHC revealed a high percentage of tumor cells that expressed nestin and EpCAM in all of the tumor samples. In addition, CD133 was highly expressed in P6 and P28 tumors, although only a small number of positive cells was identified in P34 tumor tissue. Similarly, CD24 was expressed solely in P6 and P28 tumors. By contrast, CD44^{+} cells were identified in a poorly differentiated component of P28 tumor tissue but not in the other two tumor samples. Based on the IHC results, the P28 tumor was the only one that expressed all of the tested CSC markers.

Next, multicolor flow cytometry was used to evaluate the percentage of cells that were positive for CD24, CD44, EpCAM, CD133, and their combinations in three tumor-derived cell lines (Fig 2; Table 3). For multicolor flow cytometry, we used both live cells and cells fixed in paraformaldehyde. Surprisingly, using the fixed cells, we detected very high percentages of CD24^{+}, CD44^{+}, EpCAM^{+}, and CD133^{+} cells in all of the cell lines examined (Table 3). Additionally, cells that were positive for the combinations of these markers were very common. The CD24^{+}/CD44^{+}/CD133^{+} phenotype was present in approximately 80% of the cells irrespective of the cell line. The percentages of CD24^{+}/CD44^{+}/EpCAM^{+} and CD24^{+}/CD44^{+}/CD133^{+}/EpCAM^{+} cells varied more among the cell lines, but the percentages of each ranged from 43 to 72%. Compared with their respective tumor tissues, the cell lines were markedly enriched for CD24^{+} and CD44^{+} cells. In accordance with the IHC results, the highest frequency of the cells that expressed CD24, CD44, EpCAM, and CD133 was found in the P28B cell line.

Live cells differed greatly from fixed cells with respect to positivity for CSC markers

Due to the surprising prevalence of cells in the PDAC cell lines that were positive for CSC markers, we next used live cells for subsequent flow cytometric analyses. Because fixation itself can permeabilize the cell membranes, this approach enabled us to evaluate the expression of CSC markers only on the cell surface. Using live cells for flow cytometric analyses of the expression of CD24, CD44, EpCAM, and CD133 in the PDAC cell lines, we observed a marked decrease in positivity for these markers in compared with fixed cells (Fig 2; Table 3). In the samples of live cells, CD44 was the only marker that was detected at levels that were similar to those in fixed cell samples. However, the proportions of CD24^{+}/CD44^{+}/EpCAM^{+} and CD24^{+}/CD44^{+}/CD133^{+} cells were markedly lower and ranged from 0.4 to 1.14% and from 0 to 1.43%, respectively. CD24^{+}/CD44^{+}/CD133^{+}/EpCAM^{+} cells were detected only in the P34B cell line.
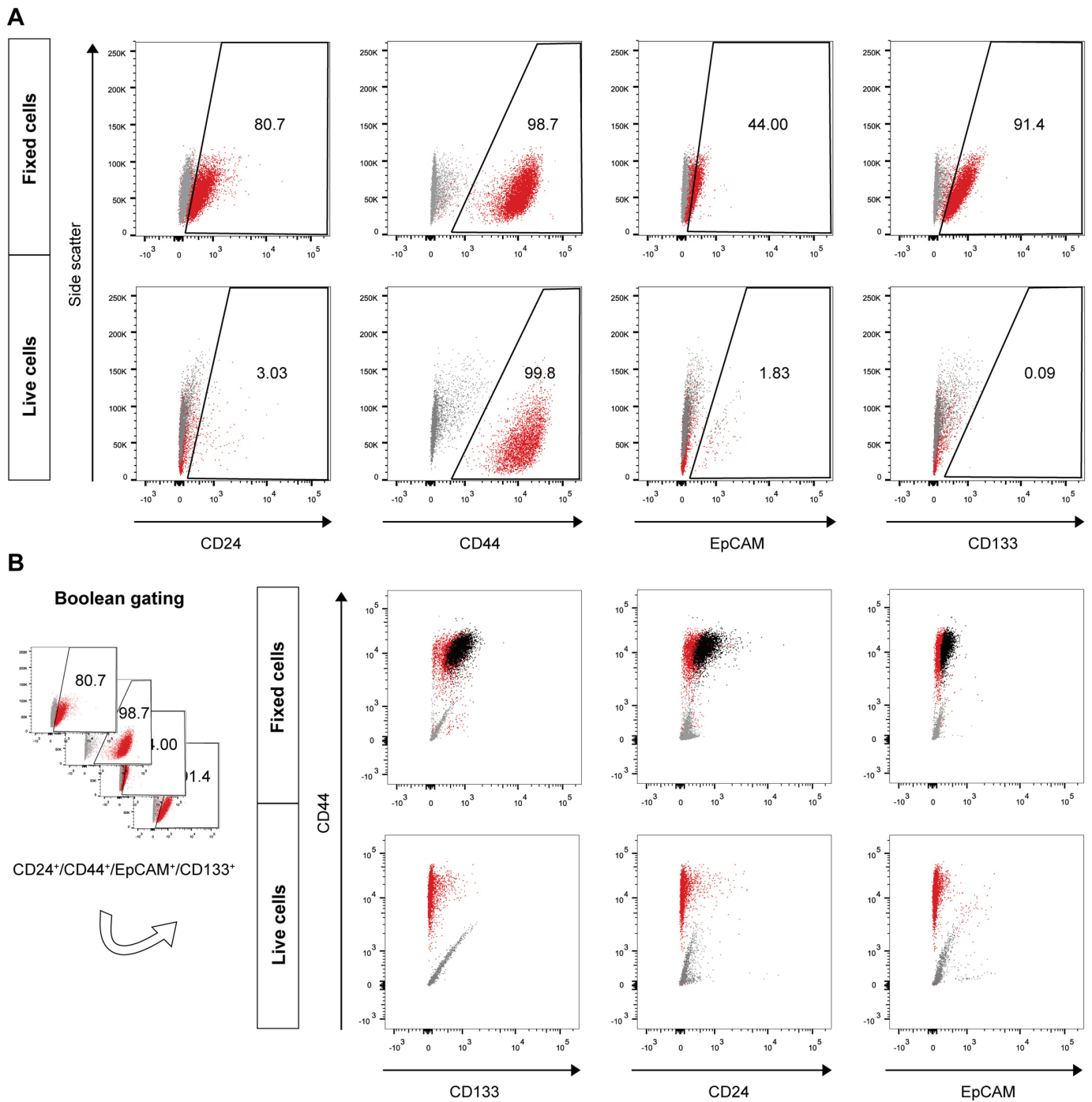
Fig 2. Flow cytometric analysis of the expression of CSC markers in fixed and live PDAC cells. (A) Dot plot diagrams depict the differences in CSC marker expression in PDAC cells when fixed or live cells were used in the flow cytometric analysis. The percentages of cells that were positive for specific markers are marked by numbers in the gated areas. (B) A Boolean gating approach was used to determine the proportion of cells that co-expressed CSC markers. An illustrative Boolean gate of the CD24$^+$/CD44$^+$/EpCAM$^+$/CD133$^+$ population (black) is shown in the dot plot diagrams. Cells stained with matched isotype control antibodies (gray) were used as controls for each CSC marker antibody (red) in both experimental designs (fixed cells and live cells). Representative data for the P6B cell line are shown. For detailed results of CSC marker expression, see Table 3.

doi:10.1371/journal.pone.0159255.g002

Table 3. Flow cytometric analysis of CSC marker expression in PDAC cell lines.

Marker	Fixed cells[a]			Live cells[a]		
	P6B	P28B	P34B	P6B	P28B	P34B
CD24+	80.70	79.10	79.10	3.03	13.00	2.52
CD44+	98.70	96.10	96.70	99.80	98.50	98.20
EpCAM+	44.00	78.60	57.50	1.83	4.08	2.28
CD133+	91.40	94.90	89.60	0.09	0	6.70
CD24+/CD44+/EpCAM+	43.20	72.10	55.10	0.40	0.76	1.14
CD24+/CD44+/CD133+	79.70	78.10	78.00	0.06	0	1.43
CD24+/CD44+/CD133+/EpCAM+	43.20	71.90	55.00	0	0	1.14

[a]Proportions of cells positive for expression of individual CSC marker or combination of markers are indicated as percentages.

doi:10.1371/journal.pone.0159255.t003

Gene expression profiling identified a pro-tumorigenic profile of the P28B cell line that highly co-expressed CSC markers

To verify the expression of CSC markers observed at the protein level and investigate possible differences among the PDAC cell lines, we next evaluated gene expression at the mRNA level. In the first step, we performed qRT-PCR for the genes that encode the CSC markers (Fig 3). qRT-PCR revealed upregulated mRNA expression of the proteins CD24, CD44, and EpCAM in P28B cells. As clinical data show, the P28B cell line was derived from the tumor of the patient with the shortest overall survival (P28, Table 1). IHC, flow cytometry and qRT-PCR results all revealed that P28B cells also expressed the highest levels of CSC markers among the tested cell lines. To investigate this phenomenon more thoroughly, we employed gene expression profile analysis. Using this method, we detected 344 genes that were upregulated (fold-change ≥ 2), and 258 genes that were downregulated (fold-change ≤ 0.5) in the P28B cells compared with the expression profiles of P6B and P34B cell lines.

To analyze the biological functions of the differentially expressed genes in P28B cells, we performed gene ontology analysis (Table 4; S3 Table). Most of the upregulated genes were found to be associated with cell surface receptor signaling (18.8% of the upregulated genes) or
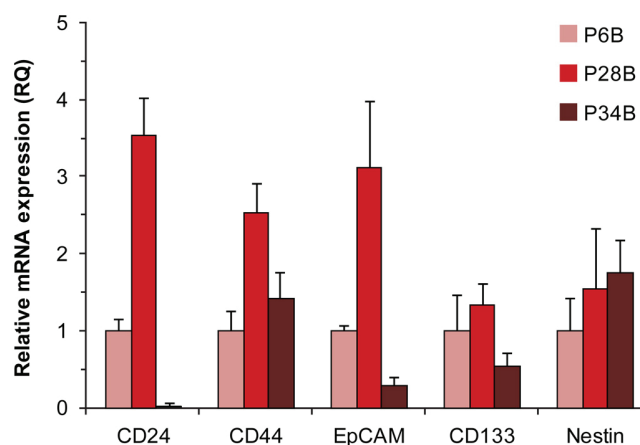
Fig 3. qRT-PCR analysis of CSC marker expression. P6B cell line served as the arbitrary calibrator of the gene expression. The error bars indicate the calculated maximum (RQMax) and minimum (RQMin) expression levels that represent the standard error of the mean expression level (RQ value).

doi:10.1371/journal.pone.0159255.g003

Table 4. Gene ontology analysis of genes differentially expressed in P28B cells.

Biological process	Number of genes	P value
Upregulated genes (fold-change ≥ 2)		
Cell surface receptor linked signal transduction	65	< 0.001
Cell adhesion	32	< 0.001
G-protein coupled receptor protein signaling pathway	30	0.049
Ion transport	29	< 0.001
Cell-cell signaling	28	< 0.001
Regulation of cell proliferation	26	0.007
Response to wounding	22	0.001
Immune response	20	0.061
Cell motion	16	0.034
Downregulated genes (fold-change ≤ 0.5)		
Regulation of cell proliferation	29	< 0.001
Cell motion	20	< 0.001
Regulation of apoptosis	18	0.039
Immune response	17	0.022
Cell adhesion	17	0.024
Mitotic cell cycle	11	0.026
Vasculature development	10	0.006

Upregulated (fold-change ≥ 2) and downregulated (fold-change ≤ 0.5) genes in P28B cells compared with P6B and P34B cells were analyzed for gene ontology. Gene ontology analysis was performed using GOTERM_BP_FAT database in DAVID functional annotation tool.

doi:10.1371/journal.pone.0159255.t004

cell adhesion (9.3%). Downregulated genes were linked to the regulation of cell proliferation (11.2% of the downregulated genes), cell motility (7.6%) or regulation of apoptosis (7%). Furthermore, a review of the literature revealed that the vast majority of the upregulated genes have been reported to have pro-tumorigenic potential, whereas about one-third of the downregulated genes were found to suppress tumorigenesis (Table 5; S4 Table). To validate the results obtained by expression profiling, we performed qRT-PCR analysis of five pro-tumorigenic and five anti-tumorigenic genes in samples from three different passages of each cell line (Fig 4). In agreement with the microarray data, all selected anti-tumorigenic genes were significantly ($P < 0.001$) downregulated in P28B cells, whereas the expression of pro-tumorigenic genes was significantly ($P < 0.001$) upregulated compared with that of P6B and P34B cells. Taken together, these analyses revealed a specific pro-tumorigenic profile of the P28B cell line that was highly enriched in cells that co-expressed CSC markers. By contrast, the lower expression of CSC markers in the P6B and P34B cell lines reflected differences in the expression profiles of these cell lines compared with the profile of P28B cells.

To further analyze the expression profile of P28B cells compared with that of P6B and P34B cells, we performed a functional protein interaction network analysis of the differentially expressed genes. Using Cytoscape software with the Reactome FI plug-in, we created an interaction network that enabled us to visualize expression profiling data combined with information on the interactions of the proteins encoded by the respective genes (Fig 5). This approach clearly showed the most prominent genes whose expression was upregulated or downregulated in P28B cells compared with the other two cell lines. Downregulated genes included *FYN*, *RAC2*, *GNG2*, *PLK1* and *MET*. Of the upregulated genes, *LYN*, *WNT2*, *KIT*, *TEK* (*TIE2*) and *ARRB1* were identified.

Table 5. Differentially expressed genes in P28B cells grouped by their role in tumorigenesis.

Role in cancer	Number of genes	Genes
Upregulated genes (fold-change ≥ 2)		
Pro-tumorigenic	62	ABCC4, ADAMTS7, ADM, ANO1, BAMBI, CD24, CP, CSF1, CXCL14, CXCR7, CYP1A1, EDN1, ELMO1, ENTPD1, EPHA6, F3, FGFR4, FZD6, FZD7, GFRA1, GPR183, GPR56, GPR65, GRIA4, CHRM3, IL6R, ITGB3, JAM2, KIT, LAMA3, LPAR3, LYN, MCAM, MITF, NCAM2, NLK, NOG, NOX4, P2RY1, PMP22, PREX2, PTGER4, PTHLH, RPS6KA5, SCN5A, SEMA4D, SEMA6A, SHC3, SLC4A4, SMAD9, SORT1, TEK, TFAP2C, TRPA1, TRPC3, TRPC6, TRPV2, UCP2, VTN, WFDC1, WNT2, WNT2B
Anti-tumorigenic	10	DSC2, DSC3, FOXF1, GBP2, PENK, PPAP2A, RELN, RGS6, TNFSF10, TXNIP
Mixed	9	ADAMTS8, CD9, DSG2, F11R, CHL1, ITGA8, NPY, SMURF2, UNC5C
Downregulated genes (fold-change ≤ 0.5)		
Pro-tumorigenic	28	ADRA2A, ARHGEF2, BGN, CENPF, CTSS, DLGAP5, ENPP2, GLI3, HORMAD1, CHST11, IL1A, IL1B, IL6, JAG1, KCNMA1, MET, MSX2, NFIB, NRP1, PLAUR, PLK1, PTX3, SEMA3C, SERPINE1, SPOCK1, TPBG, VASH2, VCAN
Anti-tumorigenic	18	CCND2, CDH13, CLDN11, EMILIN2, EPHB2, GAS1, CHST11, KLF4, KYNU, NEFL, PCDH10, PLA2G4A, RARB, SERPINB2, SLIT2, SRPX, TGFBR3, UNC5B
Mixed	16	ASPM, BUB1B, CD74, CDC6, CDKN3, CLU, CTH, ENPEP, FYN, ITGA2, ITGA3, POSTN, PRRX1, RAC2, TOP2A, UACA

The role of individual genes in tumorigenesis was determined based on the literature review (S4 Table).

doi:10.1371/journal.pone.0159255.t005
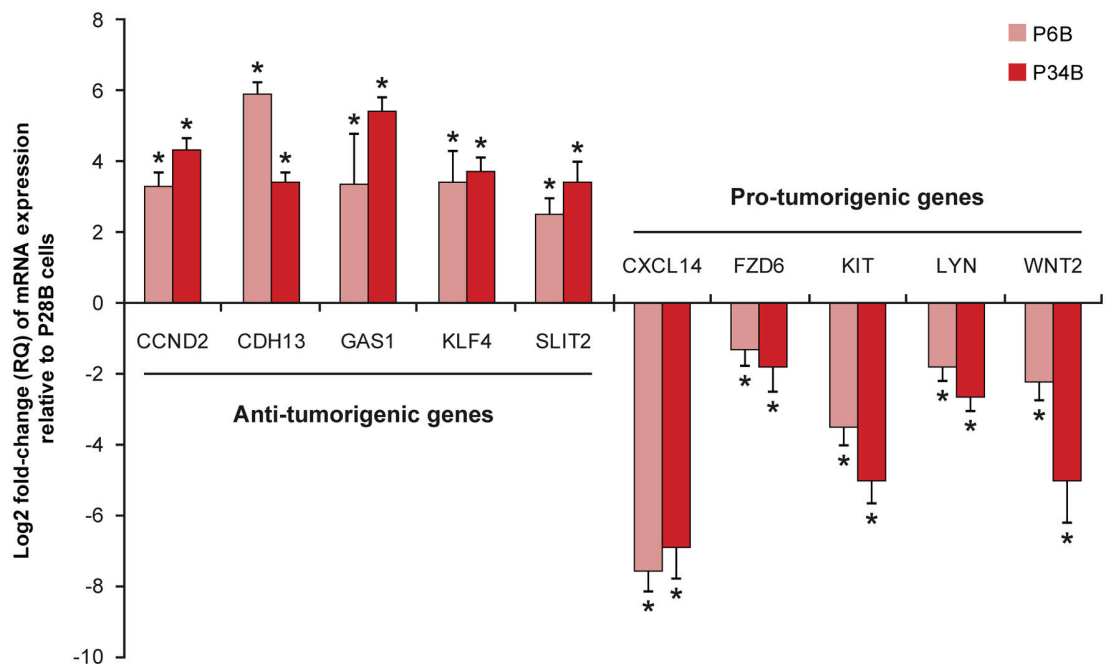
Fig 4. Validation of pro-tumorigenic expression profile of P28B cells by qRT-PCR. Five anti-tumorigenic and five pro-tumorigenic genes were selected based on the microarray data and their expression was validated by qRT-PCR. The graph shows the expression levels of the respective genes in P6B and P34B cells relative to that in P28B cell line, which served as the arbitrary calibrator. The bars represent the mean expression level (RQ value) of three biological replicates; the data are presented in log2 scale. The calculated maximum (RQMax) and minimum (RQMin) expression levels are indicated by error bars. *$P < 0.001$, indicates significant differences from P28B cell line.

doi:10.1371/journal.pone.0159255.g004
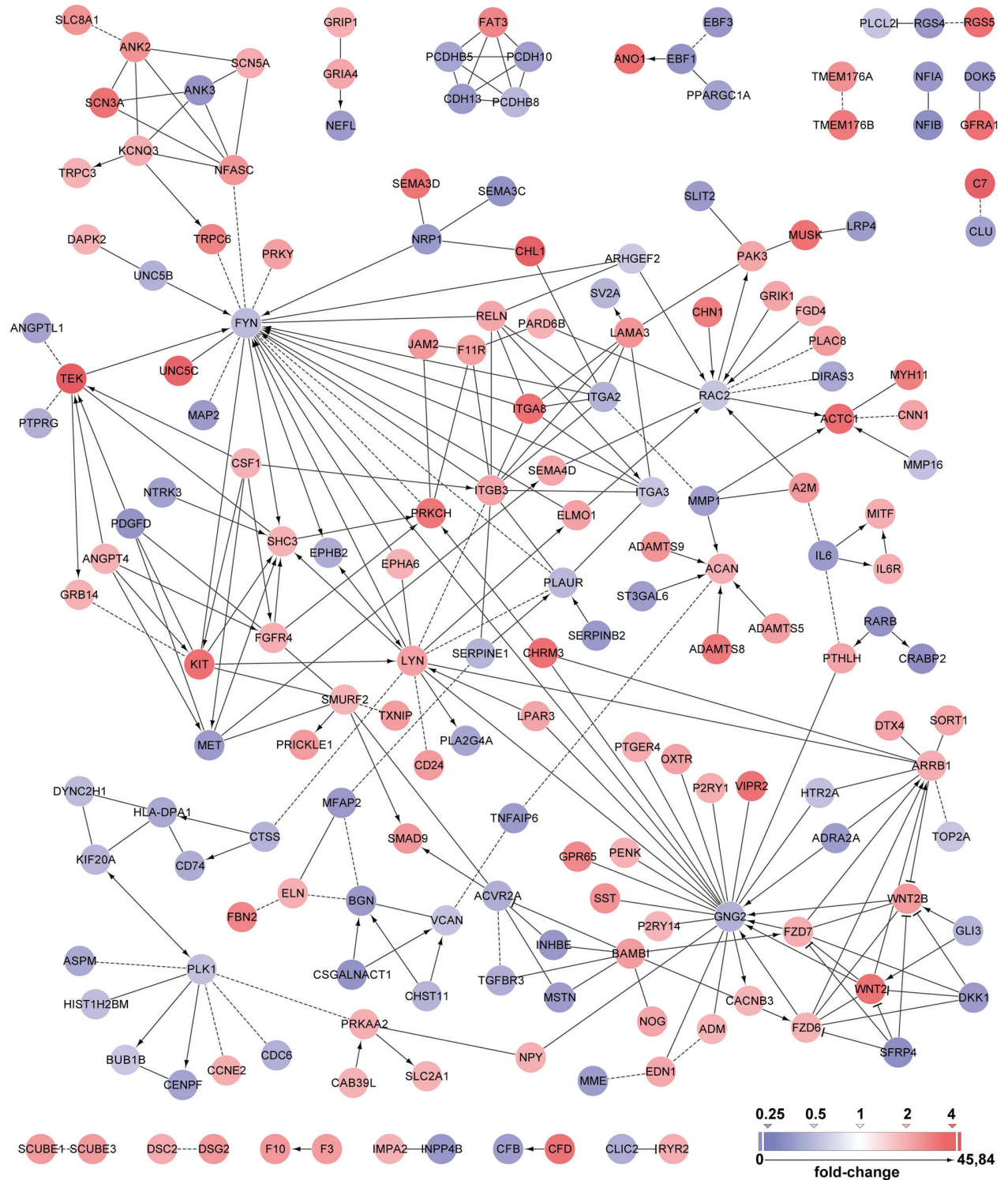
Fig 5. Functional protein network analysis based on a set of differentially expressed genes in P28B cells. A set of upregulated (fold-change ≥ 2) and downregulated (fold-change ≤ 0.5) genes in P28B cells compared with P6B and P34B cells was visualized with Cytoscape. A Reactome FI plug-in was used to analyze the functional network of proteins that are encoded by the respective genes. The fold-change values of gene expression are depicted as tints of blue (downregulated genes) or red (upregulated genes) color.

doi:10.1371/journal.pone.0159255.g005

Together, our results indicated that a high proportion of cells that expressed CSC markers corresponded with a pro-tumorigenic expression profile. In addition, the highest expression of CSC markers was found in the tumor sample taken from the patient with the shortest survival and also in the P28B cell line that was derived from this tumor.

Discussion

Although pancreatic CSCs were described nearly ten years ago as CD44^{+}/ CD24^{+}/EpCAM^{+} cells [3] or CD133^{+} cells [4], no study has determined the co-expression of all of these markers in PDAC either directly in the tumor samples or in the human PDAC cell lines derived from primary tumors. Therefore, the present study was focused on a detailed analysis of the expression of putative CSC markers (CD24, CD44, EpCAM, CD133 and nestin) in 3 pairs of matched primary PDAC tissue samples and derived cell lines.

We detected the expression of all of the examined markers in each tumor cell line. Markedly high levels of nestin were detected in all cell lines and corresponding tumors. Because nestin was expressed in most of the cells, these results suggest that nestin is not suitable as a CSC marker in PDAC, a finding that is in accordance with the results of our previous study [15]. Therefore, we omitted nestin from further flow cytometric co-expression analyses. In the cell lines, flow cytometric analysis of fixed cells revealed a high proportion of cells that expressed CSC markers. IHC confirmed that the expression patterns of the CSC markers were similar in the corresponding tumor tissues, although CD24 and CD44 expression levels were considerably lower. An increased proportion of CD24^{+} and CD44^{+} cells in PDAC cell lines compared with the original tumor tissues might indicate that these cells had a selective advantage in cell culture. This finding is in agreement with other studies that reported high percentages of CD44^{+} cells in pancreatic cell lines compared with PDAC tumor tissues [16, 17]. However, in these studies, the cell lines that were used were not derived from the examined tumors; therefore, it is difficult to determine the baseline expression levels of these markers in the original tumor tissues for comparison. Our study is the first to show that the proportion of CD44^{+} and/ or CD24^{+} cells increases in PDAC-derived cell lines compared with the corresponding tumor tissues. This phenomenon should be considered when performing *in vitro* studies of CSCs in PDAC.

Surprisingly, flow cytometric analysis of fixed cells showed that CD24, CD44, CD133, or EpCAM, as evaluated separately, are expressed in more than 80% of cells irrespective of the cell line and marker (except EpCAM in P6B and P34B cells). These values are much higher than those that have been previously reported [16, 17]. However, when live cells were used in the flow cytometry experiments, we detected a significant decrease in the proportion of CD24^{+}, CD133^{+} and EpCAM^{+} cells (Table 3). Using this approach, the levels of positivity for each of these markers were comparable to those in the aforementioned studies [16, 17]. Only CD44 expression in live cells was detected at the same level as in fixed cells (Table 3). Nevertheless, the reason for this discrepancy is obvious. It is widely known that fixation with paraformaldehyde permeabilizes the cell membranes and therefore enables the antibody to bind to the proteins that are localized within the cell. By contrast, live cells have intact membranes, and antibodies can bind only to extracellular epitopes of the proteins. This means that when fixed cells were used for flow cytometry, we could also detect cells that expressed the CSC markers within the cell.

It was previously thought that most CSC marker proteins performed their functions at the cell surface. However, growing evidence has indicated that the subcellular localization of CSC markers can vary greatly, possibly leading to completely different effects of these proteins on cell signaling, proliferation, invasiveness, and metastatic potential. Therefore, the distinct

subcellular localization of CSC markers may result in different patient outcomes. For example, several studies have reported cytoplasmic localization of CD24 in PDAC [18, 19] as well as in other tumor types [20–27]. Cytoplasmic CD24 expression has been identified as a marker of poor prognosis in gastric cancer [25], colorectal cancer [22, 23], ovarian cancer [20, 21] and malignant neoplasms of the salivary glands [26]. However, little is known concerning the functional role of CD24 within the cell. It has been reported that intracellular CD24 may inhibit the invasiveness of PDAC cells [19]. Nevertheless, a recently published study showed that intracellular CD24 promotes the growth of prostate cancer cells through the inhibition of p14ARF, resulting in decreased levels of p53 and p21 [27]. In that study, the authors also reported that CD24 positivity increased substantially when detection was performed with fixed cells. Recently, very similar findings have also been shown in breast cancer [28]. These observations are in agreement with our results and indicate that a significant amount of CD24 protein may be located in the cytoplasm of PDAC cells.

CD133 is another marker that we examined, and the cell surface immunoreactivity of this protein was significantly lower than the intracellular immunoreactivity. Originally, CD133 was introduced as a marker of pancreatic CSCs that is expressed in approximately 2% of PDAC cells [4]. Several flow cytometric studies then reported a similar low proportion of CD133$^+$ cells (0–28%) in PDAC [16, 17]. However, these results are in contrast with the high (up to 100%) CD133 positivity of cells detected by IHC even in the aforementioned studies [16, 17, 29]. IHC analysis also demonstrated that a significant amount of CD133 was localized within the cytoplasm of PDAC cells [29], a finding that is in agreement with our results (Tables 2 and 3). We and other groups have recently shown that membranous localization of CD133 may be altered in tumor cells and that intracellular CD133 may be involved in cell signaling pathways [9, 30–33]. Furthermore, the correlation of high intracellular CD133 expression with poor prognosis has been found in different types of tumors [33–36]. The results of the present study note the need for better understanding of the role of the intracellular expression of CSC markers in PDAC. Considering that flow cytometric analyses in previously published studies were typically performed to detect cell surface expression in live cells, these studies might have significantly underestimated the expression levels of CD24 (a maximum of 30% CD24$^+$ cells were reported [3, 16, 17]) and CD133 in PDAC cells, which may lead to misinterpretation of the results as discussed by other authors [37].

In the present study, we showed for the first time that cells co-expressing CD24, CD44, EpCAM, and CD133 are present in human PDAC cell lines derived from primary tumors. Moreover, CD24$^+$/CD44$^+$/EpCAM$^+$/CD133$^+$ cells represented a significant population of cells (range, 43.2 to 71.9%) among the cell lines. By contrast, the proportion of cells that co-expressed these markers at the cell surface was very limited (range, 0 to 1.43%) as indicated by flow cytometry with live cells (Table 3). These differences in subcellular localization represent a practical restriction in the isolation of CD24/CD44/EpCAM/CD133-positive and -negative cell populations. Sorting the cells based on cell surface labeling alone could be problematic because a large proportion of cells that express CSC markers within the cell would be sorted into negative fractions, likely compromising the results of further experiments. In a recent comprehensive study, Huang et al. reported that both CSC marker-positive (CSC$^+$) and -negative (CSC$^-$) populations of cells could initiate tumors in immunodeficient mice [38]. For various tumor types, they showed that not only were CSC$^+$ cells able to produce CSC$^-$ cells but CSC$^-$ cells could produce CSC$^+$ cells over long-term period in culture. These results suggested that tumorigenic cells might not be able to be distinguished by common CSC markers due to the phenotypic plasticity of tumor cells. However, the expression of CSC markers was evaluated only by flow cytometry followed by cell sorting. Because the authors used only live (non-permeabilized) cells in their experiments, they might have overlooked the cells that expressed CSC

markers localized in the cytoplasm or cell nucleus. This might also explain why the expression of CSC markers was detected in CSC⁻ cells by PCR. We speculate that the shift of CSC marker proteins from the cytoplasm to the plasma membrane and vice versa could, to a certain extent, explain the phenotypic plasticity of the FACS-sorted cells observed by Huang *et al.* and other groups [38–40]. Nevertheless, we suggest that the detection of CSC markers located within the cell should be included in future studies to validate and extend the data that are based solely on cell surface expression.

Our results revealed that the proportion of CD24⁺/CD44⁺/EpCAM⁺/CD133⁺ cells differed among the cell lines and that the highest number of cells that co-expressed all of these markers was detected in the P28B cell line, which was derived from the tumor of the patient with the shortest overall survival. Therefore, we decided to further analyze the differences among the cell lines using gene expression profiling to identify genes that may be associated with high expression levels of CSC markers. For this reason, the expression profile of P28B cells was compared with the profiles of P6B and P34B cells. Gene ontology analysis and a review of the literature revealed a specific pro-tumorigenic expression profile of P28B cells (Table 5; S4 Table). As high tumorigenic potential is a widely accepted hallmark of CSCs, this result clearly corresponds to the increased proportion of cells that co-express CSC markers in the P28B cell line. However, it should be noted that the pro-tumorigenic expression profile of P28B cells does not imply stemness of CD24⁺/CD44⁺/EpCAM⁺/CD133⁺ cells and subsequent functional *in vivo* assays are needed to determine whether CD24⁺/CD44⁺/EpCAM⁺/CD133⁺ phenotype specifically identifies PDAC cells which fulfill all the criteria defining CSCs. Of the 602 differentially expressed genes in P28B cells, the 10 most prominent genes were identified using functional protein network analysis. These genes could represent potential targets in PDAC because their expression was associated with the co-expression of CSC markers.

Fyn and Lyn are non-receptor tyrosine kinases that belong to the Src family. It has been reported that *LYN* expression is downregulated during embryonic stem cell differentiation, whereas *FYN* expression remains constant [41]. Lyn facilitates glioblastoma cell survival [42], and *LYN* expression is associated with migration and invasion in breast cancer [43]. In a study on pancreatic cancer, the downregulation of Lyn kinase activity reduced invasiveness and migration of the cells [44]. In the present study, we found that *LYN* expression was notably upregulated in P28B cells. In a colorectal cancer study, Su *et al.* reported that the overexpression of CD24 promoted cancer cell invasion through the activation of Lyn and its interaction with Erk1/2 [45]. Patients whose tumors had a lower expression of CD24 or Lyn had a higher survival rate. In accordance with these results, we showed the upregulation of *CD24* and *LYN* in P28B cells, which were derived from the tumors of patient with the shortest overall survival. This indicates that the overexpression of the CD24/Lyn axis might also play a role in PDAC. By contrast, the expression of Fyn kinase was downregulated in P28B cells. The overexpression of Fyn has been detected in various cancers, but its role in cancer is controversial [46–48]. Fyn has been reported to correlate with the metastasis of PDAC, while the inhibition of Fyn decreased liver metastasis in nude mice [47]. By contrast, the expression of Fyn kinase induces the differentiation and growth arrest of neuroblastoma cells [46]. Moreover, Fyn is downregulated in advanced tumor stages, and its downregulation predicts the short-term survival of patients with neuroblastoma. This is in agreement with our results where the downregulation of Fyn was observed in the P28B cell line. However, the exact role of Fyn kinase in PDAC has yet to be determined.

Of the other downregulated genes in P28B cells, *GNG2* was the most prominent. This gene encodes the Gγ2 subunit that forms Gβγ dimers of heterotrimeric G proteins [49]. Although it was reported that the overexpression of GNG2 inhibits the migration and invasiveness of melanoma cells [50], little is known about the function of *GNG2* in PDAC or in other tumor types.

Our study presents the first evidence that the downregulation of *GNG2* is associated with CD24^{+}/CD44^{+}/EpCAM^{+}/CD133^{+} cells and might indicate a poor prognosis in patients with PDAC.

Recently, Yu *et al.* published a study that analyzed the expression profiles of circulating pancreatic tumor cells [51]. They determined that the expression of *WNT2* was upregulated in these cells. Their additional functional experiments showed that Wnt2 promotes anchorage-independent cell survival and the metastatic potential of pancreatic cancer cells. These results are in accordance with our findings as follows: *WNT2* was overexpressed in the P28B cell line, which contains the highest proportion of cells that express CSC markers and is derived from the tumor of the patient with the shortest overall survival. Moreover, expression profiling revealed that inhibitors of Wnt (i.e., DKK1 [52] and SFRP4 [53]) were downregulated in P28B cells compared with the other two cell lines. We also showed the upregulation of WNT2B, FZD7 and FZD6, which are other components of the Wnt signaling pathway. Recently, WNT2B was found to correlate with poor prognosis in PDAC [54], FZD6 expression was reported to be a marker of tumorigenic stem-like cells [55], and FZD7 was required for the maintenance of an undifferentiated phenotype of embryonic stem cells [56]. The upregulation of these genes in P28B cells indicates that the Wnt pathway was activated in cells that were highly positive for CSC markers. These results support the hypothesis that Wnt pathway signaling is of high importance in PDAC tumorigenesis [57].

Conclusions

Our study showed that putative CSC markers (i.e., CD24, CD44, EpCAM, CD133, and nestin) are highly expressed in PDAC. Although the expression of these markers was enhanced in PDAC-derived cell lines, the expression pattern of each individual cell line corresponded to that of the original corresponding tumor specimen. We demonstrated that a large proportion of cells expressed some typically membranous CSC markers (i.e., CD24, EpCAM and CD133) solely within the cell. Thus, these proteins may also play other currently unknown roles in the cytoplasm of PDAC cells, and further research is necessary to determine the biological significance of this finding. Most importantly, our study is the first to show that CD24^{+}/CD44^{+}/EpCAM^{+}/CD133^{+} cells are present in human PDAC cell lines derived from primary tumors. Although CD24^{+}/CD44^{+}/EpCAM^{+}/CD133^{+} cells were common under *in vitro* conditions, we showed that a higher proportion of these cells in the PDAC cell line corresponded with a pro-tumorigenic gene expression profile. Upregulated Wnt signaling, upregulated expression of *LYN*, and downregulation of *FYN* expression were primarily associated with the proportion of cells that co-expressed CSC markers. In summary, these results suggest that CD24^{+}/CD44^{+}/EpCAM^{+}/CD133^{+} cells may be of further interest in the research of PDAC and emphasize the need for further studies that would investigate whether CD24^{+}/CD44^{+}/EpCAM^{+}/CD133^{+} phenotype specifically identifies pancreatic CSCs.

Supporting Information

S1 Table. Primary, conjugated primary and secondary antibodies used in this study.
(PDF)

S2 Table. Primer sequences used for qRT-PCR.
(PDF)

S3 Table. List of upregulated and downregulated genes in P28B cells according to the gene ontology analysis.
(PDF)

S4 Table. The role of differentially expressed genes in tumorigenesis—review of literature.
(PDF)

Acknowledgments

Author Contributions

Conceived and designed the experiments: JS RV. Performed the experiments: JS MH TL PN. Analyzed the data: JS RV JN. Wrote the paper: JS RV MH JN. Provided the patients' clinical data: PK. Participated in the collection of the human tissue samples: MH.

References

1. Balic A, Dorado J, Alonso-Gomez M, Heeschen C. Stem cells as the root of pancreatic ductal adenocarcinoma. Exp Cell Res. 2012; 318(6): 691–704. doi: 10.1016/j.yexcr.2011.11.007 PMID: 22119145

2. Seufferlein T, Bachet JB, Van Cutsem E, Rougier P. Pancreatic adenocarcinoma: ESMO-ESDO Clinical Practice Guidelines for diagnosis, treatment and follow-up. Ann Oncol. 2012; 23 Suppl 7: vii33–40. PMID: 22997452

3. Li C, Heidt DG, Dalerba P, Burant CF, Zhang L, Adsay V, et al. Identification of pancreatic cancer stem cells. Cancer Res. 2007; 67(3): 1030–7. PMID: 17283135

4. Hermann PC, Huber SL, Herrler T, Aicher A, Ellwart JW, Guba M, et al. Distinct populations of cancer stem cells determine tumor growth and metastatic activity in human pancreatic cancer. Cell Stem Cell. 2007; 1(3): 313–23. doi: 10.1016/j.stem.2007.06.002 PMID: 18371365

5. Lee CJ, Li C, Simeone DM. Human pancreatic cancer stem cells: implications for how we treat pancreatic cancer. Transl Oncol. 2008; 1(1): 14–8. PMID: 18607507

6. Matsuda Y, Kure S, Ishiwata T. Nestin and other putative cancer stem cell markers in pancreatic cancer. Med Mol Morphol. 2012; 45(2): 59–65. doi: 10.1007/s00795-012-0571-x PMID: 22718289

7. Li C, Wu JJ, Hynes M, Dosch J, Sarkar B, Welling TH, et al. c-Met is a marker of pancreatic cancer stem cells and therapeutic target. Gastroenterology. 2011; 141(6): 2218–27.e5. doi: 10.1053/j.gastro.2011.08.009 PMID: 21864475

8. Veselska R, Kuglik P, Cejpek P, Svachova H, Neradil J, Loja T, et al. Nestin expression in the cell lines derived from glioblastoma multiforme. BMC Cancer. 2006; 6: 32. PMID: 16457706

9. Nunukova A, Neradil J, Skoda J, Jaros J, Hampl A, Sterba J, et al. Atypical nuclear localization of CD133 plasma membrane glycoprotein in rhabdomyosarcoma cell lines. Int J Mol Med. 2015; 36(1): 65–72. doi: 10.3892/ijmm.2015.2210 PMID: 25977066

10. Skoda J, Neradil J, Zitterbart K, Sterba J, Veselska R. EGFR signaling in the HGG-02 glioblastoma cell line with an unusual loss of EGFR gene copy. Oncol Rep. 2014; 31(1): 480–7. doi: 10.3892/or.2013.2864 PMID: 24270553

11. Livak KJ, Schmittgen TD. Analysis of relative gene expression data using real-time quantitative PCR and the $2^{-\Delta\Delta CT}$ method. Methods. 2001; 25: 402–8. PMID: 11846609

12. Huang da W, Sherman BT, Lempicki RA. Bioinformatics enrichment tools: paths toward the comprehensive functional analysis of large gene lists. Nucleic Acids Res. 2009; 37(1): 1–13. doi: 10.1093/nar/gkn923 PMID: 19033363

13. Huang da W, Sherman BT, Lempicki RA. Systematic and integrative analysis of large gene lists using DAVID bioinformatics resources. Nat Protoc. 2009; 4(1): 44–57. doi: 10.1038/nprot.2008.211 PMID: 19131956

14. Shannon P, Markiel A, Ozier O, Baliga NS, Wang JT, Ramage D, et al. Cytoscape: a software environment for integrated models of biomolecular interaction networks. Genome Res. 2003; 13(11): 2498–504. PMID: 14597658

15. Lenz J, Karasek P, Jarkovsky J, Muckova K, Dite P, Kala Z, et al. Clinicopathological correlations of nestin expression in surgically resectable pancreatic cancer including an analysis of perineural invasion. J Gastrointestin Liver Dis. 2011; 20(4): 389–96. PMID: 22187705

16. Kure S, Matsuda Y, Hagio M, Ueda J, Naito Z, Ishiwata T. Expression of cancer stem cell markers in pancreatic intraepithelial neoplasias and pancreatic ductal adenocarcinomas. Int J Oncol. 2012; 41(4): 1314–24. doi: 10.3892/ijo.2012.1565 PMID: 22824809

17. Bunger S, Barow M, Thorns C, Freitag-Wolf S, Danner S, Tiede S, et al. Pancreatic carcinoma cell lines reflect frequency and variability of cancer stem cell markers in clinical tissue. Eur Surg Res. 2012; 49 (2): 88–98. doi: 10.1159/000341669 PMID: 22948659

18. Jacob J, Bellach J, Grutzmann R, Alldinger I, Pilarsky C, Dietel M, et al. Expression of CD24 in adeno-carcinomas of the pancreas correlates with higher tumor grades. Pancreatology. 2004; 4(5): 454–60. PMID: 15256807

19. Taniuchi K, Nishimori I, Hollingsworth MA. Intracellular CD24 inhibits cell invasion by posttranscrip-tional regulation of BART through interaction with G3BP. Cancer Res. 2011; 71(3): 895–905. doi: 10.1158/0008-5472.CAN-10-2743 PMID: 21266361

20. Kristiansen G, Denkert C, Schluns K, Dahl E, Pilarsky C, Hauptmann S. CD24 is expressed in ovarian cancer and is a new independent prognostic marker of patient survival. Am J Pathol. 2002; 161(4): 1215–21. PMID: 12368195

21. Choi YL, Kim SH, Shin YK, Hong YC, Lee SJ, Kang SY, et al. Cytoplasmic CD24 expression in advanced ovarian serous borderline tumors. Gynecol Oncol. 2005; 97(2): 379–86. PMID: 15863133

22. Weichert W, Denkert C, Burkhardt M, Gansukh T, Bellach J, Altevogt P, et al. Cytoplasmic CD24 expression in colorectal cancer independently correlates with shortened patient survival. Clin Cancer Res. 2005; 11(18): 6574–81. PMID: 16166435

23. Choi YL, Xuan YH, Lee SJ, Park SM, Kim WJ, Kim HJ, et al. Enhanced CD24 Expression in Colorectal Cancer Correlates with Prognostic Factors. Korean J Pathol. 2006; 40: 103–11.

24. Bircan S, Kapucuoglu N, Baspinar S, Inan G, Candir O. CD24 expression in ductal carcinoma in situ and invasive ductal carcinoma of breast: an immunohistochemistry-based pilot study. Pathol Res Pract. 2006; 202(8): 569–76. PMID: 16828238

25. Chou YY, Jeng YM, Lee TT, Hu FC, Kao HL, Lin WC, et al. Cytoplasmic CD24 expression is a novel prognostic factor in diffuse-type gastric adenocarcinoma. Ann Surg Oncol. 2007; 14(10): 2748–58. PMID: 17680316

26. Soave DF, Oliveira da Costa JP, da Silveira GG, Ianez RC, de Oliveira LR, Lourenco SV, et al. CD44/CD24 immunophenotypes on clinicopathologic features of salivary glands malignant neoplasms. Diagn Pathol. 2013; 8: 29. doi: 10.1186/1746-1596-8-29 PMID: 23419168

27. Wang L, Liu R, Ye P, Wong C, Chen GY, Zhou P, et al. Intracellular CD24 disrupts the ARF-NPM inter-action and enables mutational and viral oncogene-mediated p53 inactivation. Nat Commun. 2015; 6: 5909. doi: 10.1038/ncomms6909 PMID: 25600590

28. Rostoker R, Abelson S, Genkin I, Ben-Shmuel S, Sachidanandam R, Scheinman EJ, et al. CD24(+) cells fuel rapid tumor growth and display high metastatic capacity. Breast Cancer Res. 2015; 17: 78. doi: 10.1186/s13058-015-0589-9 PMID: 26040280

29. Kim HS, Yoo SY, Kim KT, Park JT, Kim HJ, Kim JC. Expression of the stem cell markers CD133 and nestin in pancreatic ductal adenocarcinoma and clinical relevance. Int J Clin Exp Pathol. 2012; 5(8): 754–61. PMID: 23071857

30. Skoda J, Nunukova A, Loja T, Zambo I, Neradil J, Mudry P, et al. Cancer stem cell markers in pediatric sarcomas: Sox2 is associated with tumorigenicity in immunodeficient mice. Tumor Biol. 2016; doi: 10.1007/s13277-016-4837-0

31. Chen H, Luo Z, Dong L, Tan Y, Yang J, Feng G, et al. CD133/prominin-1-mediated autophagy and glu-cose uptake beneficial for hepatoma cell survival. PLoS One. 2013; 8(2): e56878. doi: 10.1371/journal.pone.0056878 PMID: 23437259

32. Shimozato O, Waraya M, Nakashima K, Souda H, Takiguchi N, Yamamoto H, et al. Receptor-type pro-tein tyrosine phosphatase kappa directly dephosphorylates CD133 and regulates downstream AKT activation. Oncogene. 2015; 34(15): 1949–60. doi: 10.1038/onc.2014.141 PMID: 24882578

33. Huang M, Zhu H, Feng J, Ni S, Huang J. High CD133 expression in the nucleus and cytoplasm predicts poor prognosis in non-small cell lung cancer. Dis Markers. 2015; 2015: 986095. doi: 10.1155/2015/986095 PMID: 25691807

34. Sasaki A, Kamiyama T, Yokoo H, Nakanishi K, Kubota K, Haga H, et al. Cytoplasmic expression of CD133 is an important risk factor for overall survival in hepatocellular carcinoma. Oncol Rep. 2010; 24 (2): 537–46. PMID: 20596644

35. Jao SW, Chen SF, Lin YS, Chang YC, Lee TY, Wu CC, et al. Cytoplasmic CD133 expression is a reli-able prognostic indicator of tumor regression after neoadjuvant concurrent chemoradiotherapy in patients with rectal cancer. Ann Surg Oncol. 2012; 19(11): 3432–40. doi: 10.1245/s10434-012-2394-3 PMID: 22739652

36. Hashimoto K, Aoyagi K, Isobe T, Kouhuji K, Shirouzu K. Expression of CD133 in the cytoplasm is asso-ciated with cancer progression and poor prognosis in gastric cancer. Gastric Cancer. 2014; 17(1): 97–106. doi: 10.1007/s10120-013-0255-9 PMID: 23558457

37. Kristiansen G, Machado E, Bretz N, Rupp C, Winzer KJ, Konig AK, et al. Molecular and clinical dissection of CD24 antibody specificity by a comprehensive comparative analysis. Lab Invest. 2010; 90(7): 1102–16. doi: 10.1038/labinvest.2010.70 PMID: 20351695

38. Huang SD, Yuan Y, Tang H, Liu XH, Fu CG, Cheng HZ, et al. Tumor cells positive and negative for the common cancer stem cell markers are capable of initiating tumor growth and generating both progenies. PLoS One. 2013; 8(1): e54579. doi: 10.1371/journal.pone.0054579 PMID: 23349932

39. Meyer MJ, Fleming JM, Ali MA, Pesesky MW, Ginsburg E, Vonderhaar BK. Dynamic regulation of CD24 and the invasive, CD44posCD24neg phenotype in breast cancer cell lines. Breast Cancer Res. 2009; 11(6): R82. doi: 10.1186/bcr2449 PMID: 19906290

40. Botchkina IL, Rowehl RA, Rivadeneira DE, Karpeh MS Jr, Crawford H, Dufour A, et al. Phenotypic sub-populations of metastatic colon cancer stem cells: genomic analysis. Cancer Genomics Proteomics. 2009; 6(1): 19–29. PMID: 19451087

41. Zhang X, Simerly C, Hartnett C, Schatten G, Smithgall TE. Src-family tyrosine kinase activities are essential for differentiation of human embryonic stem cells. Stem Cell Res. 2014; 13(3 Pt A): 379–89. doi: 10.1016/j.scr.2014.09.007 PMID: 25305536

42. Liu WM, Huang P, Kar N, Burgett M, Muller-Greven G, Nowacki AS, et al. Lyn facilitates glioblastoma cell survival under conditions of nutrient deprivation by promoting autophagy. PLoS One. 2013; 8(8): e70804. doi: 10.1371/journal.pone.0070804 PMID: 23936469

43. Choi YL, Bocanegra M, Kwon MJ, Shin YK, Nam SJ, Yang JH, et al. LYN is a mediator of epithelial-mesenchymal transition and a target of dasatinib in breast cancer. Cancer Res. 2010; 70(6): 2296–306. doi: 10.1158/0008-5472.CAN-09-3141 PMID: 20215510

44. Fu Y, Zagozdzon R, Avraham R, Avraham HK. CHK negatively regulates Lyn kinase and suppresses pancreatic cancer cell invasion. Int J Oncol. 2006; 29(6): 1453–8. PMID: 17088984

45. Su N, Peng L, Xia B, Zhao Y, Xu A, Wang J, et al. Lyn is involved in CD24-induced ERK1/2 activation in colorectal cancer. Mol Cancer. 2012; 11:43. doi: 10.1186/1476-4598-11-43 PMID: 22731636

46. Berwanger B, Hartmann O, Bergmann E, Bernard S, Nielsen D, Krause M, et al. Loss of a FYN-regulated differentiation and growth arrest pathway in advanced stage neuroblastoma. Cancer Cell. 2002; 2 (5): 377–86. PMID: 12450793

47. Chen ZY, Cai L, Bie P, Wang SG, Jiang Y, Dong JH, et al. Roles of Fyn in pancreatic cancer metastasis. J Gastroenterol Hepatol. 2010; 25(2): 293–301. doi: 10.1111/j.1440-1746.2009.06021.x PMID: 19968749

48. Saito YD, Jensen AR, Salgia R, Posadas EM. Fyn: a novel molecular target in cancer. Cancer. 2010; 116(7): 1629–37. doi: 10.1002/cncr.24879 PMID: 20151426

49. Modarressi MH, Taylor KE, Wolfe J. Cloning, characterization, and mapping of the gene encoding the human G protein gamma 2 subunit. Biochem Biophys Res Commun. 2000; 272(2): 610–5. PMID: 10833460

50. Yajima I, Kumasaka MY, Yamanoshita O, Zou C, Li X, Ohgami N, et al. GNG2 inhibits invasion of human malignant melanoma cells with decreased FAK activity. Am J Cancer Res. 2014; 4(2): 182–8. PMID: 24660107

51. Yu M, Ting DT, Stott SL, Wittner BS, Ozsolak F, Paul S, et al. RNA sequencing of pancreatic circulating tumour cells implicates WNT signalling in metastasis. Nature. 2012; 487(7408): 510–3. doi: 10.1038/nature11217 PMID: 22763454

52. Niida A, Hiroko T, Kasai M, Furukawa Y, Nakamura Y, Suzuki Y, et al. DKK1, a negative regulator of Wnt signaling, is a target of the beta-catenin/TCF pathway. Oncogene. 2004; 23(52): 8520–6. PMID: 15378020

53. Ford CE, Jary E, Ma SS, Nixdorf S, Heinzelmann-Schwarz VA, Ward RL. The Wnt gatekeeper SFRP4 modulates EMT, cell migration and downstream Wnt signalling in serous ovarian cancer cells. PLoS One. 2013; 8(1): e54362. doi: 10.1371/journal.pone.0054362 PMID: 23326605

54. Jiang H, Li F, He C, Wang X, Li Q, Gao H. Expression of Gli1 and Wnt2B correlates with progression and clinical outcome of pancreatic cancer. Int J Clin Exp Pathol. 2014; 7(7): 4531–8. PMID: 25120849

55. Cantilena S, Pastorino F, Pezzolo A, Chayka O, Pistoia V, Ponzoni M, et al. Frizzled receptor 6 marks rare, highly tumourigenic stem-like cells in mouse and human neuroblastomas. Oncotarget. 2011; 2 (12): 976–83. PMID: 22249030

56. Fernandez A, Huggins IJ, Perna L, Brafman D, Lu D, Yao S, et al. The WNT receptor FZD7 is required for maintenance of the pluripotent state in human embryonic stem cells. Proc Natl Acad Sci U S A. 2014; 111(4): 1409–14. doi: 10.1073/pnas.1323697111 PMID: 24474766

57. Vaz A, Ponnusamy M, Seshacharyulu P, Batra S. A concise review on the current understanding of pancreatic cancer stem cells. Journal of Cancer Stem Cell Research. 2014; 2: e1004. PMID: 26451384

Zambo I, Hermanova M, Zapletalova D, **Skoda J**, Mudry P, Kyr M, Zitterbart K, Sterba J, Veselska R. Expression of nestin, CD133 and ABCG2 in relation to the clinical outcome in pediatric sarcomas. *Cancer Biomarkers*. 2016;17(1):107-16. (JCR 2016, IF = 2.274; Q3 – Oncology)

Nunukova A, Neradil J, **Skoda J**, Jaros J, Hampl A, Sterba J, Veselska R. Atypical nuclear localization of CD133 plasma membrane glycoprotein in rhabdomyosarcoma cell lines. *International Journal of Molecular Medicine*. 2015;36:65-72. (JCR 2015, IF = 2.348; Q3 – Medicine, Research & Experimental)

Atypical nuclear localization of CD133 plasma membrane glycoprotein in rhabdomyosarcoma cell lines

ALENA NUNUKOVA[1], JAKUB NERADIL[1,2], JAN SKODA[1,3], JOSEF JAROS[4], ALES HAMPL[4], JAROSLAV STERBA[2,3] and RENATA VESELSKA[1,3]

[1]Department of Experimental Biology, Faculty of Science, Masaryk University; [2]Regional Centre for Applied Molecular Oncology, Masaryk Memorial Cancer Institute; [3]Department of Pediatric Oncology, University Hospital Brno; [4]Department of Histology and Embryology, Faculty of Medicine, Masaryk University, 61137 Brno, Czech Republic

Abstract. CD133 (also known as prominin-1) is a cell surface glycoprotein that is widely used for the identification of stem cells. Furthermore, its glycosylated epitope, AC133, has recently been discussed as a marker of cancer stem cells in various human malignancies. During our recent experiments on rhabdomyosarcomas (RMS), we unexpectedly identified an atypical nuclear localization of CD133 in a relatively stable subset of cells in five RMS cell lines established in our laboratory. To the best of our knowledge, this atypical localization of CD133 has not yet been proven or analyzed in detail in cancer cells. In the present study, we verified the nuclear localization of CD133 in RMS cells using three independent anti-CD133 antibodies, including both rabbit polyclonal and mouse monoclonal antibodies. Indirect immunofluorescence and confocal microscopy followed by software cross-section analysis, transmission electron microscopy and cell fractionation with immunoblotting were also employed, and all the results undeniably confirmed the presence of CD133 in the nuclei of stable minor subpopulations of all five RMS cell lines. The proportion of cells showing an exclusive nuclear localization of CD133 ranged from 3.4 to 7.5%, with only minor differences observed among the individual anti-CD133 antibodies. Although the role of CD133 in the cell nucleus remains unclear, these results clearly indicate that this atypical nuclear localization of CD133 in a minor subpopulation of cancer cells is a common phenomenon in RMS cell lines.

Introduction

CD133 (also known as prominin-1) is a glycoprotein that is typically localized to the plasma membrane. The molecule consists of five transmembrane domains, two large extracellular loops, an extracellular N-terminus and an intracellular C-terminus. Eight potential glycosylation sites have been identified within the extracellular domains, with four per loop. Human CD133 is encoded by the *PROM1* gene, which is located in chromosomal region 4p15.32. At least seven CD133 isoforms resulting from alternative splicing have been described in humans (1,2).

CD133 is widely used to identify stem cells, and its glycosylated epitope, AC133, has recently been discussed as a marker of cancer stem cells (CSCs) in various human malignancies (2-4). In our previous studies, we identified CD133-positive cells that presented typical membrane positivity in two of the most common types of pediatric sarcomas, osteosarcoma (5) and rhabdomyosarcoma (RMS) (6). The expression of CD133 in these two solid tumors, as well as the tumorigenicity of CD133-positive cells, has been confirmed by other research groups (7-10). Therefore, CD133 is currently accepted as one of the markers of a CSC phenotype in pediatric sarcomas, including RMS (11-13).

During our recent study aimed at the analysis of CSC markers in pediatric sarcomas, we noted a surprising result: a stable subset of cells in each of five RMS cell lines examined exhibited an exclusive nuclear localization of CD133 (these data are published in this article). To date, a similar localization of this antigen has been described only in one case report of breast cancer (14) and in a large study on lung cancer (15) using immunohistochemical methods, nevertheless, without any verification or systematic description. For this reason, in this study, we sought to analyze this interesting phenomenon in detail using three independent anti-CD133 commercial antibodies (Fig. 1).

Correspondence to: Professor Renata Veselska, Department of Experimental Biology, Faculty of Science, Masaryk University, Kotlarska 2, 61137 Brno, Czech Republic
E-mail: veselska@sci.muni.cz

Materials and methods

Cell culture. Five cell lines derived from pediatric patients with RMS were included in this study: NSTS-8, NSTS-9, NSTS-11, NSTS-22 and NSTS-28. The first three cell lines were described in our previous study (6), and the last two were derived using the same procedure to generate primary cultures (16). All cell lines were authenticated by the immunodetection of MyoD, and the subtype was distinguished using *FKHR* break detection by fluorescence *in situ* hybridization (FISH). Authentication using MyoD detection was performed in the same passages as the experiments; FISH analysis of the *FKHR* break was completed up to passage 10. The cell lines were maintained in Dulbecco's modified Eagle's medium (DMEM) supplemented with 20% fetal calf serum, 2 mM glutamine, 100 IU/ml penicillin and 100 μg/ml streptomycin (all purchased from GE Healthcare Europe GmbH, Freiburg, Germany). The cells were maintained under standard conditions at 37˚C in a humified atmosphere containing 5% CO_2 and were subcultured once or twice per week. The Research Ethics Committee of the School of Science (Masaryk University, Brno, Czech Republic) approved the study protocol, and a written statement of informed consent was obtained from each participant or his/her legal guardian prior to participation in this study. A brief description of the cohort of patients included in this study is provided in Table I.

Indirect immunofluorescence. The cells were cultivated on coverslips in Petri dishes for one day and then rinsed with phosphate-buffered saline (PBS) and fixed with 3% paraformaldehyde (Sigma-Aldrich, St. Louis, MO, USA) at room temperature for 20 min. After washing again with PBS, non-specific binding was blocked with 3% bovine serum albumin (BSA; Sigma-Aldrich) in PBS for 10 min. The cells were then incubated with primary antibody at 37˚C for 60 min, washed three times in PBS and then incubated with the corresponding secondary antibody at 37˚C for 45 min. Rabbit polyclonal anti-CD133 (Cat. no. ab19898, dilution 1:70; Abcam, Cambridge, UK), mouse monoclonal anti-CD133 (clone 17A6.1, Cat. no. MAB4399, dilution 1:100; Millipore, Billerica, MA, USA), mouse monoclonal anti-AC133 (clone AC133, Cat. no. 130-090-422, dilution 1:4; Miltenyi Biotec, Bergisch Gladbach, Germany), and mouse monoclonal anti-α-tubulin antibody (clone: TU-01, Cat. no. 11-250, dilution 1:100; Exbio, Vestec, Czech Republic), which served as a control, were used as the primary antibodies. Anti-rabbit Alexa Fluor 488 (Cat. no. A11008, dilution 1:200) and anti-mouse Alexa Fluor 488 antibody (Cat. no. A11001, dilution 1:200) (both from Invitrogen, Paisley, UK) were used as the secondary antibodies. After a final wash with PBS, the cell nuclei were counterstained with 0.05% Hoechst 33342 (Life Technologies, Carlsbad, CA, USA) for 10 min, and the coverslips were mounted using Dako fluorescence mounting medium (Dako, Glostrup, Denmark). An Olympus BX-51 microscope was used for sample evaluation; micrographs were captured using an Olympus DP72 CCD camera and analyzed using the Cell P imaging system (Olympus, Tokyo, Japan). At least 200 cells were evaluated overall within discrete areas of each sample, and the samples were prepared from at least three independent passages of all examined cell lines. The mean percentages of cells showing exclusive nuclear CD133 localization were determined for entire samples of individual cell lines. For the detailed examination of CD133 nuclear localization, the same protocol for indirect immunofluorescence was employed, and the specimens were then examined using an Olympus FluoView-500 confocal imaging system combined with an inverted Olympus IX-81 microscope. The images were recorded using an Olympus DP70 CCD camera and analyzed using analySIS FIVE software (Soft Imaging System GmbH, Muenster, Germany) and an Olympus FluoView Confocal Laser Scanning Microscope System 4.3.

Transmission electron microscopy (TEM). To perform the immunodetection of CD133 in ultrathin sections, the cells grown on coverslips were rinsed with PBS and fixed in 3% paraformaldehyde (Sigma-Aldrich) and 0.1% glutaraldehyde (AppliChem GmbH, Darmstadt, Germany) in PBS at room temperature for 60 min. Following a PBS rinse and dehydration, the cells were embedded in LR White medium (Polysciences Inc., London, UK). The labeling of the ultrathin sections was performed on grids. CD133 was detected using mouse monoclonal anti-CD133 antibody (dilution 1:25; Millipore) and a gold particle-conjugated secondary antibody (anti-mouse IgG 20 nm gold, Cat. no. ab27242, dilution 1:40; Abcam). Ultrathin sections incubated without primary antibody or with the TU-01 primary monoclonal antibody against α-tubulin (dilution 1:200; Exbio) were used as controls. Following immunodetection, the specimens were contrasted with 2.5% uranyl acetate (PLIVA-Lachema, Brno, Czech Republic) for 10 min and with Reynolds solution (Sigma-Aldrich) for 6 min at room temperature. The specimens were then observed under a Morgagni 268(D) transmission electron microscope (FEI Co., Hillsboro, OR, USA). The images were captured using an Olympus Veleta TEM CCD camera and analyzed using iTEM Olympus Soft Imaging Solution (Olympus).

Immunoblot analysis. To analyze the nuclear and cytoplasmic fractions, a Nuclear Protein Extraction kit (Thermo Fisher Scientific, Rockford, IL, USA) was used according to the manufacturer's instructions. A 20 μl sample of protein extract was loaded onto an 8% sodium dodecyl sulfate (SDS)-polyacrylamide gel and separated by electrophoresis. Subsequently, the proteins were transferred onto polyvinylidene difluoride (PVDF) membranes (Bio-Rad Laboratories, Hercules, CA, USA), blocked in 5% non-fat milk at room temperature for 60 min, and incubated with primary antibodies, rabbit polyclonal anti-CD133 (Abcam), mouse monoclonal anti-α-tubulin (Exbio), or rabbit monoclonal anti-lamin B2 antibody (clone: D8P3U, Cat. no. 12255S; Cell Signaling Technology, Danvers, MA, USA) at a 1:1,000 dilution overnight at 4˚C. Anti-α-tubulin and anti-lamin B2 served as the controls for the purity of the cytoplasmic and nuclear cell fractions, respectively. After washing with Tris-buffered saline (TBS)-Tween-20, the membranes were incubated with the corresponding horseradish peroxidase (HRP)-conjugated secondary antibodies anti-mouse IgG-HRP (cat. no. A9917, dilution 1:5,000; Sigma-Aldrich) and anti-rabbit IgG-HRP antibodies (cat. no. 7074, dilution 1:5,000; Cell Signaling Technology) at room temperature for 60 min. Signal detection was performed using ECL Prime Western Blotting Detection

Table I. Description of patients from whom tumor samples were obtained to establish the rhabdomyosarcoma cell lines and the results concerning the mean percentage of cells with an exclusive nuclear localization of CD133.

Cell line	Gender	Age (years)	RMS type	No. of passages analyzed	Mean percentage of cells with exclusive nuclear localization of CD133		
					Anti-CD133 antibody (rabbit polyclonal)	Anti-CD133 antibody (mouse monoclonal)	Anti-AC133 antibody (mouse monoclonal)
NSTS-8	F	21	A	15-18	4.6	6.1	3.4
NSTS-9	M	17	A	13-18	4.6	5.2	4.1
NSTS-11	F	16	E	11-19	3.8	4.6	6.6
NSTS-22	F	5	A	11-15	4.0	6.0	6.4
NSTS-28	M	8	A	12-16	4.1	5.2	7.5

M, male; F, female; RMS, rhabdomyosarcoma. Tumor type: A, alveolar; E, embryonal.
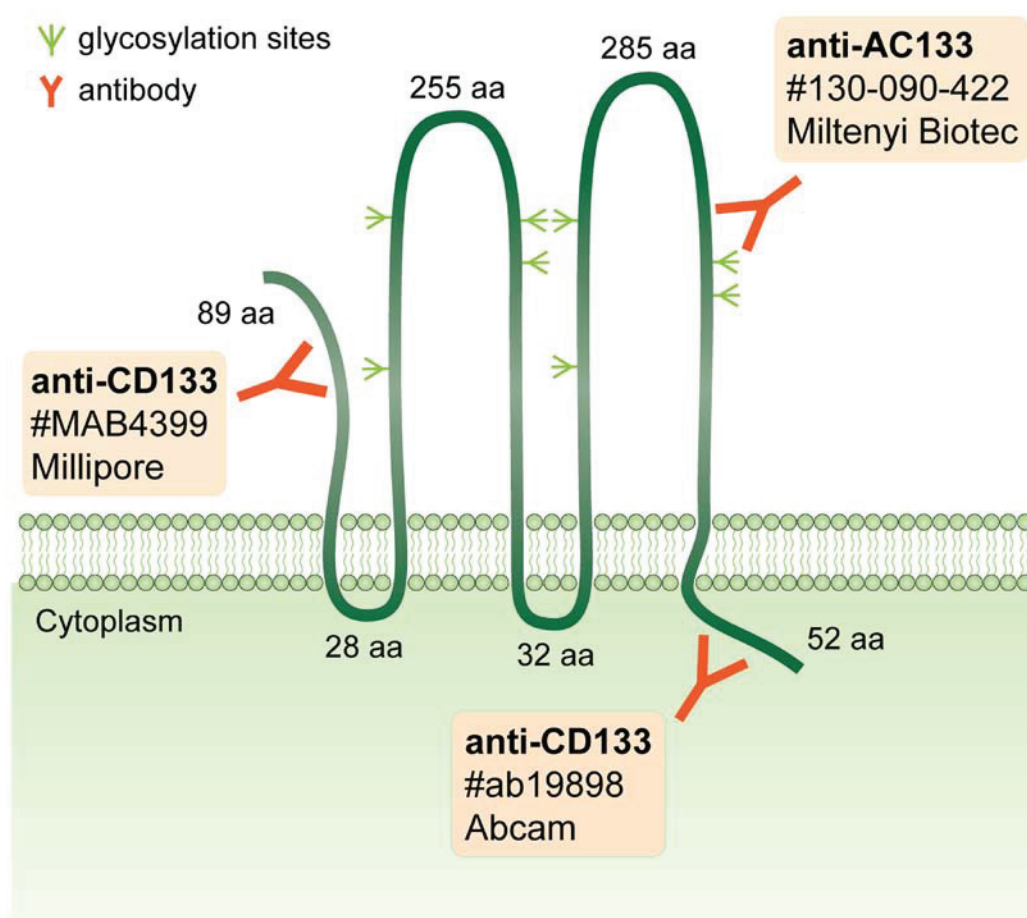

Figure 1. Overview of epitopes of the anti-CD133 and anti-AC133 antibodies used in this study. For each antibody, the catalogue number and manufacturer are indicated. Potential glycosylation sites, as well as length of the N-terminal region, the intracellular and extracellular loops and the C-terminal region of CD133 are depicted.

Reagent (GE Healthcare) according to the manufacturer's instructions.

Results

For all five RMS cell lines examined in this study, we performed a detailed analysis of the presence of cells with nuclear CD133 positivity using indirect immunofluorescence with three independent anti-CD133 antibodies (Fig. 1). A subset of cells showed only nuclear CD133 positivity, i.e., no detectable membrane or cytoplasmic positive signal. The results were markedly similar in all five cell lines analyzed, regardless of the primary antibody utilized, and the proportion ranged from 3.4 to 7.5%, with only minor differences observed among the
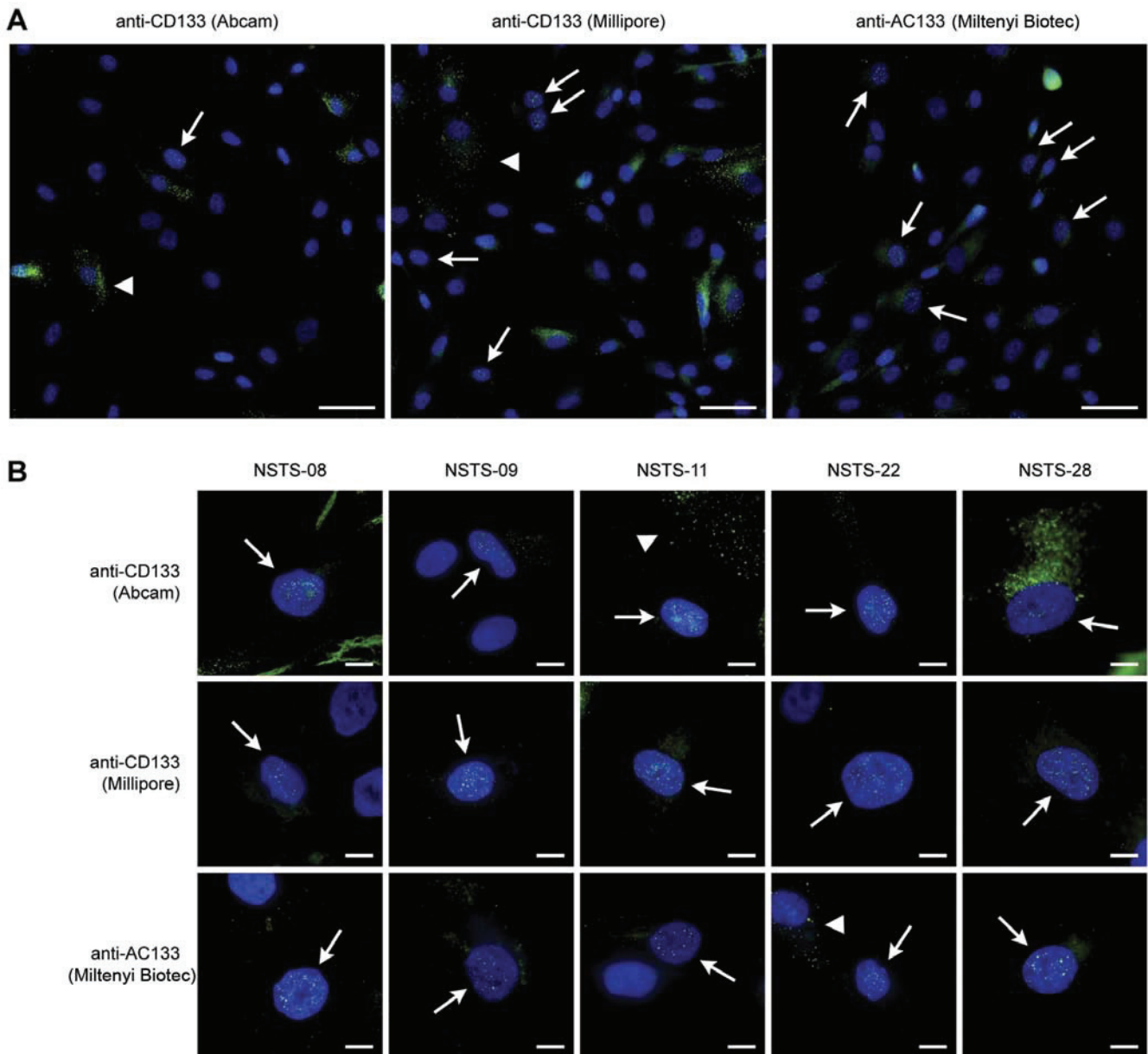
Figure 2. Nuclear localization of CD133 in rhabdomyosarcoma cells. (A) Example of the frequency of cells with CD133 nuclear positivity in the NSTS-11 cell line, as detected using three independent primary antibodies. Cells with exclusive nuclear positivity for CD133 are indicated by arrows; cells with the typical membrane positivity are indicated by arrowheads. (B) Details of cells that exhibited exclusive nuclear positivity for CD133 in all five rhabdomyosarcoma cell lines. CD133 was stained by indirect immunofluorescence using Alexa Fluor 488-labeled secondary antibodies (green), and the nuclei were counterstained with Hoechst 33342 (blue). Scale bars, (A) 50 μm and (B) 10 μm.

individual anti-CD133 antibodies (Fig. 2A and Table I). We also performed a detailed morphological analysis of the cells that exhibited exclusive nuclear positivity for CD133 (Fig. 2B); as can be seen on these micrographs, the pattern of CD133 nuclear positivity was markedly similar in all of the cell lines.

To confirm the presence of CD133 in the nuclei of the RMS cells visualized using indirect immunofluorescence, we employed confocal microscopy and software cross-section analysis through these CD133-positive nuclei (Fig. 3). As is apparent from the results, the localization of the fluorescence signal for CD133 was detected within the cell nuclei both on the software cross-sections (Fig. 3B) and on the plot diagrams of the fluorescence intensity (Fig. 3D).

Furthermore, we also used immunogold labeling with TEM to verify the localization of CD133 in the nuclei of the RMS cells. To avoid any artifacts associated with this methodological approach, the accumulation of three or more gold particles together was considered to indicate a positive signal. The results clearly indicated the presence of CD133 in both the nuclei and nucleoli (Fig. 4A and B).

These results are all completely consistent with the microscopic observations described above (Fig. 2): the software cross-sections also showed clear, punctuate signals for CD133 within the nucleus (Fig. 3B and D), i.e., no diffuse positivity throughout the entire nucleus was observed. Nevertheless, the TEM micrographs also showed the presence of CD133
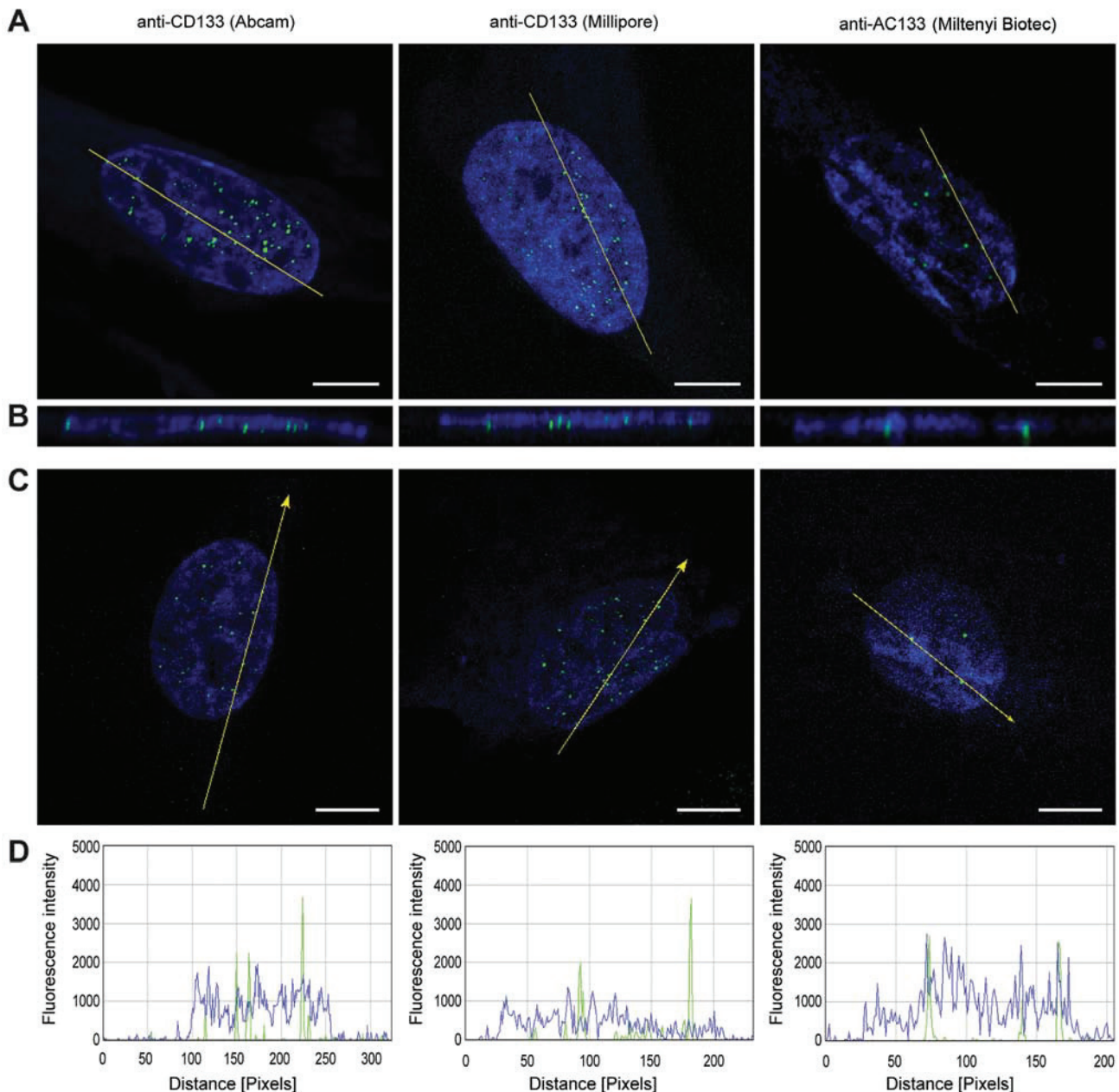
Figure 3. Confocal microscopy analysis of CD133-positive cell nuclei. (A) The planes of software cross-sections through the CD133-positive nuclei are highlighted by simple yellow lines. (B) The cross-sections at these yellow lines are shown at the bottom. (C) The yellow arrows indicate lines drawn across individual CD133-positive nuclei in the confocal image; (D) matching plots reporting the fluorescence intensity according to these arrows are given below. CD133 was stained by indirect immunofluorescence using Alexa Fluor 488-labeled secondary antibodies (green), and nuclei were counterstained with Hoechst 33342 (blue). Scale bars, 5 μm.

in the nucleoli (Fig. 4B), and this observation corresponds with the diffuse positivity for CD133 observed in some of the nucleoli (Fig. 2B). In addition to cells with the typical membrane positivity or exclusive nuclear positivity for CD133, we also sporadically noted clusters of positive signals in the cytoplasm near the cell nucleus or very close to the nuclear envelope (Fig. 4B).

Final confirmation of the results achieved through microscopic methods was carried out by immunoblot analysis of the cytoplasmic and nuclear fractions of all five RMS cell lines. The presence of CD133-specific bands of various intensities was detected in all nuclear fractions, in addition to the strong CD133-specific bands in the cytoplasmic fractions (Fig. 4C).

The purity of both subcellular fractions was confirmed by the presence/absence of α-tubulin and lamin B2. These results are completely in accordance with our other findings (reported above) achieved by indirect immunofluorescence and TEM, i.e., in all five RMS cell lines, the presence of a small subpopulation of cells with CD133 in the nucleus was revealed.

Discussion

As described above, we unexpectedly identified an atypical nuclear localization of CD133 in a relatively stable subset of cells in five RMS cell lines established in our laboratory. To date, this atypical localization of CD133 was described in one
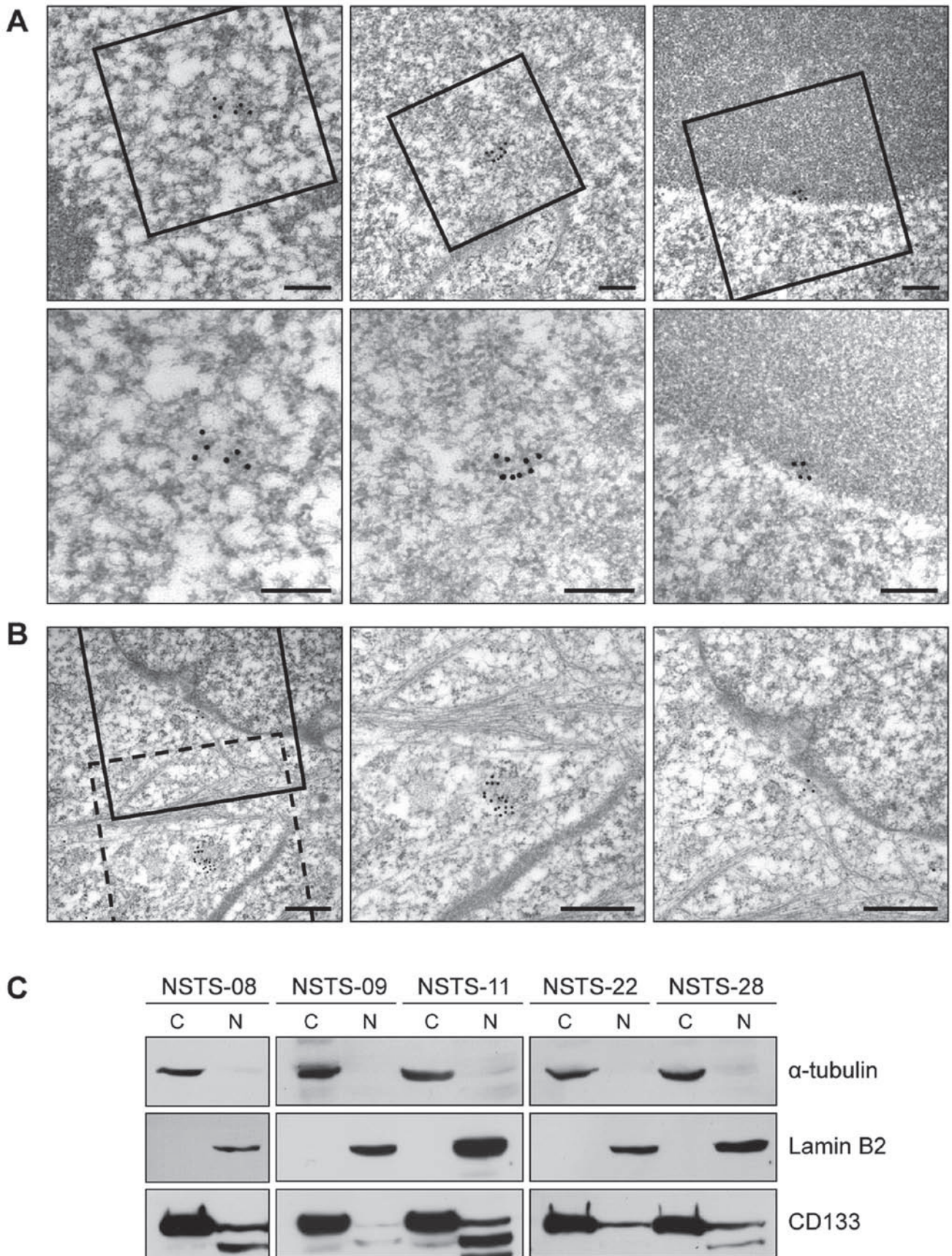
Figure 4. Detection of CD133 in the nuclei of rhabdomyosarcoma cells using transmission electron microscopy and immunoblot analysis. (A) Presence of CD133 in cell nuclei and nucleoli; more detailed images of the positive signal for CD133 in the highlighted square areas are presented on the bottom row. (B) The presence of CD133 in the cytoplasm near the nucleus (dashed square) and very close to the nuclear envelope (solid square). More detailed images of the positive signal for CD133 in the highlighted square areas, as indicated above, are shown on the right side. Representative labeling of CD133 in NSTS-28 cells is shown; CD133 was detected using 20 nm gold particles. Scale bars: (A) 250 nm and (B) 500 nm. (C) Nuclear/cytoplasmic fractionation followed by immunoblotting was performed using a rabbit polyclonal anti-CD133 primary antibody; α-tubulin and lamin B2 were used to confirm the purity of the fractions.

case report on breast cancer (14) and in a large study of prognostic markers on lung cancer (15) using immunohistochemical methods. Nevertheless, published data on CD133 expression in human cancer cells are partly inconsistent, possibly due to different analytical tools, as well as methodological limitations and pitfalls (2). For this reason, results obtained by immunohistochemistry or flow cytometry must be confirmed with alternative antibodies and should be complemented by the utilization of different detection methods of either protein or transcript (2). Furthermore, the glycosylation of CD133 epitopes in relation to the CSC phenotype should be also taken into account, particularly if the antibodies against AC133 epitope are commercially available (17).

In this study, we verified the nuclear localization of CD133 in RMS cells using three independent anti-CD133 antibodies, including both rabbit polyclonal and mouse monoclonal antibodies (Fig. 1). Indirect immunofluorescence and confocal microscopy followed by software cross-section analysis, TEM and cell fractionation with immunoblotting were also employed, and all the results undeniably confirmed the presence of CD133 in the nuclei of stable minor subpopulations of all five RMS cell lines.

These results strongly support the hypothesis that a stable subpopulation of cells with nuclear positivity for CD133 is a common phenomenon in RMS cell lines. Surprisingly, and to the best of our knowledge, similar results have not been reported to date for RMS cells. Although certain micrographs from our previous study showed cells with an accumulation of fluorescent signal for CD133 in the nucleus (6), we assumed that this finding was an artifact resulting from the use of a rabbit polyclonal antibody against CD133, (which was the only anti-CD133 antibody available at the time), although we had never detected similar nuclear positivity for CD133 in osteosarcoma or glioblastoma cell lines using the same antibody (5,18). Other authors investigating CD133 expression in RMS and RMS cell lines have not described the pattern of CD133 positivity in detail, and no micrographs of the individual cells are available in their published articles (9,10).

Very recently, one publication has mentioned the nuclear localization of CD133 in triple-negative breast cancer cells as revealed by immunohistochemistry; nevertheless, this study is a case report based on only one simple descriptive method and therefore does not include any continuing systematic analysis of this apparently interesting finding. Moreover, two of three methods listed in this article, quantitative RT-PCR and flow cytometry, are not suitable for identifying the cell surface, cytoplasmic or nuclear localization of any protein (14).

To date, another study concerning the possible value of CD133 as a prognostic indicator of survival in patients with non-small cell lung cancer (NSCLC) was just published. These interesting results suggest that CD133 expression in the nucleus of NSCLC cells was related to tumor diameter, tumor differentiation and the TNM stage. Kaplan-Meier survival and Cox regression analyses revealed that a high CD133 expression in the nucleus, as well as in the cytoplasm also predicted the poor prognosis of NSCLC (15).

As mentioned above, in addition to cells with the typical membrane positivity or exclusive nuclear positivity for CD133, clusters of positive signals in the cytoplasm near the cell nucleus or very close to the nuclear envelope were also sporadically noted. This finding is in accordance with our previously published observations of sporadic cytoplasmic positivity for CD133 in RMS cells (6), as well as with the deposition of CD133 in cytoplasmic vesicles that has been described in osteosarcoma (19) and the recently suggested mechanism of CD133 internalization and trafficking into lysosomes through interactions between CD133 and the histone deacetylase HDAC6 (20).

Taken together, our results undeniably confirmed the presence of CD133 in the cell nuclei of stable minor subpopulations in RMS cell lines. These results, although surprising and novel, were achieved through three independent methods using three independent antibodies purchased from three separate suppliers.

Nevertheless, the main question of what is the exact role of CD133 in the nucleus of RMS cells remains unanswered. In a previous study on breast cancer, the authors suggested that CD133 in the nucleus may act as transcriptional regulator and is most likely associated with a poor prognosis; however, this conclusion is largely speculative in this case report (14). By contrast, the most recent findings on NSCLC undoubtedly proved the association of nuclear positivity for CD133 poor prognosis in these patients (15).

Although a similar function of another type of surface molecule internalized into the cell nucleus, receptor tyrosine kinases, has been reported (21-23), CD133 belongs to a distinct class of cell membrane proteins, and the analogies to this process are therefore limited. Furthermore, recent studies also discuss the involvement of internalized CD133 in cell signaling pathways, such as the canonical Wnt pathway (20), or report an association between CD133 and the PI3K/Akt pathway (24-26). Regardless, the elucidation of the possible role of CD133 in the nucleus of cancer cells should be based on detailed descriptions of the localization and interactions of CD133 with other molecules in the cell nucleus. These experiments will be the focus of our upcoming study on this interesting phenomenon.

Acknowledgements

References

1. Corbeil D, Karbanová J, Fargeas CA and Jászai J: Prominin-1 (CD133): Molecular and cellular features across species. Adv Exp Med Biol 777: 3-24, 2013.
2. Grosse-Gehling P, Fargeas CA, Dittfeld C, Garbe Y, Alison MR, Corbeil D and Kunz-Schughart LA: CD133 as a biomarker for putative cancer stem cells in solid tumours: Limitations, problems and challenges. J Pathol 229: 355-378, 2013.
3. Friedman GK and Gillespie GY: Cancer stem cells and pediatric solid tumors. Cancers (Basel) 3: 298-318, 2011.
4. Xia P: Surface markers of cancer stem cells in solid tumors. Curr Stem Cell Res Ther 9: 102-111, 2014.
5. Veselska R, Hermanova M, Loja T, Chlapek P, Zambo I, Vesely K, Zitterbart K and Sterba J: Nestin expression in osteosarcomas and derivation of nestin/CD133 positive osteosarcoma cell lines. BMC Cancer 8: 300, 2008.
6. Sana J, Zambo I, Skoda J, Neradil J, Chlapek P, Hermanova M, Mudry P, Vasikova A, Zitterbart K, Hampl A, et al: CD133 expression and identification of CD133/nestin positive cells in rhabdomyosarcomas and rhabdomyosarcoma cell lines. Anal Cell Pathol (Amst) 34: 303-318, 2011.

7. Di Fiore R, Santulli A, Ferrante RD, Giuliano M, De Blasio A, Messina C, Pirozzi G, Tirino V, Tesoriere G and Vento R: Identification and expansion of human osteosarcoma-cancer-stem cells by long-term 3-aminobenzamide treatment. J Cell Physiol 219: 301-313, 2009.

8. Tirino V, Desiderio V, Paino F, De Rosa A, Papaccio F, Fazioli F, Pirozzi G and Papaccio G: Human primary bone sarcomas contain CD133⁺ cancer stem cells displaying high tumorigenicity in vivo. FASEB J 25: 2022-2030, 2011.

9. Walter D, Satheesha S, Albrecht P, Bornhauser BC, D'Alessandro V, Oesch SM, Rehrauer H, Leuschner I, Koscielniak E, Gengler C, *et al*; CWS Study Group: CD133 positive embryonal rhabdomyo-sarcoma stem-like cell population is enriched in rhabdospheres. PLoS One 6: e19506, 2011.

10. Pressey JG, Haas MC, Pressey CS, Kelly VM, Parker JN, Gillespie GY and Friedman GK: CD133 marks a myogenically primitive subpopulation in rhabdomyosarcoma cell lines that are relatively chemoresistant but sensitive to mutant HSV. Pediatr Blood Cancer 60: 45-52, 2013.

11. Veselska R, Skoda J and Neradil J: Detection of cancer stem cell markers in sarcomas. Klin Onkol 25: 2S16-2S20, 2012.

12. Dela Cruz FS: Cancer stem cells in pediatric sarcomas. Front Oncol 3: 168, 2013.

13. Satheesha S and Schafer BW: Cancer stem cells in pediatric sarcomas. In: Stem Cells and Cancer Stem Cells. Hayat MA (ed). Springer, Dordrecht, pp111-126, 2014.

14. Cantile M, Collina F, D'Aiuto M, Rinaldo M, Pirozzi G, Borsellino C, Franco R, Botti G and Di Bonito M: Nuclear localization of cancer stem cell marker CD133 in triple-negative breast cancer: A case report. Tumori 99: e245-e250, 2013.

15. Huang M, Zhu H, Feng J, Ni S and Huang J: High CD133 expression in the nucleus and cytoplasm predicts poor prognosis in non-small cell lung cancer. Dis Markers 2015: 986095, 2015.

16. Veselska R, Kuglik P, Cejpek P, Svachova H, Neradil J, Loja T and Relichova J: Nestin expression in the cell lines derived from glioblastoma multiforme. BMC Cancer 6: 32, 2006.

17. Bidlingmaier S, Zhu X and Liu B: The utility and limitations of glycosylated human CD133 epitopes in defining cancer stem cells. J Mol Med Berl 86: 1025-1032, 2008.

18. Loja T, Chlapek P, Kuglik P, Pesakova M, Oltova A, Cejpek P and Veselska R: Characterization of a GM7 glioblastoma cell line showing CD133 positivity and both cytoplasmic and nuclear localization of nestin. Oncol Rep 21: 119-127, 2009.

19. Tirino V, Desiderio V, d'Aquino R, De Francesco F, Pirozzi G, Graziano A, Galderisi U, Cavaliere C, De Rosa A, Papaccio G and Giordano A: Detection and characterization of CD133⁺ cancer stem cells in human solid tumours. PLoS One 3: e3469, 2008.

20. Mak AB, Nixon AM, Kittanakom S, Stewart JM, Chen GI, Curak J, Gingras AC, Mazitschek R, Neel BG, Stagljar I and Moffat J: Regulation of CD133 by HDAC6 promotes β-catenin signaling to suppress cancer cell differentiation. Cell Rep 2: 951-963, 2012.

21. Wang SC and Hung MC: Nuclear translocation of the epidermal growth factor receptor family membrane tyrosine kinase receptors. Clin Cancer Res 15: 6484-6489, 2009.

22. Mills IG: Nuclear translocation and functions of growth factor receptors. Semin Cell Dev Biol 23: 165-171, 2012.

23. Carpenter G and Liao HJ: Receptor tyrosine kinases in the nucleus. Cold Spring Harb Perspect Biol 5: a008979, 2013.

24. Takenobu H, Shimozato O, Nakamura T, Ochiai H, Yamaguchi Y, Ohira M, Nakagawara A and Kamijo T: CD133 suppresses neuro-blastoma cell differentiation via signal pathway modification. Oncogene 30: 97-105, 2011.

25. Wei Y, Jiang Y, Zou F, Liu Y, Wang S, Xu N, Xu W, Cui C, Xing Y, Liu Y, *et al*: Activation of PI3K/Akt pathway by CD133-p85 interaction promotes tumorigenic capacity of glioma stem cells. Proc Natl Acad Sci USA 110: 6829-6834, 2013.

26. Shimozato O, Waraya M, Nakashima K, Souda H, Takiguchi N, Yamamoto H, Takenobu H, Uehara H, Ikeda E, Matsushita S, *et al*: Receptor-type protein tyrosine phosphatase κ directly dephos-phorylates CD133 and regulates downstream AKT activation. Oncogene 34: 1949-1960 2014.

Sana J, Zambo I, **Skoda J**, Neradil J, Chlapek P, Hermanova M, Mudry P, Vasikova A, Zitterbart K, Hampl A, Sterba J, Veselska R. CD133 expression and identification of CD133/nestin positive cells in rhabdomyosarcomas and rhabdomyosarcoma cell lines. *Analytical Cellular Pathology*. 2011;34:303-18. (JCR 2011, IF = 0.917; Q4 – Oncology)

CD133 expression and identification of CD133/nestin positive cells in rhabdomyosarcomas and rhabdomyosarcoma cell lines

Jiri Sana[a,1], Iva Zambo[b,1], Jan Skoda[a,c], Jakub Neradil[a,c], Petr Chlapek[a,c], Marketa Hermanova[b], Peter Mudry[c], Alzbeta Vasikova[d], Karel Zitterbart[c], Ales Hampl[e], Jaroslav Sterba[c] and Renata Veselska[a,c,*]

[a]Laboratory of Tumor Biology and Genetics, Department of Experimental Biology, School of Science, Masaryk University, Brno, Czech Republic
[b]1st Institute of Pathologic Anatomy, St. Anne's University Hospital and School of Medicine, Masaryk University, Brno, Czech Republic
[c]Department of Pediatric Oncology, University Hospital Brno and School of Medicine, Masaryk University, Brno, Czech Republic
[d]Center of Molecular Biology and Gene Therapy, Department of Internal Medicine - Hematooncology, University Hospital Brno and School of Medicine, Masaryk University, Brno, Czech Republic
[e]Department of Histology and Embryology, School of Medicine, Masaryk University, Brno, Czech Republic

Abstract. *Background*: Co-expression of CD133, cell surface glycoprotein, and nestin, an intermediate filament protein, was determined to be a marker of neural stem cells and of cancer stem cells in neurogenic tumors.

Methods: We examined the expression of CD133 and nestin in ten tumor tissue samples taken from patients with rhabdomyosarcomas and in five rhabdomyosarcoma cell lines. Immunohistochemistry and immunofluorescence were used to examine FFPE tumor tissue samples. Cell lines were analyzed by immunofluorescence, immunoblotting, flow cytometry, and RT-PCR. Functional assays (clonogenic *in vitro* assay and tumorigenic *in vivo* assay) were also performed using these cell lines.

Results: CD133 and nestin were detected in all 10 tumor tissue samples and in all 5 cell lines; however, the frequency of CD133+, Nes+, and CD133+/Nes+ cells, as well as the intensity of fluorescence varied in individual samples or cell lines. The expression of CD133 and nestin was subsequently confirmed in all cell lines by immunoblotting. Furthermore, we observed an increasing expression of CD133 in relation to the cultivation. All cell lines were positive for Oct3/4 and nucleostemin; NSTS-11 cells were also able to form xenograft tumors in mice.

Conclusion: Our results represent the first evidence of CD133 expression in rhabdomyosarcoma tissue and in rhabdomyosarcoma cell lines. In addition, the co-expression of CD133 and nestin as well as results of the functional assays suggest a possible presence of cancer cells with a stem-like phenotype in these tumors.

Keywords: Rhabdomyosarcoma, CD133, nestin, cancer stem cells, stem cell related markers

---

[1] Both authors contributed equally to this work.

*Corresponding author: Renata Veselska, Laboratory of Tumor Biology and Genetics, Department of Experimental Biology, School of Science, Masaryk University, Kotlarska 2, 611 37 Brno, Czech Republic. Tel.: +420 549 49 7905; Fax: +420 549 49 5533; E-mail: veselska@sci.muni.cz.

1. Introduction

CD133 (also known as prominin-1) was originally described in two independent studies as a plasma membrane glycoprotein in mouse neuroepithelial stem cells and as an antigenic marker expressed on the CD34+ population of hematopoietic stem cells in humans [21, 44]. This molecule contains five-transmembrane domains, two large glycosylated extracellular loops, an extracellular N-terminus, and an intracellular C-terminus [21, 44, 46]. CD133 localizes to microvilli and other protrusions of the apical plasma membrane in various cell types [6, 44]. Although the biological function of CD133 is still not known, the above-mentioned localization indicates that CD133 may act as an organizer of plasma membrane protrusions and affect cell polarity as well as interactions with nearby cells and with the extracellular matrix [5, 6, 9].

In humans, this protein is encoded by a gene on locus 4p15.32. The molecular weight of CD133 ranges from 89 to 120 kDa, depending on its glycosylation status [12, 13, 32]. However, truncated forms of CD133 with a lower molecular weight have been described recently [26, 41].

CD133, usually in combination with other specific markers, is widely used to identify stem cells in various human tissues, such as bone marrow [21, 46], CNS [40], prostate [29], or kidney [31]. Immunodetection has also showed that CD133 is frequently expressed in many types of human tumors and tumor cell lines; it was detected in cells from neurogenic tumors [33, 34], prostate carcinomas [4], hepatocellular carcinomas [35], renal carcinomas [3], colorectal carcinomas [28], melanomas [23], pancreatic adenocarcinomas [16], lung carcinomas [11], ovarian carcinomas [14], osteosarcomas [42], endometrial carcinomas [30], acute lymphoblastic leukemias [7], and synovial sarcomas [36].

At present, co-expression of glycosylated CD133 and nestin, a class VI intermediate filament protein, is considered to be a marker of cancer stem cells (CSCs) or tumor initiating cells (TICs). This was experimentally proven in glioblastoma multiforme [19, 27] and in melanoma [23]. Furthermore, the co-expression of CD133 and nestin was also shown in medulloblastomas [33], pilocytic astrocytomas [33], oligoastrocytomas [45], and in osteosarcomas [42].

Here, we present our results regarding CD133 and nestin expression in ten tumor tissue samples taken from patients with rhabdomyosarcomas and in five cell lines derived from these tumors.

2. Material and methods

2.1. Tumor samples

Ten samples of rhabdomyosarcoma tissues were included in this study. These samples were taken from seven patients (5 males, 2 females; age range: 2–21 years old). Formalin-fixed and paraffin-embedded (FFPE) surgical samples of neoplastic tissues were retrieved from the files of the Department of Pathology, University Hospital Brno, Czech Republic, and of the Department of Oncological and Experimental Pathology, Masaryk Memorial Cancer Institute, Brno, Czech Republic. Histological sections stained with hematoxylin-eosin (H-E) were reviewed by two pathologists (IZ and MH), and representative tissue blocks were selected for immunohistochemical and immunofluorescence analysis. Cell lines were derived from respective biopsy samples that were taken from patients surgically treated for rhabdomyosarcoma; all samples for cell cultures were coded and processed in the laboratory in an anonymous manner. The Research Ethics Committee of the University Hospital Brno approved the study protocol, and a written statement of informed consent was obtained from each participant prior to their participation in this study. A description of the cohort of patients included in this study is provided in Table 1.

2.2. PCR analysis of the tumor samples

Reverse transcriptase (RT) two-step nested PCR for fusion transcript PAX3-FKHR and one-step RT-PCR for fusion transcript PAX7-FKHR were used according to published methods [1, 37]. Briefly, extraction of total RNA from a patient's tumor samples was performed using an RNeasy Mini Kit (Qiagen, Hilden, Germany) according to the instruction manual. An initial amount of 1 μg RNA was used for reverse transcription using random hexamers and MuLV reverse transcriptase (Applied Biosystems, Foster City, CA, USA). PCR products were electrophoresed on a 2% agarose gel and visualized after ethidium bromide staining. For all positive assays, the PCR product was confirmed by standard direct nucleotide sequencing.

2.3. Cell cultures

Starting with primary cultures, fresh specimens of tumor tissue were processed as described previously

Table 1
Description of patient cohort and characterization of analyzed tumors

Tumor sample	Gender	Age	Tumor type	Time of biopsy	Translocation in tumor tissue	Cell line	Translocation in cell line
1	M	13	A	DG	positive PAX3/FKHR	-	-
2	M	17	A	DG	positive PAX3/FKHR	NSTS-09	21.3%
3	F	16	E	NACHT	negative PAX3,PAX7/FKHR	NSTS-11	2.7%
4	M	7	E	DG	negative PAX3,PAX7/FKHR	-	-
5	F	2	E	DG	negative PAX3,PAX7/FKHR	NSTS-12	2.3%
6	M	2	A	DG	positive PAX3/FKHR	-	-
7a	F	21	A	DG	positive PAX3/FKHR	NSTS-08	22.3%
7b				NACHT	not available	NSTS-10	20.3%
7c				PROG	positive PAX3/FKHR	-	-
7d				PROG	not available	-	-

Notes: Gender: M, male; F, female. Age at the time of diagnosis: years. Tumor type: A, alveolar; E, embryonal. Time of biopsy: DG, diagnostic; NACHT, after neo-adjuvant chemotherapy; PROG, progression of the disease. Translocation in tumor tissue: translocation *PAX3/PAX7-FKHR* as detected by RT-PCR analysis. Translocation in cell line: *FKHR* break of as detected by FISH analysis.

[42, 43]. The primary cultures were maintained in DMEM supplemented with 20% fetal calf serum, 2 mM glutamine, and antibiotics: 100 IU/ml penicillin and 100 μg/ml streptomycin (all purchased from PAA Laboratories, Linz, Austria) and cultivated under standard conditions at 37°C in an atmosphere of 95% air : 5% CO_2. Once the specimen pieces had attached, the volume of the medium was gradually increased to 5 ml over the next 48 hours. As soon as the outgrowing cells covered approximately 60% of the surface, they were trypsinized, diluted, and transferred into a new flask. A similar procedure was used for further subcultivations of all cell lines that were derived from the primary cultures.

2.4. FISH analysis of the cell lines

Using Poseidon[TM] probes ON FKHR Break (Kreatech Diagnostics, Amsterdam, Netherlands), we examined all the above described rhabdomyosarcoma cell lines. For FISH analysis, cell suspensions were hypotonized with 75 mM KCl and fixed in methanol/acetic acid (3 : 1, vol:vol). Cell suspensions were spread onto microscopic slides and chemically aged in 2 × SSC for 30 min at 37°C. The slides were then dehydrated in 70%, 80%, and 96% ethanol for 2 min each and air-dried. Codenaturation was performed for 5 min at 75°C, and following hybridization, was allowed to proceed overnight at 37°C. Hybridized slides were then washed sequentially in 0.5 × SSC for 3 min at 75°C and 2 × SSC for 1 min at room temperature and were mounted in DAPI Counterstain (Kreatech). An Olympus BX-61 microscope was used

for FISH evaluation. Micrographs were captured by Vosskühler 1300D CCD camera and analyzed using Lucia 4.80 - KARYO/FISH/CGH software (Laboratory Imaging, Prague, Czech Republic). At least 150, but most often 300, interphase nuclei were scored for *FKHR* (13q14) gene status.

2.5. FFPE immunohistochemistry

Immunohistochemical detection of both nestin and CD133 was performed on 4 μm thick tissue sections applied to positively charged slides. The sections were deparaffinized in xylene and rehydrated through a graded alcohol series. Antigen retrieval was performed in a Pascal calibrated pressure chamber (DAKO, Glostrup, Denmark) by heating the sections in modified citrate buffer (DAKO) at pH 6.1 (CD133 IHC) or in Tris/EDTA buffer (DAKO) at pH 9.0 (nestin IHC) for 40 min at 97°C. Endogenous peroxidase activity was quenched in 3% hydrogen peroxide in methanol for 10 min, followed by incubation at room temperature with a rabbit polyclonal antibody against CD133 (No. ab19898, dilution 1 : 200, Abcam, Cambridge, UK) for 60 min or a mouse monoclonal antibody against nestin (clone 10C2, dilution 1 : 200, Millipore, Billerica, MA, USA) for 90 min. A streptavidin-biotin peroxidase detection system was used according to the manufacturer's instructions (Vectastain Ellite ABC Kit, Vector Laboratories, Burlingame, CA, USA); 3,3'-diaminobenzidine was used as a chromogen (DAB, DAKO). Slides were counterstained with Gill's hematoxylin. Tissue sections of glioblastoma multiforme served as external positive controls for the anti-nestin

antibody; Nes+ or CD133+ endothelial cells in rhabdomyosarcoma tissue samples were used as internal positive controls. Negative controls were prepared by incubating samples without primary antibody. Evaluation of immunohistochemical results was performed using a uniform microscope and camera setting (Olympus BX51 microscope and DP70 camera).

2.6. Evaluation of FFPE immunohistochemistry

For CD133, only specific membranous positivity was scored; however, cytoplasmic immunopositivity was observed in a variable proportion of tumor cells in all examined samples (see explanation in discussion). For nestin, cytoplasmic immunostaining was regarded as positive. The intensity of staining and the percentages of positive tumor cells (TC) were evaluated by two pathologists (IZ and MH) independently, using a light microscope at $\times 400$ magnification. At least five discrete foci of neoplastic infiltration were analyzed, and the average staining intensity and the percentage of CD133+ or Nes+ cells of the entire covered area were determined. The percentage of CD133+ or Nes+ TC was categorized into four levels: $\pm$ (<2% CD133+ or Nes+ TC), + (2–10% CD133+ or Nes+ TC), ++ (11–50% CD133+ or Nes+ TC), and +++ (51–100% CD133+ or Nes+ TC). The intensity of immunostaining was graded as very weak ($\pm$), weak (+), medium (++), and strong (+++). The intensity of immunostaining was also evaluated in endothelial cells, which were used as an internal positive control.

2.7. FFPE immunofluorescence

After deparaffinization and rehydration of the tissue sections, antigen retrieval was carried out under same conditions as mentioned above. Rabbit polyclonal anti-CD133 antibody (No. ab19898, dilution 1 : 50, Abcam) or mouse monoclonal anti-nestin antibody (clone 10C2, dilution 1 : 200, Millipore) were used as primary antibodies. Tissue sections were incubated with primary antibodies at room temperature for 30 min or 90 min, respectively. Then appropriate secondary antibodies, i.e., goat anti-rabbit antibody conjugated with TRITC (No. TI-1000, dilution 1 : 100, Vector) or goat anti-mouse antibody conjugated with FITC (No. AP124F, dilution 1 : 50, Millipore) were applied for 45 min or 60 min, respectively. Subsequently, slides

were mounted with mounting medium (No. S3025, Faramount Aqueous Mounting Medium, DAKO). A uniform microscope and camera setting (Nikon Eclipse 80i microscope and DS-Fi1 camera) was used for the evaluation of immunofluorescence results. Micrographs were analyzed using NIS-Elements BR 3.0 software (Laboratory Imaging).

2.8. Evaluation of FFPE immunofluorescence

Both for CD133 and nestin, the frequency of clearly positive cells (membranous positivity for CD133 and cytoplasmic positivity for nestin) was determined as follows: + (sporadically positive TC), ++ (dispersedly positive TC) and +++ (abundant positive TC). In CD133 immunofluorescence, weak cytoplasmic positivity was observed in sporadic TC in all examined cases. The slides were evaluated by two pathologists (IZ and MH) independently, using a fluorescent microscope at $\times 400$ magnification.

2.9. Immunofluorescence of cell lines

To immunostain for CD133 and nestin, cell suspensions at a concentration of 10^4 cells per ml were seeded on glass coverslips and grown under standard conditions for 24 h. Cells were then washed in PBS, fixed with 3% para-formaldehyde (Sigma-Aldrich, St. Louis, USA) in PBS for 20 min at room temperature. The cells were subsequently washed in PBS and incubated for 10 min with 2% BSA (PAA) to block nonspecific binding of the secondary antibodies. CD133 and nestin were visualized by indirect immunofluorescence. Rabbit polyclonal anti-CD133 antibody (No. ab19898, dilution 1 : 100, Abcam) and mouse monoclonal human-specific anti-nestin antibody (clone 10C2, dilution 1 : 200, Millipore) were used as primary antibodies. The cells were treated with primary antibodies at 37°C for 1 h and washed three times in PBS. Corresponding secondary antibodies, i.e., anti-rabbit antibody conjugated with TRITC (No. T6778, dilution 1 : 160, Sigma) or anti-mouse antibody conjugated with FITC (No. F8521, dilution 1 : 160, Sigma), were applied under the same conditions. Finally, the cells were mounted onto glass slides in Vectashield mounting medium containing DAPI (Vector). The cells were observed using an Olympus BX-61 fluorescence microscope. Micrographs were captured with a CCD camera COHU 4910 and ana-

lyzed using Lucia 4.80 software – KARYO/FISH/CGH (Laboratory Imaging, Prague, Czech Republic).

2.10. Evaluation of immunofluorescence on cell lines

The percentage and intensity of immunostaining (immunoreactivity) of CD133+ or Nes+ cells were evaluated at discrete areas of each sample. The samples were prepared from several various passages of all examined cell lines. The average percentage of positive cells and the intensity of immunostaining were determined for entire samples of individual cell lines. The percentage of CD133+ or Nes+ cells was categorized into six levels: (+), ~1% CD133+ or Nes+ cells; +, 1–10% CD133+ or Nes+ cells; +(+), ~10% CD133+ or Nes+ cells; ++, 10–50% CD133+ or Nes+ cells; ++(+), ~50% CD133+ or Nes+ cells; +++, >50% CD133+ or Nes+ cells. The intensity of immunostaining (immunoreactivity) was categorized into three levels: +, weak; ++, medium; +++, strong.

2.11. Flow cytometry

Cell suspensions at identical concentrations were seeded onto Petri dishes ($60 \, cm^2$) and grown under standard conditions. Evaluation of CD133 expression was performed from the second to the sixth day of cultivation at 24 h intervals. For CD133 and isotype control cell surface indirect immunostaining, cells were detached using 1 mM EDTA (PAA), fixed with 3% para-formaldehyde (Sigma) in PBS overnight at $4°C$ and then washed in PBS. The cells were treated either with rabbit polyclonal anti-CD133 primary antibody (No. ab19898, Abcam) or rabbit polyclonal isotype control (No. ab37416, Abcam) at 6 μg/ml for 40 min at $4°C$ and washed in PBS. Anti-rabbit IgG conjugated with FITC (No. F9887, dilution 1 : 160, Sigma) was applied as a secondary antibody under the same conditions. Cytometric analysis was performed using a FACS Canto^TM II (BD Biosciences). Ten thousand events per sample were evaluated using WinMDI 2.8 software. After completion of the flow cytometric analysis, the remaining cell suspensions were mounted onto glass slides and observed using a Nikon Eclipse 80i fluorescence microscope in combination with a DS-Fi1 camera. Micrographs were taken at 24 h intervals using the same microscope and camera settings.

2.12. Immunoblotting

Whole-cell extracts were loaded onto polyacrylamide gels, electrophoresed, and blotted onto polyvinylidene difluoride membranes (Bio-Rad Laboratories GmbH, Germany). The membranes were blocked with 5% nonfat milk in PBS with 0.1% Tween 20 (PBS-T), then incubated either with rabbit polyclonal anti-CD133 primary antibody (No. ab19898, Abcam), mouse monoclonal anti-nestin primary antibody (clone 10C2, Millipore) or mouse monoclonal anti-alpha tubulin primary antibody (clone TU-01, Exbio, Prague, Czech Republic) diluted 1 : 1000 in blocking solution at $4°C$ overnight. After rinsing with PBS-T, the membranes were incubated with corresponding secondary antibodies at room temperature for 45 min; i.e., anti-mouse IgG antibody peroxidase conjugate (No. A9917, Sigma) or anti-rabbit IgG antibody peroxidase conjugate (No. A2074, Sigma) diluted 1 : 5000. Each step was followed by at least three 10-min washes in PBS-T. ECL-Plus detection was performed according to the manufacturer's instructions (Amersham, GE Healthcare, UK).

2.13. PCR analysis of the cell lines

For RT-PCR, total RNA was extracted with GenElute™ Mammalian Total RNA Miniprep Kit (Sigma-Aldrich). For all samples, equal amounts of RNA (25 ng of RNA per 1 μl of total reaction content) was reverse transcribed into cDNA using M-MLV (Top-Bio, Prague, Czech Republic) and oligo-dT (Qiagen) priming. PCR was carried out in 50 μl reactions containing 0,5 μM of each primer and 10 μl of diluted cDNA. Following primer sequences were used: Oct3/4, 5′-GCAAAGCAGAAACCCTCGT-3′ (forward) and 5′-ACACTCGGACCACATCCTTC-3′ (reverse); Nucleostemin, 5′-TGCGAAGTCCAGCAA GTATTG-3′ (forward) and 5′-AATGAGGCACCTGT CCACTC-3′ (reverse); GAPDH, 5′-AGCCACATCGC TCAGACACC-3′ (forward) and 5′-GTACTCAGCGC CAGCATCG-3′ (reverse). PCR conditions include a first step of 4 minutes at $94°C$, a second step of 30 cycles of 30 seconds at $94°C$, 30 seconds annealing step at $60°C$, 45 seconds at $72°C$ and a final step of 5 minutes at $72°C$. Final products were examined by gel electrophoresis on 1% agarose.

2.14. *Clonogenicity assay in vitro*

The cells were trypsinized, single cells were manually transferred with a micropipette under microscope into separate wells of 96-well microtiter plates and were cultivated under standard conditions (see 2.3. for details). A capability of cells to proliferate and to form colonies was examined every two days for two weeks and documented using an Olympus CKX41 inverted microscope in combination with an Olympus SP-350 camera.

2.15. *Tumorigenicity assay in vivo*

Enzymaticaly dissociated cell suspension of NSTS-11 cells at concentration of 1.5×10^6 cells per 100 µl was injected subcutaneously in three 8-week-old female NOD/SCID mice. The mice were examined every three days for the presence of subcutaneous tumors. After appearance of the tumors, the mice were sacrificed and tumor tissue was collected. Each tumor was dissected into two equal parts: one of them was processed for primary culture (see 2.3.), the second was fixed in 10% buffered formalin for 24 hours, routinely processed for histological examination and embedded in paraffin. Tissue sections of FFPE samples were stained with H-E and examined. Immunohistochemical analysis was performed (see 2.5. and 2.6. for details). Monoclonal mouse anti-human desmin (clone

D33, dilution 1 : 100, DAKO), monoclonal mouse anti-human muscle actin (clone HHF35, dilution 1 : 50, DAKO) and polyclonal rabbit anti-human myoglobin (dilution 1 : 500, Novocastra Lab., Newcastle upon Tyne, UK) were employed to confirm myogenic differentiation of xenograft tumors. For desmin IHC, antigen retrieval was performed in a Pascal calibrated pressure chamber (DAKO) by heating the section in modified citrate buffer at pH 6.1. Myoglobin and muscle actin IHC was performed without antigen retrieval. The incubation time for all these primary antibodies was 60 minutes. A peroxidase conjugated polymer detection system was used for desmin, muscle actin and myoglobin detection (EnVision^{TM} + Dual Link, HRP rabbit/mouse, DAKO), 3,3′-diaminobenzidine was used as a chromogen (DAB, DAKO). Detection of nestin and CD133 in xenograft tumors was performed as described above (see 2.5. and 2.6. for details).

3. Results

3.1. *CD133 and nestin detection in the rhabdomyosarcoma tumor tissue*

The results of nestin and CD133 expression in rhabdomyosarcomas by immunohistochemical (IHC) and immunofluorescence (IF) detection are summarized in Table 2.

Table 2

Immunohistochemical and immunofluorescence analysis of CD133 and nestin expression in rhabdomyosarcomas

Tumor sample	Tumor type	IF CD133	IHC CD133			IF Nestin	IHC Nestin		
			% TC	IR TC	IR EC		% TC	IR TC	IR EC
1	A	+	±	+++	+++	+++	+++	+	+
2	A	+	±	+++	++	+++	++	+	++
3	E	+	±	+	++	+	++	+	+
4	E	+	+	+	++	+	++	++	++
5	E	+	±	++	+++	++	+++	+	±
6	A	+	±	+++	+++	+++	+++	+	+
7a		+	±	++	+++	++	+++	++	±
7b		+	±	++	+++	++	+++	++	++
	A								
7c		+	±	+++	+++	+++	+++	+	+
7d		+	±	++	+++	++	+++	+	+

Notes: Expression of CD133 and nestin was examined on formaline-fixed, paraffin embedded tissue samples of rhabdomyosarcomas using both immunofluorescence (IF) and immunohistochemistry (IHC). Evaluation of IF: + (sporadically positive TC), ++ (dispersedly positive TC) and +++ (abundant positive TC). Evaluation of IHC: % TC, percentage of nestin-positive or CD133-positive tumor cells (±, <2%; +, 2–10%; ++, 11–50%; +++, 51–100%). IR TC, intensity of immunostaining (immunoreactivity) in tumor cells (±, very weak; +, weak; ++, medium; +++, strong). IR EC, intensity of immunostaining (immunoreactivity) in endothelial cells (±, very weak; +, weak; ++, medium; +++, strong). Tumor type: A, rhabdomyosarcoma, alveolar type; E, rhabdomyosarcoma, embryonal type.
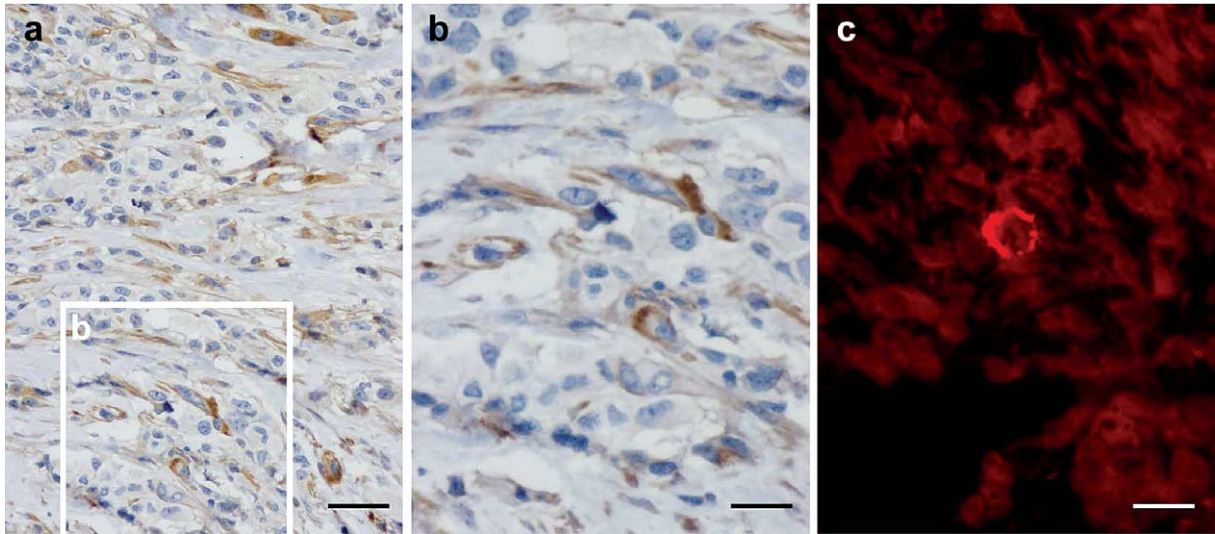
Fig. 1. Immunohistochemical and immunofluorescence analysis of CD133 expression in rhabdomyosarcomas tissues. Both IHC (a, b) and IF (c) revealed membranous CD133 positivity in only small number of tumor cells. Nonspecific cytoplasmic positivity was revealed in a significant proportion of tumor cells (a, b). Immunohistochemistry with Gill's hematoxylin counterstain (a, b); indirect immunofluorescence using TRITC-labeled secondary antibody (c). Bars, 100 μm (a), 50 μm (b), 50 μm (c).

In all examined cases, IF detection of membranous CD133 positivity was revealed in only a few tumor cells dispersed throughout the tumor tissues (Fig. 1c). Both CD133 IHC (Fig. 1b) and IF revealed not only membranous positivity in sporadic tumor cells, but also a nonspecific cytoplasmic positivity in a variable proportion of tumor cells (Fig. 1a).

Nestin expression was identified using both IHC and IF in all examined tumor samples (Fig. 2). The intensity of cytoplasmic IHC staining varied from strong (Fig. 2a) to weak (Fig. 2b). Similarly, the frequency of positive tumor cells revealed both by IHC and IF ranged from a strong, diffuse positivity (Fig. 2a and c) to a sporadic, medium to weak cytoplasmic nestin immunostaining in a subset of tumor cells (Fig. 2b and d).

3.2. Expression of CD133 and nestin in rhabdomyosarcoma cell lines

CD133 was observed in the form of a clear, membranous signal in all five newly derived rhabdomyosarcoma cell lines using indirect immunofluorescence (Table 3, Fig. 3). However, the percentage and the intensity of immunostaining (immunoreactivity) of CD133+ cells varied among individual cell lines (Table 3, Fig. 3c and d). The presence of CD133 was

subsequently verified using immunoblotting, and a 75-kDa band specific for CD133 was detected in all five cell lines examined (Fig. 4a).

Furthermore, using the NSTS-11 cell line, we experimentally determined that CD133 expression in cell populations seeded at the same concentrations increased over the course of a six-day cultivation (Fig. 5). Using a fluorescence microscope, we observed an increase of CD133+ fluorescence intensity in individual cells (Fig. 5a). The same results were also achieved by immunoblotting (Fig. 5b). Using flow cytometry, approximately a 193 percent increase in CD133 fluorescence intensity (FI) was noted from day 2 to day 6 in the cell populations (Fig. 5c).

Similar to CD133, nestin was observed in all examined cell lines, and both the percentage and the intensity of immunostaining of Nes+ cells varied among individual cell lines (Table 3, Fig. 3). Using immunoblotting, we confirmed that nestin is present in all five cell lines, and the specific bands detected were 300 kDa, 270 kDa and 100 kDa (Fig. 4b). Nevertheless, Nes+ cells only represent minor subpopulations, and the level of immunostaining was lower, compared to CD133+ cells (Table 3). Additionally, all Nes+ cells expressed CD133, but not all CD133+ cells expressed nestin (Fig. 3c and d). In contrast to the changes in CD133 expression mentioned above, expression of
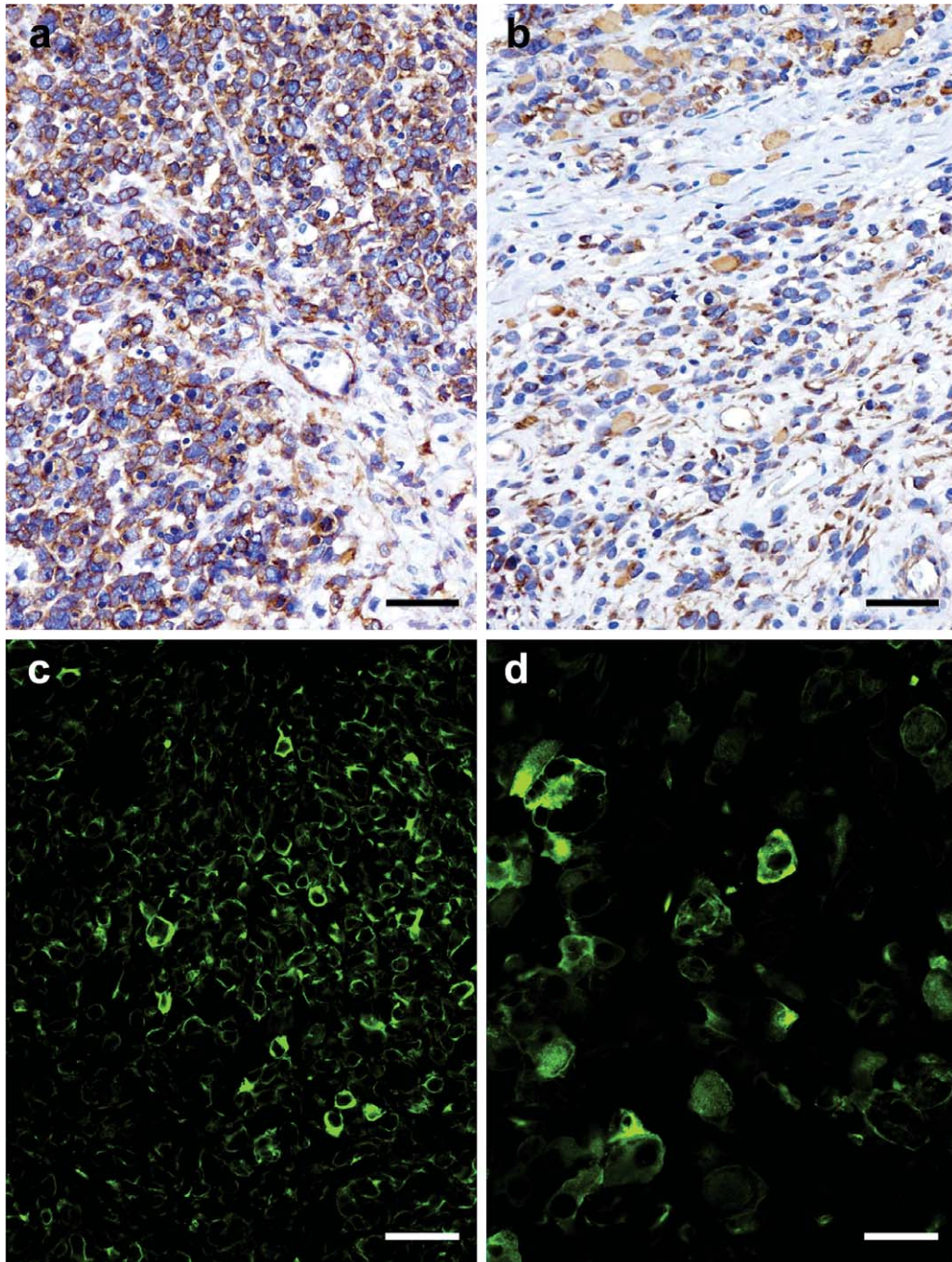
Fig. 2. Immunohistochemical and immunofluorescence analysis of nestin expression in rhabdomyosarcomas tissues. Strong, diffuse cytoplasmic positivity in the majority of tumor cells with an internal positive control of Nes+ endothelial cells; sample 8 (a). Medium cytoplasmic nestin immunostaining in a subset of dispersed tumor cells; sample 7 (b). Nestin expression in a significant proportion of tumor cells; sample 8 (c). Nestin expression in individual tumor cells; sample 4 (d). Immunohistochemistry with Gill's hematoxylin counterstain (a, b); indirect immunofluorescence using FITC-labeled secondary antibody (c, d). Bars, 100 μm (a, b, c), 50 μm (d).

Table 3

Expression of CD133 and nestin in the rhabdomyosarcoma cell lines

Cell line	Tumor type	CD133		Nestin	
		% TC	IR TC	% TC	IR TC
NSTS-08	A	+++	++	+	+
NSTS-09	A	++(+)	+++	+(+)	++
NSTS-10	A	+++	++	+(+)	++
NSTS-11	E	++	++/+++	+(+)	+
NSTS-12	E	+++	++/+++	(+)	+

Notes: Expression of CD133 and nestin in cell lines was examined using indirect immunofluorescence method. % TC, percentage of CD133/nestin positive tumor cells: (+), ∼1%; +, 1–10%; +(+), ∼10%; ++, 10–50%; ++(+), ∼50%; +++, >50%. IR TC, intensity of immunostaining (immunoreactivity) in tumor cells: +, weak; ++, medium; +++, strong. Tumor type: A, rhabdomyosarcoma, alveolar type; E, rhabdomyosarcoma, embryonal type.

nestin in cell populations was not altered during the cultivation.

3.3. Detection of CD133 and nestin in different samples from the same patient

As mentioned in Table 1, four FFPE tissue samples and two derived cell lines were obtained from the same patient suffering from rhabdomyosarcoma during the progression of the disease. This situation gave us the unique opportunity to analyze possible changes in CD133 and nestin expression in tumor tissue of the same patient in relation to the clinical course of the disease and to the applied therapy.

A 21-year-old woman was diagnosed with alveolar rhabdomyosarcoma of the left forearm and regional axillary lymph nodes, IRS stage III (tumor sample No. 7a, NSTS-08 cell line). She was treated according to protocol "EpSSG RMS 2005" very high risk arm with systemic chemotherapy of ifosfamide, vincristine, actinomycin D, and doxorubicin. After three initial courses, the patient was re-evaluated by PET and MRI imaging and determined to have a stable disease response. The tumor was inoperable without mutilating surgery, but amputation was rejected by the patient. Locoregional marginal surgery was performed, and she achieved 1st complete remission (tumor sample No. 7b, NSTS-10 cell line). Despite a second line of chemotherapy with irinotecan and vincristine, radiotherapy and metronomic antiangiogenic therapy, she relapsed in the regional lymph nodes on her shoulder (tumor sample No. 7c); her event-free survival was 13 months. Salvage chemotherapy with topote-

can and carboplatin was administered, but again, stable disease was found upon imaging. Following resection (tumor sample No. 7d) and radiotherapy, she achieved a 2nd complete remission. Several months later, she was diagnosed with a 3rd locoregional relapse on her shoulder; her event-free survival was 7 months. After a discussion with the patient, a dendritic cell vaccine against PAX3/FKHR protein was prepared. Meanwhile, concomitant chemotherapy with irinotecan, vincristine, and temodal, and radiotherapy were administered. Amputation was not accepted by the patient, despite a poor prognosis for survival. Unfortunately, the patient was diagnosed with metastatic relapse in the bones and bone marrow nine months later. As an experimental approach, a dendritic cell vaccine was applied together with palliative radiotherapy to a pathologic fracture of the vertebra. Currently, the experimental treatment with vincristine, cyclophosphamide, bevacizumab, sirolimus and valproate was administered. The overall survival of this patient is 39 months, and her prognosis remains very poor; such patients usually survive no more than three years after diagnosis.

Analysis of CD133 and nestin expression in all four tumor samples taken from this patient at various stages of the disease (see above) showed a sporadic occurrence of CD133+ cells with relatively strong immunoreactivity and a high proportion of Nes+ cells with medium to weak immunoreactivity. The frequency both of CD133+ and Nes+ cells did not change significantly during the course of the disease (Table 2).

The cell lines derived from the primary tumor (NSTS-08 cell line) and from the tumor tissue after the first chemotherapy treatment (NSTS-10 cell line) also showed the very same frequency of CD133+ and/or Nes+ cells; and the immunoreactivity for both of these markers was stable in both of these cell lines (Table 3).

3.4. Expression of stem cell markers in rhabdomyosarcoma cell lines

To confirm the presence of cells with stem cell related markers in rhabdomyosarcoma cell lines, we employed RT-PCR for detection of Oct3/4 (POU5F1) and nucleostemin (GNL3) that are considered to be markers of the embryonic stem cells. All five cell lines were identified as positive for both of these markers (Fig. 6); however, their expression partly differed among cell lines: a strong expression of Oct3/4 was
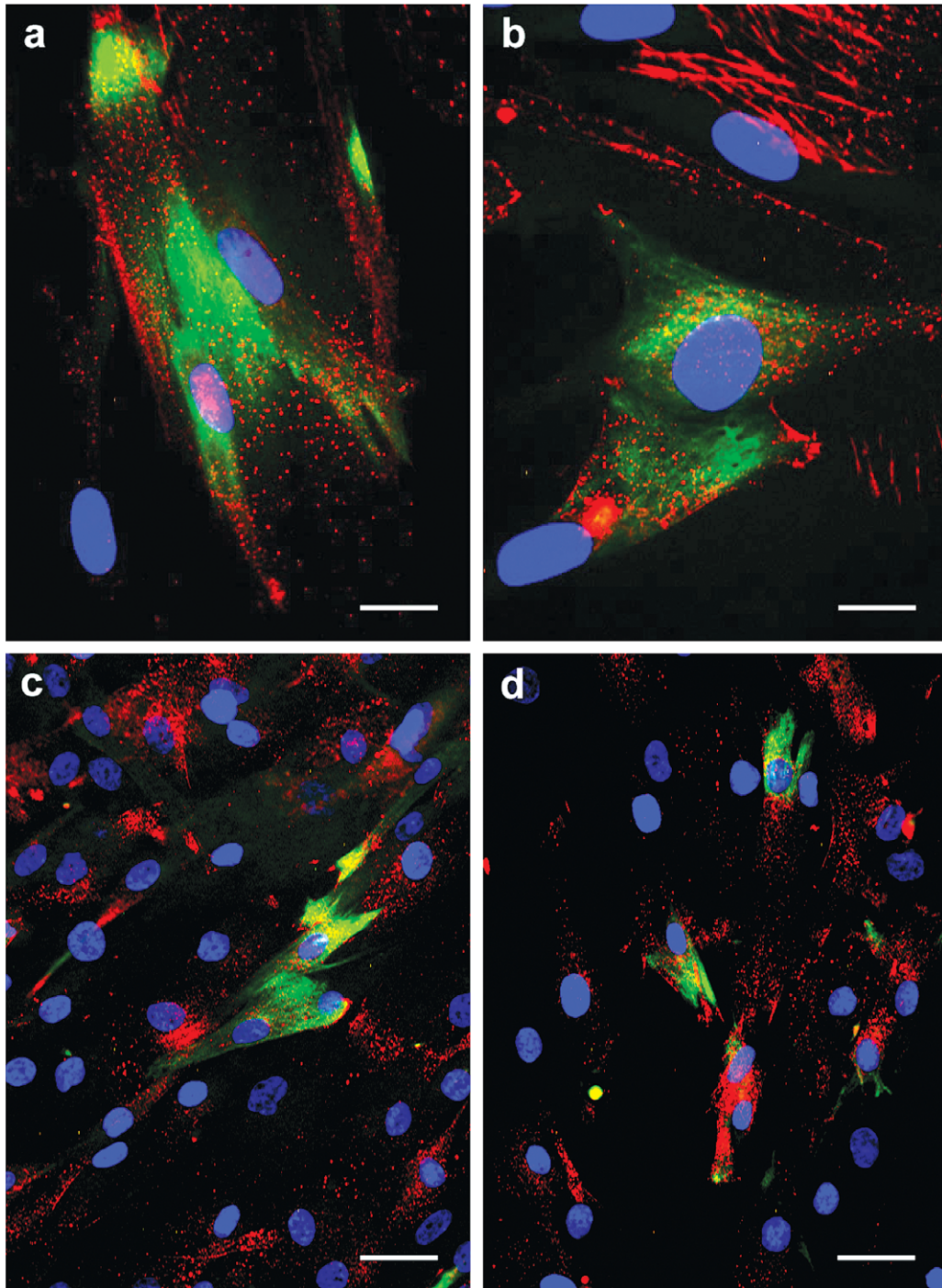
Fig. 3. Expression of CD133 and nestin in rhabdomyosarcoma cell lines. Representative double labeling for CD133 and nestin in NSTS-9 (a, b) and NSTS-8 (c, d) rhabdomyosarcoma cell lines. CD133 showed predominantly membranous positivity, visible as a dotted CD133 signal (red) on the cell surface (a-d). Invaginations of plasma membrane accumulating CD133 signals (red) led to the stripped pattern in a small subset of cells (b). CD133 (red) and nestin (green) stained by indirect immunofluorescence using TRITC-labeled secondary antibody and FITC-labeled secondary antibody, respectively; counterstaining with DAPI. Bars, 25 μm (a, b), 50 μm (c, d).
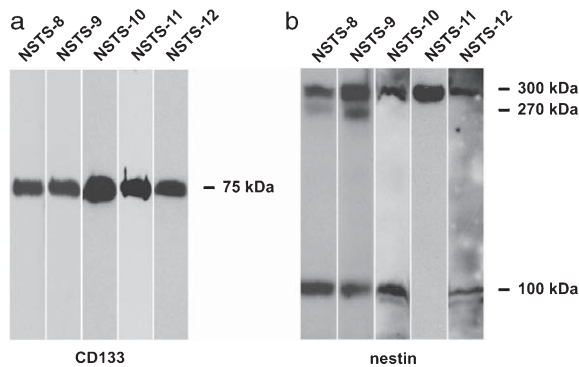
Fig. 4. Immunoblot analysis of the CD133 and nestin expression in rhabdomyosarcoma cell lines. Analysis of the CD133 expression in all five rhabdomyosarcoma cell lines (a). Analysis of the nestin expression in all five rhabdomyosarcoma cell lines (b).

identified in NSTS-8, NSTS-9, and NSTS-12 cell lines, a medium in NSTS-10 and a low expression in NSTS-11, while a medium expression of nucleostemin was detected in all cell lines with exception of NSTS-10 that showed only low level of nucleostemin expression (Fig. 6).

3.5. Functional assays using NSTS-11 cells

To confirm the presence of cells with cancer stem cell phenotype in our cell lines, we performed preliminary functional assays on NSTS-11 cell line. Clonogenicity *in vitro* assay showed that 5 to 10 % of isolated cells were able under standard *in vitro* conditions to form colonies containing more than 50 cells (Fig.7).

Furthermore, the tumorigenicity *in vivo* assay clearly confirmed the ability of NSTS-11 cells to originate xenograft tumors in NOD/SCID mice (Fig. 8). All three mice injected with NSTS-11 cell suspensions developed subcutaneous tumors in the same positions (Fig. 8a-c) within 12 weeks after injection. The diameter of all three tumors was about 10 mm (Fig. 8 d-f). Histological examination of all these xenograft tumors showed neoplastic highly mitotically active proliferation of undifferentiated dominantly spindle-shaped cells admixed with number of round, strap- or tadpole-shaped eosinophilic rhabdomyoblasts in a partially myxoid stroma (Fig. 8g-i). Moreover, the cross-striation of several cells has been displayed in all examined tumor samples. Histopathological findings correlate with the diagnosis of embryonal rhabdomyosarcoma. Myogenic differentiation was

additionally proved immunohistochemically in all three xenograft tumors (Table 4).

4. Discussion

The focus of our study was on the detection of CD133 and nestin in rhabdomyosarcoma cells. Ten samples of rhabdomyosarcoma tumor tissue and five cell lines derived from these tumors were examined using immunodetection methods; RT-PCR and functional assays were also employed to analyze the cell lines. Expression of both CD133 and nestin was microscopically determined in all tissue samples and cell lines; in the cell lines, these finding were confirmed by immunoblotting. Cells with distinct membranous positivity for CD133 occurred only sporadically in tumor tissues, although the proportion of Nes+ cells was markedly higher in the same tissues. In contrast, all five rhabdomyosarcoma cell lines showed an increased frequency of CD133+ cells, only some of which were concurrently Nes+. Above all, our research provides the first evidence of CD133 expression in rhabdomyosarcomas.

CD133 glycoprotein is considered to be a marker of the CSC phenotype in many kinds of tumors, usually in combination with other cell surface or intracellular molecules; for example: with nestin in CNS tumors [9, 24, 33, 34, 47], with CD44 in hepatocellular carcinomas [20, 48] and in colon carcinomas [15], with CD44 and $\alpha_1\beta_2^{hi}$ in prostate carcinomas [4], and with ABCG2 in pancreatic adenocarcinomas [25] and in osteosarcomas [10]. Nevertheless, expression of CD133 alone was also reported as a CSC phenotype in colon carcinomas [28], in non-small-cell lung carcinomas [2, 38], in ovarian carcinomas [8] and in endometrial carcinomas [30].

The detection of cells showing membranous positivity for CD133 that were only sporadically dispersed in rhabdomyosarcoma tumor tissues suggests that these cells may act as CSCs/TICs in this tumor type. In cell lines derived from the same tumors, we noted a markedly higher proportion of CD133+ cells; this difference may be explained by clonal selection for this phenotype under *in vitro* conditions. Since our results are the first evidence of CD133 expression in rhabdomyosarcoma cells, we verified these findings by immunoblotting cell lysates from five rhabdomyosarcoma cell lines examined in this study. Immunoblot results undoubtedly showed the CD133 expression;
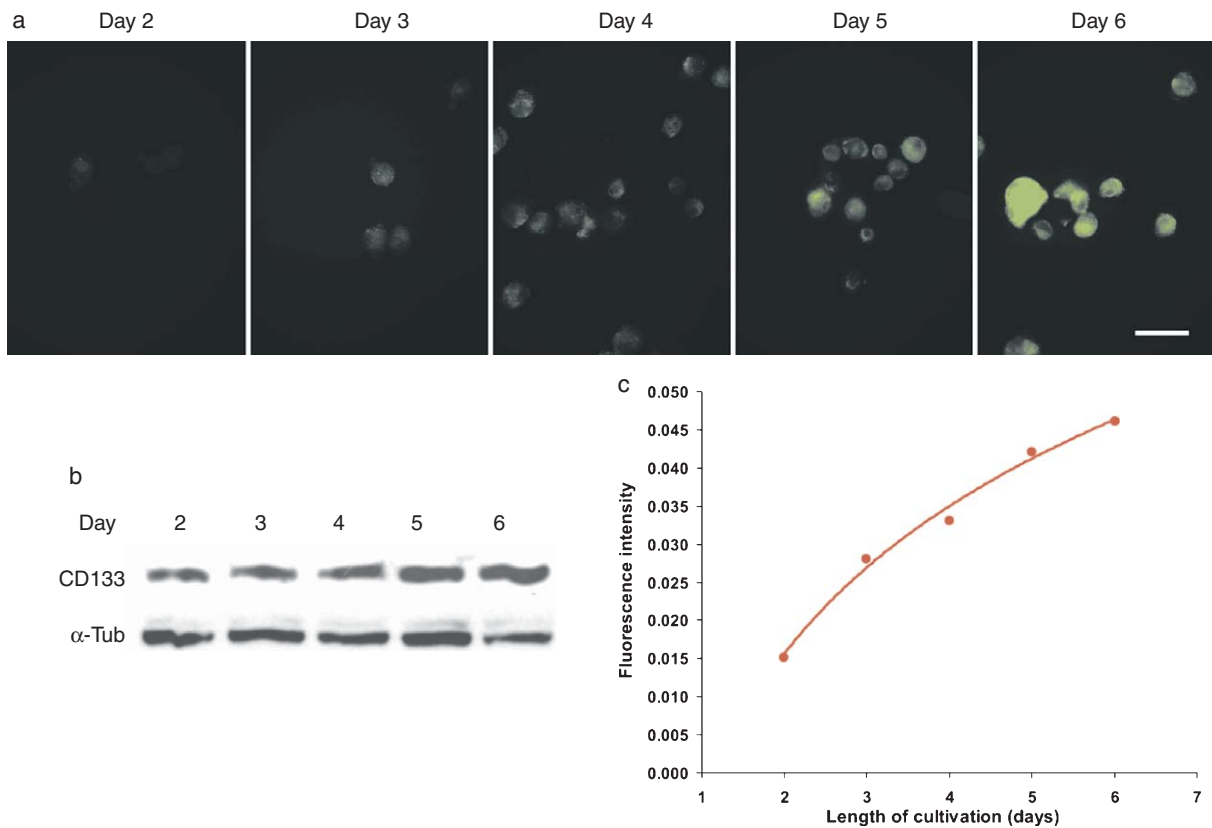
Fig. 5. CD133 expression changes in the rhabdomyosarcoma cell line NSTS-11 during a six-day cultivation. Cell suspensions were stained against CD133 (green) by indirect immunofluorescence using a FITC-labeled secondary antibody and were simultaneously analyzed using a fluorescence microscope; bar 50 μm (a) and by flow-cytometry (c). Fluorescence intensity (FI) is calculated as a quotient of difference; FITC-A log_{CD133} median fluorescence intensity (MFI) with FITC-A log_{Iso} MFI, and FSC-A where: FITC-A log_{CD133} is calculated as the mean ($n = 2$) of medians FITC-A log in samples immunostained with rabbit polyclonal anti-CD133 primary antibody, FITC-A log_{Iso} is calculated as a mean ($n = 2$) of medians FITC-A log in samples immunostained with rabbit polyclonal isotype control, FSC-A is calculated as a mean ($n = 4$) of medians FSC-A above mentioned all samples. FI = (FITC-A log_{CD133} – FITC-A log_{Iso}) / FSC-A. Immunoblot analysis of the CD133 expression changes during a six-day cultivation (b). Alpha-tubulin (α-Tub) served as a loading control.

a specific 75-kDa band was detected in all cell lines, suggesting the presence of a truncated form of CD133 that was described by two independent studies [26, 41].

During the *in vitro* experiments, we also noted increased fluorescence in individual CD133+ cells in relation to a prolonged cultivation time. For this reason, we measured the cell populations seeded at the same concentrations and at the same time. By flow cytometry, we confirmed a substantial increase in fluorescence of the whole cell population during a six-day cultivation; non-specific fluorescence and the average size of individual cells was taken into account in this experiment. In parallel, we used a fluorescence microscope to confirm the increase of CD133 labeling in individ-
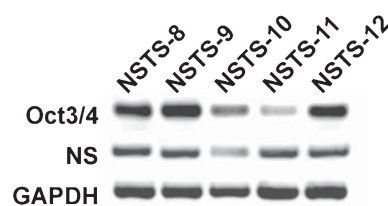

Fig. 6. RT-PCR analysis of stemness markers in rhabdomyosarcoma cell lines. Expression of Oct3/4 and nucleostemin was analyzed in all five of these cell lines; GAPDH served as a control.

ual cells. Moreover, these microscopic observations suggest not only membranous, but also cytoplasmic localization of CD133 molecules. These findings are in agreement with another study on osteosarcoma
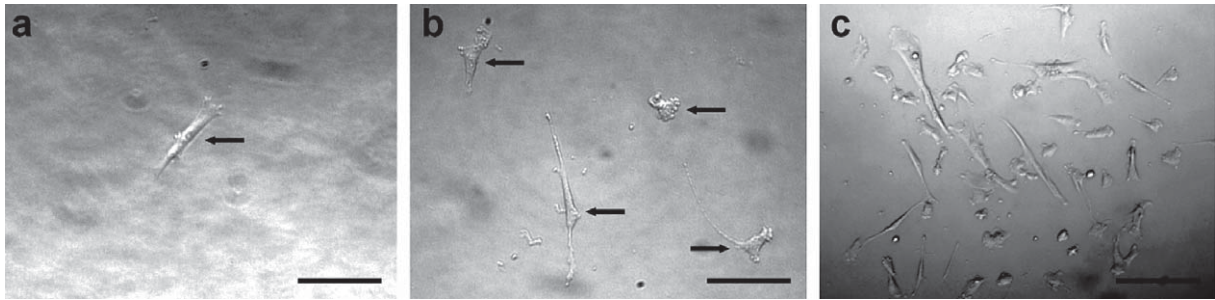
Fig. 7. Clonogenicity assay *in vitro* using NSTS-11 cell line. During two weeks of cultivation, single isolated cells (7a) were able to proliferate (7b) and to form colonies containing more than 50 cells (7c). Bars, 100 μm (a, b), 200 μm (c).
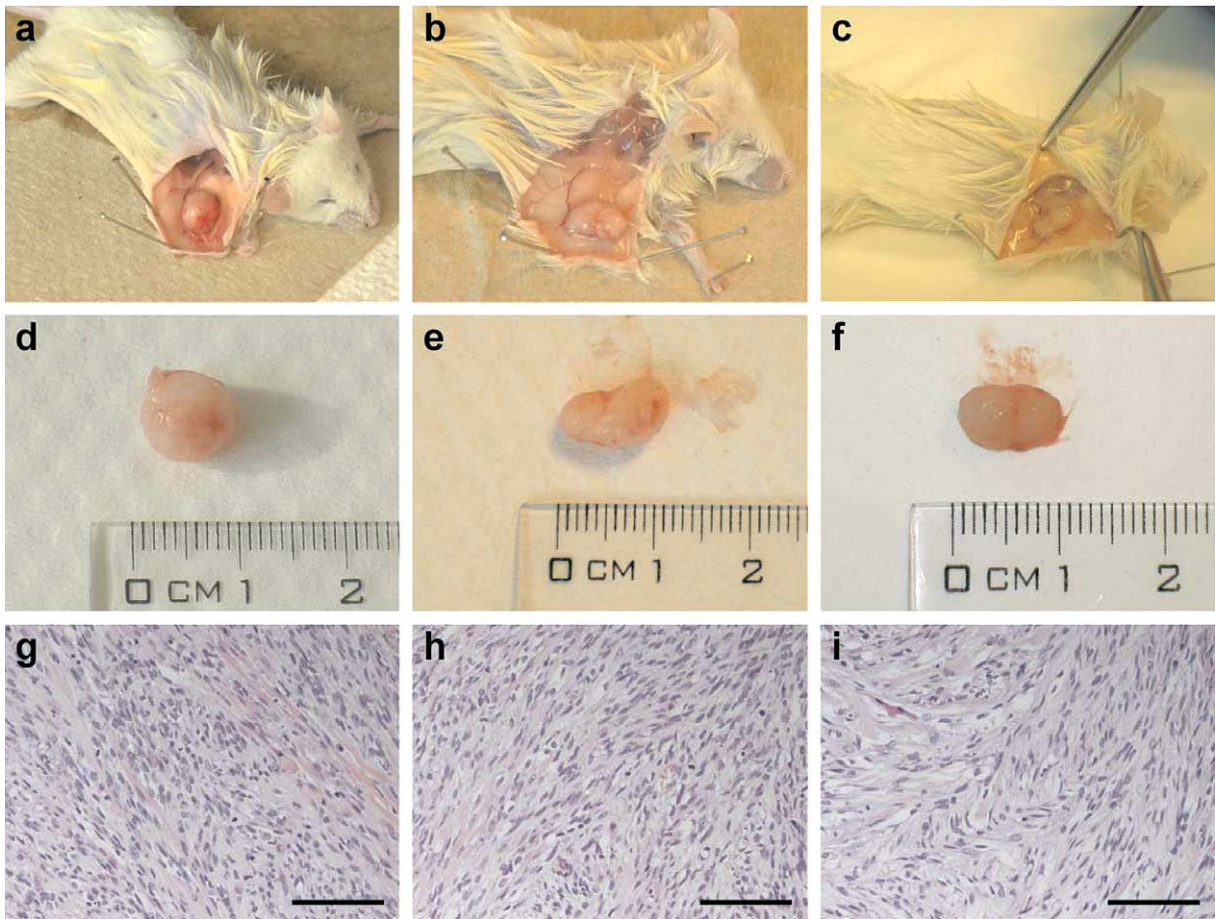

Fig. 8. Tumorigenicity *in vivo* assay using NSTS-11 cell line. Subcutaneous xenograft tumors in NOD/SCID mice at 81–84 days after injection of NSTS-11 cells (8a-c). Size of all three tumors was about 10 mm in diameter (8d-f). Histological examination of these tumors showed a pattern corresponding to the diagnosis of embryonal rhabdomyosarcoma; bars, 200 μm (8g-i).

cells, in which the deposition of CD133 into cytoplasmic vesicles was visualized by confocal microscopy [39].

Based on our previous study of osteosarcoma cell lines, in which the co-expression of CD133 and nestin was described in sarcomas for the first time [42], we

Table 4
Immunohistochemical analysis of NSTS-11 xenograft tumors in mice

Tumor	Myoglobin	Desmin	Muscle actin	Nestin	CD133
M3A138	++	++	++	+++	±
M3B138	+	++	++	+++	±
M3C138	+	++	++	+++	±

Notes: Expression of myogenic differentiation markers (myoglobin, desmin, muscle actin), CD133 and nestin was examined on formalin-fixed, paraffin embedded tissue samples of xenograft tumors using immunohistochemistry (IHC). Evaluation of IHC: percentage of positive tumor cells (±, <2%; +, 2–10%; ++, 11–50%; +++, 51–100%).

also examined the rhabdomyosarcoma samples and derived cell lines for the detection of this intermediate filament protein. Although nestin expression was reported in many tumor types including sarcomas [18], and nestin was originally described in rhabdomyosarcoma cells twelve years ago [17], there is no published work describing a possible co-expression of nestin and CD133 in rhabdomyosarcomas.

Our microscopy results confirmed that nestin is expressed in all our rhabdomyosarcoma samples as well as in all the derived rhabdomyosarcoma cell lines. Immunoblotting was employed to verify nestin expression in the examined cell lines; 300 kDa, 270 kDa and 100 kDa specific bands were detected in all of them. The 300 kDa and 270 kDa bands correspond to post-translationally-modified forms of nestin; the 100 kDa band is probably nestin that has been cleaved by lysate cryoconservation, as reported by the antibody manufacturer.

More interestingly, the expression pattern of nestin was inversely correlated to that of CD133; we detected a relatively high proportion of Nes+ cells in tumor tissues together with a sporadic occurrence of CD133+ cells, whereas CD133+ cells predominated the cell populations of all examined cell lines, including Nes+ cells, under *in vitro* conditions. Furthermore, all Nes+ cells in the cultures showed positivity for CD133 simultaneously; i.e. their phenotype was CD133+/Nes+, while CD133-/Nes+ cells were never been detected in the cell cultures.

Taken together, the sporadic occurrence of CD133+ cells (with distinct membranous positivity) in tumor tissues and a minor proportion of CD133+/Nes+ in cell cultures suggest that these cancer cells with expression of stem cell related markers may represent a CSCs/TICs phenotype in rhabdomyosarcomas. Posi-

tivity of all five examined cell lines for Oct3/4 and nucleostemin that are required for maintaining stem cell state [10] is in accordance with this idea. The hypothesis on CSCs/TICs phenotype is also partially supported by CD133 and nestin detection in different tumor samples taken from the same patient at various stages of the disease. The relatively stable frequency of CD133+ cells in tumor samples during cancer progression in this patient may indicate a resistance of these cells to the applied chemotherapy. Similarly, the presence of these cells in sample No.3 that was taken after neoadjuvant chemotherapy also suggests their CSCs/TICs phenotype.

Moreover, results of preliminary functional assays using our rhabdomyosarcoma cell lines also suggest the presence of a CSCs/TICs fraction in these cell lines. Nevertheless, further detailed functional studies of CD133+/Nes+ rhabdomyosarcoma cells are required to confirm their possible CSCs/TICs phenotype.

To summarize, the most important result of our study is the first evidence of CD133 expression in rhabdomyosarcomas and the corresponding rhabdomyosarcoma cell lines. Using immunodetection methods, we confirmed the expression of CD133 and nestin in all examined tumor samples and in all cell lines derived from them. The low incidence of CD133+ cells in tumor tissues and of CD133+/Nes+ cells in cultures as well as results of preliminary functional assays suggest a possible stem-like phenotype of cells showing co-expression of these markers. We also showed increasing expression of CD133 in rhabdomyosarcoma cells and probable accumulation of this glycoprotein in cytoplasmic vesicles during cultivation. Our results represent the first important step toward the forthcoming studies on CSCs/TICs detection in rhabdomyosarcomas.

References

[1] F.G. Barr, J. Chatten, C.M. D'Cruz, A.E. Wilson, L.E. Nauta, L.M. Nycum, J.A. Biegel and R.B. Womer, Molecular assays for chromosomal translocations in the diagnosis of pediatric soft tissue sarcomas, *JAMA* **273** (1995), 553–557.

[2] G. Bertolini, L. Roz, P. Perego, M. Tortoreto, E. Fontanella, L. Gatti, G. Pratesi, A. Fabbri, F. Andriani, S. Tinelli, E. Roz, R. Caserini, T. Camerini, L. Mariani, D. Delia, E. Calabrò, U. Pastorino and G. Sozzi, Highly tumorigenic lung cancer CD133+ cells display stem-like features and are spared by cisplatin treatment, *Proc Natl Acad Sci USA* **106** (2009), 16281–16286.

[3] S. Bruno, B. Bussolati, C. Grange, F. Collino, M.E. Graziano, U. Ferrando and G. Camussi, CD133+ renal progenitor cells contribute to tumor angiogenesis, *Am J Pathol* **169** (2006), 2223–2235.

[4] A.T. Collins, P.A. Berry, C. Hyde, M.J. Stower and N.J. Maitland, Prospective identification of tumorigenic prostate cancer stem cells, *Cancer Res* **65** (2005), 10946–10951.

[5] D. Corbeil, K. Röper, C.A. Fargeas, A. Joester and W.B. Huttner, Prominin: A story of cholesterol, plasma membrane protrusions and human pathology, *Traffic* **2** (2001), 82–91.

[6] D. Corbeil, K. Röper, A. Hellwig, M. Tavian, S. Miraglia, S.M. Watt, P.J. Simmons, B. Peault, D.W. Buck and W.B. Huttner, The human AC133 hematopoietic stem cell antigen is also expressed in epithelial cells and targeted to plasma membrane protrusions, *J Biol Chem* **275** (2000), 5512–5520.

[7] C.V. Cox, P. Diamanti, R.S. Evely, P.R. Kearns and A. Blair, Expression of CD133 on leukemia-initiating cells in childhood ALL, *Blood* **113** (2009), 3287–3296.

[8] M.D. Curley, V.A. Therrien, C.L. Cummings, P.A. Sergent, C.R. Koulouris, A.M. Friel, D.J. Roberts, M.V. Seiden, D.T. Scadden, B.R. Rueda and R. Foster, CD133 expression defines a tumor initiating cell population in primary human ovarian cancer, *Stem Cells* **27** (2009), 2875–2883.

[9] P. Dell'Albani, Stem cell markers in gliomas, *Neurochem Res* **33** (2008), 2407–2415.

[10] R. Di Fiore, A. Santulli, R.D. Ferrante, M. Giuliano, A. De Blasio, C. Messina, G. Pirozzi, V. Tirino, G. Tesoriere and R. Vento, Identification and expansion of human osteosarcoma-cancer-stem cells by long-term 3-aminobenzamide treatment, *J Cell Physiol* **219** (2009), 301–313.

[11] A. Eramo, F. Lotti, G. Sette, E. Pilozzi, M. Biffoni, A. Di Virgilio, C. Conticello, L. Ruco, C. Peschle and R. De Maria, Identification and expansion of the tumorigenic lung cancer stem cell population, *Cell Death Differ* **15** (2008), 504–514.

[12] C.A. Fargeas, W.B. Huttner and D. Corbeil, Nomenclature of prominin-1 (CD133) splice variants - an update, *Tissue Antigens* **69** (2007), 602–606.

[13] C.A. Fargeas, A. Joester, E. Missol-Kolka, A. Hellwig, W.B. Huttner and D. Corbeil, Identification of novel Prominin-1/CD133 splice variants with alternative C-termini and their expression in epididymis and testis, *J Cell Sci* **117** (2004), 4301–4311.

[14] G. Ferrandina, G. Bonanno, L. Pierelli, A. Perillo, A. Procoli, A. Mariotti, M. Corallo, E. Martinelli, S. Rutella, A. Paglia, G. Zannoni, S. Mancuso and G. Scambia, Expression of CD133-1 and CD133-2 in ovarian cancer, *Int J Gynecol Cancer* **18** (2008), 506–514.

[15] N. Haraguchi, M. Ohkuma, H. Sakashita, S. Matsuzaki, F. Tanaka, K. Mimori, Y. Kamohara, H. Inoue and M. Mori, CD133+ CD44+ population efficiently enriches colon cancer initiating cells, *Ann Surg Oncol* **15** (2008), 2927–2933.

[16] H. Immervoll, D. Hoem, P.O. Sakariassen, O.J. Steffensen and A. Molven, Expression of the "stem cell marker" CD133 in pancreas and pancreatic ductal adenocarcinomas, *BMC Cancer* **8** (2008), 48.

[17] M. Kobayashi, G. Sjöberg, S. Söderhäll, U. Lendahl, B. Sandstedt and T. Sejersen, Pediatric rhabdomyosarcomas express the intermediate filament nestin, *Pediatr Res* **43** (1998), 386–392.

[18] O. Krupkova, T. Loja, I. Zambo and R. Veselska, Nestin expression in human tumors and tumor cell lines, *Neoplasma* **57** (2010), 291–298.

[19] G. Liu, X. Yuan, Z. Zeng, P. Tunici, H. Ng, I.R. Abdulkadir, L. Lu, D. Irvin, K.L. Black and J.S. Yu, Analysis of gene expression and chemoresistance of CD133+ cancer stem cells in glioblastoma, *Mol Cancer* **5** (2006), 67.

[20] S. Ma, K.W. Chan, L. Hu, T.K. Lee, J.Y. Wo, I.O. Ng, B.J. Zheng and X.Y. Guan, Identification and characterization of tumorigenic liver cancer stem/progenitor cells, *Gastroenterology* **132** (2007), 2542–2556.

[21] S. Miraglia, W. Godfrey, A.H. Yin, K. Atkins, R. Warnke, J.T. Holden, R.A. Bray, E.K. Waller and D.W. Buck, A novel five-transmembrane hematopoietic stem cell antigen: Isolation, characterization, and molecular cloning, *Blood* **90** (1997), 5013–5021.

[22] E. Monzani, F. Facchetti, E. Galmozzi, E. Corsini, A. Benetti, C. Cavazzin, A. Gritti, A. Piccinini, D. Porro, M. Santinami, G. Invernici, E. Parati, G. Alessandri and C.A. La Porta, Melanoma contains CD133 and ABCG2 positive cells with enhanced tumourigenic potential, *Eur J Cancer* **43** (2007), 935–936.

[23] Y.R. Na, S.H. Seok, D.J. Kim, J.H. Han, T.H. Kim, H. Jung and J.H. Park, Zebrafish embryo extracts promote sphere-forming abilities of human melanoma cell line, *Cancer Sci* **100** (2009), 1429–1433.

[24] J. Neuzil, M. Stantic, R. Zobalova, J. Chladova, X. Wang, L. Prochazka, L. Dong, L. Andera and S.J. Ralph, Tumour-initiating cells vs. cancer 'stem' cells and CD133: What's in the name? *Biochem Biophys Res Commun* **355** (2007), 855–859.

[25] M. Olempska, P.A. Eisenach, O. Ammerpohl, H. Ungefroren, F. Fendrich and H. Kalthoff, Detection of tumor stem cell markers in pancreatic carcinoma cell lines, *Hepatobiliary Pancreat Dis Int* **6** (2007), 92–97.

[26] T.L. Osmond, K.W. Broadley and M.J. McConnell, Glioblastoma cells negative for the anti-CD133 antibody AC133 express a truncated variant of the CD133 protein, *Int J Mol Med* **25** (2010), 883–888.

[27] G.J. Pilkington, Cancer stem cells in the mammalian central nervous system, *Cell Prolif* **38** (2005), 423–433.

[28] L. Ricci-Vitiani, D.G. Lombardi, E. Pilozzi, M. Biffoni, M. Todaro, C. Peschle and R. De Maria, Identification and expansion of human colon cancer-initiating cells, *Nature* **445** (2007), 111–115.

[29] G.D. Richardson, C.N. Robson, S.H. Lang, D.E. Neal, N.J. Maitland and A.T. Collins, CD133 a novel marker for human prostatic epithelial stem cells, *J Cell Sci* **117** (2004), 3539–3545.

[30] S. Rutella, G. Bonanno, A. Procoli, A. Mariotti, M. Corallo, M.G. Prisco, A. Eramo, C. Napoletano, D. Gallo, A. Perillo, M. Nuti, L. Pierelli, U. Testa, G. Scambia and G. Ferrandina, Cells with characteristics of cancer stem/progenitor cells express the CD133 antigen in human endometrial tumors, *Clin Cancer Res* **15** (2009), 4299–4311.

[31] C. Sagrinati, G.S. Netti, B. Mazzinghi, E. Lazzeri, F. Liotta, F. Frosali, E. Ronconi, C. Meini, M. Gacci, R. Squecco, M. Carini, L. Gesualdo, F. Francini, E. Maggi, F. Annunziato, L. Lasagni, M. Serio, S. Romagnani and P. Romagnani, Isolation and characterization of multipotent progenitor cells from the Bowman's capsule of adult human kidneys, *J Am Soc Nephrol* **17** (2006), 2443–2456.

[32] S.V. Shmelkov, R. St Clair, D. Lyden and S. Rafii, AC133/ CD133/Prominin-1, *Int J Biochem Cell Biol* **37** (2005), 715–719.

[33] S.K. Singh, I.D. Clarke, M. Terasaki, V.E. Bonn, C. Hawkins, J. Squire and P.B. Dirks, Identification of a cancer stem cell in human brain tumors, *Cancer Res* **63** (2003), 5821–5828.

[34] S.K. Singh, C. Hawkins, I.D. Clarke, J.A. Squire, J. Bayani, T. Hide, R.M. Henkelman, M.D. Cusimano and P.B. Dirks, Identification of human brain tumour initiating cells, *Nature* **432** (2004), 396–401.

[35] A. Suetsugu, M. Nagaki, H. Aoki, T. Motohashi, T. Kunisada and H. Moriwaki, Characterization of CD133+ hepatocellular carcinoma cells as cancer stem/progenitor cells, *Biochem Biophys Res Commun* **351** (2006), 820–824.

[36] J. Terry and T. Nielsen, Expression of CD133 in synovial sarcoma, *Appl Immunohistochem Mol Morphol* **18** (2010), 159–165.

[37] B. Thomson, D. Hawkins, J. Felgenhauer and J.P. Radich, RT-PCR evaluation of peripheral blood, bone marrow and peripheral blood stem cells in children and adolescents undergoing VACIME chemotherapy for Ewing's sarcoma and alveolar rhabdomyosarcoma, *Bone Marrow Transplant* **24** (1999), 527–533.

[38] V. Tirino, R. Camerlingo, R. Franco, D. Malanga, A. La Rocca, G. Viglietto, G. Rocco and G. Pirozzi, The role of CD133 in the identification and characterisation of tumour-initiating cells in non-small-cell lung cancer, *Eur J Cardiothorac Surg* **36** (2009), 446–453.

[39] V. Tirino, V. Desiderio, R. d'Aquino, F. De Francesco, G. Pirozzi, A. Graziano, U. Galderisi, C. Cavaliere, A. De Rosa, G. Papaccio and A. Giordano, Detection and characterization of CD133+ cancer stem cells in human solid tumours, *PLoS One* **3** (2008), e3469.

[40] N. Uchida, D.W. Buck, D. He, M.J. Reitsma, M. Masek, T.V. Phan, A.S. Tsukamoto, F.H. Gage and I.L. Weissman, Direct isolation of human central nervous system stem cells, *Proc Natl Acad Sci USA* **97** (2000), 14720–14725.

[41] D.J. Vander Griend, W.L. Karthaus, S. Dalrymple, A. Meeker, A.M. DeMarzo and J.T. Isaacs, The role of CD133 in normal human prostate stem cells and malignant cancer-initiating cells, *Cancer Res* **68** (2008), 9703–9711.

[42] R. Veselska, M. Hermanova, T. Loja, P. Chlapek, I. Zambo, K. Vesely, K. Zitterbart and J. Sterba, Nestin expression in osteosarcomas and derivation of nestin/CD133 positive osteosarcoma cell lines, *BMC Cancer* **8** (2008), 300.

[43] R. Veselska, P. Kuglik, P. Cejpek, H. Svachova, J. Neradil, T. Loja and J. Relichova, Nestin expression in the cell lines derived from glioblastoma multiforme, *BMC Cancer* **6** (2006), 32.

[44] A. Weigmann, D. Corbeil, A. Hellwig and W.B. Huttner, Prominin, a novel microvillispecific polytopic membrane protein of the apical surface of epithelial cells, is targeted to plasmalemmal protrusions of non-epithelial cells, *Proc Natl Acad Sci USA* **94** (1997), 12425–12430.

[45] L. Yi, Z.H. Zhou, Y.F. Ping, J.H. Chen, X.H. Yao, H. Feng, J.Y. Lu, J.M. Wang and X.W. Bian, Isolation and characterization of stem cell-like precursor cells from primary human anaplastic oligoastrocytoma, *Mod Pathol* **20** (2007), 1061–1068.

[46] A.H. Yin, S. Miraglia, E.D. Zanjani, G. Almeida-Porada, M. Ogawa, A.G. Leary, J. Olweus, J. Kearney and D.W. Buck, AC133, a novel marker for human hematopoietic stem and progenitor cells, *Blood* **90** (1997), 5002–5012.

[47] M. Zhang, T. Song, L. Yang, R. Chen, L. Wu, Z. Yang and J. Fang, Nestin and CD133: Valuable stem cell-specific markers for determining clinical outcome of glioma patients, *J Exp Clin Cancer Res* **27** (2008), 85.

[48] Z. Zhu, X. Hao, M. Yan, M. Yao, C. Ge, J. Gu and J. Li, Cancer stem/progenitor cells are highly enriched in CD133+ CD44+ population in hepatocellular carcinoma, *Int J Cancer* **126** (2010), 2067–2078.